1-1-2011

Two dimensional rate gyro bias estimation for precise pitch and roll attitude determination utilizing a dual arc accelerometer array

William Scorse

Recommended Citation

Scorse, William, "Two dimensional rate gyro bias estimation for precise pitch and roll attitude determination utilizing a dual arc accelerometer array" (2011). Thesis. Rochester Institute of Technology. Accessed from

TWO DIMENSIONAL RATE GYRO BIAS ESTIMATION FOR PRECISE PITCH AND ROLL ATTITUDE DETERMINATION UTILIZING A DUAL ARC ACCELEROMETER ARRAY

By

WILLIAM T. SCORSE

Thesis submitted to the Faculty of the Department of Mechanical Engineering at
the Rochester Institute of Technology in partial fulfillment
of the requirements for the degree of

Master of Science
in
Mechanical Engineering

Approved by:

Dr. Agamemnon Crassidis -*Thesis Advisor*
Department of Mechanical Engineering ________________________

Dr. Tuhin Das
Department of Mechanical Engineering ________________________

Dr. Mark Kempski
Department of Mechanical Engineering ________________________

Dr. Jason Kolodziej
Department of Mechanical Engineering ________________________

Dr. Wayne Walter
Department of Mechanical Engineering ________________________

Dr. Edward Hensel
Department Head of Mechanical Engineering ________________________

Rochester, New York
January, 2011

Keywords: Attitude Estimation, Bias Estimation, Kalman Filtering, Rigid Body Dynamics, Euler Kinematics

PERMISSION TO REPRODUCE THESIS

TWO DIMENSIONAL RATE GYRO BIAS ESTIMATION FOR PRECISE PITCH AND ROLL ATTITUDE DETERMINATION UTILIZING A DUAL ARC ACCELEROMETER ARRAY

I, William T. Scorse, hereby grant permission to the Wallace Memorial Library of Rochester Institute of Technology to reproduce my thesis in the whole or part. Any reproduction will not be for commercial use or profit.

Date:______________________________ Signature:______________________________

January 2011

Abstract

In this thesis, a previously developed, novel one-dimensional attitude estimation device is expanded through the development and implementation of an innovative method for estimation of two-dimensional attitude making use of a unique low-cost, dual arc accelerometer array measuring longitudinal and transverse rotational rates in real-time. The device and method proposed is an expansion of a previously developed method for one-dimensional attitude determination and rate gyro bias estimation utilizing a one-dimensional accelerometer array. This new revolutionary device utilizes a dual arc accelerometer array and an algorithm for accurate and reliable two-dimensional attitude determination and rate gyro bias estimation in real-time. The method determines the local gravitational field vector from which attitude information can be resolved. Upon determining the location of the local gravitational field vector relative to two consecutive accelerometer sensors, the orientation of the device may then be estimated and the attitude determined. However, this measurement is discrete in nature; therefore, integrated rate gyro measurements are used to determine attitude information resulting in a continuous signal. However, attitude estimates and measurements produced by instantaneous rate sensors and gyroscope integration tend to drift over time due to drift and bias inherent to the rate gyro sensor. The integration of the acquired instantaneous rate signals amplify measurement errors leading to an undependable and imprecise estimate of the vehicles true attitude and orientation. A method for compensation of these errors is proposed in this work resulting in a highly accurate and continuous attitude estimate. For this thesis, simulations of the proposed method and device will be conducted with the inclusion of characteristic, real-world sensor noise and bias estimates produced from corrupted and biased sensors to analyze and assess the feasibility and validity of the proposed method and system configuration for two-dimensional attitude determination. The end goal of this work is to produce a precise and reliable longitudinal and transverse attitude estimation array capable of measuring rate senor and gyro bias online so as to produce highly accurate and reliable pitch and roll angle tracking in real-time while under subjection to simulated flight conditions and scenarios. While this thesis is an expansion of a previously developed device and method, it is a departure from past works in that a new, two-dimensional accelerometer array arc is utilized and additional rotational dimensions are being included in the simulated analysis.

Acknowledgments

I would like to thank the faculty and staff of the Mechanical Engineering department at the Rochester Institute of Technology for providing me with the guidance and assistance necessary to have a truly great educational experience. In particular, I would like to thank Dr. Agamemnon Crassidis for his tutelage, guidance, and faith in my abilities to grow and improve as an individual and engineer. I would like to thank Dr. Mark Kempski, Dr. Tuhin Das, Dr. Jason Kolodziej, and Dr. Wayne Walter for their patience and help donated during the course of my education at RIT. Finally, I would like to thank my family and friends for their support and constant encouragement during my years as a student at RIT.

Those who would attain to any marked degree of excellence in a chosen pursuit must work, and work hard for it, prince or peasant.

~ Bayard Taylor

The greatest results in life are usually attained by simple means and the exercise of ordinary qualities. These may for the most part be summed in these two: common-sense and perseverance.

~ Owen Feltham

Contents

List of Tables

List of Figures

Nomenclature

PARAMETERS

X, Y, Z : Primary, Secondary, and Tertiary Coordinate System Axes
i, j, k : Primary, Secondary, and Tertiary Unit Vector Directions
Ø, θ, ψ : Bank, Elevation, and Heading Euler Angles
p, q, r : Roll, Pitch, and Yaw Vehicle Angular Rates
u, v, w : Primary, Secondary, and Tertiary Body Velocities
F : Force Vector
W : Weight Vector
M : Moment Vector
V : Velocity Vector
m : Vehicle Mass
g : Acceleration due to gravity
$\vec{\omega}$: Vehicle Angular Rate Vector
$\overleftrightarrow{I}$: Inertia Tensor
σ : Turbulence Intensity
Θ : Euler Total Rotation Angle
L, M, N : Primary, Secondary, and Tertiary Scalar Moments
T : Transformation Matrix
I_{NxN} : N element by N element Identity Matrix
DCTM : Direct Cosine Transformation Matrix
$\boldsymbol{\Omega}$: Spatial Frequency
Q : Unit Quaternion – 4 by 1 Column Vector
q : Quaternion Vector
q_0 : Quaternion Scalar Element

SUPERSCRIPTS AND SUBSCRIPTS

^{T} : Transpose of Matrix or Vector
* : Quaternion Conjugate
vehicle : Relative to Vehicle Coordinate Frame
reference : Relative to Reference or Inertial Coordinate Frame
ref : Relative to Reference Frame
E : Earth-Fixed Coordinate Frame
EC : Earth-Centered Coordinate Frame
Earth-Body : Earth-Fixed Coordinate Frame to Body-Fixed Coordinate Frame
body : Body-Fixed Coordinate Frame
Body-Earth : Body-Fixed Coordinate Frame to Earth-Fixed Coordinate Frame
Earth : Earth-Fixed Coordinate Frame
i : Relating to *ith* Accelerometer of Accelerometer Array

Imp : Imposed Translational (Inertial) Loading due to Vehicle Maneuvers
Imposed : Imposed Translational (Inertial) Loading due to Vehicle Maneuvers
Man : Angular Displacement due to Vehicle Maneuvers
Maneuver : Angular Displacement due to Vehicle Maneuvers
Static : Static Condition of the Device Angular Displacement
Z, CG : Mounting at the center-of-gravity of the vehicle along the vehicle tertiary axis
CG : Center-of-Gravity
d : Device
$_{z,\,i}$: *ith* accelerometer measuring acceleration relative to the vehicle's tertiary axis

Mathematical Operators

$|x|$: Scalar or Vector Magnitude = $\sqrt{x_1^2 + \ldots + x_n^2}$
● : Dot Product
× : Cross Product or designation of Matrix rows and Columns
* : Multiplication
S_φ : Sine of φ
C_φ : Cosine of φ

Chapter 1

Introduction

1.1 Background

Accurate and reliable attitude estimation is critical for determining a vehicle's orientation within a multi-dimensional operating environment and for the execution of aircraft and vehicle maneuvers during vital operations requiring up to date attitude estimates in real-time. Traditionally, the attitude and orientation of an aircraft or vehicle can be described by three consecutive rotations characterized through the use of Euler angles for bank, elevation, and heading, where the aircraft's or vehicle's body orientation is related to a fixed frame of reference. For static or trim flight conditions, Euler angles may be measured and calculated directly because the motion of the vehicle is insignificant. However, during dynamic maneuvers, Euler angles may be calculated and determined from the instantaneous integration of the vehicle's body rotational rates that transform the inertial frame of reference fixed to the Earth, where a flat Earth assumption is assumed. For problems addressing aircraft dynamics and orientation, the flat Earth assumption where Earth is used as an inertial frame of reference is characteristically used. This is known as the Earth-fixed coordinate frame.

The measurement of motion relative to an aircraft's or vehicle's frame of reference is typically measured through the use of angular and translational rate sensors integrated with initial conditions relative the fixed, inertial frame of reference. This integration of sensor measurements relative to the fixed reference frame produces a measureable instantaneous vehicle displacement. Common sensors typically used to measure inertial quantities are accelerometers, inclinometers, magnetometers, and GPS. Rate gyroscopes are more commonly used for describing and measuring aircraft or vehicle motion through rotational rates. However, in real-world applications operating in various environments, the accurate measurement of vehicle movement and orientation has proven to be complicated due to the inherent sensor and rate gyro biases existing due to operational hardware or environmental noises and conditions. The integration of these bias effects over time for the determination of a vehicle's attitude estimate will result in large errors that deviate greatly from the vehicle's true orientation and displacement. This effect is commonly referred to as a drift effect. To accommodate for these drift effects from inherent sensor and rate gyro biases, magnetic field sensors or GPS receivers may be used to reduce and eliminate drift effects. Constraints limiting the use of such additional receivers and sensors are increased size, weight, and monetary costs which make the implementation of such additional measurement units and systems unreasonable for such applications as micro and unmanned air vehicles or robotic applications. To account for such limiting design constraints as size and weight, implementation of filtering techniques such as a Kalman filter has become common practice in the industrial world for online attitude estimation of the aircraft or vehicle. Assimilating both sensor measurements and an algorithm method to handle sensor biases enables a precise and dependable online solution for accurate determination of an aircraft's or vehicle's attitude and orientation in real-time.

This thesis expands upon a previously proposed device consisting of a one-dimensional accelerometer array fused with a rate gyro for estimating longitudinal pitching motion by developing a innovative, two-dimensional dual arc accelerometer array incorporated with rate gyros and an expanded attitude determination and sensor bias estimation algorithm intended for the study of variable, simulated aircraft loading scenarios. To determine the feasibility of the proposed expanded attitude determination method, the algorithm developed was implemented in a full nonlinear aircraft model executing variable maneuvers with sensor biases, noise, and environmental turbulence present during the simulations performed. The validation of this new and innovative method for two-dimensional attitude determination and rate gyro bias estimation algorithm was demonstrated through a comparative analysis of the estimated parameters and the true vehicle parameters for attitude and rate gyro bias respectively. While this study is a continuation and expansion of prior work, the feasibility assessment conducted in this work is a major step toward achieving the final goal of a highly accurate and reliable three-dimensional attitude determination device targeted for micro air vehicle and unmanned air vehicle applications without compromising such constraints as size, weight, power consumption, and overall cost.

1.2 Innovation and Motivation for Current Work

The work and research performed in this feasibility study is focused on the design and development of a two-dimensional, dual-arc accelerometer array for highly accurate and reliable longitudinal and transverse attitude estimation coupled with an algorithm for effective and precise rate gyro bias elimination utilizing low-cost sensors in order to accurately and repeatedly produce vehicle orientation in real-time. This work is an expansion of previous work, were the fundamental concept was previously applied to the simulation of a nonlinear aircraft performing longitudinal maneuvers for precise and reliable pitch attitude estimation. This thesis expands on the previous work completed by implementing an innovative two-dimensional dual arc accelerometer array in a full nonlinear aircraft simulation for both longitudinal and transverse maneuvers. The main goal and focus of this revolutionary device and configuration is to provide highly accurate and reliable on-line attitude and rate gyro bias estimates without the need for traditional INS systems, GPS systems, or magnetometers that may be used.

The configuration of the device consists of two semi-circular arcs containing 13 equally spaced accelerometers with rate gyros positioned at the center of the device, or the center of the arcs respectively. The offset distance and orientation relative to the center-of-gravity of the device are implemented and utilized in the algorithm method developed to determine the orientation and attitude of the vehicle and provide accurate rate gyro bias estimates in real-time. Figure 1.1 displays the proposed device setup and orientation for the longitudinal, or pitch plane array, and the transverse, or the roll plane array of the dual-arc accelerometer array respectively.

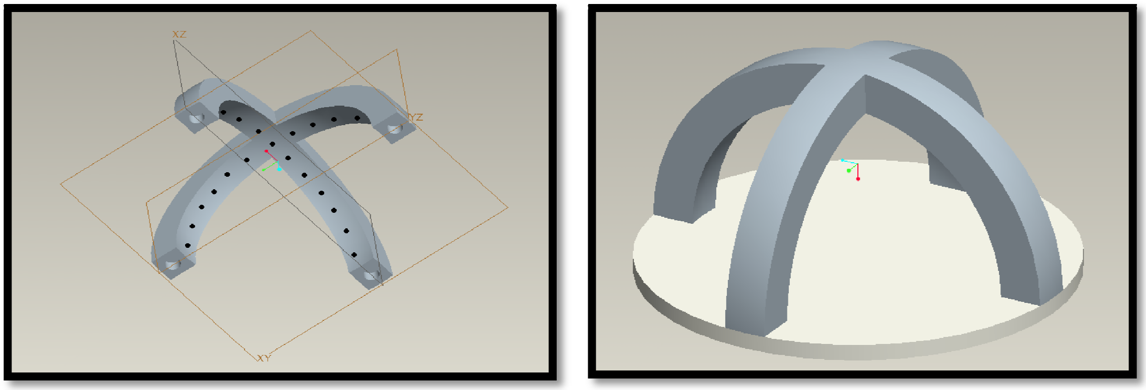

Figure 1.1: Dual-Arc Accelerometer Array Configuration

The dual-arc accelerometer array shown in Figure 1.1 was utilized for both longitudinal and transverse attitude determination and rate gyro bias estimation in real-time. Consisting of 13 accelerometers positioned equidistant from one another along both the longitudinal and transverse arcs, a separation of 15 degrees is consistent between each accelerometer as shown in Figures 1.2 and 1.3 for the pitch plane array and roll plane array respectively.

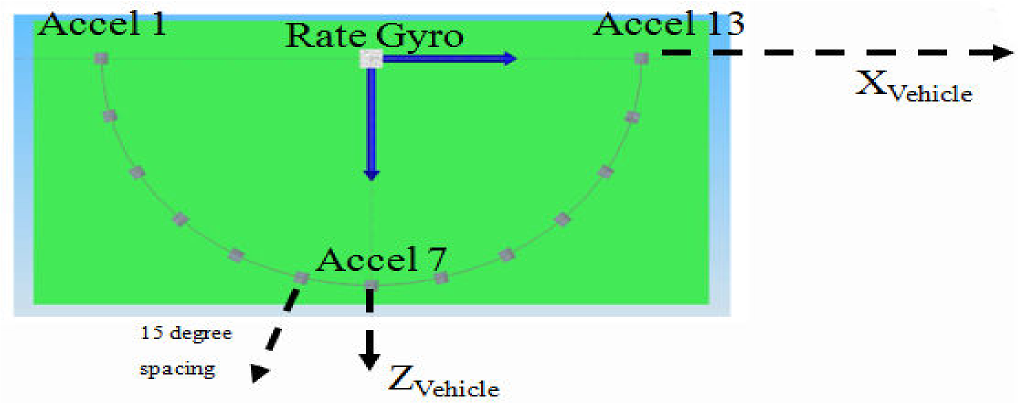

Figure 1.2: Pitch Plane Array Configuration

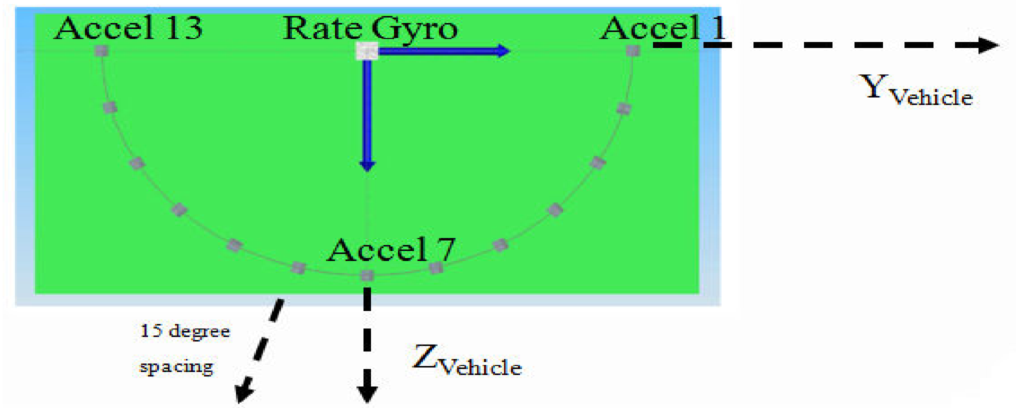

Figure 1.3: Roll Plane Array Configuration

The innovative device configuration and estimation algorithm developed will be implemented and assessed in a full nonlinear operating environment and compared to the true simulated aircraft parameters and sensor biases, and evaluated through the use of Simulink® and MATLAB®. The outline for the research and work conducted in this thesis is as follows:

1. Design and Implement a full nonlinear aircraft simulation model able to produce and replicate highly dynamic, real-world flight conditions and maneuvers.

2. Design and develop a highly precise and reliable attitude determination and rate gyro bias estimation algorithm utilizing the dual-arc accelerometer array configuration.

3. Implement and assess the feasibility of the device configuration and algorithm method developed within a full nonlinear operating environment consisting of rate sensor noise, biases, and environmental conditions consistent with real-world operating scenarios.

4. Analyze and contrast the parameter estimates of the dual-arc accelerometer array with the true values of the aircraft simulation model.

Chapter 2

Theory Development

2.1 Rigid Body Dynamics

2.1.1 Coordinate System Representations [3, 4, 24, 44, 49]

Traditional simulation of a rigid body's attitude is represented by three Euler angles, or angular displacement parameters about a references axis and coordinate system frame. Translational displacement representation in respect to a fixed axes or coordinate system in three-dimensional or Cartesian space may be described by three translational parameters. Therefore, the translational and rotational representation of a rigid body for means of accurate and reliable aircraft simulation, in terms of body position and orientation, is a combination of three translational displacements and three rotational displacements about a reference coordinate system.

When developing precise and dependable aircraft simulation models and algorithms, a major need and concern arises for the correct and appropriate definition of governing coordinate system frames. In terms of navigation; position, velocity, and attitude knowledge with respect to the Earth is essential for accurate and reliable aircraft simulation modeling. In contrast to this, when dealing with aircraft simulation modeling with respect to overall aircraft performance, position and velocity are needed with respect to the Earth's atmosphere. The former is utilized in this work, with all coordinate systems being right-handed and orthogonal.

Body – Fixed Coordinate Frame

In this study, the body-fixed coordinate frame is when the origin and axes of the coordinate frame are fixed with respect to the structure and geometry of the aircraft or rigid body. In this coordinate frame, the origin lies at the center-of-gravity of the aircraft or rigid body, where x_B is the primary axis, y_B is the secondary axis, and z_B is the tertiary axis as shown in Figure 2.1. The body-fixed coordinate frame then rotates and translates about a defined stationary, reference, coordinate frame [44].

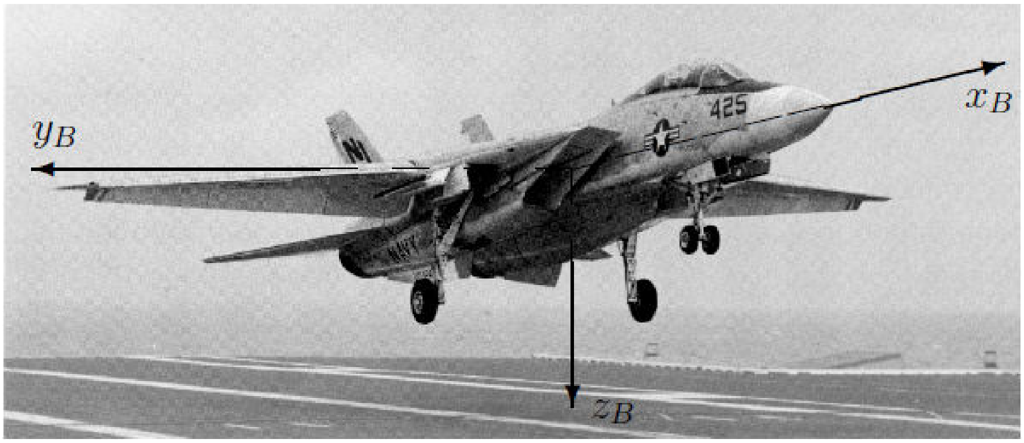

Figure 2.1: Body-Fixed Coordinate Frame [44]

Earth – Fixed Coordinate Frame

The Earth – fixed coordinate frame has its origin fixed to an arbitrary point located along the surface of the Earth, where the assumption is made that the Earth is represented by a uniform sphere. In the Earth – fixed coordinate frame, the primary axis, x_E, points due North. The secondary axis, y_E, points due East. The tertiary axis, z_E, points inward toward the center of the Earth as shown in Figure 2.2. Typically, in the aerospace community, this frame of reference is also known as the "Flat – Earth" assumption, and will be utilized throughout this work.

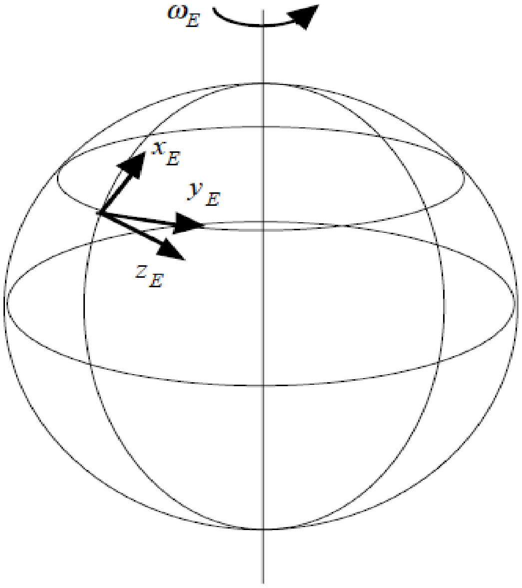

Figure 2.2: Earth – Fixed Coordinate Frame [44]

Earth – Centered Coordinate Frame

Implicated by its name, the Earth – centered coordinate frame has its origin located at the center of the Earth. Once a fixed position along the surface of the Earth has been defined, the axes may then be selected arbitrarily as shown by Figure 2.3.

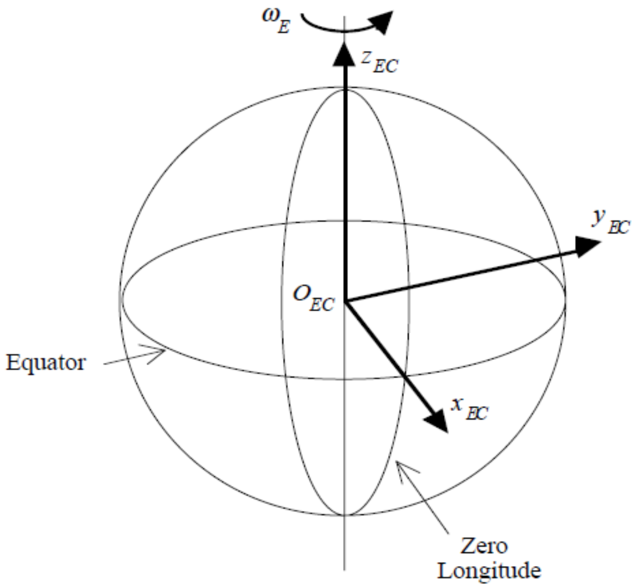

Figure 2.3: Earth – Centered Coordinate Frame [44]

Euler Angle Representation

Euler angles are angular displacement angles about the body-fixed coordinate frame known as the pitch, roll, and yaw angles. As stated previously, the primary or roll axis of the aircraft extends outward along the nose of the aircraft, the secondary or pitch axis extending out the starboard side of the aircraft, and the tertiary or yaw axis extends downward, in the direction of a cross product between the primary and secondary axes respectively. In this work, the body-fixed coordinate frame is utilized in conjunction with the Earth-fixed inertial coordinate frame as shown in Figure 2.4. Table 2.1 provides a short description and reference summation of axis designation, angle, position, and angular rate.

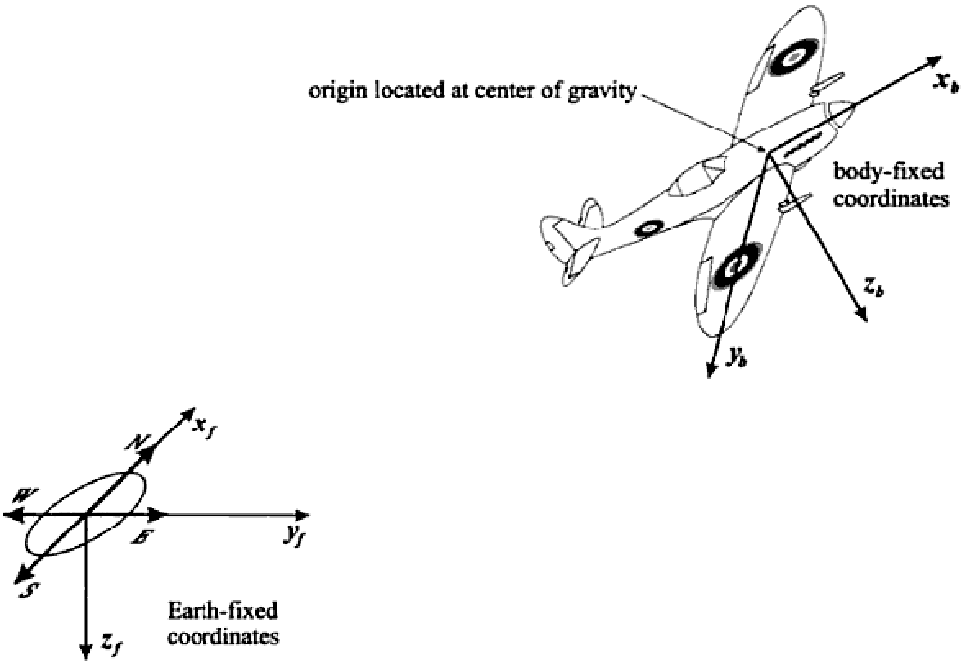

Figure 2.4: Earth – Fixed and Body – Fixed Coordinate Frames [44]

Axis Parameter	Primary Axis		Secondary Axis		Tertiary Axis	
	Earth	Body	Earth	Body	Earth	Body
Designation	X_{ref}	X_{veh}	Y_{ref}	Y_{veh}	Z_{ref}	Z_{veh}
Position	S_X	s_x	S_Y	s_y	S_Z	s_z
Velocity	V_X	u	V_Y	v	V_Z	w
Angle, φ	ϕ_E	ϕ_b	θ_E	θ_b	ψ_E	ψ_b
Angular Rate, ω	$\dot{\phi}$	p	$\dot{\theta}$	q	$\dot{\psi}$	r

Table 2.1: Earth and Body – Fixed Axis Parameter Definitions [6]

In addition to aircraft attitude descriptors such as Euler angle displacements through the use of the direct cosine matrix, additional attitude descriptors such as Euler – Rodrigues Quaternion Formulation must be considered and implemented when dealing with the transformation of vehicle angular displacement rates (pitch, roll, and yaw rate) due to the occurrence of the Gimbal Lock singularity condition. Gimbal Lock is a singularity condition caused by the occurrence of two rotational axes of an aircraft or vehicle pointing in the same direction [49]. This condition arises in aircraft dynamics when a vehicle achieves a pitch angle rotation of plus or minus 90 degrees from the primary reference axis. At this orientation, a divide by zero error, or singularity condition, occurs from the vehicle to reference rate transformation matrix [4].

Traditional three gimbal mechanical assemblies experience this phenomena due to their reliance on Euler angle relationships for attitude determination and is corrected through the use of an additional, fourth gimbal.

When developing aircraft simulation models, it is necessary to mathematically resolve the Gimbal Lock condition by including a fourth element to the attitude representation convention. To do this, it is necessary to construct the Euler Axis, or Eigen Axis, where the orientation of the non-inertial frame is characterized by a singular rotation through an angle, Θ, about the Euler Axis, E [4]. This comparative assessment between the Euler Axis rotation and Euler angle rotations for pitch, roll, and yaw respectively are a common practice for constructing attitude descriptors in the aerospace world. While the Gimbal Lock condition has now been resolved, a singularity condition still remains during integration of the Euler Axis when the Eigen angle is either 0 or 180 degrees. The most reliable and commonly used method for mathematically eliminating the Gimbal Lock condition is through the derivation and implementation of the Euler – Rodrigues Quaternion Formulation. The quaternion formulation is related to the Euler axis formulation through a change of variables where the previous four Euler axis descriptors are utilized to define four new, different parameters that avoid the mathematical occurrence of a singularity [3, 4].

2.1.2 Application of Newton's Second Law for a Rigid Body [3, 4, 32]

For simulation of an aircraft or vehicle in Cartesian space, rigid body equations of motion must be applied from Newton's second law, which states that the summation of all external forces acting on a rigid body must be equal to the time rate of change of the momentum of that body and the summation of all external moments acting on a body is equal to the time rate of change of the angular moment of the body as shown in Equations 2.1 and 2.2,

$$\sum F + W = \frac{d}{dt}(mV) \tag{2.1}$$

$$\sum M = \frac{d}{dt}(\overset{\rightarrow}{\omega}\overset{\leftrightarrow}{I}) \tag{2.2}$$

Where F is the net force vector acting on the body, W is the weight vector of the body, V is the translational rate vector of the body, M is the net moment vector about the body-fixed origin (center-of-gravity), m is the mass of the body, ω is the angular rate vector, and I is the inertia tensor defined by Equations 2.3, 2.4, and 2.5.

$$\left[\overset{\leftrightarrow}{I}\right] = \begin{bmatrix} I_{xx} & -I_{xy} & -I_{xz} \\ -I_{yx} & I_{yy} & -I_{yz} \\ -I_{zx} & -I_{zy} & I_{zz} \end{bmatrix} \tag{2.3}$$

$$I_{ij,i\neq j} = \iiint_m (i^2 + j^2)dm \tag{2.4}$$

$$I_{ii} = \iiint_m (j^2 + k^2)dm \tag{2.5}$$

From Equation 2.3, the Inertia tensor is symmetric about its diagonal. As discussed previously, the body-fixed coordinate frame, common to aircraft dynamics, has the x_B axis pointing forward from the center-of-gravity along the aircraft plane of symmetry. The y_B axis is normal to the plane of symmetry pointing out the right-hand side of the aircraft, and the z_B axis pointing downward within the aircraft plane of symmetry. It is typical in aircraft simulation to assume that the aircraft is symmetric about the plane created by the primary and tertiary axes, and that there is a negligible contribution to the inertia formed by the primary and secondary axes. Therefore, since the coordinate frame chosen for the aircraft is symmetric in y_B, the I_{xy}, I_{yx}, I_{yz}, and I_{zy} terms are generally set to zero. For the simulations conducted in this study, this assumption and simplification was not utilized to provide for the development of a more accurate and complete simulation model.

Equations 2.1 and 2.2 are defined for one-dimensional motion along the vehicle's body frame of reference. To correlate these equations from the vehicle's body-fixed frame to the inertial frame of reference, Equation 2.6 must be utilized so the vehicle's motion in the body frame is related to the inertial frame by an arbitrary body frame vector G_{veh}. Utilizing an angular velocity vector, $\vec{\omega}$, this relationship may be related to a reference frame vector, G_{ref}, shown in Equation 2.6 [32].

$$\frac{d}{dt}G_{ref} = \frac{d}{dt}G_{veh} + \vec{\omega}\times G_{veh} \tag{2.6}$$

Equation 2.6 is then applied to Equations 2.1 and 2.2 to relate the force and moment equations in the vehicle, body-fixed, reference frame to the inertial, Earth-Fixed, frame of reference resulting in Equations 2.7 and 2.8.

$$\sum F_{ref} + W_{ref} = \frac{d}{dt}(mV_{veh}) + \vec{\omega} \times (mV_{veh}) \tag{2.7}$$

$$\sum M_{ref} = \frac{d}{dt}(I_{veh}\vec{\omega}) + \vec{\omega} \times (I_{veh}\vec{\omega}) \tag{2.8}$$

In scalar form, Equations 2.7 and 2.8 may be written as Equations 2.9 and 2.10 for calculation of the net force and moment terms.

$$\begin{bmatrix} F_x \\ F_y \\ F_z \end{bmatrix}_{ref} = \begin{bmatrix} m(\dot{u} - vr + wq) \\ m(\dot{v} + ur + wp) \\ m(\dot{w} - uq + vp) \end{bmatrix} = W_{Ref} + F_{Aerodynamic} + F_{Thrust} \tag{2.9}$$

$$M = \begin{bmatrix} L \\ M \\ N \end{bmatrix} = \begin{bmatrix} \dot{p}I_{xx} - \dot{q}I_{xy} - \dot{r}I_{xz} \\ -\dot{p}I_{xy} + \dot{q}I_{yy} - \dot{r}I_{yz} \\ -\dot{p}I_{xz} - \dot{q}I_{yz} + \dot{r}I_{zz} \end{bmatrix} = \begin{bmatrix} qr(I_{yy} - I_{zz}) + (q^2 - r^2)I_{xy} - prI_{xy} + pqI_{xz} \\ pr(I_{zz} - I_{xx}) + (r^2 - p^2)I_{xz} - pqI_{yz} + qrI_{xy} \\ pq(I_{xx} - I_{yy}) + (p^2 - q^2)I_{xy} - qrI_{xz} + prI_{yz} \end{bmatrix} + M_{External} \tag{2.10}$$

Equation 2.9 accounts for the forces resulting from aerodynamic and propulsive forces, while Equation 2.10 accounts for additional moments arising from the aerodynamic and propulsive forces. During simulation, the thrust force on the aircraft is assumed to act along the negative primary axis, or – x_B direction. The utilized and governing nonlinear, six degree-of-freedom equations for aircraft flight are well documented [3, 4, 32, 44], with additional equations of motion utilized in the development of the nonlinear aircraft simulation provided in Appendix E.

While the equations provided in this section are the basic rigid body equations of motion and force equations governing the dynamics and stability of an aircraft, equations describing the orientation and position of the aircraft are critical to include as well when developing aircraft simulation models in three-dimensional space and are discussed in the following section.

2.1.3 Aircraft Orientation: Euler Kinematics [3, 4, 44]

In the preceding section, Newton's second law was utilized to derive equations of motion for an aircraft where the coordinate frame is fixed to the aircraft or vehicle, known as the body-fixed coordinate frame. While the body-fixed frame of reference does well when working with aircraft dynamics, simulation of an aircraft for describing position and orientation also requires a coordinate frame fixed to the Earth as previously discussed, known as the Earth-fixed coordinate frame. The position of the aircraft being simulated is then specified by the location of the origin of the body-fixed frame relative to that of the Earth-fixed frame. To do this, Euler angles must be utilized to orientate the aircraft relative to the Earth.

The body-fixed frame define by x_B, y_B, and z_B, relative to the Earth-fixed coordinate frame, x_f, y_f, and z_f, may be described in three consecutive rotations through three Euler angles in a specific sequence as shown by graphically by Figure 2.5 and summarized in Table 2.2.

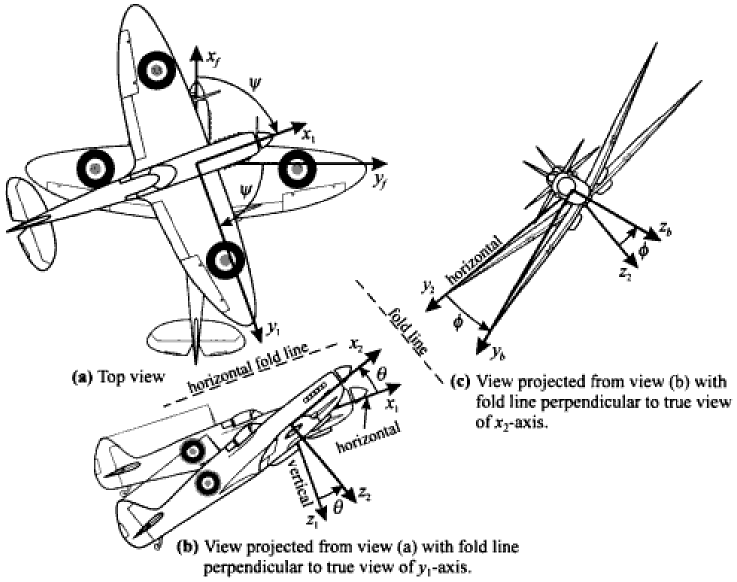

(a) Top view

(b) View projected from view (a) with fold line perpendicular to true view of y_1-axis.

(c) View projected from view (b) with fold line perpendicular to true view of x_2-axis.

Figure 2.5: Euler Angle Rotations Following the Standard Rotational Convention [4]

Rotational Axis	Rotational Description
Z_f	Rotate the Earth-fixed coordinate frame (x_f, y_f, z_f) about the z_f-axis through an angle ψ to the coordinate frame (x_1, y_1, z_1), as graphically shown in Figure 2.5a
y_1	Rotate the coordinate frame (x_1, y_1, z_1) about the y_1-axis through an angle θ to the coordinate frame (x_2, y_2, z_2), as graphically shown in Figure 2.5b
x_2	Rotate the Earth-fixed coordinate frame (x_2,y_2, z_2) about the x_2-axis through an angle ϕ to the body-fixed coordinate frame (x_b, y_b, z_b), as graphically shown in Figure 2.5c

Table 2.2: Euler Angle Rotational Convention

Utilizing the Euler angle rotations described above, the equations of motion derived for a body-fixed coordinate frame must be re-derived in terms of orientation and the position of the vehicle relative to the Earth-fixed frame of reference. Euler angles therefore allow for the orientation of the body-fixed frame of reference to be effectively related to the Earth-fixed frame of reference, as stated previously. Figure 2.6 provides a final reference for axis designation, angle, and angular rate for an aircraft operating in Cartesian space. The work conducted in this study utilizes a "3-2-1" Euler transformation sequence for the inertial Earth-fixed reference frame transformation to the body-fixed coordinate frame.

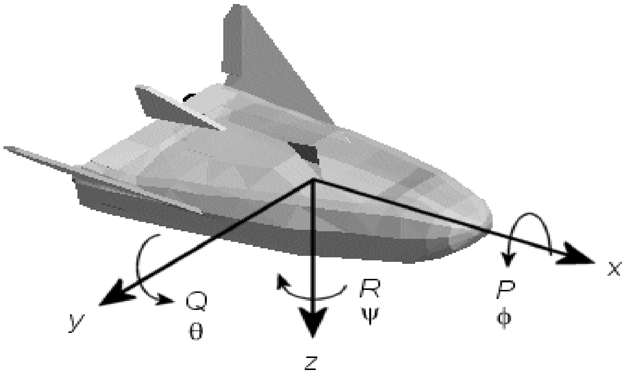

Figure 2.6: Body-Fixed Axis, Angle, and Angular Rate Designations [24]

Equations 2.11, 2.12, and 2.13 represent the rotations about the x_f, y_f, and z_f axes for a transformation from the Earth-fixed coordinate frame to the vehilce's x_B, y_B, and z_B axes respecitvely.

$$R_1 = \begin{bmatrix} 1 & 0 & 0 \\ 0 & \cos(\phi) & \sin(\phi) \\ 0 & -\sin(\phi) & \cos(\phi) \end{bmatrix} \tag{2.11}$$

$$R_2 = \begin{bmatrix} \cos(\theta) & 0 & -\sin(\theta) \\ 0 & 1 & 0 \\ \sin(\theta) & 0 & \cos(\theta) \end{bmatrix} \tag{2.12}$$

$$R_3 = \begin{bmatrix} \cos(\psi) & \sin(\psi) & 0 \\ -\sin(\psi) & \cos(\phi) & 0 \\ 0 & 0 & 1 \end{bmatrix} \tag{2.13}$$

From these relationships defined in Equations 2.11 through 2.13, Equations 2.14 and 2.15 defines the transformation matrix that performs the transformation from the inertial, Earth-fixed coordinate frame to the body-fixed coordinate frame.

$$T_{Earth-Body} = R_3 * R_2 * R_1 \tag{2.14}$$

$$T_{Earth-Body} = \begin{bmatrix} \cos(\psi) & \sin(\psi) & 0 \\ -\sin(\psi) & \cos(\psi) & 0 \\ 0 & 0 & 1 \end{bmatrix} \begin{bmatrix} \cos(\theta) & 0 & -\sin(\theta) \\ 0 & 1 & 0 \\ \sin(\theta) & 0 & \cos(\theta) \end{bmatrix} \begin{bmatrix} 1 & 0 & 0 \\ 0 & \cos(\phi) & \sin(\phi) \\ 0 & -\sin(\phi) & \cos(\phi) \end{bmatrix} \tag{2.15}$$

Combining Equations 2.11 through 2.13 in the manner given by Equation (2.16) defines the inverse transformation from the body-fixed coordinate frame to the Earth-fixed coordinate frame, as Equation 2.17.

$$T_{Body-Earth} = R_1 * R_2 * R_3 \tag{2.16}$$

$$T_{Body-Earth} = \begin{bmatrix} 1 & 0 & 0 \\ 0 & \cos(\phi) & \sin(\phi) \\ 0 & -\sin(\phi) & \cos(\phi) \end{bmatrix} \begin{bmatrix} \cos(\theta) & 0 & -\sin(\theta) \\ 0 & 1 & 0 \\ \sin(\theta) & 0 & \cos(\theta) \end{bmatrix} \begin{bmatrix} \cos(\psi) & \sin(\psi) & 0 \\ -\sin(\psi) & \cos(\psi) & 0 \\ 0 & 0 & 1 \end{bmatrix} \tag{2.17}$$

The individual matrices given in Equations 2.15 and 2.17 may now be multiplied together to form a two, single transformation matrices for each of the defined equations. At this point, it is convenient to introduce shorthand notation as,

$$s(\phi) = \sin(\phi), c(\phi) = \cos(\phi)$$

and so on.

Multiplying the individual matrices of Equations 2.15 and 2.17 together forms the transformation matrices for the Earth-fixed to body-fixed coordinate frame transformation and the body-fixed to Earth-fixed coordinate frame transformation. These matrices are given in Equations 2.18 and 2.19 respectively.

$$\begin{Bmatrix} V_{x-fixed} \\ V_{y-fixed} \\ V_{z-fixed} \end{Bmatrix} = \begin{bmatrix} c\theta c\psi & s\phi s\theta c\psi - c\phi s\psi & c\phi s\theta c\psi + s\phi s\psi \\ c\theta s\psi & s\phi s\theta s\psi + c\phi c\psi & c\phi s\theta s\psi - s\phi c\psi \\ -s\theta & s\phi c\theta & c\phi c\theta \end{bmatrix} \begin{Bmatrix} V_{x-body} \\ V_{y-body} \\ V_{z-body} \end{Bmatrix} \tag{2.18}$$

$$\begin{Bmatrix} V_{x-body} \\ V_{y-body} \\ V_{z-body} \end{Bmatrix} = \begin{bmatrix} c\theta c\psi & c\theta s\psi & -s\theta \\ s\phi s\theta c\psi - c\phi s\psi & s\phi s\theta s\psi + c\phi c\psi & s\phi c\theta \\ c\phi s\theta c\psi + s\phi s\psi & c\phi s\theta s\psi - s\phi c\psi & c\phi c\theta \end{bmatrix} \begin{Bmatrix} V_{x-fixed} \\ V_{y-fixed} \\ V_{z-fixed} \end{Bmatrix} \tag{2.19}$$

The transformation matrix given in Equation 2.18 is known as the Direct Cosine Matrix or DCM, and will be utilized throughout this work and research for transforming components of the Earth-fixed coordinate frame to the body-fixed coordinate frame of the aircraft. It is worth noting that the inverse of the transformation matrix given in Equation 2.18 is its transpose due to the nature of the inverse of square orthogonal matrices.

In the body-fixed coordinate frame, the velocity of the of the aircraft is given by u, v, and w, and in the Earth-fixed coordinate frame, the time rate of change of the position vector is designated by dx/dt, dy/dt, and dz/dt respectively. The transfer of vehicle, body-fixed rates, to inertial, Earth-fixed rates requires the utilization of the transformation matrix given in Equation 2.19 and the addition of wind components in the inertial, Earth-fixed coordinate frame as given by Equation 2.20,

$$\begin{Bmatrix} \dot{x}_{Earth-fixed} \\ \dot{y}_{Earth-fixed} \\ \dot{z}_{Earth-fixed} \end{Bmatrix} = \begin{bmatrix} c\theta c\psi & c\theta s\psi & -s\theta \\ s\phi s\theta c\psi - c\phi s\psi & s\phi s\theta s\psi + c\phi c\psi & s\phi c\theta \\ c\phi s\theta c\psi + s\phi s\psi & c\phi s\theta s\psi - s\phi c\psi & c\phi c\theta \end{bmatrix} \begin{Bmatrix} u \\ v \\ w \end{Bmatrix} + \begin{Bmatrix} V_{wind-x_f} \\ V_{wind-y_f} \\ V_{wind-z_f} \end{Bmatrix} \tag{2.20}$$

where $V_{wind\text{-}x}$, $V_{wind\text{-}y}$, and $V_{wind\text{-}z}$ are the components of the constant wind vector in the Earth-fixed coordinate frame. The integration of Equation 2.20 leads to the position of the aircraft relative to the Earth-fixed coordinate frame [4].

The relationship between angular velocities in the body-fixed frame and the Euler angular rates for the Aerospace 3-2-1 conventional rotation is given by Equation 2.21 and derived in full in Appendix A.

$$\begin{bmatrix} p \\ q \\ r \end{bmatrix} = \begin{bmatrix} 1 & 0 & -s\theta \\ 0 & c\phi & c\theta s\phi \\ 0 & -s\phi & c\theta c\phi \end{bmatrix} \begin{bmatrix} \dot{\phi} \\ \dot{\theta} \\ \dot{\psi} \end{bmatrix} \tag{2.21}$$

Equation 2.21 can be solved for the Euler rates in terms of body angular velocities and is given by Equation 2.22.

$$\begin{bmatrix} \dot{\phi} \\ \dot{\theta} \\ \dot{\psi} \end{bmatrix} = \begin{bmatrix} 1 & s\phi \tan\theta & c\phi \tan\theta \\ 0 & c\phi & -s\phi \\ 0 & s\phi \sec\theta & c\phi \sec\theta \end{bmatrix} \begin{bmatrix} p \\ q \\ r \end{bmatrix} \tag{2.22}$$

By integrating Equation 2.22, one may determine the Euler angles ψ, θ, and ϕ for the coordinate frame of interest. As previously discussed, the Gimbal Lock condition is represented in Equation 2.22 for a plus or minus 90 degree rotation, where the heading (yaw) and bank (roll) angles become unable to determine due to the parallel alignment of the roll and pitch axes [3, 4].

As previously mentioned, Euler first introduced the concept of relating a noninertial reference frame to the inertial reference frame described in terms of a single rotation known as the Euler axis or Eigen axis to eliminate the condition of parallel axes. The Euler axis developed makes use of a fourth component for orientation description. The three components describing a vector along the Euler axis are E_x, E_y, and E_z with the fourth component representing the total rotational angle, Θ. Utilizing this manner of orientation classification, an additional mathematical degree of freedom has been introduced. Figure 2.7 displays the Eigenvector and total rotation angle, Θ.

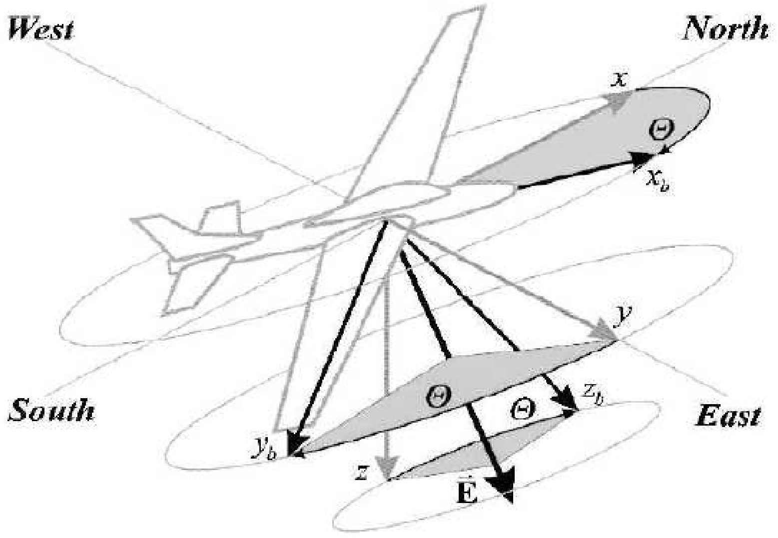

Figure 2.7: Euler Axis and Total Rotation Angle Reference [4]

During formulation of the Euler axis rotation, the components of both the inertial and noninertial coordinate frame are the same. Therefore, the vector, E, may be shown as Equation 2.23.

$$\begin{Bmatrix} E_{x-fixed} \\ E_{y-fixed} \\ E_{z-fixed} \end{Bmatrix} = \begin{Bmatrix} E_{x-body} \\ E_{y-body} \\ E_{z-body} \end{Bmatrix} \equiv \begin{Bmatrix} E_x \\ E_y \\ E_z \end{Bmatrix} \tag{2.23}$$

The components of an arbitrary vector, v, may be related from the body-fixed frame of reference to the Earth-fixed frame of reference through *Euler's Formula* [4] given by Equation 2.24,

$$\begin{Bmatrix} v_{x-body} \\ v_{y-body} \\ v_{z-body} \end{Bmatrix} = \begin{bmatrix} E_{xx} + \cos(\Theta) & E_{xy} - E_z \mathit{Sin}(\Theta) & E_{xz} - E_y \sin(\Theta) \\ E_{xy} - E_z \sin(\Theta) & E_{yy} + \cos(\Theta) & E_{yz} + E_x \sin(\Theta) \\ E_{xz} + E_y \sin(\Theta) & E_{yz} + E_x \sin(\Theta) & E_{zz} + \cos(\Theta) \end{bmatrix} \begin{Bmatrix} v_{x-fixed} \\ v_{y-fixed} \\ v_{z-fixed} \end{Bmatrix} \tag{2.24}$$

where $E_{ij} = E_i E_j (1 - \cos(\Theta))$. The inverse of the transformation matrix given in Equation 2.24 may be obtained by simply rotating through the negative of the total rotation angle utilized during the forward rotation. The inverse transformation therefore allows for the transformation of a vector from the inertial, Earth-fixed coordinate frame, to the body-fixed coordinate frame and is given by Equation 2.25.

$$\begin{Bmatrix} v_{x-fixed} \\ v_{y-fixed} \\ v_{z-fixed} \end{Bmatrix} = \begin{bmatrix} E_{xx} + \cos(\Theta) & E_{xy} - E_z Sin(\Theta) & E_{xz} + E_y \sin(\Theta) \\ E_{xy} + E_z \sin(\Theta) & E_{yy} + \cos(\Theta) & E_{yz} - E_x \sin(\Theta) \\ E_{xz} - E_y \sin(\Theta) & E_{yz} + E_x \sin(\Theta) & E_{zz} + \cos(\Theta) \end{bmatrix} \begin{Bmatrix} v_{x-body} \\ v_{y-body} \\ v_{z-body} \end{Bmatrix} \tag{2.25}$$

The relationship between the body angular rates of the aircraft and the rate of change of the Euler axis rotational parameters may be given as Equation 2.26

$$\begin{Bmatrix} \dot{\Theta} \\ \dot{E}_x \\ \dot{E}_y \\ \dot{E}_z \end{Bmatrix} = \frac{1}{2} \begin{bmatrix} 2E_x & 2E_y & 2E_z \\ E'_{xx} + C/S & E'_{xy} - E_z & E'_{xz} + E_y \\ E'_{xy} + E_z & E'_{yy} + C/S & E'_{yz} - E_x \\ E'_{xz} - E_y & E'_{yz} + E_x & E'_{zz} + C/S \end{bmatrix} \begin{Bmatrix} p \\ q \\ r \end{Bmatrix} \tag{2.26}$$

where $E'_{ij} = -E_i E_j C/S, S = \sin(\Theta/2), C = \cos(\Theta/2)$.

Equations 2.24 through 2.26 represent the kinematic transformation equations in terms of the Euler axis convention. The use of Equation 2.26 eliminates the Gimbal Lock condition at plus or minus 90 degrees; however, the use of this new equation now possesses a singularity condition when the aircraft is at an orientation of 0 or 180 degrees.

2.1.4 Quaternion Formulation

In order to avoid the singularity difficulties associated with the use of Euler angles and the large computational terms of the Direct-Cosine Matrix, another attitude representation must be utilized. The Quaternion is a commonly used method of attitude description in the aerospace community due to its freedom from the analytical complexities that are synonymous with the use of the Euler angle convention.

Quaternion Attitude Convention [4, 26, 35, 45]

The four parameters established by the formulation of the Euler axis orientation are utilized to describe four new parameters that are much more computationally less burdening. These four new parameters are defined by Equation 2.27 as

$$Q = \begin{Bmatrix} q_0 \\ q_x \\ q_y \\ q_z \end{Bmatrix} = \begin{Bmatrix} \cos(\Theta/2) \\ E_x \sin(\Theta/2) \\ E_y \sin(\Theta/2) \\ E_z \sin(\Theta/2) \end{Bmatrix} = q_0 + (q_x)\hat{\imath} + (q_y)\hat{\jmath} + (q_z)\hat{k} = \begin{Bmatrix} q_0 \\ q \end{Bmatrix} \tag{2.27}$$

and are known as the Euler-Rodrigues symmetric parameters, or alternatively, as the quaternion of finite rotation. The four parameters given by Equation 2.27 for the basis of a commonly used orientation and rigid-body rotation descriptor utilized in the aerospace community where the first element of the Quaternion is the scalar component, denoted by the 0 subscript. The other three components for the Quaternion vector, and are denoted by the x, y, and z subscripts respectively. A relationship between the four parameters of the Quaternion may be seen by squaring the four components and adding them together as shown in Equation 2.28.

$$q_0^2 + q_x^2 + q_y^2 + q_z^2 = \cos^2\left(\frac{\Theta}{2}\right) + (q_x^2 + q_y^2 + q_z^2)\sin^2\left(\frac{\Theta}{2}\right) \tag{2.28}$$

Due to the fact that there are four components governing a three axes rotation, it is necessary to eliminate the mathematical redundancy present. As previously stated, the Euler axis, E, is a unit vector. Applying the trigonometric identity given by Equation 2.29,

$$\cos^2(\Theta/2) + \sin^2(\Theta/2) = 1 \tag{2.29}$$

it may be seen that:

$$q_0^2 + q_x^2 + q_y^2 + q_z^2 = 1 \tag{2.30}$$

Quaternion Algebra and Mathematics [4, 33, 37]

In general, a quaternion is defined as

$$\{Q\} = q_0 + q_x\hat{\imath} + q_y\hat{\jmath} + q_z\hat{k} \tag{2.31}$$

A Quaternion has properties of both a scalar and a vector. While all the elements of the quaternion are real numbers, they may be designated as a hyper-complex number

Similar to complex algebra, quaternion algebra allows for the magnitude of a quaternion to be expressed like that of a complex number as shown in Equation 2.32 and the conjugate of the quaternion expressed as Equation 2.33.

$$\left|\{Q\}\right| = \sqrt{q_0^2 + q_x^2 + q_y^2 + q_z^2} \tag{2.32}$$

$$\{Q\}^* = q_0 - q_x\hat{i} - q_y\hat{j} - q_z\hat{k} \tag{2.33}$$

In terms of attitude determination, differencing a quaternion with another quaternion and multiplying quaternions by scalar terms does not either give one the overall rotation angle or change the rotation angle. To do this, a quaternion must be normalized, which requires the use of the quaternion conjugate as shown by Equation 2.34.

$$Norm(Q) = N(Q) = \frac{Q}{\sqrt{Q^* Q}} \tag{2.34}$$

The product of a quaternion, as given by Equation 2.35, consists of separate quaternion rotations where the sequence of rotation is of critical importance. The quaternion, Q, represents the first rotation and P, the second rotation. The product of a quaternion and its inverse must have a unitary value, just as the Euler transformation matrices, due to the quaternion representing a transformation from one coordinate frame to another.

$$PQ = p_0 q_0 - p \bullet q + p_0 q + q_0 p + p \times q \tag{2.35}$$

A quaternion operation is known as a quaternion rotation of an attitude vector. In a quaternion rotation, the attitude vector of the reference coordinate frame, $H_{\text{Earth-Fixed}}$, is rotated from the Earth-fixed frame of reference, to the body-fixed coordinate frame via Q. This operation produces a coordinate frame output vector, $H_{\text{Body-Fixed}}$, in the body-fixed frame as given by Equation 2.36.

$$H_{Body-Fixed} = Q * (H_{Earth-Fixed})Q = (q_0^2 - |q|^2)H_{Earth-Fixed} + 2(qq^T)H_{Earth-Fixed} - 2q_0(q \times H_{Earth-Fixed}) \tag{2.36}$$

By completing the mathematical operations, Equation 2.36 may be expanded to the derived transformation matrix given by Equation 2.37.

$$H_{Body-Fixed} = \begin{bmatrix} q_x^2 + q_0^2 - q_y^2 - q_z^2 & 2(q_x q_y + q_z q_0) & 2(q_x q_z - q_y q_0) \\ 2(q_x q_y - q_z q_0) & q_y^2 + q_0^2 - q_x^2 - q_z^2 & 2(q_y q_z - q_x q_0) \\ 2(q_x q_z + q_y q_0) & 2(q_y q_z - q_x q_0) & q_z^2 + q_0^2 - q_x^2 - q_y^2 \end{bmatrix} H_{Earth-Fixed}$$

(2.37)

In a similar manner, a transformation from the body-fixed frame to the Earth-fixed coordinate frame can be established and is presented by Equation 2.38.

$$H_{Earth-Fixed} = Q(H_{Body-Fixed})Q^* = 2(q_0^2 - 1)H_{Body-Fixed} + 2(q \bullet H_{Body-Fixed})q + 2q_0(q \times H_{Body-Fixed})$$

(2.38)

An aerospace quaternion rotation for an Earth-fixed coordinate frame to an aircraft or vehicle body-fixed frame can be established by applying Equation 2.27 to each inertial coordinate frame axis. This procedure allows for the direct formulation of rotation quaternions as defined by Equations 2.39, 2.40, and 2.41. The aerospace quaternion rotation may now be mathematically represented by Equation 2.42.

$$Rotation\ about\ the\ Earth\text{-}Fixed\ X\ axis : Q_X = \cos\left(\frac{\phi}{2}\right) + \sin\left(\frac{\phi}{2}\right)\hat{i} + 0\hat{j} + 0\hat{k}$$

(2.39)

$$Rotation\ about\ the\ Earth\text{-}Fixed\ Y\ axis : Q_Y = \cos\left(\frac{\theta}{2}\right) + 0\hat{i} + \sin\left(\frac{\theta}{2}\right)\hat{j} + 0\hat{k}$$

(2.40)

$$Rotation\ about\ the\ Earth\text{-}Fixed\ Z\ axis : Q_Z = \cos\left(\frac{\psi}{2}\right) + 0\hat{i} + 0\hat{j} + \sin\left(\frac{\psi}{2}\right)\hat{k}$$

(2.41)

$$Q_{Trans} = Q_X Q_Y Q_Z$$

(2.42)

Therefore, the total transformation equation from the Earth-fixed coordinate frame to the body-fixed coordinate frame may now be expressed as Equation 2.43.

$$H_{Body-Fixed} = Q_{Trans}{}^* H_{Earth-Fixed} Q_{Trans}$$

(2.43)

Quaternion Attitude Descriptors [4, 26, 28, 33, 37]

It is necessary to be able to relate the Euler-Rodrigues quaternion to the Euler angle formulation in order to aid in the physical description and interpretation of the Euler-Rodrigues quaternion model. To do this, a relationship must be established between the direct cosine matrix, given in Equation 2.19, and the Euler-Rodrigues formulation. This relationship is established through the use of Equation 2.44.

$$\begin{bmatrix} q_x^2+q_0^2-q_y^2-q_z^2 & 2(q_xq_y+q_zq_0) & 2(q_xq_z-q_yq_0) \\ 2(q_xq_y-q_zq_0) & q_y^2+q_0^2-q_x^2-q_z^2 & 2(q_yq_z-q_xq_0) \\ 2(q_xq_z+q_yq_0) & 2(q_yq_z-q_xq_0) & q_z^2+q_0^2-q_x^2-q_y^2 \end{bmatrix} = \begin{bmatrix} c\theta c\psi & c\theta s\psi & -s\theta \\ s\phi s\theta c\psi - c\phi s\psi & s\phi s\theta s\psi + c\phi c\psi & s\phi c\theta \\ c\phi s\theta c\psi + s\phi s\psi & c\phi s\theta s\psi - s\phi c\psi & c\phi c\theta \end{bmatrix} \tag{2.44}$$

The quaternion matrix equations relating the four terms of the Euler-Rodrigues formulation to the three Euler parameters through the use of the nine matrix components result in six additional levels of redundancy. The reduced relationship is presented by Equation 2.45 and is derived in full in Appendix B.

$$\begin{Bmatrix} q_0 \\ q_x \\ q_y \\ q_z \end{Bmatrix} = \pm \begin{Bmatrix} c_{\phi/2}c_{\theta/2}c_{\psi/2} + s_{\phi/2}s_{\theta/2}s_{\psi/2} \\ s_{\phi/2}c_{\theta/2}c_{\psi/2} - c_{\phi/2}s_{\theta/2}s_{\psi/2} \\ c_{\phi/2}s_{\theta/2}c_{\psi/2} + s_{\phi/2}c_{\theta/2}s_{\psi/2} \\ s_{\phi/2}s_{\theta/2}c_{\psi/2} - c_{\phi/2}c_{\theta/2}s_{\psi/2} \end{Bmatrix} \tag{2.45}$$

Equation 2.45 proves useful in the absence of the direct cosine matrix; however, if the transformation matrix is known, the quaternion may be determined alternatively through the use of Equation 2.46 and 2.47 which provide an alternative, direct determination of the quaternion from the off-diagonal elements of the direct cosine matrix [4].

$$q_0 = \frac{1}{2}\sqrt{1 + DCTM_{11} + DCTM_{22} + DCTM_{33}} \tag{2.46}$$

$$\begin{Bmatrix} q_x \\ q_y \\ q_z \end{Bmatrix} = \begin{Bmatrix} \frac{1}{4q_0}(DCTM_{23} - DCTM_{32}) \\ \frac{1}{4q_0}(DCTM_{31} - DCTM_{13}) \\ \frac{1}{4q_0}(DCTM_{12} - DCTM_{21}) \end{Bmatrix} \tag{2.47}$$

$Note: DCTM_{ij} = i^{th} row, and$

$j^{th} column\ of\ the\ direct\ \cos ine\ transformation\ matrix.$

Both solutions to Equation 2.45 are valid because the two solutions are mathematically possible due to the orientation of the one coordinate frame relative to another being described in terms of two right-handed rotations. Relating the quaternion back to the Euler angle representation for aircraft simulation is achieved through the use of Equation 2.48, where the Gimbal Lock singularity condition reappears [4, 28].

$$\begin{Bmatrix} \phi \\ \theta \\ \psi \end{Bmatrix} = \begin{Bmatrix} a\tan 2[2(q_0 q_x + q_y q_z),(q_0^2 + q_z^2 - q_x^2 - q_y^2) \\ a\sin[2(q_0 q_y - q_x q_z)] \\ a\tan 2[2(q_0 q_z + q_x q_y),(q_0^2 + q_x^2 - q_y^2 - q_z^2) \end{Bmatrix} \tag{2.48}$$

In order to deal with this condition, a general algorithm formulation for determining Euler angles from the corresponding quaternion components may be implemented and is shown as Equation 2.49 for attitude estimation when the condition of Gimbal Lock is possible.

$$if\,(q_0 q_y - q_x q_z = 0.5)$$

$$\begin{Bmatrix} \phi \\ \theta \\ \psi \end{Bmatrix} = \begin{Bmatrix} a\sin[2q_x / \cos(\pi/4)] + \psi \\ \pi/2 \\ arbitrary \end{Bmatrix}$$

$$if\,(q_0 q_y - q_x q_z = -0.5)$$

$$\begin{Bmatrix} \phi \\ \theta \\ \psi \end{Bmatrix} = \begin{Bmatrix} a\sin[2q_x / \cos(\pi/4)] - \psi \\ -\pi/2 \\ arbitrary \end{Bmatrix}$$

$$else$$

$$\begin{Bmatrix} \phi \\ \theta \\ \psi \end{Bmatrix} = \begin{Bmatrix} a\tan 2[2(q_0 q_x + q_y q_z), (q_0^2 + q_z^2 - q_x^2 - e_y^2) \\ a\sin[2(q_0 q_y - q_x q_z)] \\ a\tan 2[2(q_0 q_z + q_x q_y), (q_0^2 + q_x^2 - q_y^2 - q_z^2) \end{Bmatrix} \tag{2.49}$$

Quaternion Formulation for a Constantly Rotating Rigid-Body [4, 26, 28, 33]

Formulation of a closed-form quaternion solution for a rigid-body under constant rotation is possible; however, this condition is more common to spacecraft rather than aircraft applications [26].

The development of a closed-form quaternion solution to an aircraft experiencing constant angular rates is an excellent method for verification and validation of the numerical algorithm method derived and implemented to integrate the quaternion formulation. Therefore, for a rigid-body rotating at a constant angular velocity, the governing system of differential equations may be written in quaternion form as Equations 2.50 and 2.51.

$$\{\dot{Q}\} = [\mathrm{K}]\{Q\} = 0 \tag{2.50}$$

$$[\mathrm{K}] = \frac{1}{2}\begin{bmatrix} 0 & -p & -q & -r \\ p & 0 & r & -q \\ q & -r & 0 & p \\ r & q & -p & 0 \end{bmatrix}$$

(2.51)

The solution to the first-order linear differential equation given as Equation 2.50 is presented as Equation 2.52 with the full derivation presented in Appendix B.

$$\{Q\} = \left[[i]\cos(\omega t/2) + \frac{2}{\omega}[\mathrm{K}]\sin(\omega t/2) \right]\{Q\}_{t=0}$$

(2.52)

An excellent method for testing this numerical algorithm is to utilize the special case where the initial conditions of all three Euler angles are zero, given be Equation 2.53, reducing the quaternion to the form presented in Equation 2.54.

$$\begin{Bmatrix} q_0(0) \\ q_x(0) \\ q_y(0) \\ q_z(0) \end{Bmatrix} = \begin{Bmatrix} 1 \\ 0 \\ 0 \\ 0 \end{Bmatrix}$$

(2.53)

$$\begin{Bmatrix} q_0 \\ q_x \\ q_y \\ q_z \end{Bmatrix} = \begin{Bmatrix} \cos(\omega t/2) \\ (p/\omega)\sin(\omega t/2) \\ (q/\omega)\sin(\omega t/2) \\ (r/\omega)\sin(\omega t/2) \end{Bmatrix}$$

(2.54)

2.2 Signal Processing

2.2.1 Signal Noise Corruption

Contamination of sensor signals is common, if not expected, when operating in variable environments that may cause a deviation of the measured signal from the true signal. Such environments include operational environments with extreme weather conditions and fluctuations in the Earth's magnetic field that may deviate and disrupt the sensor signal. The hardware environment of the sensor also plays a role. The hardware environment may allow the interface and instrumentation of the surrounding electronics to cause interference and degradation of the signal of concern. Another consideration to signal noise corruption is the surrounding signal interface with the electronic operating environment. Interaction with surrounding electronics may cause signal corruption and inaccuracies to occur.

For accurate and reliable attitude estimation algorithms to be developed, it is necessary and critical to filter the sensor signals of concern in the presence of noise. A standard model for noise corruption is presented as Equation 2.55, where the measured value of the sensor signal is the sum of the sensor signal and the measurement noise [46].

$$\begin{array}{ccccc} Measured\ Value & = & True\ Value & + & Measurement\ Noise \\ \tilde{x} & = & x & + & v(t) \end{array} \tag{2.55}$$

2.2.2 Influence of a Biased Signal [21, 28, 33, 42, 46, 48]

The bias, or bias error, of a rate gyro is the signal output from the gyro when it is not experiencing any rotational movement. Almost all rate gyros have inherent biases in them as a source of measurement error. Typically, a gyro bias is presented as a voltage that corresponds to a rotational velocity measured in degrees per second. Unfortunately, gyro biases are not typically fixed values, but vary over time. A biased rate gyro signal may occur for a multitude of reasons ranging from errors in the manufacturing process to inaccuracies during the calibration process of the hardware setup.

Biased signals must be accounted for in the signal processing algorithm to ensure precise measurement of the signal model. Therefore, Equation 2.55 may be expanded to include a term that accounts for the signal biases that may occur [46, 48], and is shown by Equation 2.56.

$$\begin{array}{ccccccc} Measured\ Value & = & True\ Value & + & Measurement\ Noise & + & Bias \\ \tilde{x} & = & x & + & v(t) & + & b(t) \end{array} \tag{2.56}$$

Estimation of a bias associated with a rate gyro measurement may range from simple to difficult. Algorithms utilized for bias estimation depend upon the aircraft or vehicle operating environment and the information known about the rate gyro. In this work, an Extended Kalman Filter (EKF) algorithm is implemented utilizing the multi-dimensional device model, rate gyros, and accelerometer measurements operating in a multitude of scenarios.

2.2.3 The Kalman Filter [5, 26, 28, 29, 30, 31, 39]

The Kalman filter is a set of mathematical equations that provide a sequential recursive means to estimate the state of a process in a manner that minimizes the mean of the squared error, based upon actual system measurements and predicted state values [29]. The Kalman filter (KF) is a powerful state estimator because of its ability to support estimates of the past, present, and future states even when exact information and the nature of the modeled system is not known [28].

The purpose of the Kalman filter is to mathematically force the measured and estimated values of the Kalman filter's states to converge and for the covariance, or the difference in value of the estimate and true states, to be minimized during the algorithms process. Figure 2.8 displays a graphical representation of the Kalman filter's underlying mechanics.

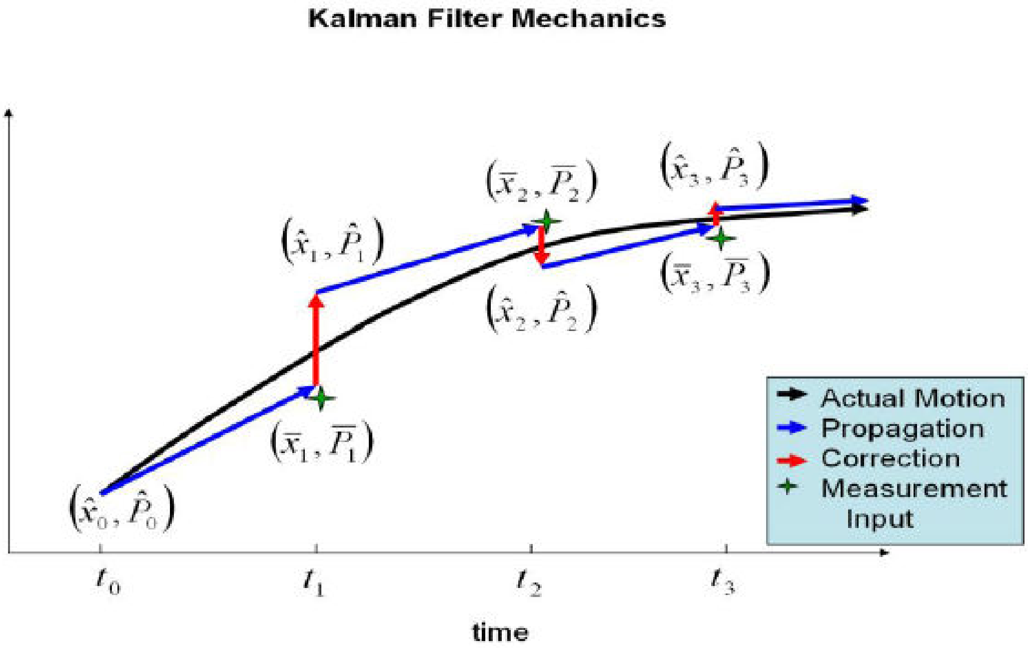

Figure 2.8: Kalman Filter Mechanics [29]

The Kalman filter was developed by R.E Kalman in 1960 when he published his paper, which has since become famous, detailing a mathematical solution to a discrete-data linear filtering problem. Since the inception of the Kalman filter, the Kalman filter has become a large subject of extensive research and application methods, especially in the area of autonomous and unmanned navigation applications.

The Extended Kalman Filter [6, 26, 28, 29, 30, 39, 48]

As discussed previously, the Kalman filter is a set of mathematical equations addressing the problem of estimating a state governed, typically, by a set of linear stochastic difference equations. In the case that the process or measurement correlation is nonlinear, an extended Kalman filter must be used. The extended Kalman filter is a Kalman filter that linearizes about the current mean and covariance [28].

Nonlinearities in modeled systems include Coulomb friction inherent to the system, centripetal forces experience in rotational systems, and sensor saturation or an imposed dead-zone of a motor model in the system. Nonlinear system models must be developed prior to operation. Unlike linear systems, nonlinear systems do not possess the superposition characteristic associated with linear systems where multiple systems may be added to one another to form a single, composite operating system. The addition of one nonlinear system to another creates a condition where the conglomerate of nonlinear systems become susceptible to multiple nonlinear system models mimicking the characteristics of the overall system, therefore not producing the true output of the overall system operation.

For a continuous-time, nonlinear system, the nonlinear state-space truth model is given as Equation 2.57.

$$\begin{gathered}\dot{\mathbf{x}}(t) = \mathbf{f}(\mathbf{x}(t), \mathbf{u}(t), t) + G(t)\mathbf{w}(t) \\ \tilde{\mathbf{y}}(t) = \mathbf{h}(\mathbf{x}(t), t) + \mathbf{v}(t)\end{gathered} \tag{2.57}$$

where f(x(t), u(t), t) and h(x(t), t) are assumed to be continuously differentiable with respect to the state, x(t). The variables w(t) and v(t) represent zero-mean Gaussian noise processes, while the control input, u(t), represents a deterministic quantity.

There are numerous ways to produce a linearized form of the Kalman filter while working in a nonlinear operating environment. The implementation of the extended Kalman filter is one of these methods. The main concept utilized in the implementation of the extended Kalman filter is that the EKF assumes that the true state is sufficiently close to the estimated state, allowing for the error dynamics to be represented fairly accurately by a Taylor-Series expansion of the first-order about a nominal state, x(t), as shown by Equation 2.58 [28, 30].

$$\mathbf{f}(x(t), \mathbf{u}(t), t) \cong \mathbf{f}(\bar{\mathbf{x}}(t), \mathbf{u}(t), t) + \left.\frac{d\mathbf{f}}{d\mathbf{x}}\right|_{\bar{\mathbf{x}}(t)} [\mathbf{x}(t) - \bar{\mathbf{x}}(t)] \tag{2.58}$$

The output equation may also be expanded upon, and is expressed as Equation 2.59.

$$\mathbf{h}(\mathbf{x}(t),t) \cong \mathbf{h}(\overline{\mathbf{x}}(t),t) + \left.\frac{d\mathbf{h}}{d\mathbf{x}}\right|_{\overline{\mathbf{x}}(t)} [\mathbf{x}(t) - \overline{\mathbf{x}}(t)] \tag{2.59}$$

In the extended Kalman filter, the current estimate of the state is used as the nominal state estimate as shown in Equation 2.60.

$$\mathbf{x}(t) = \overline{\mathbf{x}}(t) \tag{2.60}$$

Utilizing Equation 2.60, and applying it to both sides of Equations 2.58 and 2.59 allows for the formulation of Equations 2.61 and 2.62,

$$E\{\mathbf{f}(x(t),\mathbf{u}(t),t)\} = \mathbf{f}(\hat{x}(t),\mathbf{u}(t),t) \tag{2.61}$$

$$E\{\mathbf{h}(\mathbf{x}(t),t)\} = \mathbf{h}(\hat{\mathbf{x}}(t),t) \tag{2.62}$$

where the structure of the state and output estimate of the extended Kalman filter may be given as Equations 2.63 and 2.64 respectively.

$$\dot{\hat{\mathbf{x}}}(t) = \mathbf{f}(\hat{\mathbf{x}}(t),\mathbf{u}(t),t) + K(t)[\tilde{\mathbf{y}}(t) - \mathbf{h}(\hat{\mathbf{x}}(t),t)] \tag{2.63}$$

$$\hat{\mathbf{y}}(t) = \mathbf{h}(\hat{\mathbf{x}}(t),t) \tag{2.64}$$

A summary of the continuous-time extended Kalman filter is presented in Table 2.3.

System Model	$\dot{\mathbf{x}}(t)=\mathbf{f}(\mathbf{x}(t),\mathbf{u}(t),t)+G(t)\mathbf{w}(t)\sim N(\mathbf{0},Q(t))$ $\tilde{\mathbf{y}}(t)=\mathbf{h}(\mathbf{x}(t),t)+\mathbf{v}(t)\sim N(\mathbf{0},R(t))$
Initialization of the State and Covariance	$\hat{\mathbf{x}}(t_0)=\hat{\mathbf{x}}_0$ $P_0=E\left\{\tilde{\mathbf{x}}(t_0)\tilde{\mathbf{x}}^T(t_0)\right\}$
Kalman Gain	$K(t)=P(t)H^T(\hat{\mathbf{x}}(t),t)R^{-1}(t)$
Update Covariance	$\dot{P}(t)=F(\hat{\mathbf{x}}(t),t)P(t)+P(t)F^T(\hat{\mathbf{x}}(t),t)$ $-P(t)H^T(\hat{\mathbf{x}}(t),t)R^{-1}(t)H(\hat{\mathbf{x}}(t),t)P(t)+G(t)Q(t)G^T(t)$ $F(\hat{\mathbf{x}}(t),t)\equiv\left.\frac{d\,\mathrm{f}}{d\mathbf{x}}\right\|_{\hat{\mathbf{x}}(t)}$, $H(\hat{\mathbf{x}}(t),t)\equiv\left.\frac{d\mathbf{h}}{d\mathbf{x}}\right\|_{\hat{\mathbf{x}}(t)}$
Estimation "State Update"	$\dot{\hat{\mathbf{x}}}(t)=\mathbf{f}(\hat{x}(t),u(t),t)+K(t)[\tilde{y}(t)-h(\hat{x}(t),t)]$

Table 2.3: Continuous-Time Extended Kalman Filter Algorithm

The matrices, $F(\hat{\mathbf{x}}(t),t), H(\hat{\mathbf{x}}(t),t)$, are generally not consistent. Therefore, a steady-state gain cannot be determined resulting in an increased computational burden since n(n+1)/2 nonlinear equations need to be integrated in order to determine P(t). A summary of the continuous-discrete extended Kalman filter is given in Table 2.4.

System Model	$\dot{\mathbf{x}}(t) = \mathbf{f}(\mathbf{x}(t), \mathbf{u}(t), t) + G(t)\mathbf{w}(t) \sim N(\mathbf{0}, Q(t))$ $\tilde{\mathbf{y}}_k = \mathbf{h}(\mathbf{x}_k, t) + \mathbf{v}_k \sim N(\mathbf{0}, R_k)$
Initialization of the State and Covariance	$\hat{\mathbf{x}}(t_0) = \hat{\mathbf{x}}_0$ $P_0 = E\left\{\tilde{\mathbf{x}}(t_0)\tilde{\mathbf{x}}^T(t_0)\right\}$
Kalman Gain	$K_k = P_k^- H_k^T(\hat{\mathbf{x}}_k^-)[H_k(\hat{\mathbf{x}}_k^-)P_k^- H_k^T(\hat{\mathbf{x}}_k^-) + R_k]^T$ $H_k(\hat{\mathbf{x}}_k^-) \equiv \left.\frac{\partial h}{\partial x}\right\|_{\hat{\mathbf{x}}_k^-}$
Update Covariance	$\hat{\mathbf{x}}_k^+ = \hat{\mathbf{x}}_k^- + K_k[\tilde{y}_k - \mathbf{h}(\hat{\mathbf{x}}_k^-)]$ $\mathbf{P}_k^+ = [I - K_k H_k(\hat{\mathbf{x}}_k^-)]\mathbf{P}_k^-$
Estimation "State Update"	$\dot{\hat{\mathbf{x}}}(t) = \mathbf{f}(\hat{x}(t), u(t), t)$ $\dot{\mathbf{P}}(t) = F(\hat{x}(t), t)P(t) + P(t)F^T(\hat{x}(t), t) + G(t)Q(t)G^T(t)$ $F(\hat{x}(t), t) \equiv \left.\frac{\partial \mathbf{f}}{\partial \mathbf{x}}\right\|_{\hat{x}(t)}$

Table 2.4: Continuous-Discrete Extended Kalman Filter Algorithm

The approach utilized in the application and implementation of the extended Kalman filter assumes the true state is "close" to the estimated state. This restriction can be very destructive for highly nonlinear applications with large initial condition errors. Proving convergence in the extended Kalman filter is extremely difficult for simple systems where the initial conditions are not well known. Despite this, the extended Kalman filter is used heavily in practice, and is typically robust to initial condition errors, which may be verified through simulations [28].

An alternative approach to the extended Kalman filter is to linearize about the nominal state vector known *a priori*, instead of about the current state vector. For this method, the Kalman filter equations for the output estimate are given by Equations 2.65 and 2.66.

$$\begin{aligned}\dot{\hat{\mathbf{x}}}(t) &= \mathbf{f}(\bar{\mathbf{x}}(t), \mathbf{u}(t), t) + F(\bar{\mathbf{x}}(t), t)[\hat{\mathbf{x}}(t) - \bar{\mathbf{x}}(t)] \\ &+ K(t)\left\{\tilde{\mathbf{y}}(t) - \mathbf{h}(\bar{\mathbf{x}}(t), t) - H(\bar{\mathbf{x}}(t), t)[\hat{\mathbf{x}}(t) - \bar{\mathbf{x}}(t)]\right\}\end{aligned} \tag{2.65}$$

$$\hat{\mathbf{y}}(t) = \mathbf{h}(\overline{\mathbf{x}}(t),t) + H(\overline{\mathbf{x}}(t),t)[\hat{\mathbf{x}}(t) - \overline{\mathbf{x}}(t)] \tag{2.66}$$

The covariance equation remains in the same form as presented in Table 2.5, with the partial derivatives now evaluated at the nominal state rather than the current state. This approach is known as the "*Linearized Kalman Filter*" [28, 30]. Typically, the linearized Kalman filter is less accurate compared to the extended Kalman filter; however, the computational burden associated with this method is greatly reduced because the nominal state is known.

Enhancement of the extended Kalman filter accuracy may also be made by implementing a continuous linearization about the most recent estimate and then determining once again the covariance matrix, P, and Kalman gain, K. This method is known as the "*Iterated Extended Kalman Filter*" [28, 30]. The iterations of this method are given by Equations 2.66, 2.67, and 2.68 where, $\hat{\mathbf{x}}_{k_0}^{+} = \hat{\mathbf{x}}_{k}^{-}$. In this approach, the iterations are continued until the estimate no longer experiences an improvement.

$$\hat{\mathbf{x}}_{k_i}^{+} = \hat{\mathbf{x}}_{k}^{-} + K_{k_i}\left[\tilde{\mathbf{y}}_k - \mathbf{h}(\hat{\mathbf{x}}_{k_i}^{+}) - H_k(\hat{\mathbf{x}}_{k_i}^{+})(\hat{\mathbf{x}}_{k}^{-} - \hat{\mathbf{x}}_{k_i}^{+})\right] \tag{2.66}$$

$$K_{k_i} = P_k^{-} H_k^{T}(\hat{\mathbf{x}}_{k_i}^{+})\left[H_k(\hat{\mathbf{x}}_{k_i}^{+}) P_k^{-} H_k^{T}(\hat{\mathbf{x}}_{k_i}^{+}) + R_k\right]^{-1} \tag{2.67}$$

$$P_{k_i}^{+} = \left[I - K_{k_i} H_k(\hat{\mathbf{x}}_{k_i}^{+})\right] P_k^{-} \tag{2.68}$$

Kalman Filter Foundations [6, 26, 28, 30, 31, 39]

The development of a Kalman filter requires adequate knowledge of the dynamics and signal measurements that are critical to the modeled system. An initial error in the dynamic modeling of the system or the associated system noise will result in a propagated error during the entire operation period of the filter. An assumption that is often made is the vehicle or aircraft of study utilizes relatively accurate sensors and the system model implemented is generally precise.

In the Kalman filter, the state error covariance matrix, P, possess a large amount of tuning sensitivity. This tuning sensitivity is accountable when the standard deviation of the noise to signal amplitude ratio is greater than a unity value or in the case where the diagonal elements of the matrix are very close to zero in value. In the case where the diagonal elements are set very close to zero, the filter no longer continues to update the system material causing either a divergence of the filter or possibly a very long convergence time. When the ratio of standard deviation of the noise to signal amplitude is greater than unity, it may be said that the measured signals are saturated by the sensor noise resulting from failed (or failing) sensors.

To ensure the correct operation of the filter, the biases of the sensors utilized must be accurately known in order to produce a correct tracking estimate [30]. However, as long as terms of the covariance matrix are not set to zero, the filter will converge nicely to the expected estimates. The only difference will be the time to convergence.

A process in the Kalman filter known as "warm starting" is where the convergence transient of the filter is reproduced and good initial state estimates are provided [28]. This "warm starting" leads to a lower initial covariance matrix. In the case that no "a priori" state information is provided or exists, the filter may still be initialized by setting the diagonal elements of the state covariance matrix to infinity, with the off-diagonal elements of the matrix set equal to zero and some arbitrary state vectors. Initializing the state covariance matrix to infinity allows the filter to ignore the initial state estimate. Essentially, this allows the filter to act like a recursive filter in the absence of process noise. However, in the presence of process noise, the filter will ignore the initial state estimates. Therefore, the filter acts in a quasi-recursive nature until the state vector and the covariance matrix, P, can be updated and allowed to propagate.

For verification and validation of the filter operation online, the state error residuals calculated from the difference between the estimated states produced by the filter's algorithm and the input state measurements are needed. The state error cannot be calculated using the true state values because if the true states are known, the need for a filter is negligible. The variance of the estimated states, represented by the diagonal elements of the output state covariance matrix, allow for a comparative analysis of the state error determined within the $\pm 1\sigma$ and $\pm 3\sigma$ bounds [28, 30, 39]. This assessment verifies proper filter operation and order of the filter state model.

Proper operation of the filter algorithm implemented requires, from a statistical view, approximately 68% of the state error to lie within the defined $\pm 1\sigma$ bounds and approximately 99% of the state error to lie within the $\pm 3\sigma$ bounds. These statistical bounds imposed on the state error as determined from the output state covariance matrix, are developed under the assumption the filter is operating with a Gaussian distribution according to the Central Limit Theorem presented in Appendix C. An assessment such as this only verifies the steady-state operation of the filter because the state covariance update and propagation equations do not take the system inputs into account.

2.2.4 Design of an Extended Kalman Filter for Attitude Estimation Utilizing Rate Gyros [17, 26, 28, 30, 33, 34]

In this feasibility study, an extended Kalman filter algorithm was utilized to sequentially estimate the attitude and rotational rate bias values of a vehicle through the use of a dual-arc accelerometer array for producing attitude estimates utilizing low-cost sensors and rate gyroscopes. As mentioned previously, numerous parameterizations may be utilized to represent attitude. Common methods for representing attitude are through the use of Euler angles, rotational vectors, or quaternions. In this study, quaternions are implemented in the design of the extended Kalman filter since no singularities are present and the kinematic equation is bilinear.

The successful implementation of quaternions in a standard EKF model is difficult since the quaternions must obey a normalization constraint. This constraint of the quaternion mathematics can violate the linear measurement update process associated with the EKF. Therefore, a multiplicative error quaternion must be computed to deal with this short coming. Formulation and operation of the multiplicative quaternion error reduces the higher-order terms, therefore allowing the four-component quaternion to be replaced by a three-component error vector.

Multiplicative Quaternion Error Formulation for Attitude Estimation [26, 28]

The extended Kalman filter developed and implemented in this feasibility study for the purpose of accurate and reliable attitude estimation of a vehicle or aircraft operating in three-dimensional space begins with the formulation of the quaternion kinematic model given as Equation 2.69.

$$\dot{q} = \frac{1}{2}\Xi(q)w = \frac{1}{2}\Omega(w)q$$

$$Where: \quad \Xi(q) = \begin{bmatrix} q_0 I_{3x3} + [\mathbf{q}\times] \\ -\mathbf{q}^T \end{bmatrix}$$

$$q = [q_0 \ \mathbf{q}^T]^T; \ \mathbf{q} = [q_x q_y q_z]^T; \ \mathbf{q}^{-1} = \begin{bmatrix} q_0 \\ \mathbf{q} \end{bmatrix} \tag{2.69}$$

The quaternion, q, must obey a normalization constraint mentioned previously, where $qq^T = 1$. A direct design method for construction of an extended Kalman filter is to utilize Equation 2.69 in the EKF presented in Table 2.4. The additive approach used in this formulation however, will eliminate the normalization constraint necessary [26]. A simple example of this may be shown below in Equations 2.70 through 2.72 where the additive error quaternion shown as Equation 2.72 is not close to being a unit vector as the normalization constraint requires. This result shown through the use of this simple example may cause significant difficulties and errors during the filtering process of the EKF algorithm [28].

$$q = [0, 0, \sqrt{0.001}, \sqrt{0.999}]^T \tag{2.70}$$

$$\hat{q} = [0, 0, 0, 1]^T \tag{2.71}$$

$$\hat{q} - q = [0, 0, -\sqrt{0.001}, -\sqrt{0.999}]^T \tag{2.72}$$

A true approach to this problem involves the use of the multiplicative error quaternion shown below as Equation 2.73. The quaternion inverse is defined previously in Equation 2.69. Taking the derivative with respect to time of Equation 2.73 leads to the derivation of Equation 2.74, an estimate of the quaternion kinematic model, where ⊗ represents the tensor product.

$$\delta q = q \otimes \hat{q}^{-1} \tag{2.73}$$

$$\delta \dot{q} = \dot{q} \otimes \hat{q}^{-1} + q \otimes \dot{\hat{q}}^{-1} \tag{2.74}$$

$$\dot{\hat{q}} = \frac{1}{2}\Xi(\hat{q})\hat{w} = \frac{1}{2}\Omega(\hat{w})\hat{q} \tag{2.75}$$

If we take the time derivative of $\hat{q} \otimes \hat{q}^{-1} = [0,0,0,1]^T$, we obtain Equation 2.76.

$$\dot{\hat{q}} \otimes \hat{q}^{-1} + \hat{q} \otimes \dot{\hat{q}}^{-1} = 0 \tag{2.76}$$

Inserting Equation 2.75 into 2.76 gives Equation 2.77.

$$\frac{1}{2}\Omega(\hat{w})\hat{q} \otimes \hat{q}^{-1} + \hat{q} \otimes \dot{\hat{q}}^{-1} = 0 \tag{2.77}$$

Since $\hat{q} \otimes \hat{q}^{-1} = [0,0,0,1]^T$, and defining $\Omega(\hat{w})$ as Equation 2.78, Equation 2.77 may be reduced down to the form presented in Equation 2.79.

$$\Omega(w) = \begin{bmatrix} -[w\times] & w \\ -w^T & 0 \end{bmatrix} \tag{2.78}$$

$$\frac{1}{2}\begin{bmatrix} \hat{w} \\ 0 \end{bmatrix} + \hat{q} \otimes \dot{\hat{q}}^{-1} = 0 \tag{2.79}$$

Solving for $\dot{\hat{q}}^{-1}$ yields Equation 2.80 as shown below

$$\dot{\hat{q}}^{-1} = -\frac{1}{2}\hat{q}^{-1} \otimes \begin{bmatrix} \hat{w} \\ 0 \end{bmatrix} \tag{2.80}$$

Utilizing the identity given in Equation 2.81 and substituting it with Equation 2.79 into Equation 2.74, and using the definition of the multiplicative error quaternion given in Equation 2.73 gives the following formulation presented as Equation 2.82.

$$\dot{q} = \frac{1}{2}\Omega(w)q = \frac{1}{2}\begin{bmatrix} w \\ 0 \end{bmatrix} \otimes q \tag{2.81}$$

$$\delta\dot{q} = \frac{1}{2}\left\{\begin{bmatrix} w \\ 0 \end{bmatrix} \otimes \delta q - \delta q \otimes \begin{bmatrix} \hat{w} \\ 0 \end{bmatrix}\right\} \tag{2.82}$$

Defining the angular velocity as Equation 2.83, we can substitute Equation 2.83 into Equation 2.82 leading to the derivation of Equation 2.84.

$$\begin{gathered} \delta w \equiv w - \hat{w} \\ w = \hat{w} + \delta w \end{gathered} \tag{2.83}$$

$$\delta\dot{q} = \frac{1}{2}\left\{\begin{bmatrix} \hat{w} \\ 0 \end{bmatrix} \otimes \delta q - \delta q \otimes \begin{bmatrix} \hat{w} \\ 0 \end{bmatrix}\right\} + \frac{1}{2}\begin{bmatrix} \delta w \\ 0 \end{bmatrix} \otimes \delta q \tag{2.84}$$

Utilizing the identities presented in [28] and presented in this work as Equations 2.85, Equation 2.86 may be derived by substituting these identities into Equation 2.84.

$$\begin{gathered} \begin{bmatrix} \hat{w} \\ 0 \end{bmatrix} \otimes \delta q = \Omega(\hat{w})\delta q \\ \delta q \otimes \begin{bmatrix} \hat{w} \\ 0 \end{bmatrix} = \Gamma(\hat{w})\delta q \\ where:\ \Gamma(w) \equiv \begin{bmatrix} [w\times] & w \\ -w^T & 0 \end{bmatrix} \end{gathered} \tag{2.85}$$

$$\delta\dot{q} = -\begin{bmatrix} [\hat{w}\times]\delta\mathbf{q} \\ 0 \end{bmatrix} + \frac{1}{2}\begin{bmatrix} \delta w \\ 0 \end{bmatrix} \otimes \delta q \tag{2.86}$$

In Equation 2.86, the nonlinear term is presented in the last term on the right-hand side and its first-order approximation is given by

$$\frac{1}{2}\begin{bmatrix}\delta w\\ 0\end{bmatrix}\otimes\delta q\approx\frac{1}{2}\begin{bmatrix}\delta w\\ 0\end{bmatrix} \tag{2.87}$$

If Equation 2.87 is substituted into Equation 2.86, the following linearized model may be derived and is presented as Equations 2.88 and 2.89.

$$\delta\dot{q}=-[\hat{w}\times]\delta\mathbf{q}+\frac{1}{2}\delta w \tag{2.88}$$

$$\delta\dot{q}_0=0 \tag{2.89}$$

From the formulation and derivation performed, it may be seen that the fourth error-quaternion component is a constant value. Therefore, the order of the system implemented in the EKF model may be reduced by one state, reducing the overall computational burden of the filter algorithm.

Design of a Rate Gyro Model for an Extended Kalman Filter [6, 26, 28, 48]

The work completed in this feasibility study focused on the development of an algorithm and device capable of determining the attitude of a vehicle given a dual-arc accelerometer array and accurately estimate the rate gyro bias in real-time. A model widely used for simulation of this sensor was originally stated in [48] and is shown here as Equations 2.90 and 2.91

$$\omega=\tilde{\omega}-\beta-\eta_v \tag{2.90}$$

$$\dot{\beta}=\eta_u \tag{2.91}$$

where η_v *and* η_u are zero-mean Gaussian white-noise processes with covariances given by $\sigma_v^2 I_{3x3}$ *and* $\sigma_u^2 I_{3x3}$, respectively. β, represents the bias vector, and $\tilde{\omega}$ is the measured observation.

The estimated angular velocity of the vehicle may then be given as Equation 2.92 where the estimated bias differential equation may be shown as Equation 2.93.

$$\hat{\omega}=\tilde{\omega}-\hat{\beta} \tag{2.92}$$

$$\dot{\hat{\beta}} = 0$$

(2.93)

If we substitute Equation 2.90 and 2.92 into Equation 2.83 given previously, we obtain

$$\delta\omega = -(\Delta\beta + \eta_v)$$

(2.94)

where $\Delta\beta \equiv \beta - \hat{\beta}$. Inserting Equation 2.94 into Equation 2.88 given previously, we obtain

$$\delta\dot{\mathbf{q}} = -[\hat{\omega}\times]\delta\mathbf{q} - \frac{1}{2}(\Delta\beta + \eta_v)$$

(2.95)

A common simplification technique utilized is to assume a small angle approximation where $\delta\mathbf{q} \approx \delta\alpha / 2$, and $\delta\alpha$ contains the components of roll, pitch, and yaw error angles for the rotation sequence. Applying this simplification technique to Equation 2.95 gives way to the formulation of Equation 2.96.

$$\delta\dot{\alpha} = --[\hat{\omega}\times]\delta\alpha - (\Delta\beta + \eta_v)$$

(2.96)

Utilizing this approach and simplification techniques minimizes the use of factors of 1/2 and 2 in the formulation of the extended Kalman filter algorithm method and gives direct meaning to the state error-covariances, which may then be used to formulate the ±1σ and ±3σ bounds [28]. The model for the extended Kalman filter may now be given as Equation 2.97

$$\Delta\dot{\tilde{\mathbf{x}}}(t) = F(\hat{\mathbf{x}}(t),t)\Delta\tilde{\mathbf{x}}(t) + G(t)\mathbf{w}(t)$$

(2.97)

Where:

$$\Delta\tilde{\mathbf{x}}(t) \equiv \left[\delta\alpha^T(t), \Delta\beta^T(t)\right]^T$$

$$\mathbf{w}(t) \equiv \left[\eta_v^T(t)\eta_u^T(t)\right]^T$$

(2.98)

$$F(\hat{\mathbf{x}}(t),t) = \begin{bmatrix} -[\hat{\omega}(t)\times] & -I_{3x3} \\ 0_{3x3} & 0_{3x3} \end{bmatrix}, G(t) = \begin{bmatrix} -I_{3x3} & 0_{3x3} \\ 0_{3x3} & I_{3x3} \end{bmatrix}$$

(2.99)

$$Q(t) = \begin{bmatrix} \sigma_v^2 I_{3x3} & 0_{3x3} \\ 0_{3x3} & \sigma_u^2 I_{3x3} \end{bmatrix}$$

(2.100)

As it may be seen, these matrices are now 6 x 6 matrices because the order of the system has been reduced by one original state. Establishment of the sensitivity matrix, $H_k(\hat{\mathbf{x}}_{\mathbf{k}}^{\mathbf{-}})$, for implementation in the extended Kalman filter algorithm requires the use of multiple, n, vector measurements as shown in Equation 2.101, where A(q) denotes the actual attitude matrix and "diag" denotes a diagonal matrix of the correlated dimension.

$$\tilde{y}_k = \left.\begin{bmatrix} A(\mathbf{q})r_1 \\ A(\mathbf{q})r_2 \\ . \\ . \\ A(\mathbf{q})r_n \end{bmatrix}\right|_{t_k} + \left.\begin{bmatrix} \upsilon_1 \\ \upsilon_2 \\ . \\ . \\ \upsilon_n \end{bmatrix}\right|_{t_k} \equiv \mathbf{h}_k(\hat{\mathbf{x}}_k) + v_k$$

(2.101)

$$R = diag\left[\sigma_1^2 I_{3x3} \quad \sigma_2^2 I_{3x3} \quad . \quad . \quad \sigma_n^2 I_{3x3}\right]$$

(2.102)

The attitude matrix, A(q), is defined as

$$A(\mathbf{q}) = \Xi^T(q)\Psi(q)$$

(2.103)

Where:

$$\Xi(q) \equiv \begin{bmatrix} q_0 I_{3x3} + [\mathbf{q}\times] \\ -\mathbf{q}^T \end{bmatrix}$$

$$\Psi(q) \equiv \begin{bmatrix} q_0 I_{3x3} - [\mathbf{q}\times] \\ -\mathbf{q}^T \end{bmatrix}$$

(2.104)

The propagation of the attitude may then be written as

$$A(\mathbf{q}) = A(\delta\mathbf{q})A(\hat{\mathbf{q}}^-)$$

(2.105)

where the first-order approximation of the error-attitude matrix is represented by Equation 2.106 and $\delta\alpha$ once again represents the small angle approximation utilized previously.

$$A(\delta\mathbf{q}) \approx I_{3x3} - [\delta\alpha\times] \tag{2.106}$$

For an individual sensor measurement, the true and estimated body vectors may be given by Equations 2.107 and 2.108 respectively.

$$b = A(\mathbf{q})r \tag{2.107}$$

$$\hat{b}^{-} = A(\hat{\mathbf{q}}^{-})r \tag{2.108}$$

Substituting Equations 2.105 and 2.106 into Equations 2.107 and 2.108 yields Equation 2.109, where $\Delta b \equiv b - \hat{b}^{-}$.

$$\Delta b = [A(\hat{\mathbf{q}}^{-})r\times]\delta\alpha \tag{2.109}$$

With these relationships established, the sensitivity matrix may now be defined as Equation 2.110, where the number of columns is again six, the order of the reduced-order state.

$$H_k(\hat{\mathbf{x}}_k^{-}) = \left.\begin{bmatrix} [A(\hat{\mathbf{q}}^{-})r_1\times] & 0_{3x3} \\ [A(\hat{\mathbf{q}}^{-})r_2\times] & 0_{3x3} \\ \cdot & \cdot \\ \cdot & \cdot \\ [A(\hat{\mathbf{q}}^{-})r_n\times] & 0_{3x3} \end{bmatrix}\right|_{t_k} \tag{2.110}$$

With the sensitivity matrix now defined, the attitude determination and rate gyro bias estimation extended Kalman filter is summarized in Table 2.5. The first three diagonal elements of the output error-covariance matrix correspond to the attitude errors, while the last three diagonal elements correspond to the bias estimation errors. The Kalman gain, K, is determined through the use of R, the measurement-error covariance matrix and the sensitivity matrix given in Equation 2.110. The predicted performance of the extended Kalman filter algorithm for attitude and rate gyro bias estimation can be determined by checking the covariance of the diagonal elements of the attitude and bias estimation error covariance as stated previously

Initialization of the State and Covariance	$\hat{\mathbf{q}}(t_0)=\hat{\mathbf{q}}_0,\ \beta(t_0)=\beta_0$ $P(t_0)=P_0$
Kalman Gain	$K_k = P_k^- H_k^T(\hat{\mathbf{x}}_k^-)[H_k(\hat{\mathbf{x}}_k^-)P_k^- H_k^T(\hat{\mathbf{x}}_k^-)+R]^{-1}$ $H_k(\hat{\mathbf{x}}_k^-) = \left.\begin{bmatrix} [A(\hat{\mathbf{q}}^-)r_1\times]\,0_{3x3} \\ [A(\hat{\mathbf{q}}^-)r_2\times]\,0_{3x3} \\ . \quad\quad . \\ . \quad\quad . \\ [A(\hat{\mathbf{q}}^-)r_n\times]\,0_{3x3} \end{bmatrix}\right\|_{t_k}$
Update Covariance	$\hat{\hat{\mathbf{x}}}_k^+ = K_k[\tilde{y}_k - \mathbf{h}_k(\hat{\mathbf{x}}_k^-)]$ $\hat{\hat{\mathbf{x}}}_k^+ = \begin{bmatrix} \delta\hat{\alpha}_k^{+T} & \Delta\hat{\beta}_k^{+T} \end{bmatrix}^T$ $\mathbf{P}_k^+ = [I - K_k H_k(\hat{\mathbf{x}}_k^-)]\mathbf{P}_k^-$ $\mathbf{h}_k(\hat{\mathbf{x}}_k^-) = \left.\begin{bmatrix} A(\hat{\mathbf{q}}^-)r_1 \\ A(\hat{\mathbf{q}}^-)r_2 \\ . \\ . \\ A(\hat{\mathbf{q}}^-)r_n \end{bmatrix}\right\|_{t_k}$ $\hat{\mathbf{q}}_k^+ = \hat{\mathbf{q}}_k^- + \frac{1}{2}\Xi(\hat{\mathbf{q}}_k^-)\delta\hat{\alpha}_k^+,$ *renormalize quaternion* $\hat{\beta}_k^+ = \hat{\beta}_k^- + \Delta\hat{\beta}_k^+$
Estimation “State Update”	$\dot{\hat{\mathbf{q}}}(t) = \frac{1}{2}\Xi(\hat{\mathbf{q}}(t))\hat{\omega}(t)$ $\hat{\omega}(t) = \tilde{\omega}(t) - \hat{\beta}(t)$ $\dot{\mathbf{P}}(t) = F(\hat{x}(t),t)P(t) + P(t)F^T(\hat{x}(t),t) + G(t)Q(t)G^T(t)$ $F(\hat{\mathbf{x}}(t),t) = \begin{bmatrix} -[\hat{\omega}(t)\times] & -I_{3x3} \\ 0_{3x3} & 0_{3x3} \end{bmatrix}, G(t) = \begin{bmatrix} -I_{3x3} & 0_{3x3} \\ 0_{3x3} & I_{3x3} \end{bmatrix}$

Table 2.5: Extended Kalman Filter for Attitude and Rate Gyro Bias Estimation [28]

Chapter 3

Simulation Model Development

3.1 Nonlinear Aircraft Model

In this feasibility study, a nonlinear six degree-of-freedom aircraft model was utilized to verify and validate the feasibility and functionality of the innovative two-dimensional attitude estimation device and algorithm simulated in a real-world operating environment. Implementation of a nonlinear aircraft simulation model requires the use of the rigid-body equations given previously in section 2.1.2. In conjunction with the rigid-body equations, aircraft force and stability equations were utilized and are given in Appendix E for accurate and precise representation of an operational aircraft response to control surface inputs and the surrounding operating environment.

Simulation of the control surface inputs such as the horizontal tail input, asymmetric trailing-edge flap input, and symmetric rudder input, of the nonlinear aircraft model were conducted through the use of a six degree-of-freedom table look up model based on Mach number, altitude, and angle-of-attack. The simulations developed in this feasibility study were conducted for 10 second time periods at a "*cruising*" flight condition of 300 knots and an altitude of 20,000 feet.

The nonlinear plant model was implemented in conjunction with the attitude determination algorithm in three phases. The first phase of the feasibility study was to simulate the full nonlinear aircraft model performing only a pitch, or longitudinal, maneuver at the cruise flight condition, subject to the imposed loads due to aerodynamic, environmental, and thrust forces. The second phase of the feasibility study was to simulate the nonlinear aircraft model performing a roll, or transverse, maneuver only, again being subjected to the imposed loads due to the aerodynamic, environmental, and thrust forces. Upon verification of the correct operation of the proposed method, the third phase of the feasibility study was to be conducted. The third phase of the feasibility study was to conduct a combined pitch and roll (longitudinal/transverse) maneuver of the nonlinear aircraft simulation model to validate and confirm the proposed method and algorithm for accurate and reliable two-dimensional attitude estimates of both the pitch and roll angle for a maneuver operating in more than one dimension. In all three phases of the feasibility study performed, each phase was performed twice. The first iteration of each phase of the study was performed without the use of a Dryden Wind model. Upon verification of the method and algorithm operating correctly, the second iteration of each phase was implemented with the use of the Dryden Wind model to add enhanced dynamic environmental factors to the simulation model. The implementation of the Dryden Wind model allowed for the assessment and validation of the proposed methods ability to produce accurate and reliable attitude and rate gyro bias estimates while operating in a harsh and highly dynamic environment.

3.2 Dual Arc Accelerometer Array Device Model

3.2.1 Instrument Orientation [23]

For accurate simulation of an aircraft in three-dimensional, Cartesian Space, not only are the equations of motion governing the aircraft critical for successful implementation of the simulation models and algorithm, transformation equations must also be applied and developed accurately pertaining to the relationship between the reference axis and the instrument axis in order to achieve precise and reliable transformation relationships. Figure 3.1 below was utilized to establish and define the relationship between accelerometer locations and the center-of-gravity of the body-fixed axis and the reference axis. In this feasibility study, the center-of-gravity of the device and the center-of-gravity of the reference axes are the same, leading to the development of the accelerometer locations relative the device's center-of-gravity.

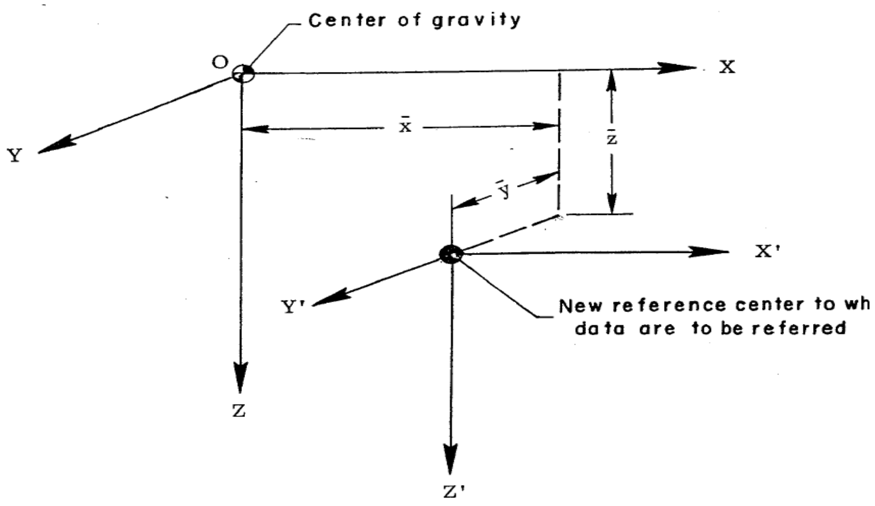

Figure 3.1: Axis System for Transformation from Vehicle C.G to new Reference C.G [23]

From Figure 3.1, three conclusions may be made with respect to the location of an accelerometer relative to the center-of-gravity location, such as:

- If the accelerometer is located forward of the center-of-gravity (CG) location, then $\bar{X}$ is positive.
- If the accelerometer is located right of the center-of-gravity (CG) location, then $\bar{Y}$ is positive.
- If the accelerometer is located down of the center-of-gravity (CG) location, then $\bar{Z}$ is positive.

Having established the accelerometer locations relative the device's center-of-gravity, the orientation of the accelerometer instrument axis may be established relative to the device reference axis for both the longitudinal and transverse accelerometer arrays. In Figure 3.2 below, the orientation of the instrument axis relative the device reference axis is established and characterized.

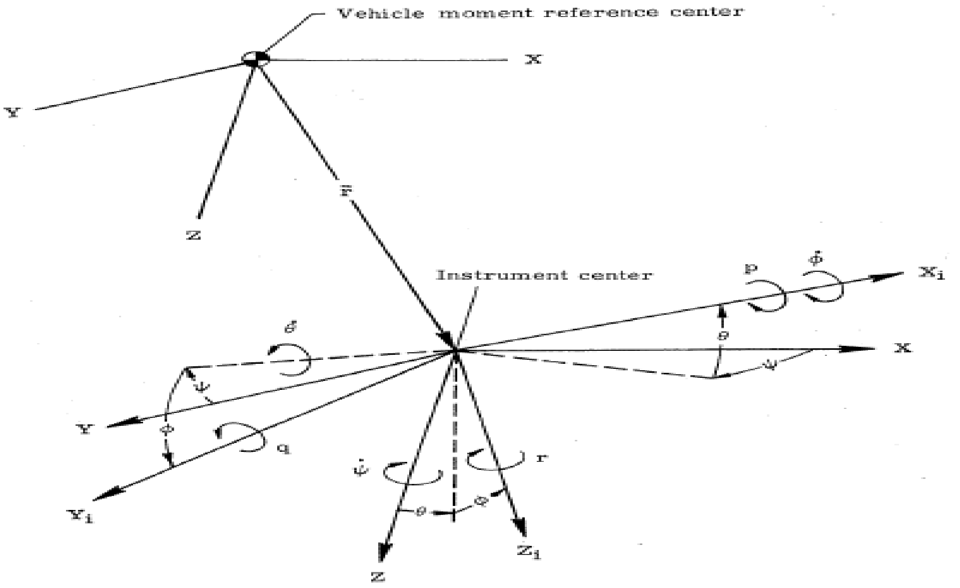

Figure 3.2: Instrument Axis Relative to the Device Reference Axis [23]

From Figure 3.2, two conclusions may be made with respect to the accelerometer orientation relative to the reference axis, such as:

- If the accelerometer is pitched up from the x-axis, then θ (pitch) is positive.
- If the accelerometer is banked downward from the y-axis, then ϕ (roll) is positive.

With the location and orientation of the instrumentation utilized relative to both the instrument axis and reference axis defined, the configuration for both the longitudinal and transverse accelerometer arrays may be established. In this feasibility study, a second accelerometer array in the transverse plane consisting of 13 additional accelerometers placed every 15 degrees about a semi-circular array will be included in order to assess and analyze movement not only in the longitudinal pitch plane, but in the transverse plane for both longitudinal and transverse maneuvers.

3.2.2 Device Configuration

The device models implemented in this feasibility study expanded up the previously [2, 6] developed and successfully implemented bias estimation algorithm and attitude determination device consisting of 13, one axis accelerometers equally spaced about a 180 degree semi-circular plane with a radius of 3 inches and a rate gyroscope positioned at the center of the device (center-of-gravity location of the device) orthogonal to the measurement plane of the axis as shown in Figure 3.3. In this figure, the device is oriented so the axes of the device are collinear with the vehicle's axes. The red axes indicate the Earth-fixed coordinate frame of reference, while the black axes indicate the reference coordinate frame of the device. The blue axes in this figure represent the body-fixed coordinate frame of the aircraft.

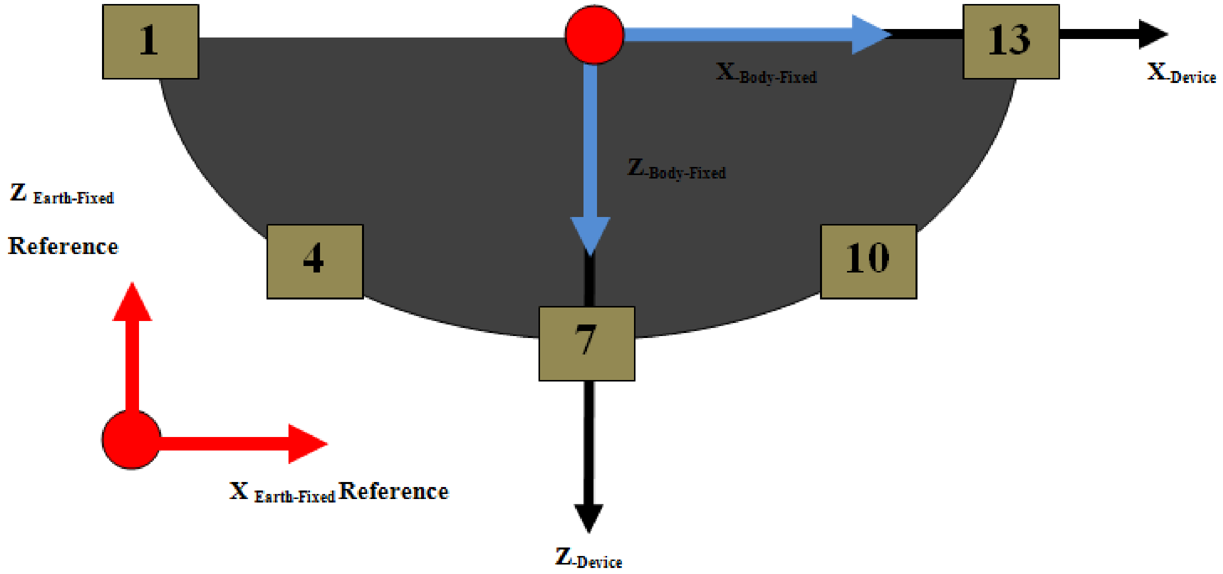

Figure 3.3: Longitudinal Pitch Array with Rate Gyro at 0 degrees of Pitch Displacement

The previously implemented method [2, 6] and device model utilized an accelerometer spacing of 15 degrees in the longitudinal, or x-z plane, beginning at negative 90 degrees pitch and moving counterclockwise about the semi-circular array to positive 90 degrees of pitch as shown once again in Figure 3.3. Therefore, in this previously established device configuration, Accelerometer # 1 lies on the negative x-axis at negative -90 degrees of pitch, Accelerometer # 4 at -45 degrees of pitch, Accelerometer # 7 lies directly on the tertiary, or z-axis, at 0 degrees, Accelerometer # 10 lies at 45 degrees of pitch, and Accelerometer # 13 lies on the positive primary axis, or x-axis of the aircraft, at 90 degrees of pitch. All angle measurements are taken with respect to the z-axis and are measured positive counterclockwise as shown in Figure 3.4.

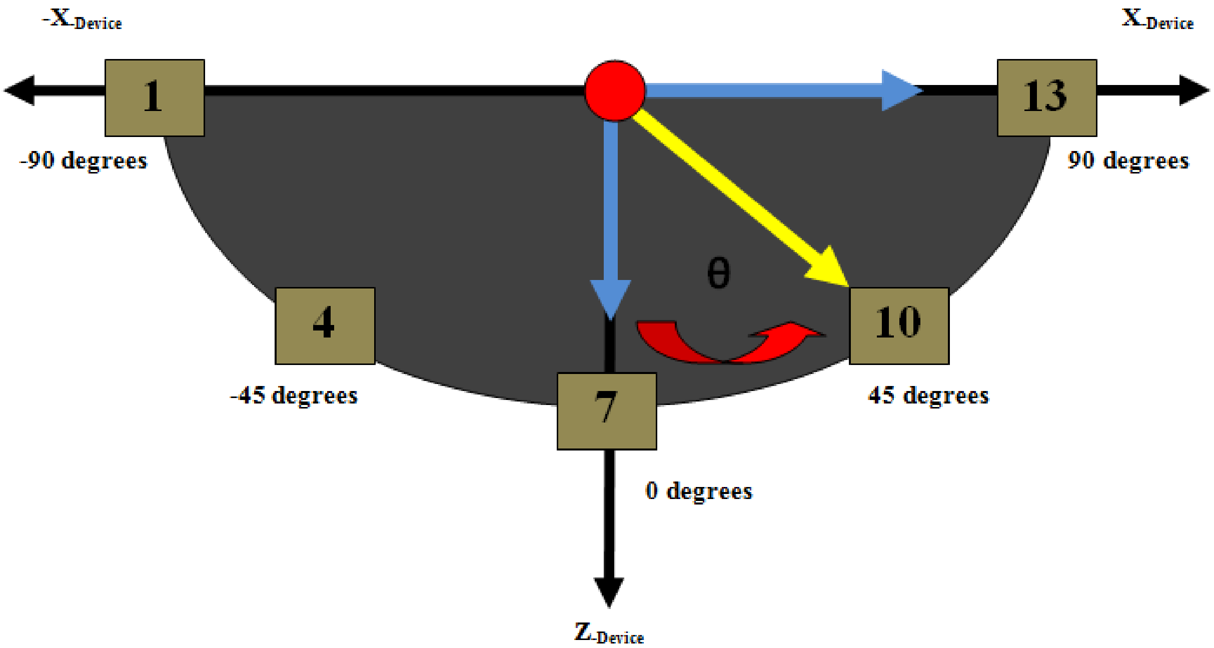

Figure 3.4: Longitudinal Pitch Array Pitch Offset Angle Convention

In this study, the previous method utilized for the development of an accurate and reliable attitude estimation device was expanded from a one-dimensional, longitudinal plane attitude estimation device to a two-dimensional, dual arc accelerometer array operating in both the longitudinal (x-z plane) and transverse (y-z) planes of motion for precise and dependable two-dimensional attitude determination. The work conducted throughout this feasibility study utilized the previously implemented orientation for the longitudinal pitch array for determining pitch attitude estimates. However, in conjunction with this configuration, a second accelerometer array consisting of an additional 13 accelerometers was implemented for the development and implementation of a transverse roll array. The configuration established for the transverse roll array is similar in nature to the previously established device. The transverse roll array consists of 13 accelerometers equally spaced about a 3 inch radius semi-circular array. As displayed in Figure 3.5, Accelerometer # 1 lies at 0 degrees of roll displacement on the positive y-axis, Accelerometer # 4 lies at 45 degrees of displacement, Accelerometer # 7 lies directly on the z-axis of the device at 90 degrees, Accelerometer # 10 lies at 135 degrees of displacement, and Accelerometer # 13 lies directly on the negative secondary, or y-axis, at 180 degrees of displacement. In the configuration of the transverse roll array, the roll angle, ϕ, is measured positive counterclockwise from the positive secondary axis, or y-axis, as depicted in Figure 3.5. Similar to the previously developed device, a rate gyro is utilized at the center-of-gravity of the device for measuring rotational rates.

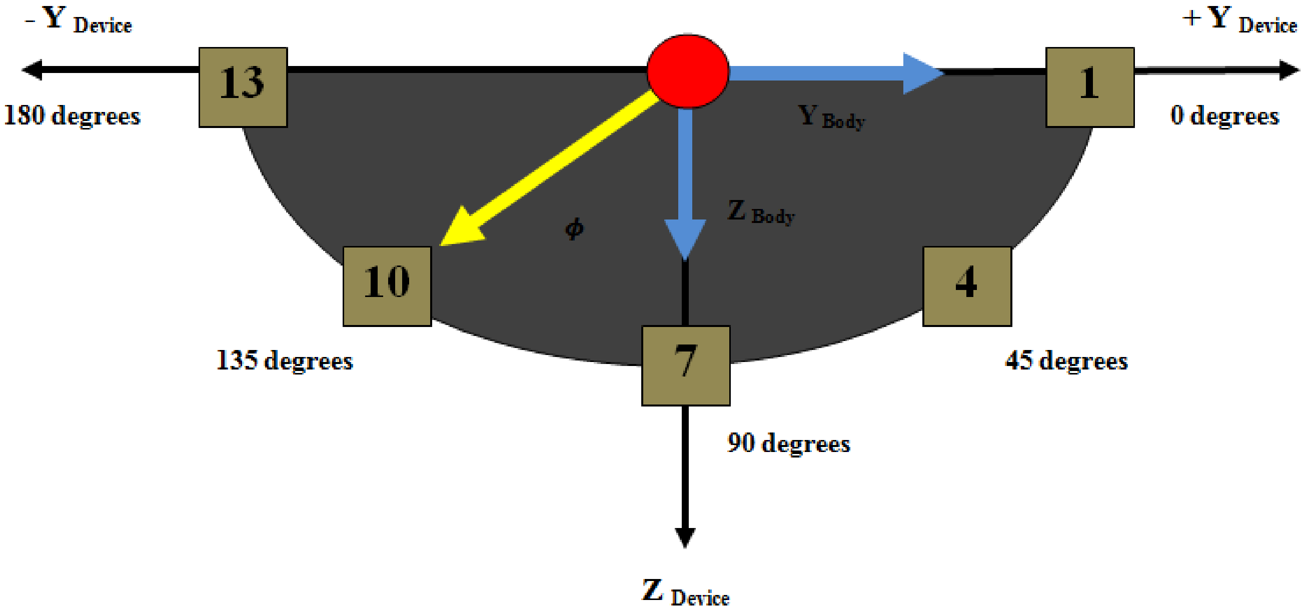

Figure 3.5: Transverse Roll Array Roll Offset Angle Convention

3.2.3 Static Operation

Longitudinal Accelerometer Array [2, 6]

An aircraft is said to be operating in a trim condition when no imposed rotational or translational accelerations are imparted upon the aircraft. When operating in this static state, the measurements of the accelerometers utilized along the longitudinal accelerometer array may be used to determine the aircrafts attitude. When the aircraft's or vehicle's primary body-fixed axis (x-axis) is parallel with the level of the ground and Accelerometer # 7 is parallel with the tertiary body-fixed axis (z-axis), the accelerometer readings denoted as $gA_{z,i}$, become a function of the offset angle, θ_i, measured from the tertiary axis. This formulation is given by Equation 3.1, where "g" represents the acceleration of gravity in gees. One gee is equal to 9.81 m/s^2 or 32.17 ft/s^2.

$$gA_{z,i} = g(\cos\theta_i) \tag{3.1}$$

On the longitudinal accelerometer array, the offset angle is taken to be negative when measured clockwise from the tertiary axis and positive when measured counterclockwise. Appendix D.1 provides a table designating each accelerometer offset angle utilized throughout this work. During a static operating condition, the only acceleration experienced by the aircraft is gravity. Therefore, accelerometer measurements during any static state in which the aircraft pitch angle, $\theta_{Maneuver}$, is not equal to zero is denoted by Equation 3.2. Figure 3.6 shows the device at a static orientation of + 45 degrees of pitch displacement.

$$gA_{z,i} = g\cos(\theta_{Maneuver} + \theta_i)$$

(3.2)

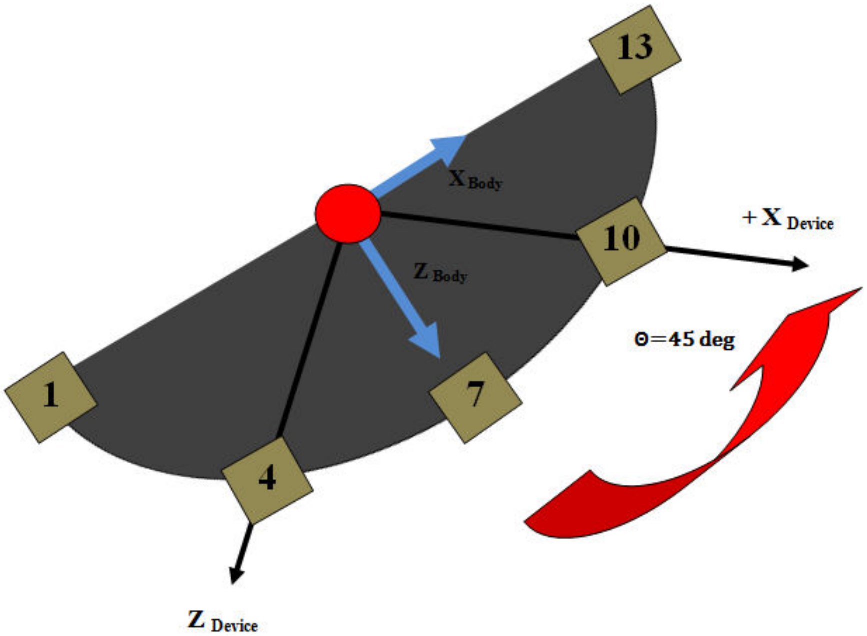

Figure 3.6: Longitudinal Accelerometer Array with Pitch Displacement of 45 degrees

Equation 3.2 may be solved for the angle calculation term, $\theta_{Maneuver}$, and is given as Equation 3.3. Maneuvers of the aircraft of the set (0, +180) degrees yield a positive accelerometer reading, $gA_{z,1}$, and a negative valued accelerometer reading for maneuvers of (0, -180) degrees. This condition yields Equation 3.4 presented below. Complete static resolution of the longitudinal array may be determined when the aircraft is at a displacement of 0 or 180 degrees, allowing Accelerometer # 7 to measure a +1 or -1 gee respectively.

$$\left|\theta_{Maneuver}\right| = ar\cos(gA_{z,i}) - \left|\theta_{i,static}\right|$$

(3.3)

$$\theta_{Maneuver} = \left|\theta_{Maneuver}\right| * (gA_{z,1})$$

(3.4)

Transverse Accelerometer Array

As previously stated, an aircraft is said to be operating in a trim condition when no imposed rotational or translational accelerations are imparted upon the aircraft. When operating in this static state, the measurements of the accelerometers on the transverse array may be utilized to determine the aircrafts attitude. When the aircraft's secondary body-fixed axis (y-axis) is parallel with the level of the ground and Accelerometer # 7 is parallel with the tertiary body-fixed axis (z-axis), the accelerometer readings denoted as $gA_{y,i}$, become a function of the offset angle, ϕ_i, measured from the secondary axis. This formulation is given by Equation 3.5, where "g" once again represents the acceleration of gravity in gees. One gee is equal to 9.81 m/s^2 or 32.17 ft/s^2.

$$gA_{y,i} = g(\sin\phi_i) \tag{3.5}$$

On the transverse accelerometer array, the offset angle is taken to be measured positive clockwise from the positive secondary axis of the aircraft. Appendix D.2 provides a table designating each accelerometer offset angle utilized on the transverse array throughout this study. During a static operating condition, the only acceleration experienced by the aircraft is gravity. Therefore, accelerometer measurements during any static state in which the aircraft pitch angle, $\phi_{Maneuver}$, is not equal to zero is denoted by Equation 3.7. Figure 3.5 shows the device at a static orientation of + 45 degrees of roll displacement.

$$gA_{y,i} = g\sin(\phi_{Maneuver} + \phi_i) \tag{3.6}$$

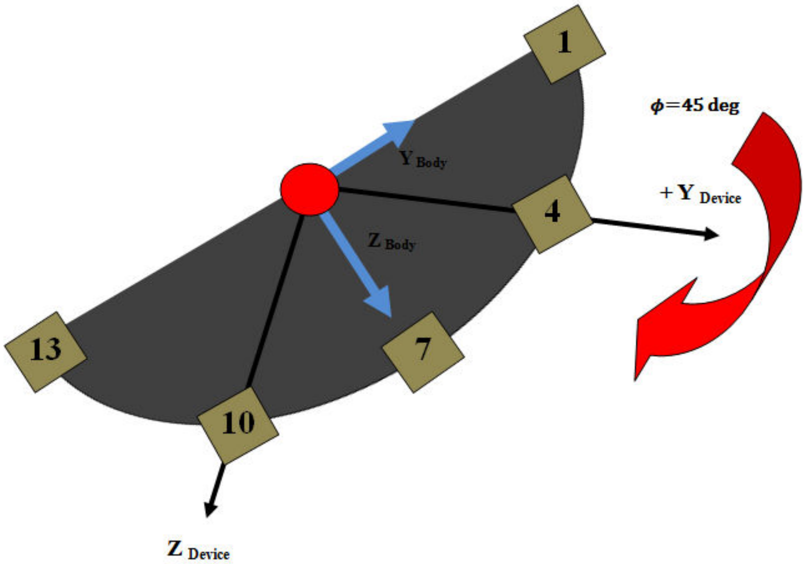

Figure 3.7: Transverse Accelerometer Array with Roll Displacement of 45 degrees

Equation 3.6 may be solved for the angle calculation term, ϕ_{Maneuver}, and is given as Equation 3.7. Maneuvers of the aircraft of the set (0, +180) degrees yield a positive accelerometer reading, $gA_{y,1}$, and a negative valued accelerometer reading for maneuvers of (0, -180) degrees. This condition yields Equation 3.8 presented below. Complete static resolution of the transverse array may be determined when the aircraft is at a displacement of 0 or 180 degrees, allowing Accelerometer # 7 to measure a +1 or -1 gee respectively.

$$\left|\phi_{Maneuver}\right| = ar\sin(gA_{y,i}) - \left|\phi_{i,static}\right| \tag{3.7}$$

$$\phi_{Maneuver} = \left|\phi_{Maneuver}\right| * (gA_{y,1}) \tag{3.8}$$

3.2.4 Loading of an Arbitrary Accelerometer

Longitudinal Accelerometer Array [2, 6, 23]

The accurate simulation and modeling of translational acceleration and rotational loading as measured by an arbitrary sensor requires the translational accelerations experienced along the vehicle axes as well as the rotational rates experienced by the vehicle to be resolved to sensor locations about the longitudinal, or pitch accelerometer array. The measured acceleration of an arbitrary sensor displaced from the vehicle center-of-gravity is given by Equation 3.9 and derived in full in Appendix D.3. The angles in Equation 3.9 are representative of the misalignment angles of an "i_{th}" accelerometer from the vehicle axes [23].

$$\begin{aligned} gA_{z,i} =& \left[gA_{x,cg} - (r^2+q^2)\overline{X}_x + (pq-\dot{r})\overline{Y}_x + (rp+\dot{q})\overline{Z}_x \right]\left(\cos(\psi_z)\sin(\theta_z)\cos(\phi_z) + \sin(\psi_z)\sin(\phi_z)\right) \\ &+ \left[gA_{y,cg} + (pq+\dot{r})\overline{X}_y - (p^2+r^2)\overline{Y}_y + (qr-\dot{p})\overline{Z}_y \right]\left(\sin(\psi_z)\sin(\theta_z)\cos(\phi_z) - \cos(\psi_z)\sin(\phi_z)\right) \\ &+ \left[gA_{z,cg} + (pr-\dot{q})\overline{X}_z - (qr+\dot{p})\overline{Y}_z + (q^2+p^2)\overline{Z}_y \right]\left(\cos(\theta_z)\cos(\phi_z)\right) \end{aligned} \tag{3.9}$$

The angular rates are given as p, q, and r for roll, pitch, and yaw rates respectively and their subsequent derivatives as $\dot{p}$, $\dot{q}$, and $\dot{r}$. The distances $\overline{X}$, $\overline{Y}$, and $\overline{Z}$ are defined as the displaced distances from the vehicle's center-of-gravity along each of the axes. In order to reduce Equation 3.9, we must first assume that $\phi = \psi = 0$ and that all $\overline{Y}$ dimensions are equal to zero within the longitudinal pitch plane. Implementing this configuration on a semi-circular array in the x-z plane for pitching motion about the y-axis, allows for polar relationships to be defined as Equations 3.10 and 3.11. Applying the defined polar relationships to Equation 3.9 allows for Equation 3.9 to be presented in a simplified form given as Equation 3.12.

$$\bar{X} = r_d \sin(\theta_i) \tag{3.10}$$

$$\bar{Z} = r_d \cos(\theta_i) \tag{3.11}$$

$$gA_{z,i} = g\left[A_{x,cg}\sin(\theta_i) + A_{z,cg}\cos(\theta_i)\right] - r_d\left[r^2\sin^2(\theta_i) - (2pr)\cos(\theta_i)\sin(\theta_i) + p^2\cos^2(\theta_i) + q^2\right] \tag{3.12}$$

Equation 3.12 utilizes both translational and rotation acceleration terms to determine the accelerometer measurements when translational components are dependent upon the accelerometer offset angles from the z-axis of the vehicle and the rotational components are dependent on the radius of departure from the vehicle's center-of-gravity.

As a result of imposed loads due to the vehicle's acceleration and the gravity vector along each axis, translational accelerations along each of the vehicle's axes occur and are given by Equation 3.13.

$$gA = \begin{bmatrix} gA_x \\ gA_y \\ gA_z \end{bmatrix}_{CG} = \begin{bmatrix} A_{x,imposed} \\ A_{y,imposed} \\ A_{z,imposed} \end{bmatrix} + g\begin{bmatrix} -\sin(\theta_{man}) \\ \cos(\theta_{man})\sin(\phi_{man}) \\ \cos(\theta_{man})\cos(\phi_{man}) \end{bmatrix} \tag{3.13}$$

Applying Equation 3.13 to Equation 3.12 along the tertiary and primary axes allows for the derivation of Equation 3.14 and 3.15 for simulation of the accelerometer measurements when the imposed translational acceleration, Euler angle orientations, and pitch, roll, and yaw vehicle rates are known for full longitudinal loading and pure rotation in the longitudinal plane. Equation 3.15 may be reduced through the use of the trigonometric identity, $\cos(\alpha + \beta) = \cos\alpha\cos\beta - \sin\alpha\sin\beta$, and is given as Equation 3.16.

Simulation of an Accelerometer under Full Longitudinal Loading

$$\begin{aligned} gA_{z,i} = {} & (A_{x,imposed}\sin(\theta_i) - g(\sin(\theta_{man})\sin(\theta_i)) + (A_{z,imposed}\cos(\theta_i) + g(\cos(\theta_i)\cos(\theta_m)\cos(\phi_i)) \\ & -r_d\left[r^2\sin^2(\theta_i) - (2pr)\cos(\theta_i)\sin(\theta_i) + p^2\cos^2(\theta_i) + q^2\right] \end{aligned} \tag{3.14}$$

Simulation of an Accelerometer under Pure Rotation in the Longitudinal Plane

$$gA_{z,i} = -g(\sin(\theta_{man})\sin(\theta_i)) + g(\cos(\theta_{man})\cos(\theta_i)) - r_d(q^2) \tag{3.15}$$

$$gA_{z,i} = g(\cos(\theta_{man} + \theta_i) - r_d(q^2) \tag{3.16}$$

Equation 3.16 is primarily utilized when the device is mounted to a rotary test bed to simulate the accelerometer readings. During static operation of the device, Equation 3.16 reduces to the form previously given by Equation 3.2.

Transverse Accelerometer Array

The accurate simulation and modeling of translational acceleration and rotational loading as measured by an arbitrary sensor requires the translational accelerations experienced along the aircraft axes as well as the rotational rates experienced by the aircraft to be resolved to sensor locations about the transverse, or roll accelerometer array, in a similar manner utilized previously for the development of the longitudinal accelerometer array equations. The measured acceleration of an arbitrary sensor displaced from the vehicle's center-of-gravity is given as Equation 3.17 and derived in full in Appendix D.3. The angles in Equation 3.17 are representative of the misalignment angles of an "i_{th}'' accelerometer from the vehicle axes [23].

$$\begin{aligned} gA_{y,i} = &\left[gA_{x,cg} - (r^2 + q^2)\overline{X}_x + (pq - \dot{r})\overline{Y}_x + (rp + \dot{q})\overline{Z}_x \right]\left(\cos(\psi_y)\sin(\theta_y)\sin(\phi_y) - \sin(\psi_y)\cos(\phi_y)\right) \\ &+\left[gA_{y,cg} + (pq + \dot{r})\overline{X}_y - (p^2 + r^2)\overline{Y}_y + (qr - \dot{p})\overline{Z}_y \right]\left(\sin(\psi_y)\sin(\theta_y)\sin(\phi_y) + \cos(\psi_y)\cos(\phi_y)\right) \\ &+\left[gA_{z,cg} + (pr - \dot{q})\overline{X}_z - (qr + \dot{p})\overline{Y}_z + (q^2 + p^2)\overline{Z}_y \right]\left(\cos(\theta_y)\sin(\phi_y)\right) \end{aligned} \tag{3.17}$$

As stated previously, the angular rates are given as p, q, and r for roll, pitch, and yaw rates respectively and their subsequent derivatives as $\dot{p}$, $\dot{q}$, and $\dot{r}$. The distances $\overline{X}$, $\overline{Y}$, and $\overline{Z}$ are defined as the displaced distances from the vehicle's center-of-gravity along each of the axes. In order to reduce Equation 3.17, we must first assume that $\theta = \psi = 0$ and that all $\overline{X}$ dimensions are equal to zero within the transverse roll plane. Implementing this configuration on a semi-circular array in the y-z plane for rolling motion about the x-axis, allows for polar relationships to be defined as Equations 3.18 and 3.19. Applying the defined polar relationships to Equation 3.17 allows for Equation 3.17 to be presented in a simplified form given as Equation 3.20.

$$\overline{Y} = r_d \cos(\phi_i) \tag{3.18}$$

$$\overline{Z} = r_d \sin(\phi_i) \tag{3.19}$$

$$gA_{y,i} = g\left[A_{y,cg}\cos(\phi_i) + A_{z,cg}\sin(\phi_i) \right] + r_d\left[(2qr)\sin(\phi_i)\cos(\phi_i) - p^2 - r^2\cos^2(\phi_i) - q^2\sin^2(\phi_i) \right] \tag{3.20}$$

Equation 3.20 utilizes both translational and rotation acceleration terms to determine the accelerometer measurements when translational components are dependent on the accelerometer offset angles from the z-axis of the vehicle and the rotational components are dependent on the radius of departure from the vehicle's center-of-gravity. As a result of the imposed loads due to the aircraft's acceleration and the gravity vector along each axis, translational accelerations along each of the vehicle's axes occur and are given previously by Equation 3.13.

Applying Equation 3.13 to Equation 3.20 along the tertiary (z-axis) and secondary (y-axis) axes allows for the derivation of Equation 3.21 and 3.22 for simulation of the accelerometer measurements when the imposed translational acceleration, Euler angle orientations, and pitch, roll, and yaw vehicle rates are known for full transverse loading and pure rotation in the transverse plane. Equation 3.22 may be reduced through the use of the trigonometric identity, $\cos(\alpha+\beta) = \cos\alpha\cos\beta - \sin\alpha\sin\beta$, and is given as Equation 3.23.

Simulation of an Accelerometer under Full Transverse Loading

$$gA_{y,i} = (A_{y,imposed}\cos(\phi_i) + g(\cos(\theta_{man})\sin(\phi_{man})\cos(\phi_i)) + (A_{z,imposed}\sin(\phi_i) + g(\cos(\theta_i)\cos(\theta_m)\sin(\phi_i)) \\ + r_d\left[(2pr)\cos(\phi_i)\sin(\phi_i) - q^2\sin^2(\phi_i) - r^2\cos^2(\phi_i) - p^2\right] \tag{3.21}$$

Simulation of an Accelerometer under Pure Rotation in the Transverse Plane

$$gA_{y,i} = g(\sin(\phi_{man})\cos(\phi_i)) + g(\cos(\phi_{man})\sin(\phi_i)) - r_d(p^2) \tag{3.22}$$

$$gA_{y,i} = g(\sin(\phi_{man} + \phi_i) - r_d(p^2) \tag{3.23}$$

Equation 3.23 may be utilized when the device is mounted to a rotary test bed to simulate the accelerometer readings in the transverse plane. During static operation of the device, Equation 3.23 reduces to the form previously given by Equation 3.6.

3.3 Dryden Wind Model [24, 47]

The work conducted in this feasibility study makes use of the ability of the two-dimensional accelerometer array to produce accurate and reliable attitude estimates while operating online in a simulated real-world environment. For accurate simulation of real-world environmental flight conditions, a Dryden wind turbulence model was implemented in order to verify and validate the ability of the method developed to produce precise and reliable real-time attitude estimates despite the presence of severe turbulence and wind.

The Dryden wind turbulence model adds turbulence to the simulation model by passing band-limited white noise through appropriate filters. In this study, the mathematical representation utilized for continuous simulation of turbulence and wind effects was the Military Specification MIL-F-8785C.

The component spectra functions utilized in this implementation of the MIL-F-8785C are given in Table 3.1. Based on the military guidelines, turbulence is defined as a stochastic process defined by a velocity spectrum [24]. For an aircraft operating at a speed, V, through a turbulence field with a defined spatial frequency of $\boldsymbol{\Omega}$, measured in radians per meter, the circular frequency, ω, is calculated by multiplying the velocity by $\boldsymbol{\Omega}$ [47].

Longitudinal	**MIL-F-8785C**
$\Phi_u(\omega)$	$\frac{2\sigma_u^2}{VL_w} \bullet \frac{1}{\left[1+\left(1.339L_u\frac{\omega}{V}\right)^2\right]^{5/6}}$
$\Phi_p(\omega)$	$\frac{\sigma_w^2}{VL_w} \bullet \frac{0.8\left(\frac{\pi L_\omega}{4b}\right)^{1/3}}{1+\left(\frac{4b\omega}{\pi V}\right)^2}$
Lateral	**MIL-F-8785C**
$\Phi_v(\omega)$	$\frac{2\sigma_v^2 L_v}{\pi V} \bullet \frac{1+\frac{8}{3}\left(1.339L_v\frac{\omega}{V}\right)^2}{\left[1+\left(1.339L_v\frac{\omega}{V}\right)^2\right]^{11/6}}$
$\Phi_r(\omega)$	$\frac{\mp\left(\frac{\omega}{V}\right)^2}{1+\left(\frac{3b\omega}{\pi V}\right)^2} \bullet \Phi_v(\omega)$
Vertical	**MIL-F-8785C**
$\Phi_w(\omega)$	$\frac{\sigma_\omega^2 L_\omega}{\pi V} \bullet \frac{1+\frac{8}{3}\left(1.339L_w\frac{\omega}{V}\right)^2}{\left[1+\left(1.339L_w\frac{\omega}{V}\right)^2\right]^{11/6}}$
$\Phi_q(\omega)$	$\frac{\mp\left(\frac{\omega}{V}\right)^2}{1+\left(\frac{4b\omega}{\pi V}\right)^2} \bullet \Phi_w(\omega)$

Table 3.1: MIL-F-8785C Component Spectra Functions [47]

The variable, b, is defined as the aircraft wingspan and the variables L_u, L_v, and L_w represent the turbulence scale length. The variables σ_u, σ_v, and σ_w represent the turbulence intensities. The term, $\Phi_p(w)$, is known as the longitudinal turbulence angular rate spectrum and is a rational function derived from a curve-fitting complex algebra function, not the vertical turbulence velocity spectrum, $\Phi_w(w)$, which is multiplied by a scale factor. In practice, the implementation of the turbulence angular rate spectrum contributes far less to the aircraft gust response than the turbulence velocity spectrum [47].

The Dryden wind turbulence model focuses on the implementation of a generated signal possessing the correct characteristics of a unit variance, band-limited white noise signal passed though forming filters. As approximations of the Von Karman velocity spectra, the forming filters utilized in the Dryden wind turbulence model are valid in a range of normalized frequencies of less than 50 radians per meter. The transfer functions utilized for the MIL-F-8785C model are given and summarized in Table 3.2 below.

Longitudinal	**MIL-F-8785C**
$H_u(s)$	$\dfrac{\sigma_u\sqrt{\dfrac{2}{\pi}\bullet\dfrac{L_u}{V}}\left(1+0.25\left(\dfrac{L_u}{V}\right)s\right)}{1+1.357\left(\dfrac{L_u}{V}\right)s+0.1987\left(\dfrac{L_u}{V}\right)^2 s^2}$
$H_p(s)$	$\sigma_w\sqrt{\dfrac{0.8}{V}}\bullet\dfrac{\left(\dfrac{\pi}{4b}\right)^{1/6}}{L_w^{1/3}\left(1+\left(\dfrac{4b}{\pi V}\right)s\right)}$
Lateral	**MIL-F-8785C**
$H_v(s)$	$\dfrac{\sigma_u\sqrt{\dfrac{1}{\pi}\bullet\dfrac{L_v}{V}}\left(1+2.7478\dfrac{L_v}{V}s+0.3398\left(\dfrac{L_v}{V}\right)^2 s^2\right)}{\left(1+2.9958\dfrac{L_v}{V}s+1.9754\left(\dfrac{L_v}{V}\right)^2 s^2+0.1539\left(\dfrac{L_v}{V}\right)^3 s^3\right)}$
$H_r(s)$	$\dfrac{\mp\dfrac{s}{V}}{\left(1+\left(\dfrac{3b}{\pi V}\right)\right)s}\bullet H_v(s)$
Vertical	**MIL-F-8785C**
$H_w(s)$	$\dfrac{\sigma_u\sqrt{\dfrac{1}{\pi}\bullet\dfrac{L_w}{V}}\left(1+2.7478\left(\dfrac{L_w}{V}\right)s+0.3398\left(\dfrac{L_w}{V}\right)^2 s^2\right)}{1+2.9958\left(\dfrac{L_w}{V}\right)s+1.9754\left(\dfrac{L_w}{V}\right)^2 s^2+0.1539\left(\dfrac{L_w}{V}\right)^3 s^3}$
$H_q(s)$	$\dfrac{\mp\dfrac{s}{V}}{\left(1+\left(\dfrac{4b}{\pi V}\right)\right)s}\bullet H_w(s)$

Table 3.2: MIL-F-8785C Forming Filter Transfer Functions [47]

When implementing the Dryden wind turbulence model, the model is divided into two distinct regions where the turbulence scale and intensities are a function of the altitude at which the simulation takes place. In this feasibility study, a medium to high altitude scale (altitude > 2000 feet) was utilized. At the medium to high altitude level, the turbulence scale lengths and intensities operate on the assumption that the turbulence is isotropic. The military reference scale lengths utilized are presented in Table 3.3 below [24].

Scale Lengths	MIL-F-8785C
L_u	2500 feet
L_v	2500 feet
L_w	2500 feet

Table 3.3: MIL-F-8785C Scale Lengths [24]

The correct turbulence intensities are critical to the implementation of the Dryden wind turbulence model. Turbulence intensities are determined from a lookup table, presented as Figure 3.8 below, providing the turbulence intensities as a function of altitude and how the probability of the turbulence intensities are being exceeded. In Figure 3.8 the turbulence axes are aligned with the body-fixed coordinates where the relationship amongst turbulence intensities is given by Equation 3.53.

$$\sigma_u = \sigma_v = \sigma_w \tag{3.53}$$

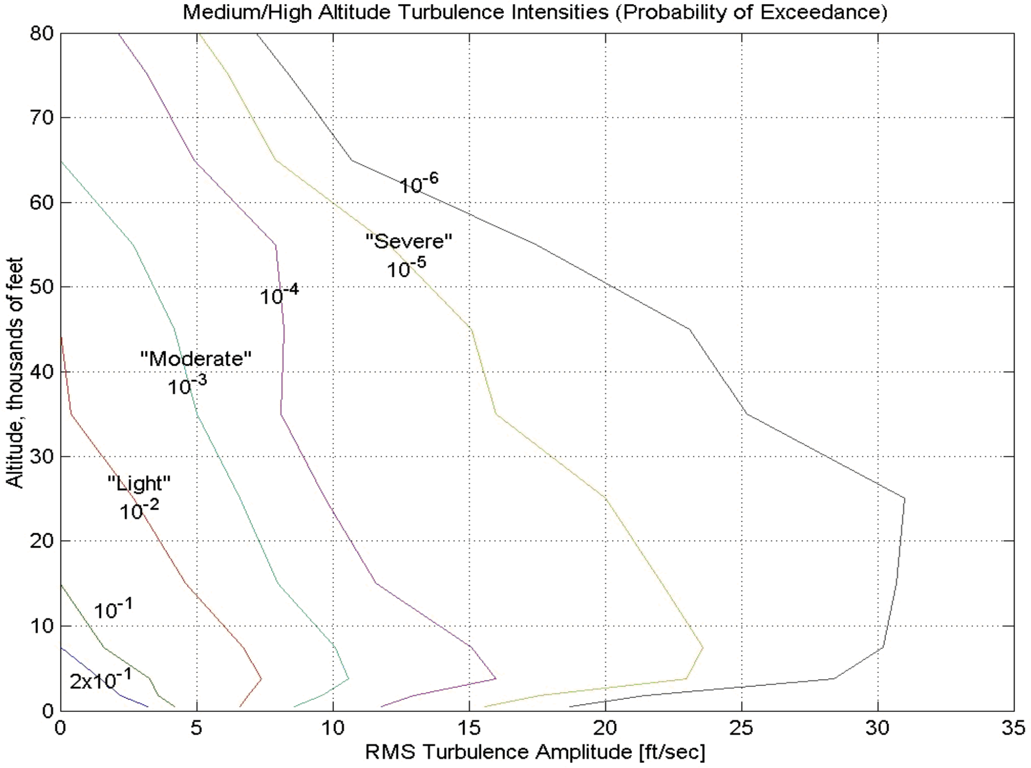

Figure 3.8 Medium/High Altitude Turbulence Intensities [24, 47]

Figures 3.9, 3.10, and 3.11 display the turbulence inputs implemented during each phase of the simulation study with a summary of the maximum turbulence inputs given in Tables 3.4, 3.5, and 3.6 respectively.

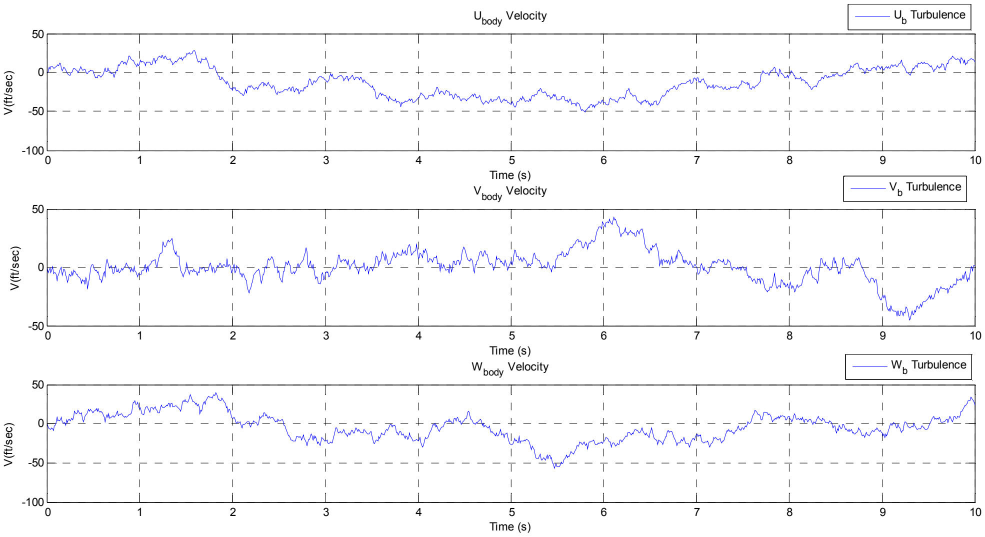

Figure 3.9: Longitudinal Maneuver – Turbulence Inputs

Longitudinal Maneuver	Maximum Turbulence Input (feet/second)
u_b	50.71
v_b	44.83
w_b	56.59

Table 3.4: Longitudinal Maneuver Maximum Turbulence Inputs

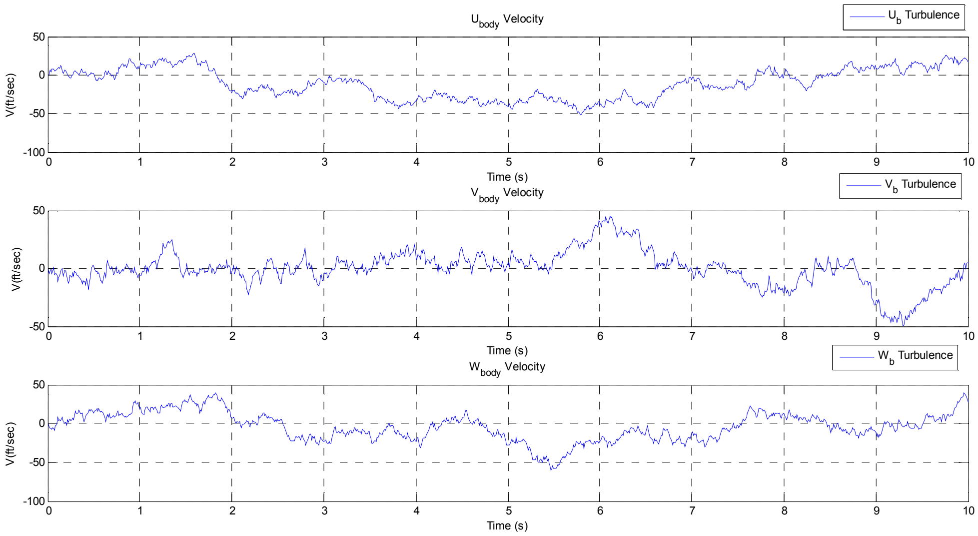

Figure 3.10: Transverse Maneuver – Turbulence Inputs

Transverse Maneuver	Maximum Turbulence Input (feet/second)
u_b	51.32
v_b	49.80
w_b	59.98

Table 3.5: Transverse Maneuver Maximum Turbulence Inputs

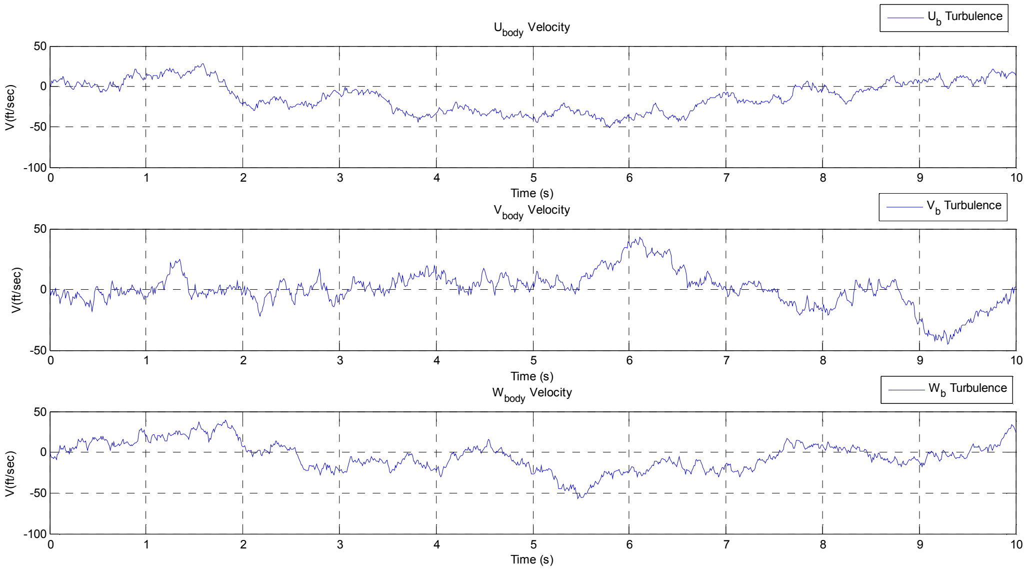

Figure 3.11: Longitudinal/Transverse Maneuver – Turbulence Inputs

Longitudinal/Transverse Maneuver	Maximum Turbulence Input (feet/second)
u_b	50.74
v_b	45.19
w_b	56.74

Table 3.6: Longitudinal/Transverse Maneuver Maximum Turbulence Inputs

Implementation of the Dryden wind turbulence model was critical in this feasibility study for accurate assessment of the proposed method to reliably produce precise and sustainable attitude and rate gyro bias estimates despite functioning in a harsh and severe operating environment. The turbulent simulations conducted in this feasibility study simulated highly vibrational characteristics with a maximum turbulence magnitude of approximately 60 feet per second (three times the level of the highest probability encountered).

3.4 Algorithm Operation

The algorithm implemented in this feasibility study makes use of the data from the rate gyro and accelerometer array measurements to calculate both longitudinal and transverse attitude estimates while continuously producing an estimate of the rate gyro bias in real-time dynamic maneuvers of the vehicle or aircraft.

3.4.1 Extended Kalman Filter Bias Estimation

An extended Kalman filter model was designed and implemented to determine the rate gyro bias and longitudinal and transverse attitude estimates from the accelerometer array and gyro measurements generated from the nonlinear aircraft model. The initial state vectors of the extended Kalman filter are set to zero degrees of longitudinal and transverse displacement. The model utilized for the extended Kalman filter implementation is given in Figure 3.12 below.

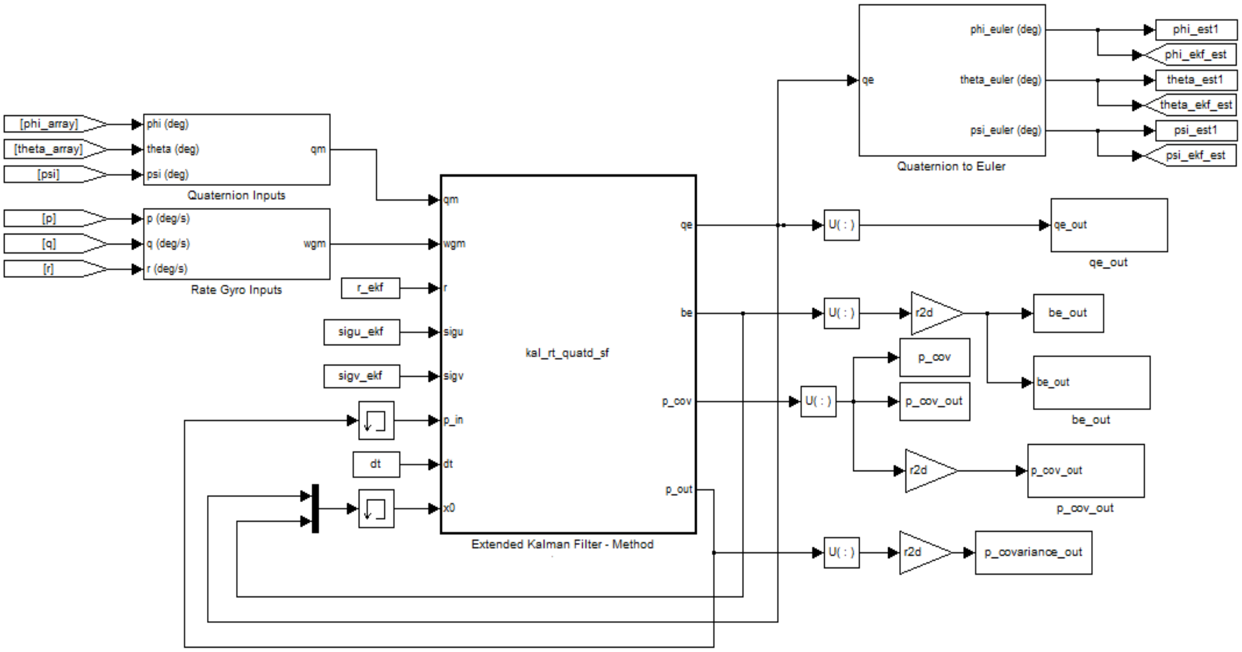

Figure 3.12: Extended Kalman Filter Diagram

The extended Kalman filter in Figure 3.12 relies on the rate gyro measurements and the attitude estimates produced by the two-dimensional accelerometer array as inputs to the system. The extended Kalman filter also relies on the measurement and initial error covariances for the rate gyro and bias measurements. In this study, the bias of the rate gyro is assumed to be unaffected by the operating conditions allowing the extended Kalman filter to be implemented with a constant noise variance. The bias of the rate gyro is assumed to be constant because once the rate gyro reaches its functional peak and a constant operating temperature; the bias varies minimally over time and may be assumed to be a constant value.

3.4.2 Parameter Estimation

In this feasibility study, parameter estimation was utilized to effectively verify and validate the accuracy of the attitude estimates produced by the extended Kalman filter. Implementing this method of verification required the use of Equations 3.54, 3.55, and 3.56 where the body velocity terms could be estimated by solving each equation for the body acceleration terms and integrating once to obtain the body velocity components [3, 4].

$$-A_{x,cg} - mg\sin(\theta_{est}) = m(\dot{u}_{est} + qw - rv) \tag{3.54}$$

$$A_{y,cg} + mg\sin(\phi_{est}) = m(\dot{v}_{est} + ru - pw) \tag{3.55}$$

$$-A_{z,cg} + mg\cos(\theta_{est})\cos(\phi_{est}) = m(\dot{w}_{est} + pv - qu) \tag{3.56}$$

The body velocity estimates may now be used in conjunction with the attitude estimates produced by the extended Kalman filter to determine the aircraft's, or vehicle's, velocity components through the use of Equation 3.57 below. The positional estimates and parameters of the aircraft may be determined by solving for $V_x, V_y, \; and \; V_z$ and then integrating once.

$$\begin{Bmatrix} V_x \\ V_y \\ V_z \end{Bmatrix} = \begin{bmatrix} c\theta_{est}c\psi_{est} & s\phi_{est}s\theta_{est}c\psi_{est} - c\phi_{est}s\psi_{est} & c\phi_{est}\,s\theta_{est}\,c\psi_{est} + s\phi_{est}s\psi_{est} \\ c\theta_{est}s\psi_{est} & s\phi_{est}s\theta_{est}s\psi_{est} + c\phi_{est}c\psi_{est} & c\phi_{est}s\theta_{est}s\psi_{est} - s\phi_{est}c\psi_{est} \\ -s\theta_{est} & s\phi_{est}c\theta_{est} & c\phi_{est}c\theta_{est} \end{bmatrix} \begin{Bmatrix} u_{est} \\ v_{est} \\ w_{est} \end{Bmatrix} \tag{3.57}$$

Determining velocity parameters and inertial position estimates through the use of simple kinematic equations for the body and aircraft velocity components and comparing them to the truth measurements produced by the nonlinear aircraft model, is a viable method to validate and confirm the extended Kalman filter's attitude estimates are accurate and reliable.

3.4.3 Hardware Considerations

The precision of the attitude and bias estimation algorithm implemented is dependent upon the configuration of the two-dimensional accelerometer array and the operational condition of the rate gyro. In this section, a brief discussion is had addressing the use of the rate gyro and the number of accelerometers utilized.

The work completed in this feasibility study addresses the primary problem of expanding upon a previously developed one-dimensional attitude and rate gyro bias estimation algorithm and device to a two-dimensional attitude array and rate gyro bias estimation algorithm operating in real-time. Is this study, a rate gyroscope model was implemented with variable zero mean white Gaussian noise and rate gyro ramp inputs with a constant rate gyro bias of 0.200 degrees per second where the rate gyroscopes are assumed to mounted at the center-of-gravity location of the accelerometer array model implemented, therefore aligning the gyro with the x-z and y-z planes of motion being assessed in this feasibility study.

This feasibility study conducted research expanding upon previous iterations of this method [2, 6] by adding an additional accelerometer array for both longitudinal and transverse attitude assessments along with an updated algorithm method for estimation of the rate gyro bias in a full nonlinear operating environment with longitudinal and transverse imposed acceleration loading. The work conducted in this study utilized 13 accelerometers on both the longitudinal and transverse accelerometer arrays displaced equally about the 180 degree arcs for 15 degrees of resolution between accelerometers. If more accelerometers would have been utilized, the accuracy of the attitude and bias estimate would have increased; however, if less accelerometers had been implemented in this study, the accuracy of the attitude and rate gyro bias estimate would have decreased due to a decrease resolution between adjacent accelerometer locations along the array. In the work conducted in this study, the number of accelerometers was maintained at 13 in order to sustain a consistent basis between studies utilizing this method and to keep the focus of this study on validating the concept of a two-dimensional accelerometer array for determining accurate and reliable attitude and rate gyro bias estimates in real-time.

Chapter 4

Simulation Results

4.1 Simulation Overview

For verification and validation of the proposed device and algorithm method, three simulation phases were conducted. Within each of the three simulation phases of the feasibility study, two simulations were constructed and assessed utilizing a full nonlinear aircraft plant model with applied rotational and translational acceleration loading along the primary, secondary, and tertiary vehicle axes. Phase I of this study included the construction of two longitudinal simulations, while Phase II consisted of two transverse simulations to simulate and assess the effectiveness of the two-dimensional accelerometer array model for estimation of the rate gyro bias online while correctly determining the longitudinal and transverse attitude. Upon verification of the simulation models and algorithm operating appropriately, Phase III of the study was conducted through the implementation of two additional simulations constructed to assess the ability of the device model and algorithm to accurately and reliably measure the rate gyro bias and estimate the longitudinal and transverse attitude for a combined longitudinal and transverse maneuver. The aircraft simulation maneuver imposed during Phase III of the simulation study was in essence a combined longitudinal and transverse maneuver.

In each phase of the simulation study, the first simulation was performed in the absence of turbulence and extreme environmental conditions. The second simulation was then implemented with the Dryden wind model, described previously in Section 3.3, to determine the effectiveness of the proposed device and algorithm to accurately estimate the rate gyro bias and correctly determine the attitude despite the presence of harsh environmental conditions and extreme vibrational effects. The turbulence implemented in the second simulation of each simulation set is modeled as an extreme operating condition; however, is of great importance when assessing the ability of the method to function and operate correctly despite the presence of severe environmental and vibrational surroundings.

Throughout this feasibility study, the accelerometer signals implemented were modeled with a zero mean white Gaussian noise input with a variance of 0.000015 gee^2. In each of the simulations conducted, the accelerometer signals from the two-dimensional accelerometer array where modeled with a different “seed” input to the Gaussian white noise so as to more accurately simulate the variability in noise inputs characteristics of real-world operating conditions. The rate gyro signals utilized in this study were modeled with a white Gaussian noise variance of 0.15 (deg/sec)^2 and a constant rate gyro bias of 0.200 degrees per second.

In addition to the device model implemented, a complimentary filter was also utilized in the developed simulation models to produce longitudinal and transverse attitude estimates during each of the simulated flight maneuvers. The complimentary filter implemented utilizes an established threshold tolerance value for reinitializing the initial conditions of the filter integrator to estimate the longitudinal and transverse attitude through the use of consecutive accelerometers. Once two consecutive accelerometers along either the longitudinal or transverse accelerometer array have identical readings within the defined threshold value, the local gravitational field vector can be localized within the given device configuration. Upon localizing the gravitational field vector, the algorithm triggers the complementary filter integrators at this state. The threshold tolerance value on the longitudinal array was set to a value of 0.0003 gees and on the transverse array a value of 0.0005 gees.

4.2 Nonlinear Aircraft Model Implementation

In this feasibility study, the nonlinear six degree-of-freedom aircraft model discussed previously in Section 3.1 and presented in Appendix E is implemented to verify and assess the overall performance and functionality of the utilized, innovative two-dimensional accelerometer device model and algorithm method simulated in a real-world operating environment. Longitudinal motion of the aircraft was performed utilizing horizontal tail inputs, while the transverse and heading motion of the aircraft was controlled using inputs to the asymmetric trailing-edge flap and symmetric rudder. The implementation of the device and proposed algorithm method was performed by simulating the nonlinear aircraft model at a "*cruise*" configuration of 300 knots and an altitude of 20,000 feet allowing for the accelerometers along each of the arrays to experience full translational loading during the maneuvers assessed in each simulation. The resulting accelerometer measurements along the longitudinal and transverse array were calculated using Equation 3.14 and 3.21 respectively and shown here as Equations 4.1 and 4.2.

Simulation of an Accelerometer under Full Longitudinal Loading

$$\begin{aligned} gA_{z,i} &= (A_{x,imposed}\sin(\theta_i) - g(\sin(\theta_{man})\sin(\theta_i)) + (A_{z,imposed}\cos(\theta_i) + g(\cos(\theta_i)\cos(\theta_m)\cos(\phi_i)) \\ &- r_d\left[r^2\sin^2(\theta_i) - (2pr)\cos(\theta_i)\sin(\theta_i) + p^2\cos^2(\theta_i) + q^2\right] \end{aligned} \tag{4.1}$$

Simulation of an Accelerometer under Full Transverse Loading

$$\begin{aligned} gA_{y,i} &= (A_{y,imposed}\cos(\phi_i) + g(\cos(\theta_{man})\sin(\phi_{man})\cos(\phi_i)) + (A_{z,imposed}\sin(\phi_i) + g(\cos(\theta_i)\cos(\theta_m)\sin(\phi_i)) \\ &+ r_d\left[(2pr)\cos(\phi_i)\sin(\phi_i) - q^2\sin^2(\phi_i) - r^2\cos^2(\phi_i) - p^2\right] \end{aligned} \tag{4.2}$$

The imposed translational and rotational loads are determined from the forces experienced by the aircraft during flight. During dynamic operation, the translational loads experienced along the vehicle's axes are a result of the vehicle thrust and aerodynamic forces experienced during the aircraft's dynamic maneuver. Operation of the aircraft in this dynamic state of abrupt maneuvers or maneuvers where the equilibrium may not be assumed to be quasi-static, allows the forces experienced during the dynamic operation of the aircraft to become unbalanced. The unbalanced forces experienced during dynamic maneuvers results in non-constant accelerations as shown in Figures 4.1 through 4.6, where "A1" through "A13" represent the output of the thirteen accelerometers utilized on each accelerometer array respectively. In a static condition, the lift force of the aircraft negates the weight force and the aircraft's thrust force negates the vehicle's drag allowing for a condition of balanced forces.

Phase I – Longitudinal Maneuver: Full Longitudinal Loading of an Accelerometer

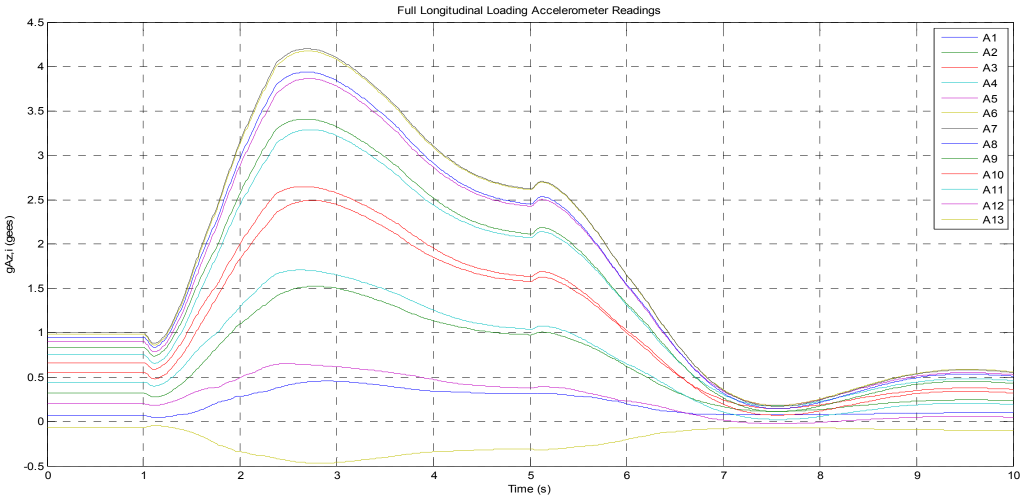

Figure 4.1: Full Longitudinal Loading of an Accelerometer during a Longitudinal Maneuver

Phase I – Longitudinal Maneuver: Full Transverse Loading of an Accelerometer

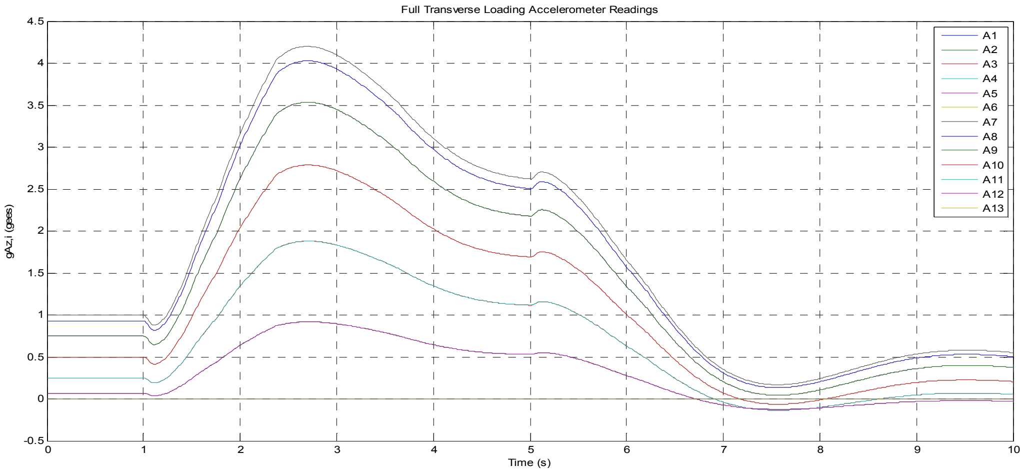

Figure 4.2: Full Transverse Loading of an Accelerometer during a Longitudinal Maneuver

Phase II – Transverse Maneuver: Full Longitudinal Loading of an Accelerometer

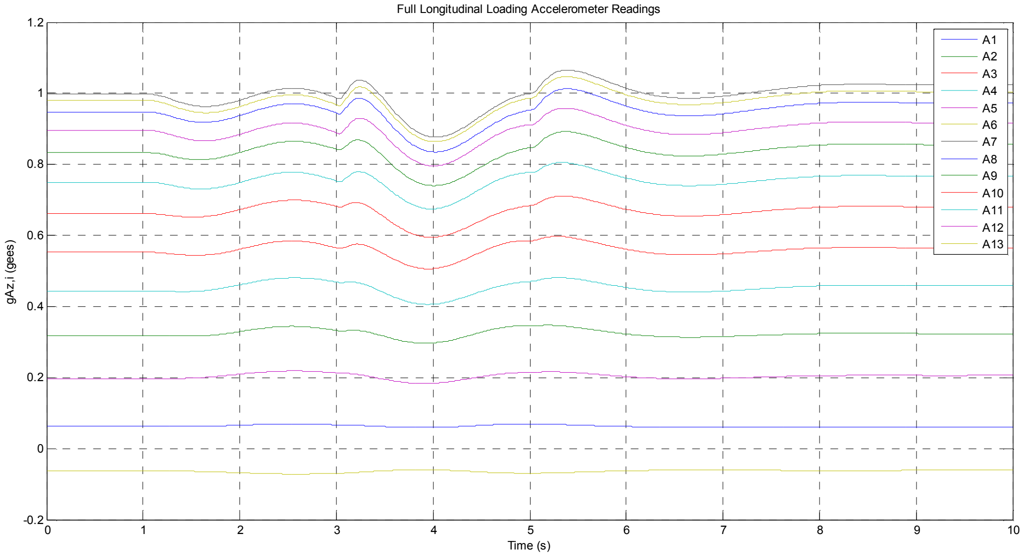

Figure 4.3: Full Longitudinal Loading of an Accelerometer during a Transverse Maneuver

Phase II – Transverse Maneuver: Full Transverse Loading of an Accelerometer

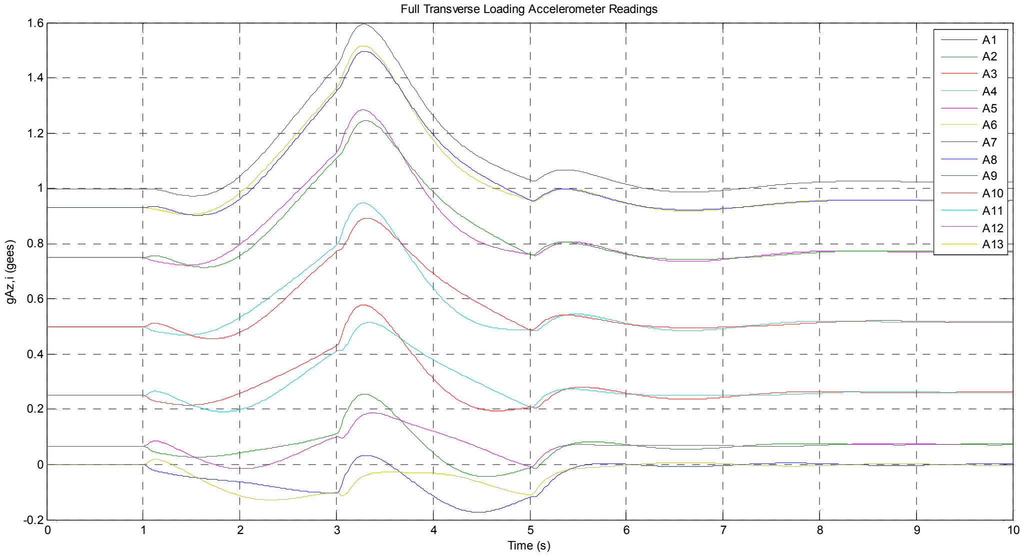

Figure 4.4: Full Transverse Loading of an Accelerometer during a Transverse Maneuver

Phase III – Longitudinal/Transverse Maneuver: Full Longitudinal Loading of an Accelerometer

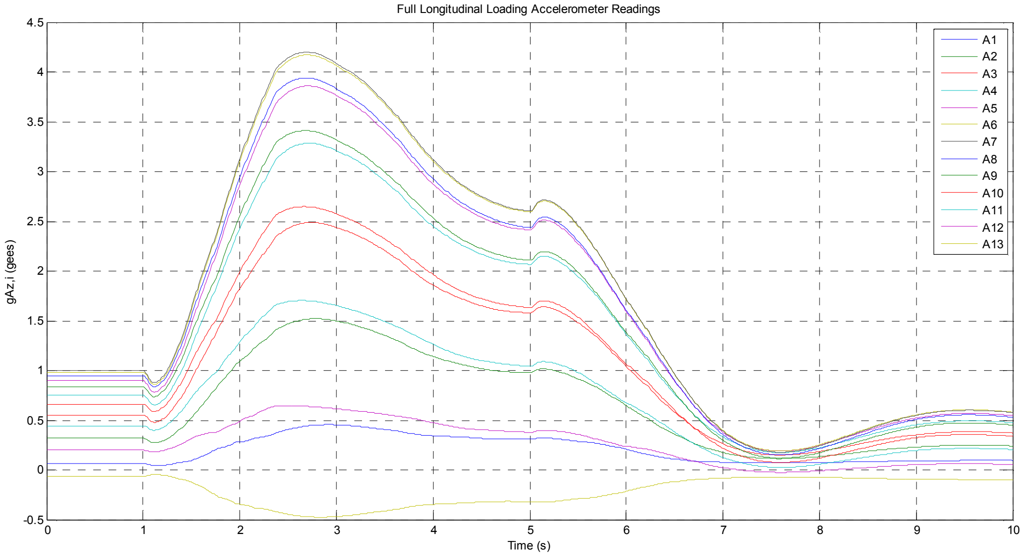

Figure 4.5: Full Longitudinal Loading of an Accelerometer during a Longitudinal/Transverse Maneuver

Phase III – Longitudinal/Transverse Maneuver: Full Transverse Loading of an Accelerometer

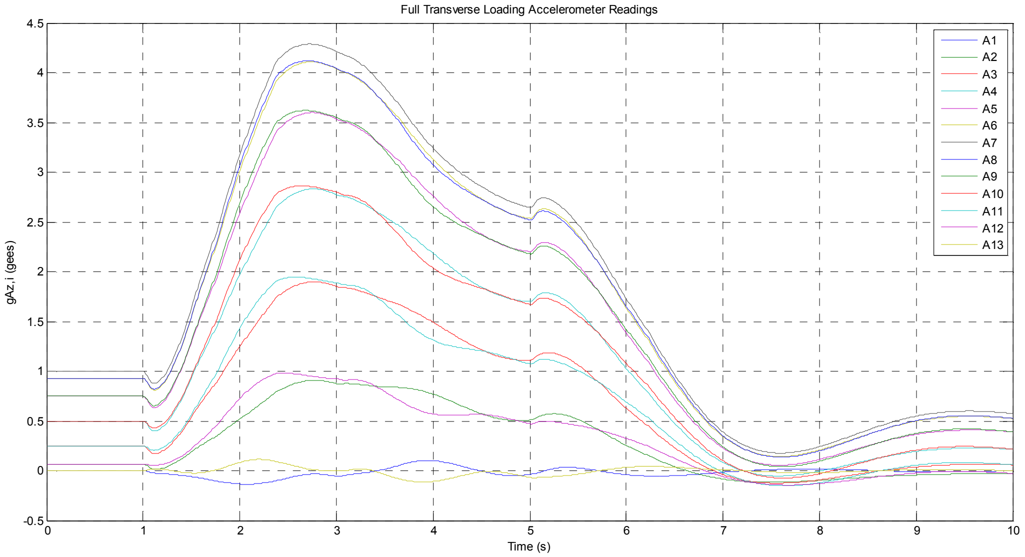

Figure 4.6: Full Transverse Loading of an Accelerometer during a Longitudinal/Transverse Maneuver

Attitude estimation for the conditions of full longitudinal and transverse loading requires knowledge of the translational accelerations experienced along the primary, secondary, and tertiary axes of the vehicle. To obtain this information, the array must be augmented with three accelerometers at the center-of-gravity location. This method is shown in Equation 3.13 where the sum of the imposed loads and weight of the aircraft is determined by the accelerometers at the center-of-gravity location. With knowledge of these values, the vehicle's longitudinal and transverse attitude may be accurately estimated using the measurements produced by the two-dimensional accelerometer array and Equations 4.1 and 4.2 respectively.

4.2.1 Algorithm for Imposed Loading Determination

Longitudinal Accelerometer Array [2, 6]

In the previous research conducted [2], linear plant models were examined that underwent both gravitational and rotational accelerations. Expanding upon this research [6], a method for estimating the imposed translational accelerations along the aircraft's primary and tertiary axes during dynamic maneuvers of the aircraft was developed. In order to ensure accurate bias estimation and attitude determination during the aircraft's or vehicle's maneuvers, the previously developed device was augmented with two additional accelerometers at the aircraft's center-of-gravity to measure the imparted translational accelerations occurring along the aircraft's primary and tertiary axes during maneuvers [6].

From Equation 3.13 the accelerometers located at the center-of-gravity location along the longitudinal array may be resolved in terms of the registered sum of imposed motion and gravitational accelerations. The total acceleration, measured in gees, experienced along the primary axis, $A_{X,CG}$, and tertiary axis, $A_{Z,CG}$, are given by Equations 4.3 and 4.4 respectively and derived in full in Appendix D.

$$A_{X,CG} = \frac{A_{X,imposed}}{g} - (\sin\theta_{Man}) \tag{4.3}$$

$$A_{Z,CG} = \frac{A_{Z,imposed}}{g} + (\cos\theta_{Man}\cos\phi_{Man}) \tag{4.4}$$

Due to the inability to directly measure the imposed translational or rotational acceleration imparted on the aircraft during maneuvers, an estimation of the imposed acceleration loads must be performed utilizing previous measurements from the accelerometer array and the accelerometers placed at the center-of-gravity of the aircraft or vehicle simulated. Rearranging Equation 4.1 in terms of the imposed translational accelerations along the tertiary and primary axes, Equations 4.5 and 4.6 may be resolved respectively. When the imposed loads along the vehicle axes are calculated, the attitude of the vehicle may be determined utilizing trigonometric relationships given in Equations 4.3 and 4.4.

Full Longitudinal Imposed Loading Calculations

$$A_{z,imposed} = \left.\frac{g[A_{z,i} - A_{x,cg}\sin(\theta_i) - (\cos(\theta_{man})\cos(\phi_{man})\cos(\theta_i))] + r_d[(r\sin(\theta_i) - p\cos(\theta_i))^2 + q^2]}{\cos(\theta_i)}\right| for, i = [2:12] \tag{4.5}$$

$$A_{x,imposed} = \left.\frac{g[A_{z,i} - A_{z,cg}\cos(\theta_i) + (\sin(\theta_{man})\sin(\theta_i))] + r_d\left[(2pr)\cos(\phi_i)\sin(\phi_i) - q^2\sin^2(\phi_i) - r^2\cos^2(\phi_i) - p^2\right]}{\sin(\theta_i)}\right| for, i = [1:6] \text{ and } [8:13] \tag{4.6}$$

For calculation of the imposed loading along the tertiary axis, Accelerometers #2 through #12 are utilized to avoid a divide by zero singularity condition due to the location of Accelerometers #1 and #13. For the determination of the imposed loading along the primary axis, Accelerometers #1 through #6 and Accelerometers # 8 through #13 are used to avoid a singularity condition due to the location of Accelerometer #7.

The imposed translational loading along the primary and tertiary axes may be solved for during pure rotational motion by resolving the $r_d(q^2)$ term directly from Accelerometer #7 that lies along the tertiary axis and from the accelerometer at the aircraft's center-of-gravity that senses acceleration along the tertiary axis, $A_{Z,CG}$. The acceleration measured by Accelerometer #7 is not influenced by the acceleration experienced along the aircraft's primary axis due to the orientation of Accelerometer #7 directly along the tertiary axis of the vehicle. Therefore, the acceleration experienced by Accelerometer #7 will register equal to the value of the accelerometer placed at the center-of-gravity location of the aircraft with the rotational component remaining present as shown in Equation 4.7.

$$\frac{r_d[q^2]}{g} = (A_{z,cg}) - (A_{z,7}) \tag{4.7}$$

A continuous attitude estimate is produced by the observer, therefore allowing for the previous estimated pitch angle, $\theta_{\text{Man, Prev}}$, to be known and utilized to produce an estimation of the current imposed translational acceleration. This result is valid because the attitude of the aircraft varies minimally over a small time interval and is shown graphically in Figure 4.7 where the maximum deviation is 0.1985 degrees from one time interval to another during the longitudinal maneuver. The algorithm method developed and implemented relies on a delayed attitude estimate from the accelerometer array therefore; Equations 4.8 and 4.9 are approximations of the imposed loads along the tertiary and primary axes for pure rotation respectively.

Pure Rotational Imposed Loading Calculations

$$\left(\frac{A_{z,imposed}}{g}\right) \approx \left(\frac{A_{z,i} - (A_{x,cg}\sin(\theta_i)) + (A_{z,cg}) - (A_{z,7})}{\cos(\theta_i)}\right) - (\cos(\theta_{man,prev}))\Bigg|\, for, i = [2:12] \tag{4.7}$$

$$\left(\frac{A_{x,imposed}}{g}\right) \approx \left(\frac{A_{z,i} - (A_{z,cg}\cos(\theta_i)) + (A_{z,cg}) - (A_{z,7})}{\sin(\theta_i)}\right) + (\sin(\theta_{man,prev}))\Bigg|\, for, i = [1:6]\ and\ [8:13] \tag{4.8}$$

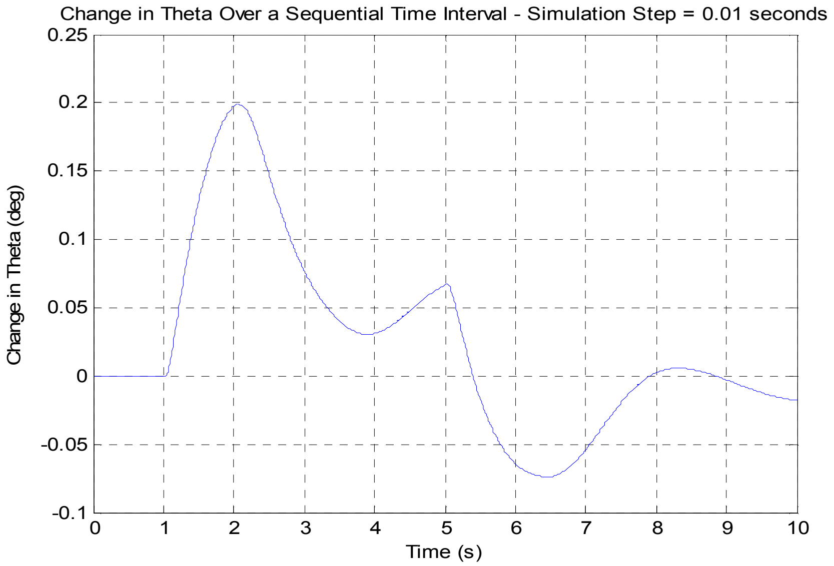

Figure 4.7: Longitudinal Attitude Change over a Time Interval

With the rotational acceleration approximations and imposed loading calculations derived, an estimate for the present vehicle longitudinal, or pitch attitude may be calculated from the previously derived equations for imposed loadings and is given by Equation 4.9, or alternatively as 4.10. Figures 4.8 through 4.13 represent the longitudinal attitude estimate determined by the accelerometer array against the truth value of the longitudinal attitude of the nonlinear aircraft model for each phase of the simulation study. Table 4.1 presents the maximum and mean attitude error experienced during each of the simulation phases.

Present Pitch Maneuver Angle Estimation

$$\theta_{maneuver,present} \approx \arctan\left[\frac{-\left[A_{x,cg} - \left(\frac{A_{x,imposed}}{g}\right)\right]}{A_{z,cg} - \left(\frac{A_{z,imposed}}{g}\right)}\right] \tag{4.9}$$

$$\theta_{maneuver,present} \approx \arcsin\left[\left(\frac{A_{x,imposed}}{g}\right) - A_{x,cg}\right] \tag{4.10}$$

Phase I – Longitudinal Maneuver: No Turbulence

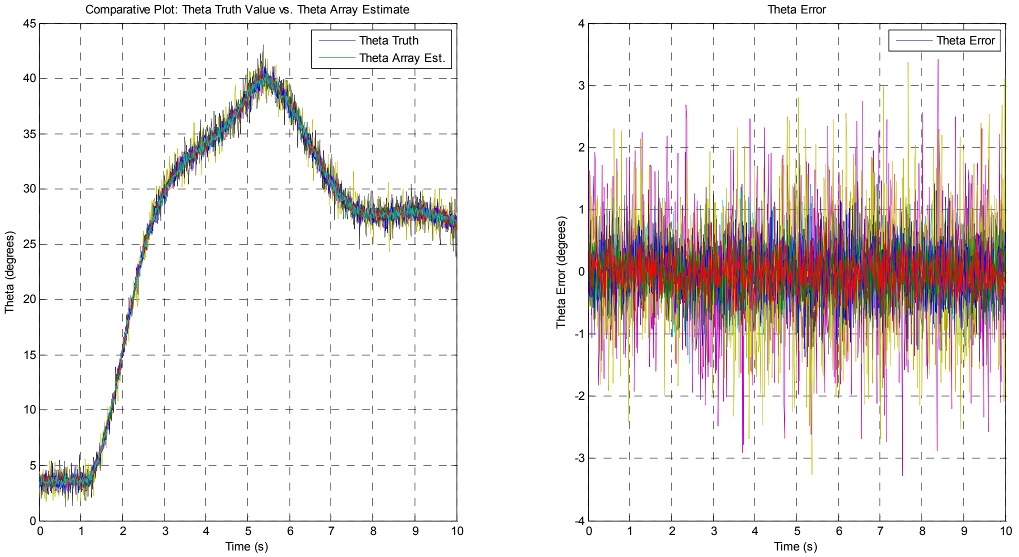

Figure 4.8: Phase I Attitude Estimation Results –Assessment of $\theta_{Estimate}$ and θ_{Truth}

Phase I – Longitudinal Maneuver: Turbulence

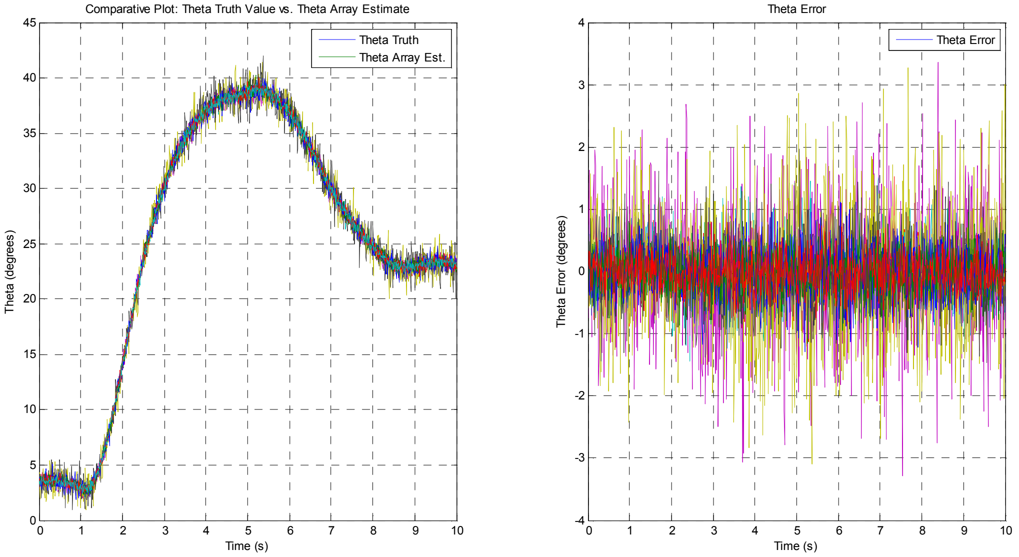

Figure 4.9: Phase I Attitude Estimation Results – Turbulence Assessment of $\theta_{Estimate}$ and θ_{Truth}

Phase II – Transverse Maneuver: No Turbulence

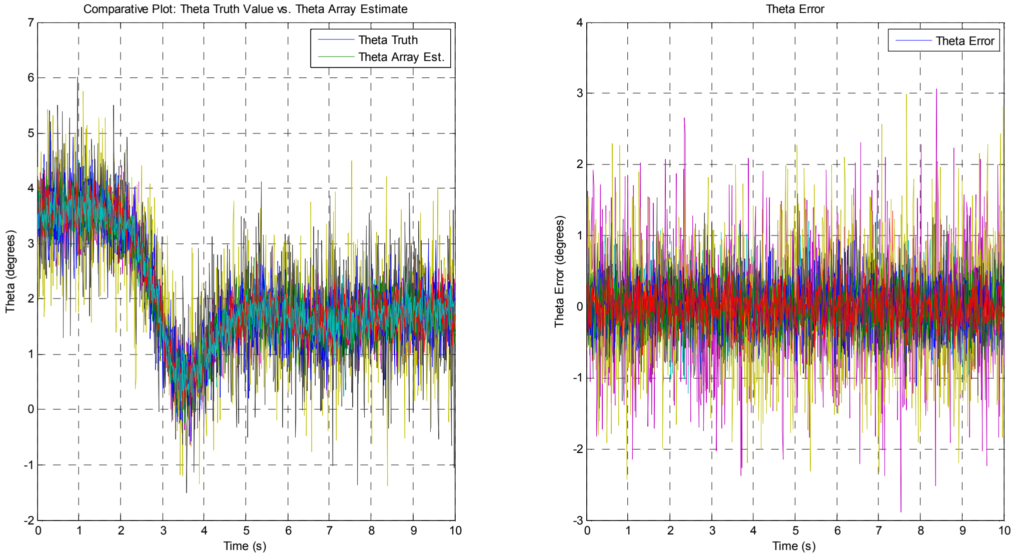

Figure 4.10: Phase II Attitude Estimation Results –Assessment of $\theta_{Estimate}$ and θ_{Truth}

Phase II – Transverse Maneuver: Turbulence

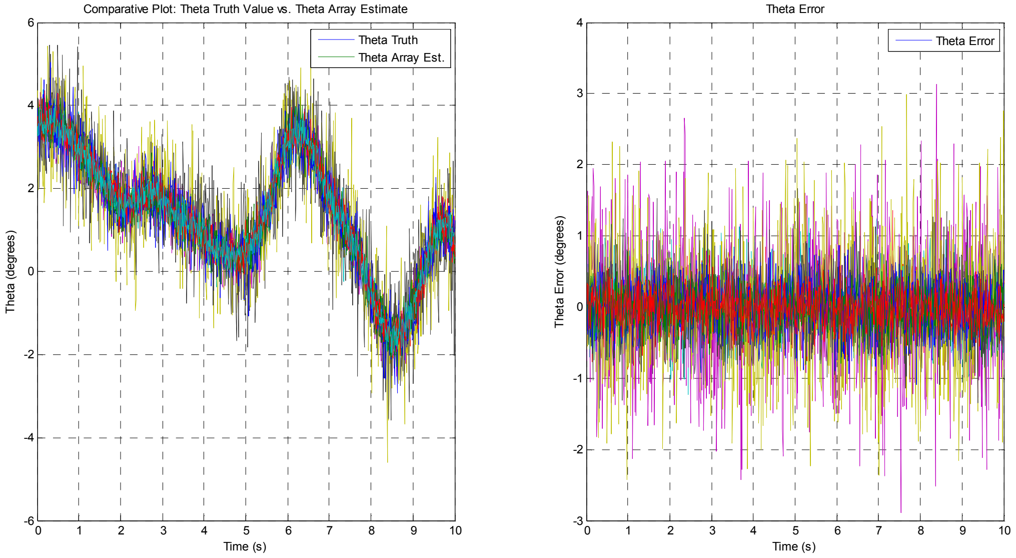

Figure 4.11: Phase II Attitude Estimation Results – Turbulence Assessment of $\theta_{Estimate}$ and θ_{Truth}

Phase III – Longitudinal/Transverse Maneuver: No Turbulence

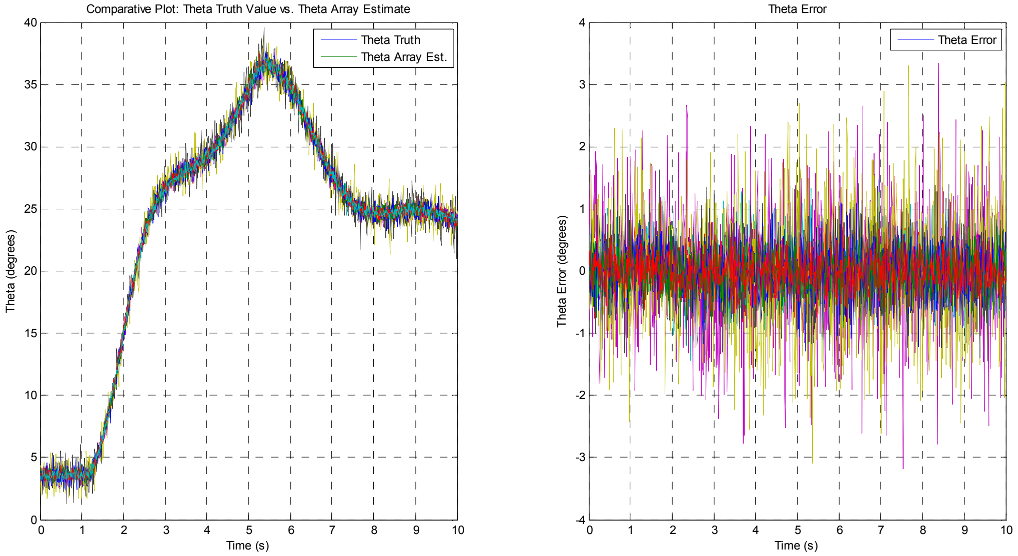

Figure 4.12: Phase III Attitude Estimation Results –Assessment of $\theta_{Estimate}$ and θ_{Truth}

Phase III– Longitudinal/Transverse Maneuver: Turbulence

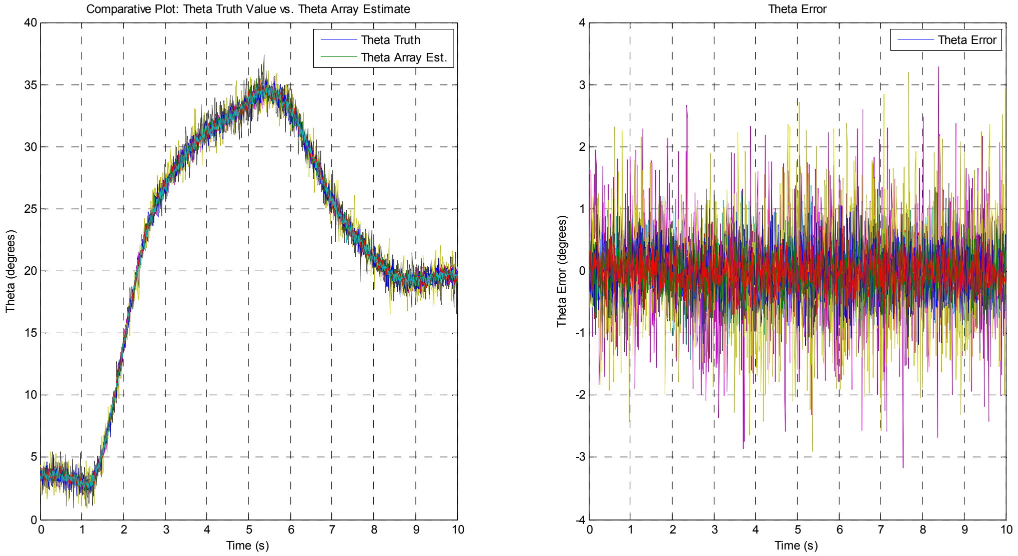

Figure 4.13: Phase III Attitude Estimation Results – Turbulence Assessment of $\theta_{Estimate}$ and θ_{Truth}

Aircraft Simulation Maneuver	Maximum Longitudinal Attitude Error (degrees)	Mean Longitudinal Attitude Error (degrees)
Longitudinal Maneuver	3.4194	1.7305
Longitudinal Maneuver with Turbulence	3.3652	1.6993
Transverse Maneuver	3.0682	1.4751
Transverse Maneuver with Turbulence	3.1306	1.4837
Longitudinal/Transverse Maneuver	3.3400	1.6742
Longitudinal/Transverse Maneuver with Turbulence	3.2912	1.6332

Table 4.1: Maximum and Mean Longitudinal Attitude Error

As shown in Table 4.1, the attitude estimate produced by the longitudinal accelerometer array relying on body rotational rates produces a fairly accurate estimate of the longitudinal attitude with maximum errors for all maneuvers being less than 3.5000 degrees and mean errors less than 1.7500 degrees. The present estimate of the longitudinal attitude is then used in conjunction with the present pitch rate determined by the rate gyroscope for estimation of the rate gyro bias.

A pure rotational acceleration estimate is needed for the implementation of the complementary filter. The triggers of the complementary filter occur when the difference between two consecutive accelerometers fall within a defined threshold value as described previously in Section 4.1. The derivation of the pure rotational approximation must be performed prior to the differencing execution of the complementary filter algorithm and is shown in Equation 4.11.

$$A_{z,i} - \left(\frac{A_{x,imposed}}{g}\right)\sin(\theta_i) - \left(\frac{A_{z,imposed}}{g}\right)\cos(\theta_i) = (\cos(\theta_{Man})\cos(\theta_i)) - (\sin(\theta_{Man})\sin(\theta_i)) - \left(\frac{r_d q^2}{g}\right) \tag{4.11}$$

The left side of Equation 4.11 is determined utilizing accelerometer readings in conjunction with the imposed loading values along the tertiary and primary axes given previously by Equations 4.7 and 4.8 respectively for pure rotation conditions. Equation 4.12 represents a pure rotation approximation of the accelerometer measurements where the imposed loading terms and therefore the effects of wind gust, turbulence, and environmental factors are subtracted out from the accelerometer signals during dynamic maneuvers.

$$A_{z,i}, PureRotationApproximation \approx A_{z,i} - \left(\frac{(A_{x,imposed})}{g}\right)\sin(\theta_i) - \left(\frac{(A_{z,imposed})}{g}\right)\cos(\theta_i) \tag{4.12}$$

Transverse Accelerometer Array

The work completed in this feasibility study focuses on the expansion of the method previously developed [2, 6] through the addition of a third accelerometer at the vehicle's center-of-gravity to measure the imposed translational accelerations that occur not only along the aircraft's primary and tertiary axes, but also along the secondary axis as well.

Utilizing the same method implemented on the longitudinal array, Equation 3.13 may be utilized to resolve the accelerometers located at the center-of-gravity location along the transverse array in terms of the registered sum of the imposed motion and gravitational accelerations. The total acceleration, measured in gees, experienced along the secondary axis, $A_{Y,CG}$, and tertiary axis, $A_{Z,CG}$, are given by Equations 4.13 and 4.14 respectively and are derived in full in Appendix D.

$$A_{Y,CG} = \frac{A_{Y,imposed}}{g} + (\cos\theta_{Man} \sin\phi_{Man}) \tag{4.13}$$

$$A_{Z,CG} = \frac{A_{Z,imposed}}{g} + (\cos\theta_{Man} \cos\phi_{Man}) \tag{4.14}$$

As stated previously, due to the inability to directly measure the imposed translational or rotational acceleration imparted on the aircraft during maneuvers, an estimation of the imposed acceleration loads must be performed utilizing previous measurements from the accelerometer arrays and the accelerometers placed at the center-of-gravity of the aircraft. Rearranging Equation 4.2 in terms of the imposed translational accelerations along the secondary and tertiary axes, Equations 4.15 and 4.16 may be resolved respectively. When the imposed loads along the vehicle axes are calculated, the attitude of the vehicle may be determined utilizing trigonometric relationships given in Equations 4.13 and 4.14.

Full Transverse Imposed Loading Calculations

$$A_{y,imposed} = \left.\frac{g[A_{y,i} - A_{z,cg}\sin(\phi_i) - (\cos(\theta_{man})\sin(\phi_{man})\cos(\phi_i))] - r_d\left[(2pr)\cos(\phi_i)\sin(\phi_i) - q^2\sin^2(\phi_i) - r^2\cos^2(\phi_i) - p^2\right]}{\cos(\phi_i)}\right| for, i = [1:6] \; and \; [8:13] \tag{4.15}$$

$$A_{z,imposed} = \left.\frac{g[A_{y,i} - A_{y,cg}\cos(\phi_i) - (\cos(\theta_{man})\cos(\phi_{man})\sin(\phi_i))] - r_d\left[(2pr)\cos(\phi_i)\sin(\phi_i) - q^2\sin^2(\phi_i) - r^2\cos^2(\phi_i) - p^2\right]}{\sin(\phi_i)}\right| for, \; i = [2:12] \tag{4.16}$$

For calculation of the imposed loading along the tertiary axis as given by Equation 4.16, Accelerometers #2 through #12 are utilized to avoid a divide by zero singularity condition due to the location of Accelerometers #1 and #13. For the determination of the imposed loading along the secondary axis, Accelerometers #1 through #6 and Accelerometers # 8 through #13 are used to avoid a singularity condition due to the location of Accelerometer #7.

The imposed translational loading along the secondary and tertiary axes may be solved for during pure rotational motion by resolving the $r_d(p^2)$ term directly from Accelerometer #7 that lies along the tertiary axis and from the accelerometer at the aircraft's center-of-gravity that senses acceleration along the tertiary axis, $A_{Z,CG}$. The acceleration measured by Accelerometer #7 is not influenced by the acceleration experienced along the aircraft's secondary axis due to the orientation of Accelerometer #7 directly along the tertiary axis of the aircraft. Therefore, the acceleration experienced by Accelerometer #7 will register equal to the value of the accelerometer placed at the center-of-gravity location of the aircraft with the rotational component remaining present as shown in Equation 4.17.

$$\frac{r_d[p^2]}{g} = (A_{z,cg}) - (A_{z,7}) \tag{4.17}$$

Discussed previously, a continuous attitude estimate is produced by the accelerometer array from both the longitudinal and transverse accelerometer arrays. Therefore the previous estimated roll angle, $\phi_{\text{Man, Prev}}$, may be known and utilized to produce an estimate of the current imposed translational acceleration. This result is valid because the attitude of the aircraft varies minimally over a small time interval and is shown graphically in Figure 4.14 where the maximum deviation is 0.2206 degrees from one time interval to another during the transverse maneuver. The algorithm method developed and implemented relies on a delayed attitude estimate from the accelerometer array. Therefore Equations 4.18 and 4.19 are approximations of the imposed loads along the tertiary and secondary axes for pure rotation respectively.

Pure Rotational Imposed Loading Calculations

$$\left(\frac{A_{z,imposed}}{g}\right) \approx \left(\frac{A_{y,i} - (A_{y,cg}\cos(\phi_i)) + (A_{z,cg}) - (A_{y,7})}{\sin(\phi_i)}\right) - (\cos(\phi_{man,prev}))\Bigg|\, for,\ i = [2:12] \tag{4.18}$$

$$\left(\frac{A_{y,imposed}}{g}\right) \approx \left(\frac{A_{y,i} - (A_{z,cg}\sin(\phi_i)) + (A_{z,cg}) - (A_{y,7})}{\cos(\phi_i)}\right) - (\sin(\phi_{man,prev}))\Bigg|\, for, i = [1:6]\ and\ [8:13] \tag{4.19}$$

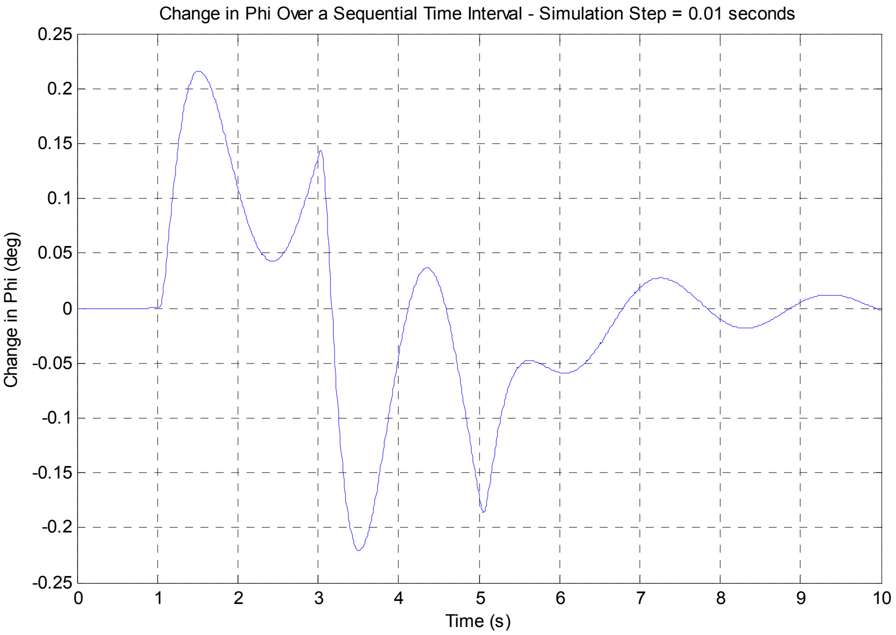

Figure 4.14: Transverse Attitude Change over a Time Interval

With the rotational acceleration approximations and imposed loading calculations derived, an estimate for the vehicle's present transverse, or roll attitude may be calculated from the previously derived equations for imposed loadings and is given by Equation 4.20. Figures 4.15 through 4.20 represent the transverse attitude estimate determined by the accelerometer array against the truth value of the transverse attitude of the nonlinear aircraft model for each phase of the simulation study. Table 4.2 presents the maximum and mean attitude error experienced during each of the simulation phases.

Present Roll Maneuver Angle Estimation

$$\phi_{maneuver,present} \approx \arctan\left[\frac{A_{y,cg} - \left(\frac{A_{y,imposed}}{g}\right)}{A_{z,cg} - \left(\frac{A_{z,imposed}}{g}\right)}\right] \tag{4.20}$$

Phase I – Longitudinal Maneuver: No Turbulence

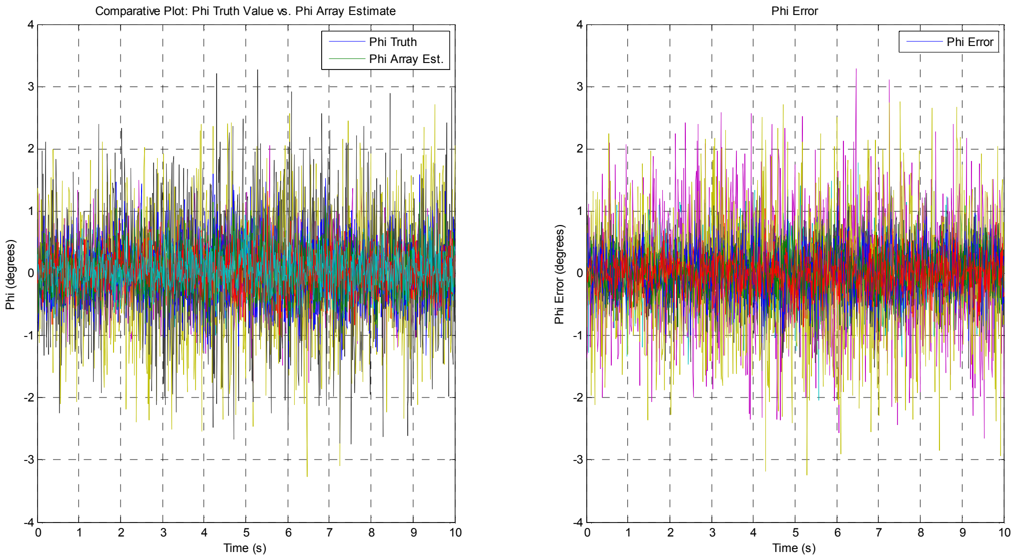

Figure 4.15: Phase I Attitude Estimation Results – Assessment of ϕ_{Estimate} and ϕ_{Truth}

Phase I – Longitudinal Maneuver: Turbulence

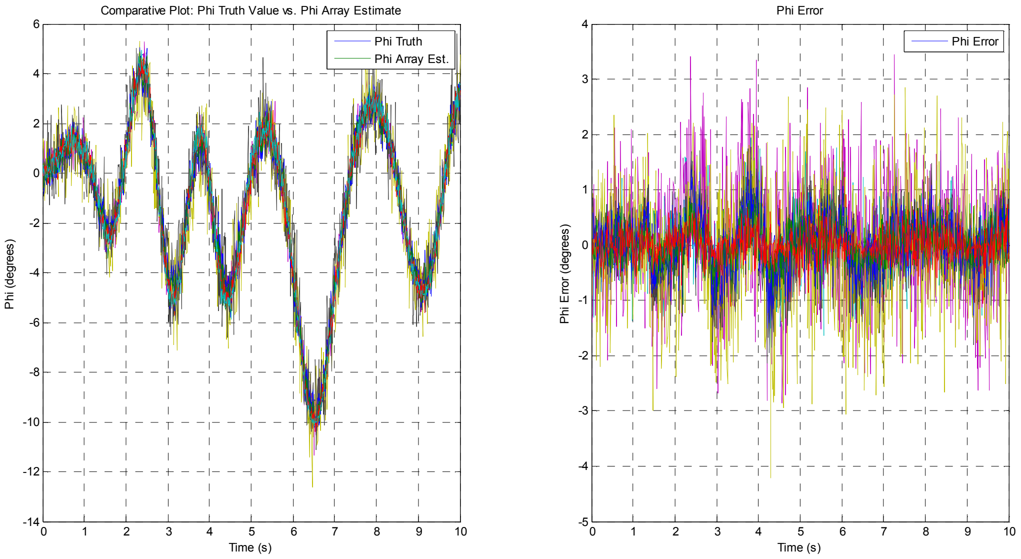

Figure 4.16: Phase I Attitude Estimation Results – Turbulence Assessment of ϕ_{Estimate} and ϕ_{Truth}

Phase II – Transverse Maneuver: No Turbulence

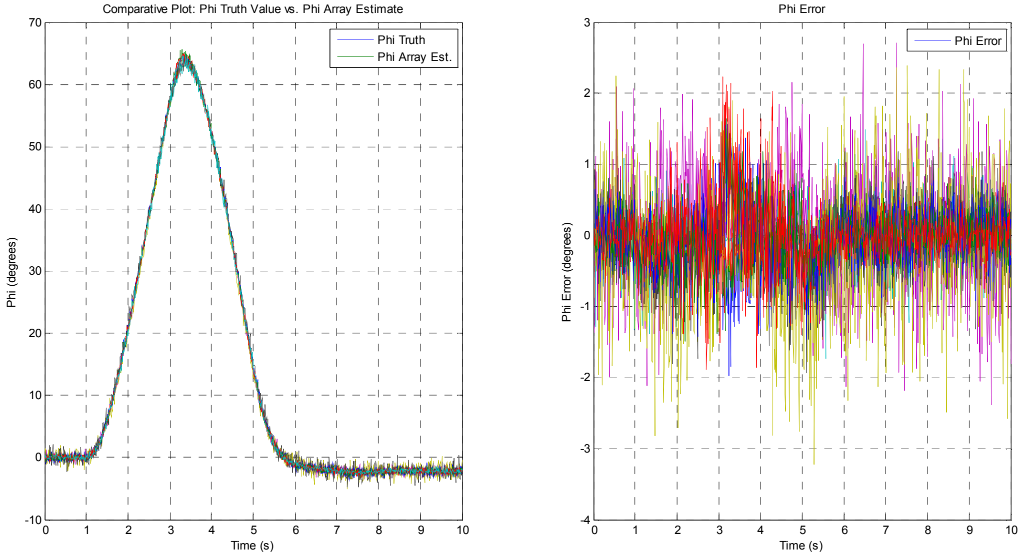

Figure 4.17: Phase II Attitude Estimation Results – Assessment of ϕ_{Estimate} and ϕ_{Truth}

Phase II – Transverse Maneuver: Turbulence

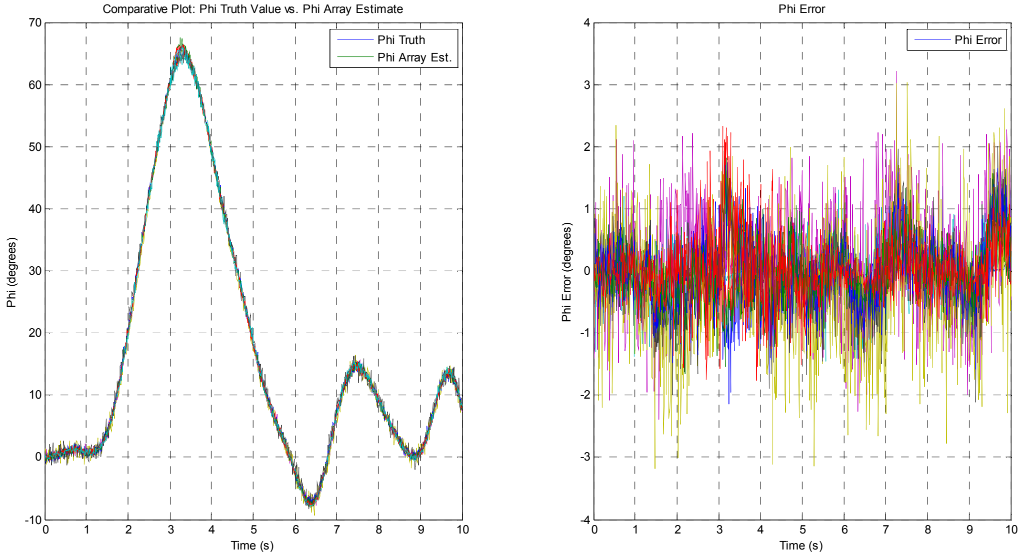

Figure 4.18: Phase II Attitude Estimation Results – Turbulence Assessment of ϕ_{Estimate} and ϕ_{Truth}

Phase III – Longitudinal/Transverse Maneuver: No Turbulence

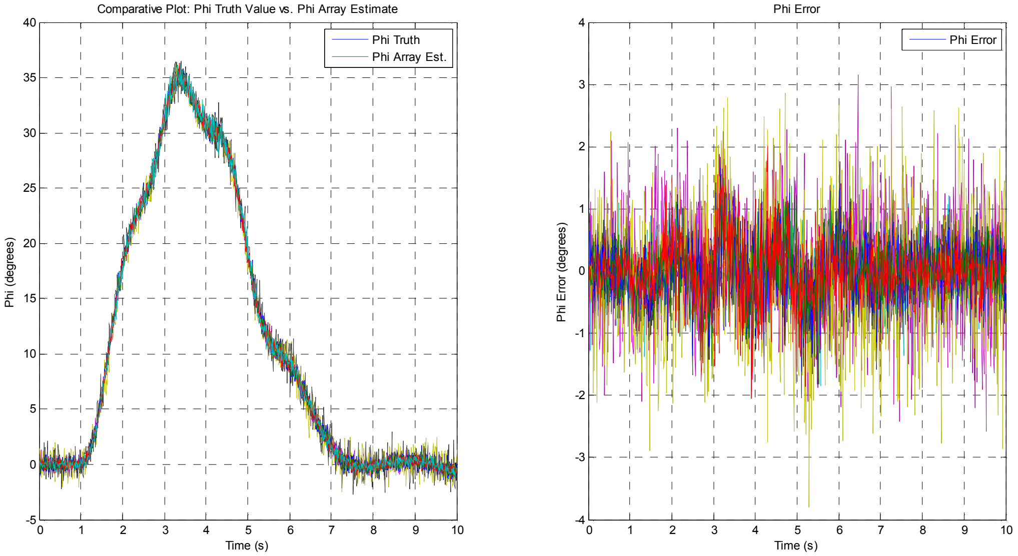

Figure 4.19: Phase III Attitude Estimation Results – Assessment of ϕ_{Estimate} and ϕ_{Truth}

Phase III – Longitudinal/Transverse Maneuver: Turbulence

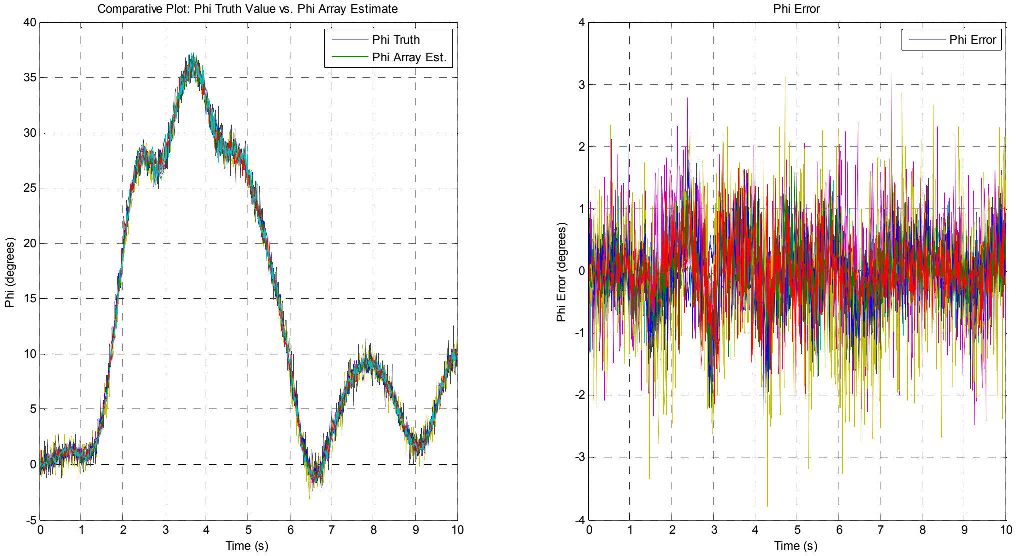

Figure 4.20: Phase III Attitude Estimation Results –
Turbulence Assessment of ϕ_{Estimate} and ϕ_{Truth}

Aircraft Simulation Maneuver	**Maximum Transverse Attitude Error (degrees)**	**Mean Transverse Attitude Error (degrees)**
Longitudinal Maneuver	3.2866	1.6609
Longitudinal Maneuver with Turbulence	4.2167	1.9752
Transverse Maneuver	3.2186	1.9803
Transverse Maneuver with Turbulence	3.2148	2.1148
Longitudinal/Transverse Maneuver	3.8026	1.9282
Longitudinal/Transverse Maneuver with Turbulence	3.7895	2.0192

Table 4.2: Maximum and Mean Transverse Attitude Error

As shown in Table 4.2, the attitude estimate produced by the transverse accelerometer array relying on body rotational rates produces a fairly accurate estimate of the transverse attitude with maximum errors for all maneuvers conducted valued at less than 4.250 degrees and mean errors less than 2.150 degrees. The present estimate of the transverse attitude is then used in conjunction with the present roll rate determined by the rate gyroscope for estimation of the rate gyro bias, just as the present estimate of the longitudinal attitude was utilized as stated previously.

A pure rotational acceleration estimate is needed for the implementation of the complementary filter. The triggers of the complementary filter occur when the difference between two consecutive accelerometers fall within a defined threshold value as described previously in Section 4.1. The derivation of the pure rotational approximation must be performed prior to the differencing execution of the complementary filter algorithm and is shown in Equation 4.21.

$$A_{y,i}-\left(\frac{A_{y,imposed}}{g}\right)\cos(\phi_i)-\left(\frac{A_{z,imposed}}{g}\right)\sin(\phi_i)=(\sin(\phi_{Man})\cos(\phi_i))+(\cos(\phi_{Man})\sin(\phi_i))-\left(\frac{r_d p^2}{g}\right) \tag{4.21}$$

The left side of Equation 4.21 is determined utilizing accelerometer readings in conjunction with the imposed loading values along the tertiary and secondary axes given previously by Equations 4.18 and 4.19 respectively for pure rotation conditions. Equation 4.22 represents a pure rotation approximation of the accelerometer measurements where the imposed loading terms and therefore the effects of wind gust, turbulence, and environmental factors are subtracted out from the accelerometer signals during dynamic maneuvers.

$$A_{y,i}, PureRotationApproximation \approx A_{y,i}-\left(\frac{(A_{y,imposed})}{g}\right)\cos(\phi_i)-\left(\frac{(A_{z,imposed})}{g}\right)\sin(\phi_i) \tag{4.22}$$

4.2.2 Signal Differencing Imposed Loading Determination

Longitudinal Accelerometer Array

The concept of signal differencing (SD) involves taking the difference of symmetric accelerometer signals along the accelerometer array, allowing for the feedback of the nonlinear bracket terms given in Equations 4.5 and 4.6 to be simplified in terms of symmetric accelerometer signals. Utilization of this method allows for a more accurate and reliable solution to the desired imposed loading terms, and ultimately the estimation of the vehicle's attitude, without a reliance on the rate gyro measurements. Therefore, in the absence or malfunction of the aircraft's rate gyro angular rate terms, the method of signal differencing may be utilized to accurately determine the value of the imposed translational and rotational accelerations for estimation of the aircraft's attitude.

Implementation of the signal differencing method requires the establishment of two symmetric planes within the longitudinal pitch array. The two symmetric planes are characterized by a left-half plane where all negative angles of θ are considered and a right-half plane where all positive angles of θ are considered. Utilizing this distinction allows for the formulation of the following two generalized forms, given by Equations 4.23 and 4.24, for the left-half and right-half plane of the longitudinal accelerometer array respectively.

Left-Half Pitch Plane: Sin (θ) = Negative

$$gA_{z,14-i} = g[A_{x,cg}abs(\sin(\theta_i)) + A_{z,cg}\cos(\theta_i)] - r_d\left[r^2\sin^2(\theta_i) - (2pr)\cos(\theta_i)abs(\sin(\theta_i)) + p^2\cos^2(\theta_i) + q^2\right] \tag{4.23}$$

Right-Half Pitch Plane: Cos (θ) = Positive

$$gA_{z,i} = g[-A_{x,cg}abs(\sin(\theta_i)) + A_{z,cg}\cos(\theta_i)] - r_d\left[r^2\sin^2(\theta_i) - (2pr)\cos(\theta_i)abs(\sin(\theta_i)) + p^2\cos^2(\theta_i) + q^2\right] \tag{4.24}$$

Derivation of the imposed loading equations, given previously as Equations 4.5 and 4.6, in terms of the signal differencing expression requires the nonlinear bracket term, $r_d[(r^2\sin^2\theta_i - (2pr)\cos\theta_i\sin\theta_i + p^2\cos^2\theta_i) + q^2]$, to be separated into two separate expressions defined by Equation 4.25.

$$r_d\left[r^2\sin^2(\theta_i) - (2pr)\cos(\theta_i)abs(\sin(\theta_i)) + p^2\cos^2(\theta_i) + q^2\right] = r_d[(r^2\sin^2(\theta_i) + p^2\cos^2(\theta_i) + q^2)] + r_d[(-2pr)\cos(\theta_i)\sin(\theta_i)] \tag{4.25}$$

Generalization of the r_d (2pr) Bracket Term

A generalized representation of the r_d (2pr) expression in terms accelerometer signals is necessary and critical due to the configuration and displacement of the accelerometer locations along the longitudinal accelerometer array. Differencing Equation 4.24 from 4.23 yields the generalized representation of the (r_d) 2pr term as an expression of symmetric accelerometer signals and is shown as Equations 4.26 and 4.27.

$$g(A_{z,14-i}-A_{z,i})=2g(A_{x,cg})abs(\sin(\theta_i))+2r_d\cos(\theta_i)abs(\sin(\theta_i)) \tag{4.26}$$

$$\frac{g\left[(A_{z,14-i}-A_{z,i})-2(A_{x,cg})abs(\sin(\theta_i))\right]}{2\left[\cos(\theta_i)abs(\sin(\theta_i))\right]}=(2pr)r_d\Bigg|\ for,\ i=[1:6] \tag{4.27}$$

Generalization of the $r_d[r^2\sin^2\theta_i+p^2\cos^2\theta_i+q^2]$ Bracket Term

Implementing the same method utilized to represent the r_d (2pr) term as an expression of symmetric accelerometer signals about the longitudinal array, the r_d $[r^2\sin^2\theta_i + p^2\cos^2\theta_i + q^2]$ is also represented in terms of symmetric accelerometer signals. However, to complete this formulation, the right-half and left-half accelerometer plane equations given previously as Equations 4.23 and 4.24 must be added together to ensure the $(2pr)(\cos\theta_i(\sin\theta_i))$ term drops out during the derivation sequence. Therefore, utilizing Equations 4.23 and 4.24, Equations 4.28 and 4.29 may be derived for the representation of the r_d $[r^2\sin^2\theta_i + p^2\cos^2\theta_i + q^2]$ term as an expression of symmetric accelerometer signals.

$$g(A_{z,14-i}+A_{z,i})=2g(A_{z,cg})(\cos(\theta_i))+2r_d\left[r^2\sin^2\theta_i+p^2\cos^2\theta_i+q^2\right] \tag{4.28}$$

$$\frac{g\left[(A_{z,14-i}+A_{z,i})-2(A_{x,cg})(\cos(\theta_i))\right]}{-2}=r_d[r^2\sin^2(\theta_i)+p^2\cos^2(\theta_i)+q^2] \tag{4.29}$$

The two expressions of the large nonlinear equation are now expressed in terms of symmetric accelerometer signals as given by Equations 4.27 and 4.29. With these two expressions now defined, the imposed loading terms defined previously as Equations 4.5 and 4.6 may be redefined and expressed solely in terms of accelerometer signals. Utilizing this method of imposed loading determination eliminates the reliance on the aircraft's angular rate terms resolved by the rate gyroscopes.

The imposed loading expression for translational and rotational loadings experienced along the aircraft's tertiary and primary axes are redefined in terms of signal differencing expressions as Equations 4.30 and 4.31 respectively.

$$A_{z,imposed} = \left. \frac{g[A_{z,i} - A_{x,cg}\sin(\theta_i) - (\cos(\theta_{man})\cos(\phi_{man})\cos(\theta_i)] + [B - A(\cos(\theta_i)\sin(\theta_i))]}{\cos(\theta_i)} \right| \mathit{for},\ i = [2:12] \tag{4.30}$$

$$A_{x,imposed} = \left. \frac{g[A_{z,i} - A_{x,cg}\cos(\theta_i) + (\sin(\theta_{man})\sin(\theta_i)] + [B - A(\cos(\theta_i)\sin(\theta_i))]}{\sin(\theta_i)} \right| \mathit{for},\ i = [1:6]\ \mathit{and}\ [8:13] \tag{4.31}$$

where "A" and "B" are defined as Equations 4.27 and 4.29 given previously.

$$A = \frac{g\left[(A_{z,14-i} - A_{z,i}) - 2(A_{x,cg})abs(\sin(\theta_i))\right]}{2(\cos(\theta_i)abs(\sin(\theta_i))}$$

$$B = \frac{g\left[(A_{z,14-i} + A_{z,i}) - 2(A_{x,cg})(\cos(\theta_i))\right]}{-2}$$

The method of differencing symmetric accelerometer signals along the longitudinal accelerometer array for resolution of the nonlinear expression and eliminating the reliance of angular rate terms resolved from the use of rate gyroscopes enables an alternative method for the algorithm scheme developed and implemented to assess and determine the imposed loads along the primary and tertiary axes respectively for means of accurate and reliable attitude estimation.

Equations 4.30 and 4.31 may now be utilized for attitude estimation in the longitudinal plane through the use of the defined Equations for estimates of the present pitch angle given previously as Equations 4.9 and 4.10. Figures 4.21 through 4.26 represent the longitudinal attitude estimate determined by the signal differencing imposed loading algorithm for longitudinal attitude estimation against the truth value of the longitudinal attitude of the aircraft simulation model for each phase of the simulation study conducted. Table 4.3 presents the maximum and mean attitude error experienced during each phase of the simulation performed.

Phase I – Longitudinal Maneuver: No Turbulence

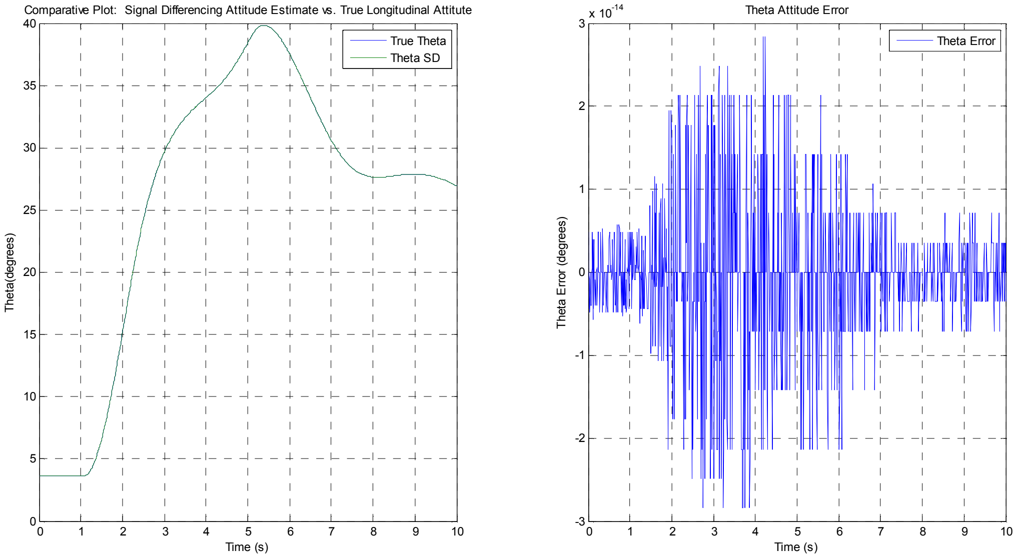

Figure 4.21: Phase I SD Attitude Estimation Results –Assessment of $\theta_{SD\text{-}Estimate}$ and θ_{Truth}

Phase I – Longitudinal Maneuver: Turbulence

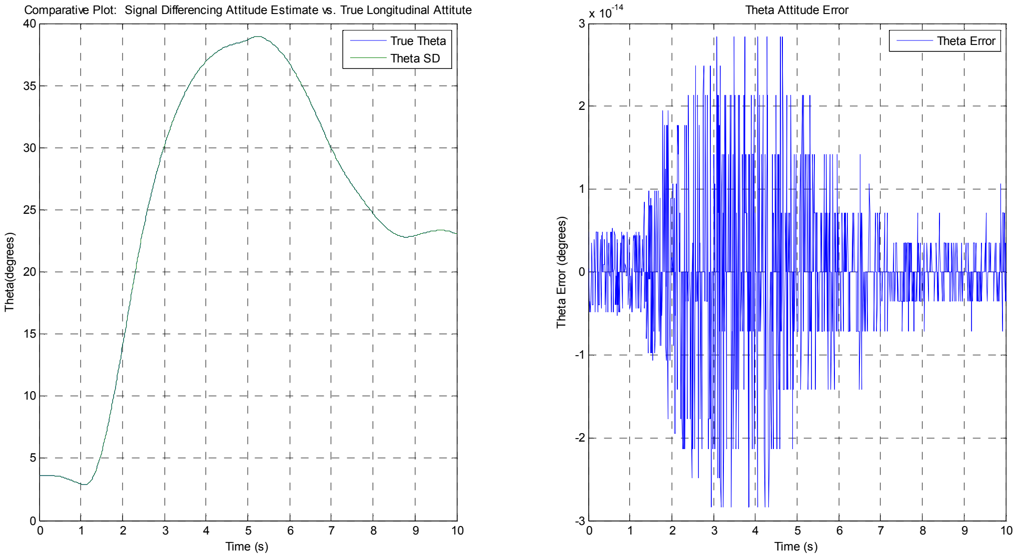

Figure 4.22: Phase I SD Attitude Estimation Results – Turbulence Assessment of $\theta_{SD\text{-}Estimate}$ and θ_{Truth}

Phase II – Transverse Maneuver: No Turbulence

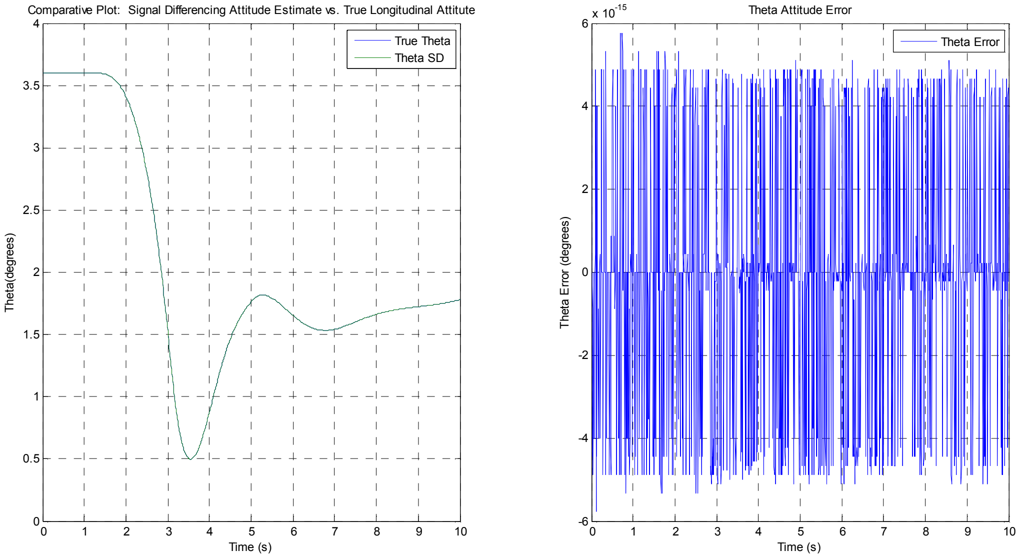

Figure 4.23: Phase II SD Attitude Estimation Results –Assessment of $\theta_{SD\text{-}Estimate}$ and θ_{Truth}

Phase II– Transverse Maneuver: Turbulence

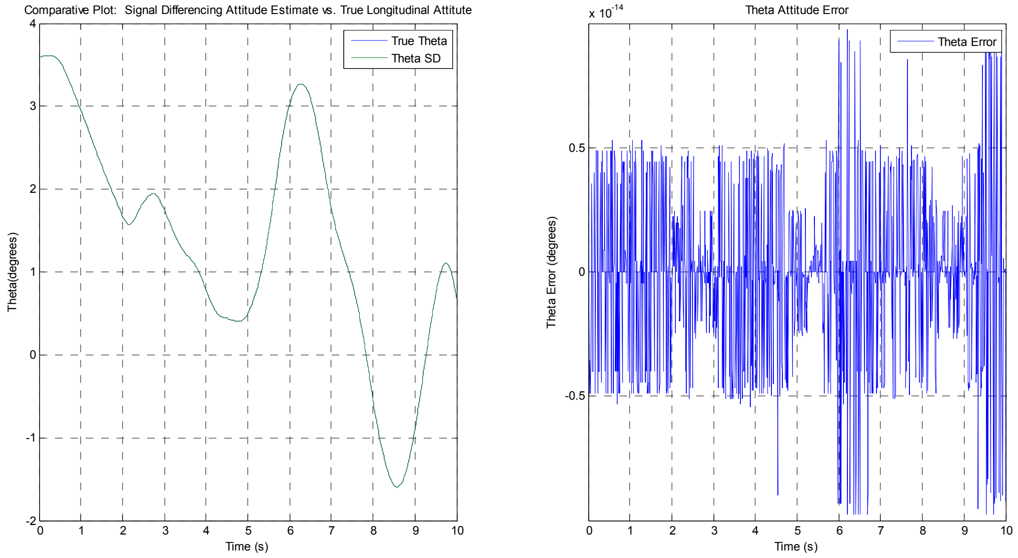

Figure 4.24: Phase II SD Attitude Estimation Results –
Turbulence Assessment of $\theta_{SD\text{-}Estimate}$ and θ_{Truth}

Phase III – Longitudinal/Transverse Maneuver: No Turbulence

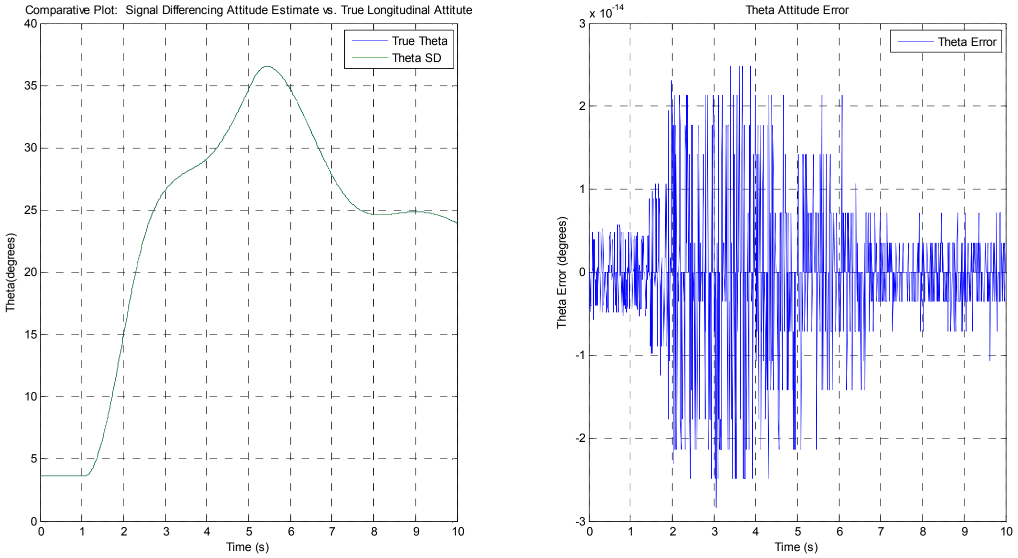

Figure 4.25: Phase III SD Attitude Estimation Results –Assessment of $\theta_{\text{SD-Estimate}}$ and θ_{Truth}

Phase III – Longitudinal/Transverse Maneuver: Turbulence

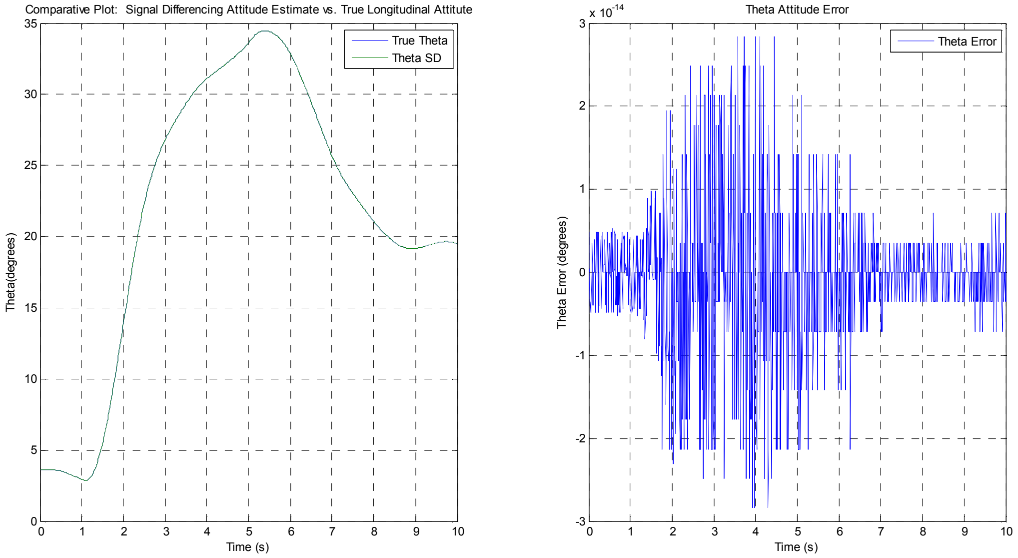

Figure 4.26: Phase III SD Attitude Estimation Results –
Turbulence Assessment of $\theta_{\text{SD-Estimate}}$ and θ_{Truth}

Aircraft Simulation Maneuver	**Maximum Longitudinal SD Attitude Error (degrees)**	**Mean Longitudinal SD Attitude Error (degrees)**
Longitudinal Maneuver	2.8422e-014	5.4253e-015
Longitudinal Maneuver with Turbulence	2.8422e-014	5.4134e-015
Transverse Maneuver	5.7732e-015	2.4505e-015
Transverse Maneuver with Turbulence	9.7700e-015	2.4390e-015
Longitudinal/Transverse Maneuver	2.8422e-014	5.2616e-015
Longitudinal/Transverse Maneuver with Turbulence	2.8422e-014	5.4546e-015

Table 4.3: Maximum and Mean Signal Differencing Longitudinal Attitude Error

As shown in Table 4.3, the attitude estimate produced by the longitudinal accelerometer array implementing the signal differencing method produces an extremely accurate estimate of the longitudinal attitude with maximum errors for all maneuvers being less than 2.8500e-14 degrees and mean errors less than 5.4600e-15 degrees.

The present estimate of the longitudinal attitude determined through the implementation of the signal differencing method is then used in conjunction with the present pitch rate determined by the rate gyroscope for estimation of the rate gyro bias. As it may be seen in Table 4.3, the longitudinal attitude error produced during the operation of the signal differencing imposed loading determination algorithm is far less than the error produced during the attitude estimation method reliant on the body rotational rates produced by the rate gyro.

Transverse Accelerometer Array

The model of signal differencing may also be implemented on the transverse accelerometer array for resolution of the large nonlinear expression in terms of symmetric accelerometer signals along the transverse array. Utilization of this method allows for a more accurate and reliable solution to the desired imposed loading terms along the secondary and tertiary axes without a reliance on the angular rate terms resolved by the use of rate gyroscopes. Therefore, in the absence or malfunction of the aircraft's rate gyro angular rate terms, the method of signal differencing may be utilized on the transverse accelerometer array to accurately determine the value of the imposed translational and rotational accelerations for precise estimation of the aircraft's present attitude.

Implementation of the signal differencing method requires the establishment of two symmetric planes within the transverse roll array. The two symmetric planes are characterized by a left-half plane where all negative angles of ϕ are considered and a right-half plane where all positive angles of ϕ are considered. Utilizing this distinction allows for the formulation of the following two generalized forms, given by Equations 4.32 and 4.33, for the left-half and right-half plane of the transverse array respectively.

Right-Half Roll Plane: Cos (ϕ) = Positive

$$gA_{y,i} = gA_{y,cg}abs(\cos(\phi_i) + gA_{z,cg}\sin(\phi_i) + r_d[(2qr)\sin(\phi_i)abs(\cos(\phi_i)) - (p^2) - (r^2\cos^2(\phi_i)) - (q^2\sin^2(\phi_i))]$$

(4.32)

Left-Half Roll Plane: Cos (ϕ) = Negative

$$gA_{y,14-i} = -gA_{y,cg}abs(\cos(\phi_i) + gA_{z,cg}\sin(\phi_i) + r_d[(2qr)\sin(\phi_i)abs(\cos(\phi_i)) - (p^2) - (r^2\cos^2(\phi_i)) - (q^2\sin^2(\phi_i))]$$

(4.33)

Derivation of the imposed loading equations along the secondary and tertiary axes, given previously by Equations 4.15 and 4.16, in terms of the signal differencing terms requires the nonlinear bracket expression, $\mathrm{r_d}[(-2\mathrm{qr})\sin\phi_\mathrm{i}\,\mathrm{abs}(\cos\phi_\mathrm{i}) - (\mathrm{p}^2) - (\mathrm{r}^2\cos^2\phi_\mathrm{i}) - (\mathrm{q}^2\sin^2\phi_\mathrm{i})]$, to be divided into two separate terms defined by Equation 4.34.

$$r_d[(2qr)\sin(\phi_i)abs(\cos(\phi_i)) - (p^2) - (r^2\cos^2(\phi_i)) - (q^2\sin^2(\phi_i))] = r_d[(2qr)\sin(\phi_i)\cos(\phi_i)] - r_d(-(p^2) - (r^2\cos^2(\phi_i)) - (q^2\sin^2(\phi_i)))]$$

(4.34)

Generalization of the $(2qr(r_d))$ Bracket Term

A generalized representation of the r_d (2qr) term is necessary and critical due to the configuration and displacement of the accelerometer locations along the transverse accelerometer array. Differencing Equation 4.32 from Equation 4.33 yields the generalized representation of the (r_d) 2qr term as an expression of symmetric accelerometer signals on the transverse array and is shown by Equation 4.35 and 4.36.

$$g(A_{y,14-i} - A_{y,i}) + 2g(A_{y,cg})abs(\cos(\phi_i)) = r_d[\_(-4qr)\sin(\phi_i)abs(\cos(\phi_i))]$$

(4.35)

$$(2qr)r_d = \left.\frac{g\left[(A_{y,14-i} - A_{y,i}) + 2(A_{y,cg})abs(\cos(\phi_i))\right]}{-2(abs\cos(\phi_i))(\sin(\phi_i))}\right| \quad for,\ i = [1:6]$$

(4.36)

Generalization of the $r_d[-(p^2) - (r^2\cos^2\phi_i) - (q^2\sin^2\phi_i)]$ Bracket Term

Implementing the same method utilized to develop a generalized representation of the r_d (2qr) term as an expression of symmetric accelerometer signals about the transverse array, the $r_d[-(p^2) - (r^2\cos^2\phi_i) - (q^2\sin^2\phi_i)]$ is represented in terms of symmetric accelerometer signals. However, to complete this formulation, the right-half and left-half accelerometer plane equations given previously as Equations 4.33 and 4.34 must be added together to ensure the (2qr) term drops out during the derivation sequence.

Therefore, summing Equations 4.33 and 4.34 allows for Equations 4.37 and 4.38 to be derived for the generalized representation of the r_d $[-p^2 - r^2\cos^2\phi_i - q^2\sin^2\phi_i]$ term as an expression of symmetric accelerometer signals along the transverse accelerometer array without a reliance on the rate gyro body rate terms.

$$g[(A_{y,14-i}+A_{y,i})-2A_{z,cg}\sin\phi_i]=2r_d[-p^2-(r^2\cos^2\phi_i)-(q^2\sin^2\phi_i)] \tag{4.37}$$

$$r_d[-(p^2)-(r^2\cos^2(\phi_i))-(q^2\sin^2(\phi_i))]=\frac{g\left[(A_{y,14-i}+A_{y,i})-2(A_{z,cg})(\sin(\phi_i))\right]}{2} \tag{4.38}$$

The two terms of the large nonlinear expression are now represented in terms of symmetric accelerometer signals along the transverse array as given by Equations 4.36 and 4.38. With these two expressions now defined, the imposed loading calculations defined previously as Equations 4.15 and 4.16 may be redefined and expressed solely in terms of accelerometer signals. Utilizing this method of imposed loading determination once again eliminates the reliance on the aircraft's angular rate terms as resolved by the rate gyro. The imposed loading expression for translational and rotational loadings experienced along the aircraft's tertiary and secondary axes are defined as Equations 4.39 and 4.40 respectively.

$$A_{z,imposed}=\frac{g[A_{y,i}-A_{y,cg}\cos(\phi_i)]-C(\cos(\phi_i)\sin(\phi_i))-D}{\sin(\phi_i)}-[\cos(\theta_{man})\cos(\phi_{man})]\Bigg|\; for,\ i=[2:12] \tag{4.39}$$

$$A_{y,imposed}=\frac{g[A_{y,i}-A_{z,cg}\sin(\phi_i)-C(\cos(\phi_i)\sin(\phi_i))-D}{\cos(\phi_i)}-[\cos(\theta_{man})\sin(\phi_{man})]\Bigg|\; for,\ i=[1:6]\ and\ [8:13] \tag{4.40}$$

where "C" and "D" are defined as Equations 4.36 and 4.38 given previously.

$$C=\frac{g\left[(A_{y,14-i}-A_{y,i})+2(A_{y,cg})abs(\cos(\phi_i))\right]}{-2(abs\cos(\phi_i))(\sin(\phi_i))}$$

$$D=\frac{g\left[(A_{y,14-i}+A_{y,i})-2(A_{z,cg})(\sin(\phi_i))\right]}{2}$$

The method of differencing symmetric accelerometer signals along the transverse accelerometer array for resolution of the nonlinear expression and eliminating the reliance of angular rate terms resolved from the use of the rate gyroscopes enables an alternative method for the algorithm scheme developed and implemented to calculate and determine the imposed loads along the secondary and tertiary axes respectively for means of accurate and reliable attitude estimation.

Equations 4.39 and 4.40 may now be utilized for attitude estimation in the transverse plane through the use of the defined equation for estimates of the present roll angle given previously as Equations 4.20. Figures 4.27 through 4.32 represent the transverse attitude estimate determined by the signal differencing imposed loading algorithm for transverse attitude estimation against the truth value of the transverse attitude of the aircraft simulation for each phase of the feasibility study. Table 4.4 presents the maximum and mean attitude error experienced during each of the simulation phases.

Phase I – Longitudinal Maneuver: No Turbulence

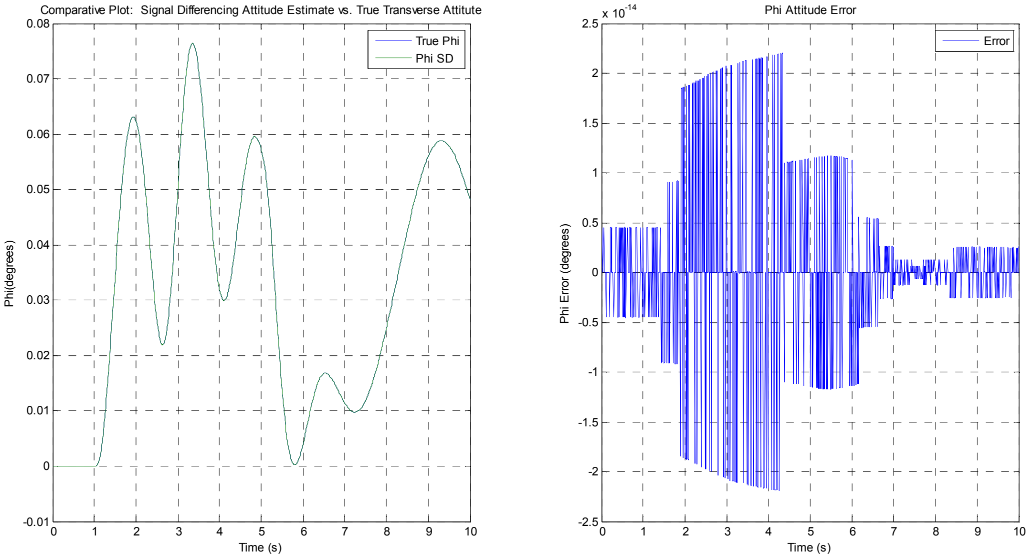

Figure 4.27: SD Attitude Estimation Results –Assessment of $\phi_{\text{SD-Estimate}}$ and ϕ_{Truth}

Phase I – Longitudinal Maneuver: Turbulence

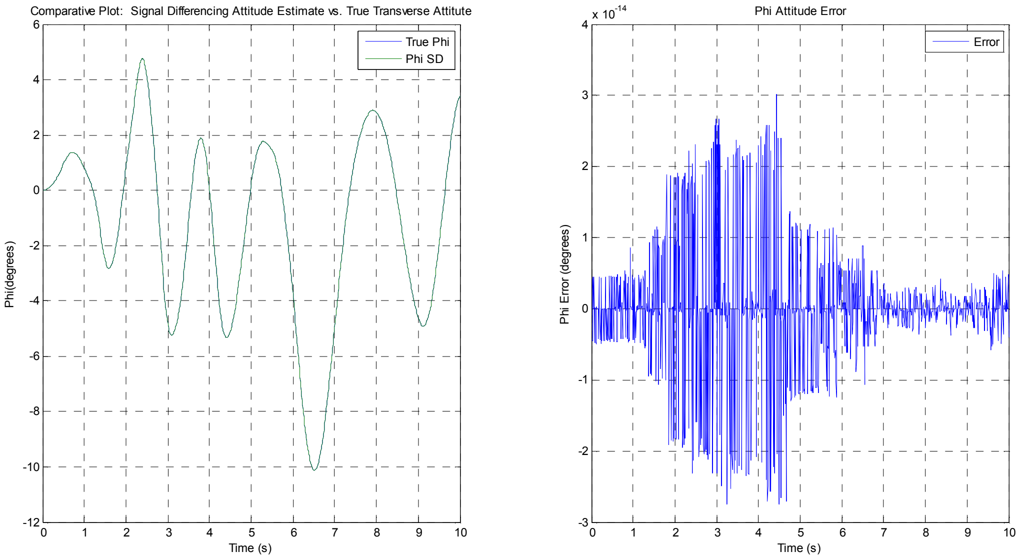

Figure 4.28: SD Attitude Estimation Results – Turbulence Assessment of $\phi_{\text{SD-Estimate}}$ and ϕ_{Truth}

Phase II – Transverse Maneuver: No Turbulence

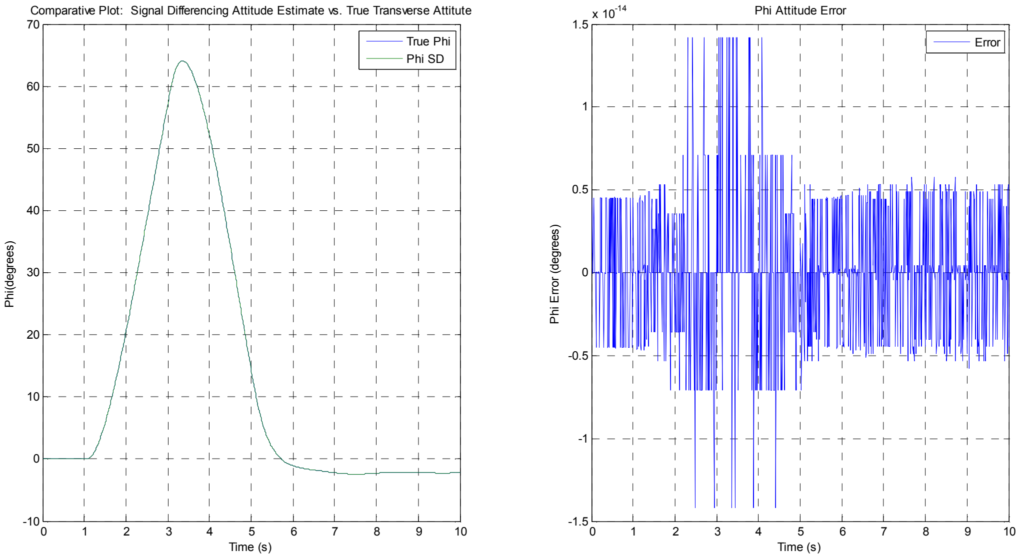

Figure 4.29: SD Attitude Estimation Results –Assessment of $\phi_{\text{SD-Estimate}}$ and ϕ_{Truth}

Phase II – Transverse Maneuver: Turbulence

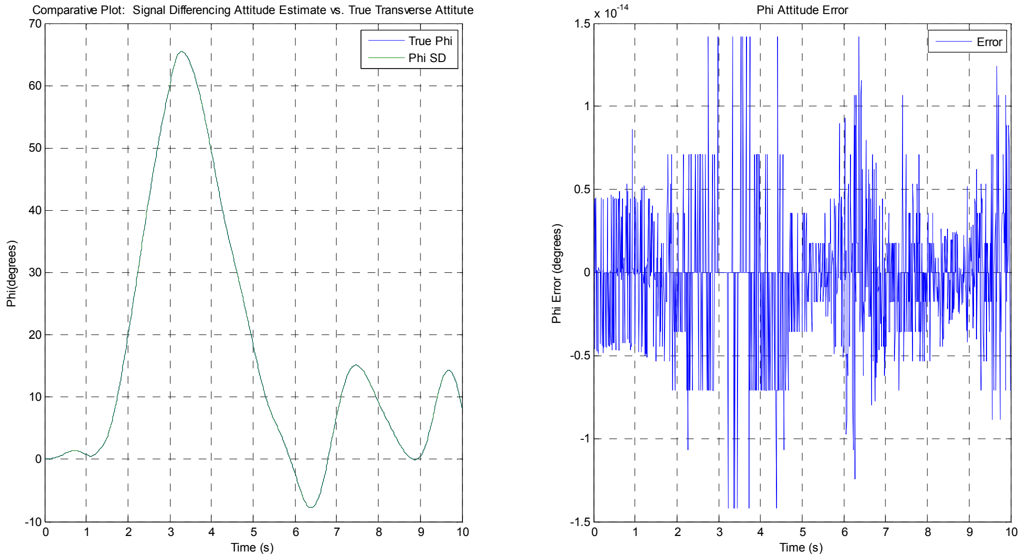

Figure 4.30: SD Attitude Estimation Results – Turbulence Assessment of $\phi_{\text{SD-Estimate}}$ and ϕ_{Truth}

Phase III – Longitudinal/Transverse Maneuver: No Turbulence

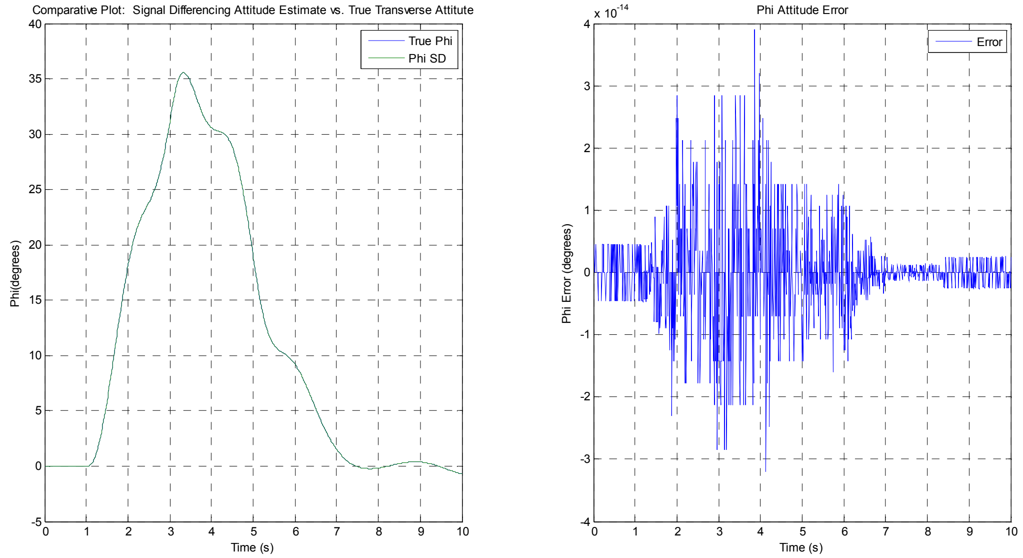

Figure 4.31: SD Attitude Estimation Results – Assessment of $\phi_{\text{SD-Estimate}}$ and ϕ_{Truth}

Phase III – Longitudinal/Transverse Maneuver: Turbulence

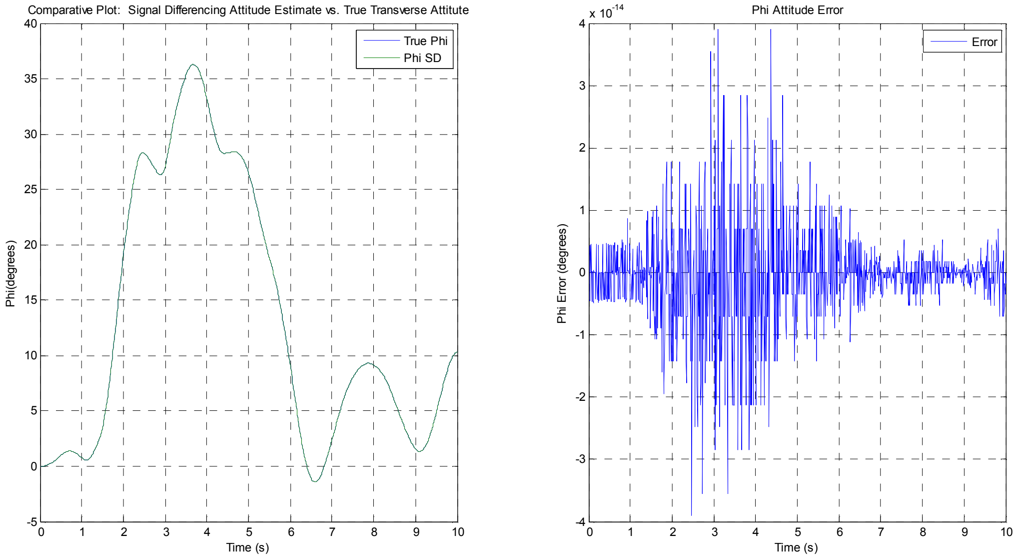

Figure 4.32: SD Attitude Estimation Results – Turbulence Assessment of $\phi_{\text{SD-Estimate}}$ and ϕ_{Truth}

Aircraft Simulation Maneuver	**Maximum Transverse SD Attitude Error (degrees)**	**Mean Transverse SD Attitude Error (degrees)**
Longitudinal Maneuver	2.1996e-014	4.5896e-015
Longitudinal Maneuver with Turbulence	3.0198e-014	5.0101e-015
Transverse Maneuver	1.4211e-014	2.6774e-015
Transverse Maneuver with Turbulence	1.4211e-014	2.8036e-015
Longitudinal/Transverse Maneuver	3.9080e-014	4.3250e-015
Longitudinal/Transverse Maneuver with Turbulence	3.9080e-014	4.7777e-015

Table 4.4: Maximum and Mean Signal Differencing Transverse Attitude Error

As shown in Table 4.4, the attitude estimate produced by the transverse accelerometer array utilizing the signal differencing method produces an extremely accurate estimate of the transverse attitude with maximum errors for all maneuvers being less than 3.9500e-14 degrees and mean errors less than 5.1000e-15 degrees.

The present estimate of the transverse attitude determined through the implementation of the signal differencing method is then used in conjunction with the present roll rate determined by the rate gyroscope for estimation of the rate gyro bias. As it may be seen in Table 4.4, the error produced during the operation of the signal differencing imposed loading determination algorithm is far less than the error produced during the attitude estimation method reliant on the body rotational rates produced by the rate gyro. Figure 4.33 displays the flow chart algorithm for the imposed loading calculation in conjunction with the attitude estimate produced by the two-dimensional accelerometer array for both the longitudinal and transverse attitudes.

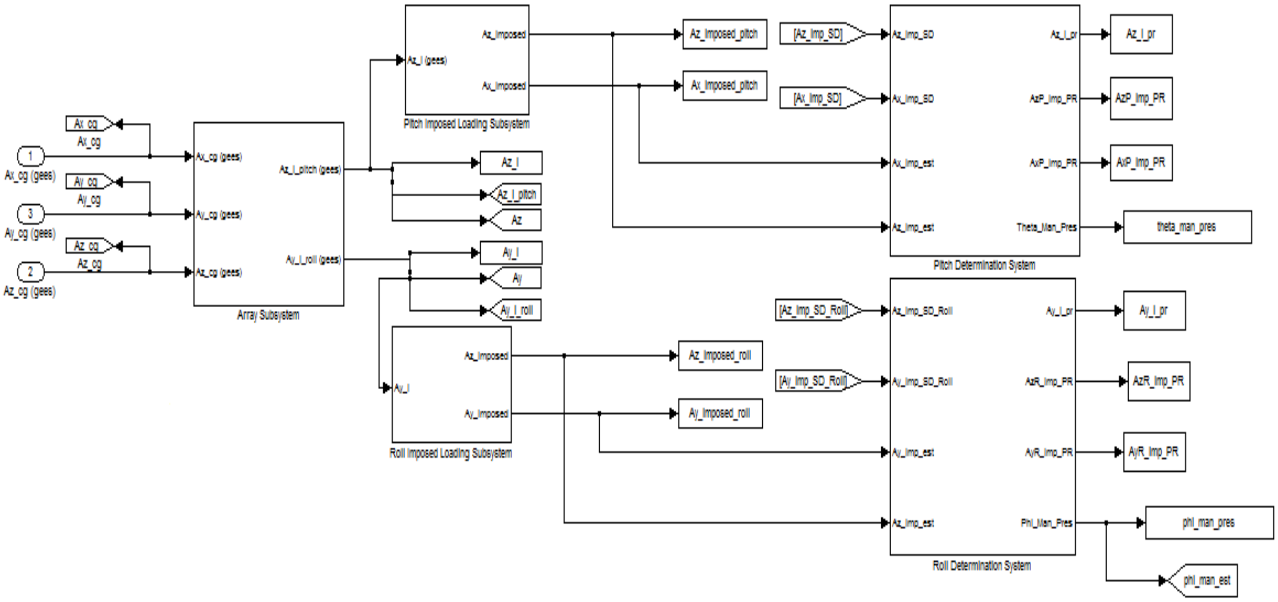

Figure 4.33: Flowchart for Full Longitudinal and Transverse Imposed Loading and Attitude Determination

Comparative Analysis of Two-Dimensional Attitude Estimation Methods

The attitude estimation results obtained from Sections 4.2.1 and 4.2.2 are summarized in Tables 4.5 and 4.6.

Aircraft Simulation Maneuver	Max Longitudinal Attitude Error (degrees)	Mean Longitudinal Attitude Error (degrees)	Max Longitudinal SD Attitude Error (degrees)	Mean Longitudinal SD Attitude Error (degrees)	Percent Decrease in Mean Error
Longitudinal Maneuver	3.4194	1.7305	2.8422e-14	5.4253e-15	≈ 100%
Longitudinal Maneuver with Turbulence	3.3652	1.6993	2.8422e-14	5.4134e-15	≈ 100%
Transverse Maneuver	3.0682	1.4751	5.7732e-15	2.4505e-15	≈ 100%
Transverse Maneuver with Turbulence	3.1306	1.4837	9.7700e-15	2.4390e-15	≈ 100%
Longitudinal/ Transverse Maneuver	3.3400	1.6742	2.8422e-14	5.2616e-15	≈ 100%
Longitudinal/ Transverse Maneuver with Turbulence	3.2912	1.6332	2.8422e-14	5.4546e-15	≈ 100%

Table 4.5: Longitudinal Array Attitude Estimation Comparison

Aircraft Simulation Maneuver	**Max Transverse Attitude Error (degrees)**	**Mean Transverse Attitude Error (degrees)**	**Max Transverse SD Attitude Error (degrees)**	**Mean Transverse SD Attitude Error (degrees)**	**Percent Decrease in Mean Error**
Longitudinal Maneuver	3.2866	1.6609	2.1996e-14	4.5896e-15	≈ 100%
Longitudinal Maneuver with Turbulence	4.2167	1.9752	3.0198e-14	5.0101e-15	≈ 100%
Transverse Maneuver	3.2186	1.9803	1.4211e-14	2.6774e-15	≈ 100%
Transverse Maneuver with Turbulence	3.2148	2.1148	1.4211e-14	2.8036e-15	≈ 100%
Longitudinal/ Transverse Maneuver	3.8026	1.9282	3.9080e-14	4.3250e-15	≈ 100%
Longitudinal/ Transverse Maneuver with Turbulence	3.7895	2.0192	3.9080e-14	4.7777e-15	≈ 100%

Table 4.6: Transverse Array Attitude Estimation Comparison

From the results presented in Tables 4.5 and 4.6, the signal differencing imposed loading algorithm produces superior attitude estimation results as compared to the imposed loading algorithm reliant on the body angular rate terms measured by the rate gyroscopes. While one of the main advantages of the signal differencing method is the drastic improvement in attitude estimation accuracy, another considerable advantage of the signal differencing method is the non-reliance of the method on the body angular rate terms and solely on the accelerometer signals produced by the two-dimensional accelerometer array.

4.3 Extended Kalman Filter Bias Estimation

The extended Kalman filter algorithm described previously in Section 2.2.3 was implemented with the imposed loading algorithm derived in Section 4.2.2. From the results obtained in Section 4.2.2, the signal differencing imposed loading method was utilized in conjunction with the extended Kalman filter attitude and bias estimation algorithm due to the accuracy of the process to produce accurate and reliable estimations of the vehicle's attitude despite the presence of severe environmental conditions.

In each phase of the feasibility study conducted, the extended Kalman filter was implemented for estimation of the rate gyro bias and determination of the vehicle's attitude according to Section 2.2.3 over a 10 second time interval. The sampling time of the extended Kalman filter was set to 0.01 seconds with the attitude estimates provided by the signal differencing algorithm and accelerometer measurements according to Section 4.2.2. The process noise and measurement noise standard deviations are listed in Table 4.7. The rate gyro variance was set to 0.15 $(\text{deg/sec})^2$, yielding a standard deviation, σ, equal to 0.3873 degrees per second. The extended Kalman filter was used to estimate the rate gyro bias in real-time utilizing the attitude estimates produced by the two-dimensional accelerometer array.

To allow for proper convergence of the covariance matrix within the ±1σ and ±3σ bounds, the extended Kalman filter was implemented with turbulent and non-turbulent bias process noise and gyro process noise variances. The initial state estimates implemented are those discussed previously in Section 2.2.4, while the initial state covariance matrix was given diagonal elements as described in Table 4.7 to ensure proper convergence of the extended Kalman filter's covariance matrix. The bias process noise variance was implemented with the same value in both the turbulent and non-turbulent operating environments because the values are independent of the operating environment unlike the accelerometer and rate gyro measurements. Feasibility simulations were conducted utilizing the EKF parameter values given in Table 4.7 for each phase of the study conducted. The results from each simulation study conducted are presented in the following sections.

Extended Kalman Filter Parameters Values		
Parameter		**Value**
P_0^a		1×10^{9}
P_0^b		1×10^{-4}
P_0		$Diag[P_0^a P_0^a P_0^a P_0^b P_0^b P_0^b]$
$\sigma_u(rad/\sec^{3/2})$	Non-Turbulent	1×10^{-6}
	Turbulent	1×10^{-5}
$\sigma_v(rad/\sec^{1/2})$	Non-Turbulent	1×10^{-2}
	Turbulent	1×10^{-2}
$\beta(\deg/\sec)$		0.2
$\Gamma(\deg/\sec/hour)$		0.05

Table 4.7: EKF Parameter Values

4.3.1 Phase I Study – Longitudinal Aircraft Maneuver

Phase I – Longitudinal Maneuver: No Turbulence

The extended Kalman filter derived previously in Section 2.2.3 with the parameter values given in Table 4.7 was implemented as an observer to the nonlinear aircraft simulation model to improve upon the attitude and rate gyro bias estimation online. A comparison of the attitude determined by the dual-arc accelerometer array algorithm developed in Section 4.2.1 with the observer estimates utilizing the EKF algorithm are shown in Figures 4.34 through 4.37 where Table 4.8 presents a summary of maximum and mean attitude and rate gyro bias estimation errors. In this phase of the analysis, no turbulence was injected into the simulation model.

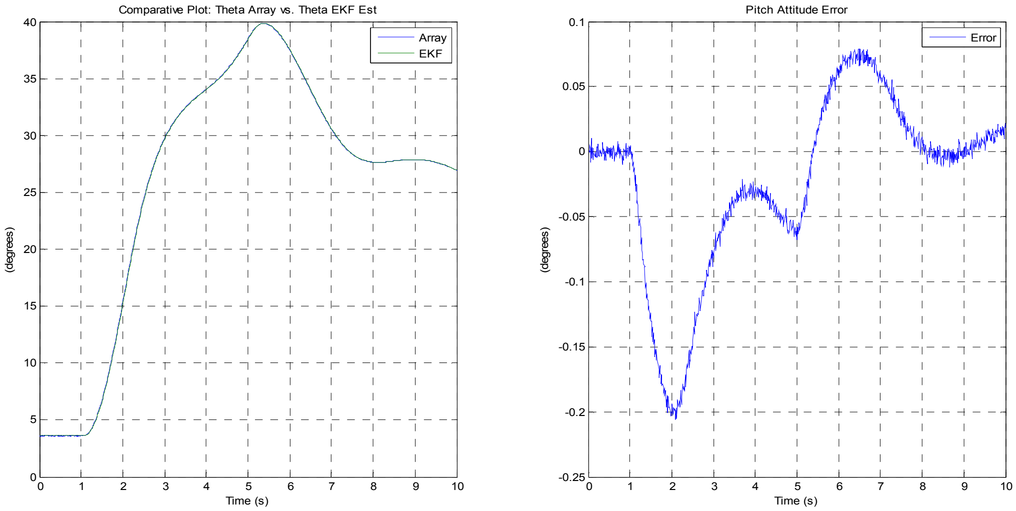

Figure 4.34: Nonlinear Pitch Attitude Tracking Results – Phase I No Turbulence

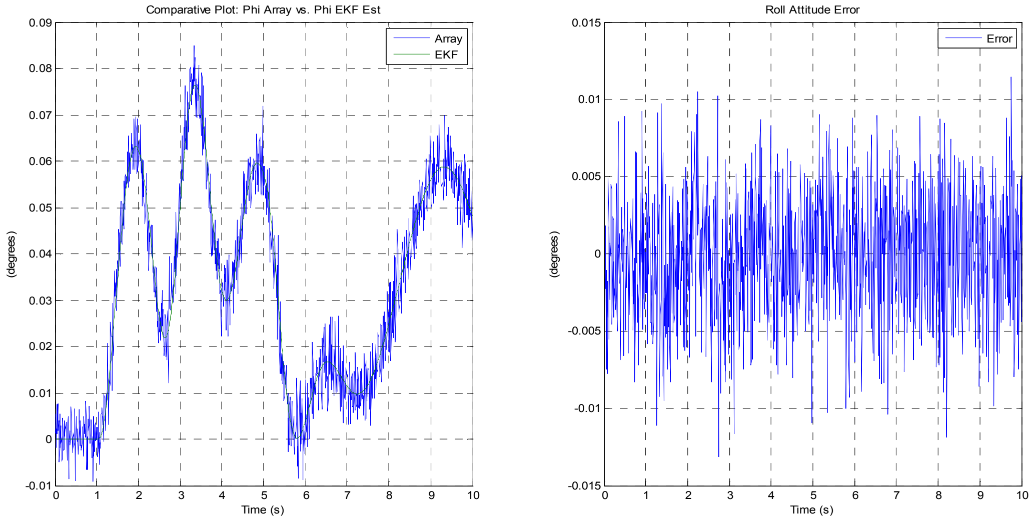

Figure 4.35: Nonlinear Roll Attitude Tracking Results – Phase I No Turbulence

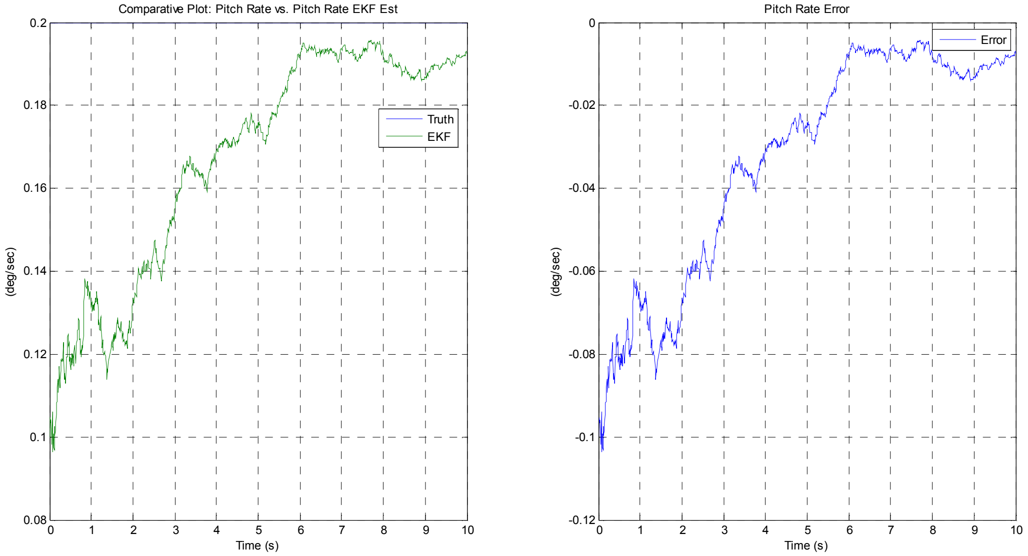

Figure 4.36: Nonlinear Pitch Rate Bias Estimation Results – Phase I No Turbulence

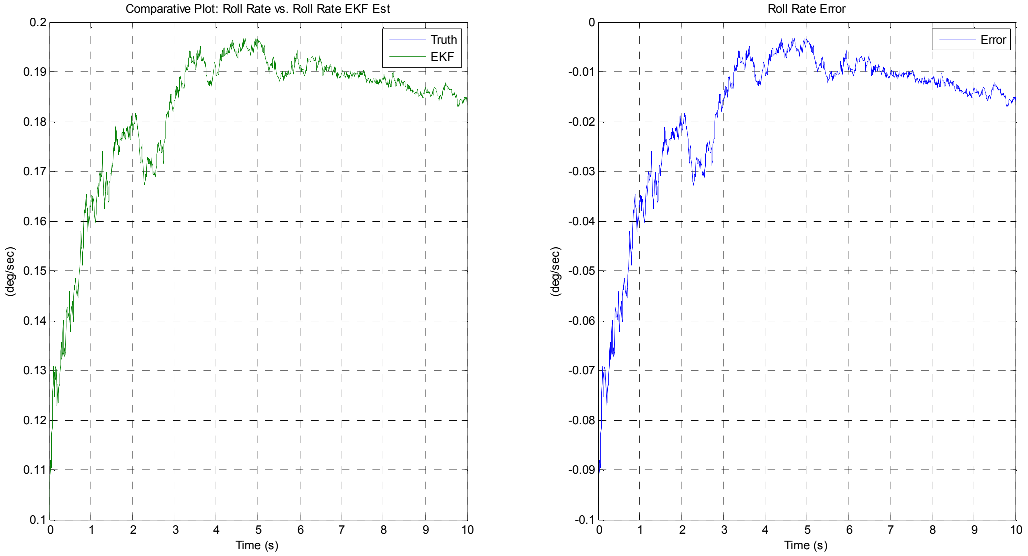

Figure 4.37: Nonlinear Roll Rate Bias Estimation Results – Phase I No Turbulence

Phase I Maximum and Mean Error Results No Turbulence					
Rate Gyro Bias (deg/sec)	**Rate Gyro Slope (deg/sec/hr)**	**Phase I – Longitudinal Maneuver with No Turbulence**			
0.2	0.05	θ Max Absolute Error (deg)	θ Mean Absolute Error (deg)	Max Bias Absolute Error (deg/sec)	Mean Bias Absolute Error (deg/sec)
		0.20607	0.05015	0.10369	0.03305
		ϕ Max Absolute Error (deg)	ϕ Mean Absolute Error (deg)	Max Bias Absolute Error (deg/sec)	Mean Bias Absolute Error (deg/sec)
		0.01315	0.00332	0.10000	0.01840

Table 4.8: Maximum and Mean Attitude and Bias Estimation Results – Phase I No Turbulence

From the simulation performed, the attitude estimates for both the longitudinal and transverse attitude of the vehicle stay within a ±0.250 degrees error, while Figures 4.36 and 4.37 show a maximum bias error of ±0.125 degrees per second as displayed and summarized in Table 4.8.

Additionally, plots of the pitch and roll rate bias estimation errors are provided for an assessment of the ±1σ and ±3σ bounds on the rate gyro. The rate gyro variance for the study conducted was set to 0.15 (degrees/second)^2. Taking the square root of this value gives a standard deviation, σ, of 0.3873 degrees/second. Figures 4.38 demonstrate how the extended Kalman filter provides accurate and well behaved pitch and roll bias estimation errors bounded by the rate gyro signal.

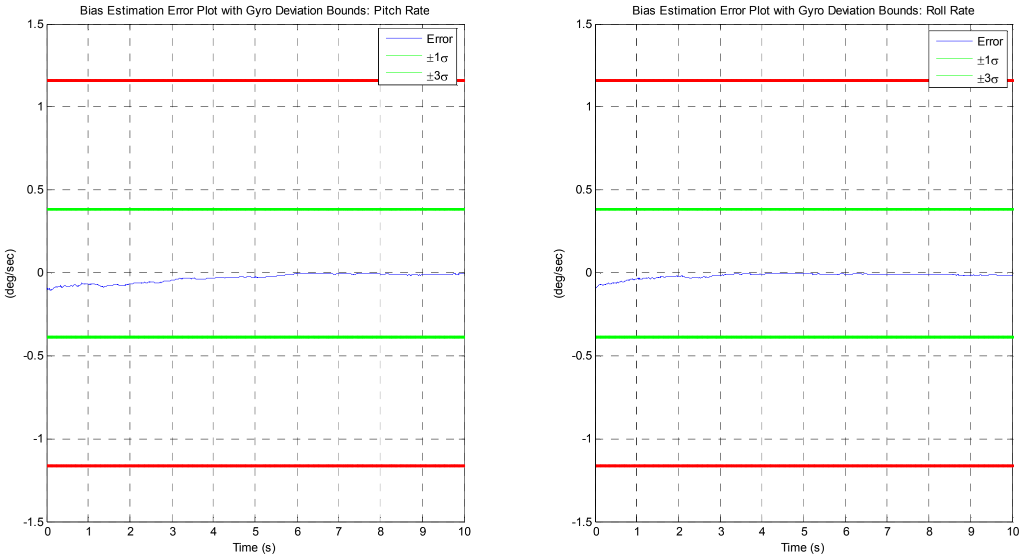

Figure 4.38: Nonlinear EKF Bias Estimation Error with Bounds – Phase I No Turbulence
]

The maximum bias error is acceptable due to the error remaining in the ±1σ and ±3σ bounds of ± 0.3873 degrees per second and ± 1.1619 degrees per second imposed from the rate gyro noise variance as displayed in Figure 4.38. Staying within these statistical bounds is essential because 99.7% of a normally distributed value lies within the ±3σ bounds and 68.3% within the ±1σ bounds [41]. Therefore, the extended Kalman filter rate gyro bias and attitude estimation algorithm implemented in Phase I of this study with no turbulence injections proves to produce accurate and reliable attitude tracking results and rate gyro bias estimations in real-time.

The simulation plant model utilized in this feasibility study was nonlinear; therefore the EKF parameters were checked to ensure proper filter operation and convergence. The check for correct filter operation is conducted by comparing the attitude tracking and rate gyro bias estimation errors against the ±1σ and ±3σ values taken from the diagonal elements of the extended Kalman filters covariance matrix, P. Figures 4.39 and 4.40 demonstrate a properly operating extended Kalman filter due to the attitude and bias estimation errors versus variance operating within the ±1σ and ±3σ bounds established by the covariance matrix of the EKF.

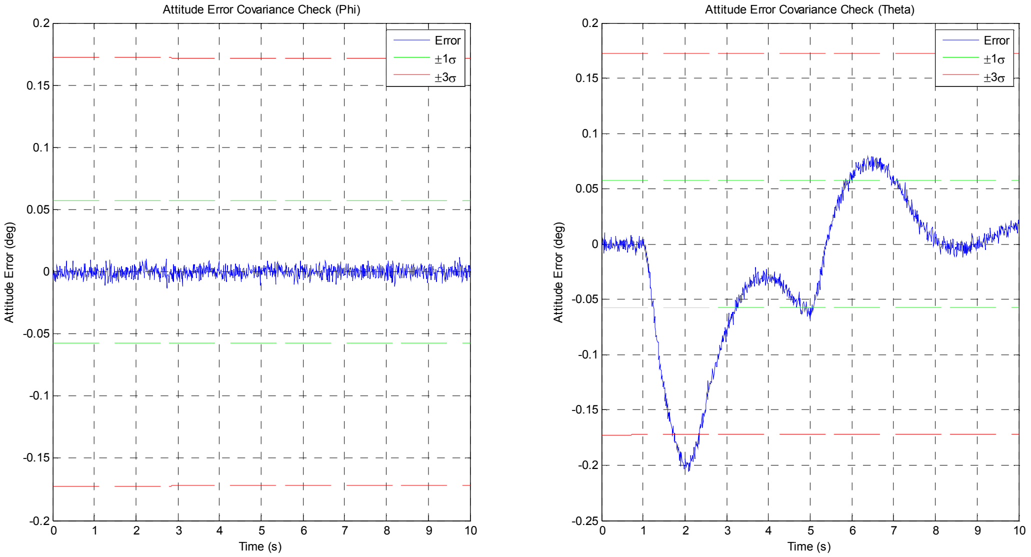

Figure 4.39: Nonlinear Attitude Error Covariance Check – Phase I No Turbulence

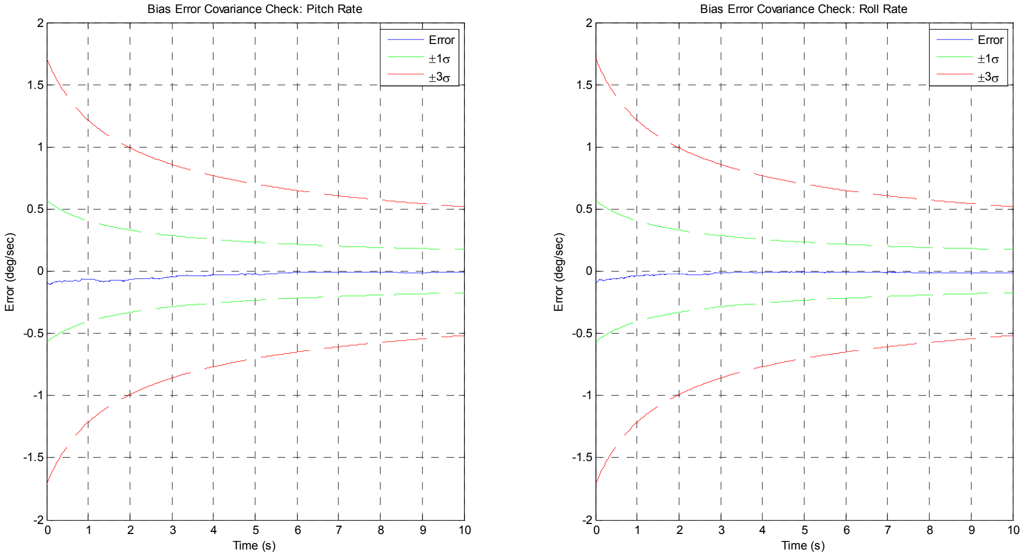

Figure 4.40: Nonlinear Bias Error Covariance Check – Phase I No Turbulence

Phase I – Longitudinal Maneuver: Turbulence

A comparison of the attitude determined by the dual-arc accelerometer array algorithm developed in Section 4.2.1 with the observer estimates utilizing the EKF algorithm are shown in Figures 4.41 through 4.44 where Table 4.9 presents a summary of maximum and mean attitude and rate gyro bias estimation errors. In this phase of the analysis, turbulence was injected into the simulation model through the use of the Dryden wind and turbulence model discussed previously in Section 3.3 where the maximum turbulence input to the simulation model approaches approximately 60 feet per second. The injection of such severe turbulence and vibrational effects is utilized to display the robustness of the algorithm developed and implemented to produce accurate and reliable attitude and rate gyro bias estimates while operating in harsh environments.

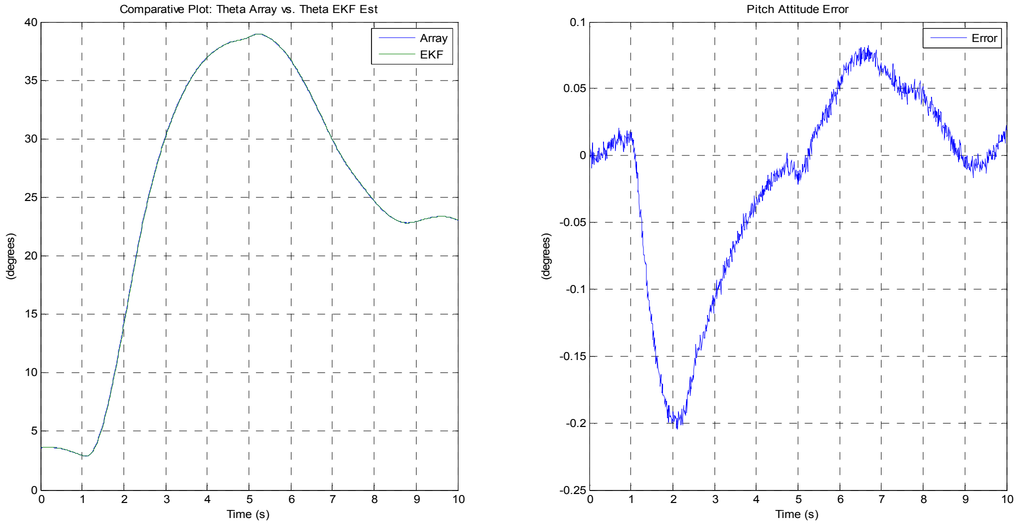

Figure 4.41: Nonlinear Pitch Attitude Tracking Results – Phase I with Turbulence

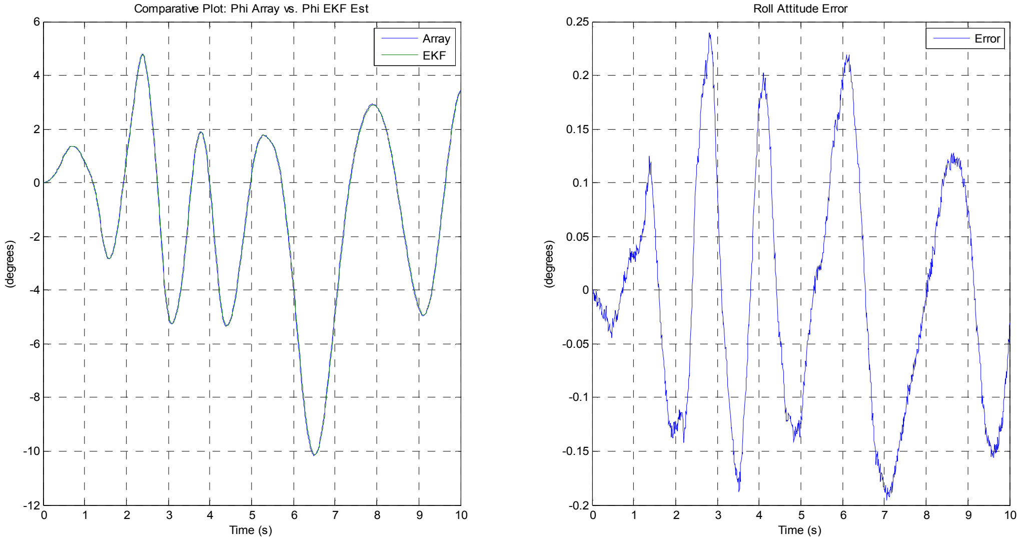

Figure 4.42: Nonlinear Roll Attitude Tracking Results – Phase I with Turbulence

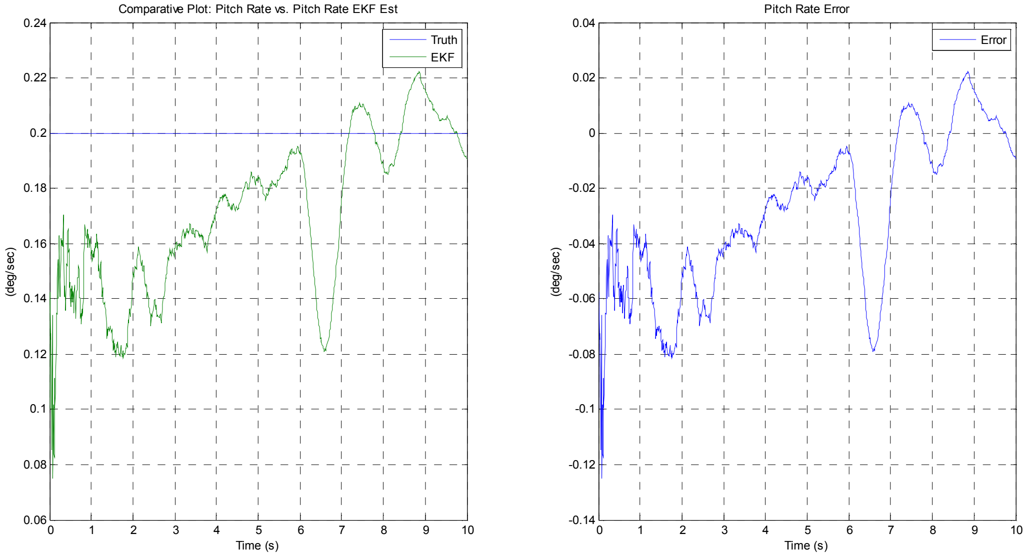

Figure 4.43: Nonlinear Pitch Rate Bias Estimation Results – Phase I with Turbulence

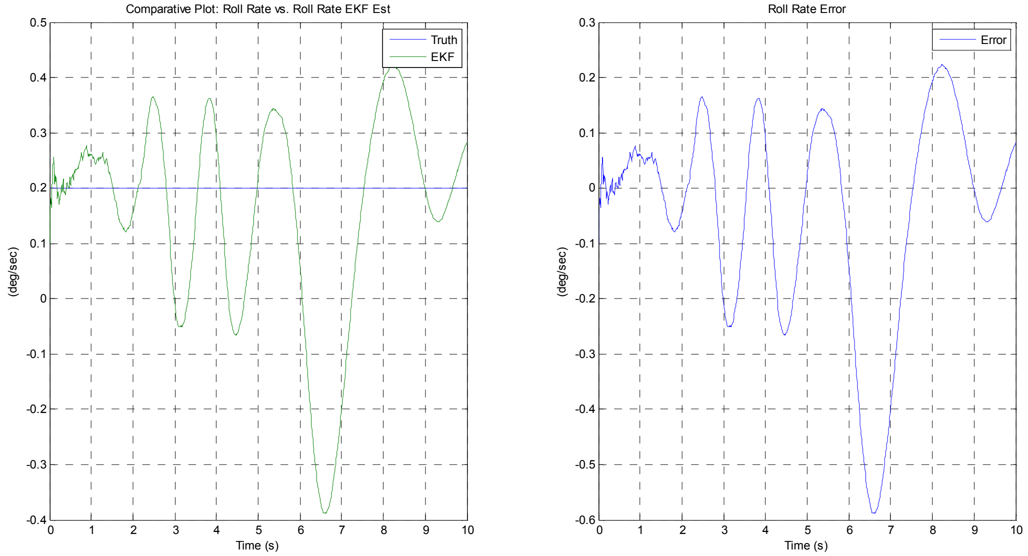

Figure 4.44: Nonlinear Roll Rate Bias Estimation Results – Phase I with Turbulence

Phase I Maximum and Mean Error Results with Turbulence					
Rate Gyro Bias (deg/sec)	**Rate Gyro Slope (deg/sec/hr)**	**Phase I – Longitudinal Maneuver with Turbulence**			
0.2	0.05	θ Max Absolute Error (deg)	θ Mean Absolute Error (deg)	Max Bias Absolute Error (deg/sec)	Mean Bias Absolute Error (deg/sec)
		0.20478	0.05422	0.12495	0.03271
		ϕ Max Absolute Error (deg)	ϕ Mean Absolute Error (deg)	Max Bias Absolute Error (deg/sec)	Mean Bias Absolute Error (deg/sec)
		0.23970	0.09496	0.58871	0.13752

Table 4.9: Maximum and Mean Attitude and Bias Estimation Results – Phase I with Turbulence

From the simulation performed, the attitude estimates for both the longitudinal and transverse attitude of the vehicle stay within a ±0.250 degrees error while Figure 4.43 and 4.44 shows a maximum bias error of ±0.600 degrees per second as displayed and summarized in Table 4.9. Staying within these statistical bounds is once again essential because 99.7% of a normally distributed value lies within the $\pm 3\sigma$ bounds and 68.3% within the $\pm 1\sigma$ bounds [41]. Therefore, the extended Kalman filter rate gyro bias and attitude estimation algorithm implemented in Phase I of this study with severe turbulence injections proves to provide accurate and reliable attitude tracking results and rate gyro bias estimations in real-time.

Additionally, plots of the pitch and roll rate bias estimation errors are provided for an assessment of the $\pm 1\sigma$ and $\pm 3\sigma$ bounds on the rate gyro. Figures 4.45 demonstrate how the extended Kalman filter provides accurate and well behaved pitch and roll bias estimation errors bounded by the rate gyro signal.

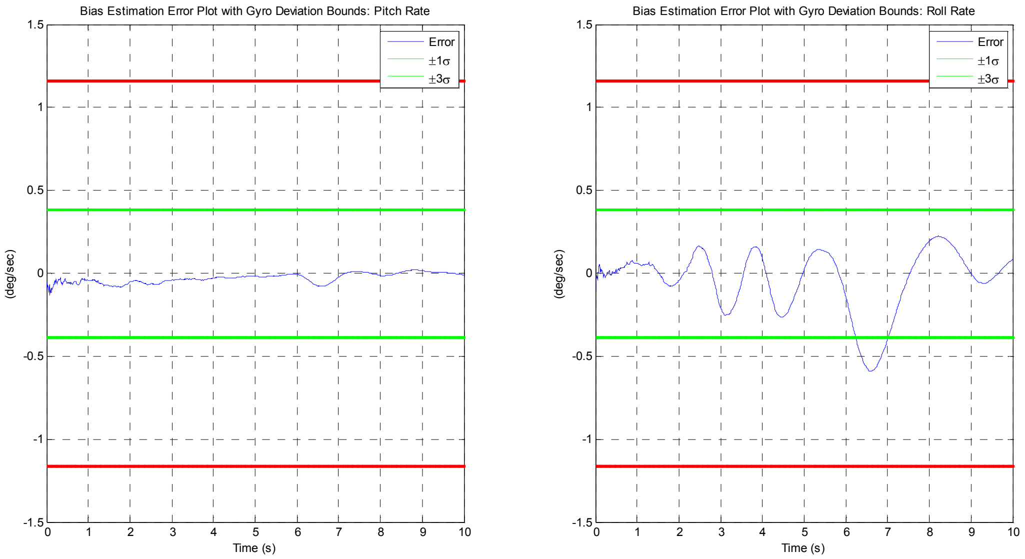

Figure 4.45: Nonlinear EKF Bias Estimation Error with Bounds – Phase I with Turbulence

The maximum bias error is acceptable due to the error remaining in the ±1σ and ±3σ bounds of ± 0.3873 degrees per second and ± 1.1619 degrees per second imposed from the rate gyro noise variance as displayed in Figure 4.45.

The check for correct filter operation is once again conducted by comparing the attitude tracking and rate gyro bias estimation errors against the ±1σ and ±3σ values taken from the diagonal elements of the extended Kalman filters covariance matrix, P. Figures 4.46 and 4.47 demonstrate a properly operating extended Kalman filter due to the attitude and bias estimation errors versus variance operating within the ±1σ and ±3σ bounds established by the covariance matrix of the EKF.

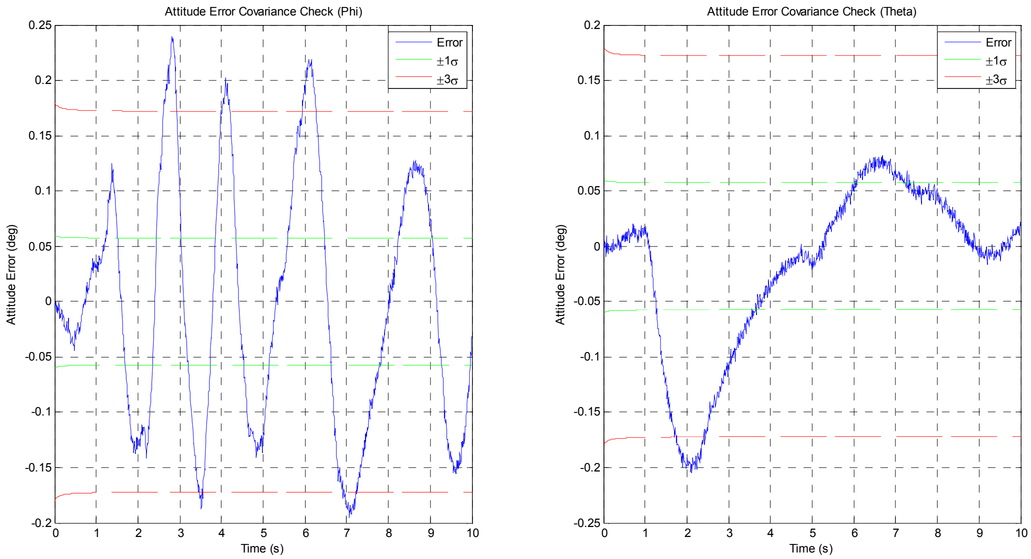

Figure 4.46: Nonlinear Attitude Error Covariance Check – Phase I with Turbulence

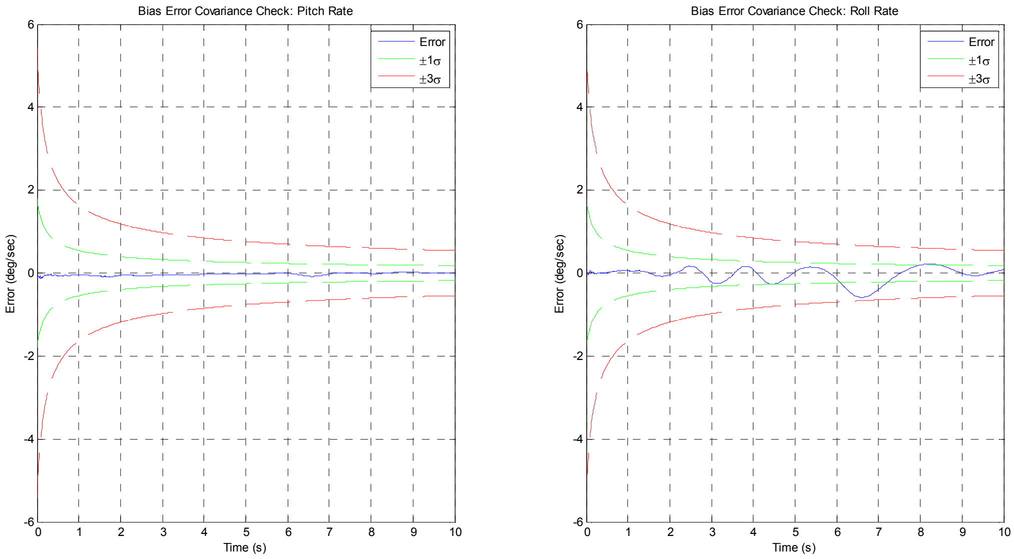

Figure 4.47: Nonlinear Bias Error Covariance Check – Phase I with Turbulence

Utilizing the EKF parameters given previously in Table 4.7, the rate gyro bias magnitude was varied between values of 0.2 and 10 degrees/second while the rate gyro bias slope was varied between values of 0 and 1 degree/second/hour in order examine and assess the sensitivity of the extended Kalman filter implemented to changes in rate gyro bias magnitude and slope. The results of the Phase I assessment are summarized in Tables 4.10 through 4.13 given below.

Impact of Changing Rate Gyro Bias Magnitude with a Constant Slope					
Phase I: Longitudinal Maneuver No Turbulence					
Rate Gyro Bias Slope (deg/sec/hr)	Bias (deg/sec)	θ Max Absolute Error (deg)	θ Mean Absolute Error (deg)	Max Bias Absolute Error (deg/sec)	Mean Bias Absolute Error (deg/sec)
0.0	0.2	0.20607	0.05018	0.10369	0.03308
	1	0.20866	0.05112	0.90000	0.22516
	3	0.21513	0.05413	2.90000	0.70535
	5	0.22160	0.05727	4.90000	1.18550
	10	0.23778	0.06548	9.90000	2.38600
0.5	0.2	0.20607	0.05018	0.10369	0.03279
	1	0.20866	0.05111	0.90000	0.22486
	3	0.21513	0.05413	2.90000	0.70505
	5	0.22161	0.05727	4.90000	1.18520
	10	0.23778	0.06548	9.90000	2.38570
1.0	0.2	0.20607	0.05018	0.10369	0.03249
	1	0.20866	0.05111	0.90000	0.22457
	3	0.21514	0.05413	2.90000	0.70476
	5	0.22161	0.05727	4.90000	1.18500
	10	0.23778	0.06548	9.90000	2.38540
Phase I: Longitudinal Maneuver with Turbulence					
Rate Gyro Bias Slope (deg/sec/hr)	Bias (deg/sec)	θ Max Absolute Error (deg)	θ Mean Absolute Error (deg)	Max Bias Absolute Error (deg/sec)	Mean Bias Absolute Error (deg/sec)
0.0	0.2	0.20478	0.05422	0.12495	0.03272
	1	0.20514	0.05429	0.90000	0.06738
	3	0.20604	0.05463	2.90000	0.15968
	5	0.20694	0.05506	4.90000	0.25292
	10	0.20919	0.05635	9.90000	0.48601
0.5	0.2	0.20478	0.05422	0.12495	0.03261
	1	0.20514	0.05429	0.90000	0.06713
	3	0.20604	0.05463	2.90000	0.15934
	5	0.20694	0.05505	4.90000	0.25258
	10	0.20919	0.05635	9.90000	0.48567
1.0	0.2	0.20478	0.05422	0.12495	0.03250
	1	0.20514	0.05429	0.90000	0.06689
	3	0.20604	0.05463	2.90000	0.15900
	5	0.20694	0.05505	4.90000	0.25224
	10	0.20919	0.05635	9.90000	0.48533

Table 4.10: Sensitivity of Extended Kalman Filter to Changes in Rate Gyro Bias Magnitude with Constant Rate Gyro Slope – Phase I Pitch Attitude and Bias Summary

Impact of Changing Rate Gyro Bias Magnitude with a Constant Slope

Phase I: Longitudinal Maneuver No Turbulence

Rate Gyro Bias Slope (deg/sec/hr)	Bias (deg/sec)	ϕ Max Absolute Error (deg)	ϕ Mean Absolute Error (deg)	Max Bias Absolute Error (deg/sec)	Mean Bias Absolute Error (deg/sec)
0.0	0.2	0.01315	0.00332	0.10000	0.01843
	1	0.01529	0.00393	0.90000	0.21051
	3	0.03414	0.00740	2.90000	0.69070
	5	0.05354	0.01182	4.90000	1.17090
	10	0.10360	0.02372	9.90000	2.37140
0.5	0.2	0.01315	0.00332	0.10000	0.01814
	1	0.01529	0.00393	0.90000	0.21021
	3	0.03414	0.00740	2.90000	0.69040
	5	0.05354	0.01182	4.90000	1.17060
	10	0.10360	0.02372	9.90000	2.37110
1.0	0.2	0.01315	0.00332	0.10000	0.01784
	1	0.01529	0.00393	0.90000	0.20992
	3	0.03414	0.00740	2.90000	0.69011
	5	0.05354	0.01182	4.90000	1.17030
	10	0.10360	0.02372	9.90000	2.37080

Phase I: Longitudinal Maneuver with Turbulence

Rate Gyro Bias Slope (deg/sec/hr)	Bias (deg/sec)	ϕ Max Absolute Error (deg)	ϕ Mean Absolute Error (deg)	Max Bias Absolute Error (deg/sec)	Mean Bias Absolute Error (deg/sec)
0.0	0.2	0.23970	0.09496	0.58876	0.13752
	1	0.23943	0.09510	0.90000	0.15312
	3	0.23874	0.09546	2.90000	0.22183
	5	0.23805	0.09583	4.90000	0.29762
	10	0.23633	0.09677	9.90000	0.51140
0.5	0.2	0.23970	0.09496	0.58831	0.13752
	1	0.23943	0.09510	0.90000	0.15309
	3	0.23874	0.09546	2.90000	0.22176
	5	0.23805	0.09583	4.90000	0.29750
	10	0.23633	0.09677	9.90000	0.51117
1.0	0.2	0.23970	0.09496	0.58786	0.13752
	1	0.23943	0.09510	0.90000	0.15306
	3	0.23874	0.09546	2.90000	0.22168
	5	0.23805	0.09583	4.90000	0.29737
	10	0.23633	0.09677	9.90000	0.51093

Table 4.11: Sensitivity of Extended Kalman Filter to Changes in Rate Gyro Bias Magnitude with Constant Rate Gyro Slope – Phase I Roll Attitude and Bias Summary

Tables 4.10 and 4.11 assessed the sensitivity of the extended Kalman filter to changes in the rate gyro bias magnitude while maintaining a constant rate gyro bias slope. Tables 4.12 and 4.13 display a summary of attitude determination and bias estimation results for sensitivity of the extended Kalman filter to changes in the rate gyro bias magnitude while maintaining a constant rate gyro bias slope for Phase I of the feasibility study conducted.

Impact of Changing Rate Gyro Bias Slope with Constant Bias Magnitude					
Phase I: Longitudinal Maneuver No Turbulence					
Rate Gyro Bias (deg/sec)	Rate Gyro Bias Slope (deg/sec/hr)	θ Max Absolute Error (deg)	θ Mean Absolute Error (deg)	Max Bias Absolute Error (deg/sec)	Mean Bias Absolute Error (deg/sec)
0.2	0.0	0.20607	0.05018	0.10369	0.03308
	0.5	0.20607	0.05018	0.10369	0.03279
	1.0	0.20607	0.05018	0.10369	0.03249
1	0.0	0.20866	0.05111	0.90000	0.22516
	0.5	0.20866	0.05111	0.90000	0.22486
	1.0	0.20866	0.05111	0.90000	0.22457
3	0.0	0.21513	0.05413	2.90000	0.70535
	0.5	0.21513	0.05413	2.90000	0.70505
	1.0	0.21514	0.05413	2.90000	0.70476
5	0.0	0.22160	0.05727	4.90000	1.18550
	0.5	0.22161	0.05727	4.90000	1.18520
	1.0	0.22161	0.05727	4.90000	1.18500
10	0.0	0.23778	0.06548	9.90000	2.38600
	0.5	0.23778	0.06548	9.90000	2.38570
	1.0	0.23778	0.06548	9.90000	2.38540
Phase I: Longitudinal Maneuver with Turbulence					
Rate Gyro Bias (deg/sec)	Rate Gyro Bias Slope (deg/sec/hr)	θ Max Absolute Error (deg)	θ Mean Absolute Error (deg)	Max Bias Absolute Error (deg/sec)	Mean Bias Absolute Error (deg/sec)
0.2	0.0	0.20478	0.05422	0.12495	0.03272
	0.5	0.20478	0.05422	0.12495	0.03261
	1.0	0.20478	0.05422	0.12495	0.03250
1	0.0	0.20514	0.05429	0.90000	0.06738
	0.5	0.20514	0.05429	0.90000	0.06713
	1.0	0.20514	0.05429	0.90000	0.06689
3	0.0	0.20604	0.05463	2.90000	0.15968
	0.5	0.20604	0.05463	2.90000	0.15934
	1.0	0.20604	0.05463	2.90000	0.15900
5	0.0	0.20694	0.05506	4.90000	0.25292
	0.5	0.20694	0.05505	4.90000	0.25258
	1.0	0.20694	0.05505	4.90000	0.25224
10	0.0	0.20919	0.05635	9.90000	0.48601
	0.5	0.20919	0.05635	9.90000	0.48567
	1.0	0.20919	0.05635	9.90000	0.48533

Table 4.12: Sensitivity of Extended Kalman Filter to Changes in Rate Gyro Bias Slope with Constant Rate Gyro Bias Magnitude – Phase I Pitch Attitude and Bias Summary

Impact of Changing Rate Gyro Bias Slope with Constant Bias Magnitude					
Phase I: Longitudinal Maneuver No Turbulence					
Rate Gyro Bias (deg/sec)	Rate Gyro Bias Slope (deg/sec/hr)	ϕ Max Absolute Error (deg)	ϕ Mean Absolute Error (deg)	Max Bias Absolute Error (deg/sec)	Mean Bias Absolute Error (deg/sec)
0.2	0.0	0.01315	0.00332	0.10000	0.01843
	0.5	0.01315	0.00332	0.10000	0.01814
	1.0	0.01315	0.00332	0.10000	0.01784
1	0.0	0.01529	0.00393	0.90000	0.21051
	0.5	0.01529	0.00393	0.90000	0.21021
	1.0	0.01529	0.00393	0.90000	0.20992
3	0.0	0.03414	0.00740	2.90000	0.69070
	0.5	0.03414	0.00740	2.90000	0.69040
	1.0	0.03414	0.00741	2.90000	0.69011
5	0.0	0.05354	0.00118	4.90000	1.17090
	0.5	0.05354	0.01181	4.90000	1.17060
	1.0	0.05354	0.01182	4.90000	1.17030
10	0.0	0.10360	0.02372	9.90000	2.37140
	0.5	0.10360	0.02372	9.90000	2.37110
	1.0	0.10360	0.02373	9.90000	2.37080
Phase I: Longitudinal Maneuver with Turbulence					
Rate Gyro Bias (deg/sec)	Rate Gyro Bias Slope (deg/sec/hr)	ϕ Max Absolute Error (deg)	ϕ Mean Absolute Error (deg)	Max Bias Absolute Error (deg/sec)	Mean Bias Absolute Error (deg/sec)
0.2	0.0	0.23970	0.09496	0.58876	0.13752
	0.5	0.23970	0.09496	0.58831	0.13752
	1.0	0.23970	0.09496	0.58786	0.13752
1	0.0	0.23943	0.09510	0.90000	0.15312
	0.5	0.23943	0.09510	0.90000	0.15309
	1.0	0.23942	0.09510	0.90000	0.15306
3	0.0	0.23874	0.09546	2.90000	0.22183
	0.5	0.23874	0.09546	2.90000	0.22176
	1.0	0.23874	0.09546	2.90000	0.22168
5	0.0	0.23805	0.09583	4.90000	0.29762
	0.5	0.23805	0.09583	4.90000	0.29750
	1.0	0.23805	0.09583	4.90000	0.29737
10	0.0	0.23633	0.09677	9.90000	0.51140
	0.5	0.23633	0.09677	9.90000	0.51117
	1.0	0.23633	0.09677	9.90000	0.51093

Table 4.13: Sensitivity of Extended Kalman Filter to Changes in Rate Gyro Bias Slope with Constant Rate Gyro Bias Magnitude – Phase I Roll Attitude and Bias Summary

The results of the Phase I study conducted show bias magnitude has little to negligible effect on the attitude estimation of the EKF and noticeable effect on the bias estimate as the bias magnitude imposed increases. From the study performed, the results show that varying the bias magnitude has more effect on attitude and bias estimation results as compared to varying the rate gyro bias slope. For the Phase I simulation study, the bias estimate is reasonable and the attitude estimate does not drift outside of the acceptable range of ±1 degree based on instrumentation from [49]. The inaccuracies of the algorithm method implemented result from accelerometer and rate gyro measurement noises and severe turbulence effects causing a highly dynamical operating environment.

4.3.2 Phase II Study – Transverse Aircraft Maneuver

Phase II – Transverse Maneuver: No Turbulence

Phase II of the feasibility study focused on the implementation of the extended Kalman filter derived previously in Section 2.2.3 implemented as an observer to the nonlinear aircraft simulation model to improve upon the attitude and rate gyro bias estimation for a transverse or roll maneuver of the nonlinear aircraft simulation plant model. A comparison of the attitude determined by the dual-arc accelerometer array algorithm developed in Section 4.2.1 with the observer estimates utilizing the EKF algorithm are shown in Figures 4.48 through 4.51 where Table 4.14 presents a summary of maximum and mean attitude and rate gyro bias estimation errors. In this phase of the analysis, no turbulence was injected into the simulation model.

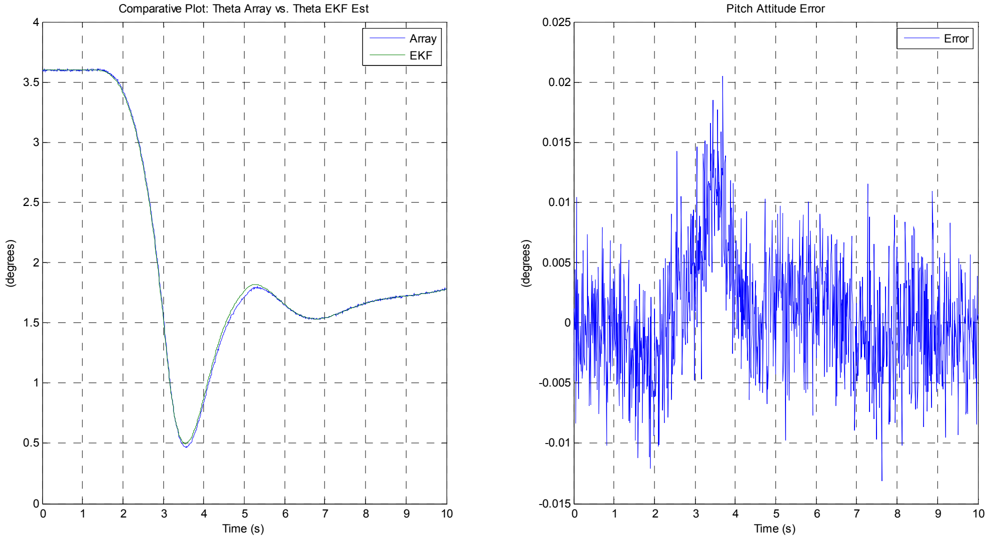

Figure 4.48: Nonlinear Pitch Attitude Tracking Results – Phase II No Turbulence

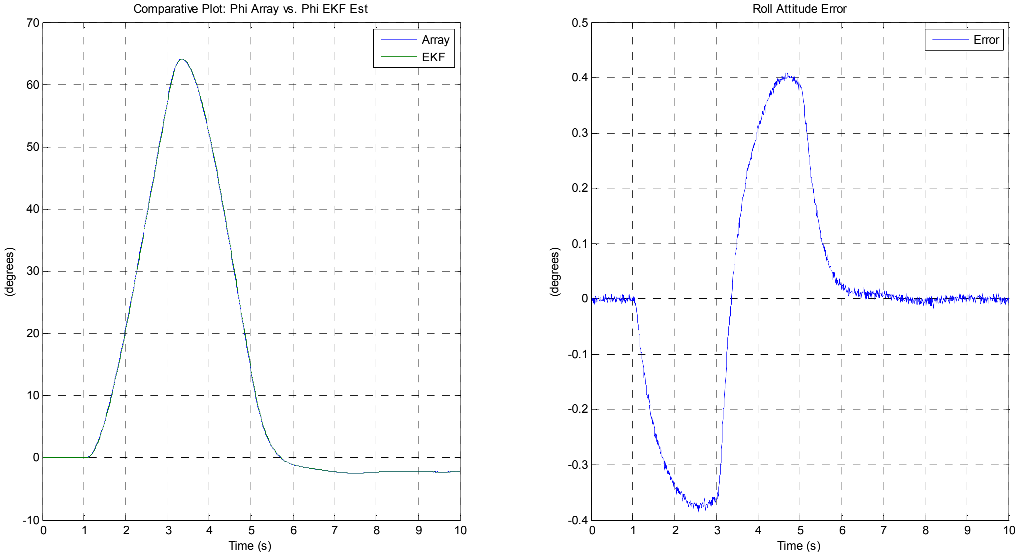

Figure 4.49: Nonlinear Roll Attitude Tracking Results – Phase II No Turbulence

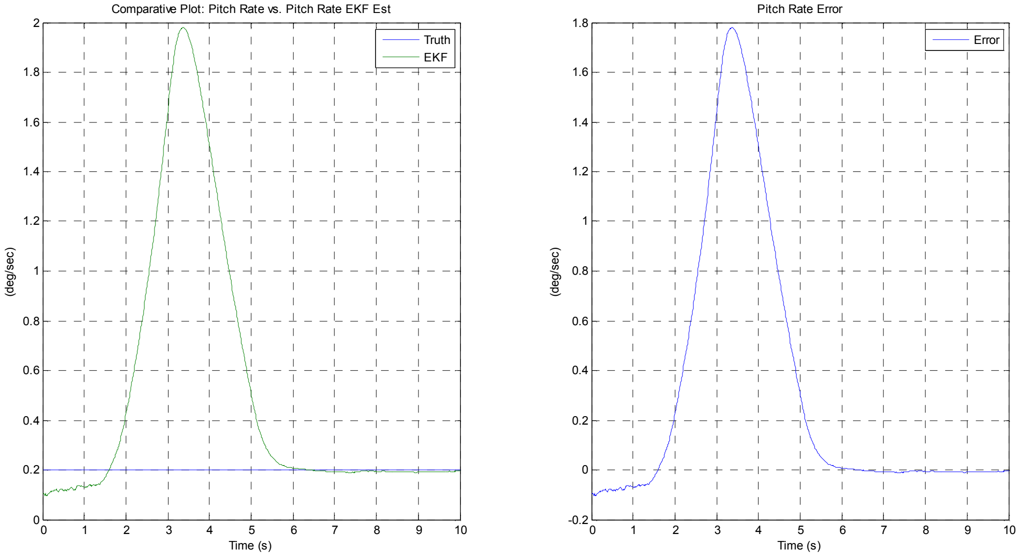

Figure 4.50: Nonlinear Pitch Rate Bias Estimation Results – Phase II No Turbulence

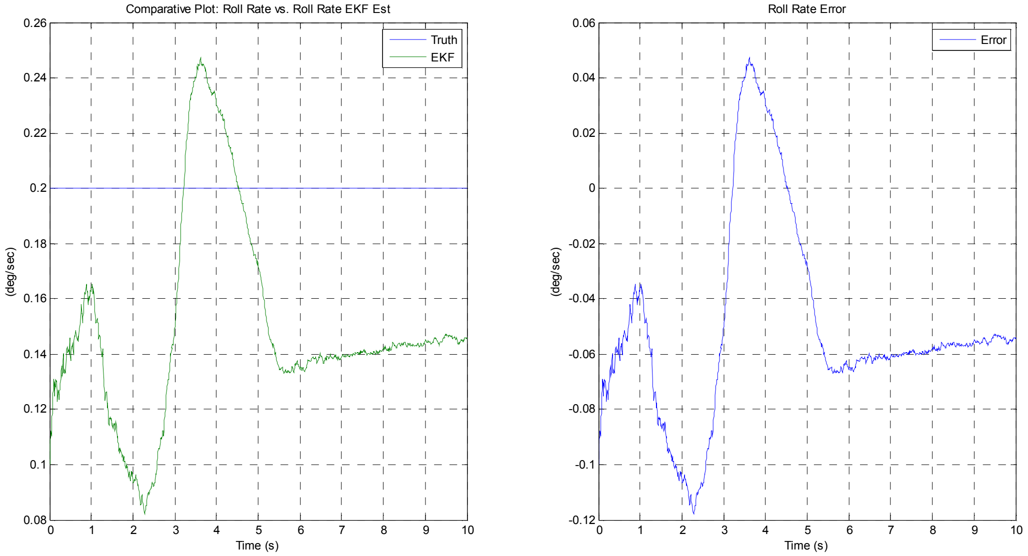

Figure 4.51: Nonlinear Roll Rate Bias Estimation Results – Phase II No Turbulence

Phase II Maximum and Mean Error Results No Turbulence					
Rate Gyro Bias (deg/sec)	**Rate Gyro Slope (deg/sec/hr)**	**Phase II – Transverse Maneuver with No Turbulence**			
0.2	0.05	θ Max Absolute Error (deg)	θ Mean Absolute Error (deg)	Max Bias Absolute Error (deg/sec)	Mean Bias Absolute Error (deg/sec)
		0.02046	0.00392	1.78140	0.34301
		ϕ Max Absolute Error (deg)	ϕ Mean Absolute Error (deg)	Max Bias Absolute Error (deg/sec)	Mean Bias Absolute Error (deg/sec)
		0.40759	0.13165	0.11779	0.05733

Table 4.14: Maximum and Mean Attitude and Bias Estimation Results – Phase II No Turbulence

From the simulation performed, the attitude estimates for both the longitudinal and transverse attitude of the vehicle stay within a ±0.410 degrees error, while Figures 4.50 and 4.51 show a maximum bias error of ±0.1.800 degrees per second as displayed and summarized in Table 4.14.

As was previously done in Phase I of the study, plots of the pitch and roll rate bias estimation errors are provided for an assessment of the ±1σ and ±3σ bounds on the rate gyro. The rate gyro variance for the Phase II of the study were kept consistent and set to 0.15 (degrees/second)^2. Figure 4.52 demonstrates how the extended Kalman filter provides accurate and well behaved pitch and roll bias estimation errors bounded by the rate gyro signal.

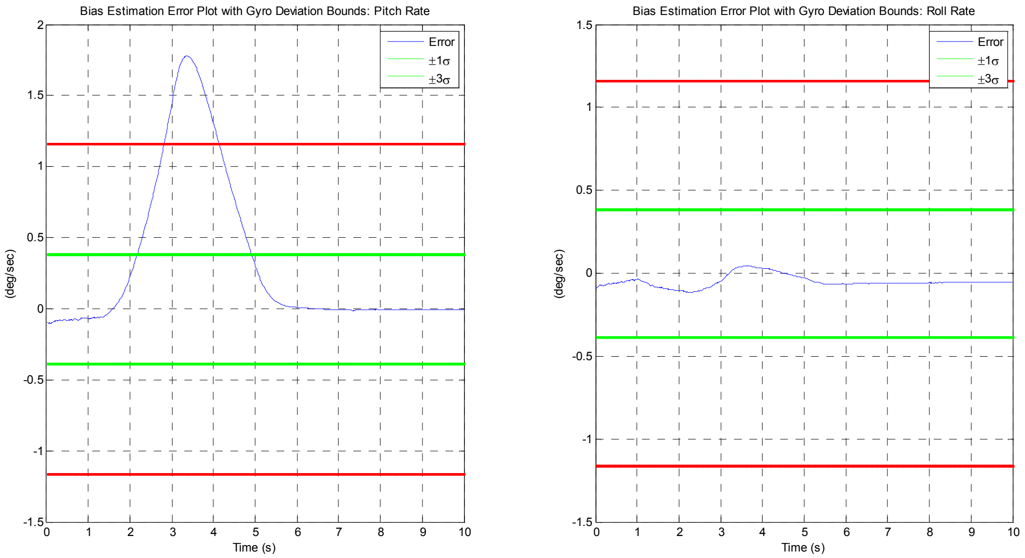

Figure 4.52: Nonlinear EKF Bias Estimation Error with Bounds – Phase II No Turbulence

The maximum bias error is acceptable due to the error remaining in the ±1σ and ±3σ bounds of ± 0.3873 degrees per second and ± 1.1619 degrees per second imposed from the rate gyro noise variance as displayed in Figure 4.52. While the maximum bias error lies outside the ±3σ bounds, the error is very minimal and as the simulation time increases, shows excellent convergence within the imposed rate gyro signal bounds. Staying within these statistical bounds is one again essential because 99.7% of a normally distributed value lies within the ±3σ bounds and 68.3% within the ±1σ bounds [41]. Therefore, the extended Kalman filter rate gyro bias and attitude estimation algorithm implemented in Phase II of this study with no turbulence injections proves to provide accurate and reliable attitude tracking results and rate gyro bias estimations in real-time.

The extended Kalman filter parameters were checked to ensure proper filter operation for the transverse maneuver imposed. The check for correct filter operation is once again conducted by comparing the attitude tracking and rate gyro bias estimation errors against the ±1σ and ±3σ values taken from the diagonal elements of the extended Kalman filters covariance matrix, P. Figures 4.53 and 4.54 demonstrate a properly operating extended Kalman filter due to the attitude and bias estimation errors versus variance operating within the ±1σ and ±3σ bounds established by the covariance matrix of the EKF.

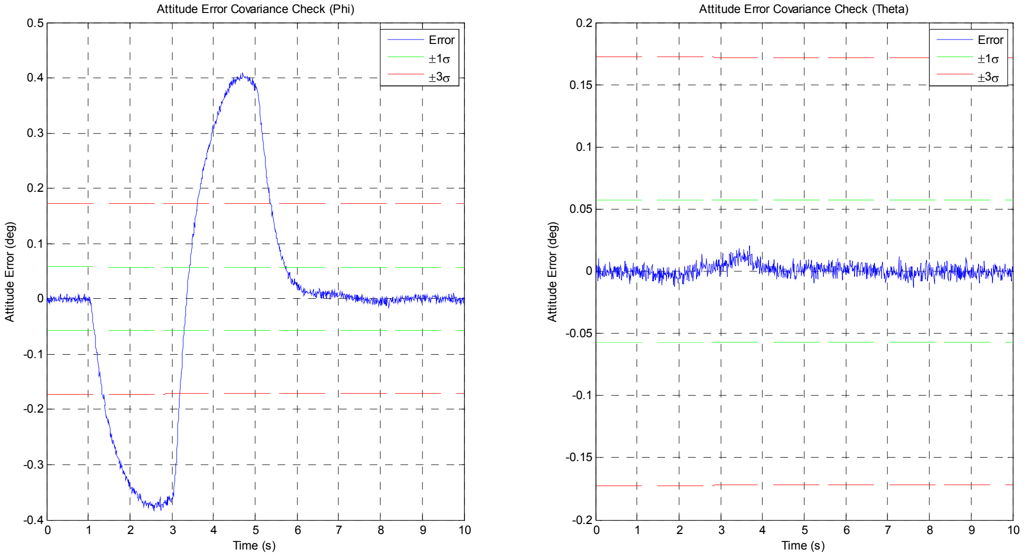

Figure 4.53: Nonlinear Attitude Error Covariance Check – Phase II No Turbulence

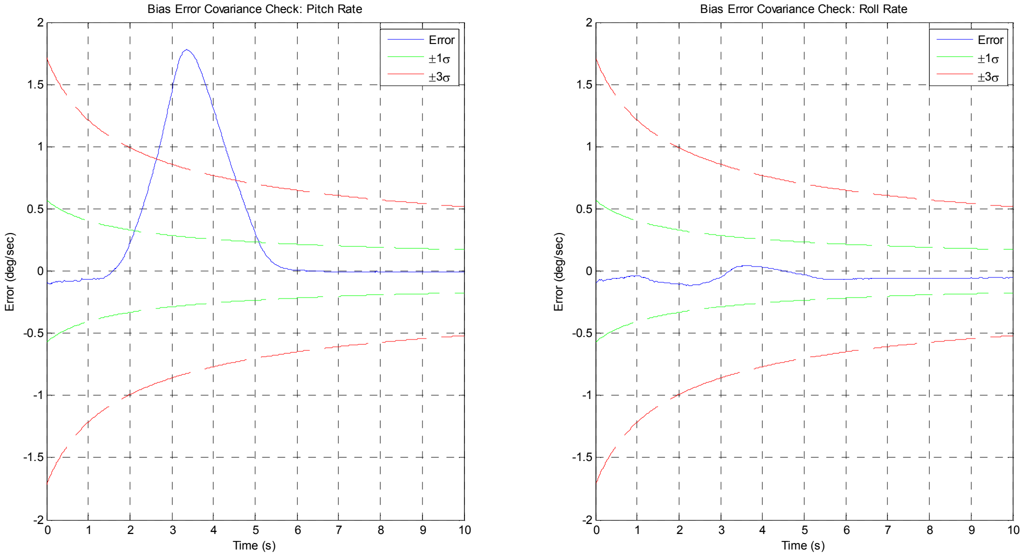

Figure 4.54: Nonlinear Bias Error Covariance Check – Phase II No Turbulence

Phase II – Transverse Maneuver: Turbulence

A comparison of the attitude determined by the dual-arc accelerometer array algorithm developed in Section 4.2.1 with the observer estimates is once again assessed utilizing the EKF algorithm and are shown in Figures 4.55 through 4.58 where Table 4.15 presents a summary of maximum and mean attitude and rate gyro bias estimation errors. In this phase of the analysis, turbulence was injected into the simulation model through the use of the Dryden wind and turbulence model from Section 3.3 where the maximum turbulence input to the simulation model approaches approximately 60 feet per second. The injection of such severe turbulence and vibrational effects is utilized in this Phase II portion of the feasibility study to display the robustness of the algorithm developed and implemented to produce accurate and reliable attitude and rate gyro bias estimates while operating in harsh environments and multiple dimensions.

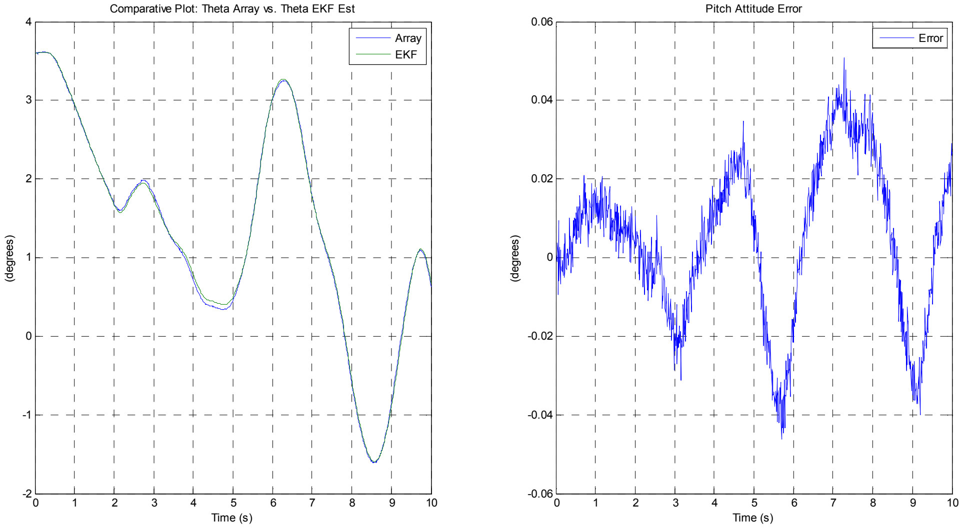

Figure 4.55: Nonlinear Pitch Attitude Tracking Results – Phase II with Turbulence

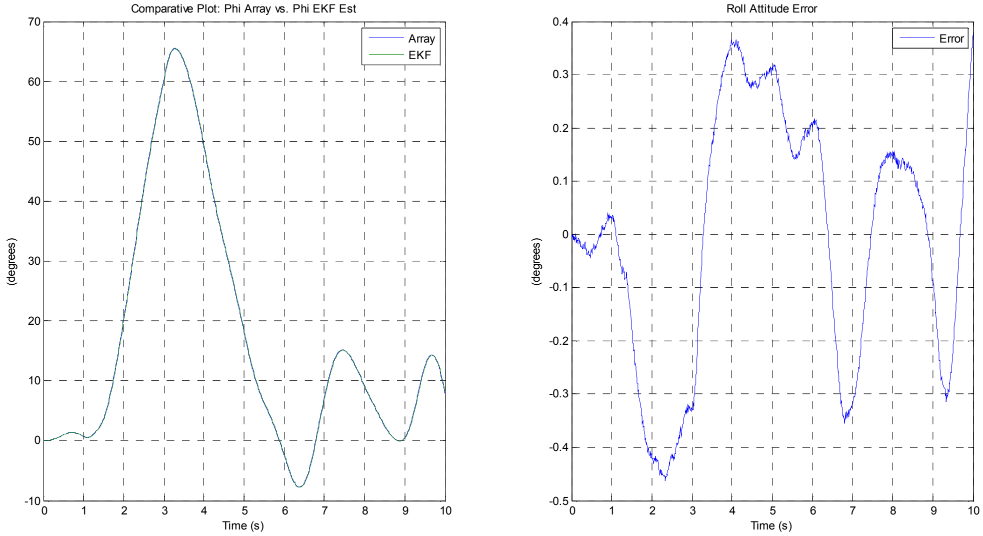

Figure 4.56: Nonlinear Roll Attitude Tracking Results – Phase II with Turbulence

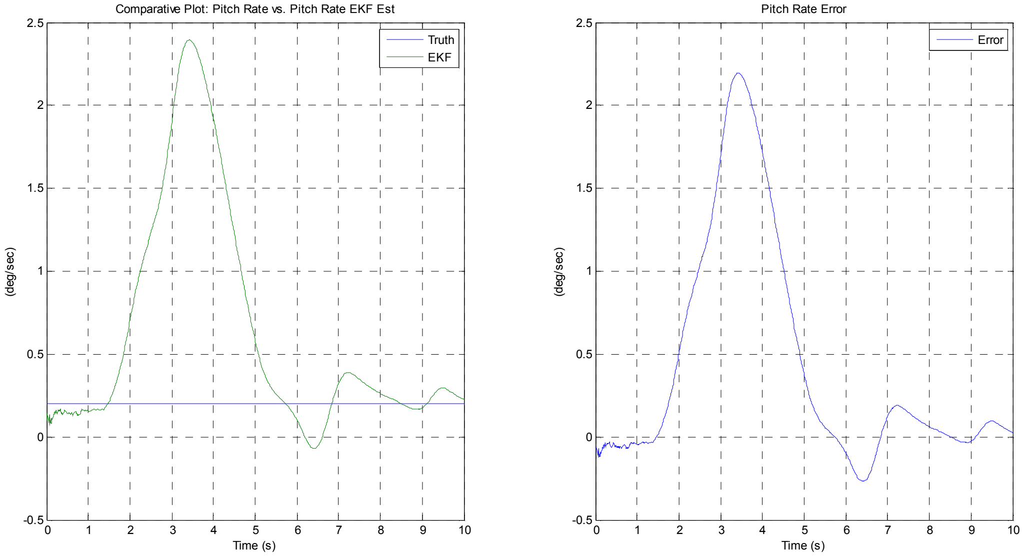

Figure 4.57: Nonlinear Pitch Rate Bias Estimation Results – Phase II with Turbulence

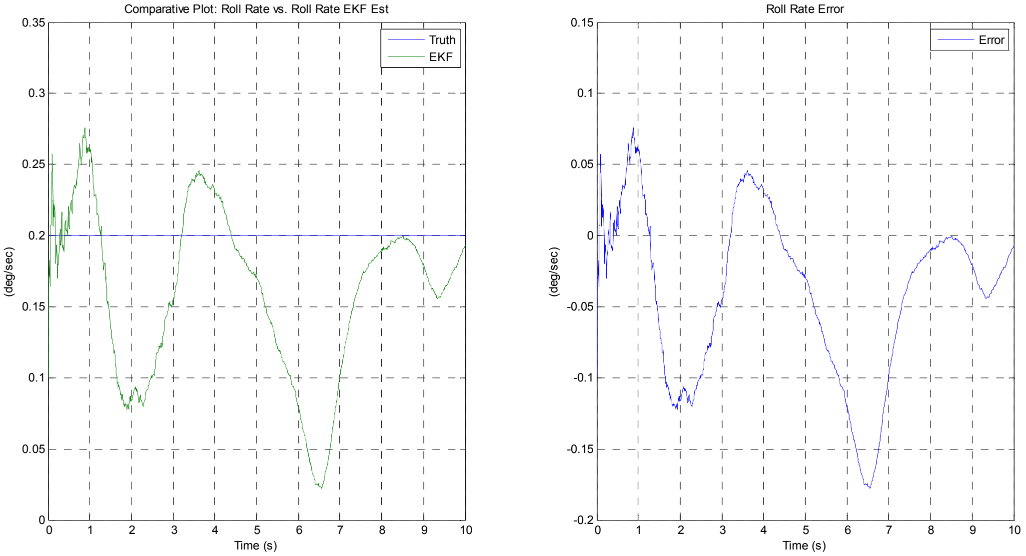

Figure 4.58: Nonlinear Roll Rate Bias Estimation Results – Phase II with Turbulence

Phase II Maximum and Mean Error Results with Turbulence					
Rate Gyro Bias (deg/sec)	**Rate Gyro Slope (deg/sec/hr)**	**Phase II – Transverse Maneuver with Turbulence**			
0.2	0.05	θ Max Absolute Error (deg)	θ Mean Absolute Error (deg)	Max Bias Absolute Error (deg/sec)	Mean Bias Absolute Error (deg/sec)
		0.05083	0.01659	2.19600	0.47764
		ϕ Max Absolute Error (deg)	ϕ Mean Absolute Error (deg)	Max Bias Absolute Error (deg/sec)	Mean Bias Absolute Error (deg/sec)
		0.46355	0.19930	0.17773	0.05399

Table 4.15: Maximum and Mean Attitude and Bias Estimation Results – Phase II with Turbulence

From the Phase II simulations performed with turbulence injections, the attitude estimates for both the longitudinal and transverse maximum attitude of the vehicle stay within a ±0.500 degrees error, while Figures 4.57 and 4.58 show a maximum bias error of ±0.2.200 degrees per second as displayed and summarized in Table 4.15.

Additionally, plots of the pitch and roll rate bias estimation errors are provided for an assessment of the ±1σ and ±3σ bounds on the rate gyro. Figures 4.59 demonstrate how the extended Kalman filter provides accurate and well behaved pitch and roll bias estimation errors bounded by the rate gyro signal. While the maximum bias error lies outside the ±3σ bounds, the error is very minimal and as the simulation time increases, shows excellent convergence within the imposed rate gyro signal bounds at a simulation time above approximately five seconds.

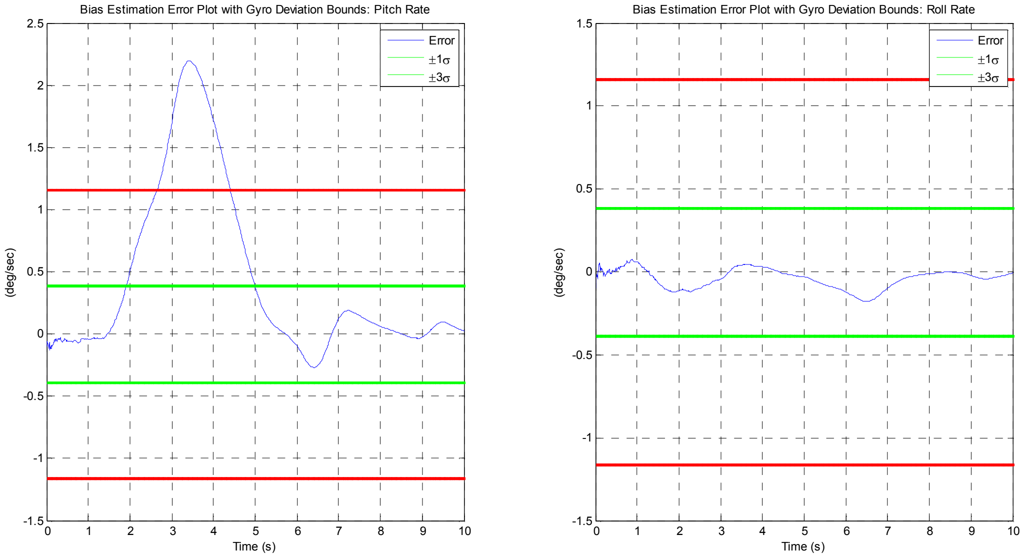

Figure 4.59: Nonlinear EKF Bias Estimation Error with Bounds – Phase II with Turbulence

The maximum bias error is acceptable due to the error remaining in the ±1σ and ±3σ bounds of ± 0.3873 degrees per second and ± 1.1619 degrees per second imposed from the rate gyro noise variance as displayed in Figure 4.59. Staying within these statistical bounds is one again essential because 99.7% of a normally distributed value lies within the ±3σ bounds and 68.3% within the ±1σ bounds [41]. Therefore, the extended Kalman filter rate gyro bias estimation and attitude determination algorithm implemented in Phase II of this study with severe turbulence injections proves to provide accurate and reliable attitude tracking results and rate gyro bias estimations in real-time.

The check for correct filter operation in this Phase II, turbulent, portion of the feasibility study is once again conducted by comparing the attitude tracking and rate gyro bias estimation errors against the ±1σ and ±3σ values taken from the diagonal elements of the extended Kalman filters covariance matrix, P. Figures 4.60 and 4.61 demonstrate a properly operating extended Kalman filter due to the attitude and bias estimation errors versus variance operating within the ±1σ and ±3σ bounds established by the covariance matrix of the EKF.

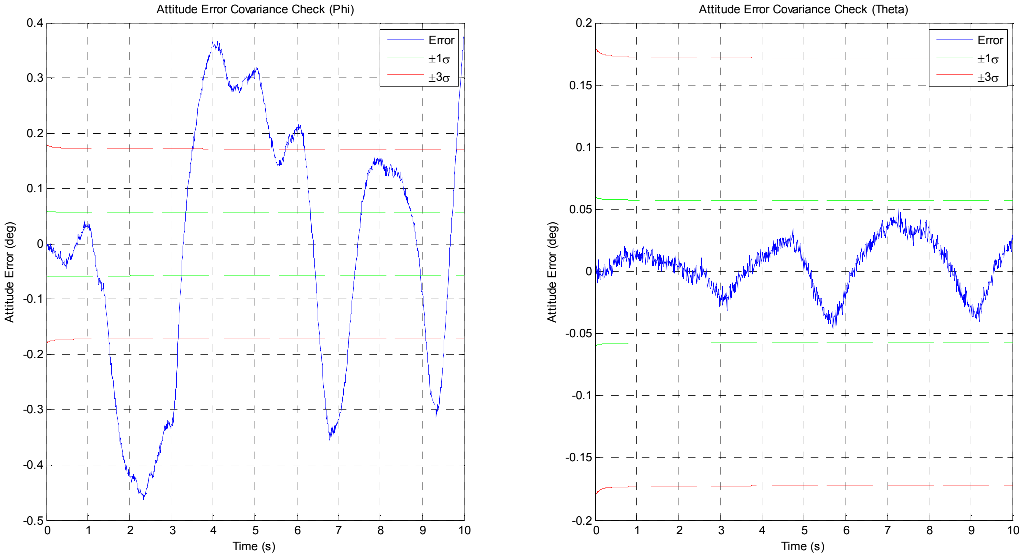

Figure 4.60: Nonlinear Attitude Error Covariance Check – Phase II with Turbulence

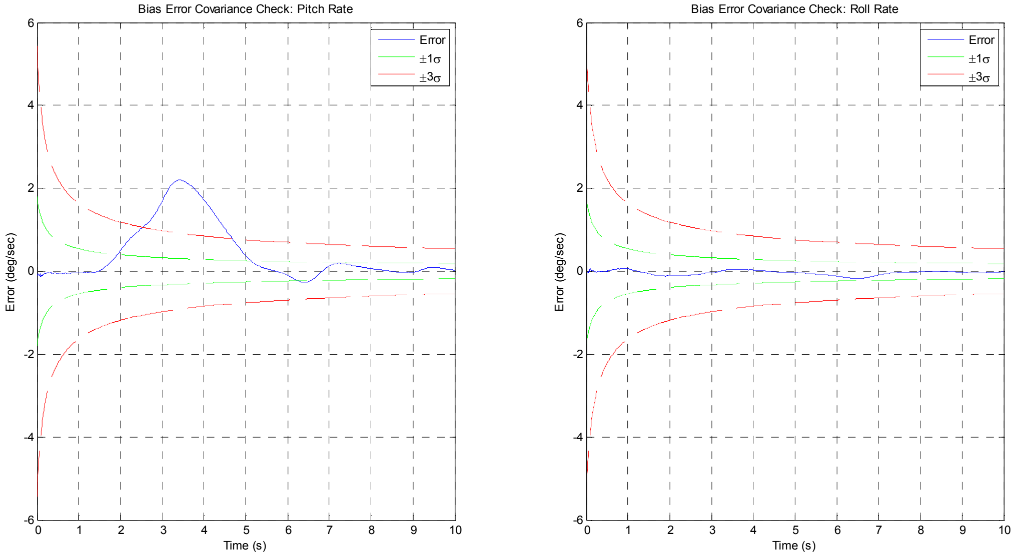

Figure 4.61: Nonlinear Bias Error Covariance Check – Phase II with Turbulence

Utilizing the EKF parameters given previously in Table 4.7, the rate gyro bias magnitude was varied between values of 0.2 and 10 degrees/second while the rate gyro bias slope was varied between values of 0 and 1 degree/second/hour in order examine and assess the sensitivity of the extended Kalman filter implemented to changes in rate gyro bias magnitude and slope. The results of the Phase II assessment are summarized in Tables 4.16 through 4.19 given below.

Impact of Changing Rate Gyro Bias Magnitude with a Constant Slope					
Phase II: Transverse Maneuver No Turbulence					
Rate Gyro Bias Slope (deg/sec/hr)	Bias (deg/sec)	θ Max Absolute Error (deg)	θ Mean Absolute Error (deg)	Max Bias Absolute Error (deg/sec)	Mean Bias Absolute Error (deg/sec)
0.0	0.2	0.02046	0.00392	1.78140	0.34302
	1	0.01875	0.00433	1.59810	0.40333
	3	0.03473	0.00715	2.90000	0.64570
	5	0.05359	0.01108	4.90000	0.96253
	10	0.10270	0.02274	9.90000	2.03690
0.5	0.2	0.02046	0.00392	1.78160	0.34293
	1	0.01875	0.00433	1.59830	0.40316
	3	0.03473	0.00716	2.90000	0.64550
	5	0.05359	0.01108	4.90000	0.96229
	10	0.10270	0.02275	9.90000	2.03660
1.0	0.2	0.02046	0.00392	1.78170	0.34285
	1	0.01875	0.00433	1.59850	0.40299
	3	0.03473	0.00716	2.90000	0.64529
	5	0.05359	0.01109	4.90000	0.96206
	10	0.10270	0.02275	9.90000	2.03630
Phase II: Transverse Maneuver with Turbulence					
Rate Gyro Bias Slope (deg/sec/hr)	Bias (deg/sec)	θ Max Absolute Error (deg)	θ Mean Absolute Error (deg)	Max Bias Absolute Error (deg/sec)	Mean Bias Absolute Error (deg/sec)
0.0	0.2	0.05083	0.01659	2.19600	0.47762
	1	0.05072	0.01654	2.17330	0.48961
	3	0.05045	0.01655	2.90000	0.52405
	5	0.05277	0.01667	4.90000	0.56397
	10	0.10270	0.01726	9.90000	0.68302
0.5	0.2	0.05082	0.01659	2.19620	0.47778
	1	0.05071	0.01654	2.17350	0.48975
	3	0.05044	0.01655	2.90000	0.52414
	5	0.05277	0.01667	4.90000	0.56399
	10	0.10270	0.01726	9.90000	0.68290
1.0	0.2	0.05082	0.01658	2.19640	0.47795
	1	0.05071	0.01654	2.17380	0.48989
	3	0.05044	0.01655	2.90000	0.52423
	5	0.05277	0.01667	4.90000	0.56402
	10	0.10270	0.01726	9.90000	0.68277

Table 4.16: Sensitivity of Extended Kalman Filter to Changes in Rate Gyro Bias Magnitude with Constant Rate Gyro Slope– Phase II Pitch Attitude and Bias Summary

Impact of Changing Rate Gyro Bias Magnitude with a Constant Slope					
Phase II: Transverse Maneuver No Turbulence					
Rate Gyro Bias Slope (deg/sec/hr)	Bias (deg/sec)	ϕ Max Absolute Error (deg)	ϕ Mean Absolute Error (deg)	Max Bias Absolute Error (deg/sec)	Mean Bias Absolute Error (deg/sec)
0.0	0.2	0.40759	0.13165	0.11780	0.05735
	1	0.40619	0.13215	0.90000	0.24212
	3	0.40268	0.13405	2.90000	0.72231
	5	0.39917	0.13623	4.90000	1.20250
	10	0.40935	0.14258	9.90000	2.40300
0.5	0.2	0.40759	0.13164	0.11769	0.05711
	1	0.40618	0.13215	0.90000	0.24182
	3	0.40267	0.13405	2.90000	0.72201
	5	0.39916	0.13623	4.90000	1.20220
	10	0.40935	0.14258	9.90000	2.40270
1.0	0.2	0.40758	0.13164	0.11758	0.05688
	1	0.40618	0.13215	0.90000	0.24153
	3	0.40267	0.13405	2.90000	0.72172
	5	0.39916	0.13623	4.90000	1.20190
	10	0.40935	0.14258	9.90000	2.40240
Phase II: Transverse Maneuver with Turbulence					
Rate Gyro Bias Slope (deg/sec/hr)	Bias (deg/sec)	ϕ Max Absolute Error (deg)	ϕ Mean Absolute Error (deg)	Max Bias Absolute Error (deg/sec)	Mean Bias Absolute Error (deg/sec)
0.0	0.2	0.46355	0.19930	0.17777	0.05402
	1	0.46388	0.19948	0.90000	0.07995
	3	0.46470	0.19992	2.90000	0.17066
	5	0.46552	0.20038	4.90000	0.26390
	10	0.46757	0.20153	9.90000	0.49698
0.5	0.2	0.46355	0.19930	0.17732	0.05375
	1	0.46388	0.19948	0.90000	0.07966
	3	0.46470	0.19992	2.90000	0.17032
	5	0.46552	0.20038	4.90000	0.26356
	10	0.46757	0.20153	9.90000	0.49664
1.0	0.2	0.46355	0.19930	0.17688	0.05349
	1	0.46388	0.19948	0.90000	0.07936
	3	0.46470	0.19992	2.90000	0.16998
	5	0.46552	0.20038	4.90000	0.26322
	10	0.46757	0.20153	9.90000	0.49630

Table 4.17: Sensitivity of Extended Kalman Filter to Changes in Rate Gyro Bias Magnitude with Constant Rate Gyro Slope – Phase II Roll Attitude and Bias Summary

Tables 4.16 and 4.17 assessed the sensitivity of the extended Kalman filter to changes in the rate gyro bias magnitude while maintaining a constant rate gyro bias slope. Tables 4.18 and 4.19 display a summary of attitude determination and bias estimation results for sensitivity of the extended Kalman filter to changes in the rate gyro bias slope while maintaining a constant rate gyro bias magnitude for Phase II of the feasibility study conducted.

Impact of Changing Rate Gyro Bias Slope with Constant Bias Magnitude					
Phase II: Transverse Maneuver No Turbulence					
Rate Gyro Bias (deg/sec)	Rate Gyro Bias Slope (deg/sec/hr)	θ Max Absolute Error (deg)	θ Mean Absolute Error (deg)	Max Bias Absolute Error (deg/sec)	Mean Bias Absolute Error (deg/sec)
0.2	0.0	0.02046	0.00392	1.78140	0.34302
	0.5	0.02046	0.00392	1.78160	0.34293
	1.0	0.02045	0.00392	1.78170	0.34285
1	0.0	0.01875	0.00433	1.59810	0.40333
	0.5	0.01875	0.00433	1.59830	0.40316
	1.0	0.01874	0.00433	1.59850	0.40299
3	0.0	0.03473	0.00716	2.90000	0.64570
	0.5	0.03473	0.00716	2.90000	0.64550
	1.0	0.03473	0.00716	2.90000	0.64529
5	0.0	0.05359	0.01108	4.90000	0.96253
	0.5	0.05359	0.01108	4.90000	0.96229
	1.0	0.05359	0.01109	4.90000	0.96206
10	0.0	0.10270	0.02274	9.90000	2.03690
	0.5	0.10270	0.02275	9.90000	2.03660
	1.0	0.10270	0.02275	9.90000	2.03630
Phase II: Transverse Maneuver with Turbulence					
Rate Gyro Bias (deg/sec)	Rate Gyro Bias Slope (deg/sec/hr)	θ Max Absolute Error (deg)	θ Mean Absolute Error (deg)	Max Bias Absolute Error (deg/sec)	Mean Bias Absolute Error (deg/sec)
0.2	0.0	0.05083	0.01659	2.19600	0.47762
	0.5	0.05082	0.01659	2.19620	0.47778
	1.0	0.05082	0.01658	2.19640	0.47795
1	0.0	0.05072	0.01654	2.17330	0.48961
	0.5	0.05071	0.01654	2.17350	0.48975
	1.0	0.05071	0.01654	2.17380	0.48989
3	0.0	0.05045	0.01655	2.90000	0.52405
	0.5	0.05044	0.01655	2.90000	0.52414
	1.0	0.05044	0.01655	2.90000	0.52423
5	0.0	0.05277	0.01667	4.90000	0.56397
	0.5	0.05277	0.01667	4.90000	0.56399
	1.0	0.05277	0.01667	4.90000	0.56402
10	0.0	0.10270	0.01726	9.90000	0.68302
	0.5	0.10270	0.01726	9.90000	0.68290
	1.0	0.10270	0.01726	9.90000	0.68277

Table 4.18: Sensitivity of Extended Kalman Filter to Change in Rate Gyro Bias Slope with Constant Rate Gyro Bias Magnitude – Phase II Pitch Attitude and Bias Summary

Impact of Changing Rate Gyro Bias Slope with Constant Bias Magnitude					
Phase II: Transverse Maneuver No Turbulence					
Rate Gyro Bias (deg/sec)	Rate Gyro Bias Slope (deg/sec/hr)	ϕ Max Absolute Error (deg)	ϕ Mean Absolute Error (deg)	Max Bias Absolute Error (deg/sec)	Mean Bias Absolute Error (deg/sec)
0.2	0.0	0.40759	0.13165	0.11780	0.05735
	0.5	0.40759	0.13164	0.11769	0.05711
	1.0	0.40758	0.13164	0.11758	0.05688
1	0.0	0.40619	0.13215	0.90000	0.24212
	0.5	0.40618	0.13215	0.90000	0.24182
	1.0	0.40618	0.13215	0.90000	0.24153
3	0.0	0.40268	0.13405	2.90000	0.72231
	0.5	0.40267	0.13405	2.90000	0.72201
	1.0	0.40267	0.13405	2.90000	0.72172
5	0.0	0.39917	0.13623	4.90000	1.20250
	0.5	0.39916	0.13623	4.90000	1.20220
	1.0	0.39916	0.13623	4.90000	1.20190
10	0.0	0.40935	0.14258	9.90000	2.40300
	0.5	0.40935	0.14258	9.90000	2.40270
	1.0	0.40935	0.14258	9.90000	2.40240
Phase II: Transverse Maneuver with Turbulence					
Rate Gyro Bias (deg/sec)	Rate Gyro Bias Slope (deg/sec/hr)	ϕ Max Absolute Error (deg)	ϕ Mean Absolute Error (deg)	Max Bias Absolute Error (deg/sec)	Mean Bias Absolute Error (deg/sec)
0.2	0.0	0.46355	0.19930	0.17777	0.05402
	0.5	0.46355	0.19930	0.17732	0.05375
	1.0	0.46355	0.19930	0.17688	0.05349
1	0.0	0.46388	0.19948	0.90000	0.07995
	0.5	0.46388	0.19948	0.90000	0.07966
	1.0	0.46388	0.19948	0.90000	0.07936
3	0.0	0.46470	0.19992	2.90000	0.17066
	0.5	0.46470	0.19992	2.90000	0.17032
	1.0	0.46470	0.19992	2.90000	0.16998
5	0.0	0.46552	0.20038	4.90000	0.26390
	0.5	0.46552	0.20038	4.90000	0.26356
	1.0	0.46552	0.20038	4.90000	0.26322
10	0.0	0.46757	0.20153	9.90000	0.49698
	0.5	0.46757	0.20153	9.90000	0.49664
	1.0	0.46757	0.20153	9.90000	0.49630

Table 4.19: Sensitivity of Extended Kalman Filter to Change in Rate Gyro Bias Slope with Constant Rate Gyro Bias Magnitude – Phase II Roll Attitude and Bias Summary

The results of the Phase II study conducted show bias magnitude has little to negligible effect on the attitude estimation of the EKF and noticeable effect on the bias estimate as the bias magnitude imposed increases just as in the previous phase of the study conducted. From the simulations performed, the results show that varying the bias magnitude has more effect on attitude and bias estimation results as compared to varying the rate gyro bias slope. For the Phase II simulation study, the bias estimate is reasonable and the attitude estimate does not drift outside of the acceptable range of ±1 degrees based on instrumentation from [49]. The inaccuracies of the algorithm method implemented are once again a result from accelerometer and rate gyro measurement noises and severe turbulence effects causing a highly dynamical operating environment.

4.3.3 Phase III Study – Longitudinal/Transverse Aircraft Maneuver

Phase III – Longitudinal/Transverse Maneuver: No Turbulence

Phase III of this feasibility study focused on the implementation of the extended Kalman filter derived previously in Section 2.2.3 implemented as an observer to the nonlinear aircraft simulation model to improve upon the attitude and rate gyro bias estimation for a combined longitudinal/transverse maneuver of the nonlinear aircraft simulation plant model. A comparison of the attitude determined by the dual-arc accelerometer array algorithm developed in Section 4.2.1 with the observer estimates utilizing the EKF algorithm are shown in Figures 4.62 through 4.65 where Table 4.20 presents a summary of maximum and mean attitude and rate gyro bias estimation errors. In this Phase III portion of the analysis, no turbulence was injected into the simulation model.

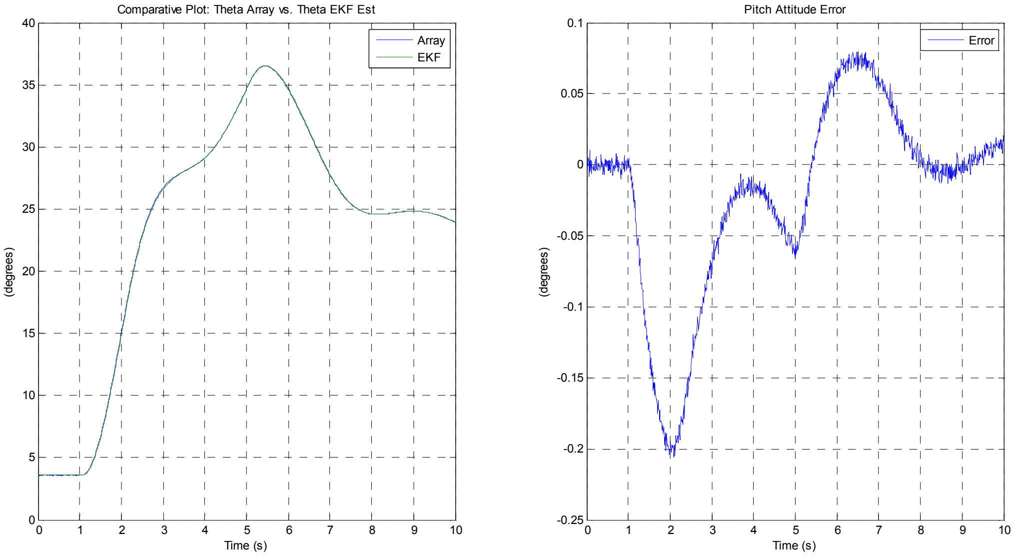

Figure 4.62: Nonlinear Pitch Attitude Tracking Results – Phase III No Turbulence

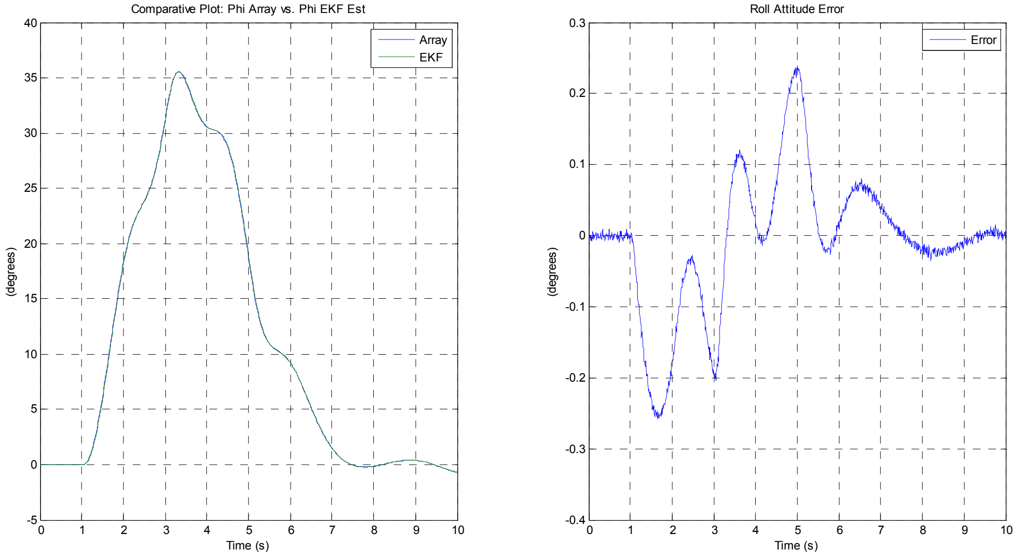

Figure 4.63: Nonlinear Roll Attitude Tracking Results – Phase III No Turbulence

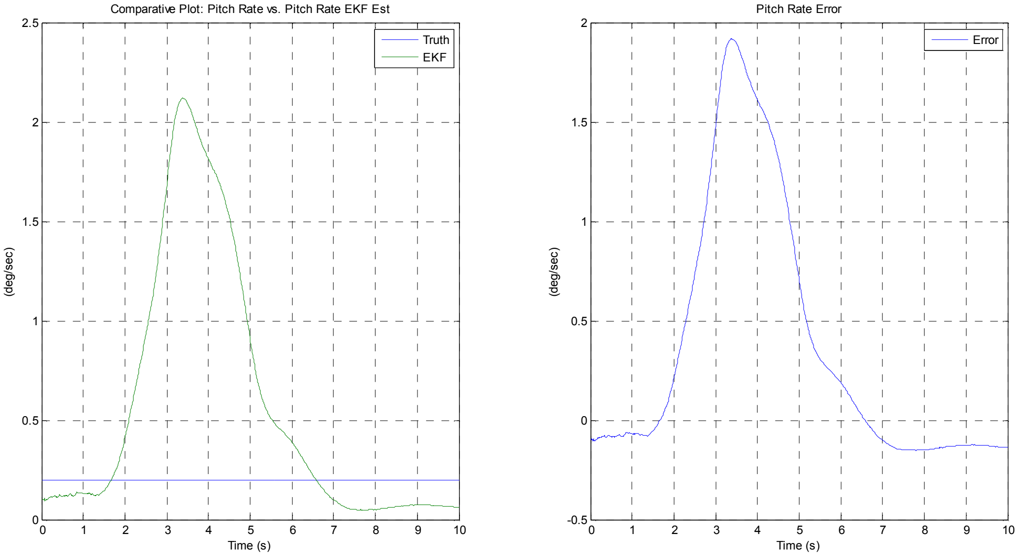

Figure 4.64: Nonlinear Pitch Rate Bias Estimation Results – Phase III No Turbulence

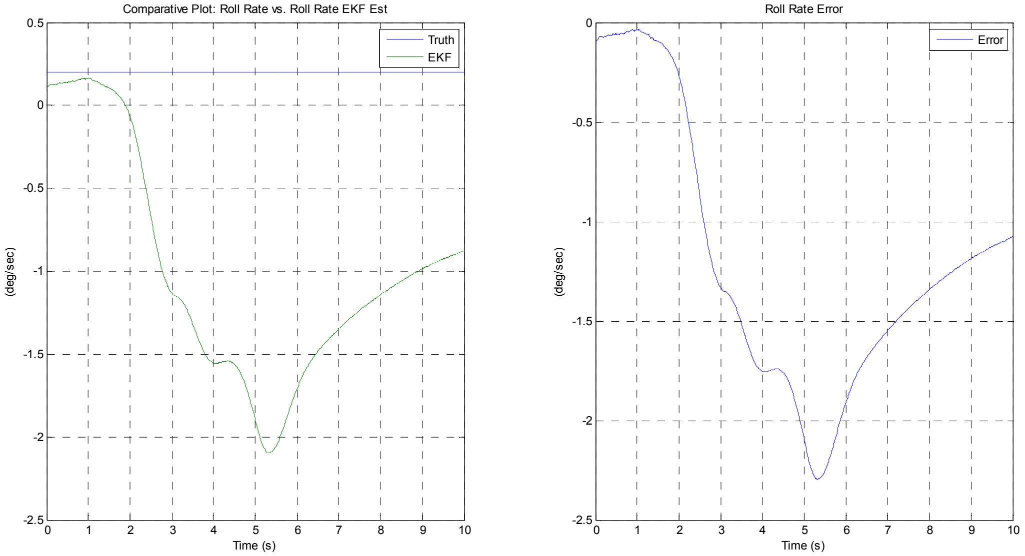
Comparative Plot: Roll Rate vs. Roll Rate EKF Est

Roll Rate Error

Figure 4.65: Nonlinear Roll Rate Bias Estimation Results – Phase III No Turbulence

Phase III Maximum and Mean Error Results No Turbulence					
Rate Gyro Bias (deg/sec)	**Rate Gyro Slope (deg/sec/hr)**	**Phase III – Longitudinal/Transverse Maneuver with No Turbulence**			
0.2	0.05	θ Max Absolute Error (deg)	θ Mean Absolute Error (deg)	Max Bias Absolute Error (deg/sec)	Mean Bias Absolute Error (deg/sec)
		0.20602	0.04766	1.92040	0.47859
		ϕ Max Absolute Error (deg)	ϕ Mean Absolute Error (deg)	Max Bias Absolute Error (deg/sec)	Mean Bias Absolute Error (deg/sec)
		0.25716	0.06274	2.29640	1.20530

Table 4.20: Maximum and Mean Attitude and Bias Estimation Results –
Phase III No Turbulence

From the Phase III simulation performed, the attitude estimates for both the longitudinal and transverse maximum error of the vehicle attitude stay within a ±0.260 degree error, while Figure 4.64 and 4.65 show a maximum bias error of ±2.300 degrees per second as displayed and summarized in Table 4.20.

As was previously done in Phase I and Phase II of the study, plots of the pitch and roll rate bias estimation errors are provided for an assessment of the $\pm 1\sigma$ and $\pm 3\sigma$ bounds on the rate gyro. The rate gyro variance for this phase of the study were kept consistent and set to 0.15 (degrees/second)^2. Figure 4.66 demonstrate how the extended Kalman filter provides accurate and well behaved pitch and roll bias estimation errors bounded by the rate gyro signal.

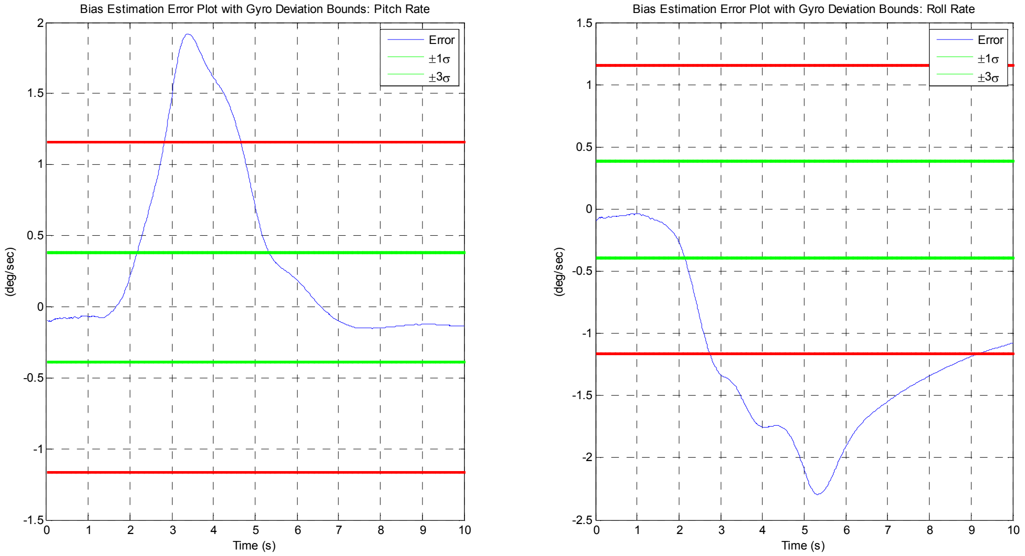

Figure 4.66: Nonlinear EKF Bias Estimation Error with Bounds – Phase III No Turbulence

The maximum bias error is acceptable due to the error remaining in the ±1σ and ±3σ bounds of ± 0.3873 degrees per second and ± 1.1619 degrees per second imposed from the rate gyro noise variance as displayed in Figure 4.66. While the maximum bias error lies outside the ±3σ bounds, the error is very minimal and as the simulation time increases, shows excellent convergence within the imposed rate gyro signal bounds. Staying within these statistical bounds is essential because 99.7% of a normally distributed value lies within the ±3σ bounds and 68.3% within the ±1σ bounds [41]. Therefore, the extended Kalman filter rate gyro bias and attitude estimation algorithm implemented in Phase III of this study with no turbulence injections proves to provide accurate and reliable attitude tracking results and rate gyro bias estimations in real-time.

The extended Kalman filter parameters were checked once again in this Phase III portion of the feasibility study to ensure proper filter operation for the combined longitudinal/transverse maneuver imposed. The check for correct filter operation again conducted by comparing the attitude tracking and rate gyro bias estimation errors against the ±1σ and ±3σ values taken from the diagonal elements of the extended Kalman filter's covariance matrix, P. Figures 4.67 and 4.68 demonstrate a properly operating extended Kalman filter due to the attitude and bias estimation errors versus variance operating within the ±1σ and ±3σ bounds established by the covariance matrix of the EKF. While the roll rate bias error covariance verification does not fall within the ±3σ bounds at the end of the simulation period, if the simulation period is expanded to 50 seconds, the roll rate bias error does converge within the ±1σ and ±3σ bounds to validate proper filter operation as shown in Figure 4.69.

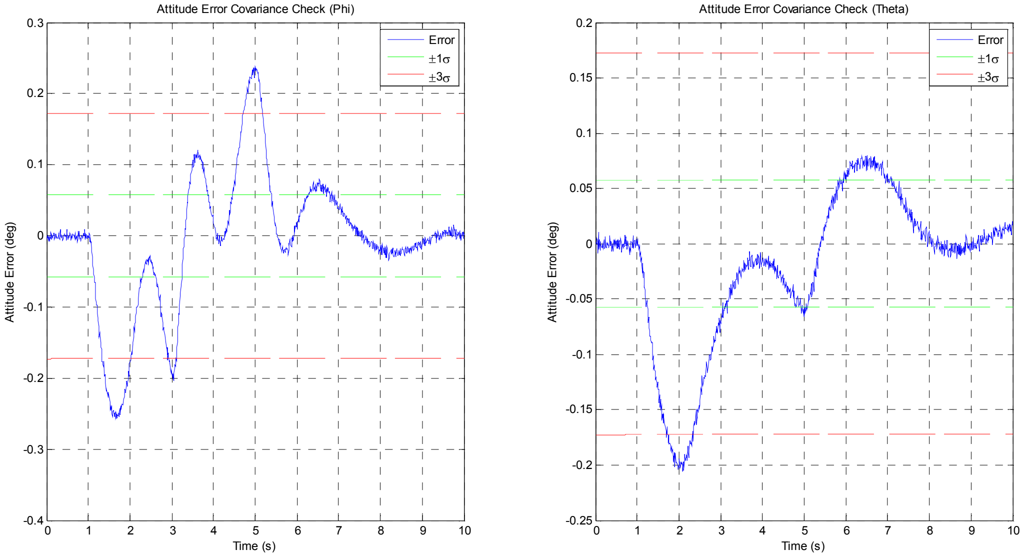

Figure 4.67: Nonlinear Attitude Error Covariance Check – Phase III No Turbulence

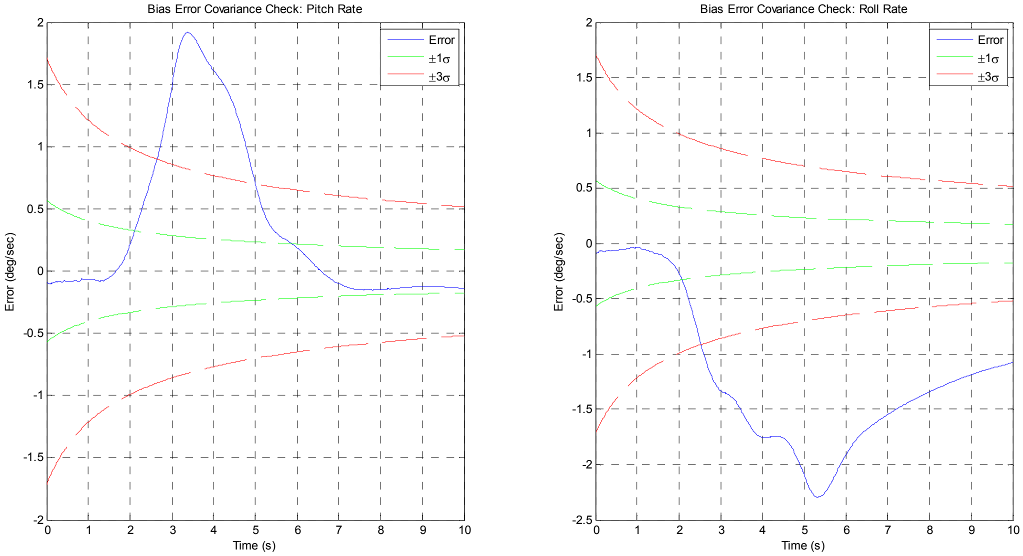

Figure 4.68: Nonlinear Bias Error Covariance Check – Phase III No Turbulence

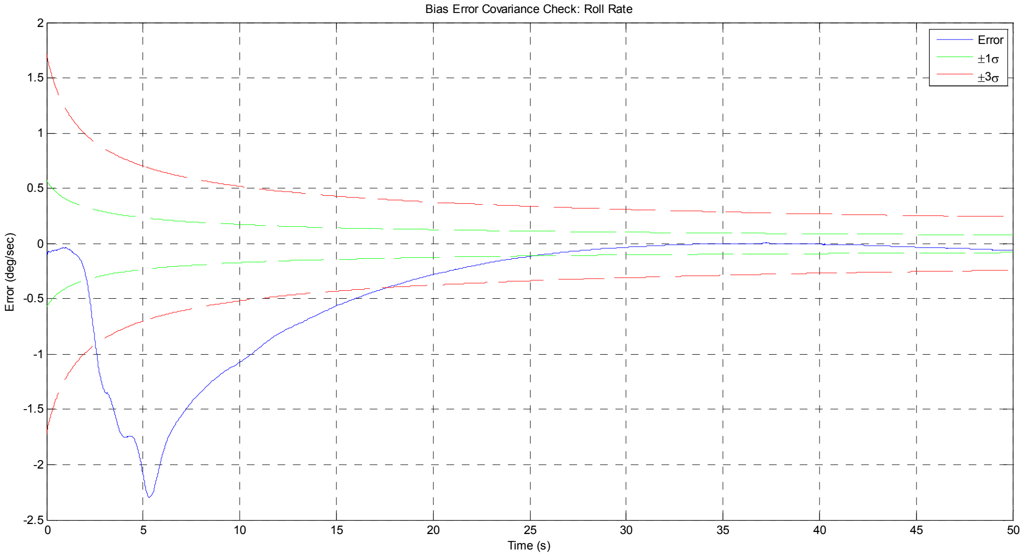

Figure 4.69: Nonlinear Bias Error Covariance Check – Phase III Simulation Period Expanded to 50 seconds No Turbulence

Phase III – Longitudinal/Transverse Maneuver: Turbulence

A comparison of the attitude determined by the dual-arc accelerometer array algorithm developed in Section 4.2.1 with the observer estimates is once again assessed utilizing the EKF algorithm and are shown in Figures 4.70 through 4.73 where Table 4.21 presents a summary of maximum and mean attitude and rate gyro bias estimation errors. In this Phase III analysis, turbulence was injected into the simulation model through the use of the Dryden wind and turbulence model from Section 3.3 where the maximum turbulence input to the simulation model approaches approximately 60 feet per second. The injection of such severe turbulence and vibrational effects is utilized in this Phase III portion of the feasibility study to display the robustness of the algorithm developed and implemented to produce accurate and reliable attitude and rate gyro bias estimates while operating in harsh environments and multiple dimensions.

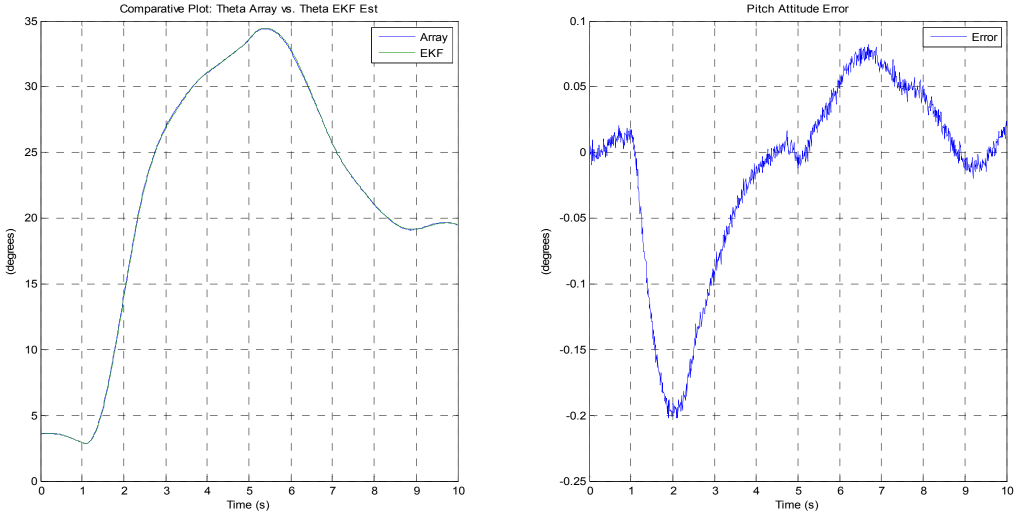

Figure 4.70: Nonlinear Pitch Attitude Tracking Results – Phase III with Turbulence

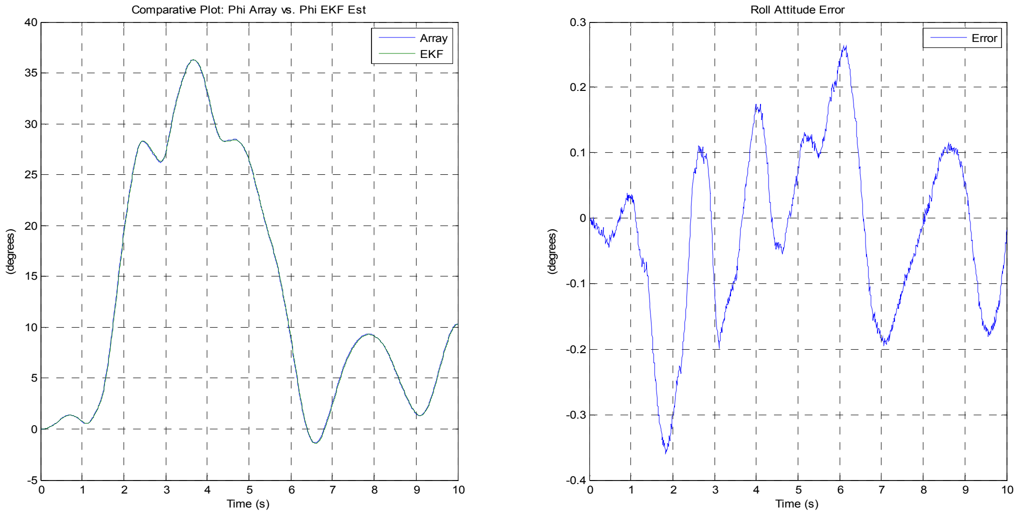

Figure 4.71: Nonlinear Pitch Attitude Tracking Results – Phase III with Turbulence

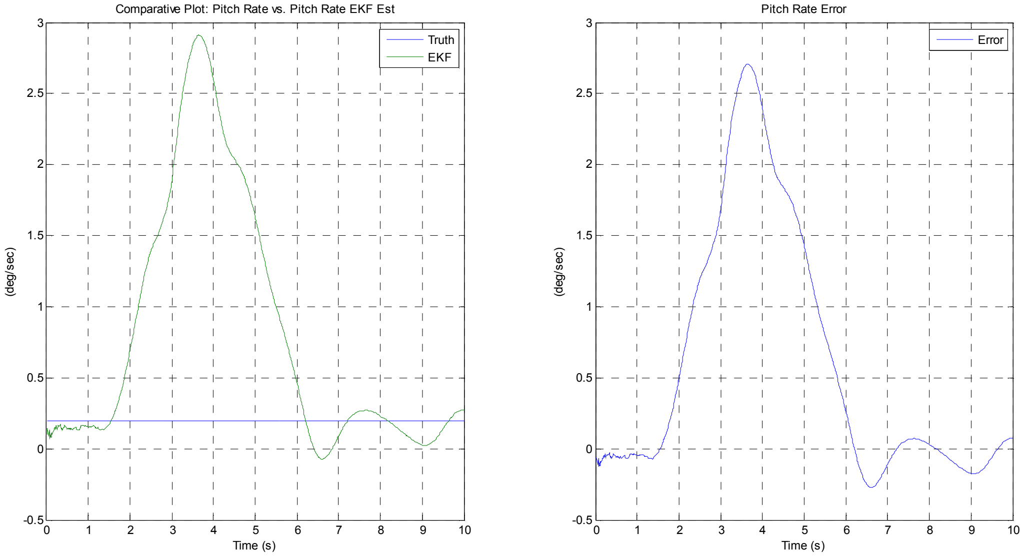

Figure 4.72: Nonlinear Pitch Rate Bias Estimation Results – Phase III with Turbulence

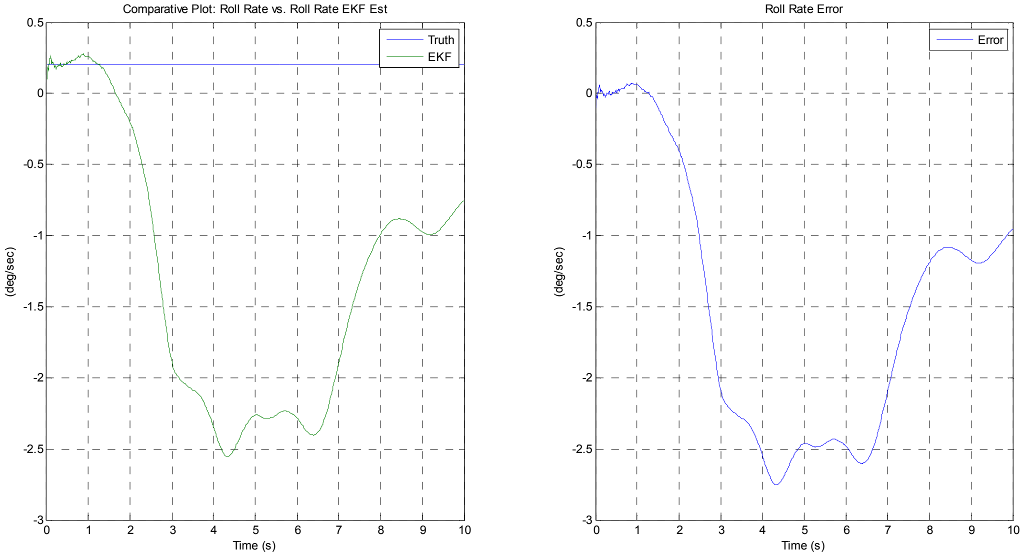

Figure 4.73: Nonlinear Roll Rate Bias Estimation Results – Phase III with Turbulence

Phase III Maximum and Mean Error Results with Turbulence					
Rate Gyro Bias (deg/sec)	**Rate Gyro Slope (deg/sec/hr)**	**Phase III – Longitudinal/Transverse Maneuver with Turbulence**			
0.2	0.05	θ Max Absolute Error (deg)	θ Mean Absolute Error (deg)	Max Bias Absolute Error (deg/sec)	Mean Bias Absolute Error (deg/sec)
		0.20238	0.05023	2.7103	0.68214
		ϕ Max Absolute Error (deg)	ϕ Mean Absolute Error (deg)	Max Bias Absolute Error (deg/sec)	Mean Bias Absolute Error (deg/sec)
		0.35895	0.10839	2.7555	1.49450

Table 4.21: Maximum and Mean Attitude and Bias Estimation Results –
Phase III with Turbulence

From the Phase III simulation performed with turbulence injections, the attitude estimates for both the longitudinal and transverse maximum attitude of the vehicle stay within a ±0.360 degree of error, while Figures 4.72 and 4.73 show a maximum bias error of ±0.2.760 degrees per second as displayed and summarized in Table 4.21.

Additionally, plots of the pitch and roll rate bias estimation errors are provided for an assessment of the ±1σ and ±3σ bounds on the rate gyro. Figure 4.74 demonstrates how the extended Kalman filter provides accurate and well behaved pitch and roll bias estimation errors bounded by the rate gyro signal. While the maximum bias errors for both pitch and roll rate bias values lie outside the ±3σ bounds, the error is very minimal over the time period and as the simulation time increases, shows excellent convergence within the imposed rate gyro signal bounds at a simulation time exceeding ten seconds.

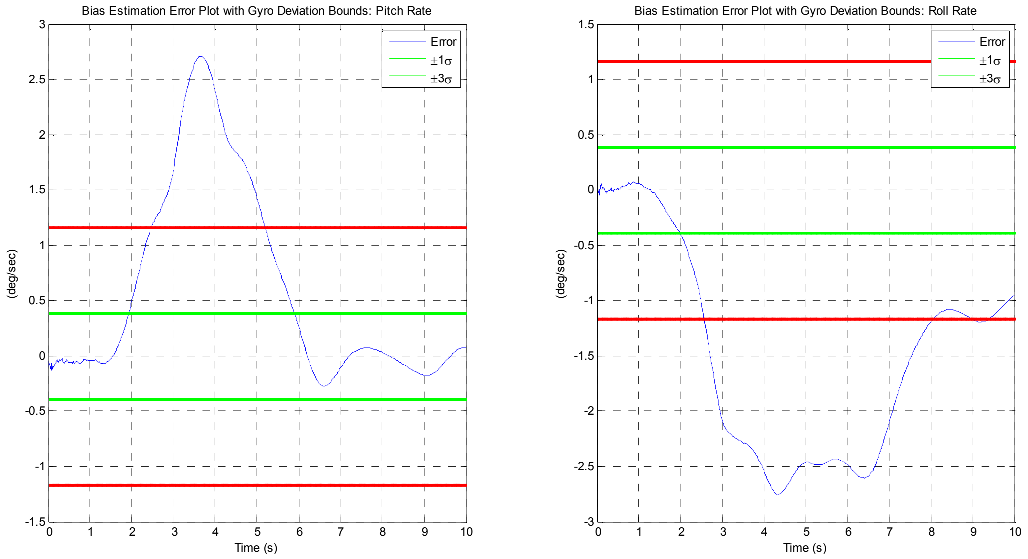
Bias Estimation Error Plot with Gyro Deviation Bounds: Pitch Rate

Bias Estimation Error Plot with Gyro Deviation Bounds: Roll Rate

Figure 4.74: Nonlinear EKF Bias Estimation Error with Bounds – Phase III with Turbulence

The maximum bias error is acceptable due to the error remaining in the ±1σ and ±3σ bounds of ± 0.3873 degrees per second and ± 1.1619 degrees per second imposed from the rate gyro noise variance as displayed in Figure 4.74. Staying within these statistical bounds is essential because 99.7% of a normally distributed value lies within the ±3σ bounds and 68.3% within the ±1σ bounds [41]. Therefore, the extended Kalman filter rate gyro bias estimation and attitude determination algorithm implemented in Phase III of this study with severe turbulence injections proves to provide accurate and reliable attitude tracking results and rate gyro bias estimations in real-time.

The check for correct filter operation in this Phase III, turbulent, portion of the feasibility study is conducted by comparing the attitude tracking and rate gyro bias estimation errors against the ±1σ and ±3σ values taken from the diagonal elements of the extended Kalman filter's covariance matrix, P. Figures 4.75 and 4.76 demonstrate a properly operating extended Kalman filter due to the attitude and bias estimation errors versus variance operating within the ±1σ and ±3σ bounds established by the covariance matrix of the EKF. While the roll rate bias error covariance verification does not fall within the ±3σ bounds at the end of the simulation period, if the simulation period is expanded to 50 seconds, the roll rate bias error does converge within the ±1σ and ±3σ bounds to validate proper filter operation as shown in Figure 4.77.

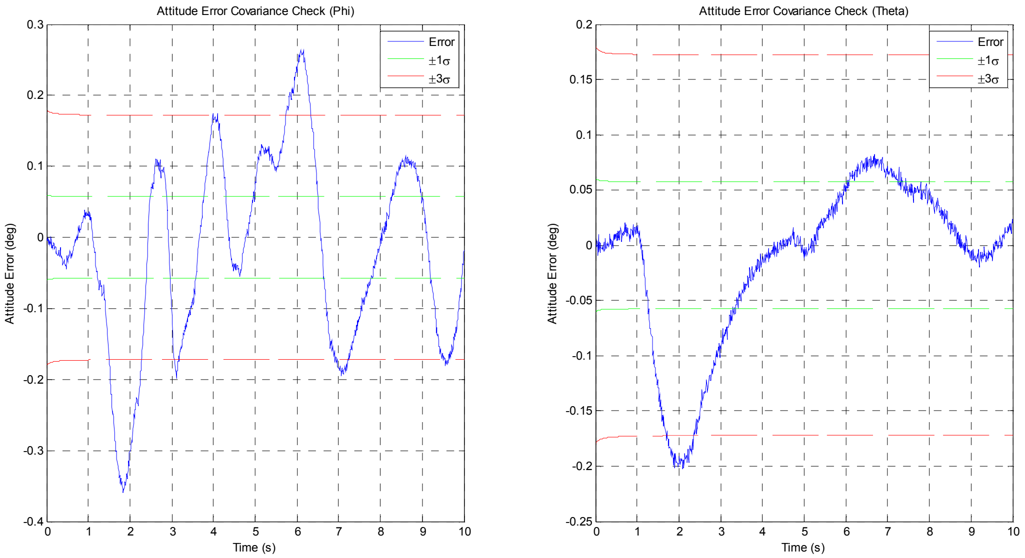

Figure 4.75: Nonlinear Attitude Error Covariance Check – Phase III with Turbulence

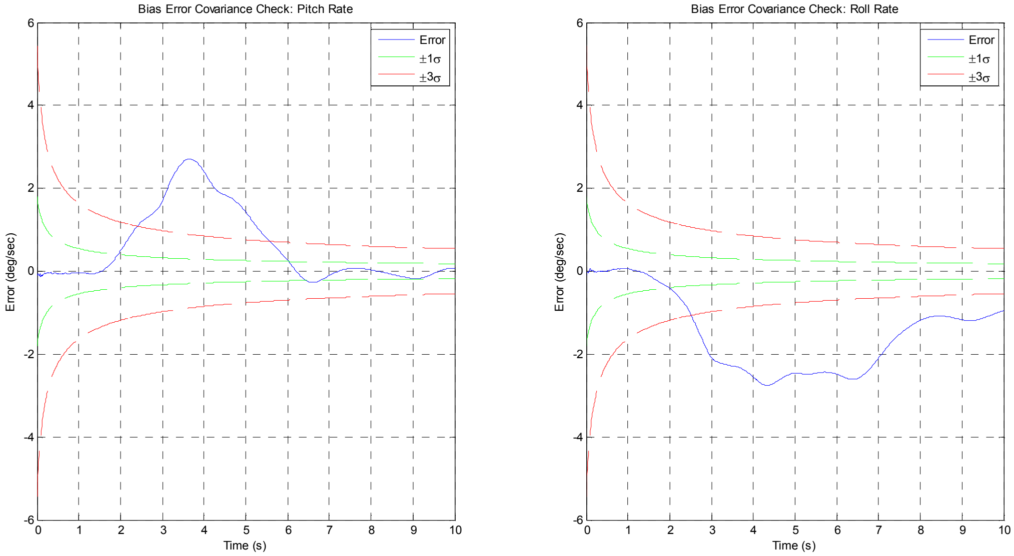

Figure 4.76: Nonlinear Bias Error Covariance Check – Phase III with Turbulence

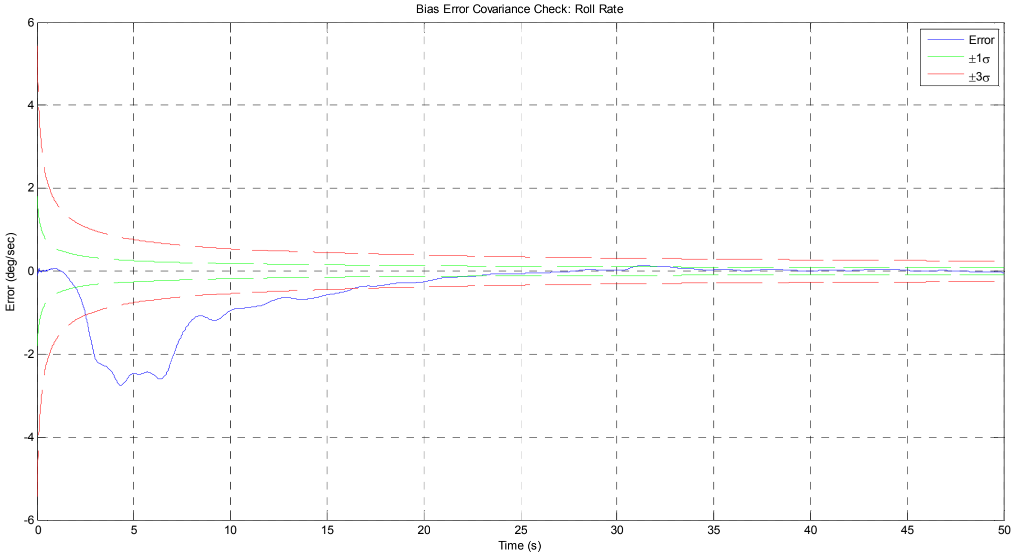

Figure 4.77: Nonlinear Bias Error Covariance Check – Phase III Simulation Period Expanded to 50 seconds with Turbulence

Utilizing the EKF parameters given previously in Table 4.7, the rate gyro bias magnitude was varied between values of 0.2 and 10 degrees/second while the rate gyro bias slope was varied between values of 0 and 1 degree/second/hour in order examine and assess the sensitivity of the extended Kalman filter implemented to changes in rate gyro bias magnitude and slope. The results of the Phase III assessment are summarized in Tables 4.22 through 4.25 given below.

Impact of Changing Rate Gyro Bias Magnitude with a Constant Slope					
Phase III: Longitudinal/Transverse Maneuver No Turbulence					
Rate Gyro Bias Slope (deg/sec/hr)	Bias (deg/sec)	θ Max Absolute Error (deg)	θ Mean Absolute Error (deg)	Max Bias Absolute Error (deg/sec)	Mean Bias Absolute Error (deg/sec)
0.0	0.2	0.20602	0.04766	1.92030	0.47860
	1	0.20860	0.04862	1.73770	0.52047
	3	0.21506	0.05169	2.90000	0.72035
	5	0.22152	0.05487	4.90000	1.00560
	10	0.23767	0.06318	9.90000	1.98420
0.5	0.2	0.20602	0.04766	1.92050	0.47853
	1	0.20860	0.04862	1.73790	0.52037
	3	0.21507	0.05169	2.90000	0.72018
	5	0.22153	0.05487	4.90000	1.00540
	10	0.23768	0.06318	9.90000	1.98390
1.0	0.2	0.20602	0.04766	1.92070	0.47846
	1	0.20861	0.02086	1.73810	0.52027
	3	0.21507	0.05169	2.90000	0.72000
	5	0.22153	0.05487	4.90000	1.00520
	10	0.23768	0.06318	9.90000	1.98360
Phase III: Longitudinal/Transverse Maneuver with Turbulence					
Rate Gyro Bias Slope (deg/sec/hr)	Bias (deg/sec)	θ Max Absolute Error (deg)	θ Mean Absolute Error (deg)	Max Bias Absolute Error (deg/sec)	Mean Bias Absolute Error (deg/sec)
0.0	0.2	0.20238	0.050223	2.71030	0.68214
	1	0.20274	0.05029	2.68900	0.69591
	3	0.20365	0.05058	2.90000	0.73362
	5	0.20456	0.05097	4.90000	0.77527
	10	0.20684	0.05219	9.90000	0.89432
0.5	0.2	0.20238	0.05022	2.71060	0.68219
	1	0.20274	0.05029	2.68920	0.69595
	3	0.20365	0.05058	2.90000	0.73362
	5	0.20456	0.05097	4.90000	0.77523
	10	0.20684	0.05219	9.90000	0.89421
1.0	0.2	0.20238	0.05022	2.71080	0.68225
	1	0.20274	0.05029	2.68950	0.69599
	3	0.20365	0.05058	2.90000	0.73363
	5	0.20456	0.05097	4.90000	0.77518
	10	0.20684	0.05219	9.90000	0.89409

Table 4.22: Sensitivity of Extended Kalman Filter to Changes in Rate Gyro Bias Magnitude with Constant Rate Gyro Slope – Phase III Pitch Attitude and Bias Summary

Impact of Changing Rate Gyro Bias Magnitude with a Constant Slope					
Phase III: Longitudinal/Transverse Maneuver No Turbulence					
Rate Gyro Bias Slope (deg/sec/hr)	Bias (deg/sec)	ϕ Max Absolute Error (deg)	ϕ Mean Absolute Error (deg)	Max Bias Absolute Error (deg/sec)	Mean Bias Absolute Error (deg/sec)
0.0	0.2	0.25716	0.06274	2.29640	1.20530
	1	0.26017	0.06344	2.42260	1.39740
	3	0.26770	0.06576	2.90000	1.87760
	5	0.27523	0.06822	4.90000	2.35780
	10	0.29407	0.07477	9.90000	3.55830
0.5	0.2	0.25716	0.06274	2.29610	1.20500
	1	0.26017	0.06344	2.42230	1.39710
	3	0.26770	0.06576	2.90000	1.87730
	5	0.27523	0.06822	4.90000	2.35750
	10	0.29407	0.07478	9.90000	3.55800
1.0	0.2	0.25716	0.06274	2.29580	1.20470
	1	0.26017	0.06344	2.42200	1.39680
	3	0.26770	0.06576	2.90000	1.87700
	5	0.27524	0.06822	4.90000	2.35720
	10	0.29407	0.07478	9.90000	3.55770
Phase III: Longitudinal/Transverse Maneuver with Turbulence					
Rate Gyro Bias Slope (deg/sec/hr)	Bias (deg/sec)	ϕ Max Absolute Error (deg)	ϕ Mean Absolute Error (deg)	Max Bias Absolute Error (deg/sec)	Mean Bias Absolute Error (deg/sec)
0.0	0.2	0.35895	0.10839	2.75550	1.49460
	1	0.35936	0.10858	2.77360	1.52480
	3	0.36040	0.10905	2.90000	1.61800
	5	0.36144	0.10953	4.90000	1.71130
	10	0.36404	0.11075	9.90000	1.94440
0.5	0.2	0.35895	0.10839	2.75520	1.49420
	1	0.35937	0.10858	2.77330	1.52450
	3	0.36040	0.10905	2.90000	1.61770
	5	0.36144	0.10953	4.90000	1.71090
	10	0.36404	0.11075	9.90000	1.94400
1.0	0.2	0.35895	0.10839	2.75490	1.49390
	1	0.35937	0.10858	2.77300	1.52410
	3	0.36040	0.10905	2.90000	1.61740
	5	0.36144	0.10953	4.90000	1.71060
	10	0.36404	0.11075	9.90000	1.94370

Table 4.23: Sensitivity of Extended Kalman Filter to Changes in Rate Gyro Bias Magnitude with Constant Rate Gyro Slope – Phase III Roll Attitude and Bias Summary

Tables 4.22 and 4.23 assessed the sensitivity of the extended Kalman filter to changes in the rate gyro bias magnitude while maintaining a constant rate gyro bias slope. Tables 4.24 and 4.25 display a summary of attitude determination and bias estimation results for sensitivity of the extended Kalman filter to changes in the rate gyro bias slope while maintaining a constant rate gyro bias magnitude for Phase III of the feasibility study conducted.

Impact of Changing Rate Gyro Bias Slope with Constant Bias Magnitude					
Phase III: Longitudinal/Transverse Maneuver No Turbulence					
Rate Gyro Bias (deg/sec)	Rate Gyro Bias Slope (deg/sec/hr)	θ Max Absolute Error (deg)	θ Mean Absolute Error (deg)	Max Bias Absolute Error (deg/sec)	Mean Bias Absolute Error (deg/sec)
0.2	0.0	0.20602	0.04766	1.92030	0.47860
	0.5	0.20602	0.04766	1.92050	0.47853
	1.0	0.20602	0.04766	1.92070	0.47846
1	0.0	0.20860	0.04862	1.73770	0.52047
	0.5	0.20860	0.04862	1.73790	0.52037
	1.0	0.20861	0.04862	1.73810	0.52027
3	0.0	0.21506	0.05169	2.90000	0.72035
	0.5	0.21507	0.05169	2.90000	0.72018
	1.0	0.21507	0.05169	2.90000	0.72000
5	0.0	0.22152	0.05487	4.90000	1.00560
	0.5	0.22153	0.05487	4.90000	1.00540
	1.0	0.22153	0.05487	4.90000	1.00520
10	0.0	0.23767	0.06318	9.90000	1.98420
	0.5	0.23768	0.06318	9.90000	1.98390
	1.0	0.23768	0.06318	9.90000	1.98360
Phase III: Longitudinal/Transverse Maneuver with Turbulence					
Rate Gyro Bias (deg/sec)	Rate Gyro Bias Slope (deg/sec/hr)	θ Max Absolute Error (deg)	θ Mean Absolute Error (deg)	Max Bias Absolute Error (deg/sec)	Mean Bias Absolute Error (deg/sec)
0.2	0.0	0.20238	0.05023	2.71030	0.68214
	0.5	0.20238	0.05022	2.71060	0.68219
	1.0	0.20238	0.05022	2.71080	0.68225
1	0.0	0.20274	0.05029	2.68900	0.69591
	0.5	0.20274	0.05029	2.68920	0.69595
	1.0	0.20274	0.05029	2.68950	0.69599
3	0.0	0.20365	0.05058	2.90000	0.73362
	0.5	0.20365	0.05058	2.90000	0.73362
	1.0	0.20365	0.05058	2.90000	0.73363
5	0.0	0.20456	0.05097	4.90000	0.77527
	0.5	0.20456	0.05097	4.90000	0.77523
	1.0	0.20456	0.05097	4.90000	0.77518
10	0.0	0.20684	0.05219	9.90000	0.89432
	0.5	0.20684	0.05219	9.90000	0.89421
	1.0	0.20684	0.05219	9.90000	0.89409

Table 4.24: Sensitivity of Extended Kalman Filter to Change in Rate Gyro Bias Slope with Constant Rate Gyro Bias Magnitude – Phase III Pitch Attitude and Bias Summary

Impact of Changing Rate Gyro Bias Slope with Constant Bias Magnitude					
Phase III: Longitudinal/Transverse Maneuver No Turbulence					
Rate Gyro Bias (deg/sec)	Rate Gyro Bias Slope (deg/sec/hr)	ϕ Max Absolute Error (deg)	ϕ Mean Absolute Error (deg)	Max Bias Absolute Error (deg/sec)	Mean Bias Absolute Error (deg/sec)
0.2	0.0	0.25716	0.062739	2.29640	1.20530
	0.5	0.25716	0.062739	2.29610	1.20500
	1.0	0.25716	0.062739	2.29580	1.20470
1	0.0	0.26017	0.063441	2.42260	1.39740
	0.5	0.26017	0.063441	2.42230	1.39710
	1.0	0.26017	0.063441	2.42200	1.39680
3	0.0	0.26770	0.065760	2.90000	1.87760
	0.5	0.26770	0.065760	2.90000	1.87730
	1.0	0.26770	0.065761	2.90000	1.87700
5	0.0	0.27523	0.068216	4.90000	2.35780
	0.5	0.27523	0.068217	4.90000	2.35750
	1.0	0.27524	0.068218	4.90000	2.35720
10	0.0	0.29407	0.074774	9.90000	3.55830
	0.5	0.29407	0.074775	9.90000	3.55800
	1.0	0.29407	0.074776	9.90000	3.55770
Phase III: Longitudinal/Transverse Maneuver with Turbulence					
Rate Gyro Bias (deg/sec)	Rate Gyro Bias Slope (deg/sec/hr)	ϕ Max Absolute Error (deg)	ϕ Mean Absolute Error (deg)	Max Bias Absolute Error (deg/sec)	Mean Bias Absolute Error (deg/sec)
0.2	0.0	0.35895	0.10839	2.75550	1.49460
	0.5	0.35895	0.10839	2.75520	1.49420
	1.0	0.35895	0.10839	2.75490	1.49390
1	0.0	0.35936	0.10858	2.77360	1.52480
	0.5	0.35937	0.10858	2.77330	1.52450
	1.0	0.35937	0.10858	2.77300	1.52410
3	0.0	0.36040	0.10905	2.90000	1.61800
	0.5	0.36040	0.10905	2.90000	1.61770
	1.0	0.36040	0.10905	2.90000	1.61740
5	0.0	0.36144	0.10953	4.90000	1.71130
	0.5	0.36144	0.10953	4.90000	1.71090
	1.0	0.36144	0.10953	4.90000	1.71060
10	0.0	0.36404	0.11075	9.90000	1.94440
	0.5	0.36404	0.11075	9.90000	1.94400
	1.0	0.36404	0.11075	9.90000	1.94370

Table 4.25: Sensitivity of Extended Kalman Filter to Change in Rate Gyro Bias Slope with Constant Rate Gyro Bias Magnitude – Phase III Roll Attitude and Bias Summary

The results of the Phase III study conducted show bias magnitude again has little to negligible effect on the attitude estimation of the EKF and noticeable effect on the bias estimate as the bias magnitude imposed increases just as was shown in the previous two phases of the study conducted. From the simulations performed, the results show that varying the bias magnitude has more effect on attitude and bias estimation results as compared to varying the rate gyro bias slope. For the Phase III simulation study utilizing a combined aircraft maneuver, the bias estimate is reasonable and the attitude estimate does not drift outside of the acceptable range of ±1 degree based on instrumentation from [49]. The inaccuracies of the algorithm method implemented are a result from accelerometer and rate gyro measurement noises and severe turbulence effects causing a highly dynamical operating environment.

4.4 Comparative Analysis of Algorithm Operation with Sensor Noise Affects

4.4.1 Comparison of Algorithm Operation with Sensor Noise Affects: Part I

The validation of the algorithm concept and operation implemented in this feasibility study for two-dimensional attitude determination and rate gyro bias estimation requires a comparative analysis of the method and noise parameters employed in this feasibility study against sensor noise parameters of similar works and studies. The sensor noise values in [50] were simulated and implemented in the nonlinear aircraft simulation model utilized in this feasibility study with the use of the extended Kalman filter algorithm from Section 4.3. Table 4.26 compares the noise parameters instituted in this study against the noise parameters in [50], where the sensor noise parameters were chosen based on manufacturer specifications and experimental data. The rate gyro bias magnitude remained at 0.200 degrees/second for this analysis since the algorithm implemented previously in Section 4.3 showed negligible variations in output errors over the simulation intervals due to changes in the magnitude of the rate gyro bias.

Sensor	**Previous Simulation Values (Standard Deviation)**	**Alternative Sensor Values (Standard Deviation)**
Accelerometer (gees)	0.00387	2.0387×10^{-4}
Rate Gyroscope (degrees/second)	0.387	0.03

Table 4.26: Previous Sensor Noise Parameters versus Alternative Sensor Noise Parameters [50]

Utilizing the values published and shown in Table 4.26 in the nonlinear aircraft simulation for Phase I of the feasibility study with the extended Kalman filter algorithm parameters used previously, the attitude and rate gyro bias estimation results are shown in Figures 4.78 and 4.79 respectively for both the longitudinal and transverse accelerometer array measurements.

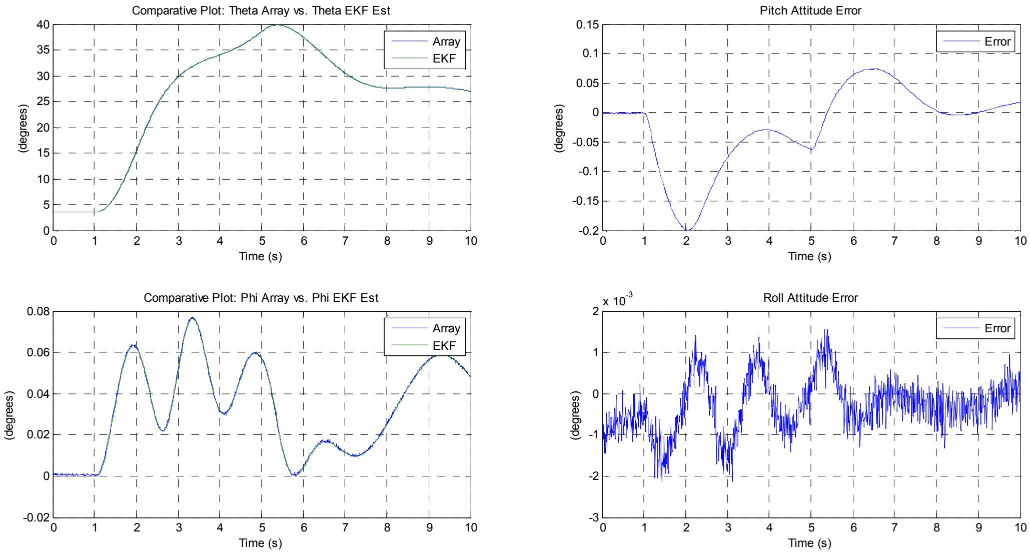

Figure 4.78: Phase I Non-Turbulent Attitude Estimation Results using Alternative Sensor Noise Values

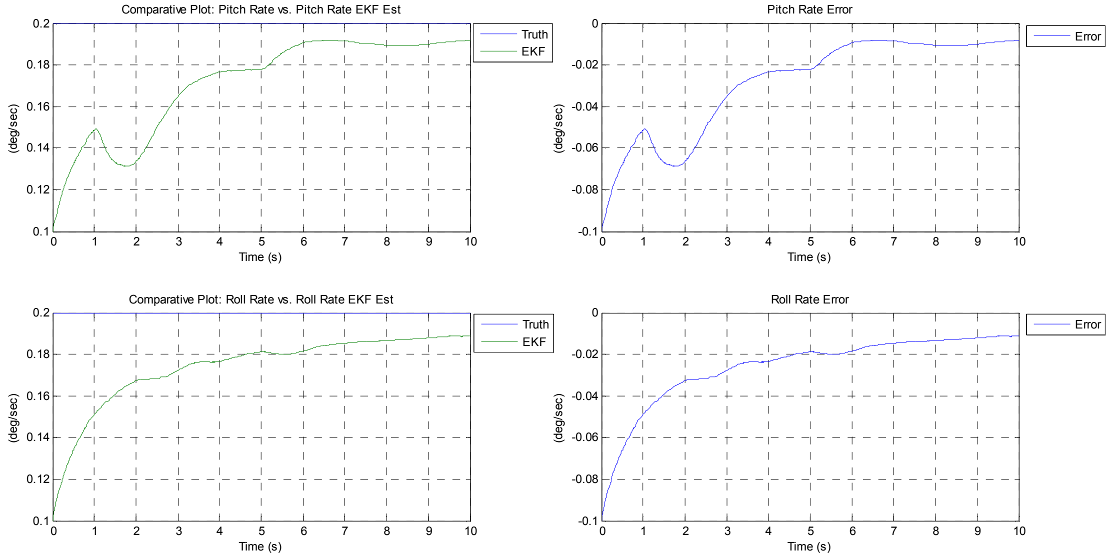

Figure 4.79: Phase I Non-Turbulent Bias Estimation Results using Alternative Sensor Noise Values

As shown in Figures 4.78 and 4.79, the attitude and rate gyro bias estimation results produced by the extended Kalman filter algorithm utilizing the alternative sensor noise parameters from [50] in the nonlinear aircraft simulation model results in relatively minimal errors for a Phase I, longitudinal maneuver without turbulence injections where the results are summarized in Table 4.27 below.

Phase I Maximum and Mean Error Results for Alternative Sensor Noise Parameters					
Rate Gyro Bias (deg/sec)	**Rate Gyro Slope (deg/sec/hr)**	**Phase I – Longitudinal Maneuver with No Turbulence**			
0.20	0.05	θ Max Absolute Error (deg)	θ Mean Absolute Error (deg)	Max Bias Absolute Error (deg/sec)	Mean Bias Absolute Error (deg/sec)
		0.19946	0.04979	0.10000	0.02882
		ϕ Max Absolute Error (deg)	ϕ Mean Absolute Error (deg)	Max Bias Absolute Error (deg/sec)	Mean Bias Absolute Error (deg/sec)
		0.00214	0.00058	0.10000	0.02589

Table 4.27: Attitude and Rate Gyro Bias Estimation Errors for Phase I Simulation with Alternative Sensor Noise Parameters

The EKF parameters were checked to ensure proper filter operation and convergence for the nonlinear simulation model utilizing the alternative sensor noise values. Figures 4.80 and 4.81 demonstrate a properly operating extended Kalman filter due to the attitude and bias estimation errors versus variance operating within the ±1σ and ±3σ bounds established by the covariance matrix of the EKF.

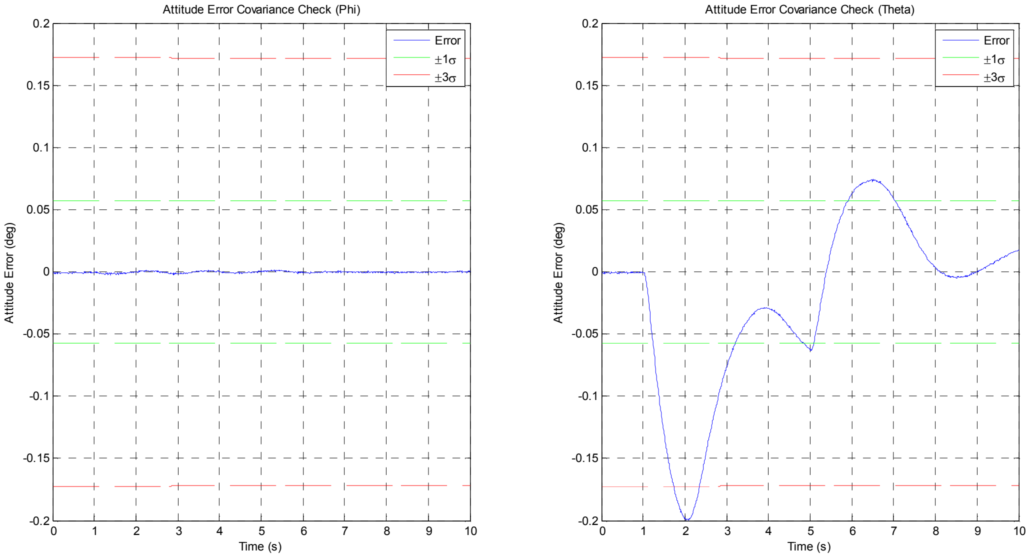

Figure 4.80: Phase I Non-Turbulent Attitude Error Covariance Check using Alternative Sensor Noise Values

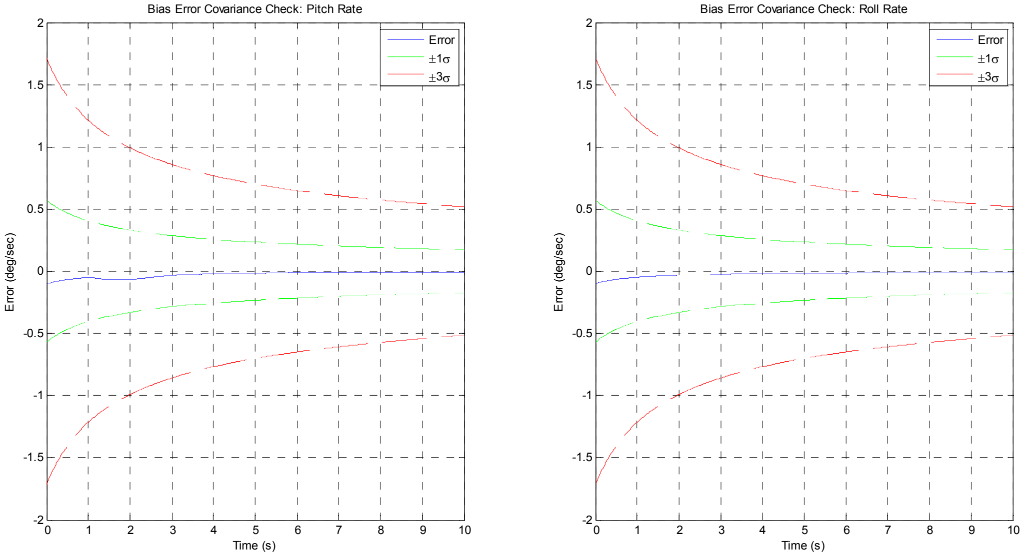

Figure 4.81: Phase I Non-Turbulent Bias Error Covariance Check with Alternative Sensor Noise Values

From Figures 4.80 and 4.81, the extended Kalman filter is shown to converge during on-line operation within the ±1σ and ±3σ bounds while utilizing the alternative sensor noise values from [50]. While the simulations conducted in this feasibility study and [50] differ, the results published in [50] address both maximum pitch and roll maneuvers of ±20 degrees with minimal pitch and roll rates. These low angular rates of the simulated maneuvers in [50] result in negligible imposed translational loads. While each phase of the simulation study was completed for the analysis of the proposed algorithm implemented in this feasibility study against the published noise parameter values, the plots were omitted in this section and are presented in Appendix F.1 for completeness.

However, Tables 4.28 and 4.29 below present a summary of the maximum and mean attitude and bias errors experienced during each phase of the study conducted utilizing the alternative sensor noise values from [50] for turbulent and non-turbulent simulations. The rate gyro bias magnitude and slope were maintained at 0.200 degrees/second and 0.05 degrees/second/hour for each simulation performed.

Maximum and Mean Attitude and Rate Gyro Bias Estimation Errors Using Sensor Noise Values: Non-Turbulent Simulations			
Phase I – Longitudinal Maneuver			
θ Max Absolute Error (deg)	θ Mean Absolute Error (deg)	ϕ Max Absolute Error (deg)	ϕ Mean Absolute Error (deg)
0.19946	0.04979	0.00214	0.00058
Max Pitch Rate Bias Absolute Error (deg/sec)	Mean Pitch Rate Bias Absolute Error (deg/sec)	Max Roll Rate Bias Absolute Error (deg/sec)	Mean Roll Rate Bias Absolute Error (deg/sec)
0.10000	0.02882	0.10000	0.02589
Phase II – Transverse Maneuver			
θ Max Absolute Error (deg)	θ Mean Absolute Error (deg)	ϕ Max Absolute Error (deg)	ϕ Mean Absolute Error (deg)
0.01106	0.00209	0.40175	0.13078
Max Pitch Rate Bias Absolute Error (deg/sec)	Mean Pitch Rate Bias Absolute Error (deg/sec)	Max Roll Rate Bias Absolute Error (deg/sec)	Mean Roll Rate Bias Absolute Error (deg/sec)
1.78530	0.34385	0.11861	0.06126
Phase III – Longitudinal/Transverse Maneuver			
θ Max Absolute Error (deg)	θ Mean Absolute Error (deg)	ϕ Max Absolute Error (deg)	ϕ Mean Absolute Error (deg)
0.19957	0.04731	0.25357	0.06218
Max Pitch Rate Bias Absolute Error (deg/sec)	Mean Pitch Rate Bias Absolute Error (deg/sec)	Max Roll Rate Bias Absolute Error (deg/sec)	Mean Roll Rate Bias Absolute Error (deg/sec)
1.92500	0.47929	2.30680	1.21280

Table 4.28: Non-Turbulent Maximum and Mean Error Values Using Alternative Sensor Values

From the simulations conducted utilizing the alternative sensor noise values for non-turbulent aircraft simulation maneuvers, the maximum longitudinal attitude errors experienced were less than ±0.200 degrees, while the maximum transverse attitude errors experienced were less than ± 0.410 degrees. The maximum pitch rate bias errors experienced during the non-turbulent simulations performed were less than ±1.950 degrees/second, while the maximum roll rate bias errors experienced during the non-turbulent simulations were less than ±2.310 degrees/second.

Maximum and Mean Attitude and Rate Gyro Bias Estimation Errors Using Sensor Noise Values: Turbulent Simulations			
Phase I – Longitudinal Maneuver			
θ Max Absolute Error (deg)	θ Mean Absolute Error (deg)	ϕ Max Absolute Error (deg)	ϕ Mean Absolute Error (deg)
0.19814	0.053995	0.23885	0.09505
Max Pitch Rate Bias Absolute Error (deg/sec)	Mean Pitch Rate Bias Absolute Error (deg/sec)	Max Roll Rate Bias Absolute Error (deg/sec)	Mean Roll Rate Bias Absolute Error (deg/sec)
0.10000	0.02570	0.59536	0.14007
Phase II – Transverse Maneuver			
θ Max Absolute Error (deg)	θ Mean Absolute Error (deg)	ϕ Max Absolute Error (deg)	ϕ Mean Absolute Error (deg)
0.04001	0.01630	0.45703	0.19918
Max Pitch Rate Bias Absolute Error (deg/sec)	Mean Pitch Rate Bias Absolute Error (deg/sec)	Max Roll Rate Bias Absolute Error (deg/sec)	Mean Roll Rate Bias Absolute Error (deg/sec)
2.20370	0.47702	0.18550	0.05799
Phase III – Longitudinal/Transverse Maneuver			
θ Max Absolute Error (deg)	θ Mean Absolute Error (deg)	ϕ Max Absolute Error (deg)	ϕ Mean Absolute Error (deg)
0.19574	0.04998	0.35537	0.10838
Max Pitch Rate Bias Absolute Error (deg/sec)	Mean Pitch Rate Bias Absolute Error (deg/sec)	Max Roll Rate Bias Absolute Error (deg/sec)	Mean Roll Rate Bias Absolute Error (deg/sec)
2.72330	0.68101	2.77480	1.50240

Table 4.29: Turbulent Maximum and Mean Error Values Using Alternative Sensor Values

From the simulations conducted utilizing the alternative sensor noise values for turbulent aircraft simulation maneuvers, the maximum longitudinal attitude errors experienced were less than ±0.200 degrees, while the maximum transverse attitude errors experienced were less than ± 0.460 degrees. The maximum pitch rate bias errors experienced during the turbulent simulations performed were less than ±2.730 degrees/second, while the maximum roll rate bias errors experienced during the turbulent aircraft simulations were less than ±2.780 degrees/second. From the simulation performed, the bias estimates produced are reasonable and the longitudinal and transverse attitude estimates do not drift outside of the acceptable range of ±1 degrees based on instrumentation from [49].

The derived and implemented algorithm method utilized in this feasibility study has already proven to provide very accurate attitude tracking results and estimates of the rate gyro biases as shown in the figures and tables provided in the previous sections. The algorithm method proposed in this work addresses the problem of accurate and reliable two-dimensional attitude and rate gyro bias estimation during dynamic aircraft simulation maneuvers subjected to large imposed acceleration loading and harsh environmental conditions. Therefore, it may be said that the algorithm utilized in this study would possess similar if not improved two-dimensional attitude and rate gyro bias estimation results when subjected to a low or negligible imposed loading and dynamical operating environments.

4.4.2 Comparison of Algorithm Operation with Sensor Noise Affects: Part II

In Section 4.4.1, the algorithm method developed and implemented in this feasibility study was assessed directly utilizing alternative sensor noise parameter values from [50]. The results found from the study completed in the previous section of this work showed accurate attitude tracking and rate gyro bias estimation results while using the alternative sensor noise values in conjunction with the extended Kalman filter algorithm developed.

While the study in Section 4.4.1 represented a direct implementation of the noise values utilized in [50], the work completed in this Part II analysis will analyze the impact of utilizing similar alternative sensor noise values from [51] while varying the magnitude of the noise inputs to the nonlinear operating system and algorithm method developed. Tables 4.30, 4.31, and 4.32 compare the sensor noise parameter values instituted in this study previously and the alternative sensor noise values similar to those utilized [51]. The rate gyro bias magnitude remained at 0.200 degrees/second for this analysis since the algorithm implemented previously in Section 4.3 showed negligible variations in output errors over the simulation intervals due to changes in the rate gyro bias magnitude.

Sensor	**Previous Simulation Values (Standard Deviation)**	**Alternative Sensor Values: ADXRS450 ±300 degree/second Rate Gyro (Standard Deviation)**
Rate Gyroscope (degrees/second)	0.3873	0.1407

Table 4.30: Previous Gyro Noise Parameters versus Alternative Gyro Noise Parameters

Sensor	**Previous Simulation Values (Standard Deviation)**	**Alternative Sensor Values: ADXL326 ±16 gee Accelerometer (Standard Deviation)**
Accelerometer (gees)	0.00387	0.00155

Table 4.31: Previous Accelerometer Noise Parameters versus Alternative Accelerometer Noise Parameters

Variation of Alternative Sensor Noise Values for Simulation			
Sensor	**Study A**	**Study B**	**Study C**
	σ	2σ	3σ
ADXRS450: Rate Gyro	0.1407	0.2814	0.4421
ADXL326: Accelerometer	0.00155	0.00310	0.00465

Table 4.32: Variation of Alternative Sensor Noise Parameter Magnitudes for Simulation

Implementing the values published for the accelerometer and rate gyro presented in Table 4.32, Studies A, B, and C were conducted using the nonlinear aircraft simulation model for Phase I of the feasibility study utilizing the extended Kalman filter algorithm method developed previously for accurate and reliable two-dimensional attitude determination and rate gyro bias estimation. Figures 4.82 and 4.83 represent the longitudinal and transverse attitude and bias estimation results respectively for Study A of the employed alternative noise parameter values as given in Table 4.32.

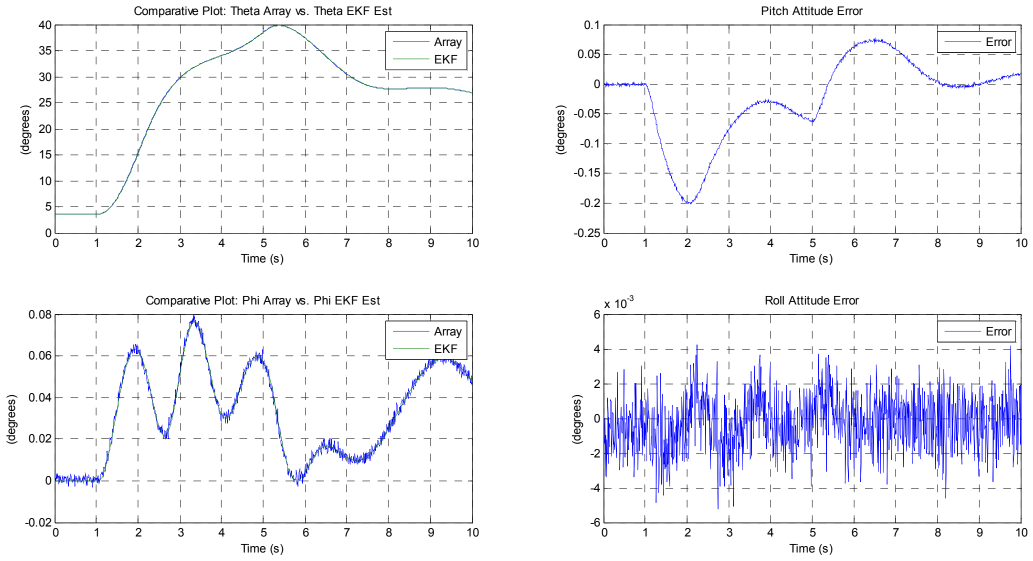
Comparative Plot: Theta Array vs. Theta EKF Est

Pitch Attitude Error

Comparative Plot: Phi Array vs. Phi EKF Est

Roll Attitude Error

Figure 4.82: Phase I - Study A Non-Turbulent Attitude Estimation Results using Alternative Sensor Noise Values

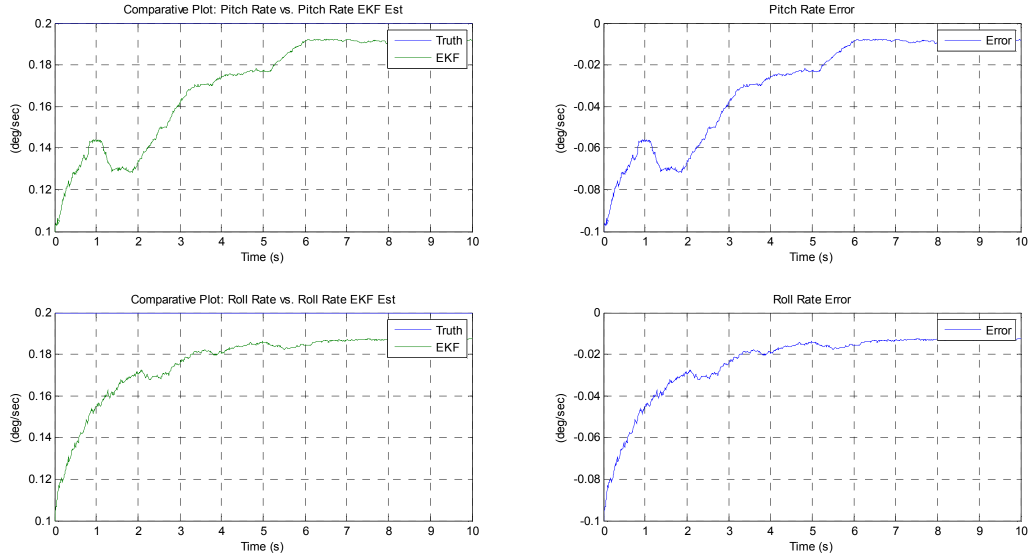
Comparative Plot: Pitch Rate vs. Pitch Rate EKF Est

Pitch Rate Error

Comparative Plot: Roll Rate vs. Roll Rate EKF Est

Roll Rate Error

Figure 4.83: Phase I - Study A Non-Turbulent Bias Estimation Results using Alternative Sensor Noise Values

As shown in Figures 4.82 and 4.83, the attitude and rate gyro bias estimation results produced by the extended Kalman filter algorithm utilizing the alternative sensor noise parameters similar to [51] and presented in Table 4.32, produce relatively minimal errors for a Phase I - Study A, longitudinal maneuver without turbulence injections and are summarized in Table 4.33 below.

Phase I-Study A Maximum and Mean Error Results for Alternative Sensor Noise Parameters					
Rate Gyro Bias (deg/sec)	**Rate Gyro Slope (deg/sec/hr)**	**Phase I – Longitudinal Maneuver with No Turbulence**			
0.20	0.05	θ Max Absolute Error (deg)	θ Mean Absolute Error (deg)	Max Bias Absolute Error (deg/sec)	Mean Bias Absolute Error (deg/sec)
		0.20150	0.04985	0.10000	0.03013
		ϕ Max Absolute Error (deg)	ϕ Mean Absolute Error (deg)	Max Bias Absolute Error (deg/sec)	Mean Bias Absolute Error (deg/sec)
		0.00526	0.00129	0.10000	0.02357

Table 4.33: Attitude and Rate Gyro Bias Estimation Errors for Phase I - Study A Simulation with Alternative Sensor Noise Parameters

The EKF parameters were checked to ensure proper filter operation and convergence for the nonlinear simulation model utilizing the alternative sensor noise values. Figures 4.84 and 4.85 demonstrate a properly operating extended Kalman filter due to the attitude and bias estimation errors versus variance operating within the ±1σ and ±3σ bounds established by the covariance matrix of the EKF.

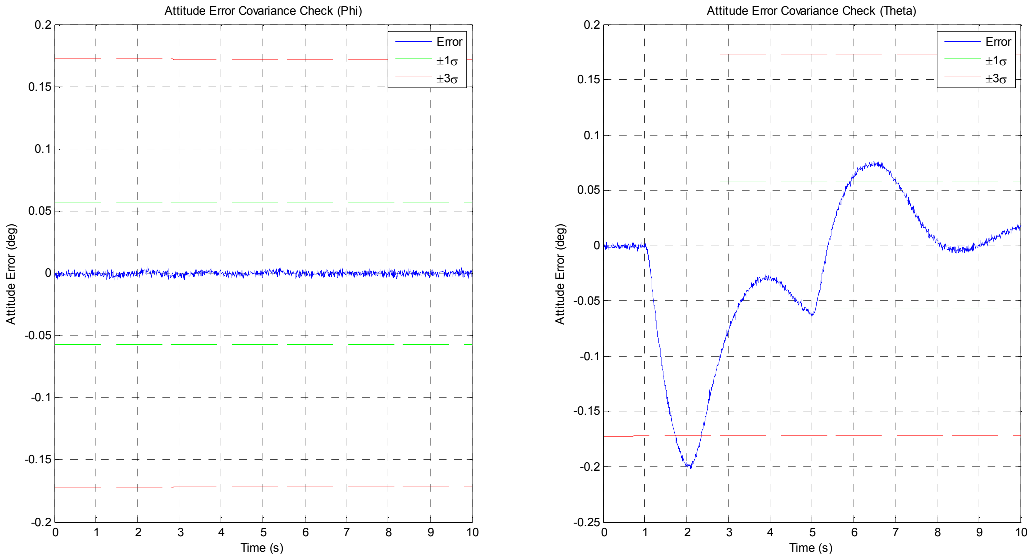

Figure 4.84: Phase I - Study A Non-Turbulent Attitude Error Covariance Check using Alternative Sensor Noise Values

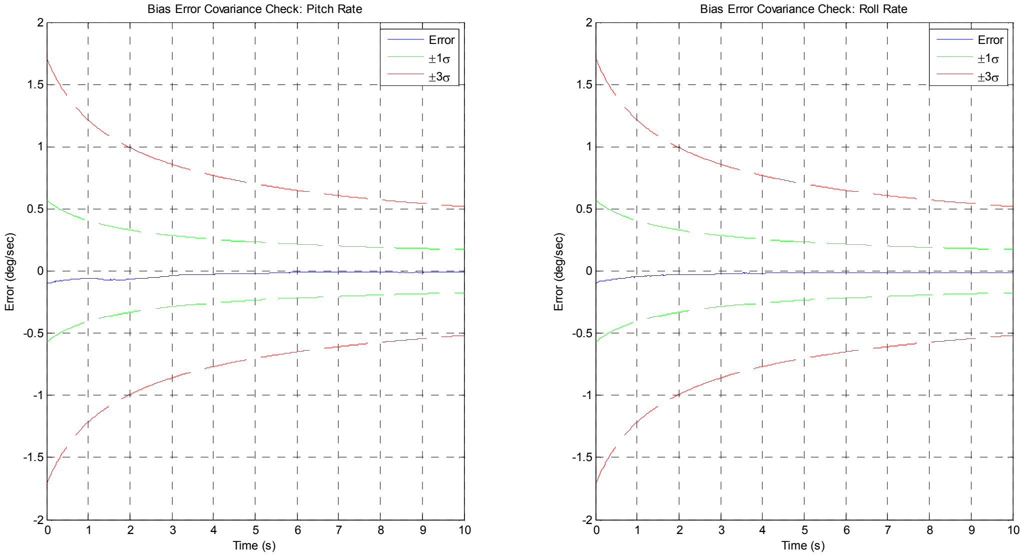

Figure 4.85: Phase I-Study A Non-Turbulent Bias Error Covariance Check using Alternative Sensor Noise Values

From Figures 4.84 and 4.85, the extended Kalman filter is shown to converge during on-line operation within the ±1σ and ±3σ bounds while utilizing the alternative sensor noise values similar to [51] and presented in Table 4.32. While the simulations conducted in this feasibility study and [51] differ, the results published in [51] address maximum roll maneuvers of 20 degrees with minimal angular rotational rates while utilizing low-cost, low power consumption, consumer off the shelf (COTS) sensors. The low angular rates of the simulated maneuvers in [51] result in negligible imposed translational loads. While each phase of the simulation study was completed for the analysis of the proposed algorithm implemented in this feasibility study against the published noise parameter values for Studies A, B, and C, the plots were omitted in this section for brevity and are presented in Appendix F.2 for completeness.

However, Tables 4.34, 4.35, and 4.36 below present a summary of the maximum and mean absolute attitude and bias errors experienced during each phase of Study A, Study B, and Study C conducted utilizing the alternative sensor noise values from Table 4.32 for turbulent and non-turbulent simulations. The rate gyro bias magnitude and slope were maintained at 0.200 degrees/second and 0.05 degrees/second/hour for each simulation performed.

From the simulations conducted utilizing the alternative sensor noise values in Table 4.32 for both non-turbulent and turbulent aircraft simulation maneuvers, the maximum attitude errors experienced were less than ±0.465 degrees, while the maximum bias errors experienced during the simulations performed were less than ±2.800 degrees/second. From the simulation studies performed, the bias estimates produced are reasonable and the longitudinal and transverse attitude estimates do not drift outside of the acceptable range of ±1 degrees based on instrumentation from [49].

Maximum and Mean Attitude and Rate Gyro Bias Estimation Errors Using Sensor Noise Values: Non-Turbulent Simulations – Study A			
Phase I – Longitudinal Maneuver			
θ Max Absolute Error (deg)	θ Mean Absolute Error (deg)	ϕ Max Absolute Error (deg)	ϕ Mean Absolute Error (deg)
0.20150	0.04985	0.00526	0.00129
Max Pitch Rate Bias Absolute Error (deg/sec)	Mean Pitch Rate Bias Absolute Error (deg/sec)	Max Roll Rate Bias Absolute Error (deg/sec)	Mean Roll Rate Bias Absolute Error (deg/sec)
0.10000	0.03013	0.10000	0.02357
Phase II – Transverse Maneuver			
θ Max Absolute Error (deg)	θ Mean Absolute Error (deg)	ϕ Max Absolute Error (deg)	ϕ Mean Absolute Error (deg)
0.01351	0.00245	0.40356	0.13094
Max Pitch Rate Bias Absolute Error (deg/sec)	Mean Pitch Rate Bias Absolute Error (deg/sec)	Max Roll Rate Bias Absolute Error (deg/sec)	Mean Roll Rate Bias Absolute Error (deg/sec)
1.78400	0.34358	0.11756	0.05994
Phase III – Longitudinal/Transverse Maneuver			
θ Max Absolute Error (deg)	θ Mean Absolute Error (deg)	ϕ Max Absolute Error (deg)	ϕ Mean Absolute Error (deg)
0.20144	0.04736	0.25468	0.06229
Max Pitch Rate Bias Absolute Error (deg/sec)	Mean Pitch Rate Bias Absolute Error (deg/sec)	Max Roll Rate Bias Absolute Error (deg/sec)	Mean Roll Rate Bias Absolute Error (deg/sec)
1.92330	0.47907	2.30350	1.21050
Maximum and Mean Attitude and Rate Gyro Bias Estimation Errors Using Sensor Noise Values: Turbulent Simulations – Study A			
Phase I – Longitudinal Maneuver			
θ Max Absolute Error (deg)	θ Max Absolute Error (deg)	ϕ Max Absolute Error (deg)	ϕ Mean Absolute Error (deg)
0.20020	0.05403	0.23911	0.09501
Max Pitch Rate Bias Absolute Error (deg/sec)	Max Pitch Rate Bias Absolute Error (deg/sec)	Max Roll Rate Bias Absolute Error (deg/sec)	Max Roll Rate Bias Absolute Error (deg/sec)
0.10000	0.02786	0.59311	0.13898
Phase II – Transverse Maneuver			
θ Max Absolute Error (deg)	θ Max Absolute Error (deg)	ϕ Max Absolute Error (deg)	ϕ Mean Absolute Error (deg)
0.04264	0.01633	0.45905	0.19921
Max Pitch Rate Bias Absolute Error (deg/sec)	Max Pitch Rate Bias Absolute Error (deg/sec)	Max Roll Rate Bias Absolute Error (deg/sec)	Max Roll Rate Bias Absolute Error (deg/sec)
2.20130	0.47716	0.18271	0.05637
Phase III – Longitudinal/Transverse Maneuver			
θ Max Absolute Error (deg)	θ Max Absolute Error (deg)	ϕ Max Absolute Error (deg)	ϕ Mean Absolute Error (deg)
0.19779	0.04999	0.35648	0.10838
Max Pitch Rate Bias Absolute Error (deg/sec)	Max Pitch Rate Bias Absolute Error (deg/sec)	Max Roll Rate Bias Absolute Error (deg/sec)	Max Roll Rate Bias Absolute Error (deg/sec)
2.71930	0.68135	2.76870	1.49970

Table 4.34: Maximum and Mean Error Values Using Alternative Sensor Values – Study A

Maximum and Mean Attitude and Rate Gyro Bias Estimation Errors Using Sensor Noise Values: Non-Turbulent Simulations – Study B			
Phase I – Longitudinal Maneuver			
θ Max Absolute Error (deg)	θ Mean Absolute Error (deg)	ϕ Max Absolute Error (deg)	ϕ Mean Absolute Error (deg)
0.20411	0.05001	0.00976	0.00244
Max Pitch Rate Bias Absolute Error (deg/sec)	Mean Pitch Rate Bias Absolute Error (deg/sec)	Max Roll Rate Bias Absolute Error (deg/sec)	Mean Roll Rate Bias Absolute Error (deg/sec)
0.10066	0.03179	0.10000	0.02062
Phase II – Transverse Maneuver			
θ Max Absolute Error (deg)	θ Mean Absolute Error (deg)	ϕ Max Absolute Error (deg)	ϕ Mean Absolute Error (deg)
0.01748	0.00323	0.40586	0.13131
Max Pitch Rate Bias Absolute Error (deg/sec)	Mean Pitch Rate Bias Absolute Error (deg/sec)	Max Roll Rate Bias Absolute Error (deg/sec)	Mean Roll Rate Bias Absolute Error (deg/sec)
1.78250	0.34325	0.11767	0.05841
Phase III – Longitudinal/Transverse Maneuver			
θ Max Absolute Error (deg)	θ Mean Absolute Error (deg)	ϕ Max Absolute Error (deg)	ϕ Mean Absolute Error (deg)
0.20405	0.04751	0.25609	0.06253
Max Pitch Rate Bias Absolute Error (deg/sec)	Mean Pitch Rate Bias Absolute Error (deg/sec)	Max Roll Rate Bias Absolute Error (deg/sec)	Mean Roll Rate Bias Absolute Error (deg/sec)
1.92160	0.47880	2.29940	1.20750
Maximum and Mean Attitude and Rate Gyro Bias Estimation Errors Using Sensor Noise Values: Turbulent Simulations – Study B			
Phase I – Longitudinal Maneuver			
θ Max Absolute Error (deg)	θ Max Absolute Error (deg)	ϕ Max Absolute Error (deg)	ϕ Mean Absolute Error (deg)
0.20281	0.05412	0.23945	0.09497
Max Pitch Rate Bias Absolute Error (deg/sec)	Max Pitch Rate Bias Absolute Error (deg/sec)	Max Roll Rate Bias Absolute Error (deg/sec)	Max Roll Rate Bias Absolute Error (deg/sec)
0.10674	0.03062	0.59060	0.13783
Phase II – Transverse Maneuver			
θ Max Absolute Error (deg)	θ Max Absolute Error (deg)	ϕ Max Absolute Error (deg)	ϕ Mean Absolute Error (deg)
0.04731	0.01645	0.46162	0.19926
Max Pitch Rate Bias Absolute Error (deg/sec)	Max Pitch Rate Bias Absolute Error (deg/sec)	Max Roll Rate Bias Absolute Error (deg/sec)	Max Roll Rate Bias Absolute Error (deg/sec)
2.19830	0.47742	0.17945	0.054628
Phase III – Longitudinal/Transverse Maneuver			
θ Max Absolute Error (deg)	θ Max Absolute Error (deg)	ϕ Max Absolute Error (deg)	ϕ Mean Absolute Error (deg)
0.20041	0.05010	0.35789	0.10838
Max Pitch Rate Bias Absolute Error (deg/sec)	Max Pitch Rate Bias Absolute Error (deg/sec)	Max Roll Rate Bias Absolute Error (deg/sec)	Max Roll Rate Bias Absolute Error (deg/sec)
2.71420	0.68180	2.76110	1.49640

Table 4.35: Maximum and Mean Error Values Using Alternative Sensor Values – Study B

Maximum and Mean Attitude and Rate Gyro Bias Estimation Errors Using Sensor Noise Values: Non-Turbulent Simulations – Study C			
Phase I – Longitudinal Maneuver			
θ Max Absolute Error (deg)	θ Mean Absolute Error (deg)	*ϕ* Max Absolute Error (deg)	*ϕ* Mean Absolute Error (deg)
0.20709	0.05027	0.01490	0.00377
Max Pitch Rate Bias Absolute Error (deg/sec)	Mean Pitch Rate Bias Absolute Error (deg/sec)	Max Roll Rate Bias Absolute Error (deg/sec)	Mean Roll Rate Bias Absolute Error (deg/sec)
0.10526	0.03370	0.10000	0.17252
Phase II – Transverse Maneuver			
θ Max Absolute Error (deg)	θ Mean Absolute Error (deg)	*ϕ* Max Absolute Error (deg)	*ϕ* Mean Absolute Error (deg)
0.02200	0.00429	0.40848	0.13184
Max Pitch Rate Bias Absolute Error (deg/sec)	Mean Pitch Rate Bias Absolute Error (deg/sec)	Max Roll Rate Bias Absolute Error (deg/sec)	Mean Roll Rate Bias Absolute Error (deg/sec)
1.78080	0.34288	0.11785	0.05680
Phase III – Longitudinal/Transverse Maneuver			
θ Max Absolute Error (deg)	θ Mean Absolute Error (deg)	*ϕ* Max Absolute Error (deg)	*ϕ* Mean Absolute Error (deg)
0.20703	0.04775	0.25770	0.06285
Max Pitch Rate Bias Absolute Error (deg/sec)	Mean Pitch Rate Bias Absolute Error (deg/sec)	Max Roll Rate Bias Absolute Error (deg/sec)	Mean Roll Rate Bias Absolute Error (deg/sec)
1.91970	0.47848	2.29480	1.20410
Maximum and Mean Attitude and Rate Gyro Bias Estimation Errors Using Sensor Noise Values: Turbulent Simulations – Study C			
Phase I – Longitudinal Maneuver			
θ Max Absolute Error (deg)	θ Max Absolute Error (deg)	*ϕ* Max Absolute Error (deg)	*ϕ* Mean Absolute Error (deg)
0.20579	0.05428	0.23983	0.09496
Max Pitch Rate Bias Absolute Error (deg/sec)	Max Pitch Rate Bias Absolute Error (deg/sec)	Max Roll Rate Bias Absolute Error (deg/sec)	Max Roll Rate Bias Absolute Error (deg/sec)
0.13437	0.03379	0.58774	0.13750
Phase II – Transverse Maneuver			
θ Max Absolute Error (deg)	θ Max Absolute Error (deg)	*ϕ* Max Absolute Error (deg)	*ϕ* Mean Absolute Error (deg)
0.05264	0.01667	0.46455	0.19932
Max Pitch Rate Bias Absolute Error (deg/sec)	Max Pitch Rate Bias Absolute Error (deg/sec)	Max Roll Rate Bias Absolute Error (deg/sec)	Max Roll Rate Bias Absolute Error (deg/sec)
2.19480	0.47776	0.17684	0.05384
Phase III – Longitudinal/Transverse Maneuver			
θ Max Absolute Error (deg)	θ Max Absolute Error (deg)	*ϕ* Max Absolute Error (deg)	*ϕ* Mean Absolute Error (deg)
0.20339	0.05030	0.35950	0.10840
Max Pitch Rate Bias Absolute Error (deg/sec)	Max Pitch Rate Bias Absolute Error (deg/sec)	Max Roll Rate Bias Absolute Error (deg/sec)	Max Roll Rate Bias Absolute Error (deg/sec)
2.70840	0.68233	2.75260	1.49370

Table 4.36: Maximum and Mean Error Values Using Alternative Sensor Values – Study C

4.5 Complementary Filter Triggering Estimation

In addition to the device model and extended Kalman filter algorithm implemented, a complimentary filter was also utilized in the developed simulation models to produce longitudinal and transverse attitude estimates during each of the simulated flight maneuvers through dynamic triggering of a predefined threshold value along the longitudinal and transverse accelerometer arrays. A complementary filter is essentially a frequency domain filter. In a sense, the complementary filter may be defined as the utilization of two or more transfer functions, which are mathematical complements of one another as shown in Equation 4.41. Therefore, the complementary filter either blends or fuses similar or redundant data from variable inputs in order to determine and generate a robust estimate of a single state input.

$$\left(\hat{\theta},\hat{\phi}\right)_{CF}=\frac{\tau^2 s}{\left(\tau s+1\right)^2}\left(\dot{\theta},\dot{\phi}\right)_{Euler}+\frac{2\tau s+1}{\left(\tau s+1\right)^2}\left(\theta,\phi\right)_{Man} \tag{4.41}$$

The work completed in this feasibility study utilizes two complementary filters for accurate and reliable verification of the longitudinal and transverse attitude estimates through the implementation of dynamic triggering at predefined threshold values. The complementary filter implemented utilizes an established threshold tolerance value for reinitializing the complementary filter initial conditions to estimate the longitudinal and transverse attitude through the use of consecutive accelerometer pairs along each array since the attitude is known precisely at that condition. The dynamic triggering algorithm implemented for reinitialization of the complementary filter is shown in Figure 4.86.

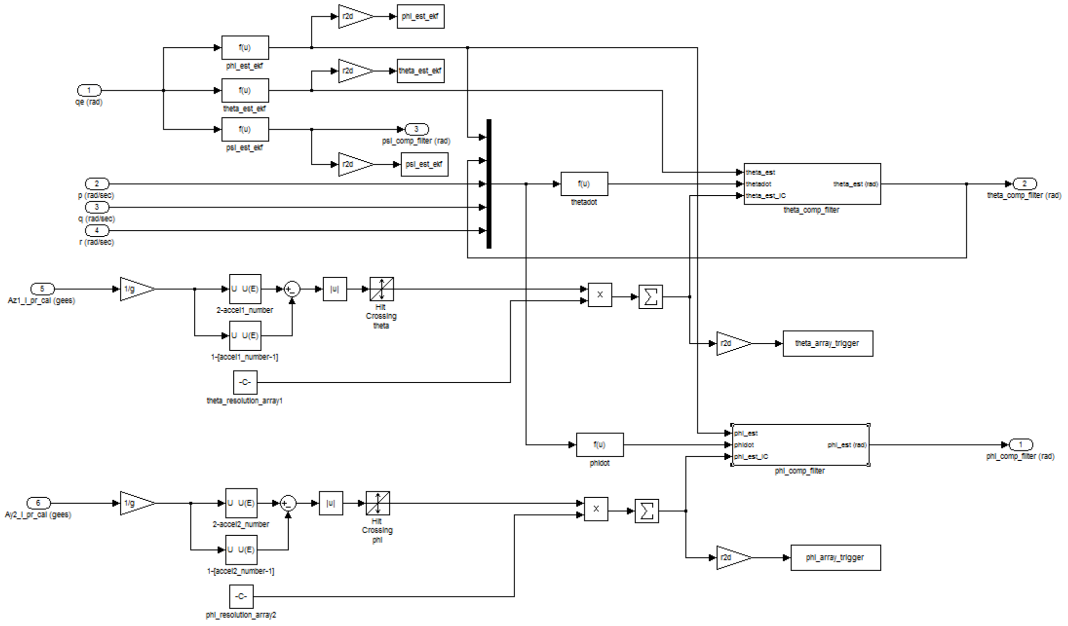

Figure 4.86: Complementary Filter Dynamic Triggering Algorithm

The threshold tolerance value on the longitudinal array was tuned to a value of 0.0003 gees and on the transverse array a value of 0.0005 gees. Figures 4.87 through 4.104 display the longitudinal and transverse attitude estimates during each phase of the simulation study determined by the complementary filter with the implementation of the dynamic triggering reinitialization algorithm. Tables 4.37 through 4.42 display the maximum and mean attitude errors during each phase of the simulation conducted.

Phase I – Longitudinal Maneuver: No Turbulence

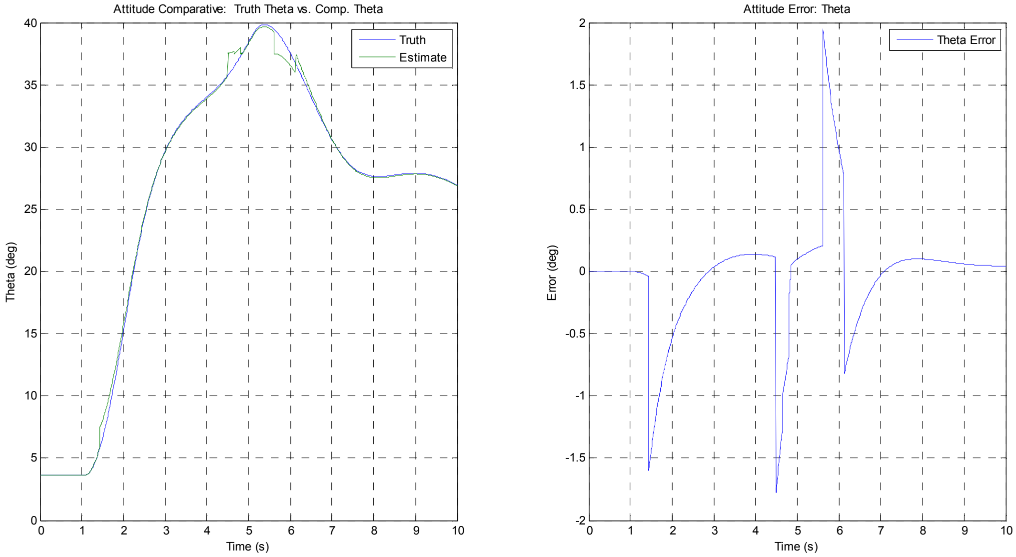

Figure 4.87: Complementary Filter Attitude Estimation –

Phase I No Turbulence: θ Comparison

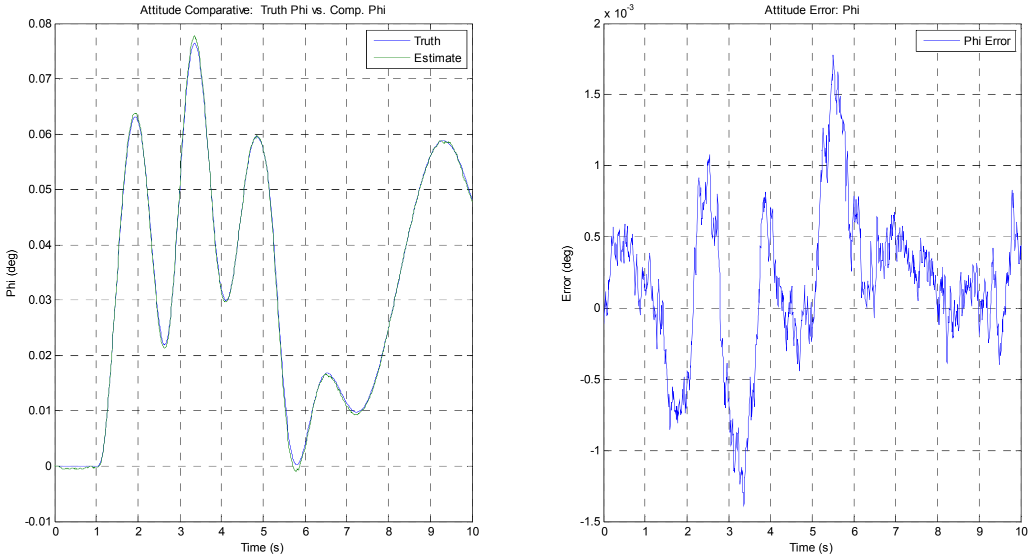

Figure 4.88: Complementary Filter Attitude Estimation –

Phase I No Turbulence: ϕ Comparison

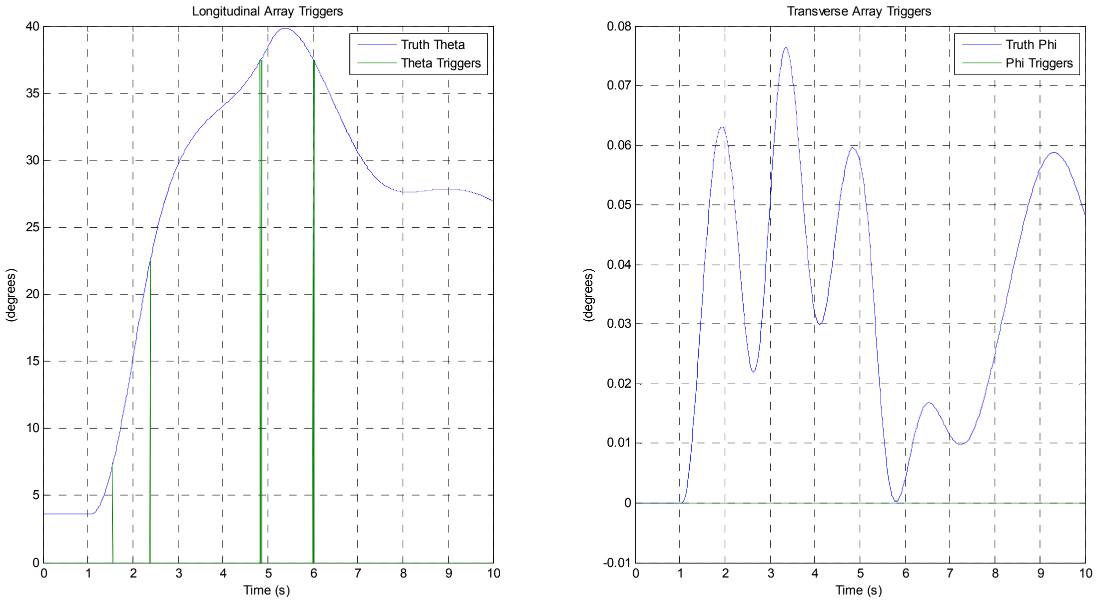

Figure 4.89: Complementary Filter Longitudinal and Transverse Array Reinitialization Triggers – Phase I No Turbulence

Figure 4.89 shows the longitudinal and transverse accelerometer array trigger magnitudes during a pure longitudinal maneuver compared to the truth value of the pitch and roll angle of the aircraft during the simulation. The dynamic triggers of the complementary filter occurred at 7.5 degree increments of resolution based on 13 accelerometers placed around the two 180 degree accelerometer arcs and are verified in the Figure 4.89 as being operational during the longitudinal maneuver along the longitudinal array. This result is expected because no motion is maneuver is imposed in the transverse, or y-z, plane of motion during the simulation of the aircraft.

Longitudinal Maneuver – No Turbulence	**Maximum Absolute Error (degrees)**
$Phase\ I:\ \theta_{Max-Error}$	0.1978
$Phase\ I:\ \phi_{Max-Error}$	0.0008
Longitudinal Maneuver – No Turbulence	**Mean Absolute Error (degrees)**
$Phase\ I:\ \theta_{Mean-Error}$	0.0456
$Phase\ I:\ \phi_{Mean-Error}$	0.0003

Table 4.37: Phase I – Longitudinal Maneuver No Turbulence Data Summary

The output time histories of the complementary filter attitude estimates overlaid with the true attitudes show good agreement between the true and estimated attitude time histories. The complementary filter experienced maximum attitude errors less than ±0.200 degrees and mean errors less than ±0.050 degrees during a pure longitudinal maneuver with no turbulence injected into the simulation model.

Phase I – Longitudinal Maneuver: Turbulence

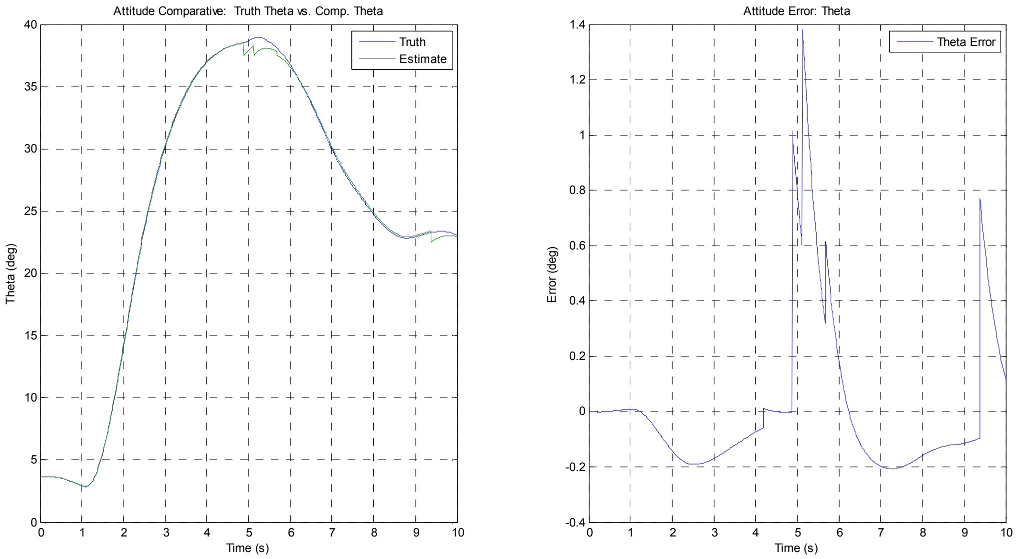

Figure 4.90: Complementary Filter Attitude Estimation – Phase I with Turbulence: θ Comparison

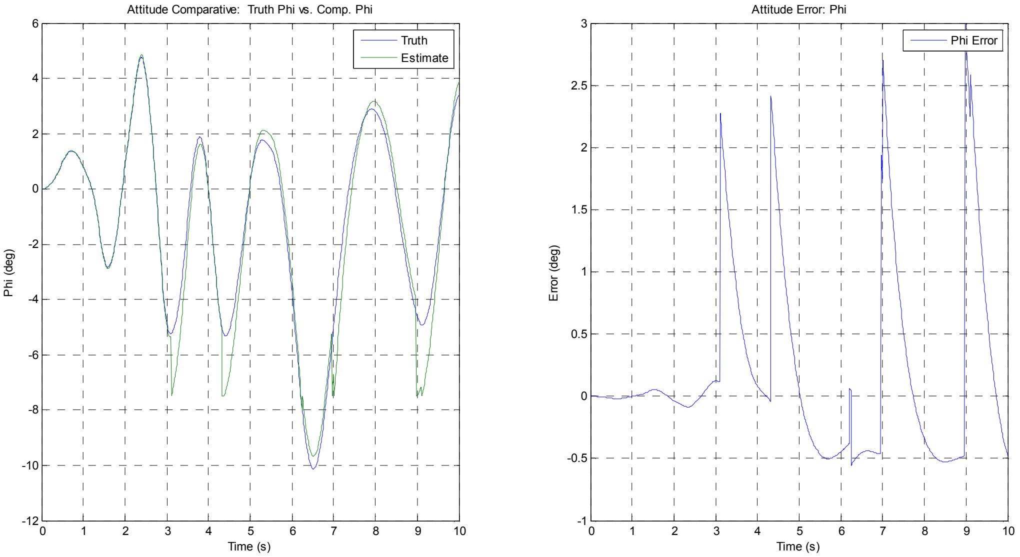

Figure 4.91: Complementary Filter Attitude Estimation – Phase I with Turbulence: ϕ Comparison

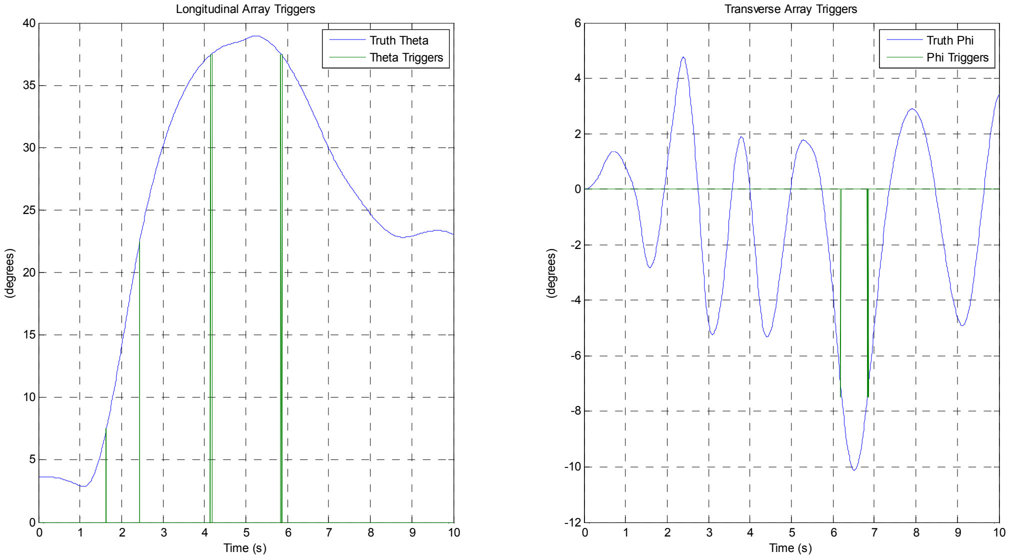

Figure 4.92: Complementary Filter Longitudinal and Transverse Array Reinitialization Triggers – Phase I with Turbulence

Figure 4.92 shows the longitudinal and transverse accelerometer array trigger magnitudes during a pure longitudinal maneuver compared to the truth value of the pitch and roll angle during the simulation. The dynamic triggers of the complementary filter occurred at 7.5 degree increments of resolution based on 13 accelerometers placed around the two 180 degree accelerometer arcs and are verified in the Figure 4.92 as being operational during the longitudinal maneuver along the longitudinal array and partially along the transverse array due to extreme vibrational effects of the simulation which causes triggers to occur in the transverse plane as well.

Longitudinal Maneuver –Turbulence	**Maximum Absolute Error (degrees)**
$Phase\ I:\ \theta_{Max-Error}$	1.3832
$Phase\ I:\ \phi_{Max-Error}$	2.9961
Longitudinal Maneuver –Turbulence	**Mean Absolute Error (degrees)**
$Phase\ I:\ \theta_{Mean-Error}$	1.8446
$Phase\ I:\ \phi_{Mean-Error}$	0.4912

Table 4.38: Phase I – Longitudinal Maneuver with Turbulence Data Summary

The output time histories of the complementary filter attitude estimates overlaid with the true attitudes show good agreement between the true and estimated attitude time histories during Phase I of the study with turbulence injected into the simulation model. The complementary filter experienced maximum attitude errors less than ±0.4000 degrees and mean errors less than ±0.7500 degrees during a pure longitudinal maneuver with turbulence.

Phase II – Transverse Maneuver: No Turbulence

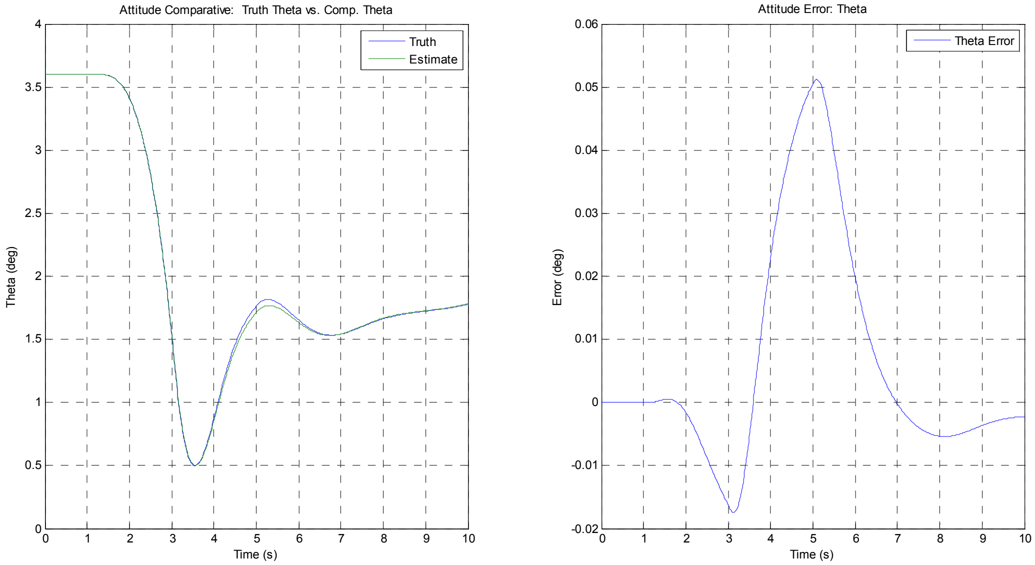

Figure 4.93: Complementary Filter Attitude Estimation –
Phase II No Turbulence: θ Comparison

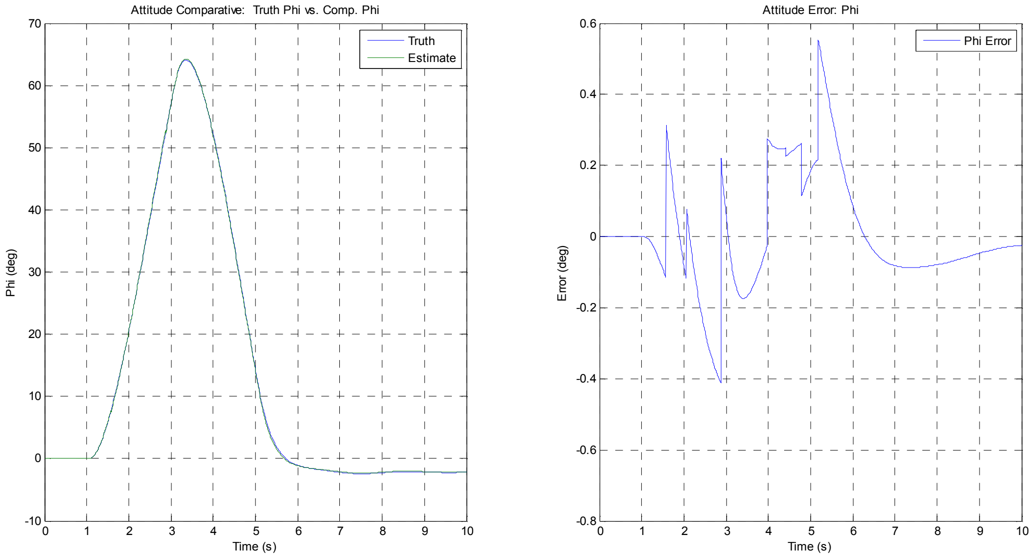

Figure 4.94: Complementary Filter Attitude Estimation –
Phase II No Turbulence: ϕ Comparison

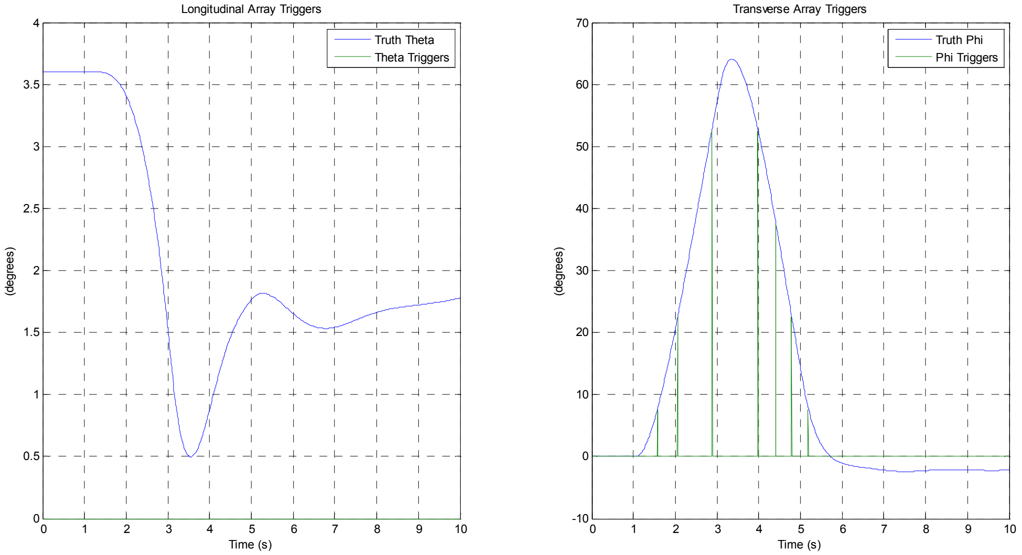

Figure 4.95: Complementary Filter Longitudinal and Transverse Array Reinitialization Triggers – Phase II No Turbulence

Figure 4.95 shows the longitudinal and transverse accelerometer array trigger magnitudes during a pure transverse maneuver compared to the truth value of the pitch and roll angle during the simulation. The dynamic triggers of the complementary filter occurred at 7.5 degree increments of resolution based on 13 accelerometers placed around the two 180 degree accelerometer arcs and are verified in the Figure 4.95 as being operational during the transverse maneuver along the transverse array only due to the aircraft experiencing no motion in the longitudinal, or x-z, plane during the simulated aircraft maneuver.

Transverse Maneuver – No Turbulence	**Maximum Absolute Error (degrees)**
$Phase\ II:\ \theta_{Max-Error}$	0.0512
$Phase\ II:\ \phi_{Max-Error}$	0.5537
Transverse Maneuver –No Turbulence	**Mean Absolute Error (degrees)**
$Phase\ II:\ \theta_{Mean-Error}$	0.0118
$Phase\ II:\ \phi_{Mean-Error}$	0.1146

Table 4.39: Phase II – Transverse Maneuver No Turbulence Data Summary

The output time histories of the complementary filter attitude estimates overlaid with the true attitudes show good agreement between the true and estimated attitude time histories during Phase II of the study with no turbulence injected into the simulation model. The complementary filter experienced maximum attitude errors less than ±0.5600 degrees and mean errors less than ±0.1200 degrees during a pure transverse maneuver.

Phase II – Transverse Maneuver: Turbulence

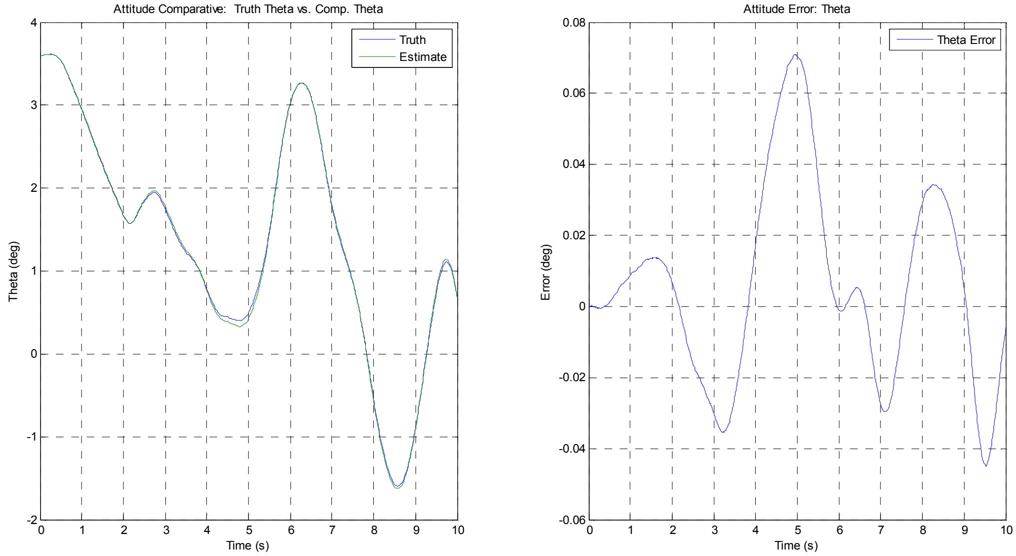

Figure 4.96: Complementary Filter Attitude Estimation –
Phase II with Turbulence: θ Comparison

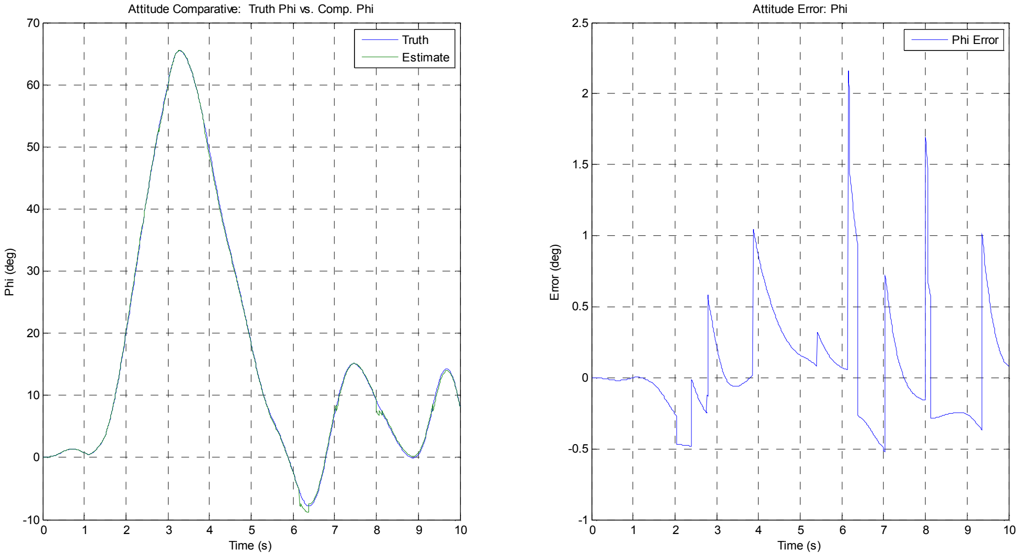

Figure 4.97: Complementary Filter Attitude Estimation –
Phase II with Turbulence: ϕ Comparison

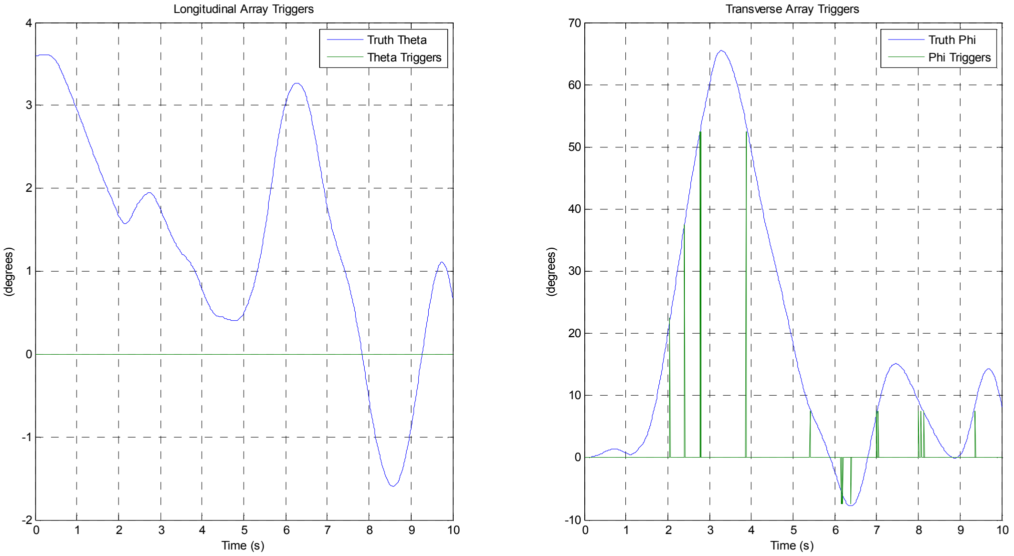

Figure 4.98: Complementary Filter Longitudinal and Transverse Array Reinitialization Triggers – Phase II with Turbulence

Figure 4.98 shows the longitudinal and transverse accelerometer array trigger magnitudes during a pure transverse maneuver compared to the truth value the pitch and roll angle during the simulation. The dynamic triggers of the complementary filter occurred again at 7.5 degree increments based on 13 accelerometers placed around the two 180 degree accelerometer arcs and are verified in the Figure 4.98 as being operational during the transverse maneuver along the transverse array only due to the aircraft experiencing no motion in the longitudinal, or x-z, plane during the simulated aircraft maneuver despite the presence of severe turbulence and vibrational effects.

Transverse Maneuver –Turbulence	**Maximum Absolute Error (degrees)**
$Phase\ II:\ \theta_{Max-Error}$	0.0708
$Phase\ II:\ \phi_{Max-Error}$	2.1657
Transverse Maneuver –Turbulence	**Mean Absolute Error (degrees)**
$Phase\ II:\ \theta_{Mean-Error}$	0.0217
$Phase\ II:\ \phi_{Mean-Error}$	0.2627

Table 4.40: Phase II – Transverse Maneuver with Turbulence Data Summary

The output time histories of the complementary filter attitude estimates overlaid with the true attitudes show good agreement between the true and estimated attitude time histories during Phase II of the study with turbulence injected into the simulation model. The complementary filter experienced maximum attitude errors less than ±0.5600 degrees and mean errors less than ±0.1200 degrees during a pure transverse maneuver.

Phase III – Longitudinal/Transverse Maneuver: No Turbulence

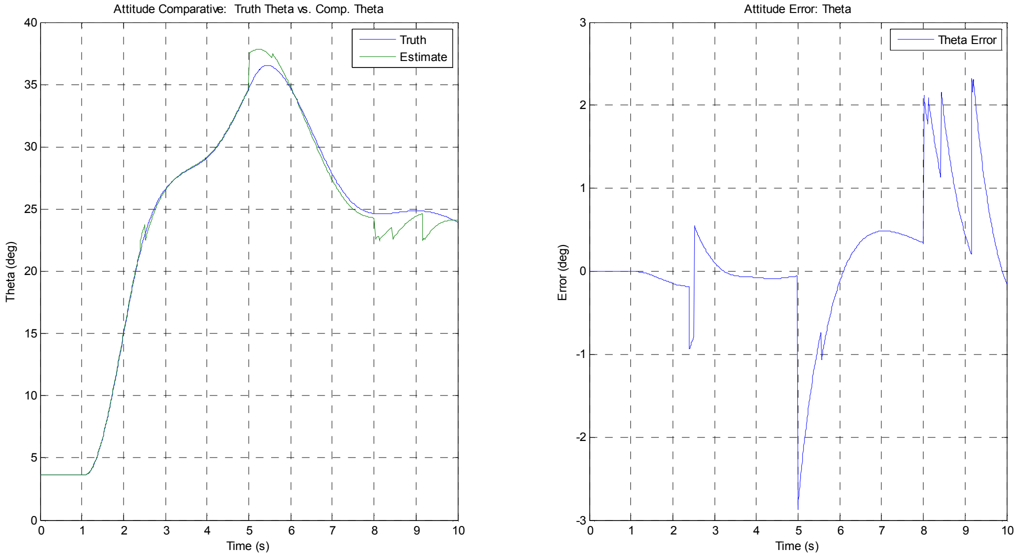

Figure 4.99: Complementary Filter Attitude Estimation –

Phase III No Turbulence: θ Comparison

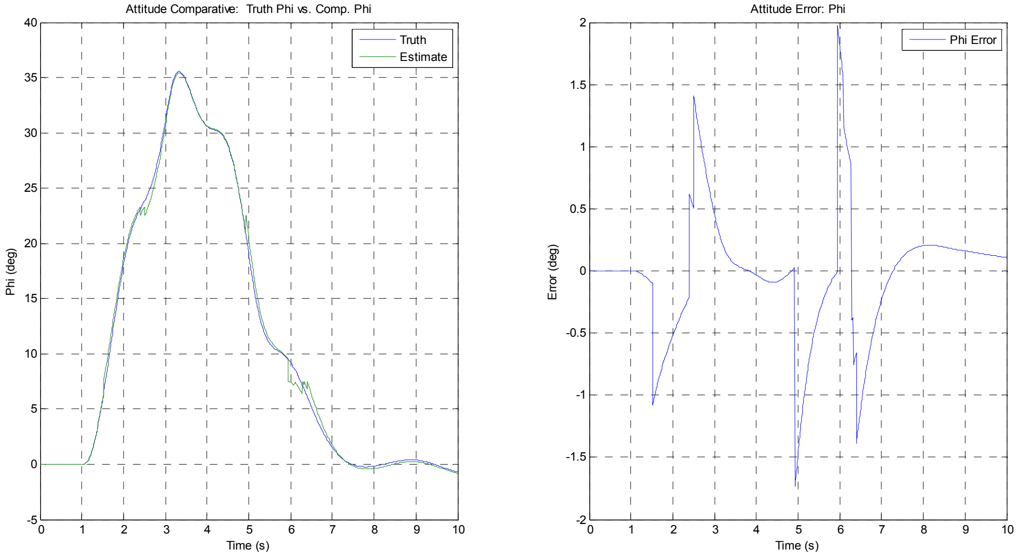

Figure 4.100: Complementary Filter Attitude Estimation –

Phase III No Turbulence: ϕ Comparison

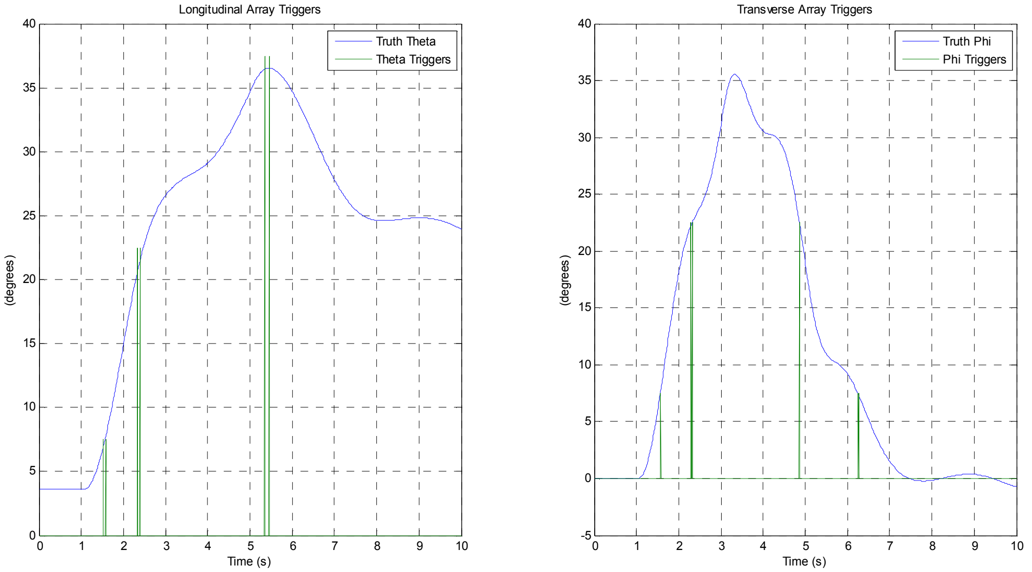

Figure 4.101: Complementary Filter Longitudinal and Transverse Array Reinitialization Triggers – Phase III No Turbulence

Figure 4.101 shows the longitudinal and transverse accelerometer array trigger magnitudes during a combined longitudinal/transverse maneuver compared to the truth value of the pitch and roll angle during the simulation. The dynamic triggers of the complementary filter occurred at 7.5 degree increments based on 13 accelerometers placed around the two 180 degree accelerometer arcs and are verified in the Figure 4.101 as being operational during the combined maneuver along the longitudinal and transverse array due to the aircraft experiencing motion in both the longitudinal and transverse plane of motion during the simulated aircraft maneuver.

Longitudinal/Transverse Maneuver –No Turbulence	**Maximum Absolute Error (degrees)**
$Phase\ III:\ \theta_{Max-Error}$	2.8706
$Phase\ III:\ \phi_{Max-Error}$	1.9755
Longitudinal/Transverse Maneuver –No Turbulence	**Mean Absolute Error (degrees)**
$Phase\ III:\ \theta_{Mean-Error}$	0.4609
$Phase\ III:\ \phi_{Mean-Error}$	0.3186

Table 4.41: Phase III – Longitudinal/Transverse Maneuver No Turbulence Data Summary

The output time histories of the complementary filter attitude estimates overlaid with the true attitudes show good agreement between the true and estimated attitude time histories during Phase III of the study for combined multi-dimensional maneuver with no turbulence injected into the simulation model. The complementary filter experienced maximum attitude errors less than ±2.0000 degrees and mean errors less than ±0.2000 degrees during the simulated aircraft maneuver.

Phase III – Longitudinal/Transverse Maneuver: Turbulence

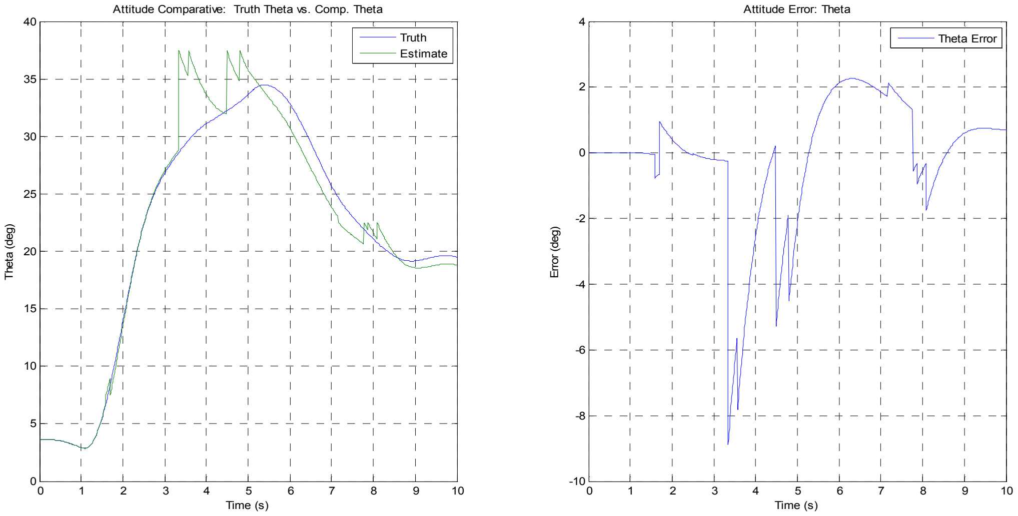

Figure 4.102: Complementary Filter Attitude Estimation –

Phase III with Turbulence: θ Comparison

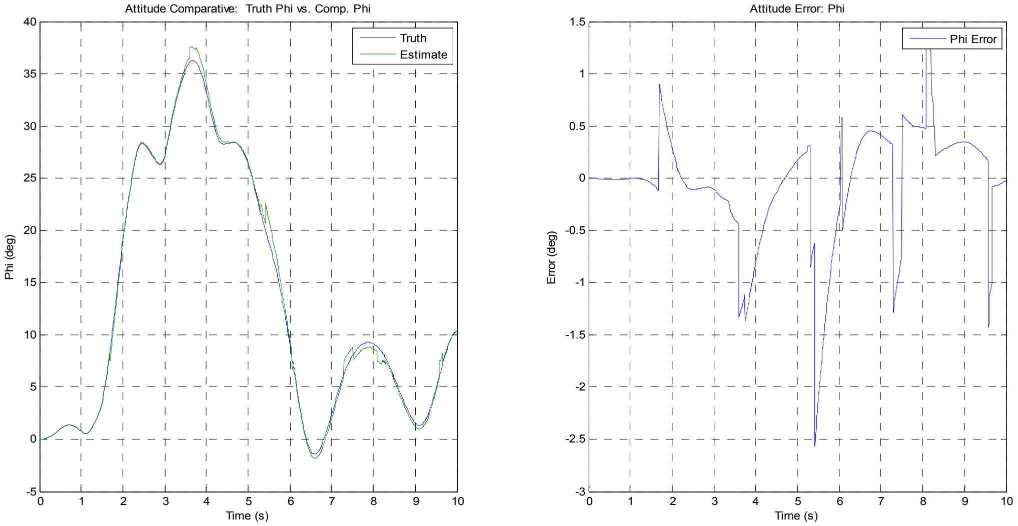

Figure 4.103: Complementary Filter Attitude Estimation –

Phase III with Turbulence: ϕ Comparison

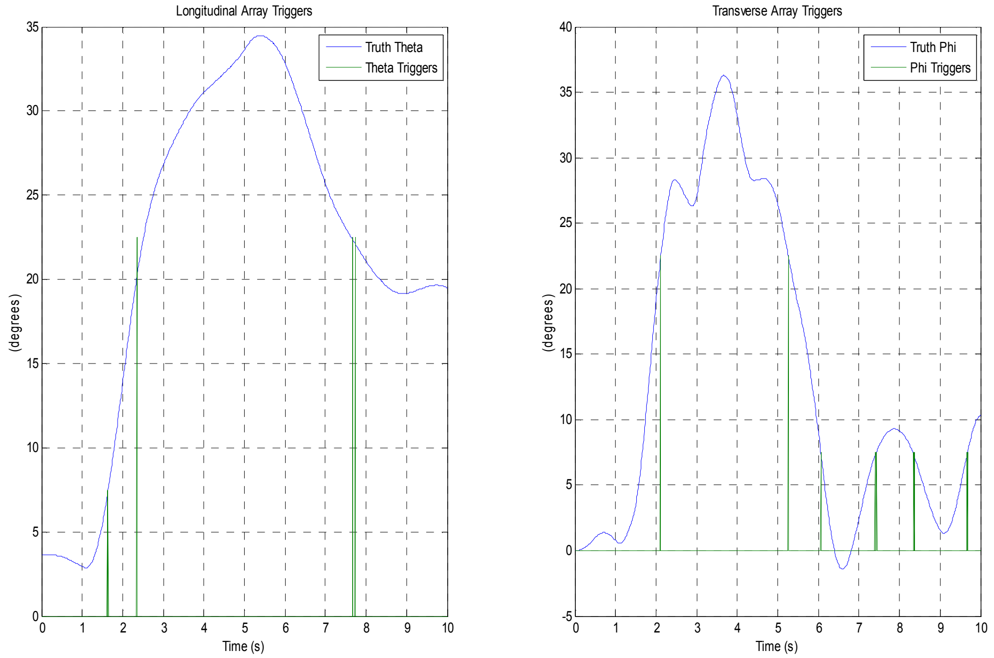

Figure 4.104: Complementary Filter Longitudinal and Transverse Array Reinitialization Triggers – Phase III with Turbulence

Figure 4.104 shows the longitudinal and transverse accelerometer array trigger magnitudes during a combined longitudinal/transverse maneuver compared to the truth value of theta and phi during the simulation. The dynamic triggers of the complementary filter occurred at 7.5 degree increments based on 13 accelerometers placed around the two 180 degree accelerometer arcs and are verified in the Figure 4.104 as being operational during the combined maneuver along the longitudinal and transverse array due to the aircraft experiencing motion in both the longitudinal and transverse plane of motion during the simulated aircraft maneuver despite the presence of severe turbulence and vibrational effects.

Longitudinal/Transverse Maneuver – Turbulence	**Maximum Absolute Error (degrees)**
$Phase\ III:\ \theta_{Max-Error}$	8.8864
$Phase\ III:\ \phi_{Max-Error}$	2.5682
Longitudinal/Transverse Maneuver – Turbulence	**Mean Absolute Error (degrees)**
$Phase\ III:\ \theta_{Mean-Error}$	1.2651
$Phase\ III:\ \phi_{Mean-Error}$	0.3733

Table 4.42: Phase III – Longitudinal/Transverse Maneuver with Turbulence Data Summary

The output time histories of the complementary filter attitude estimates overlaid with the true attitudes show good agreement between the true and estimated attitude time histories during Phase III of the study for combined multi-dimensional maneuver with turbulence injected into the simulation model. The complementary filter experienced maximum attitude errors less than ±2.5000 degrees and mean errors less than ±0.2500 degrees during the simulated aircraft maneuver.

4.6 Inertial Position and Parameter Estimation

A focus of this feasibility study was the assessment and verification of the developed model and algorithm methods ability to provide accurate and reliable inertial position and parameter estimates through the use of mathematical and kinematic relationships. Equations 3.54, 3.55, and 3.56 given previously in Section 3.4.2 may be utilized and solved for the body acceleration terms along the primary, secondary, and tertiary axes respectively. These equations and their respective derivations for the body accelerations terms are presented in this section as Equations 4.42, 4.43, and 4.44 respectively.

$$\dot{u}_{est} = \frac{1}{m}(-A_{x,cg} - mg\sin(\theta_{est})) - qw + rv \tag{4.42}$$

$$\dot{v}_{est} = pw - ru + \frac{1}{m}\left(A_{y,cg} + mg\sin(\phi_{est})\right) \tag{4.43}$$

$$\dot{w}_{est} = qu - pv - \frac{1}{m}\left(A_{z,cg} - mg\cos(\theta_{est})\cos(\phi_{est})\right) \tag{4.44}$$

Equations 4.42, 4.43, and 4.44 may then be integrated once to obtain the body velocity estimates needed to solve for the aircraft velocity parameters given previously as Equation 3.57 in Section 3.4.2. Integration of the body velocity parameters give a valid inertial position estimate of the aircraft during each phase of the simulation study. Figure 4.105 shows the algorithm method utilized where the attitude estimates produced by the extended Kalman filter are utilized as input parameters to the inertial position estimate equations.

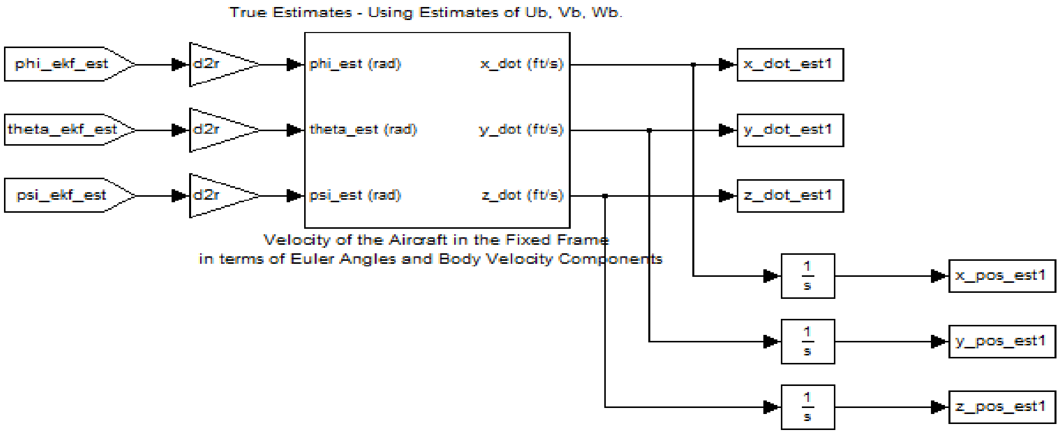

Figure 4.105: Aircraft Velocity Parameter and Inertial Position Estimation Algorithm

Aircraft parameter and inertial position estimates were obtained during each of the three phases of the simulation study and the results are shown in Figures 4.106 through 4.111. Table 4.43 presents the maximum and mean errors occurred during each phase of the study.

Phase I – Longitudinal Maneuver: No Turbulence

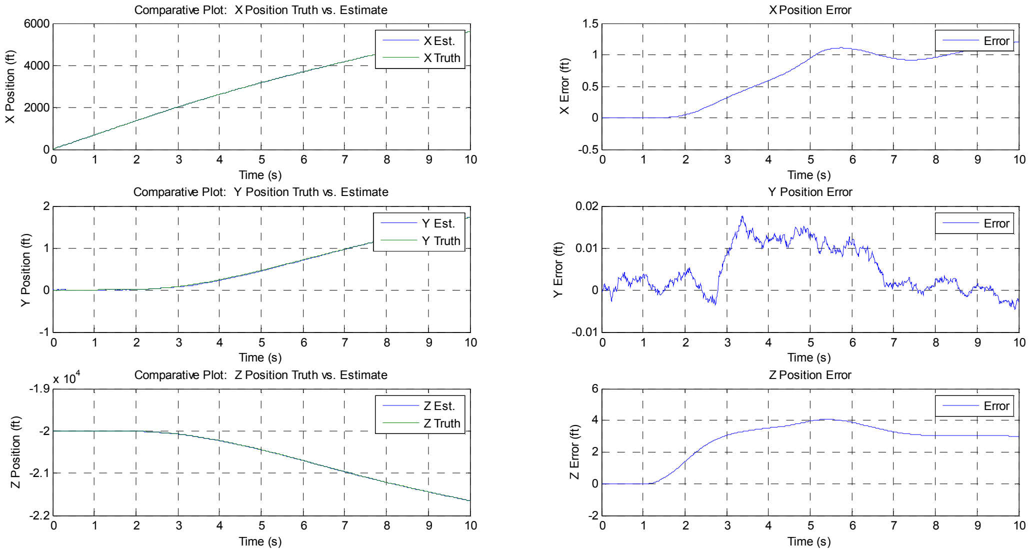

Figure 4.106: Inertial Position Estimates – Longitudinal Maneuver No Turbulence

Phase I – Longitudinal Maneuver: Turbulence

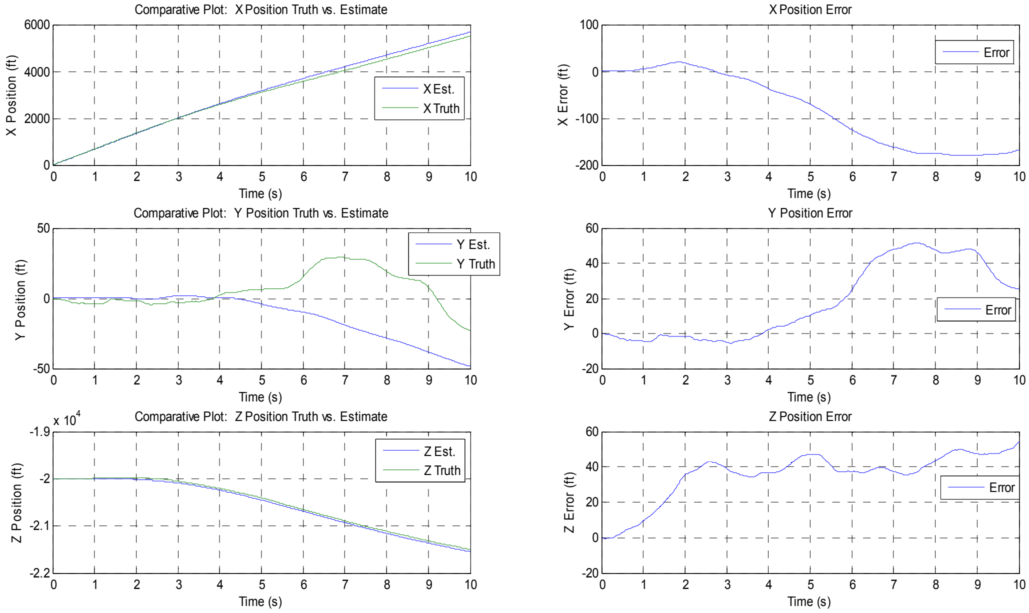

Figure 4.107: Inertial Position Estimates – Longitudinal Maneuver with Turbulence

Phase II – Transverse Maneuver: No Turbulence

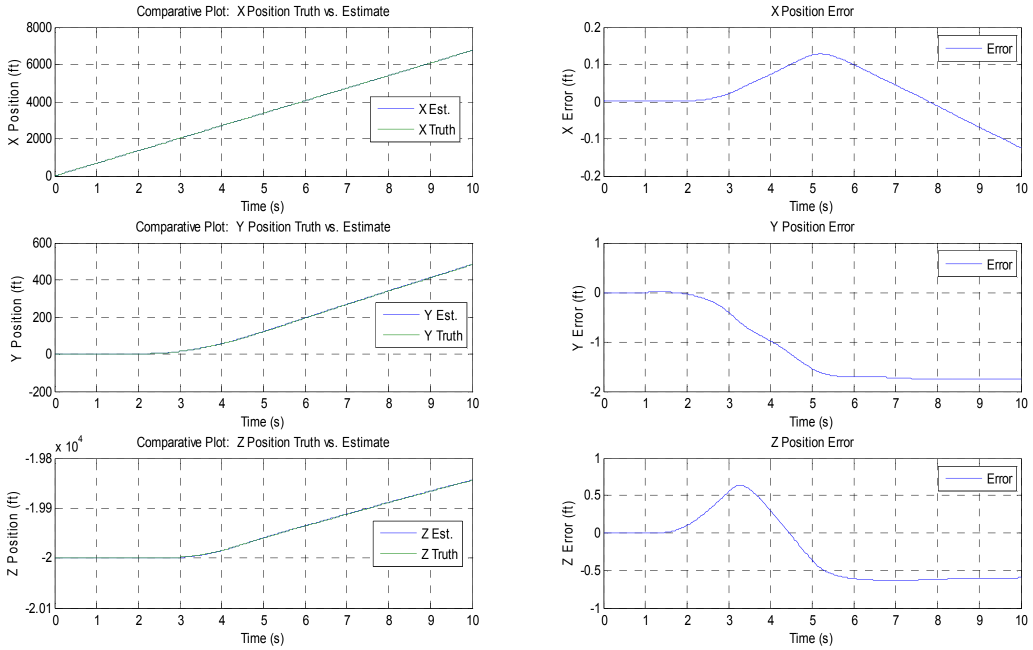

Figure 4.108: Inertial Position Estimates – Transverse Maneuver No Turbulence

Phase II – Transverse Maneuver: Turbulence

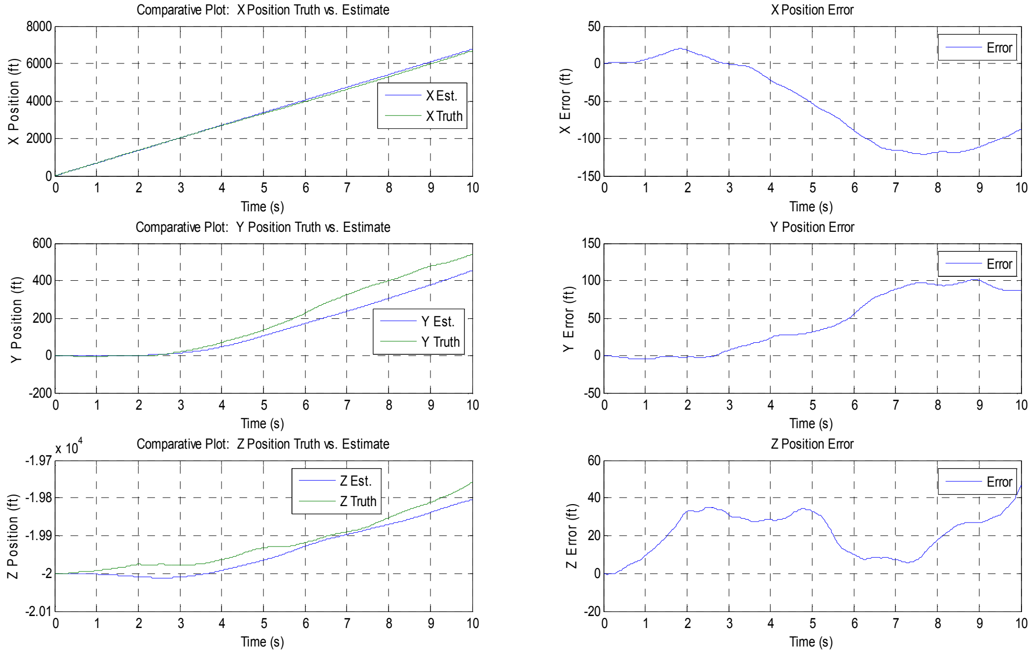

Figure 4.109: Inertial Position Estimates – Transverse Maneuver with Turbulence

Phase III – Longitudinal/Transverse Maneuver: No Turbulence

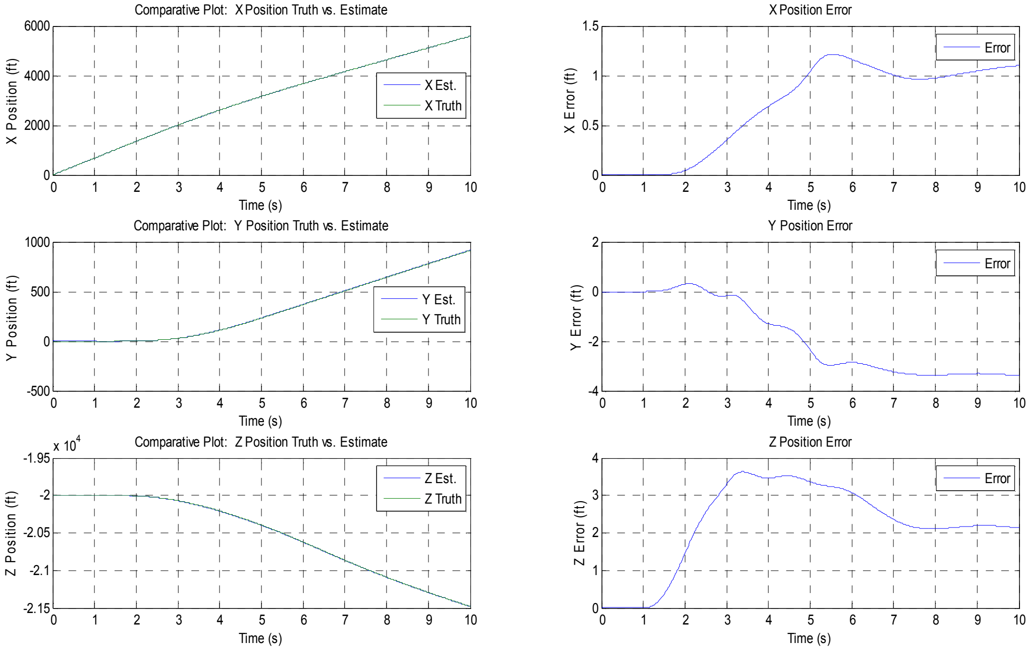

Figure 4.110: Inertial Position Estimates – Longitudinal/Transverse Maneuver No Turbulence

Phase III – Longitudinal/Transverse Maneuver: Turbulence

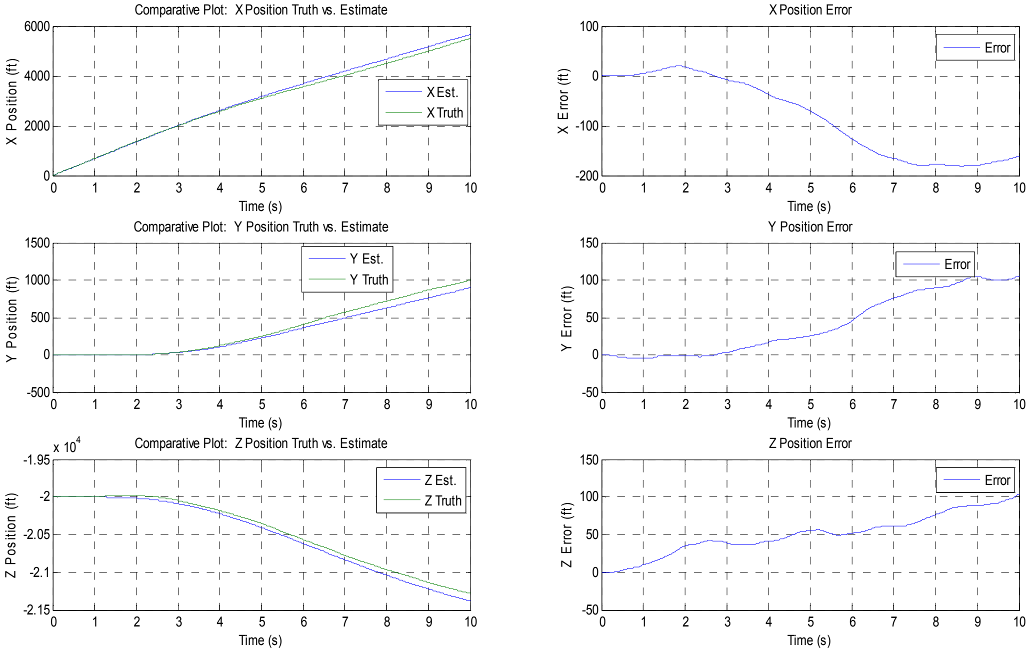

Figure 4.111: Inertial Position Estimates – Longitudinal/Transverse Maneuver with Turbulence

Inertial Position Parameter	Maximum Absolute Error (feet)	Mean Absolute Error (feet)
Phase I – Longitudinal Maneuver with No Turbulence		
X	1.1967	0.6551
Y	0.0095	0.0041
Z	4.0625	2.6531
Phase I – Longitudinal Maneuver with Turbulence		
X	179.3200	86.1520
Y	51.6700	20.2240
Z	54.3900	35.6400
Phase II – Transverse Maneuver with No Turbulence		
X	0.1378	0.0502
Y	1.7607	1.0778
Z	0.6374	0.4022
Phase II – Transverse Maneuver with Turbulence		
X	121.6530	58.0000
Y	101.0810	44.7430
Z	46.7620	21.3120
Phase III – Longitudinal/Transverse Maneuver with No Turbulence		
X	1.2153	0.6869
Y	3.3836	1.8367
Z	3.6284	2.2432
Phase III – Longitudinal/Transverse Maneuver with Turbulence		
X	180.5910	86.6910
Y	105.2200	41.6250
Z	103.8510	50.5190

Table 4.43: Inertial Position Estimation Maximum and Mean Error Summary

From the time history plots displayed in Figures 4.106 through 4.111, it may be shown during simulated aircraft maneuvers not experiencing turbulence, the algorithm and method implemented provides relatively good estimates of the vehicle's inertial position in real-time. During each phase of the simulation study conducted, maximum positional errors in the x-direction did not exceed ±1.25 feet, in the y-direction ±3.40 feet, and in the z-direction maximum errors were less than ±4.25 feet. During simulated aircraft maneuvers exposed to extreme turbulence and vibrational effects, the maximum error in the x-direction was approximately ±180 feet, in the y-direction ±106 feet, and in the z-direction ±104 feet. While these values are large deviations from the true inertial position of the aircraft, the turbulence injected and simulated during each phase of the simulation study utilizing the Dryden wind and turbulence model, discussed in Section 3.3, were exposed to turbulence and vibrational effects upwards of 60 feet per second, or three times the highest likely turbulence to be experience during any real-world flight condition. Deviations and errors in the attitude estimates during turbulent flight simulations will cause an increase and propagation in the error of the inertial position estimates determined during the duration of the simulated aircraft maneuver.

Chapter 5

Conclusion and Future Work

5.1 Conclusion

In this feasibility study, the ability of an innovative, low-cost, two-dimensional accelerometer array to estimate and eliminate a rate gyro bias online for accurate and reliable two-dimensional attitude estimation was assessed and verified. The device and algorithm method implemented in this feasibility study was an expansion of a previous work; however, is a unique departure from previous studies and conventional parameter identification and attitude estimation due to the implementation of a two-dimensional, cost-effective, accelerometer array utilizing the measurement of one inertial reference vector, gravity. The development of this device provides numerous benefits over conventional reference frame sensors and inertial measurement units such as GPS and inclinometers which are largely susceptible to environmental conditions, signal interruption, or the governing dynamics of the operating system. The method implemented and assessed in this study provides a robust algorithm method for estimation of the rate gyro bias and two-dimensional attitude determination through the algorithm's ability to measure and eliminate the imposed acceleration loads imparted upon the vehicle due to the dynamics of the vehicle maneuver and the affects of the environmental operating conditions.

The developed method and algorithm implemented in this feasibility study expanded upon previous research conducted by expanding the previous one-dimensional analysis in the longitudinal plane, to a multi-dimensional assessment in both the longitudinal and transverse planes by utilizing cost-effective accelerometers along two 180 degree arcs and a rate gyro placed at the center-of-gravity location with an extended Kalman filter algorithm for rate gyro bias estimation yielding robust longitudinal and transverse attitude estimation in real-time. The accelerometer and rate gyro measurements were simulated utilizing rotational displacements, center-of-gravity accelerations, and rotational rate outputs from a constructed nonlinear six degree-of-freedom aircraft simulation model. Simulation of the nonlinear aircraft model included highly dynamical maneuvers and operating environments resulting in imposed loads up to 3.5 gees. The rate gyro was simulated with an imposed, constant 0.200 degree/second bias magnitude and rate gyro slope of 0.050 degrees/second/hour. The algorithm implemented produced a bias estimation maximum error of ±2.750 degrees/second during non-turbulent maneuvers and ±2.850 degrees/second during maneuvers injected with maximum body axis velocities of up to 60 feet per second through the use of a Dryden wind gust model. Maximum attitude estimation errors produced from the extended Kalman filter for longitudinal attitude estimates were shown to be approximately ±0.210 degrees, while transverse attitude estimates experienced maximum attitude errors of ±0.400 degrees for simulated aircraft maneuvers subject to non-turbulent flight conditions. Aircraft simulation maneuvers subjected to imposed turbulence inputs experience maximum attitude error of up to ±0.220 degrees for longitudinal attitude estimates and ±0.470 degrees for transverse attitude estimates.

The inertial position estimation algorithm implemented resulted in maximum position errors of up to 4.00 feet during non-turbulent flight conditions and maximum position errors of up to 180 feet during simulated aircraft maneuvers with turbulence injections of up to 60 feet per second. The end result of this feasibility study is the development and successful implementation of a two-dimensional, dual-arc accelerometer array model fused with an algorithm method composed of mathematical operations and kinematic relationships requiring knowledge of sensor operating parameters and the accelerometer array location relative the aircraft's center-of-gravity location. The characteristics of the developed two-dimensional accelerometer array enable the device not only to be cost-effective, but easily implementable in a variety of applications requiring critical and robust attitude estimation such as unmanned air and micro air vehicles, and terrestrial or marine applications.

5.2 Future Work

The work conducted in this feasibility study and research initiative focused on the development and implementation of a two-dimensional accelerometer array for accurate and reliable rate sensor bias estimation for precise attitude determination of the longitudinal and transverse angle measurement during simulated highly dynamic flight conditions. This study focused on system modeling development of the proposed two-dimensional accelerometer array and signal simulation development to assess and validate the functionality and feasibility of the device in a real-world, nonlinear operating environment. However, a real-world test platform capable of imposing rotational and translational accelerations for evaluation of the developed algorithm and method of operations is required for verification and validation of the hardware configuration in a real-world operating environment.

The next research phase is the development and testing of a miniaturized, two-dimensional attitude determination and rate gyro bias estimation algorithm coupled with an accelerometer bias estimation and clipping compensation algorithm for precise attitude and inertial position estimation.

In the next phase of work and research conducted, prototype hardware testing is to be performed on a relevant test platform such as a laboratory testing, shaker table testing and implementation on a highly dynamic vehicle such as a sounding rocket or flight test vehicle. Testing of the method and device developed in a such a manner would offer significant verification and validation testing of the proposed hardware prototype as shown in Figure 5.1.

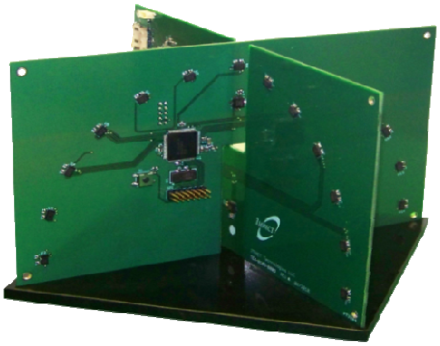

Figure 5.1: Prototype Hardware Accelerometer Based Attitude Estimation Device

Bibliography

[1] M.A. Abid. SPACECRAFT SENSORS. John Wiley and Sons, 2005.

[2] A.L. Crassidis and W.W. Walter. ATTITUDE ESTIMATION USING AN ACCELEROMETER AND RATE GYRO BASED DEVICE. In *Proceedings at AIAA Atmospheric Flight Mechanics Conference and Exhibit*, August 2006**.**

[3] R.C. Nelson. FLIGHT STABILITY AND AUTOMATIC CONTROL. McGraw-Hill, 1998.

[4] W.F. Phillips. MECHANICS OF FLIGHT. John Wiley & Sons, 2004.

[5] T. Lefebvre, H. Bruyninckx, and J. De Schutter. KALMAN FILTERS FOR NONLINEAR SYSTEMS: A COMPARISON OF PERFORMANCE. In *IEEE Transactions on Automatic Control*, October 2001.

[6] R.M. Weisman. *Robust Longitudinal Rate Gyro Bias Estimation for Reliable Pitch Attitude Observation through Utilization of a Displaced Accelerometer Array*, Master of Science Thesis Rochester Institute of Technology Department of Mechanical Engineering, December 2008.

[7] K. Lo and H. Kimura. RECURSIVE ESTIMATION METHODS FOR DISCRETE SYSTEMS. In *IEEE Transactions on Automatic Control,* Vol. 48, No. 11, November 2003.

[8] J. Thienel and R. M. Sanner. A COUPLED NONLINEAR SPACECRAFT ATTITUDE CONTROLLER AND OBSERVER WITH AN UNKNOWN CONSTANT GYRO BIAS AND GYRO NOISE. In *IEEE Transactions on Automatic Control,* Vol. 48, No. 11, November 2003.

[9] Y. Oshman and F. Landis Markley. SPACECRAFT ATTITUDE/RATE ESTIMATION USING VECTOR-AIDED GPS OBSERVATIONS. In *IEEE Transactions on Aerospace and Electronic Systems,* Vol. 35, No. 3*,* July 1999.

[10] D. Choukroun, I. Y. Bar-Itzhack, and Y. Oshman. NOVEL QUATERNION KALMAN FILTER. In *IEEE Transactions on Aerospace and Electronic Systems,* Vol. 42, No. 1, January 2006.

[11] J. Ting-Yung Wen. THE ATTITUDE CONTROL PROBLEM. In *IEEE Transactions on Automatic Control,* Vol. 36, No. 10, October 1991.

[12] Y. Oshman and M. Isakow. MINI-UAV ATTITUDE ESTIMATION USING AN INERTIALLY STABALIZED PAYLOAD. In *IEEE Transactions on Aerospace and Electronic Systems,* Vol. 35, No. 4, October 1999.

[13] R. A. Iltis. STATE ESTIMATION USING AN APPROXIMATE REDUCED STATISTICS ALGORITHM. In *IEEE Transactions on Aerospace and Electronic Systems,* Vol. 35, No. 4, October 1999.

[14] T. Kim and C. Webb. SIGMA POINT KALMAN FILTERING FOR INTEGRATED GPS AND INERTIAL NAVIGATION. In *IEEE Transactions on Aerospace and Electronic Systems,* Vol. 35, No. 4, October 1999.

[15] Y. Soo Suh. ATTITUDE ESTIMATION BY MULTI-MODE KALMAN FILTERS. In *IEEE Transactions on Industrial Electronics*, Vol. 53, No. 4, August 2006.

[16] L. Cheng, Z. Zhaoying, and F. Xu. ATTITUDE DETERMINATION FOR MAVs USING A KALMAN FILTER. In *Tsinghua Science and Technology,* ISSN 1007-0214 03/25 pp593-597, Volume 13, Number 5, October 2008.

[17] J.K. Hall, N.B. Knoebel, and T.W.McLain. QUATERNION ATTITUDE ESTIMATION FOR MAVS USING A MULTIPLICATIVE EXTENDED KALMAN FILTER. In *IEEE Position, Location, and Navigation Symposium*, May, 2008.

[18] H. Rehbinder and X. Hu. DRIFT-FREE ATTITUDE ESTIMATION FOR ACCELERATED RIGID BODIES. In *Proceedings of 2001 IEEE International Conference on Robotics and Automation*, Vol. 4, May 2001.

[19] A. Tayebi, S. McGilvray, A. Roberts, and M. Moallem. ATTITUDE ESTIMATION AND STABILIZATION OF A RIGID BODY USING LOW COST SENSORS. In *46th IEEE Conference on Decision and Control*, December 2007.

[20] C. Jizheng, Y. Jianping, and F. Qun. FLIGHT VEHICLE ATTITUDE DETERMINATION USING THE MODIFIED RODRIQUES PARAMETERS. In *Chinese Jouirnal of Aeronautics,* Vol. 21, Number 5, October 2008.

[21] Y.I. Akcayir and Y. Ozkazanc. GYROSCOPE DRIFT ESTIMATION IN LAND NAVIGATION SYSTEMS. In *Proceedings of IEEE Conference on Control Applications*. Institute of Electrical and Electronics Engineers, 2003.

[22] W. Gao, Q. Nie, G. Zai, and H. Jia. GYROSCOPE DRIFT ESTIMATION IN TIGHLY-COUPLED INS/GPS NAVIGATION SYSTESMS. In *Proceedings of IEEE Conference on Industrial Electronics and Applications*. Institute of Electrical and Electronics Engineers, 2007.

[23] T.G. Gainer and S. Hoffman. SUMMARY OF TRANSFORMATION AND EQUATIONS OF MOTION USED IN FREE FLIGHT AND WIND TUNNEL DATA AND REDUCTION ANALYSIS, NASA-SP-3070, NASA Langley Research Center, 1972.

[24] The Math Works Inc., http://www.mathworks.com/. Coordinate Systems for Modeling, 2008.

[25] D.C. Montgomery and G.C. Runger. APPLIED STATSTICS AND PROBABILITY FOR ENGINEERS. John Wiley & Sons, 1994.

[26] E.J. Lefferts, F.L. Markley, and M.D. Shuster. KALMAN FILTERING FOR SPACECRAFT ATTITUDE ESTIMATION. *Journal of Guidance and Control*, 5(5):417-429, 1982.

[27] N. Metni, J. Pflimlin, T. Hamel, and P. Soueres. ATTITUDE AND GYRO BIAS ESTIMATION FOR A VTOL UAV. *Control Engineering Practice*, 14:1511-1520, 2006.

[28] J.L. Crassidis and J.L. Junkins. OPTIMAL ESTIMATION OF DYNAMIC SYSTEMS. Chapman & Hall/CRC, 2004.

[29] G. Welch and G. Bishop. AN INTRODUCTION TO THE KALMAN FILTER. UNC-Chapel Hill, TR 95-041, July 24, 2006.

[30] P. Zarchan and H. Musoff. FUNDAMENTALS OF KALMAN FILTERING: A PRACTICAL APPROACH. Progress in Astronautics and Aeronautics. American Institute of Aeronautics and Astronautics, Volume 232, Third Edition, 2009.

[31] R.F. Stengel. OPTIMAL CONTROL AND ESTIMATION. Dover Publications Inc, 1994.

[32] S. Ying. ADVANCED DYNAMICS. American Institute of Aeronautics and Astronautics, 1997.

[33] M.D. Shuster and W.F. Dellinger. SPACECRAFT ATTITUDE DETERMINATION AND CONTROL. *Fundamentals of Space Systems*, 2nd Edition. 236-325, Ed. V.L. Pisacane. 2005. Oxford University Press.

[34] R. Yadlin. ATTITUDE DETERMINATION AND BIAS ESTIMATION USING KALMAN FITLERING. Software and Analysis Team Lead, FalconSAT-5, U.S. Air Force Academy Small Satellite Research Laboratory.

[35] N. Huges. QUATERNION TO EULER ANGLE CONVERSION FOR ARBITRARY ROTATION SEQUENCE USING GEOMETRIC METHODS. Braxton Technologies, Colorado Springs, Colorado, 80915.

[36] N.A. Denison. *Automated Carrier Landing of an Unmanned Combat Aerial Vehicle Using Dynamic Inversion,* Master of Science Thesis Air Force Institute of Technology, Department of Aeronautical and Astronautical Engineering, June 2007.

[37] J. Diebel. REPRESENTING ATTITUDE: EULER ANGLES, UNIT QUATERNIONS, AND ROTATION VECTORS. Stanford University, October 2006.

[38] J.L. Marins, Y. Xun, E.R. Bachman, R.B. McGhee, and M.J. Zyda. AN EXTENDED KALMAN FILTER FOR QUATERION-BASED ORIENTATION ESTIMATION USING MARG SENSORS. In *Proceedings of the 2001 IEEE/RSJ International Conference on Intelligent Robots and Systems,* Maui, Hawaii, USA, Oct. 29 - Nov. 03, 2001.

[39] M.I. Ribeiro. KALMAN AND EXTENDED KALMAN FITLERS: CONCEPT, DERIVATION, AND PROPERTIES. Institute for Systems and Robotics, February 2004.

[40] H.G. Campbell. MATRICES WITH APPLICATIONS. Meredith Corporation, 1968.

[41] D.C. Montgomery, C.G. George, and N.F. Hubele. ENGINEERING STATISTICS. John Wiley & Sons, 2004

[42] J.G. Proakis and D.G. Manolakis. DIGITAL SIGNAL PROCESSING: PRINCIPLES, ALGORITHMS, AND APPLICATIONS. Pearson Prentice Hall, 2007.

[43] K. Ogata. DISCRETE-TIME CONTROL SYSTEMS. Prentice Hall, 1995.

[44] W.C. Durham. AIRCRAFT DYNAMICS AND CONTROL. Virginia Polytechnic Institute and State University. Blacksburg, Virginia. 2002

[45] J.B. Kuipers. QUATERNIONS AND ROTATION SEQUENCES: A PRIMER WITH APPLICATIONS TO ORBITS, AEROSPACE, AND VIRTUAL REALITY. Princeton University Press, 1999.

[46] R.L. Farrenkopf. GENERALIZED RESULTS FOR PRECISION ATTITUDE REFERENCE SYSTEMS USING GYROS. *AIAA Paper 74-903*, 1974.

[47] S. Gage. CREATING A UNIFIED GRAPHICAL WIND TURBULENCE MODEL FROM MULTIPLE SPECIFICATIONS. In *Proceedings at AIAA Modeling and Simulation Technologies Conference and Exhibit*, 11-14 August 2003**.**

[48] R.L. Farrenkopf. ANALYTIC STEADY-STATE ACCURACY SOLUTIONS FOR TWO COMMON SPACECRAFT ATTITUDE ESTIMATORS. *Journal of Guidance and Control*, Vol.1, No.4, July-Aug. 1978, pp. 282-284.

[49] D.H. Titterton. STRAPDOWN INERTIAL NAVIGATION TECHNOLOGY. Institution of Engineering and Technology, 2nd edition, 2004.

[50] D. Kingston and R.W. Beard. REAL-TIME ATTITUDE AND POSITION ESTIMATION FOR SMALL UAVs USING LOW-COST SENSORS. In *AIAA 3rd Unmanned Unlimited Technical Conference*, Chicago, Illinois, 2004. AIAA.

[51] D. Dacheng, L. Liu, and D. Xiaojing. A LOW-COST ATTITUDE ESTIMATION SYSTEM FOR UAV APPLICATIONS. In *Proceedings of IEEE Control and Decision Conference*, May 26-28, 2010.

Appendices

Appendix A

Aerospace Transformations

A.1 Translational Vector Sequence [2, 3, 4, 6, 28, 32]

Resolution of displacements in a body-fixed coordinate frame relative to an Earth-fixed coordinate frame of reference by means of a rotational angle sequence is presented in the figures and trigonometric identities shown in this section for derivation of the necessary and appropriate rotational matrices. The standard aerospace rotation sequence is utilized to derive the displacements in a body-fixed coordinate frame to an Earth-fixed coordinate frame of reference.

Consider a rotation of the x_f, y_f, z_f frame about the z_f-axis thorugh a rotation angle, ψ, allowing the new frame of reference to be represented as x_1, y_1, z_1 as shown in Figure A.1. Equation A.1 relates the displacements in the body-fixed frame relative to the Earth-fixed coordinate frame through the transformation reference frame.

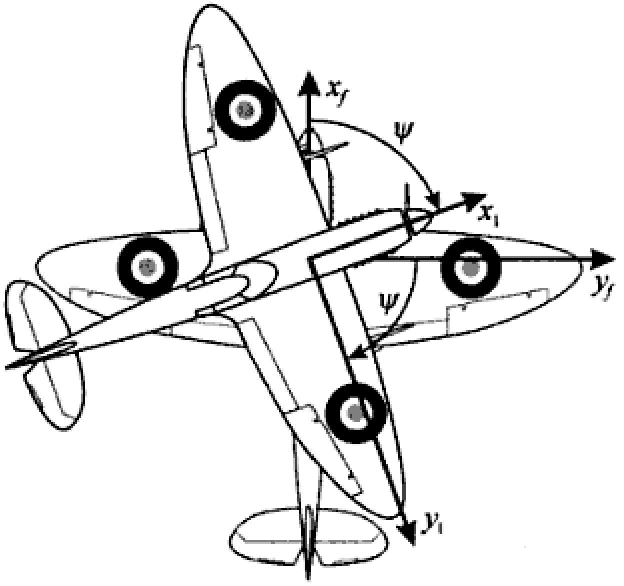

Figure A.1: Rotation about the Z-Axis [4]

$$R_3 = \begin{bmatrix} \cos\psi & \sin\psi & 0 \\ -\sin\psi & \cos\psi & 0 \\ 0 & 0 & 1 \end{bmatrix}$$

(A.1)

Consider a rotation of the x_1, y_1, z_1 coordinate frame about the y_1-axis through a rotation angle, θ, to the coordinate system defined as x_2, y_2, z_2 as shown in Figure A.2. Equation A.2 represents the rotation sequence through the rotation angle, θ.

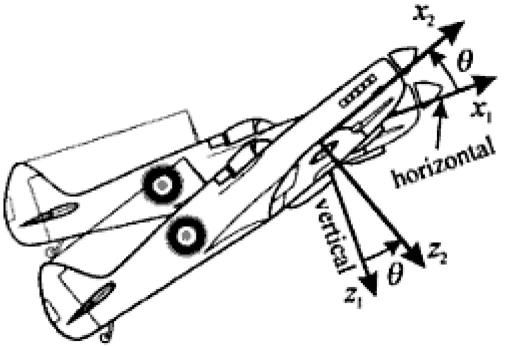

Figure A.2: Rotation about the Y-Axis [4]

$$R_2 = \begin{bmatrix} \cos\theta & 0 & -\sin\theta \\ 0 & 1 & 0 \\ \sin\theta & 0 & \cos\theta \end{bmatrix} \tag{A.2}$$

Consider a rotation of the x_2, y_2, z_2 coordinate frame about the x_2-axis through a rotation angle, ϕ, to the coordinate system defined as the body-fixed coordinate frame of x_b, y_b, z_b as shown in Figure A.3. Equation A.3 represents the third rotation sequence through the rotation angle, ϕ.

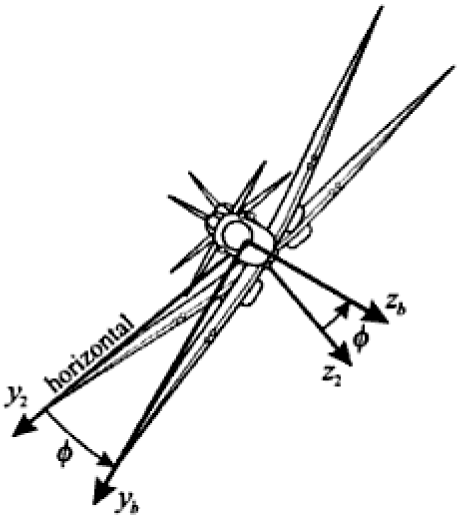

Figure A.3: Rotation about the X-Axis [4]

$$R_1 = \begin{bmatrix} 1 & 0 & 0 \\ 0 & \cos\phi & \sin\phi \\ 0 & -\sin\phi & \cos\phi \end{bmatrix} \tag{A.3}$$

The rotation about a general normalized axis, $\hat{a}$, through a particular rotation angle, β, is defined by Equation A.4 as given in [32].

$$R(\beta,\hat{a}) = \cos\beta\mathbf{I} + (1-\cos\beta)\hat{a}\hat{a}^T - \sin\beta[\hat{a}x] \tag{A.4}$$

$$Where:\ [\hat{a}x] = \begin{bmatrix} 0 & -a_3 & a_2 \\ a_3 & 0 & -a_1 \\ -a_2 & a_1 & 0 \end{bmatrix}$$

A.2 Rotational Vector Sequence [4, 28, 32]

In a similar manner utilized in the previous section, the time rate of change of the Euler angles ($\dot{\phi},\dot{\theta},\dot{\psi}$), may be related to the body-fixed coordinate frame components of the angular velocity vector, (p, q, r), of the aircraft. For derivation of this sequence, it is critical to consider all rotational coordinate systems for each Euler angle. The bank angle, ϕ, is defined relative to the coordinate system x_2, y_2, z_2, while the pitch angle, θ, is defined with respect to x_1, y_1, z_1. The heading angle, ψ, is defined relative to the Earth-fixed coordinate frame, x_f, y_f, z_f. The establishment of these relationships and reference designations result in Equation A.5 for transformation between the Euler angle rates and the vehicle, or aircraft rates.

$$\begin{Bmatrix} p \\ q \\ r \end{Bmatrix} = \begin{bmatrix} 1 & 0 & 0 \\ 0 & \cos\phi & \sin\phi \\ 0 & -\sin\phi & \cos\phi \end{bmatrix} \begin{Bmatrix} \dot{\phi} \\ 0 \\ 0 \end{Bmatrix} + \begin{bmatrix} 1 & 0 & 0 \\ 0 & \cos\phi & \sin\phi \\ 0 & -\sin\phi & \cos\phi \end{bmatrix} \begin{bmatrix} \cos\theta & 0 & -\sin\theta \\ 0 & 1 & 0 \\ \sin\theta & 0 & \cos\theta \end{bmatrix} \begin{Bmatrix} 0 \\ \dot{\theta} \\ 0 \end{Bmatrix}$$
$$+ \begin{bmatrix} 1 & 0 & 0 \\ 0 & \cos\phi & \sin\phi \\ 0 & -\sin\phi & \cos\phi \end{bmatrix} \begin{bmatrix} \cos\theta & 0 & -\sin\theta \\ 0 & 1 & 0 \\ \sin\theta & 0 & \cos\theta \end{bmatrix} \begin{bmatrix} \cos\psi & \sin\psi & 0 \\ -\sin\psi & \cos\psi & 0 \\ 0 & 0 & 1 \end{bmatrix} \begin{Bmatrix} 0 \\ 0 \\ \dot{\psi} \end{Bmatrix} \tag{A.5}$$

Combining and reducing terms in Equation A.5 allows for the derivation of Equation A.6 in terms of the angular velocity vector.

$$\begin{Bmatrix} p \\ q \\ r \end{Bmatrix} = \begin{bmatrix} 1 & 0 & -\sin\theta \\ 0 & \cos\phi & \sin\phi\cos\theta \\ 0 & -\sin\phi & \cos\phi\cos\theta \end{bmatrix} \begin{Bmatrix} \dot{\phi} \\ \dot{\theta} \\ \dot{\psi} \end{Bmatrix} \tag{A.6}$$

Inverting Equation A.6 gives the Euler rates in terms of pitch, roll, and yaw rates respectively. Equation A.6 is a non-orthogonal three by three element matrix. Therefore, the implementation of matrix inverse operations is required to obtain the transformation matrix given in Equation A.7. Equation A.7 displays the mathematical phenomenon known as Gimbal Lock where $\dot{\phi}$ and $\dot{\psi}$ may not be computed due to the divide by zero singularity occurring when two axes become aligned with one another. Matrix inversion operations may be performed using the steps provided in any linear algebra or matrices book such as [40] and therefore are not provided explicitly in this work.

$$\begin{Bmatrix} \dot{\phi} \\ \dot{\theta} \\ \dot{\psi} \end{Bmatrix} = \begin{bmatrix} 1 & \sin\phi\sin\theta/\cos\theta & \cos\phi\sin\theta/\cos\theta \\ 0 & \cos\phi & -\sin\phi \\ 0 & \sin\phi/\cos\theta & \cos\phi/\cos\theta \end{bmatrix} \begin{Bmatrix} p \\ q \\ r \end{Bmatrix} \tag{A.7}$$

Appendix B

Quaternion Mathematics

This section of the Appendix provides additional mathematical background for quaternion operations, relationships, and transformations taken from [4], [28], [35], and [37].

B.1 Quaternion Algebra

A general quaternion, {Q}, is defined as Equation B.1 in the hypercomplex form.

$$\{Q\} = q_0 + q_x\hat{i} + q_y\hat{j} + q_z\hat{k} \tag{B.1}$$

Where q_0, q_x, q_y, and q_z are scalars and i, j, and k are unit vectors in Cartesian space. Given a scalar constant, C, multiplication of a quaternion by a scalar constant is shown in Equation B.2.

$$C\{Q\} = Cq_0 + Cq_x\hat{i} + Cq_y\hat{j} + Cq_z\hat{k} \tag{B.2}$$

If another quaternion, {P}, is defined in the hypercomplex form shown as Equation B.3, multiplication of two quaternions may be performed by following the quaternion multiplication rules given in Figure B.1.

$$\{P\} = p_0 + p_x\hat{i} + p_y\hat{j} + p_z\hat{k} \tag{B.3}$$

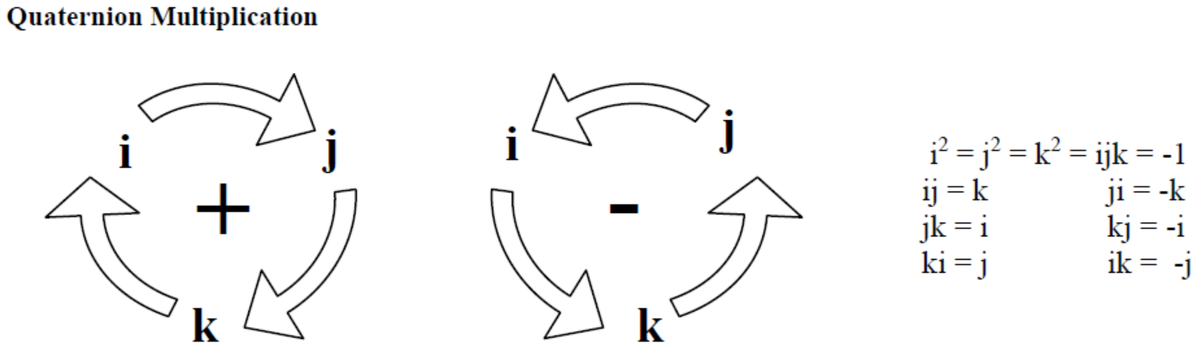

$i^2 = j^2 = k^2 = ijk = -1$

$ij = k$	$ji = -k$
$jk = i$	$kj = -i$
$ki = j$	$ik = -j$

Figure B.1: Rules for Quaternion Multiplication [35]

The product of two quaternions follows the distributive law. Therefore, the quaternion product of {Q} and {P} may be displayed as Equation (B.4).

$$\begin{aligned}\{Q\}\otimes\{P\} &= (q_0 + q_x\hat{i} + q_y\hat{j} + q_z\hat{k})\otimes(p_0 + p_x\hat{i} + p_y\hat{j} + p_z\hat{k})\\ &= (q_0p_0 - q_xp_x - q_yp_y - q_zp_z)\\ &+ (q_0p_x + q_xp_0 + q_yp_z - q_zp_y)\hat{i}\\ &+ (q_0p_y - q_xp_z + q_yp_0 + q_zp_x)\hat{j}\\ &+ (q_0p_z + q_xp_y - q_yp_x + q_zp_0)\hat{k}\end{aligned} \tag{B.4}$$

Quaternions possess properties of both scalars and vectors, but also contain similarities common with complex algebra. The magnitude of a quaternion may be defined in the same manner as a complex number or vector as shown in Equation B.5.

$$\left|\{Q\}\right| = \sqrt{q_0^2 + q_x^2 + q_y^2 + q_z^2} \tag{B.5}$$

The conjugate of the quaternion may be defined as Equation B.6.

$$\{Q\}^* = q_0 - q_x\hat{i} - q_y\hat{j} - q_z\hat{k} \tag{B.6}$$

Similar to a complex variable, the product of quaternion with its conjugate generates a scalar equal to the square of the magnitude of the quaternion as shown in Equation B.7.

$$\{Q\}\otimes\{Q\}^* = q_0^2 + q_x^2 + q_y^2 + q_z^2 = \left|\{Q\}\right|^2 \tag{B.7}$$

The derivation of the quaternion inverse is shown in the following derivation.

Given $Q^{-1}Q = QQ^{-1} = 1$ *by definition of the inverse*

Multiply by the quaternion conjugate $\{Q\}^*$

$Q^{-1}Q\{Q\}^* = \{Q\}^*QQ^{-1} = \{Q\}^*$

Therefore because $\{Q\}^*\{Q\}$ *equals the square of the norm*, $N(Q)$

$$Q^{-1} = \frac{\{Q\}^*}{N^2(Q)}$$

Because the unit quaternion is used

the norm is equal to 1. *Therefore*:

$Q^{-1} = \{Q\}^*$

B.2 Relationship between the Quaternion and Euler Angles

It is necessary in aircraft simulations to be able to relate the quaternion to the Euler angles. Such a relationship may be established from Equation 2.44 in Section 2.1.4 and is utilized as the starting point in this section.

$$\begin{bmatrix} q_x^2+q_0^2-q_y^2-q_z^2 & 2(q_xq_y+q_zq_0) & 2(q_xq_z-q_yq_0) \\ 2(q_xq_y-q_zq_0) & q_y^2+q_0^2-q_x^2-q_z^2 & 2(q_yq_z-q_xq_0) \\ 2(q_xq_z+q_yq_0) & 2(q_yq_z-q_xq_0) & q_z^2+q_0^2-q_x^2-q_y^2 \end{bmatrix} = \begin{bmatrix} c\theta c\psi & c\theta s\psi & -s\theta \\ s\phi s\theta c\psi - c\phi s\psi & s\phi s\theta s\psi + c\phi c\psi & s\phi c\theta \\ \mathrm{c}\phi \mathrm{s}\theta \mathrm{c}\psi + s\phi s\psi & c\phi s\theta s\psi - s\phi c\psi & c\phi c\theta \end{bmatrix} \tag{B.8}$$

By combining the diagonal elements of Equation B.8 with the understanding that the magnitude of the quaternion must be equal to 1, a 4x4 algebraic equation for the squares of the quaternion components may be obtained and is shown as Equation B.9.

$$\begin{bmatrix} 1 & 1 & -1 & -1 \\ 1 & -1 & 1 & -1 \\ 1 & -1 & -1 & 1 \\ 1 & 1 & 1 & 1 \end{bmatrix} \begin{Bmatrix} q_0^2 \\ q_x^2 \\ q_y^2 \\ q_z^2 \end{Bmatrix} = \begin{Bmatrix} \cos\theta\cos\psi \\ \sin\phi\sin\theta\sin\psi + \cos\phi\cos\psi \\ \cos\phi\cos\theta \\ 1 \end{Bmatrix} \tag{B.9}$$

The matrix equation is readily solved by direct elimination yielding Equation B.10.

$$\begin{Bmatrix} q_0^2 \\ q_x^2 \\ q_y^2 \\ q_z^2 \end{Bmatrix} = \frac{1}{4}\begin{Bmatrix} 1+\cos\theta\cos\psi+\sin\phi\sin\theta\sin\psi+\cos\phi\cos\theta+\cos\phi\cos\psi \\ 1-\cos\phi\cos\theta-\sin\phi\sin\theta\sin\psi-\cos\phi\cos\psi+\cos\theta\cos\psi \\ 1-\cos\theta\cos\psi-\cos\phi\cos\theta+\sin\phi\sin\theta\sin\psi+\cos\phi\cos\psi \\ 1-\cos\theta\cos\psi+\cos\phi\cos\theta-\sin\phi\sin\theta\sin\psi-\cos\phi\cos\psi \end{Bmatrix} \tag{B.10}$$

Implementing half-angle identities, Equation B.10 may be written as Equation B.11.

$$\begin{Bmatrix} q_0^2 \\ q_x^2 \\ q_y^2 \\ q_z^2 \end{Bmatrix} = \begin{Bmatrix} \left(C\phi/2C\theta/2C\psi/2+S\phi/2S\theta/2S\psi/2\right)^2 \\ \left(S\phi/2C\theta/2C\psi/2-C\phi/2S\theta/2S\psi/2\right)^2 \\ \left(C\phi/2S\theta/2C\psi/2+S\phi/2C\theta/2S\psi/2\right)^2 \\ \left(S\phi/2S\theta/2C\psi/2-C\phi/2C\theta/2S\psi/2\right)^2 \end{Bmatrix} \tag{B.11}$$

Extracting the off-diagonal elements of Equation B.8 produces Equation B.12.

$$\begin{bmatrix} 0 & 0 & 2 & 2 & 0 & 0 \\ 0 & 0 & -2 & 2 & 0 & 0 \\ 0 & -2 & 0 & 0 & 2 & 0 \\ 0 & 2 & 0 & 0 & 2 & 0 \\ 2 & 0 & 0 & 0 & 0 & 2 \\ -2 & 0 & 0 & 0 & 0 & 2 \end{bmatrix} \begin{Bmatrix} q_0q_x \\ q_0q_y \\ q_0q_z \\ q_xq_y \\ q_xq_z \\ q_yq_z \end{Bmatrix} = \begin{Bmatrix} \cos\theta\sin\psi \\ \sin\phi\sin\theta\cos\psi-\cos\phi\sin\psi \\ -\sin\theta \\ \cos\phi\sin\theta\cos\psi+\sin\phi\sin\psi \\ \sin\phi\cos\theta \\ \cos\phi\sin\theta\sin\psi-\sin\phi\cos\psi \end{Bmatrix} \tag{B.12}$$

This algebraic system may be solved by adding and subtracting appropriate pairs of equations giving way to Equation B.13. Therefore, s_0, s_x, s_y, and s_z are the unknown signs of the quaternion.

$$\begin{Bmatrix} q_0q_x \\ q_0q_y \\ q_0q_z \\ q_xq_y \\ q_xq_z \\ q_yq_z \end{Bmatrix} = \frac{1}{4}\begin{Bmatrix} \sin\phi\cos\theta - \cos\phi\sin\theta\sin\psi + \sin\phi\cos\psi \\ \cos\phi\sin\theta\cos\psi + \sin\phi\sin\psi + \sin\theta \\ \cos\theta\sin\psi - \sin\phi\sin\theta\cos\psi + \cos\phi\sin\psi \\ \cos\theta\sin\psi + \sin\phi\sin\theta\cos\psi - \cos\phi\sin\psi \\ \cos\phi\sin\theta\cos\psi + \sin\phi\sin\psi - \sin\theta \\ \sin\phi\cos\theta + \cos\phi\sin\theta\sin\psi - \sin\phi\cos\psi \end{Bmatrix} \tag{B.13}$$

Therefore, the off-diagonal elements of Equation B.8 provide only three additional pieces of information given by Equation B.14.

$$\begin{aligned} s_0s_x &= 1 \\ s_0s_y &= 1 \\ s_0s_z &= -1 \end{aligned} \tag{B.14}$$

Applying this information with Equation B.11 produces Equation 2.45 and is shown again here as Equation B.15.

$$\begin{Bmatrix} q_0 \\ q_x \\ q_y \\ q_z \end{Bmatrix} = \pm\begin{Bmatrix} c_{\phi/2}c_{\theta/2}c_{\psi/2} + s_{\phi/2}s_{\theta/2}s_{\psi/2} \\ s_{\phi/2}c_{\theta/2}c_{\psi/2} - c_{\phi/2}s_{\theta/2}s_{\psi/2} \\ c_{\phi/2}s_{\theta/2}c_{\psi/2} + s_{\phi/2}c_{\theta/2}s_{\psi/2} \\ s_{\phi/2}s_{\theta/2}c_{\psi/2} - c_{\phi/2}c_{\theta/2}s_{\psi/2} \end{Bmatrix} \tag{B.15}$$

B.3 Quaternion Calculus

Beginning with Equation 2.27 from Section 2.1.4 and restating it here as Equation B.16 yields,

$$Q = \begin{Bmatrix} q_0 \\ q_x \\ q_y \\ q_z \end{Bmatrix} = \begin{Bmatrix} \cos(\Theta/2) \\ E_x \sin(\Theta/2) \\ E_y \sin(\Theta/2) \\ E_z \sin(\Theta/2) \end{Bmatrix} = q_0 + (q_x)\hat{i} + (q_y)\hat{j} + (q_z)\hat{k} = \begin{Bmatrix} q_0 \\ q \end{Bmatrix} \tag{B.16}$$

Equation B.16 may be differentiated yielding the time rate of change of the Euler-Rodrigues symmetric parameters with respect to the time rate of change of the Euler axis parameters as shown in Equation B.17.

$$\begin{Bmatrix} \dot{q}_0 \\ \dot{q}_x \\ \dot{q}_y \\ \dot{q}_z \end{Bmatrix} = \begin{Bmatrix} -\sin(\Theta/2) \\ E_x \cos(\Theta/2) \\ E_y \cos(\Theta/2) \\ E_z \cos(\Theta/2) \end{Bmatrix} \frac{\dot{\Theta}}{2} + \begin{Bmatrix} 0 \\ \dot{E}_x \sin(\Theta/2) \\ \dot{E}_y \sin(\Theta/2) \\ \dot{E}_z \sin(\Theta/2) \end{Bmatrix} \tag{B.17}$$

Applying Equation B.16 yields,

$$\begin{Bmatrix} \dot{q}_0 \\ \dot{q}_x \\ \dot{q}_y \\ \dot{q}_z \end{Bmatrix} = \frac{1}{2} \begin{bmatrix} -q_x & -q_y & -q_z \\ q_0 & -q_z & q_y \\ q_z & q_0 & -q_x \\ -q_y & q_x & q_0 \end{bmatrix} \begin{Bmatrix} p \\ q \\ r \end{Bmatrix} \tag{B.18}$$

Equation B.18 is linear in both the noninertial angular rates and Euler-Rodrigues symmetric parameters. Therefore, it may be written as the form given previously as Equations 2.50 and 2.51 in Section 2.1.4.

$$\begin{Bmatrix} \dot{q}_0 \\ \dot{q}_x \\ \dot{q}_y \\ \dot{q}_z \end{Bmatrix} = \frac{1}{2} \begin{bmatrix} 0 & -p & -q & -r \\ p & 0 & r & -q \\ q & -r & 0 & p \\ r & q & -p & 0 \end{bmatrix} \begin{Bmatrix} q_0 \\ q_x \\ q_y \\ q_z \end{Bmatrix} \tag{B.19}$$

Derivation of the Quaternion Integral with Constant Rotation

Beginning with Equation 2.50 we have:

$$\{\dot{Q}\} = [\mathrm{K}]\{Q\} = 0 \tag{B.20}$$

Such that:

$$K = \frac{1}{2}\begin{Bmatrix} 0 & -\vec{\omega}^T \\ \vec{\omega} & -[\vec{\omega}\times] \end{Bmatrix} = \frac{1}{2}\begin{Bmatrix} 0 & -p & -q & -r \\ p & 0 & r & -q \\ q & -r & 0 & p \\ r & q & -p & 0 \end{Bmatrix} \tag{B.21}$$

$$With: \quad \vec{\omega} = [p \ q \ r]^T$$

$$[\vec{\omega}\times] = \begin{bmatrix} 0 & -r & q \\ r & 0 & -p \\ -q & p & 0 \end{bmatrix} \tag{B.22}$$

We may then solve utilizing the first order separable homogenous differential equation techniques:

$$\frac{\dot{Q}}{Q} = K \tag{B.23}$$

$$\int \frac{\dot{Q}}{Q}\, dt = \int K \; dt$$

$$\ln(Q) = Kt + C$$

$$Q = C\exp[Kt]$$

(B.24)

Where C is a constant with the value $Q_{t=t0}$ and exp represents the matrix exponential. The scalar and matrix expansion series expressions may be written as:

Scalar:

$$e^x = \exp[x] = 1 + x + \frac{x^2}{2!} + \frac{x^3}{3!} \cdots + \frac{x^n}{n!}$$

(B.25)

Matrix:

$$e^A = \exp[A] = I_{nxn} + A + \frac{AA}{2!} + \frac{AAA}{3!} + \cdots$$

$$Where: \; I \; is \; the \; Identity \; Matrix$$

(B.26)

Allowing A = Kt gives the following derivation by means of direct matrix multiplication of Equation B.21:

$$KK = -\frac{1}{4}\left|\vec{\omega}\right|^2 \mathbf{I}_{4x4}$$

$$Where: \left|\vec{\omega}\right| = \sqrt{p^2 + q^2 + r^2}$$

(B.27)

Applying Equation 2.27’s relationship and grouping the odd and even terms from the series expansion of the matrix exponential develops the following relationships:

$$e^{Kt} = \mathbf{I}_{4x4}\left(1 - \frac{\lambda^2}{2!} + \frac{\lambda^4}{4!} + \cdots\right) + \frac{2}{w}K\left(\lambda - \frac{\lambda^3}{3!} + \frac{\lambda^5}{5!} + \cdots\right)$$

$$Where: \; \lambda = \frac{\left|\vec{\omega}\right| t}{2}$$

(B.28)

Inputting trigonometric relationships for the series expansions allows Equation B.28 to become Equation B.29.

$$e^{Kt} = \left[\mathbf{I}_{4x4} \cos\left(\frac{\omega t}{2}\right) + \frac{2K}{\omega} \sin\left(\frac{\omega t}{2}\right) \right] \tag{B.29}$$

Equation B.24 then becomes Equation 2.52 and is presented as Equation B.30.

$$Q = \left[\mathbf{I}_{4x4} \cos\left(\frac{\omega t}{2}\right) + \frac{2K}{\omega} \sin\left(\frac{\omega t}{2}\right) \right] Q_{t=t_0} \tag{B.30}$$

Quaternion Integration Example

Integration of a quaternion, $Q_{t=t_0}$, with the initial conditions of the Euler angles set equal to zero and undergoing a constant rotation, $\vec{\omega}$, over time, t, results in the following solution sequence.

$$Q_{t=t_0} = \pm \begin{Bmatrix} c_{\phi/2}c_{\theta/2}c_{\psi/2} + s_{\phi/2}s_{\theta/2}s_{\psi/2} \\ s_{\phi/2}c_{\theta/2}c_{\psi/2} - c_{\phi/2}s_{\theta/2}s_{\psi/2} \\ c_{\phi/2}s_{\theta/2}c_{\psi/2} + s_{\phi/2}c_{\theta/2}s_{\psi/2} \\ s_{\phi/2}s_{\theta/2}c_{\psi/2} - c_{\phi/2}c_{\theta/2}s_{\psi/2} \end{Bmatrix} = \begin{Bmatrix} 1 \\ 0 \\ 0 \\ 0 \end{Bmatrix}$$

$$\vec{\omega} = [p\ q\ r]^T$$

$$\omega = \sqrt{p^2 + q^2 + r^2}$$

$$Q = \left[\mathbf{I}_{4x4} \cos\left(\frac{\omega t}{2}\right) + \frac{2K}{\omega} \sin\left(\frac{\omega t}{2}\right) \right] Q_{t=t_0}$$

$$Q = \begin{Bmatrix} \cos\left(\dfrac{\omega t}{2}\right) \\ \left(\dfrac{p}{\omega}\right)\sin\left(\dfrac{\omega t}{2}\right) \\ \left(\dfrac{q}{\omega}\right)\sin\left(\dfrac{\omega t}{2}\right) \\ \left(\dfrac{r}{\omega}\right)\sin\left(\dfrac{\omega t}{2}\right) \end{Bmatrix}$$

B.4 Quaternion Rotation Sequences

B.4.1 “3-2-1” Standard Aircraft Rotation Sequence [37]

The “3-2-1” standard Euler angle aircraft rotation sequence is shown in Figure B.2.

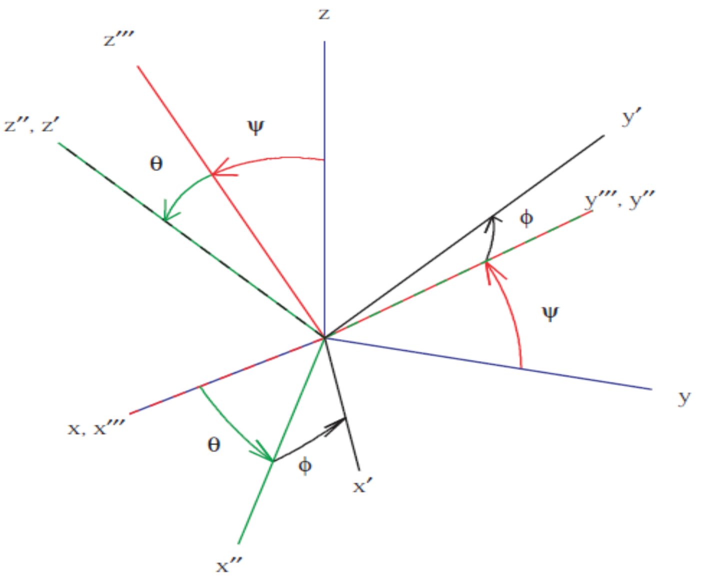

Figure B.2: Euler Angle “3-2-1” Sequence [37]

The quaternion dynamic transformation model for a standard aircraft “3-2-1” rotation is given by Equation B.31.

$$\begin{Bmatrix} \dot{q}_0 \\ \dot{q}_x \\ \dot{q}_y \\ \dot{q}_z \end{Bmatrix} = \frac{1}{2} \begin{bmatrix} -q_x & -q_y & -q_z \\ q_0 & -q_z & q_y \\ q_z & q_0 & -q_x \\ -q_y & q_x & q_0 \end{bmatrix} \begin{Bmatrix} p \\ q \\ r \end{Bmatrix} \tag{B.31}$$

The initial conditions of the "3-2-1" rotation and the conversion from quaternion formulation to Euler angle convention are given as Equations B.32 and B.33 respectively.

$$\begin{aligned}
q_0(0) &= \cos\left(\frac{\psi}{2}\right)\cos\left(\frac{\theta}{2}\right)\cos\left(\frac{\phi}{2}\right) + \sin\left(\frac{\psi}{2}\right)\sin\left(\frac{\theta}{2}\right)\sin\left(\frac{\phi}{2}\right) \\
q_x(0) &= \cos\left(\frac{\psi}{2}\right)\cos\left(\frac{\theta}{2}\right)\sin\left(\frac{\phi}{2}\right) - \sin\left(\frac{\psi}{2}\right)\sin\left(\frac{\theta}{2}\right)\cos\left(\frac{\phi}{2}\right) \\
q_y(0) &= \cos\left(\frac{\psi}{2}\right)\sin\left(\frac{\theta}{2}\right)\cos\left(\frac{\phi}{2}\right) + \sin\left(\frac{\psi}{2}\right)\cos\left(\frac{\theta}{2}\right)\sin\left(\frac{\phi}{2}\right) \\
q_z(0) &= \sin\left(\frac{\psi}{2}\right)\cos\left(\frac{\theta}{2}\right)\cos\left(\frac{\phi}{2}\right) - \cos\left(\frac{\psi}{2}\right)\sin\left(\frac{\theta}{2}\right)\sin\left(\frac{\phi}{2}\right)
\end{aligned} \tag{B.32}$$

$$\begin{aligned}
\theta &= \arcsin(q_0 q_y - q_x q_z) \\
\phi &= \arctan\left(\frac{2(q_0 q_x + q_y q_z)}{1 - 2(q_x^2 + q_y^2)}\right) \\
\psi &= \arctan\left(\frac{2(q_0 q_z + q_x q_y)}{1 - 2(q_y^2 + q_z^2)}\right)
\end{aligned} \tag{B.33}$$

B.4.2 “1-2-3” Standard Spacecraft Rotation Sequence [37]

The “1-2-3” standard Euler angle spacecraft rotation sequence is shown in Figure B.3.

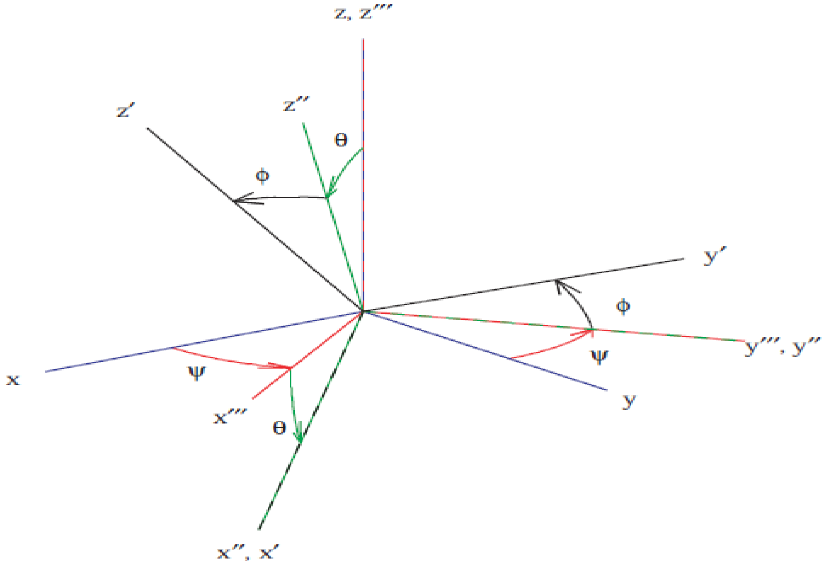

Figure B.3: Euler Angle “1-2-3” Sequence [37]

The quaternion dynamic transformation model for a standard aircraft “1-2-3” rotation is given by Equation B.34.

$$\begin{Bmatrix} \dot{q}_0 \\ \dot{q}_x \\ \dot{q}_y \\ \dot{q}_z \end{Bmatrix} = \frac{1}{2} \begin{bmatrix} -q_z & -q_y & -q_x \\ q_y & -q_z & q_0 \\ q_x & q_0 & -q_z \\ -q_0 & q_x & q_y \end{bmatrix} \begin{Bmatrix} p \\ q \\ r \end{Bmatrix} \tag{B.34}$$

The initial conditions of the “1-2-3” rotation and the conversion from quaternion formulation to Euler angle convention are given as Equations B.35 and B.36 respectively.

$$\begin{aligned} q_0(0) &= \sin\left(\frac{\phi}{2}\right)\cos\left(\frac{\theta}{2}\right)\cos\left(\frac{\psi}{2}\right) + \cos\left(\frac{\phi}{2}\right)\sin\left(\frac{\theta}{2}\right)\sin\left(\frac{\psi}{2}\right) \\ q_x(0) &= \cos\left(\frac{\phi}{2}\right)\sin\left(\frac{\theta}{2}\right)\cos\left(\frac{\psi}{2}\right) - \sin\left(\frac{\phi}{2}\right)\cos\left(\frac{\theta}{2}\right)\sin\left(\frac{\psi}{2}\right) \\ q_y(0) &= \cos\left(\frac{\phi}{2}\right)\cos\left(\frac{\theta}{2}\right)\sin\left(\frac{\psi}{2}\right) + \sin\left(\frac{\phi}{2}\right)\sin\left(\frac{\theta}{2}\right)\cos\left(\frac{\psi}{2}\right) \\ q_z(0) &= \cos\left(\frac{\phi}{2}\right)\cos\left(\frac{\theta}{2}\right)\cos\left(\frac{\psi}{2}\right) - \sin\left(\frac{\phi}{2}\right)\sin\left(\frac{\theta}{2}\right)\sin\left(\frac{\psi}{2}\right) \end{aligned} \tag{B.35}$$

$$\begin{aligned}
\theta &= \arcsin(q_0 q_y + q_x q_z) \\
\phi &= \arctan 2\left(\frac{-2(q_x q_y - q_0 q_z)}{-q_0^2 - q_x^2 + q_y^2 + q_z^2}\right) \\
\psi &= \arctan 2\left(\frac{-2(q_0 q_x - q_y q_z)}{q_0^2 - q_x^2 - q_y^2 + q_z^2}\right)
\end{aligned} \tag{B.36}$$

Appendix C

Extended Kalman Filter Supplement

C.1 Statistical Information [6, 28, 30, 31, 41, 43]

A summation of the calculation of the statistical variables and nomenclature utilized in the construction of the extended Kalman filter are presented in Table C.1.

Variable	Process	Description
$\mathbf{x}$	Measured/Estimated	State Vector
x	Measured/Estimated	State Scalar
$w \sim N(0,Q)$	Random Number	Normal distribution between 0 and Q
$\mu = E\{x\}$	$\int_{-\infty}^{\infty} xpdf[x,t]dx$	Mean of x
$\sigma^2 = V\{x\}$	$\int_{-\infty}^{\infty} (x-\mu)^2 pdf[x,t]dx$	Variance of x
σ	$\sqrt{V\{x\}}$	Standard Deviation of x
P	$E\left\{\left(\hat{\mathbf{x}} - \mathbf{x}\right)\left(\hat{\mathbf{x}} - \mathbf{x}\right)^T\right\}$	State Error Covariance Matrix
Q	$\begin{bmatrix} E\{p^2\} & E\{pq\} \\ E\{pq\} & E\{q^2\} \end{bmatrix}$	Process Noise Covariance
R	$E\left\{(x-\mu)(x-\mu)^T\right\}$	Measurement Noise Covariance

Table C.1: Summary of Statistical Variables

The most commonly accepted distribution for state estimation utilizes the Gaussian random process. For a scalar, x, the Gaussian or normal probability density function is shown as Equation C.1 and for a multidimensional case for a vector, X, Equation C.2 [41].

$$p(x) = \frac{1}{\sigma\sqrt{2\pi}} \exp\left[-\frac{(x-\mu)^2}{2\sigma^2}\right] \tag{C.1}$$

$$p(\mathbf{x}) = \frac{1}{\det[(2\pi R)]^{1/2}} \exp\left[-\frac{1}{2}(\mathbf{x}-\mu)^T R^{-1}(\mathbf{x}-\mu) \right] \tag{C.2}$$

The notation for this distribution is displayed as Equation C.3.

$$p(\mathbf{x}) \sim N(\mu, R) \tag{C.3}$$

The central limit theorem states a given distribution with mean, μ, and variance, σ^2, the sample distribution (regardless of the original shape of the distribution) will approach a Gaussian distribution with mean, μ, and variance, σ^2/N, as the sample size, N, continues to increase [41]. The limiting form of the distribution may be shown as Equation C.4.

$$Z = \frac{\overline{X} - \mu}{\sigma\sqrt{n}} \tag{C.4}$$

For a zero-mean Gaussian white-noise process, the following properties hold true:

$$\begin{gathered} E\{\mathbf{x}\} = \mu = 0 \\ \sigma^2 = E\{(x-\mu)^2\} \end{gathered} \tag{C.5}$$

For a normal or Gaussian distribution with a mean, μ, and standard deviation, σ, the probabilities associated with a normal or Gaussian distribution are shown in Table C.2 [41].

Bounds	**Percentage of data within the Bounds**
$P(\mu-\sigma < X < \mu+\sigma)$	0.6827
$P(\mu-2\sigma < X < \mu+2\sigma)$	0.9545
$P(\mu-3\sigma < X < \mu+3\sigma)$	0.9973

Table C.2: Data Distribution for a Gaussian or Normal Distribution

C.2 Continuous to Discrete Transformation [30, 42, 43]

Continuous and discrete-time data measurements occur in different manners. While continuous-time domain measurements signify a collection of a continuous stream of data representing exactly what is being measured, in the same manner as an analog measurement, digital or discrete-time data measurements sample a continuous stream at discrete data points Creating a representation of a discrete-time signal in the continuous-time domain requires data utilized in discrete measurement collection to be extrapolated using recursive mathematical techniques or by being held constant. This is commonly known as a first-order and zero-order hold respectively. A first-order hold retains the value of the previous sample, along with the present sample, and predicts, by extrapolation the next sample value. A higher-order hold such as a second-order hold will reconstruct a signal more accurately; however, is subject to an undesirable time delay in the period.

The conversion process utilized in digital signal processing of a transformation from the continuous-time to discrete-time representation is accomplished through the use of a bilinear transformation or "Tustin Method's". The bilinear transformation is a first-order approximation of the natural logarithmic function mapping the z-plane to the s-plane given Equation C.6 and the sampling interval, T.

$$z = e^{sT} \tag{C.6}$$

The sampling interval is then used in the first-order Padé approximation given as Equation C.7.

$$z = e^{sT} \approx \frac{1}{1 - sT} \tag{C.7}$$

In discrete-time, the matrix, T_k, may be found by substituting "s" as a function of "z" This relationship uses the Laplace transform of the continuous-time matrix, $T(t)$, as shown in Equation C.8.

$$T_k = T(s)\big|_{s=f(z)} \tag{C.8}$$

The derivation method utilizes the Padé approximation as given in Equation C.9, where a zero-order hold is represented by n =1 and a first-order hold by n = 2.

$$s^n = \left(\frac{1 - z^{-1}}{T} \right)^n \tag{C.9}$$

The inverse of this mapping and the first-order bilinear approximation is shown in the sequence presented by Equation C.10.

$$\begin{aligned} s &= \frac{1}{T}\ln(z) \\ &\approx \frac{2}{T}\frac{z-1}{z+1} \\ &\approx \frac{2}{T}\frac{1-z^{-1}}{1+z^{-1}} \end{aligned} \tag{C.10}$$

An alternative approach to utilizing a Taylor-Series expansion of a fundamental matrix, Φ , for a system which uses a time invariant state transition matrix with no external input or noise may be used. In state-space formulation, the equation is given by

$$\dot{x} = Fx \tag{C.11}$$

The fundamental matrix is then used to propagate the state forward for any time, t_0 to t_f, as shown in Equations C.12 and C.13. Utilizing the inverse Laplace transform.

$$x(t) = \Phi(t - t_0)x(t_0) \tag{C.12}$$

$$\Phi(t) = \mathscr{L}^{-1}[(s\mathbf{I} - F)^{-1}] \tag{C.13}$$

Taking the inverse Laplace transform allows for the fundamental matrix, Φ , in continuous-time to be expressed and approximated through the use of a Taylor-Series expansion.

$$\Phi(t) = e^{Ft} = \mathbf{I} + Ft + \frac{(Ft)^2}{2!} + \frac{(Ft)^3}{3!} \cdots \frac{(Ft)^n}{n!} \tag{C.14}$$

The discrete-time fundamental matrix, Φ_k, may be determined by evaluating the continuous-time fundamental matrix at the sampling time, T_s, and with an approximation utilizing the first two terms of the Taylor-Series expansion.

$$\Phi_k = \Phi(T_s) \tag{C.15}$$

Appendix D

Two-Dimensional Accelerometer Array Supplement

D.1 Longitudinal Array Offsets

Accelerometer	Offset from Accelerometer #7 – Degrees (Radians)
1	-90 (-1.5708)
2	-75 (-1.3090)
3	-60 (-1.0472)
4	-45 (-.78540)
5	-30 (-.52360)
6	-15 (-.26180)
7	0 (0)
8	15 (-.26180)
9	30 (-.52360)
10	45 (-.78540)
11	60 (-1.0472)
12	75 (-1.3090)
13	90 (-1.5708)

Table D.1: Longitudinal Accelerometer Array Offsets [2, 6]

D.2 Transverse Array Offsets

Accelerometer	Offset from Accelerometer #1 – Degrees (Radians)
1	0 (0)
2	15 (.26180)
3	30 (.52360)
4	45 (.78540)
5	60 (1.0472)
6	75 (1.3090)
7	90 (1.5708)
8	105 (1.8326)
9	120 (2.0944)
10	135 (2.3562)
11	150 (2.6180)
12	165 (2.8798)
13	180 (3.1416)

Table D.2: Transverse Accelerometer Array Offsets

D.3 Resolution of Center-of-Gravity Acceleration to Device Location [23, 32]

For accurate and reliable operation of the two-dimensional accelerometer array, the acceleration experienced at the center-of-gravity of the vehicle must be resolved to the device accelerometer locations. Allow the inertial reference system to be represented as XYZ and the vehicle reference system to be represented as xyz for both translational and rotational systems. R is the position vector of the origin of the xyz system, where r and r' are position vectors of point P in the XYZ and xyz systems respectively. The variable, r, represents the distance from the inertial frame origin to a particular accelerometer on the device, while r' represents the distance from the vehicle's center-of-gravity to the same accelerometer location. The angular rotation rate is given as $\vec{\omega}$. These parameters are shown in Figure D.1 from [32]. The derivation utilized in this section assumes the vehicle to be a rigid-body with respect to the manner in which the device is mounted to the vehicle.

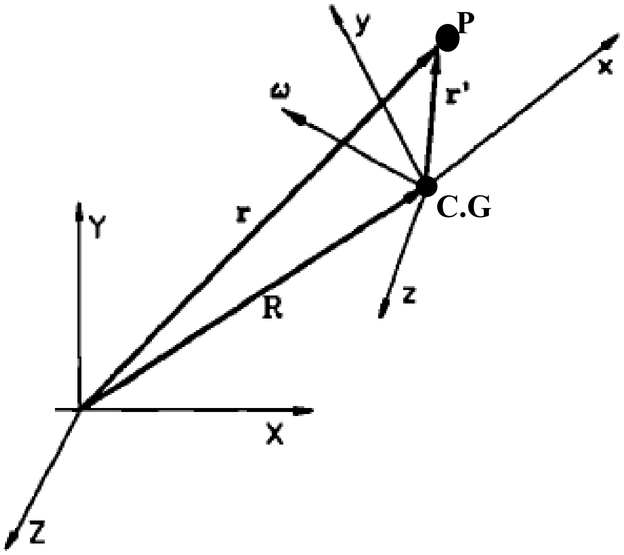

Figure D.1: Translational and Rotational Reference System Relative to an Inertial Frame of Reference [32]

Therefore

$$\vec{r} = \vec{R} + \vec{r}^{\,'} \tag{D.1}$$

Differentiating Equation D.1 with respect to time yields Equation D.2.

$$\begin{gathered}\dot{\vec{r}} = \dot{\vec{R}} + \dot{\vec{r}}^{\,'} + (\vec{\omega} \times \vec{r}^{\,'}) \\ \vec{v}_i = \dot{\vec{r}} = \dot{\vec{R}}' + \dot{\vec{r}}^{\,'} + (\vec{\omega} \times \vec{r}^{\,'})\end{gathered} \tag{D.2}$$

The variable v_i is the linear velocity term experienced by the ith accelerometer in the inertial coordinate frame system. Due to the rotation of the vehicle about the vehicle's center-of-gravity, the $\vec{\omega}\times\vec{r}^{\,'}$ term arises where $\vec{\omega}$ is the rotation rate vector of the vehicle. Differencing Equation D.2 gives the acceleration of the device in the reference coordinate frame where Equation D.3 results from the collection of like terms and the introduction of acceleration as the second derivative of position.

$$\ddot{\vec{r}} = \ddot{\vec{R}} + \ddot{\vec{r}}^{\,'} + \vec{\omega}\times\dot{\vec{r}}^{\,'} + \vec{\omega}\times\vec{r}^{\,'} + \vec{\omega}\times\dot{\vec{r}}^{\,'} + \vec{\omega}\times\vec{\omega}\times\vec{r}$$

$$\vec{a}_i = \ddot{\vec{r}} = \ddot{\vec{R}} + \ddot{\vec{r}}^{\,'} + 2(\vec{\omega}\times\dot{\vec{r}}^{\,'}) + \dot{\vec{\omega}}\times\vec{r}^{\,'} + \vec{\omega}\times\vec{\omega}\times\vec{r}^{\,'} \tag{D.3}$$

In Equation D.3, a_i represents the acceleration measured by the ith accelerometer in the inertial frame of reference. The derivatives of the vector, R, are the velocity and acceleration vectors experienced by the center-of-gravity, origin, and of the vehicle. Newton's second law must now be applied assuming there is no change in the mass of the vehicle.

$$\vec{F} = \frac{d}{dt}(m\vec{v}) = \cancel{\dot{m}}\vec{v} + m\dot{\vec{v}} = m\vec{a} \tag{D.4}$$

As stated previously, the vehicle is a rigid body. Therefore, r' is constant because it is the distance from the vehicle's center-of-gravity to the accelerometer locations along the device arrays. Thus, the subsequent derivatives are zero and Equations D.5 and D.6 may be brought about from Equation D.2 and D.3. Equations D.5 and D.6 define the velocity and acceleration at the accelerometer locations in the inertial coordinate frame when the translational velocity, acceleration of the vehicle's center-of-gravity, and the vehicle's rotational rates and distance from the vehicle's center-of-gravity to the device center-of-gravity are known precisely. The last term in Equation D.5 along with the last two terms in Equation D.6 is representative of the moment arm contribution to the measured velocity and acceleration of a displaced accelerometer.

$$\vec{v}_i = \vec{V}_{veh} + (\vec{\omega}\times\vec{r}^{\,'}) \tag{D.5}$$

$$\vec{a}_i = \ddot{\vec{R}} + \dot{\vec{\omega}}\times\vec{r}\,' + \vec{\omega}\times\vec{\omega}\times\vec{r}\,' = \vec{a}_{veh} + \dot{\vec{\omega}}\times\vec{r}\,' + \vec{\omega}\times\vec{\omega}\times\vec{r}\,' \tag{D.6}$$

In this work, resolution of the vehicle's accelerations at the center-of-gravity to the instrument location is considered only. Therefore, Equation D.5 is not utilized. The sensor coordinate frame axes for both the longitudinal and transverse accelerometer arrays are assumed to be orthogonal and only translated along the vehicle coordinate frame axes. Thus, carrying out the first cross-product for the ith accelerometer gives the following derivation as Equation D.7.

$$\dot{\vec{\omega}} \times r' = \begin{Bmatrix} \dot{p} \\ \dot{q} \\ \dot{r} \end{Bmatrix} \times \begin{Bmatrix} \bar{x}_i \\ \bar{y}_i \\ \bar{z}_i \end{Bmatrix} = \begin{vmatrix} \hat{i} & \hat{j} & \hat{k} \\ \dot{p} & \dot{q} & \dot{r} \\ \bar{x}_i & \bar{y}_i & \bar{z}_i \end{vmatrix} = \begin{Bmatrix} (\dot{q}\bar{z}_i - \dot{r}\bar{y}_i)\hat{i} \\ -(\dot{p}\bar{z}_i - \dot{r}\bar{x}_i)\hat{j} \\ (\dot{p}\bar{y}_i - \dot{q}\bar{x}_i)\hat{k} \end{Bmatrix} \tag{D.7}$$

$$Where: \begin{Bmatrix} \bar{x}_i \\ \bar{y}_i \\ \bar{z}_i \end{Bmatrix} = \begin{Bmatrix} Fuselage\ Station_{C.G} - Fuselage\ Station_{Vehicle\ C.G} \\ Buttline\ Station_{C.G} - Buttline\ Station_{Vehicle\ C.G} \\ Waterline\ Station_{C.G} - Waterline\ Station_{Vehicle\ C.G} \end{Bmatrix} \tag{D.8}$$

Performing the vector triple product gives the following derivation sequence as Equation D.9.

$$\vec{\omega} \times \vec{\omega} \times \vec{r}\,' = \begin{Bmatrix} p \\ q \\ r \end{Bmatrix} \times \begin{Bmatrix} p \\ q \\ r \end{Bmatrix} \times \begin{Bmatrix} \bar{x}_i \\ \bar{y}_i \\ \bar{z}_i \end{Bmatrix} = \begin{Bmatrix} p \\ q \\ r \end{Bmatrix} \times \begin{Bmatrix} (q\bar{z}_i - r\bar{y}_i)\hat{i} \\ -(p\bar{z}_i - r\bar{x}_i)\hat{j} \\ (p\bar{y}_i - q\bar{x}_i)\hat{k} \end{Bmatrix} =$$

$$\begin{vmatrix} \hat{i} & \hat{j} & \hat{k} \\ p & q & r \\ (q\bar{z}_i - r\bar{y}_i) & -(p\bar{z}_i - r\bar{x}_i) & (p\bar{y}_i - q\bar{x}_i) \end{vmatrix} = \begin{Bmatrix} \left(qp\bar{y}_i - q^2\bar{x}_i + rp\bar{z}_i - r^2\bar{x}_i\right)\hat{i} \\ -\left(p^2\bar{y}_i - pq\bar{x}_i - rq\bar{z}_i - r^2\bar{y}_i\right)\hat{j} \\ \left(-p^2\bar{z}_i + pr\bar{x}_i - q^2\bar{z}_i + qr\bar{y}_i\right)\hat{k} \end{Bmatrix}$$

$$Simplifying\ yields: \vec{\omega} \times \vec{\omega} \times \vec{r}\,' = \begin{Bmatrix} \left(-(q^2 + r^2)\bar{x}_i + pq\bar{y}_i + rp\bar{z}_i\right)\hat{i} \\ -\left(-pq\bar{x}_i + (p^2 + r^2)\bar{y}_i - rq\bar{z}_i\right)\hat{j} \\ \left(pr\bar{x}_i + qr\bar{y}_i - (q^2 + p^2)\bar{z}_i\right)\hat{k} \end{Bmatrix} \tag{D.9}$$

Substituting Equation D.7 and Equation D.9 into Equation D.6 allows for the acceleration of the vehicle's center-of-gravity to an ith accelerometer translated along the vehicle axes to be resolved and is shown as Equation D.10.

$$\vec{a}_i = \begin{Bmatrix} \vec{a}_x \\ \vec{a}_y \\ \vec{a}_z \end{Bmatrix}_{CG} + \begin{Bmatrix} -(q^2 + r^2) & (pq - \dot{r}) & (rp + \dot{q}) \\ (pq + \dot{r}) & -(p^2 - r^2) & (rq - \dot{p}) \\ (pr - \dot{q}) & (qr + \dot{p}) & -(p^2 + q^2) \end{Bmatrix} \begin{Bmatrix} \overline{x}_i \\ \overline{y}_i \\ \overline{z}_i \end{Bmatrix} \tag{D.10}$$

The proposed two-dimensional accelerometer array device possesses accelerometers rotated about the vehicle's primary and secondary axes. Therefore, a transformation must be applied to Equation D.10 to account for axis misalignment angles. Because the angular displacement of the accelerometers along each array from the vehicle axes are known, the use of the fixed-reference frame to body-fixed coordinate frame transformation may be applied where the vehicle coordinate frame becomes the reference frame and the accelerometer is the body being rotated from the reference coordinate frame. Applying the transformation, $T_{Earth-Body}$, previously from Equation 2.14 to Equation D.5 and D.6 gives Equations D.11 and D.12 respectively.

$$\vec{v}_{i,misalign} = T_{Earth-Body} * \left[\vec{V}_i + (\vec{\omega} \times \vec{r}\,') \right] \tag{D.11}$$

$$\vec{a}_{i,misalign} = T_{Earth-Body} * \left[\vec{a}_i + \dot{\vec{\omega}} \times \vec{r}\,' + \vec{\omega} \times \vec{\omega} \times \vec{r} \right] \tag{D.12}$$

Where the transformation, $T_{Earth-Body}$, is stated again using the misalignment angles of the ith accelerometer as shown in Equation D.13.

$$T_{Earth-Body} = \begin{bmatrix} \cos\theta_i \cos\psi_i & \cos\theta_i \sin\psi_i & -\sin\theta_i \\ \sin\phi_i \sin\theta_i \cos\psi_i - \cos\phi_i \sin\psi_i & \sin\phi_i \sin\theta_i \sin\psi_i + \cos\phi_i \cos\psi_i & \sin\phi_i \cos\theta_i \\ \cos\phi_i \sin\theta_i \cos\psi_i + \sin\phi_i \sin\psi_i & \cos\phi_i \sin\theta_i \sin\psi_i - \sin\phi_i \cos\psi_i & \cos\phi_i \cos\theta_i \end{bmatrix} \tag{D.13}$$

With the transformation equation, $T_{Earth-Body}$, now defined, the acceleration of the vehicle's center-of-gravity to the ith accelerometer for each vehicle axis may be resolved and are shown as Equations D.14, D.15, and D.16.

$$\vec{a}_{x,i\ misalign} = \vec{a}_{x,i} \left[\cos\theta_{x,i} \cos\psi_{x,i} \right] + \vec{a}_{y,i} \left[\cos\theta_{x,i} \sin\psi_{x,i} \right] - \vec{a}_{z,i} \left[\sin\theta_{x,i} \right] \tag{D.14}$$

$$\begin{aligned}\vec{a}_{y,i\ misalign} &= \vec{a}_{x,i}\left[\sin\phi_{y,i}\sin\theta_{y,i}\cos\psi_{y,i} - \cos\phi_{y,i}\sin\psi_{y,i}\right]\\ &+\vec{a}_{y,i}\left[\sin\phi_{y,i}\sin\theta_{y,i}\sin\psi_{y,i} + \cos\phi_{y,i}\cos\psi_{y,i}\right]\\ &+\vec{a}_{z,i}\left[\sin\phi_{y,i}\cos\theta_{y,i}\right]\end{aligned} \tag{D.15}$$

$$\begin{aligned}\vec{a}_{z,i\ misalign} &= \vec{a}_{x,i}\left[\cos\phi_{z,i}\sin\theta_{z,i}\cos\psi_{z,i} + \sin\phi_{z,i}\sin\psi_{z,i}\right]\\ &+\vec{a}_{y,i}\left[\cos\phi_{z,i}\sin\theta_{z,i}\sin\psi_{z,i} - \sin\phi_{z,i}\cos\psi_{z,i}\right]\\ &+\vec{a}_{z,i}\left[\cos\phi_{z,i}\cos\theta_{z,i}\right]\end{aligned} \tag{D.16}$$

Where:

$$\begin{aligned}\vec{a}_{x,i} &= \vec{a}_{x,CG} - (q^2 + r^2)\overline{x}_x + (pq - \dot{r})\overline{y}_x + (rp + \dot{q})\overline{z}_x\\ \vec{a}_{y,i} &= \vec{a}_{y,CG} + (pq + \dot{r})\overline{x}_y + (p^2 + r^2)\overline{y}_y - (rq + \dot{p})\overline{z}_y\\ \vec{a}_{z,i} &= \vec{a}_{z,CG} + (pr - \dot{q})\overline{x}_z + (qr - \dot{p})\overline{y}_z - (p^2 + q^2)\overline{z}_z\end{aligned} \tag{D.17}$$

D.4 Simulated Acceleration Measurements

The following are accelerometer measurements along the longitudinal accelerometer array, $gA_{z,i}$, and accelerometer measurements along the transverse accelerometer array, $gA_{y,i}$, for each aircraft simulation maneuver performed. The accelerometer measurements along each accelerometer array are shown with and without Gaussian noise inputs, where the variance of the accelerometer noise inputs were simulated at a value of 0.000015 gee^2.

Phase I – Longitudinal Maneuver with No Turbulence

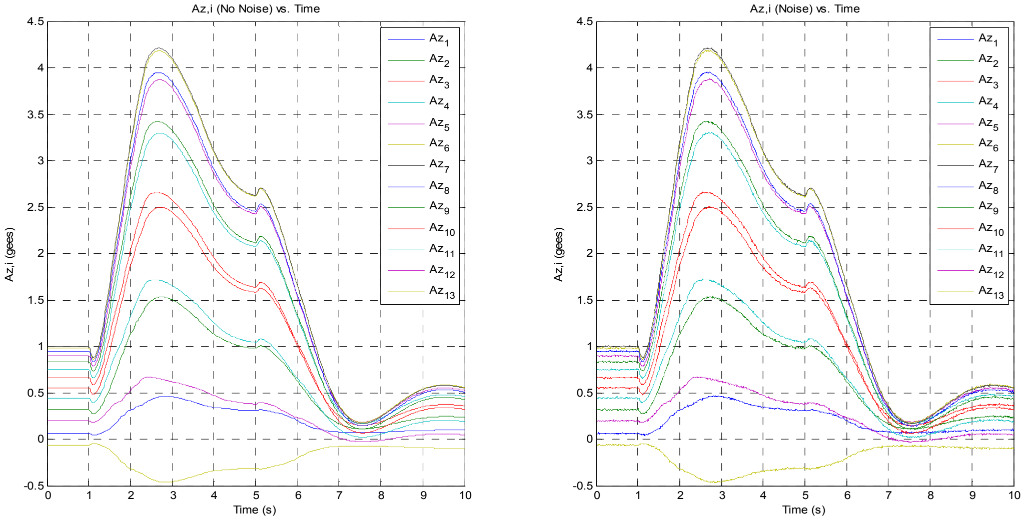

Figure D.2: Longitudinal Accelerometer Array Measurements – Phase I Nonlinear Aircraft Model

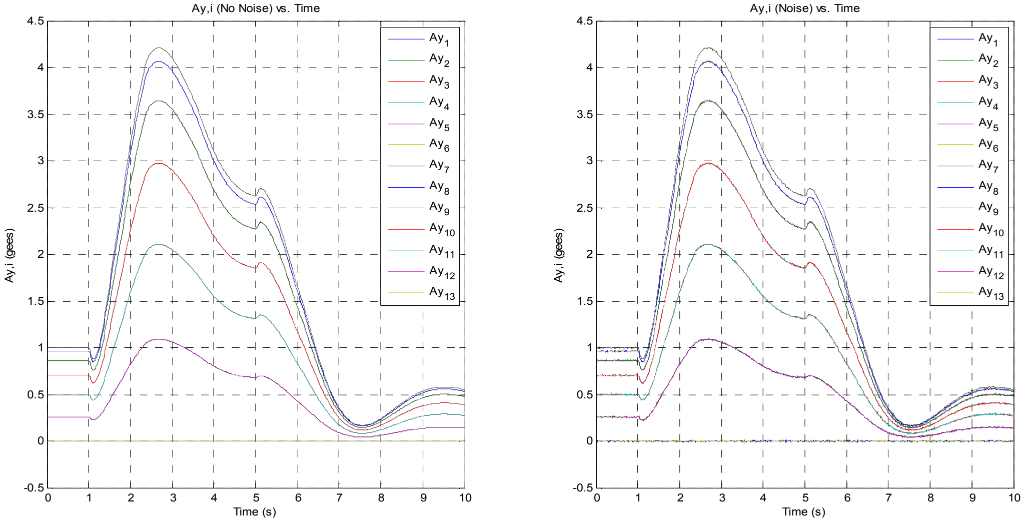

Figure D.3: Transverse Accelerometer Array Measurements – Phase I Nonlinear Aircraft Model

Phase I – Longitudinal Maneuver with Turbulence

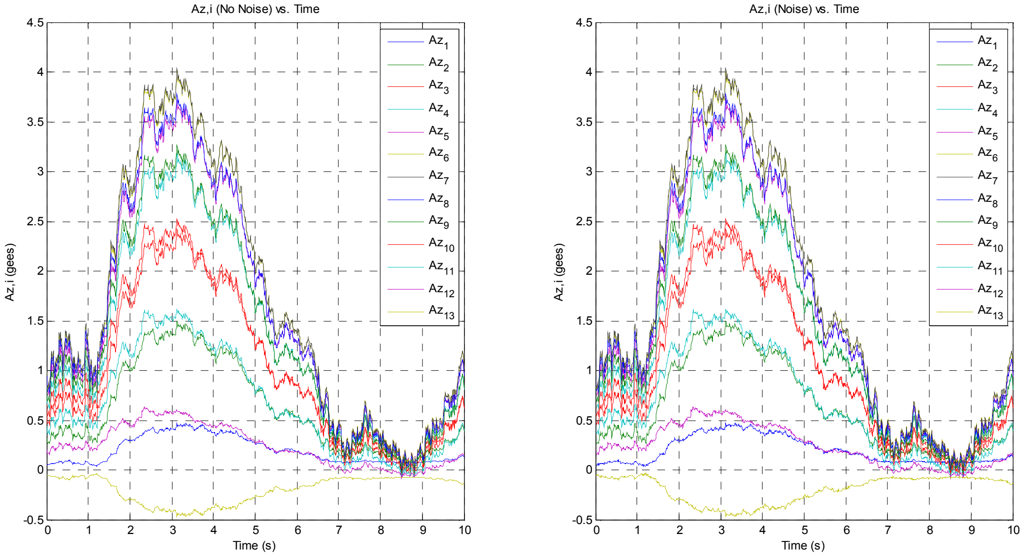

Figure D.4: Longitudinal Accelerometer Array Measurements – Phase I Nonlinear Aircraft Model with Turbulence

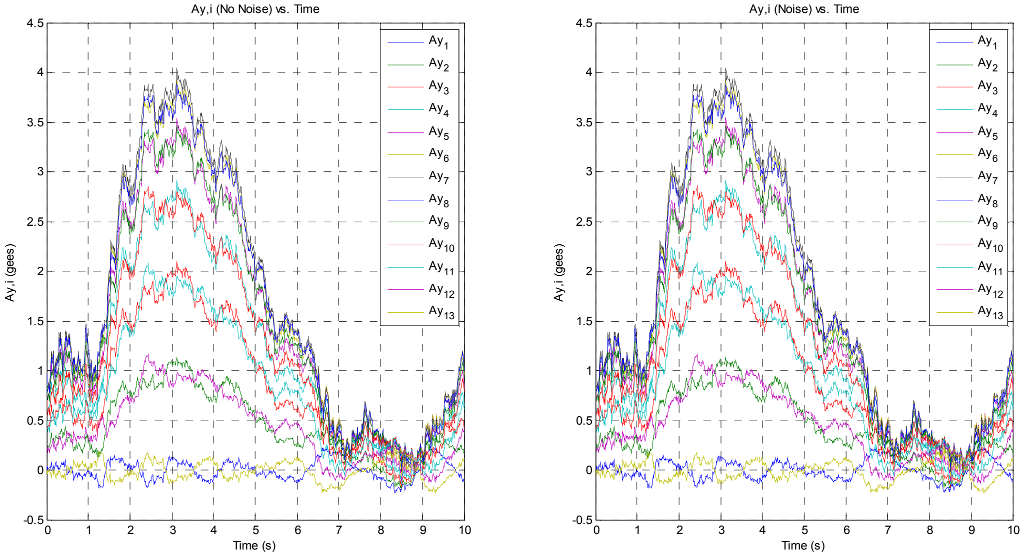

Figure D.5: Transverse Accelerometer Array Measurements – Phase I Nonlinear Aircraft Model with Turbulence

Phase II – Transverse Maneuver with No Turbulence

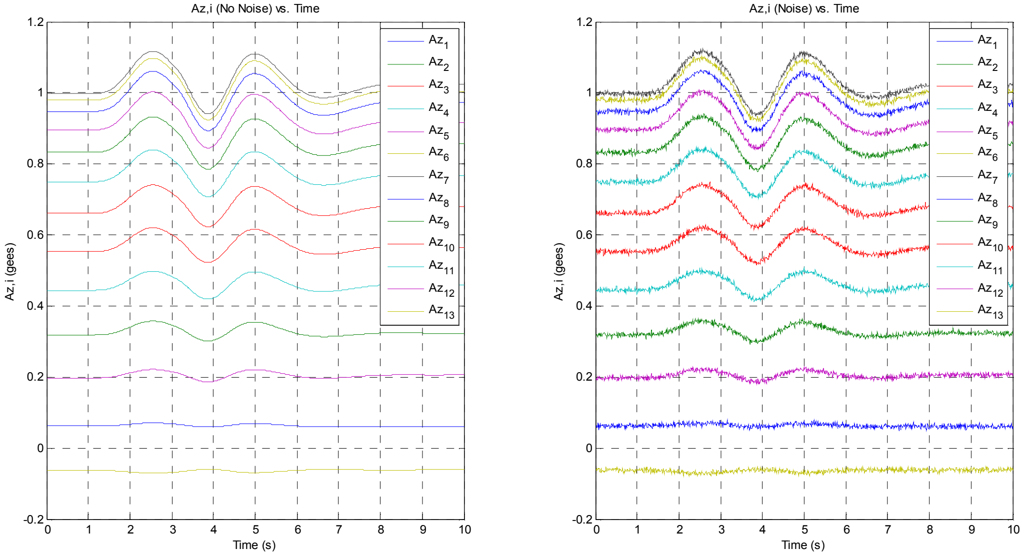

Figure D.6: Longitudinal Accelerometer Array Measurements –
Phase II Nonlinear Aircraft Model

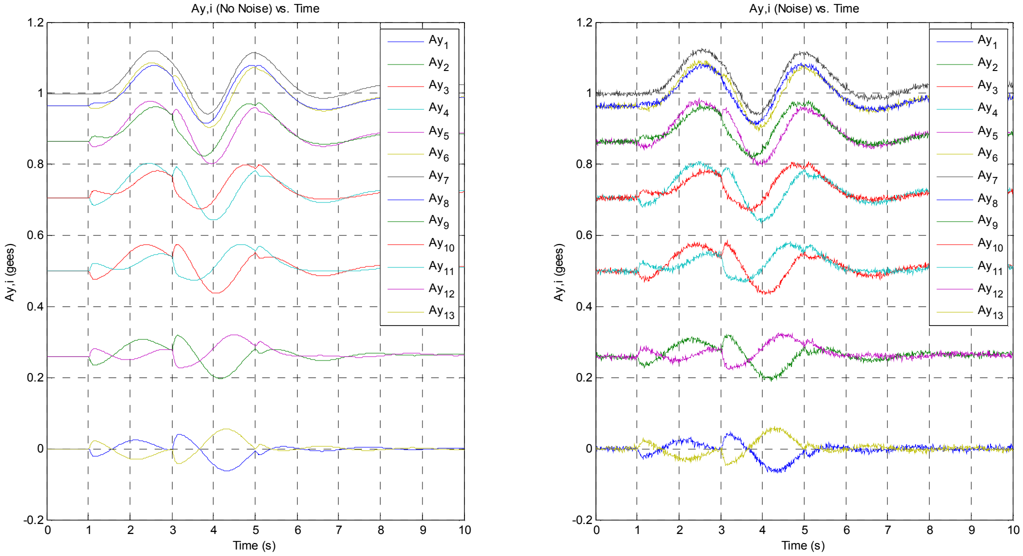

Figure D.7: Transverse Accelerometer Array Measurements –
Phase II Nonlinear Aircraft Model

Phase II – Transverse Maneuver with Turbulence

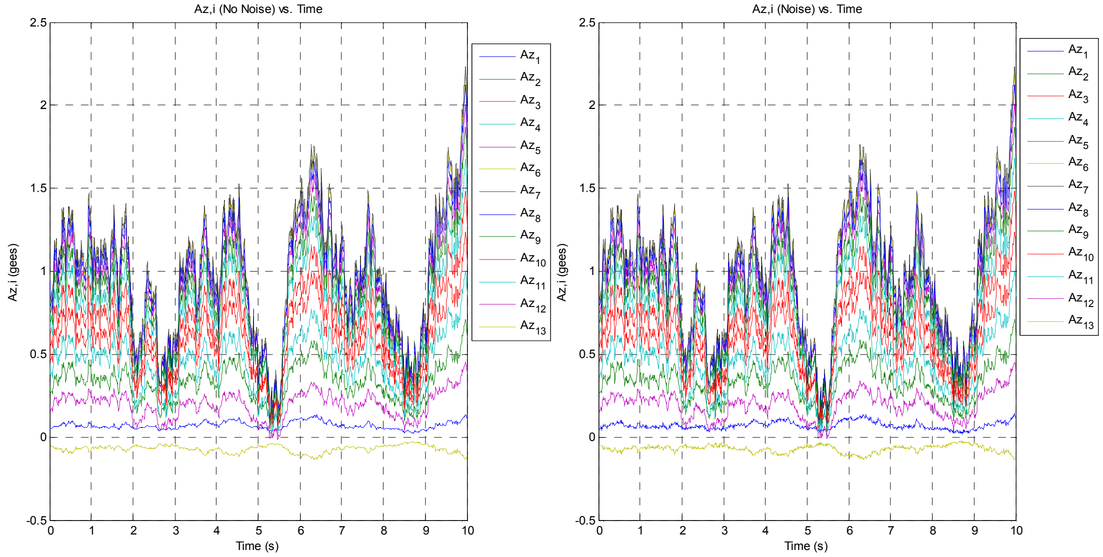

Figure D.8: Longitudinal Accelerometer Array Measurements – Phase II Nonlinear Aircraft Model with Turbulence

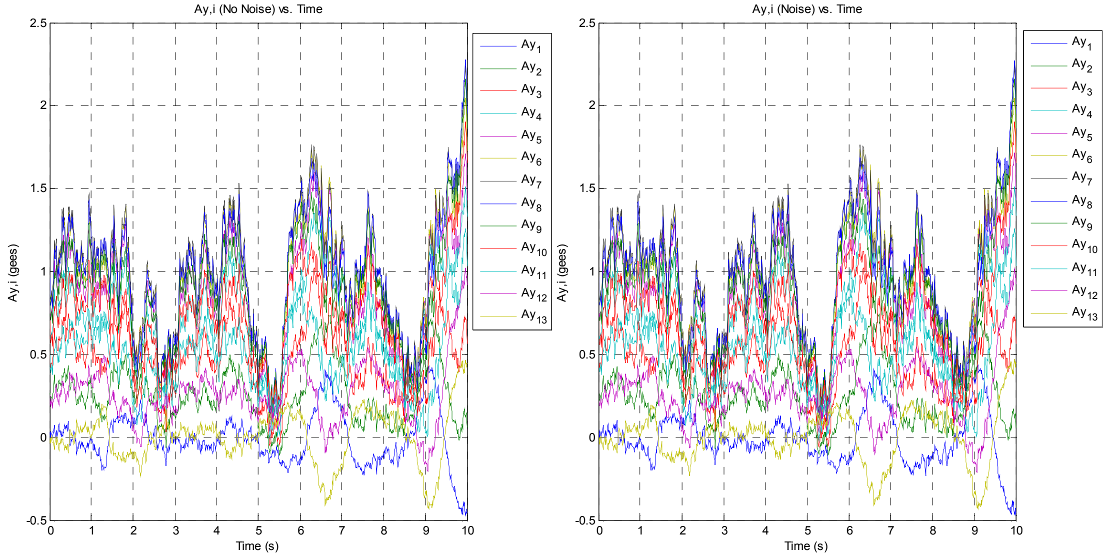

Figure D.9: Transverse Accelerometer Array Measurements – Phase II Nonlinear Aircraft Model with Turbulence

Phase III – Longitudinal/Transverse Maneuver with No Turbulence

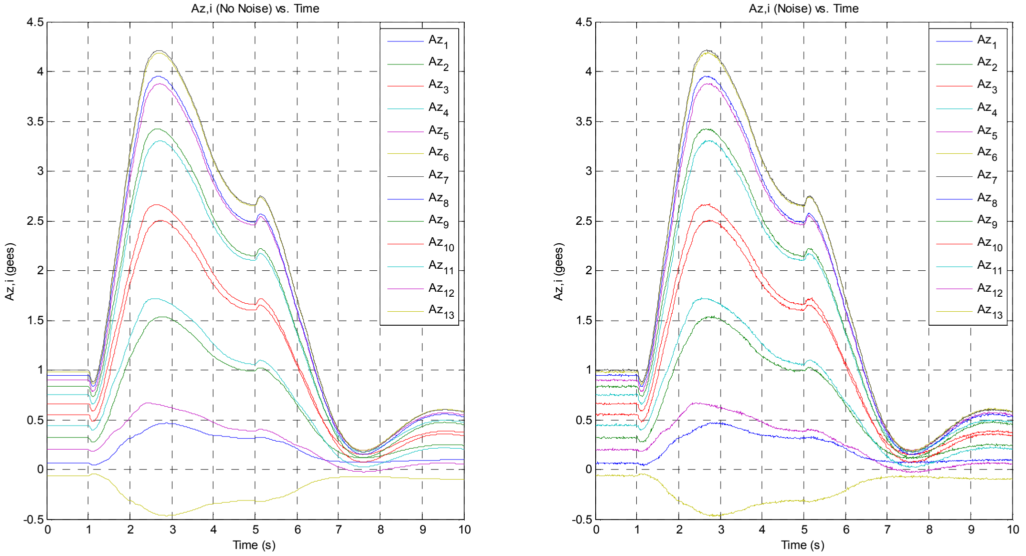

Figure D.10: Longitudinal Accelerometer Array Measurements – Phase III Nonlinear Aircraft Model

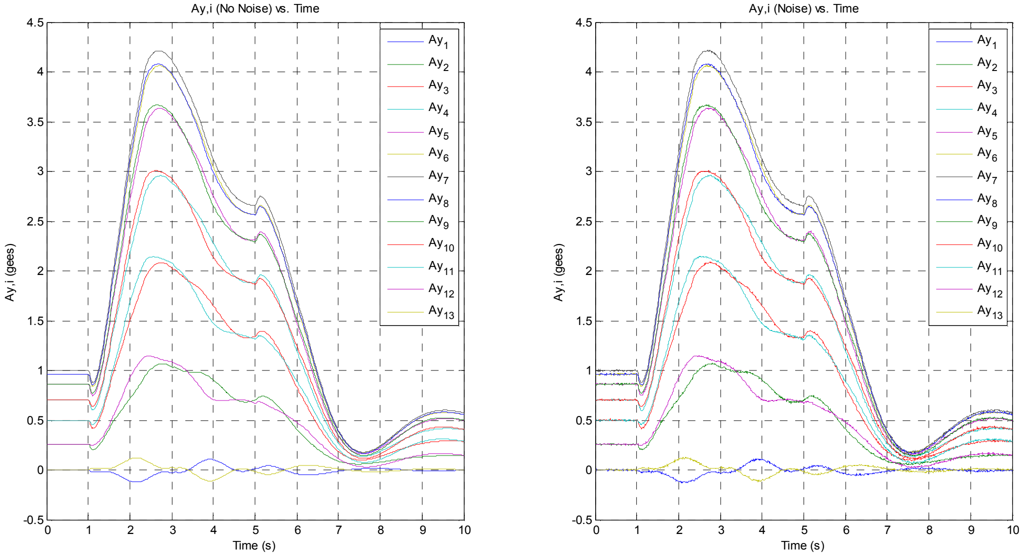

Figure D.11: Transverse Accelerometer Array Measurements – Phase III Nonlinear Aircraft Model

Phase III – Longitudinal/Transverse Maneuver with Turbulence

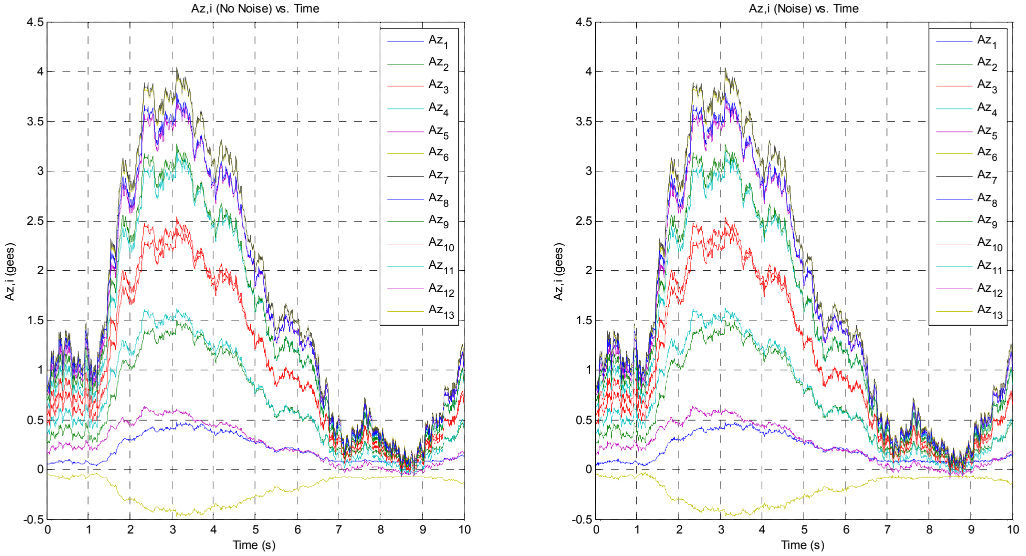

Figure D.12: Longitudinal Accelerometer Array Measurements – Phase III Nonlinear Aircraft Model with Turbulence

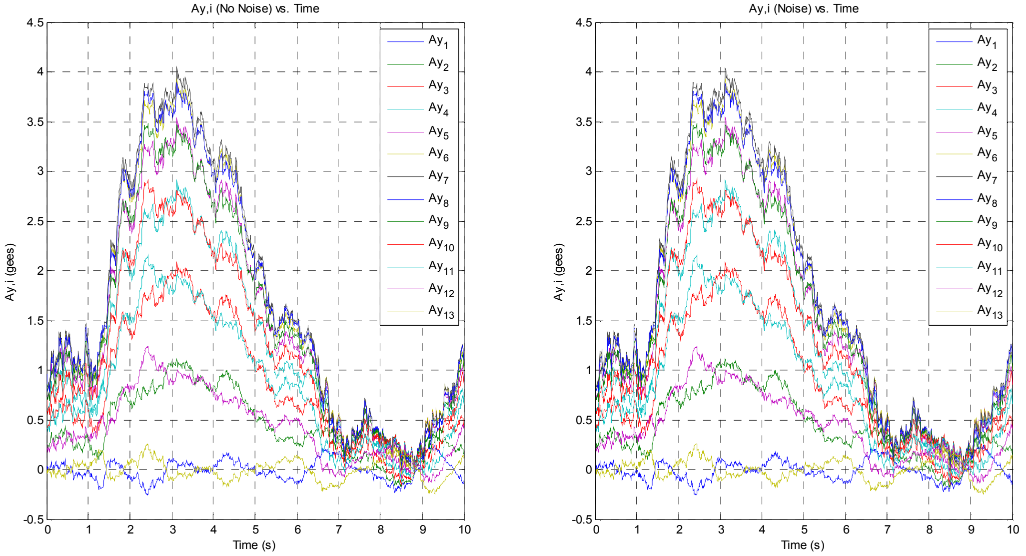

Figure D.13: Transverse Accelerometer Array Measurements – Phase III Nonlinear Aircraft Model with Turbulence

D.5 Simulated Imposed Loading Measurements

The following figures are the imposed loading measurements along the vehicle axes during each of the simulated aircraft maneuvers performed. In each of the figures generated, "Gen" refers to the imposed loading calculation determined through the use of the body angular rate terms discussed in Section 4.2.1. The term, "SD" refers to the imposed loading calculation determined through the use of the signal differencing method as discussed in Section 4.2.2.

Phase I – Longitudinal Maneuver with No Turbulence

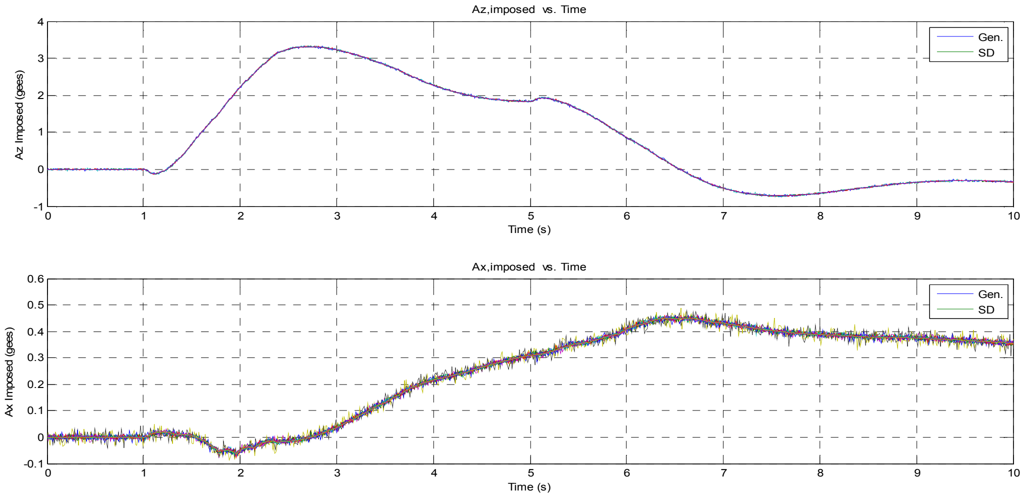

Figure D.14: Phase I Longitudinal Array Imposed Load Measurements – Nonlinear Aircraft Model

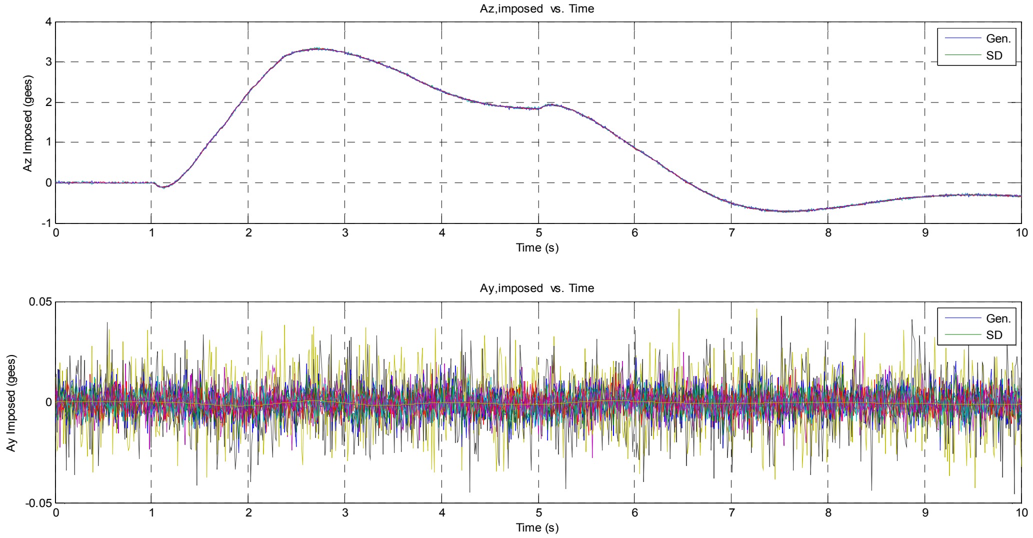

Figure D.15: Phase I Transverse Array Imposed Load Measurements – Nonlinear Aircraft Mode

Phase I – Longitudinal Maneuver with Turbulence

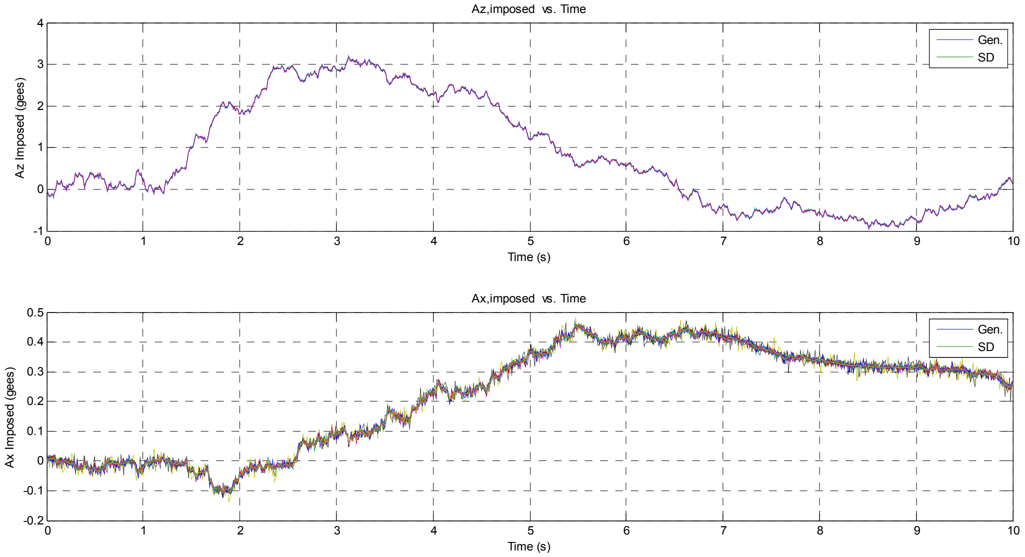

Figure D.16: Phase I Longitudinal Array Imposed Load Measurements – Nonlinear Aircraft Model with Turbulence

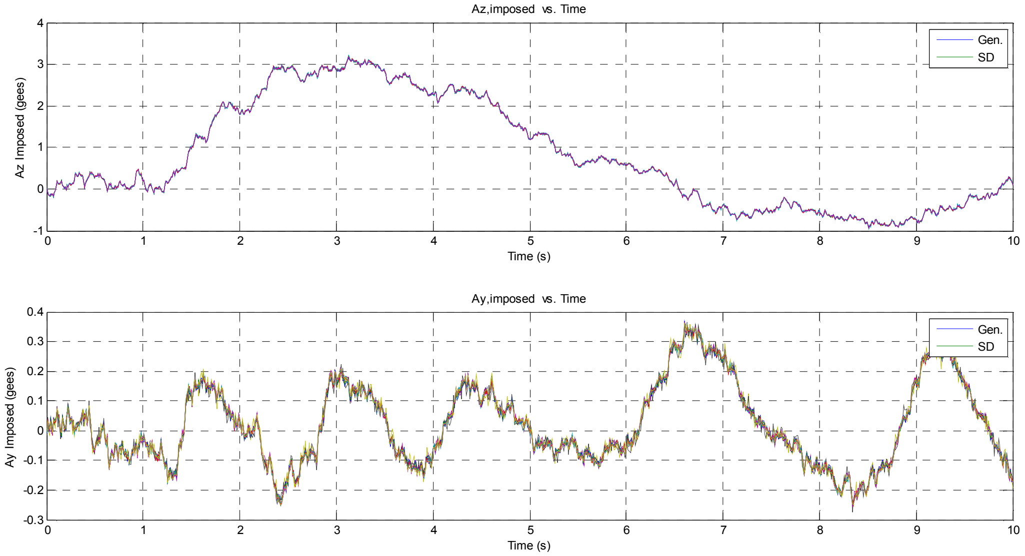

Figure D.17: Phase I Transverse Array Imposed Load Measurements – Nonlinear Aircraft Model with Turbulence

Phase II – Transverse Maneuver with No Turbulence

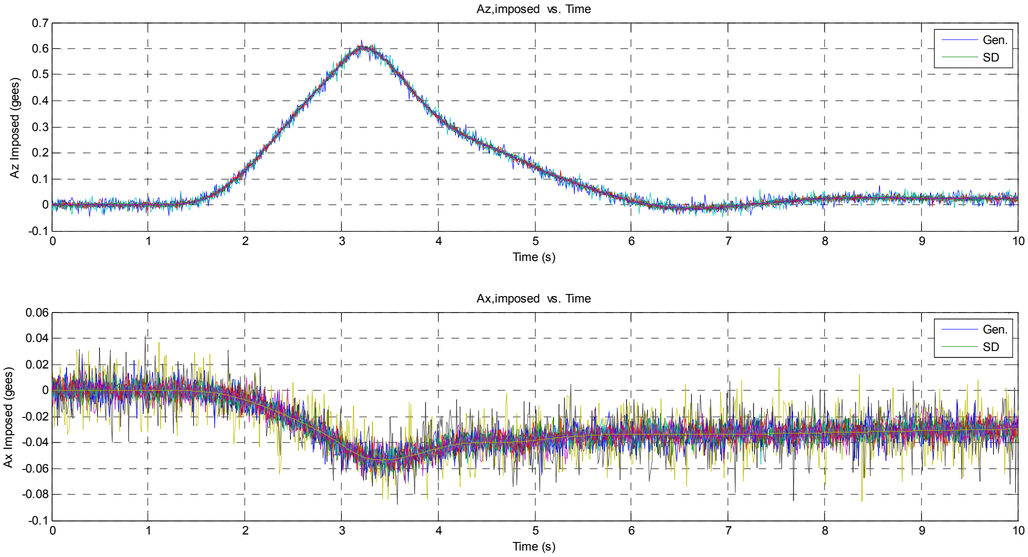

Figure D.18: Phase II Longitudinal Array Imposed Load Measurements – Nonlinear Aircraft Model

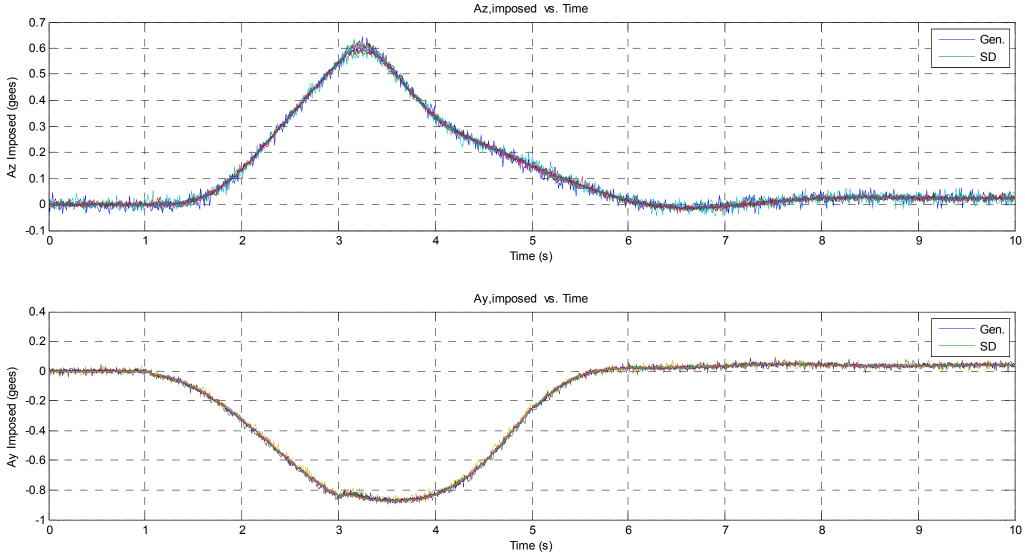

Figure D.19: Phase II Transverse Array Imposed Load Measurements – Nonlinear Aircraft Model

Phase II – Transverse Maneuver with Turbulence

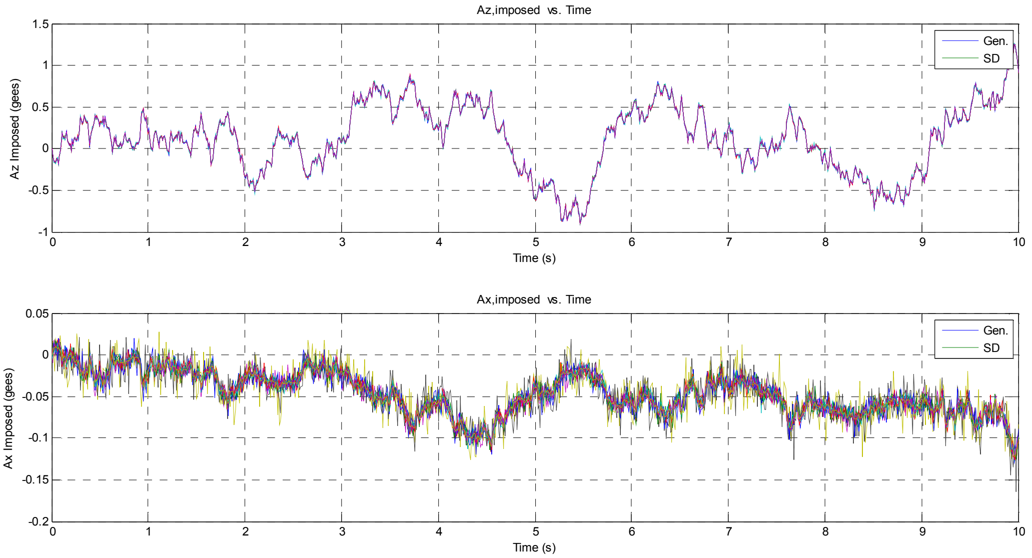

Figure D.20: Phase II Longitudinal Array Imposed Load Measurements – Nonlinear Aircraft Model with Turbulence

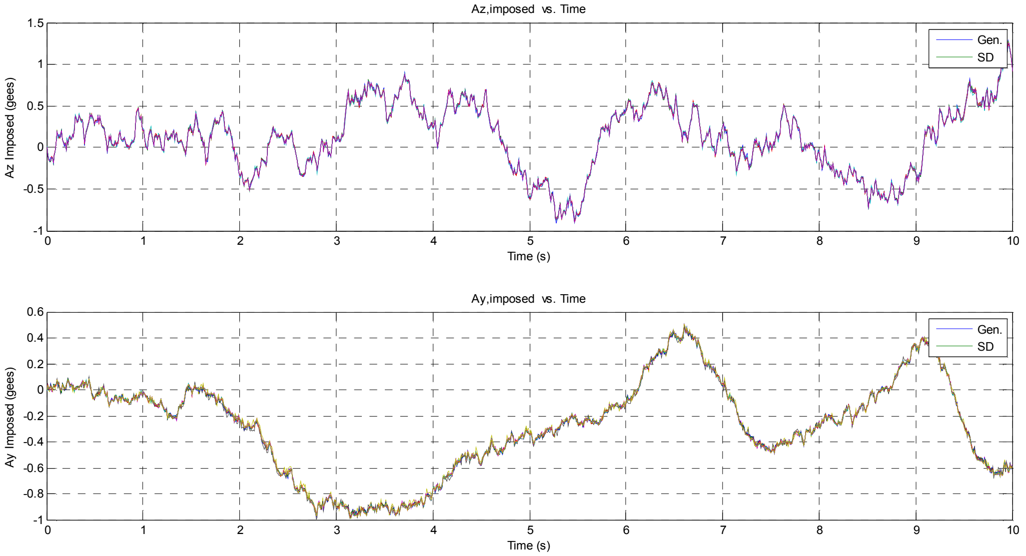

Figure D.21: Phase II Transverse Array Imposed Load Measurements – Nonlinear Aircraft Model with Turbulence

Phase III – Longitudinal/Transverse Maneuver with No Turbulence

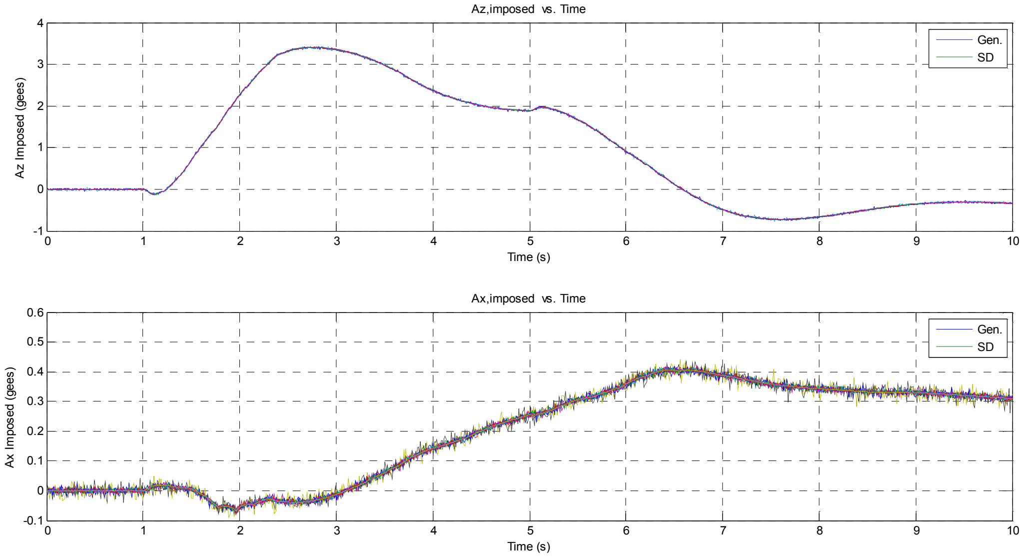

Figure D.22: Phase III Longitudinal Array Imposed Load Measurements – Nonlinear Aircraft Model

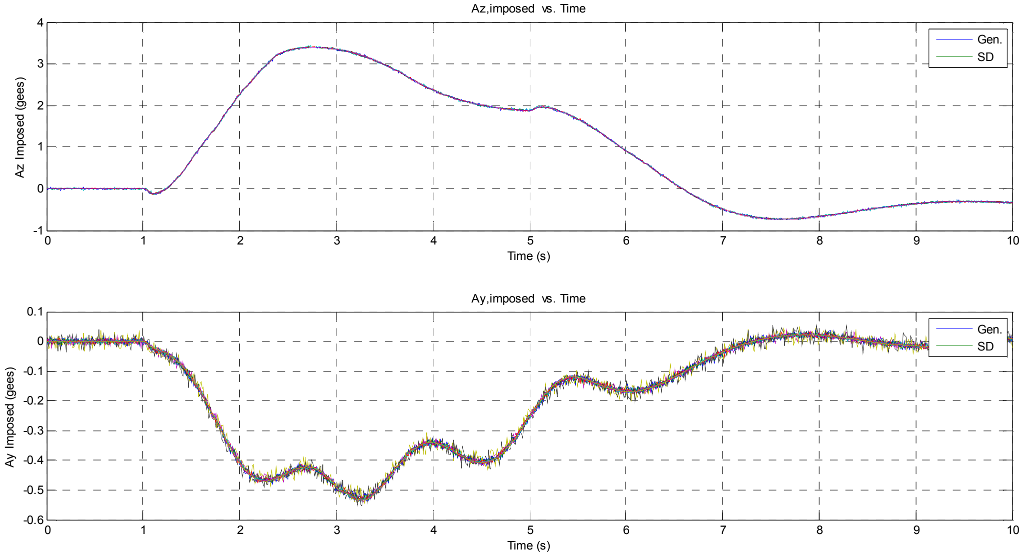

Figure D.23: Phase III Transverse Array Imposed Load Measurements – Nonlinear Aircraft Model

Phase III – Longitudinal/Transverse Maneuver with Turbulence

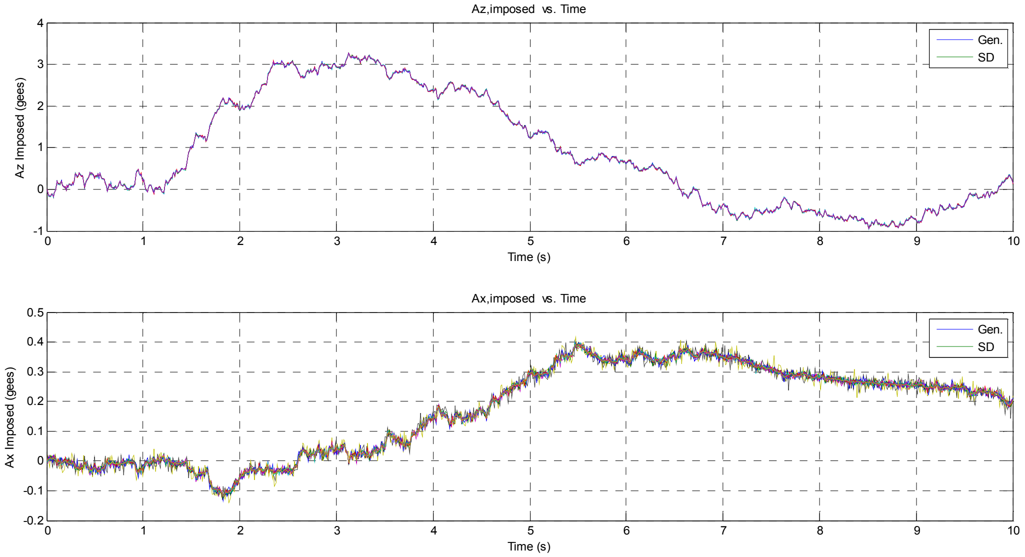

Figure D.24: Phase III Longitudinal Array Imposed Load Measurements – Nonlinear Aircraft Model with Turbulence

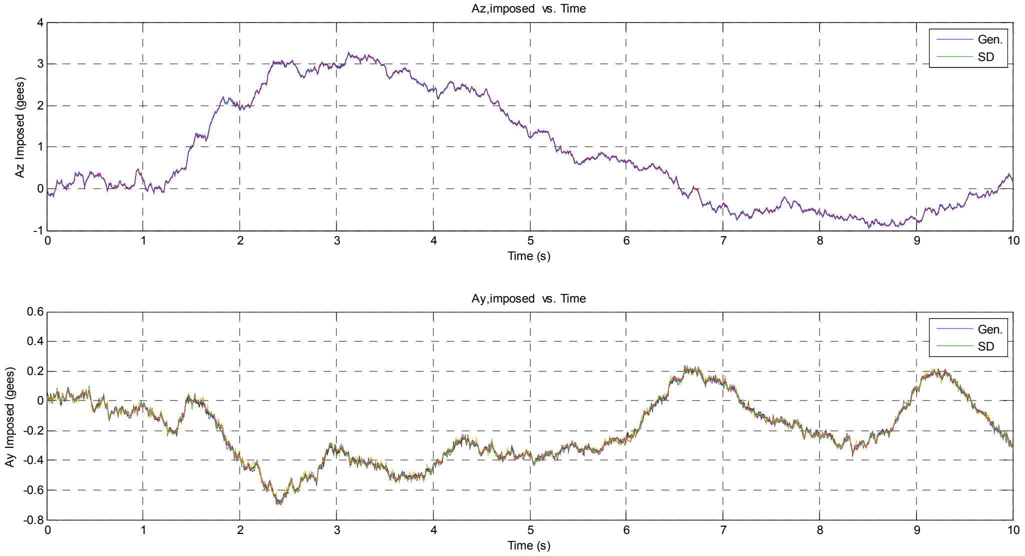

Figure D.25: Phase III Transverse Array Imposed Load Measurements – Nonlinear Aircraft Model with Turbulence

D.6 Two-Dimensional Accelerometer Array Simulink Models

The figures presented in this section display the two-dimensional accelerometer array models constructed and implemented in Simulink.

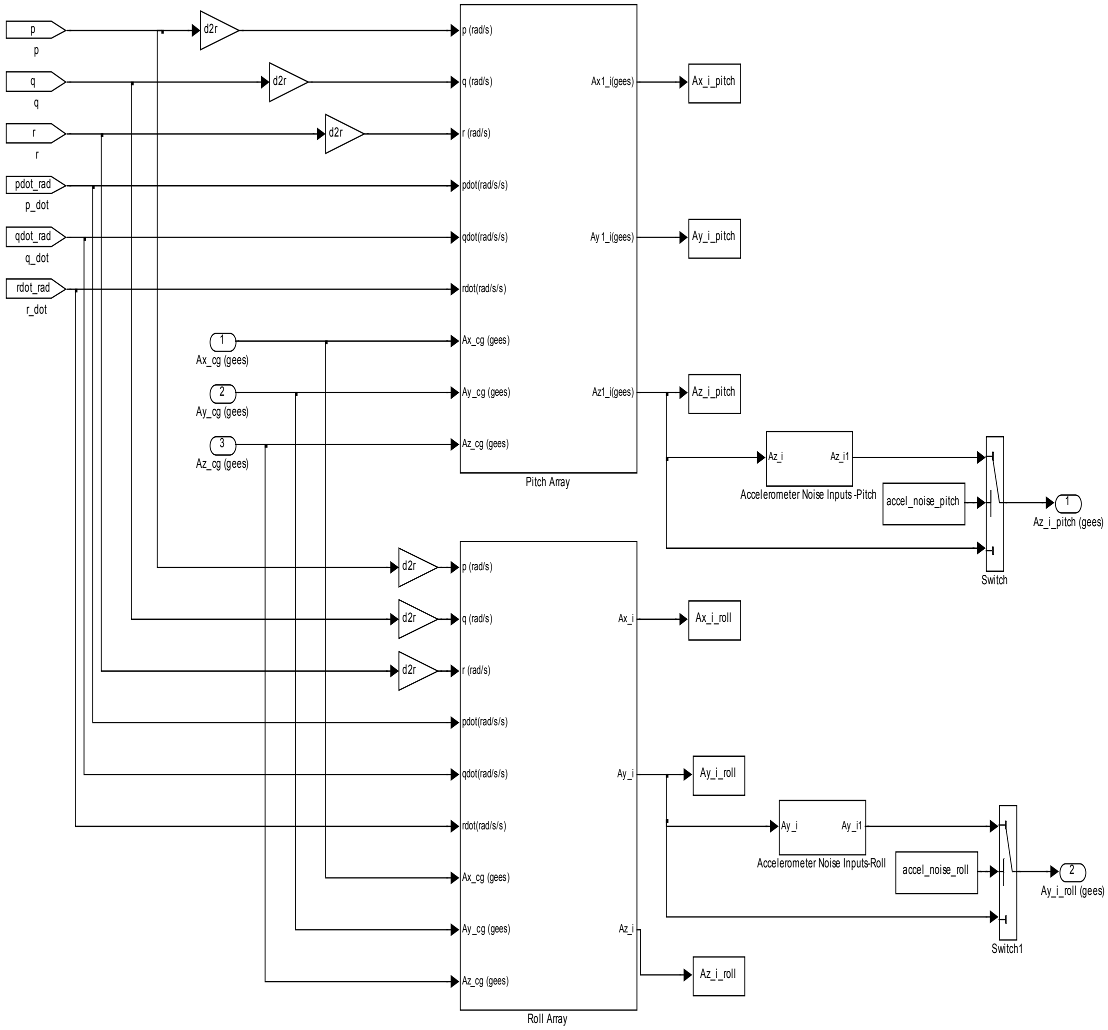

Figure D.26: Generalized Longitudinal and Transverse Accelerometer Measurement Systems

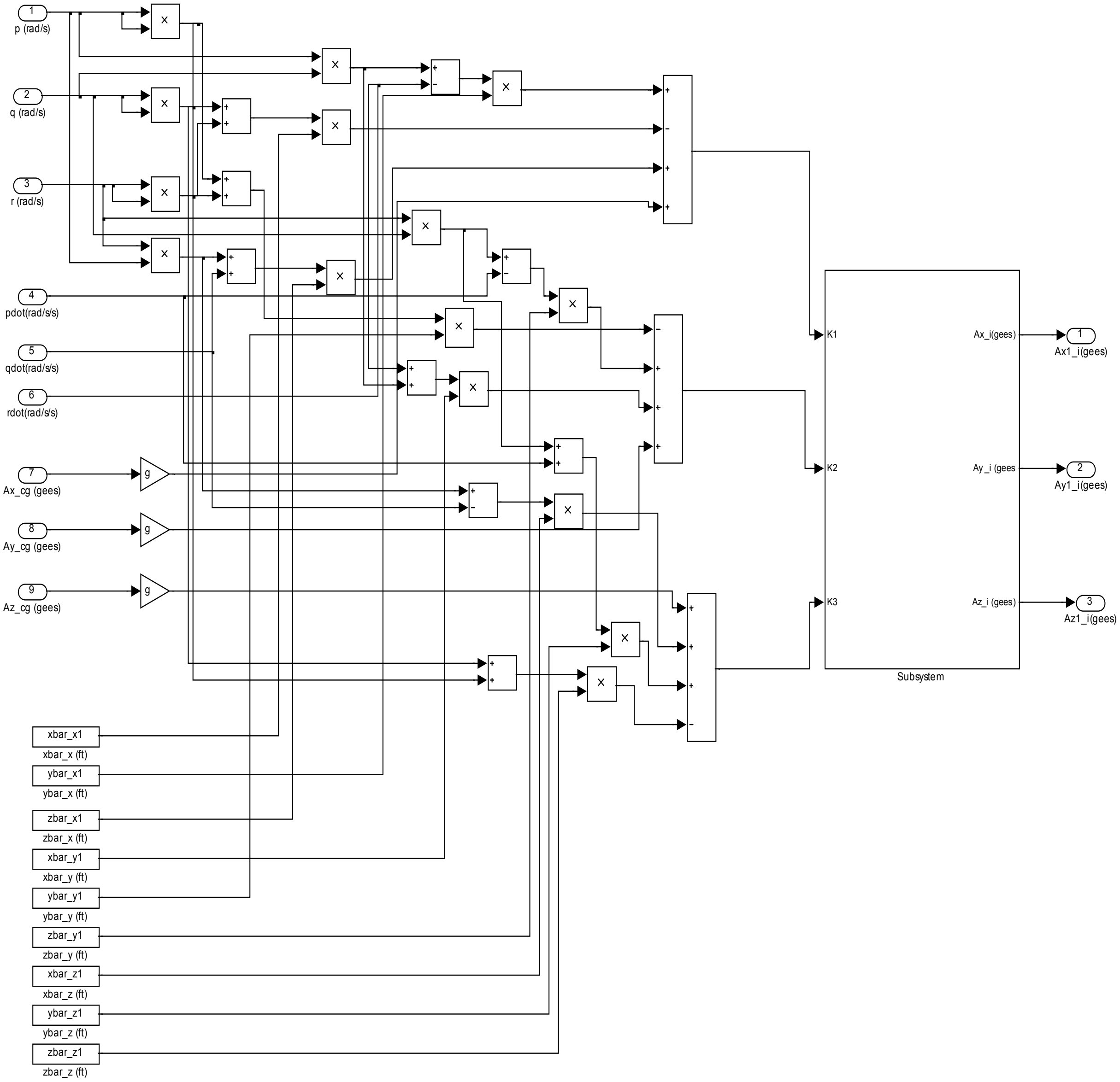

Figure D.27: Longitudinal Accelerometer Array Measurement Subsystem

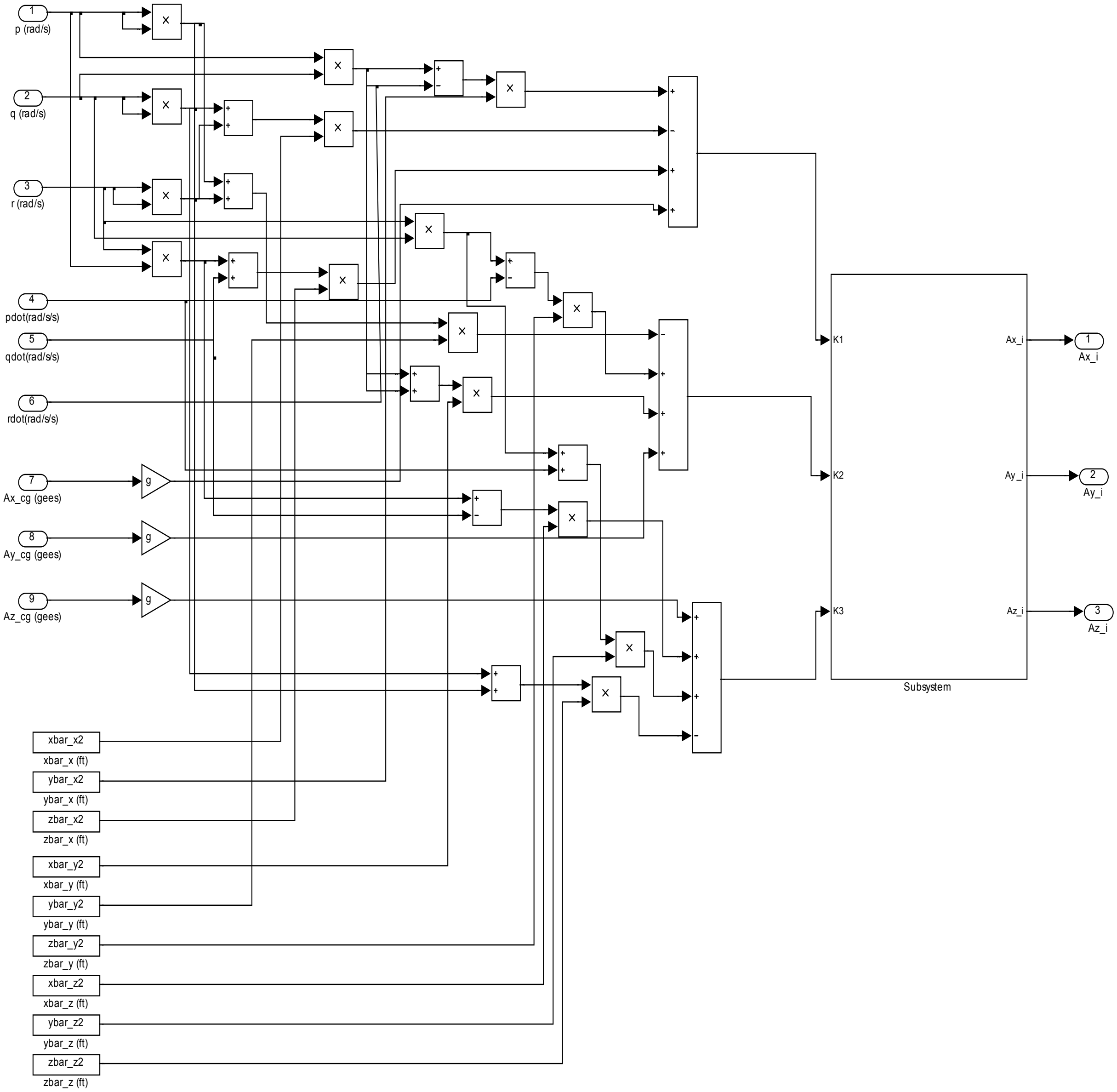

Figure D.28: Transverse Accelerometer Array Measurement Subsystem

Appendix E

Nonlinear Aircraft Model

E.1 Modeling Equations

In addition to the rigid-body equations of motion provided in Section 2.1.2, additional equations are needed to fully describe and characterize the motion of an aircraft. This section of work utilizes references [3], [4], and [32] to provide the additional derivations necessary for correct and accurate construction of the rigid-body nonlinear aircraft simulation model.

E.1.1 Aircraft Stability Axes Coordinate Frame

The stability axes coordinate frame of an aircraft simulation model utilizes three primary parameters such as the true velocity of the aircraft, V_T, defined as the magnitude of the body axes velocities. The angle-of-attack, α, which is the angle of pitch of the aircraft relative to the oncoming wind. And third, the yaw or heading angle, β, relative to the oncoming wind. Equations E.1 through E.6 provide the necessary transformation equations from the vehicle's body axes to the stability axes and stability axes back to the vehicle's body axes.

Body Axes to Stability Axes:

$$\alpha = \tan^{-1}\left(\frac{w}{u}\right) \tag{E.1}$$

$$\beta = \sin^{-1}\left(\frac{v}{V_T}\right) \tag{E.2}$$

$$V_T = \sqrt{u^2 + v^2 + w^2} \tag{E.3}$$

Stability Axes to Body Axes:

$$u = V_T \cos\alpha \cos\beta \tag{E.4}$$

$$v = V_T \sin\beta \tag{E.5}$$

$$w = V_T \sin\alpha \cos\beta \tag{E.6}$$

The force equations utilized are:

$$\dot{\alpha} = q - \left(p\cos\alpha + r\sin\alpha\right)\tan\beta - \frac{LOM}{V_T\cos\beta}$$

$$+\frac{g}{V_T\cos\beta}\left(\cos\theta\cos\phi\cos\alpha + \sin\theta\sin\alpha\right) \tag{E.7}$$

$$\dot{\beta} = p\sin\alpha - r\cos\alpha + \frac{1}{V_T}\left(YOM\cos\beta + DOM\sin\beta\right)$$

$$+\frac{g}{V_T}\left(\cos\theta\sin\phi\cos\beta + \sin\theta\sin\beta\cos\alpha - \cos\theta\cos\phi\sin\beta\sin\alpha\right) \tag{E.8}$$

$$\dot{V}_T = YOM\sin\beta - DOM\cos\beta$$

$$+g\left[\left(\cos\theta\cos\phi\sin\alpha - \sin\theta\cos\alpha\right)\cos\beta + \cos\theta\sin\phi\sin\beta\right] \tag{E.9}$$

Where:

$$DOM = \frac{D - T\cos\alpha}{m},\ YOM = \frac{Y}{m},\ LOM = \frac{L + T\sin\alpha}{m} \tag{E.10}$$

It is also assumed that the thrust force, T, acts along the positive primary axis of the aircraft, x_b. For longitudinal and transverse acceleration loading of the accelerometers along each array, the primary, secondary, and tertiary acceleration loading at the aircraft's center-of-gravity must be defined respectively. Figure E.1 displays the normal and axial forces and moments, along with the lift and drag force directions. The angle-of-attack is also shown in Figure E.1

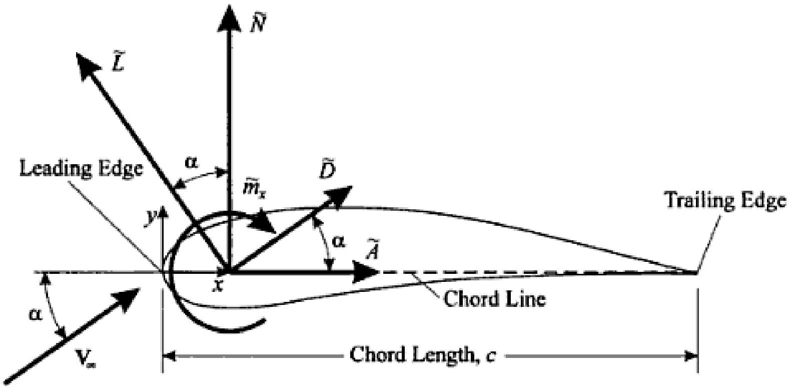

Figure E.1: Forces and Moments in the Normal and Axial Directions along an Airfoil [4]

In Figure E.1, the velocity is represented by $\vec{V}$, flowing over the airfoil and the drag, $\vec{D}$, acting collinear. The lift variable, $\vec{L}$, is perpendicular to the drag force. The variable $\vec{A}$ represents the axial force direction of the airfoil, while $\vec{N}$ represents the airfoil normal vector. The angle-of-attack is given as α, which represents the angle between the vehicle's primary axis, x_b, and the vehicle's velocity vector. Utilizing Figure E.1, the lift and drag forces acting along the vehicle's primary, secondary, and tertiary axes may be determined yielding the imposed, inertial accelerations measured by the accelerometers placed at the vehicle's center-of gravity.

Equations E.11, E.12, and E.13 summarize the vehicle's imposed loading and the weight of the vehicle. The imposed inertial loads, $F_{\mathbf{X_b},\mathbf{Imposed}}$, $F_{\mathbf{Y_b},\mathbf{Imposed}}$, and $F_{\mathbf{Z_b},\mathbf{Imposed}}$ result from the thrust and aerodynamic forces imparted on the vehicle during the simulated maneuvers performed.

$$A_{X,CG} = F_{\mathbf{X_b},\mathbf{Imposed}} + W_{x_b} \tag{E.11}$$

$$A_{Y,CG} = F_{\mathbf{Y_b},\mathbf{Imposed}} + W_{y_b} \tag{E.12}$$

$$A_{Z,CG} = F_{\mathbf{Z_b},\mathbf{Imposed}} + W_{z_b} \tag{E.13}$$

Since Newton's second law is being applied, the gravitational force in the body-fixed coordinate frame must also be expressed in the Earth-fixed coordinate frame. The gravitational force is given as (0, 0, W) in the Earth-fixed frame. Therefore, the gravitational force vector in the body-fixed coordinate frame is given as

$$\begin{Bmatrix} W_{x_b} \\ W_{y_b} \\ W_{z_b} \end{Bmatrix} = mg \begin{Bmatrix} -\sin(\theta) \\ \sin(\phi)\cos(\theta) \\ \cos(\phi)\cos(\theta) \end{Bmatrix} \tag{E.14}$$

E.1.2 Stability Derivatives and Aircraft Nomenclature

The forces and moments acting upon an aircraft are the sum of the loads due to the gravitational force, aerodynamic loading, and thrust. The force vector, $F_{\text{Aerodynamic}}$, given previously in Equation 2.9 may be written in conjunction with the body-fixed gravitational components as Equation E.15. Figure E.2 displays the body-fixed coordinate frame components of the gravitational force.

$$\vec{F}+\vec{W}=\frac{1}{2}pV^2S\begin{Bmatrix}C_L\\C_D\\C_Y\end{Bmatrix}+T\begin{Bmatrix}\cos(\alpha_{T0})\\0\\-\sin(\alpha_{T0})\end{Bmatrix}+mg\begin{Bmatrix}-\sin(\theta)\\\sin(\phi)\cos(\theta)\\\cos(\phi)\cos(\theta)\end{Bmatrix}$$

$$=\overline{q}S\begin{Bmatrix}C_L\\C_D\\C_Y\end{Bmatrix}+T\begin{Bmatrix}\cos(\alpha_{T0})\\0\\-\sin(\alpha_{T0})\end{Bmatrix}+mg\begin{Bmatrix}-\sin(\theta)\\\sin(\phi)\cos(\theta)\\\cos(\phi)\cos(\theta)\end{Bmatrix}$$

(E.15)

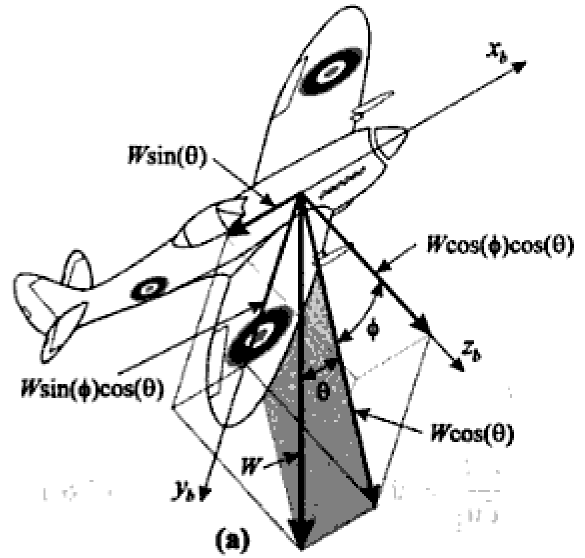

Figure E.2: Gravitational Forces in the Body-Fixed Coordinate Frame [4]

The external moment vector, M_{External}, given previously in Equation 2.10 may be written as Equation E.16. Figure E.3 represents the body-fixed components of the aerodynamic forces and moments.

$$\vec{M}=\frac{1}{2}pV^2S\begin{Bmatrix}bC_l\\cC_m\\bC_n\end{Bmatrix}=\overline{q}S\begin{Bmatrix}bC_l\\cC_m\\bC_n\end{Bmatrix}$$

(E.16)

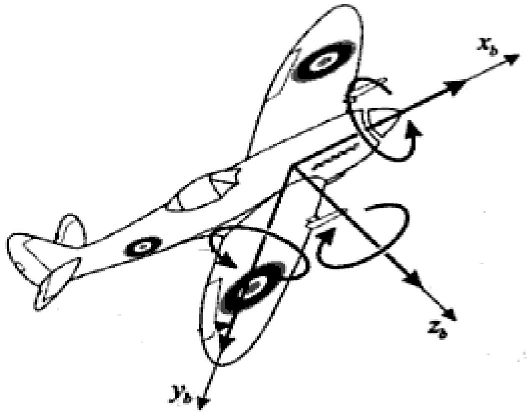

Figure E.3: Aerodynamic Forces and Moments in the Body-Fixed Coordinate Frame [4]

The force and moment coefficients are shown below in Equations E.17 through E.22.

Force Coefficients

$$C_L = C_{L_0} + C_{L_\alpha}\alpha + \frac{c}{2V_T}\left(C_{L_q}q + C_{L_{\dot{\alpha}}}\dot{\alpha}\right) + C_{L_{\delta_e}}\delta_e + C_{L_{\delta_f}}\delta_f$$

(E.17)

$$C_D = C_{D_0} + C_{D_\alpha}\alpha + \frac{c}{2V_T}\left(C_{D_q}q + C_{D_{\dot{\alpha}}}\dot{\alpha}\right) + C_{D_{\delta_e}}\delta_e + C_{D_{\delta_f}}\delta_f$$

(E.18)

$$C_Y = C_{Y_0} + C_{Y_\beta}\beta + \frac{b}{2V_T}\left(C_{Y_p}p + C_{Y_r}r\right) + C_{Y_{\delta_a}}\delta_a + C_{Y_{\delta_r}}\delta_r$$

(E.19)

Moment Coefficients

$$C_l = C_{l_0} + C_{l_\beta}\beta + \frac{b}{2V_T}\left(C_{l_p}p + C_{l_r}r\right) + C_{l_{\delta_a}}\delta_a + C_{l_{\delta_r}}\delta_r$$

(E.20)

$$C_m = C_{m_0} + C_{m_\alpha}\alpha + \frac{c}{2V_T}\left(C_{m_q}q + C_{m_{\dot{\alpha}}}\dot{\alpha}\right) + C_{m_{\delta e}}\delta_e + C_{m_{\delta f}}\delta_f$$

(E.21)

$$C_n = C_{n_0} + C_{n_\beta}\beta + \frac{b}{2V_T}\left(C_{n_p}p + C_{n_r}r\right) + C_{n_{\delta_a}}\delta_a + C_{n_{\delta_r}}\delta_r$$

(E.22)

The constants and stability derivatives utilized in the nonlinear aircraft simulation model during this feasibility study conducted are given in Tables E.1 through E.7 along with their respective values. In Tables E.1 through E.6, the “naught” terms represent dimensionless parameters while the other parameters are per radian. Figures E.4, E.5, and E.6 represent the aircraft response parameters during each phase of the feasibility study conducted.

Phase I – Longitudinal Maneuver

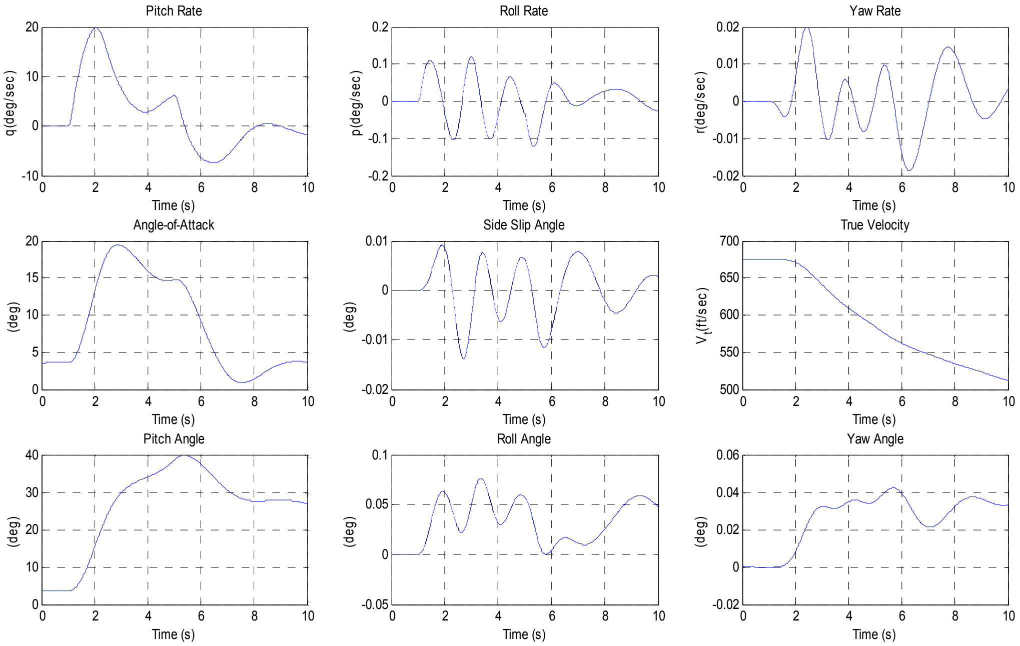

Figure E.4: Longitudinal Maneuver Aircraft Simulation Parameters

Phase II – Transverse Maneuver

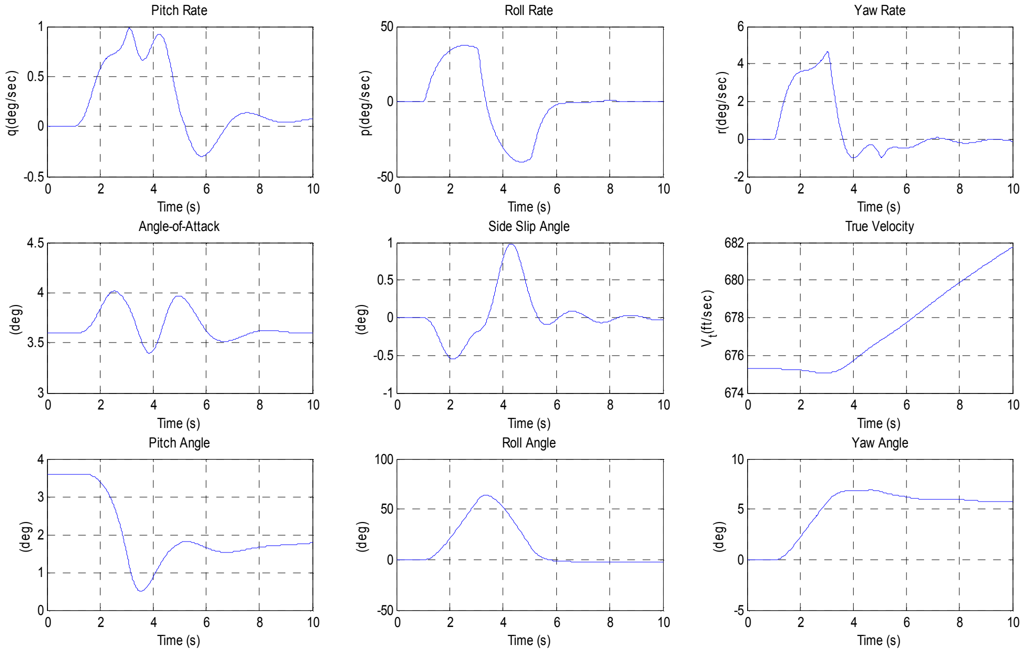

Figure E.5: Transverse Maneuver Aircraft Simulation Parameters

Phase III – Longitudinal/Transverse Maneuver

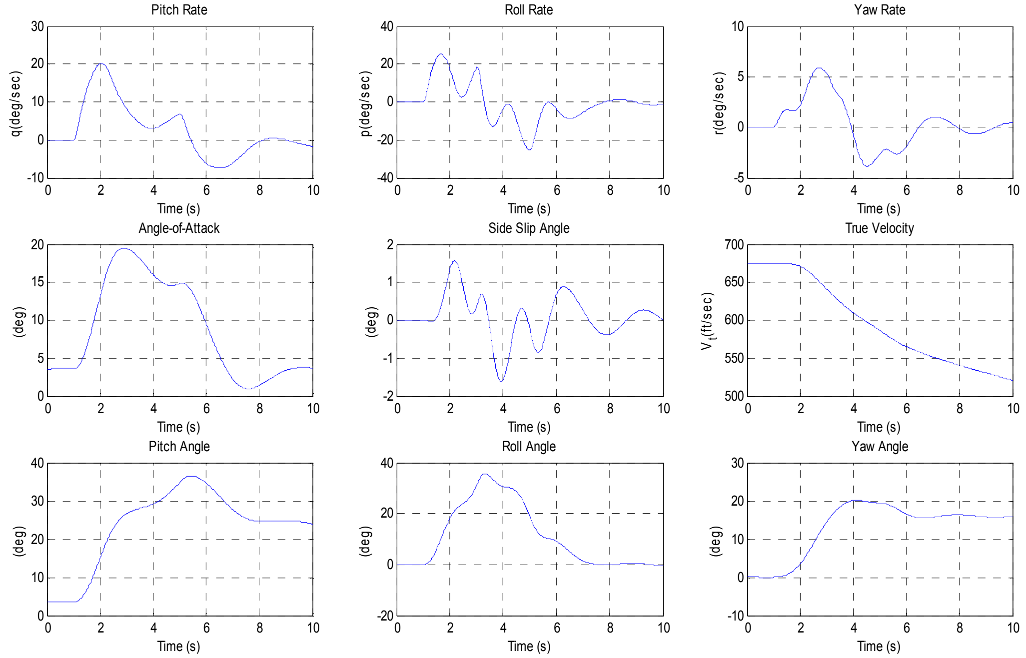

Figure E.6: Longitudinal/Transverse Maneuver Aircraft Simulation Parameters

Variable	Description	Value
C_L	Total Lift Coefficient	Equation E.17
C_{L_0}	Initial Lift Coefficient	0.459069
C_{L_α}	Lift Change with respect to α	4.566721
$C_{L_{\dot\alpha}}$	Lift Change with respect to $\dot\alpha$	2.420000
C_{L_q}	Lift Change with respect to pitch rate	8.049999
$C_{L_{\delta_e}}$	Lift Change with respect to δ_e	0.423988
$C_{L_{\delta_f}}$	Lift Change with respect to δ_f	1.145916

Table E.1: Lift Force Aerodynamic Coefficients

Variable	Description	Value
C_D	Total Drag Coefficient	Equation E.18
C_{D_0}	Initial Drag Coefficient	0.040905
C_{D_α}	Drag Change with respect to α	0.469378
$C_{D_{\dot\alpha}}$	Drag Change with respect to $\dot\alpha$	0.0
C_{D_q}	Drag Change with respect to pitch rate	0.0
$C_{D_{\delta_e}}$	Drag Change with respect to δ_e	0.017762
$C_{D_{\delta_f}}$	Drag Change with respect to δ_f	0.0

Table E.2: Drag Force Aerodynamic Coefficients

Variable	**Description**	**Value**
C_Y	Total Side Force Coefficient	Equation E.19
C_{Y_0}	Initial Side Force Coefficient	0.0
C_{Y_β}	Side Force Change with respect to β	-0.675760
C_{Y_p}	Side Force Change with respect to roll rate	0.0
C_{Y_r}	Side Force Change with respect to yaw rate	0.0
$C_{Y_{\delta_a}}$	Side Force Change with respect to δ_a	0.0
$C_{Y_{\delta_r}}$	Side Force Change with respect to δ_r	-0.658901

Table E.3: Side Force Aerodynamic Coefficients

Variable	**Description**	**Value**
C_l	Total Rolling Moment Coefficient	Equation E.20
C_{l_0}	Initial Rolling Moment Coefficient	0.0
C_{l_β}	Rolling Moment Change with respect to β	-0.023000
C_{l_p}	Rolling Moment Change with respect to roll rate	-0.450000
C_{l_r}	Rolling Moment Change with respect to yaw rate	0.2650000
$C_{l_{\delta_a}}$	Rolling Moment change with respect to δ_a	-0.1719860
$C_{l_{\delta_r}}$	Rolling Moment change with respect to δ_r	-0.0022900

Table E.4: Rolling Moment Aerodynamic Coefficients

Variable	Description	Value
C_m	Total Pitching Moment Coefficient	Equation E.21
C_{m_0}	Initial Pitching Moment Coefficient	0.489826
C_{m_α}	Pitching Moment Change with respect to α	-4.585108
C_{m_q}	Pitching Moment Change with respect to pitch rate	-0.366000
$C_{m_{\dot{\alpha}}}$	Pitching Moment Change with respect to $\dot{\alpha}$	-11.00000
$C_{m_{\delta e}}$	Pitching Moment change with respect to δ_e	-1.972694
$C_{m_{\delta f}}$	Pitching Moment change with respect to δ_f	0.0

Table E.5: Pitching Moment Aerodynamic Coefficients

Variable	Description	Value
C_n	Total Yawing Moment Coefficient	Equation E.22
C_{n_0}	Initial Yawing Moment Coefficient	0.0
C_{n_β}	Yawing Moment Change with respect to β	0.254531
C_{n_p}	Yawing Moment Change with respect to roll rate	-0.11000
C_{n_r}	Yawing Moment Change with respect to yaw rate	-0.20000
$C_{n_{\delta_a}}$	Yawing Moment change with respect to δ_a	0.021772
$C_{n_{\delta_r}}$	Yawing Moment change with respect to δ_r	-0.107716

Table E.6: Yawing Moment Aerodynamic Coefficients

Variable	Description	Value
$\bar{q}$	Dynamic Pressure	$\frac{1}{2}\rho V_T^2$
S	Wing Platform Area	300.00 ft
b	Wingspan	30.00 ft
c	Wing Chord	11.32 ft
m	Aircraft Mass	756.53 slugs
p	Air Density	0.001496 slug/ft^3
g	Acceleration of Gravity	32.17 ft/sec^2
I_{xx}	Primary Axis Mass Moment of Inertia	8691.46 slug-ft^2
I_{yy}	Secondary Axis Mass Moment of Inertia	70668.58 slug-ft^2
I_{zz}	Tertiary Axis Mass Moment of Inertia	70418.67 slug-ft^2
I_{xz}	Cross Product Mass Moment of Inertia	0.0 slug-ft^2
I_{xy}	Cross Product Mass Moment of Inertia	151.44 slug-ft^2
I_{yz}	Cross Product Mass Moment of Inertia	0.0 slug-ft^2

Table E.7: Aircraft Aerodynamic Constants

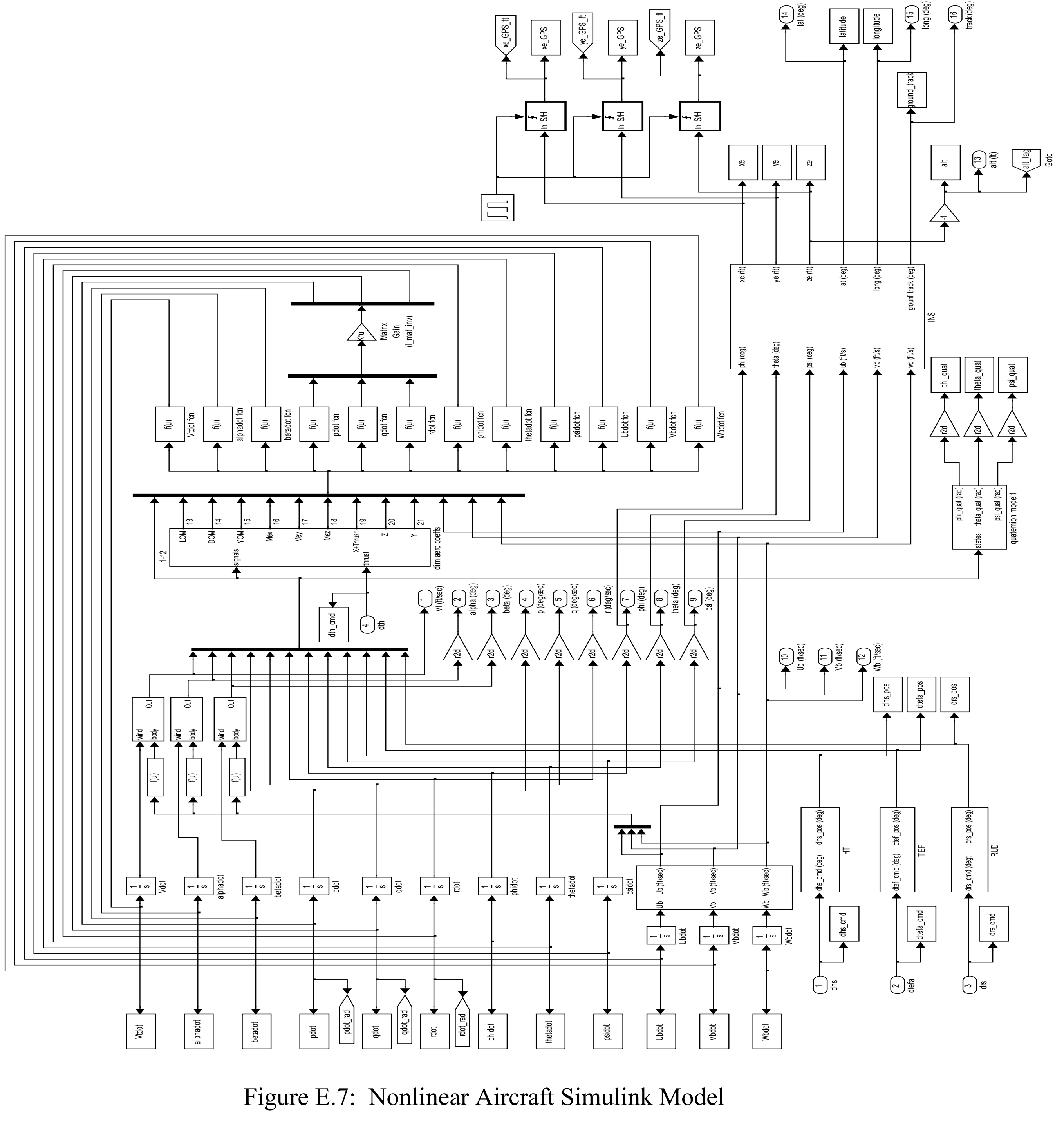

Figure E.7: Nonlinear Aircraft Simulink Model

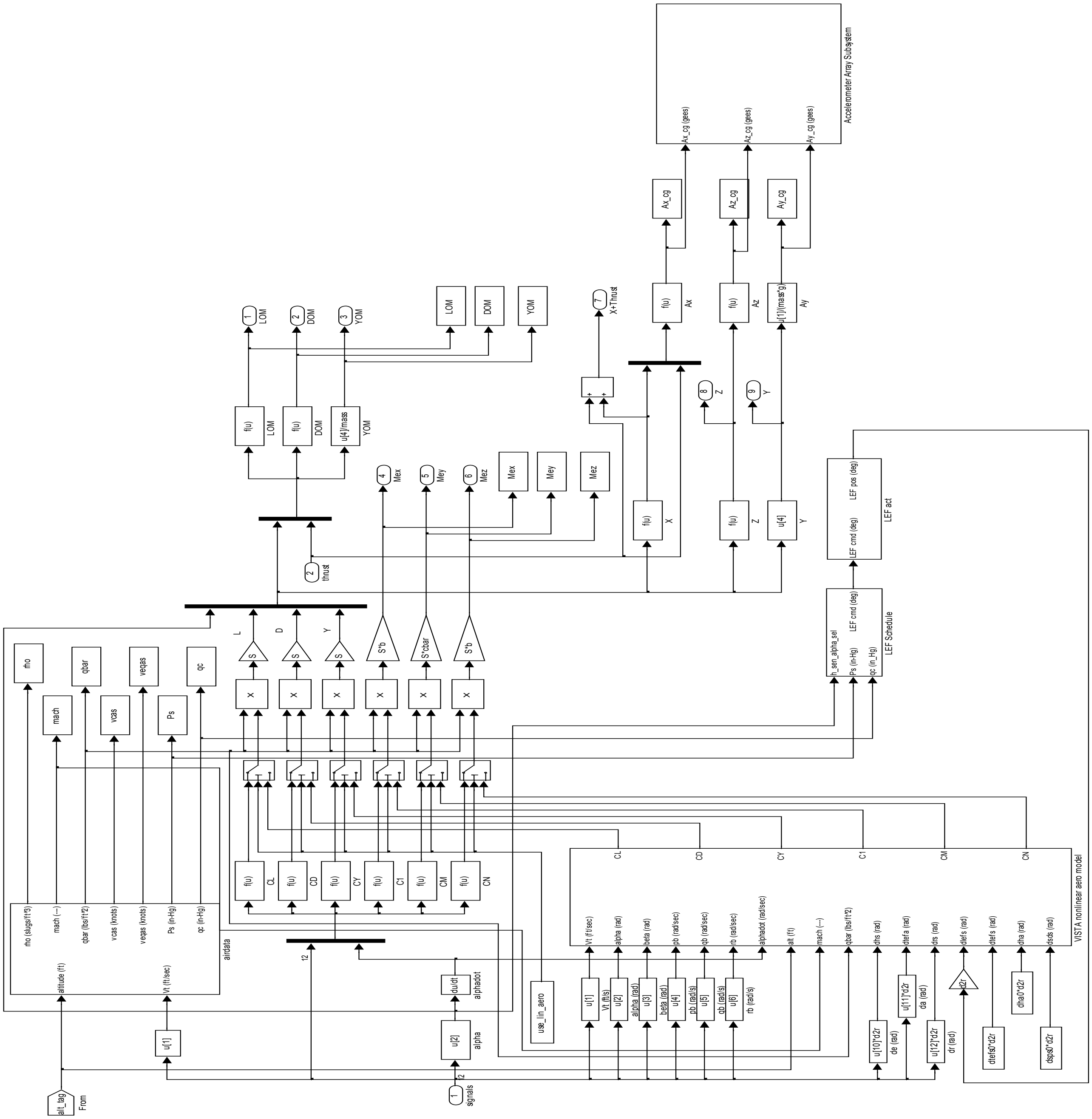

Figure E.8: Simulink Aerodynamic and Equations of Motion Model

Appendix F

Supplemental Figures

This appendix section displays additional figures in support of the work and study conducted.

F.1 Section 4.4.1 – Comparative Analysis of Algorithm Operation and Sensor Noise Affects: Part I

In this section of the appendix, supplemental figures omitted from Section 4.4.1 for conciseness are presented for each phase of the feasibility study conducted to demonstrate correct operation of the algorithm method developed utilizing sensor noise values as given in [50]. A summation of the maximum and mean absolute attitude and bias estimation errors for each phase of the feasibility study performed was presented previously in Section 4.4.1 in Tables 4.28 and 4.29 for non-turbulent and turbulent aircraft simulation maneuvers respectively.

F.1.1 Phase I: Non-Turbulent Longitudinal Aircraft Simulation Maneuver – Part I

This phase of the study was previously conducted and displayed in Section 4.4.1. The results and conclusions developed from the performed nonlinear simulations are presented in completeness in Section 4.4.1.

F.1.2 Phase I: Turbulent Longitudinal Aircraft Simulation Maneuver – Part I

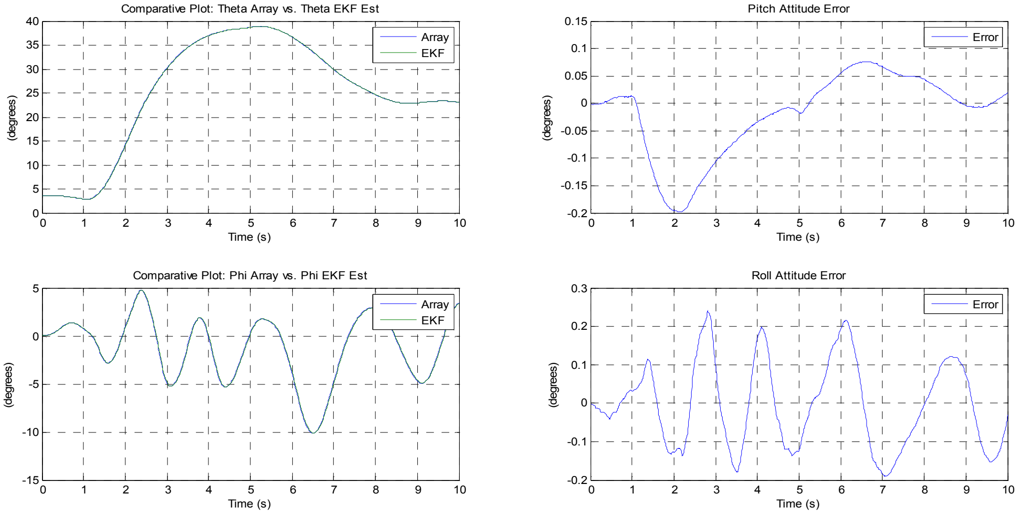

Figure F.1: Phase I Turbulent Attitude Estimation Results using Sensor Noise Values

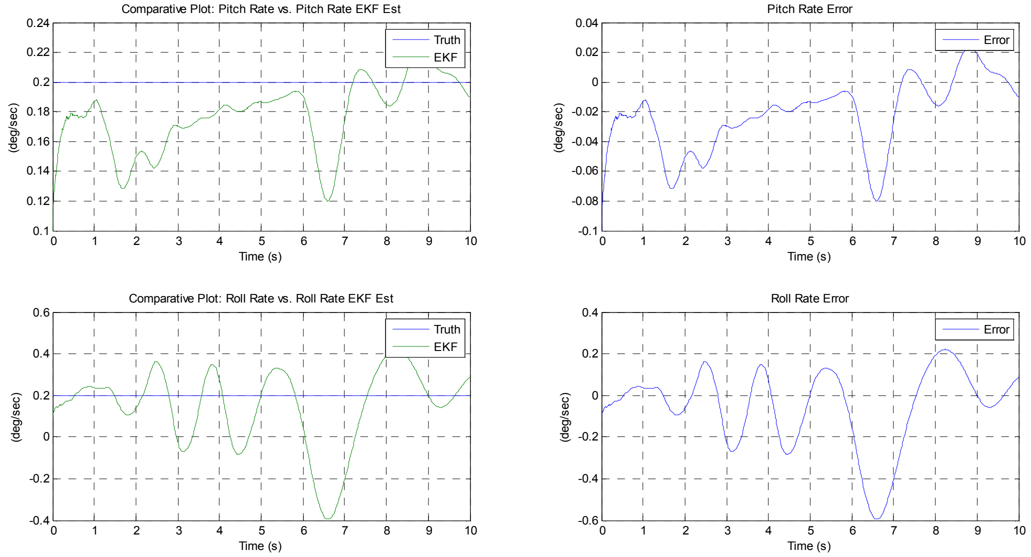

Figure F.2: Phase I Turbulent Bias Estimation Results using Sensor Noise Values

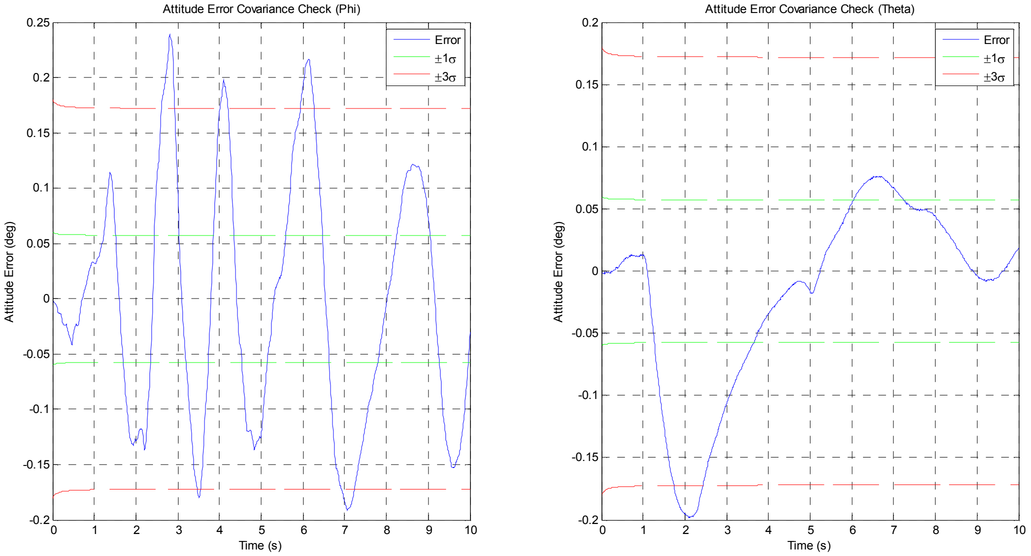

Figure F.3: Phase I Turbulent Attitude Error Covariance Check using Sensor Noise Values

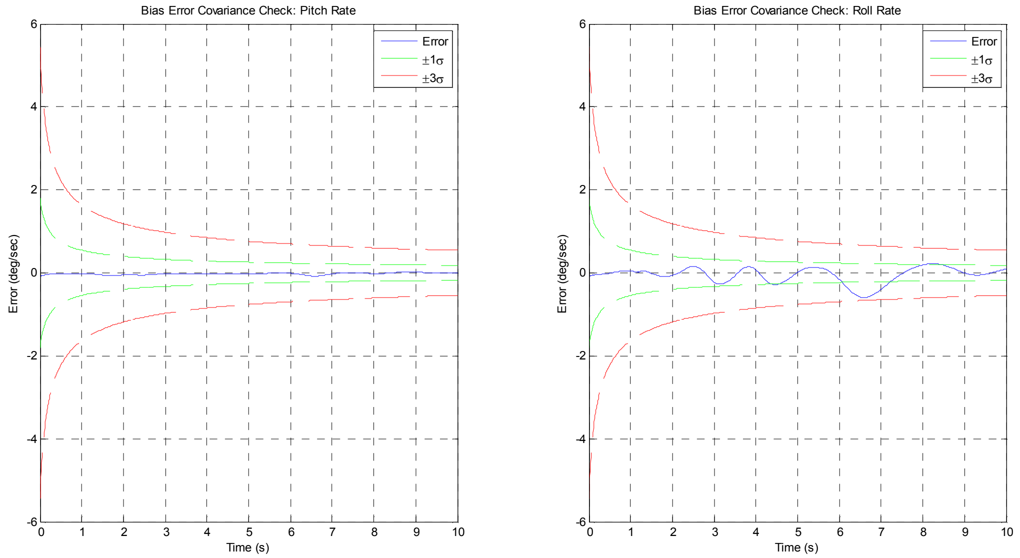

Figure F.4: Phase I Turbulent Bias Error Covariance Check using Sensor Noise Values

F.1.3 Phase II: Non-Turbulent Transverse Aircraft Simulation Maneuver – Part I

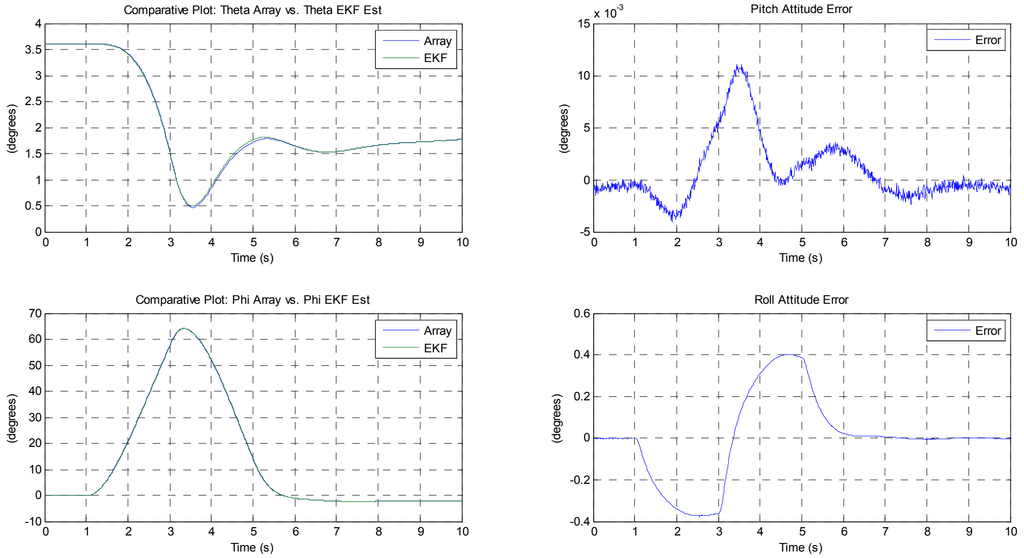

Figure F.5: Phase II Non-Turbulent Attitude Estimation Results using Sensor Noise Values

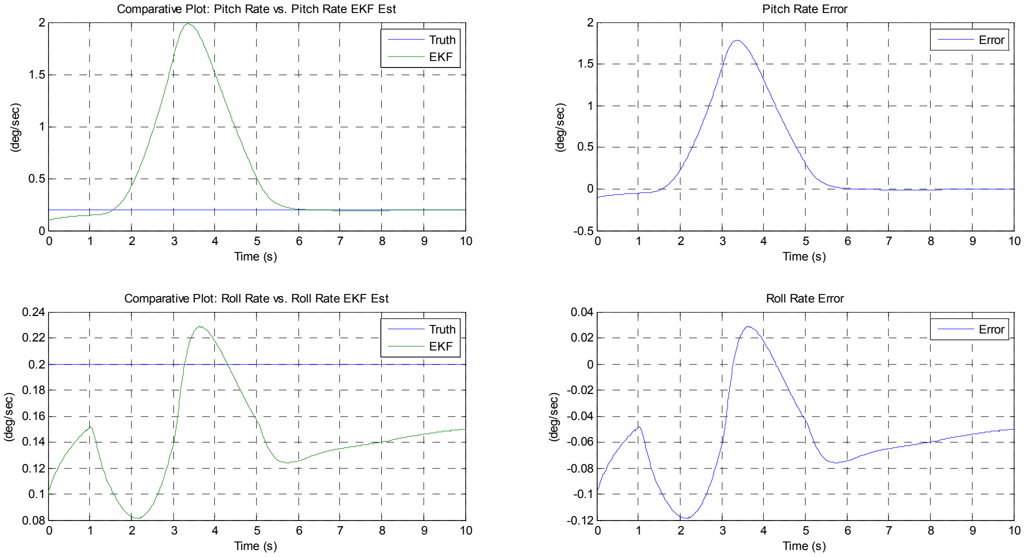

Figure F.6: Phase II Non-Turbulent Bias Estimation Results using Sensor Noise Values

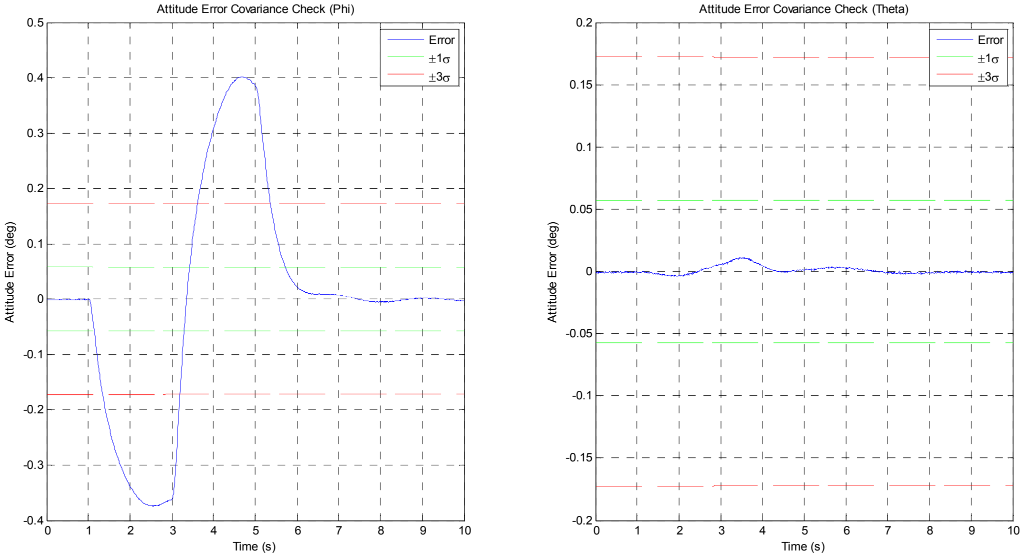

Figure F.7: Phase II Non-Turbulent Attitude Error Covariance Check using Sensor Noise Values

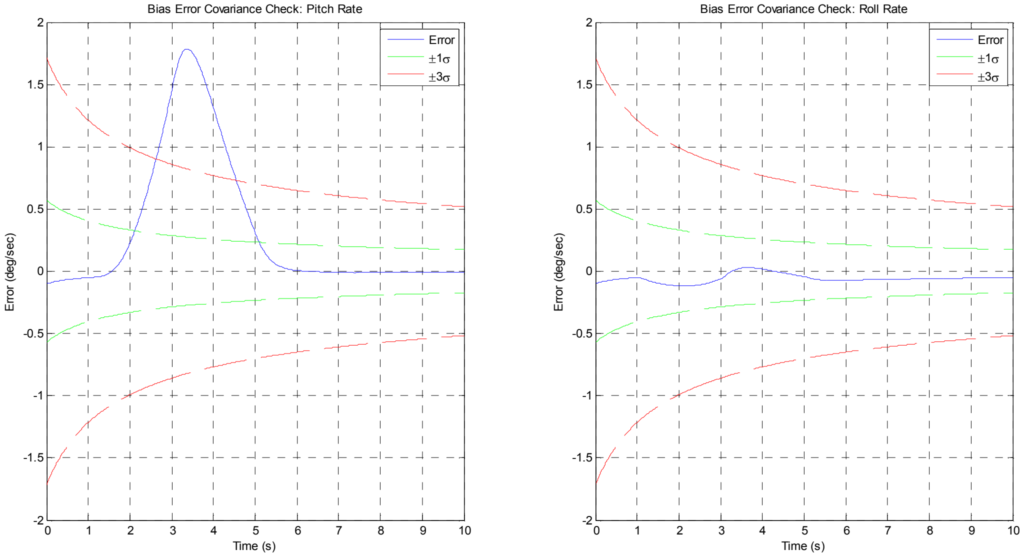

Figure F.8: Phase II Non-Turbulent Bias Error Covariance Check using Sensor Noise Values

F.1.4 Phase II: Turbulent Transverse Aircraft Simulation Maneuver – Part I

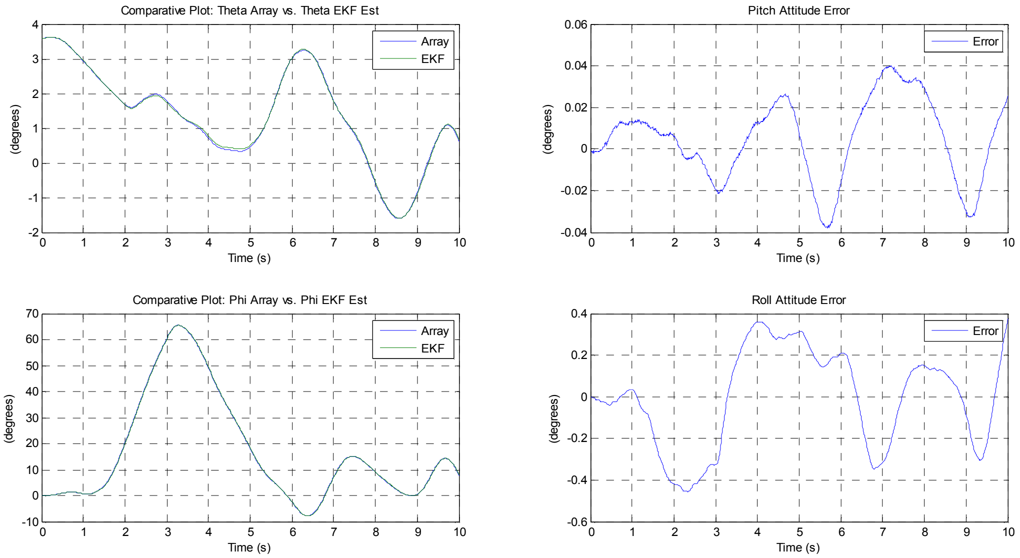

Figure F.9: Phase II Turbulent Attitude Estimation Results using Sensor Noise Values

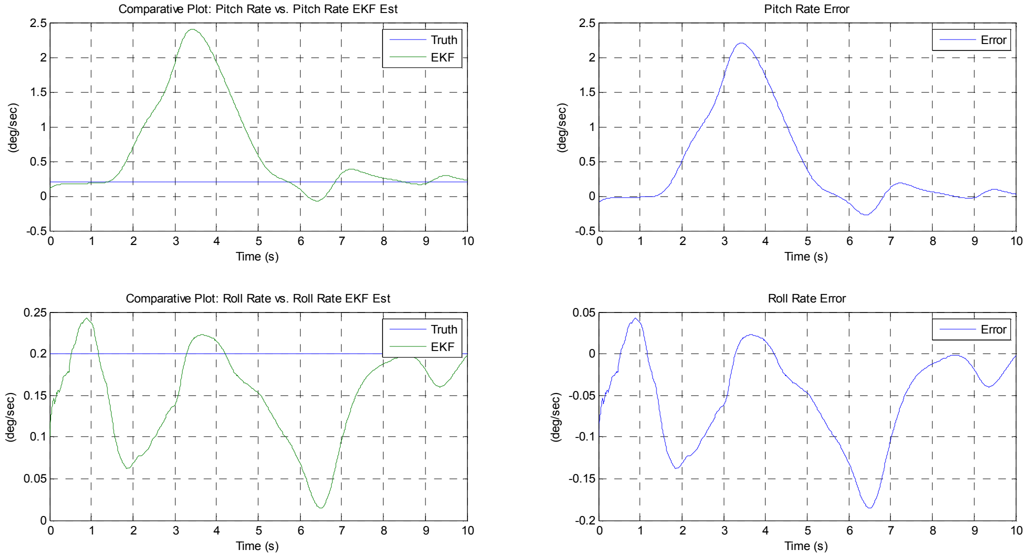

Figure F.10: Phase II Turbulent Bias Estimation Results using Sensor Noise Values

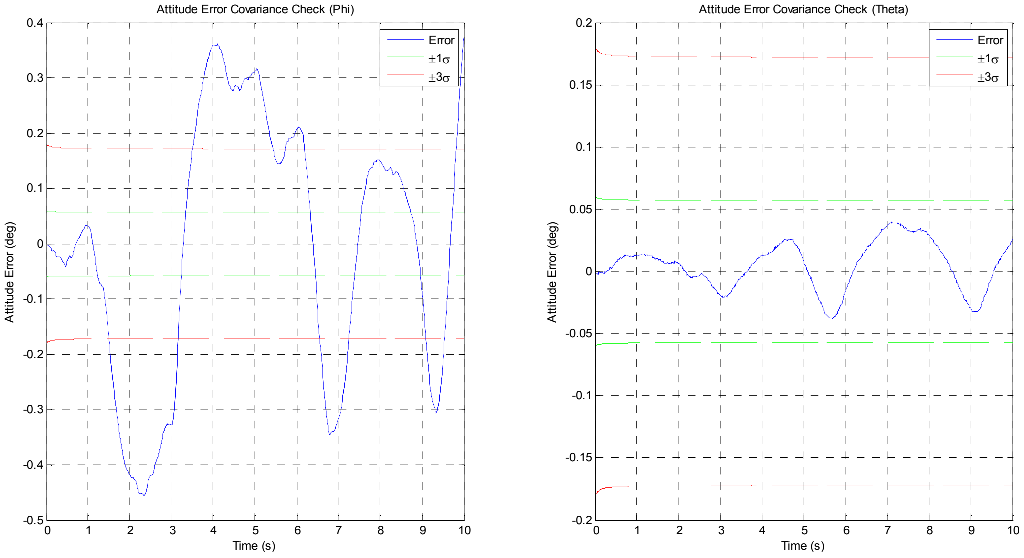

Figure F.11: Phase II Turbulent Attitude Error Covariance Check using Sensor Noise Values

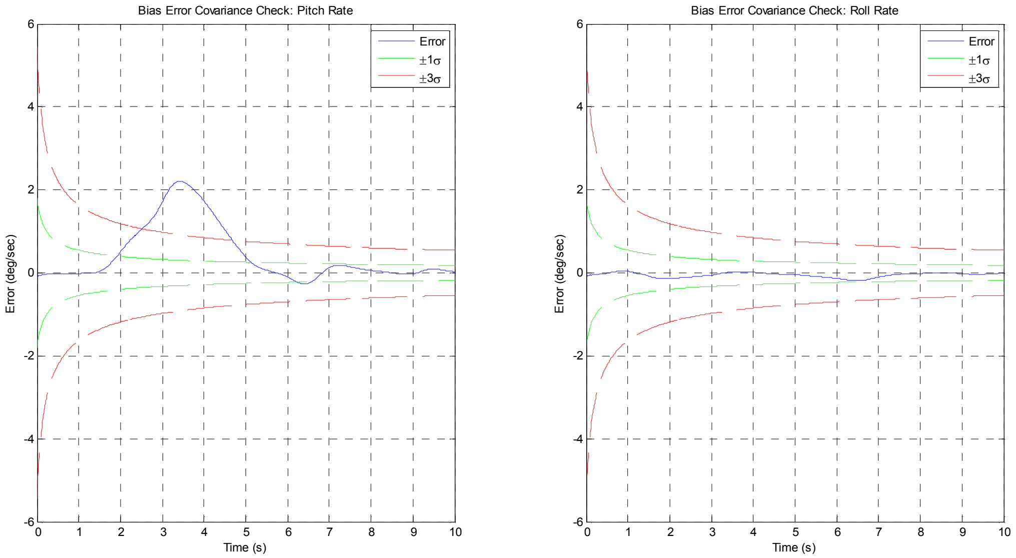

Figure F.12: Phase II Turbulent Bias Error Covariance Check using Sensor Noise Values

F.1.5 Phase III: Non-Turbulent Longitudinal/Transverse Aircraft Simulation Maneuver – Part I

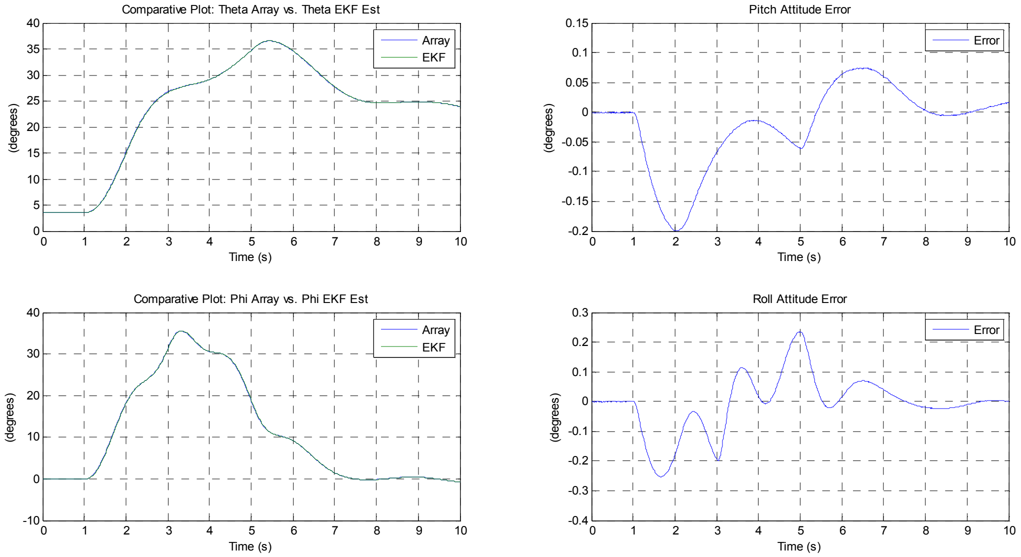

Figure F.13: Phase III Non-Turbulent Attitude Estimation Results using Sensor Noise Values

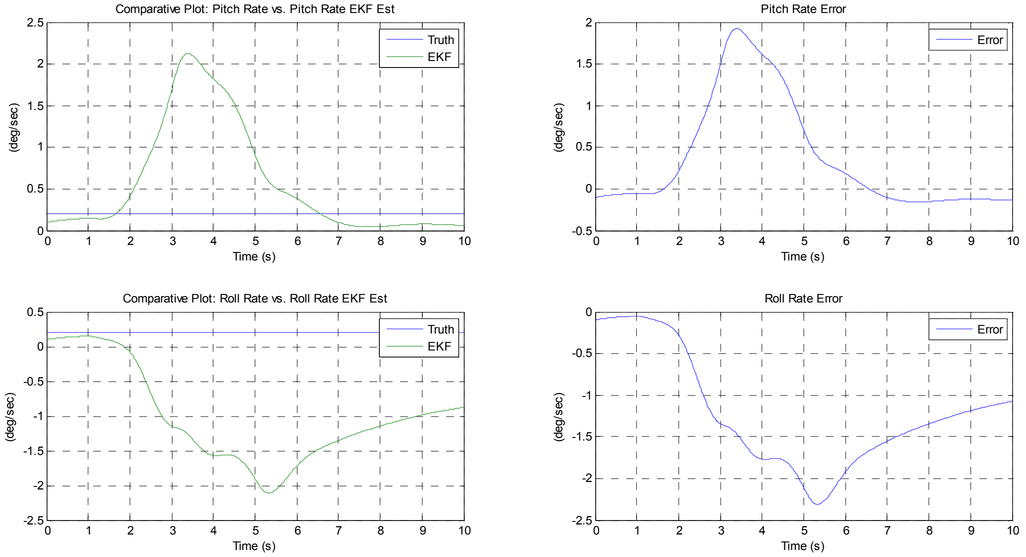

Figure F.14: Phase III Non-Turbulent Bias Estimation Results using Sensor Noise Values

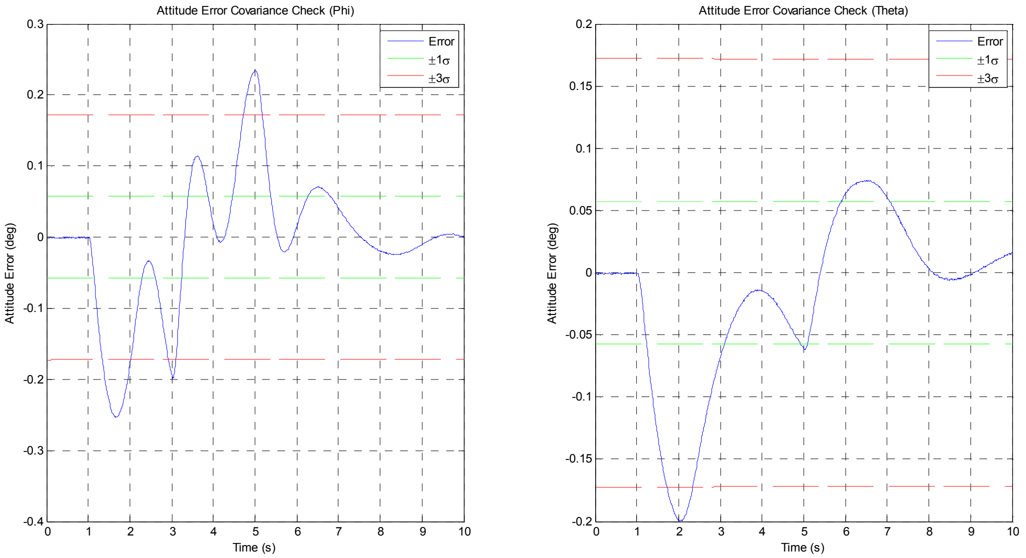

Figure F.15: Phase III Non-Turbulent Attitude Error Covariance Check using Sensor Noise Values

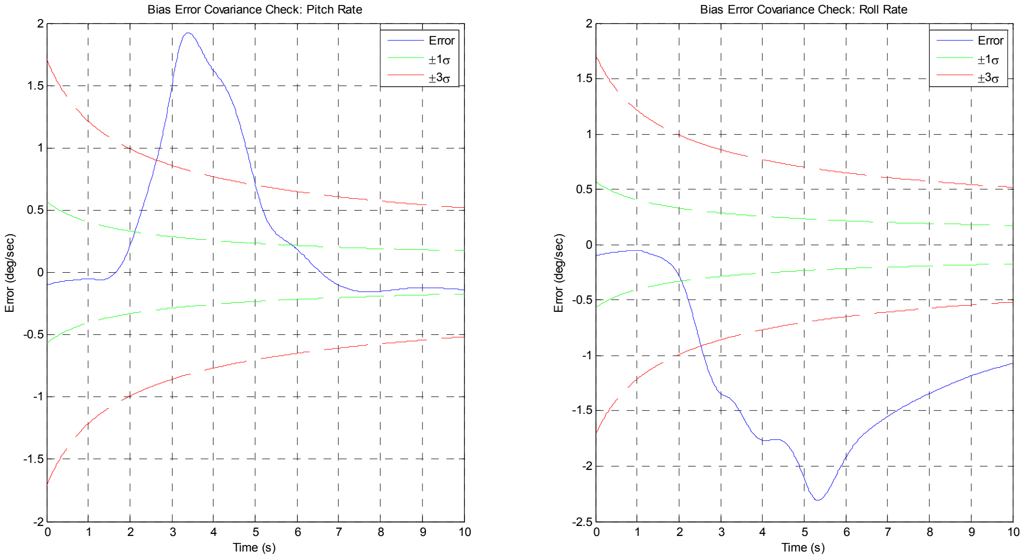

Figure F.16: Phase III Non-Turbulent Bias Error Covariance Check using Sensor Noise Values

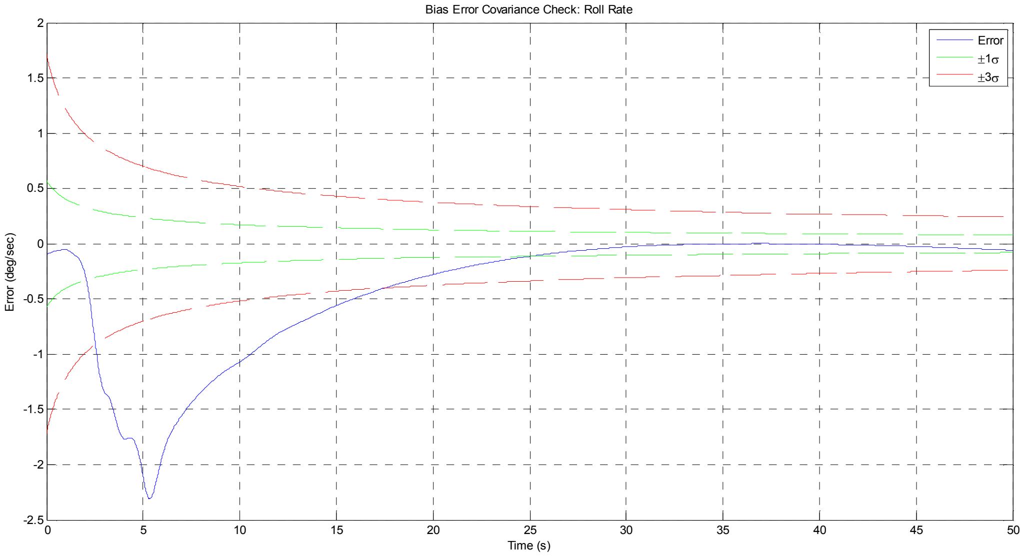

Figure F.17: Phase III Non-Turbulent Roll Rate Bias Error Covariance Check using Sensor Noise Values with Simulation Expanded to 50 Seconds.

F.1.6 Phase III: Turbulent Longitudinal/Transverse Aircraft Simulation Maneuver – Part I

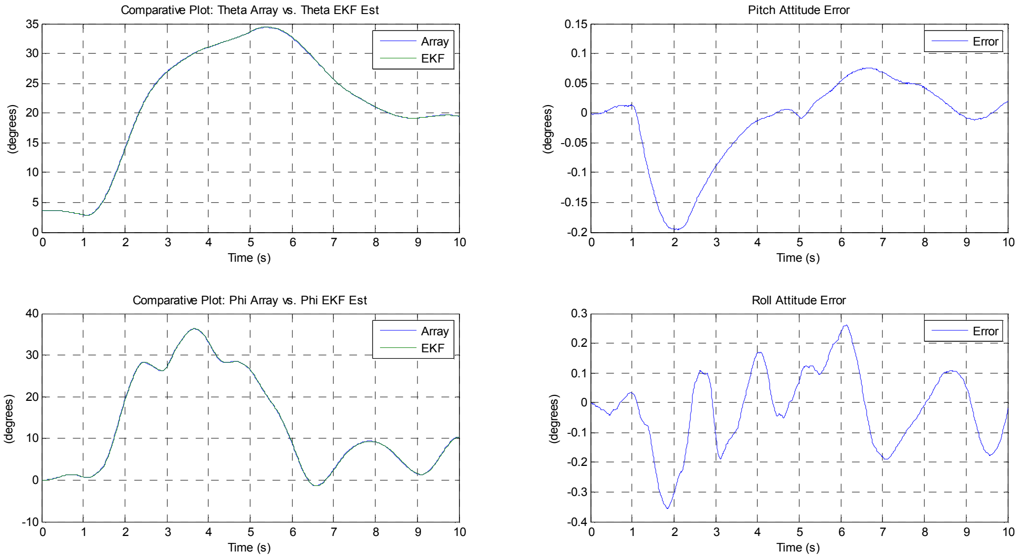

Figure F.18: Phase III Turbulent Attitude Estimation Results using Sensor Noise Values

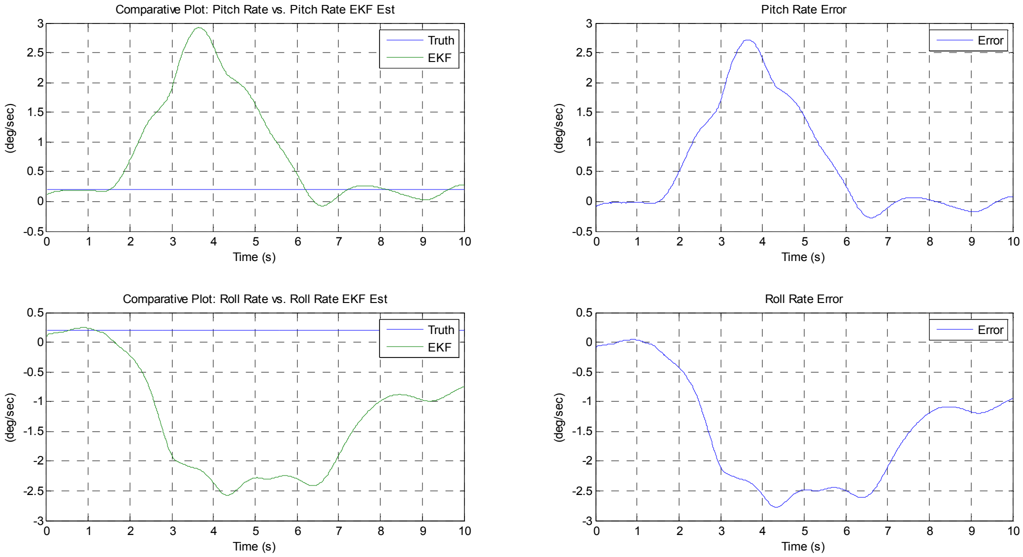

Figure F.19: Phase III Turbulent Bias Estimation Results using Sensor Noise Values

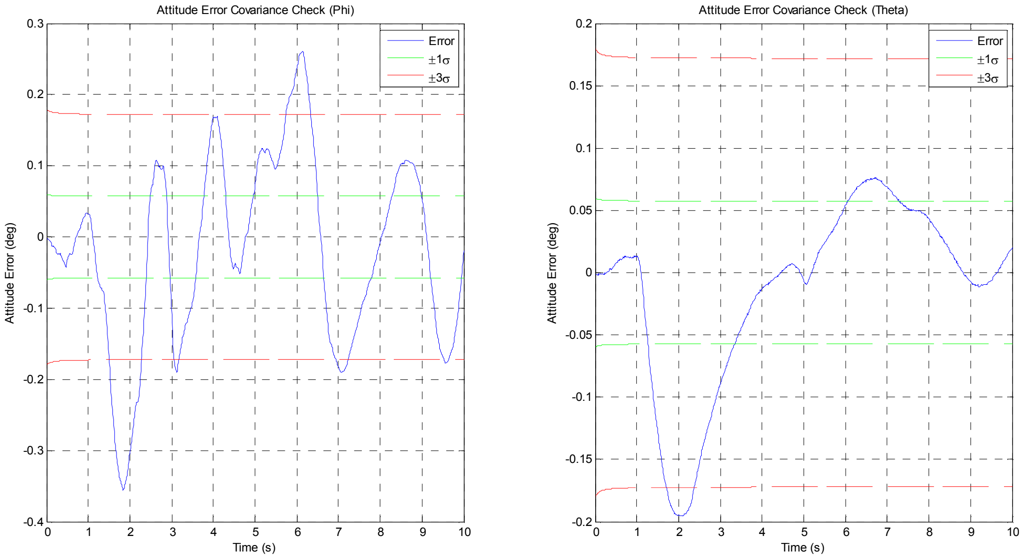
Attitude Error Covariance Check (Phi)

Attitude Error Covariance Check (Theta)

Figure F.20: Phase III Turbulent Attitude Error Covariance Check using Sensor Noise Values

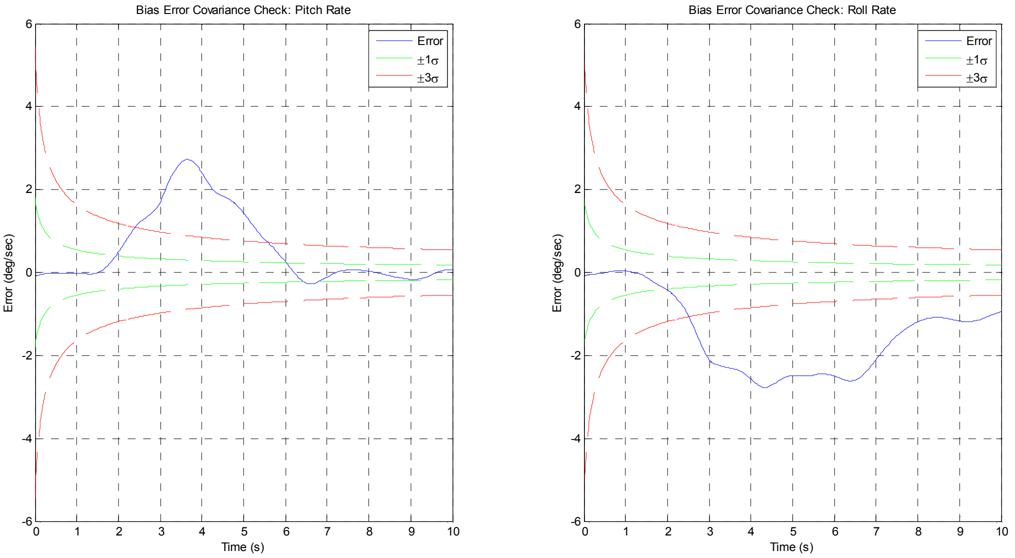
Bias Error Covariance Check: Pitch Rate

Bias Error Covariance Check: Roll Rate

Figure F.21: Phase III Turbulent Bias Error Covariance Check using Sensor Noise Values

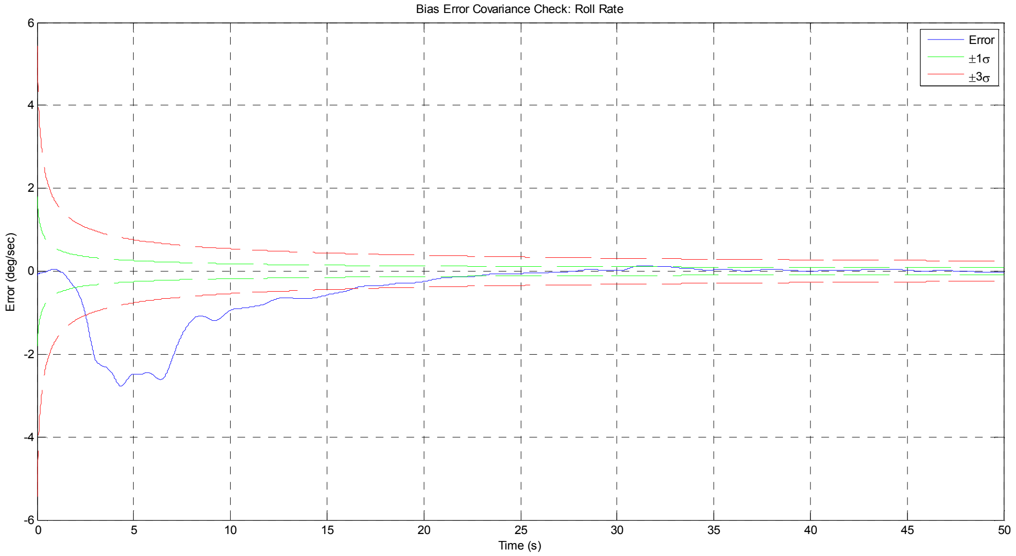

Figure F.22: Phase III Turbulent Roll Rate Bias Error Covariance Check using Sensor Noise Values with Simulation Expanded to 50 Seconds.

F.2 Section 4.4.2 – Comparative Analysis of Algorithm Operation and Sensor Noise Affects: Part II

In this section of the appendix, supplemental figures omitted from Section 4.4.2 for brevity are presented for each phase of the feasibility study conducted to demonstrate correct operation of the algorithm method developed utilizing sensor noise values similar to those given in [51] and presented previously in Table 4.32 in Section 4.4.2. A summation of the maximum and mean absolute attitude and bias estimation errors for each phase of the feasibility study performed was presented previously in Section 4.4.2 in Tables 4.34, 4.35, and 4.36 for non-turbulent and turbulent aircraft simulation maneuvers respectively.

F.2.1 Phase I: Non-Turbulent Longitudinal Aircraft Simulation Maneuver – Part II

Nonlinear Aircraft Simulation: Study A

This phase of the study was previously conducted and displayed in Section 4.4.2. The results and conclusions developed from the performed nonlinear simulations are presented in completeness in Section 4.4.2.

Nonlinear Aircraft Simulation: Study B

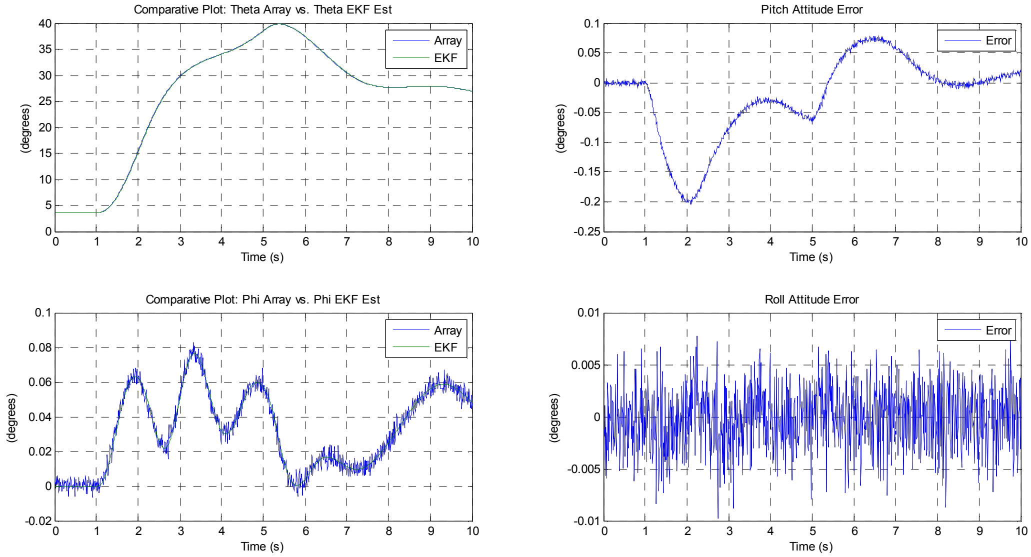

Figure F.23: Phase I Non-Turbulent Attitude Estimation Results using Sensor Noise Values: Part II - Study B

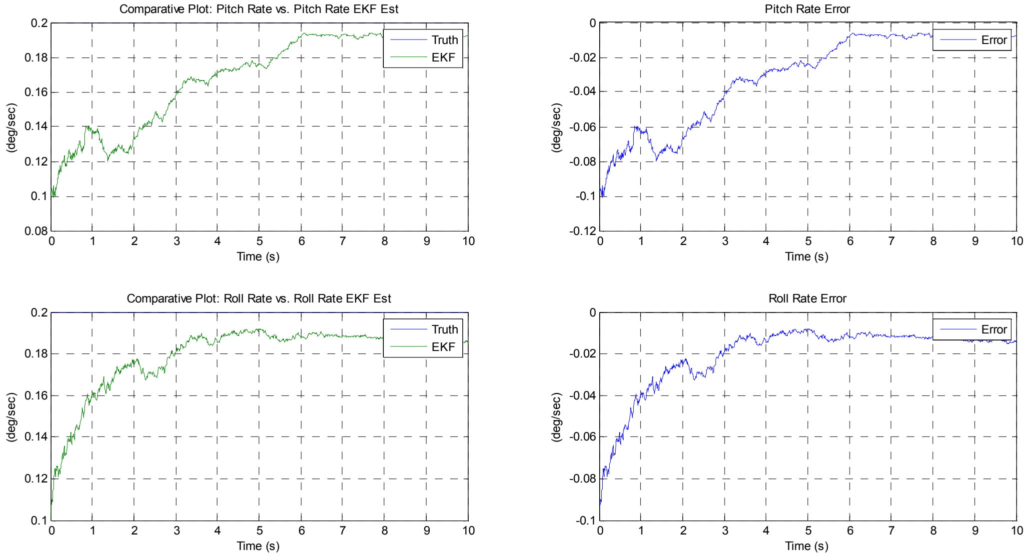

Figure F.24: Phase I Non-Turbulent Bias Estimation Results using Sensor Noise Values: Part II - Study B

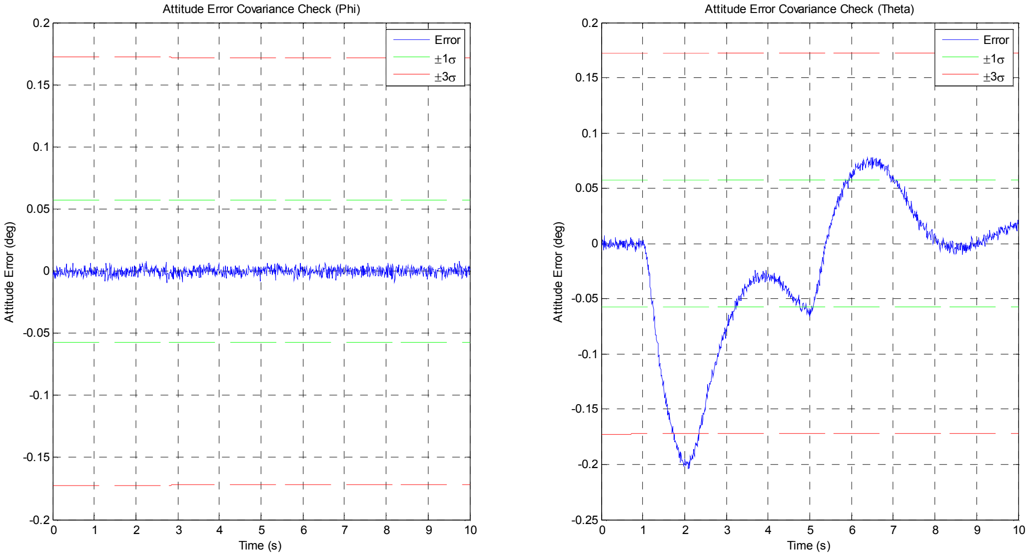

Figure F.25: Phase I Non-Turbulent Attitude Error Covariance Check using Sensor Noise Values: Part II - Study B

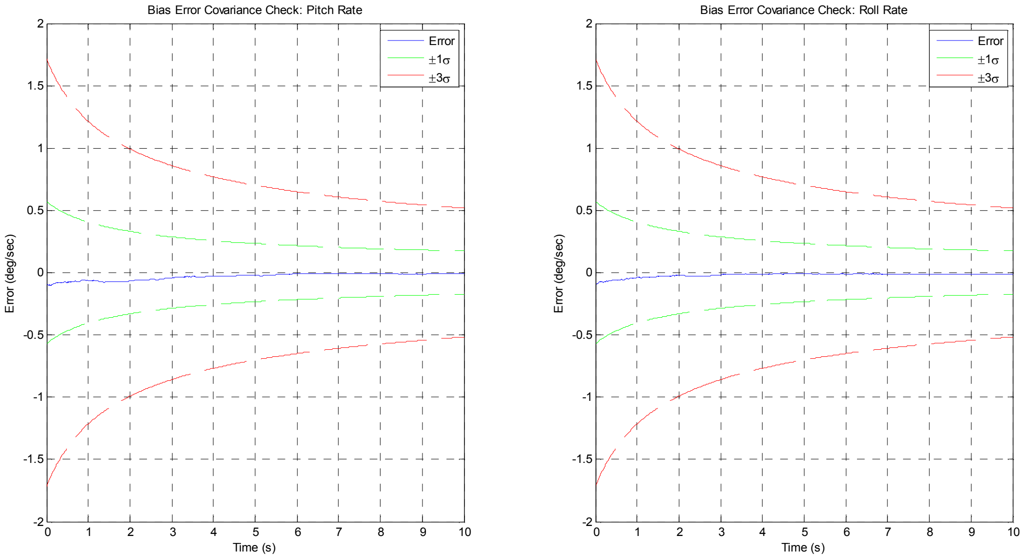

Figure F.26: Phase I Non-Turbulent Bias Error Covariance Check using Sensor Noise Values: Part II - Study B

Nonlinear Aircraft Simulation: Study C

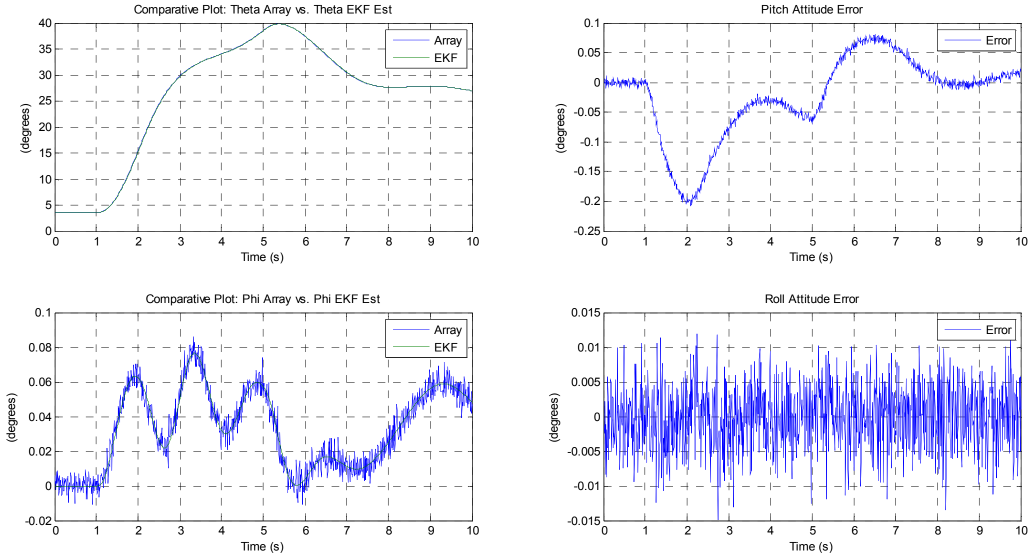

Figure F.27: Phase I Non-Turbulent Attitude Estimation Results using Sensor Noise Values: Part II - Study C

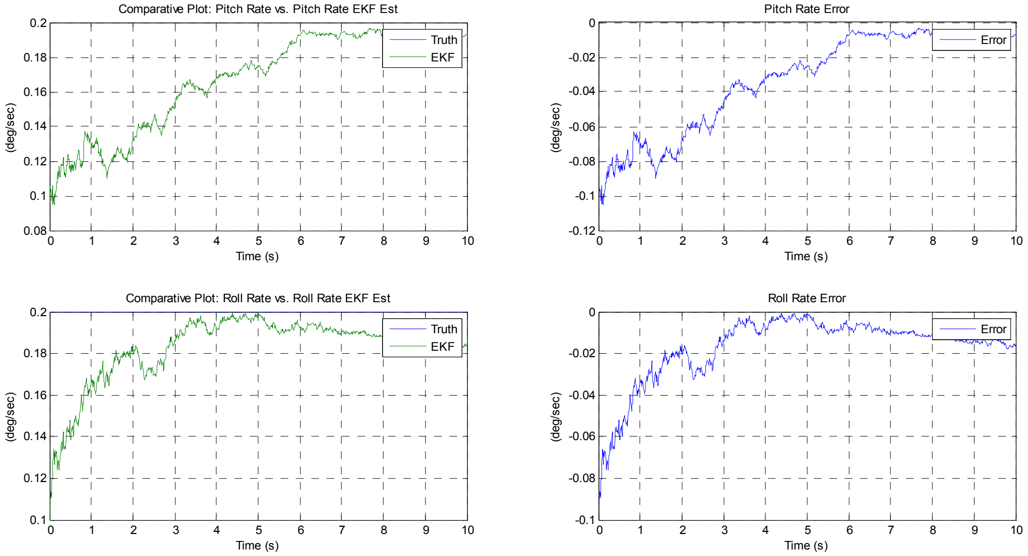

Figure F.28: Phase I Non-Turbulent Bias Estimation Results using Sensor Noise Values: Part II - Study C

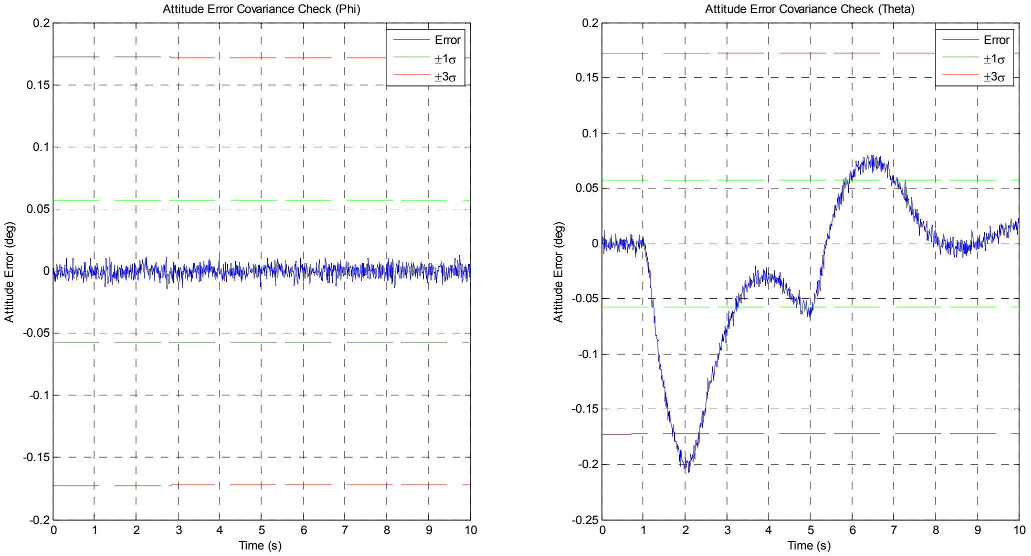

Figure F.29: Phase I Non-Turbulent Attitude Error Covariance Check using Sensor Noise Values: Part II - Study C

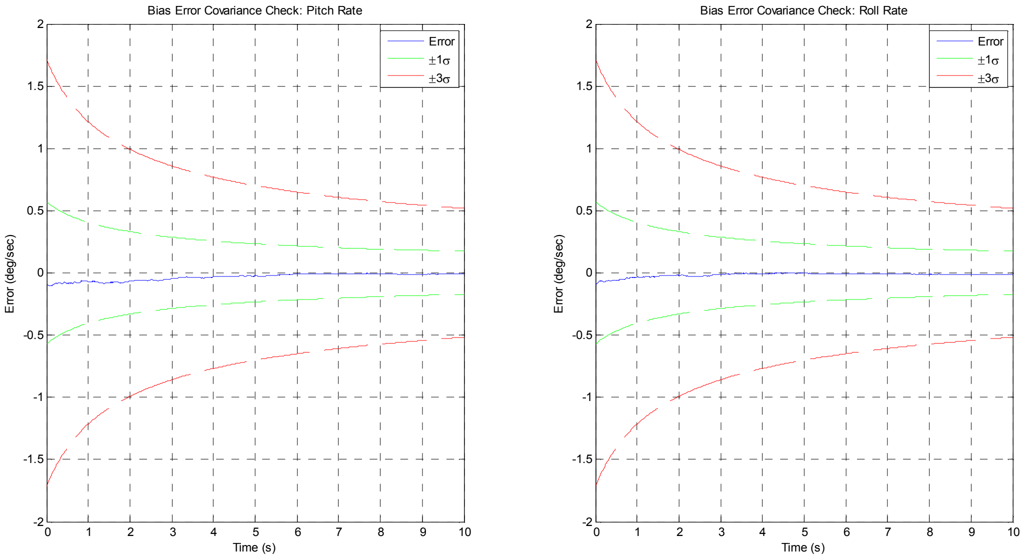

Figure F.30: Phase I Non-Turbulent Bias Error Covariance Check using Sensor Noise Values: Part II - Study C

F.2.2 Phase I: Turbulent Longitudinal Aircraft Simulation Maneuver – Part II

Nonlinear Aircraft Simulation: Study A

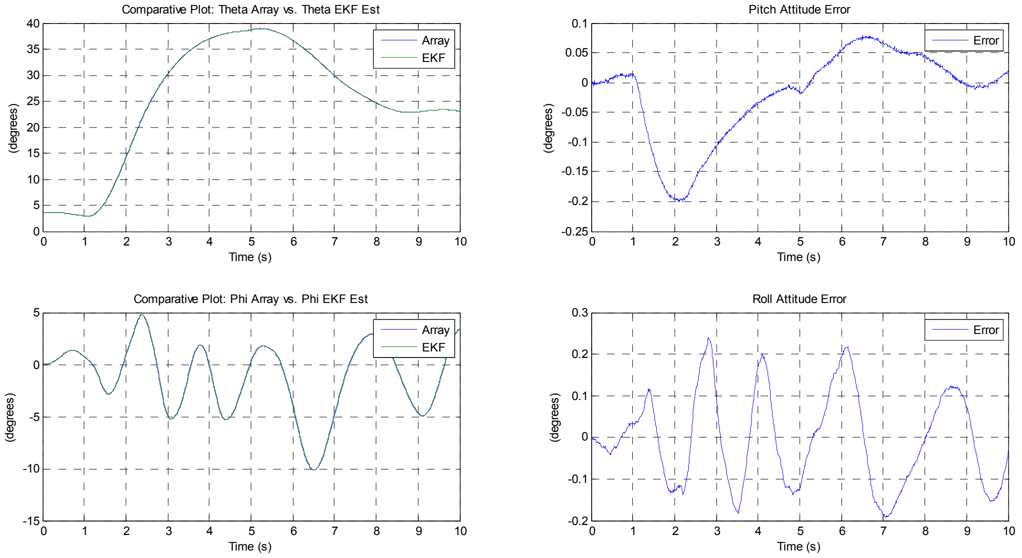

Figure F.31: Phase I Turbulent Attitude Estimation Results using Sensor Noise Values: Part II - Study A

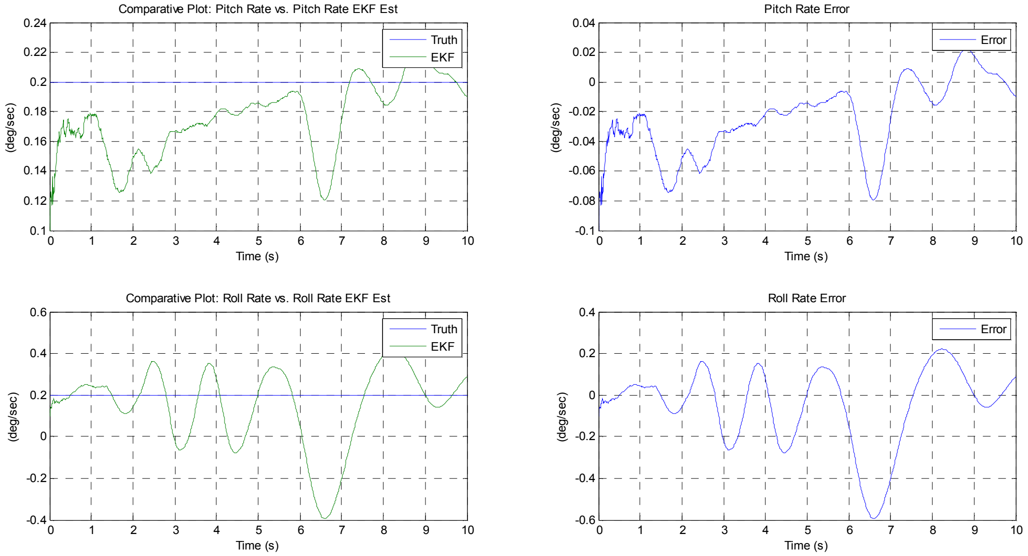

Figure F.32: Phase I Turbulent Bias Estimation Results using Sensor Noise Values: Part II - Study A

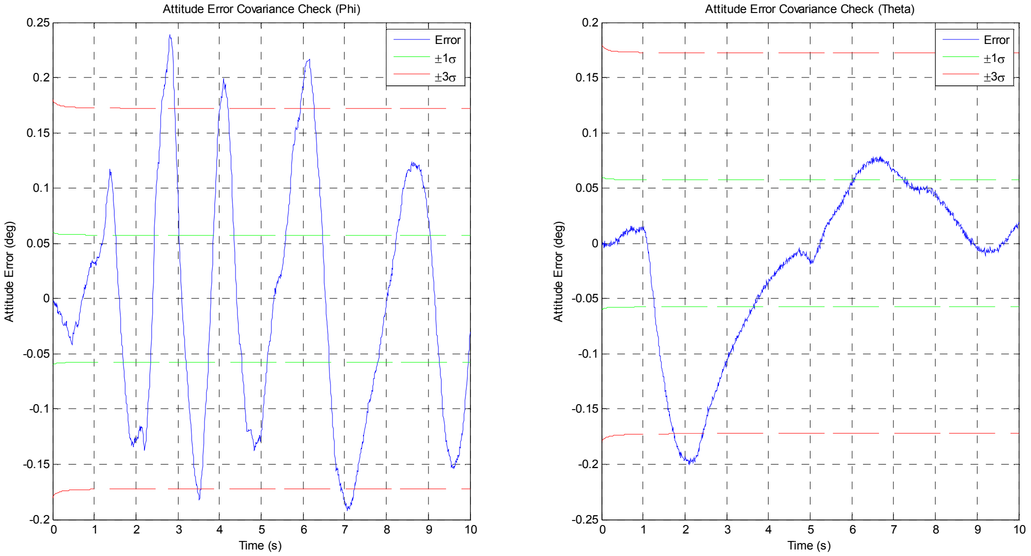

Figure F.33: Phase I Turbulent Attitude Error Covariance Check using Sensor Noise Values: Part II - Study A

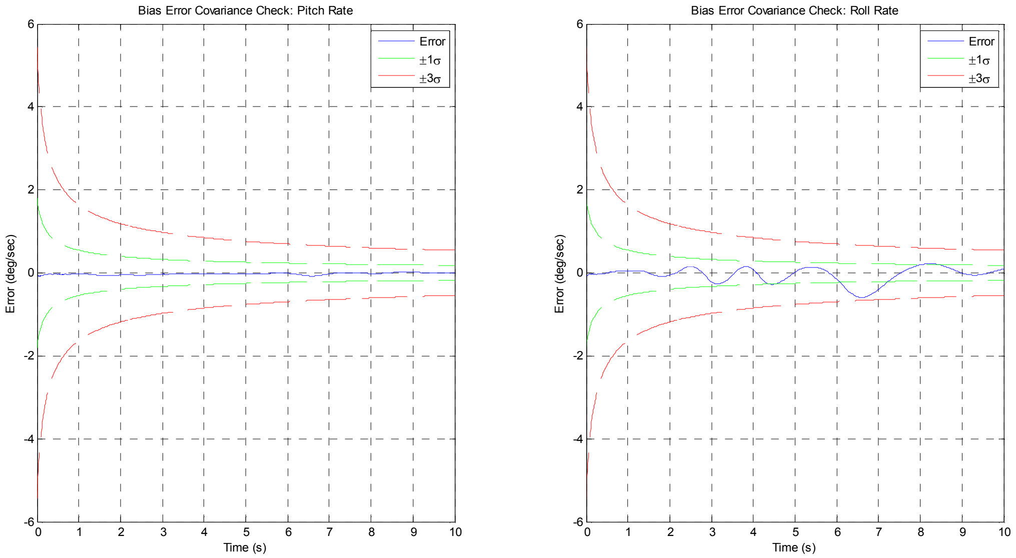

Figure F.34: Phase I Turbulent Bias Error Covariance Check using Sensor Noise Values: Part II - Study A

Nonlinear Aircraft Simulation: Study B

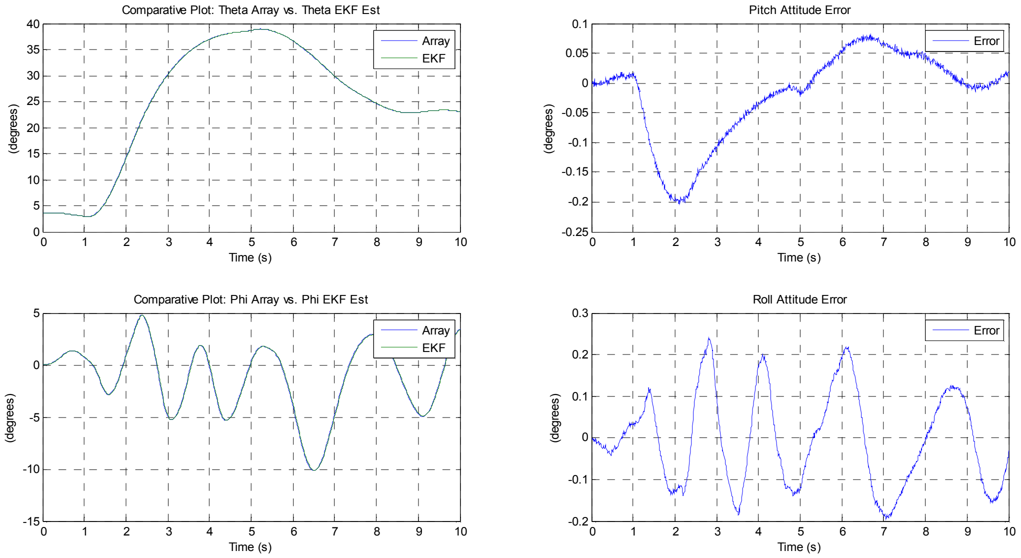

Figure F.35: Phase I Turbulent Attitude Estimation Results using Sensor Noise Values: Part II - Study B

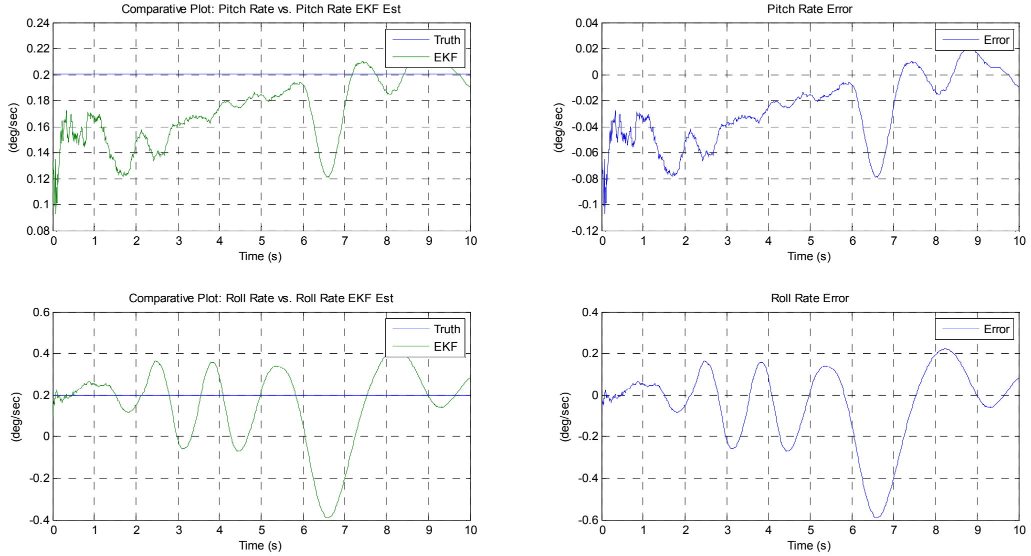
Comparative Plot: Pitch Rate vs. Pitch Rate EKF Est

Pitch Rate Error

Comparative Plot: Roll Rate vs. Roll Rate EKF Est

Roll Rate Error

Figure F.36: Phase I Turbulent Bias Estimation Results using Sensor Noise Values: Part II - Study B

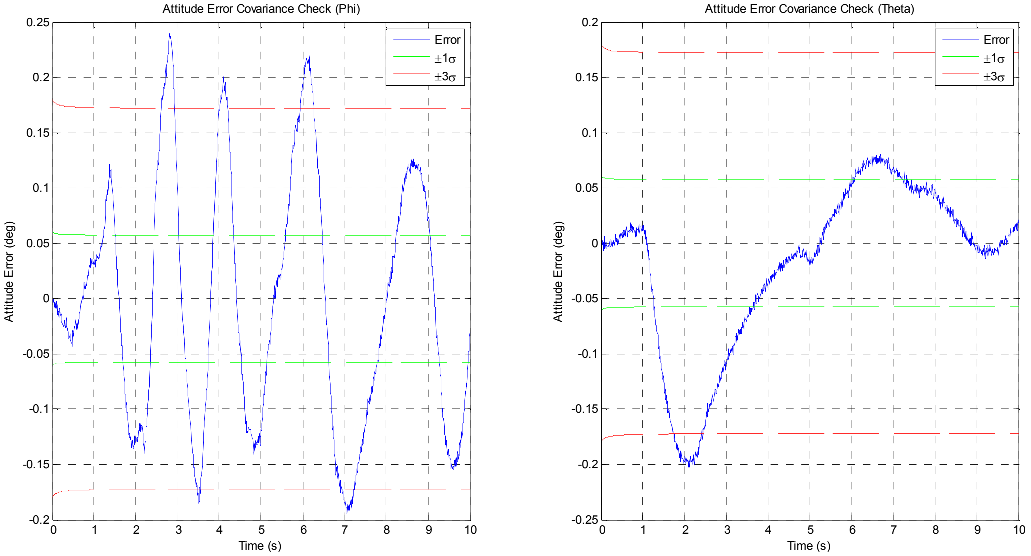
Attitude Error Covariance Check (Phi)

Attitude Error Covariance Check (Theta)

Figure F.37: Phase I Turbulent Attitude Error Covariance Check using Sensor Noise Values: Part II - Study B

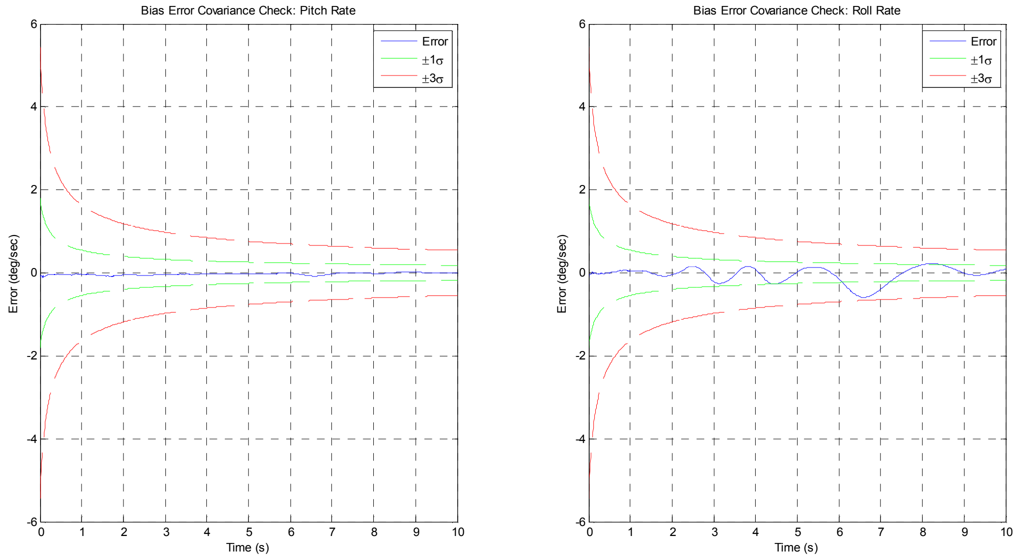

Figure F.38: Phase I Turbulent Bias Error Covariance Check using Sensor Noise Values: Part II - Study B

Nonlinear Aircraft Simulation: Study C

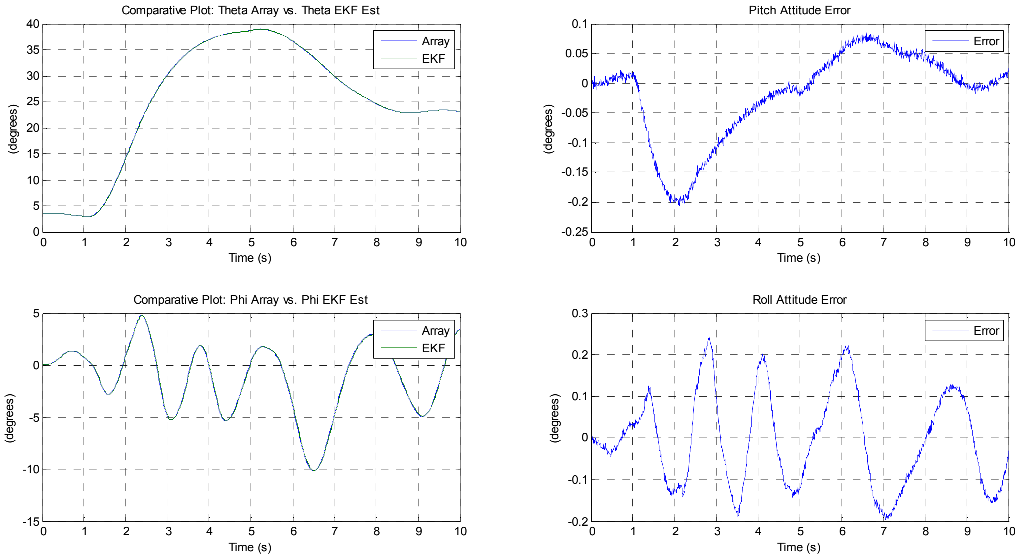

Figure F.39: Phase I Turbulent Attitude Estimation Results using Sensor Noise Values: Part II - Study C

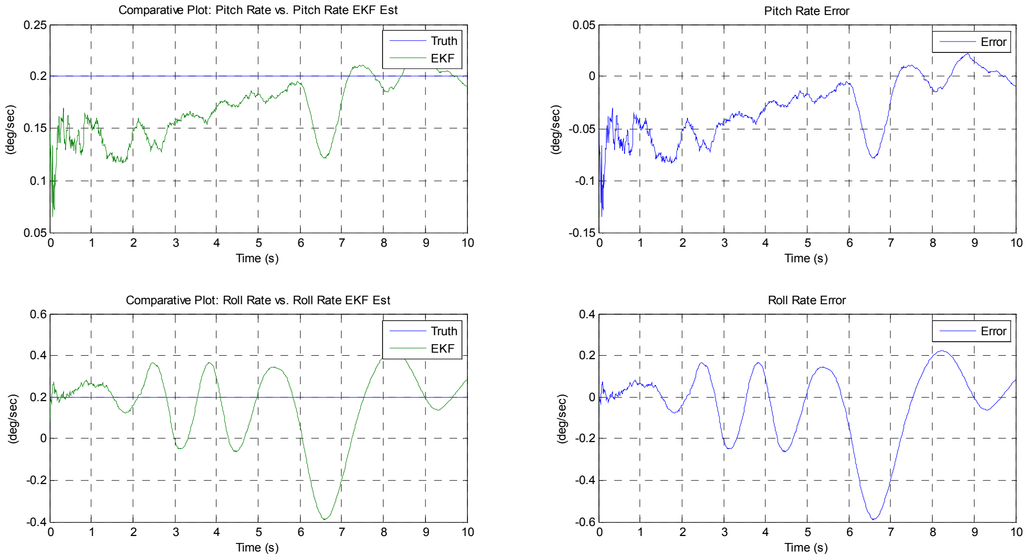

Figure F.40: Phase I Turbulent Bias Estimation Results using Sensor Noise Values: Part II - Study C

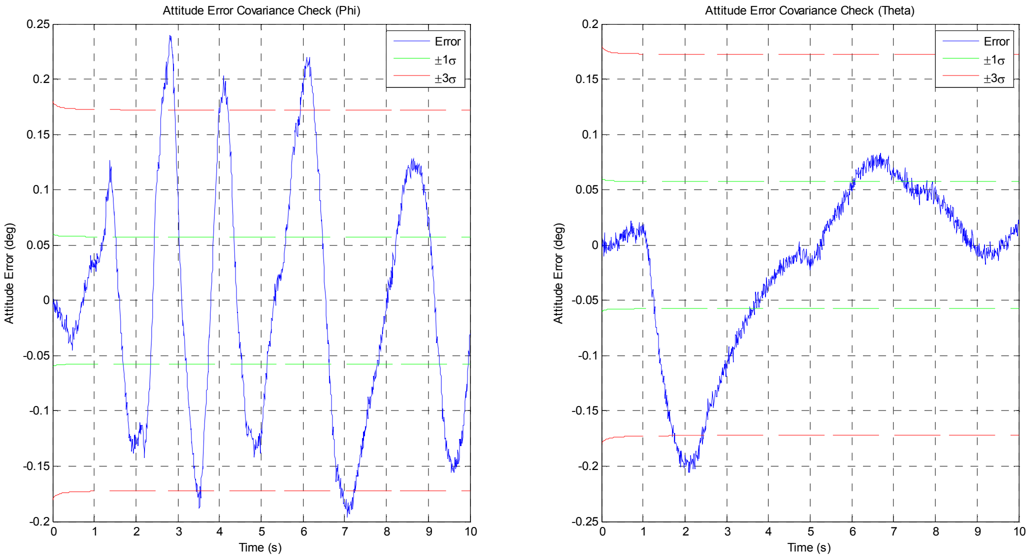

Figure F.41: Phase I Turbulent Attitude Error Covariance Check using Sensor Noise Values: Part II - Study C

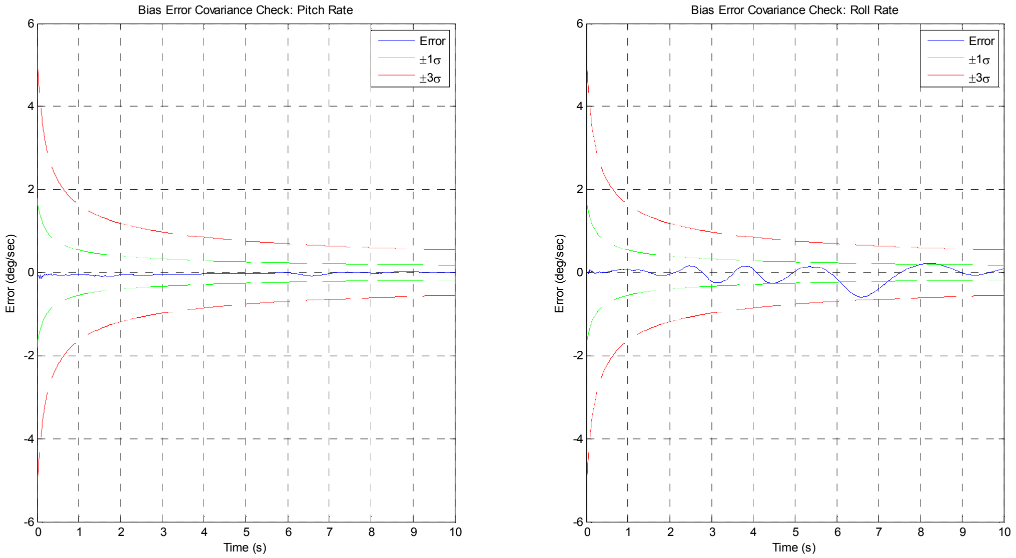

Figure F.42: Phase I Turbulent Bias Error Covariance Check using Sensor Noise Values: Part II - Study C

F.2.3 Phase II: Non-Turbulent Transverse Aircraft Simulation Maneuver – Part II

Nonlinear Aircraft Simulation: Study A

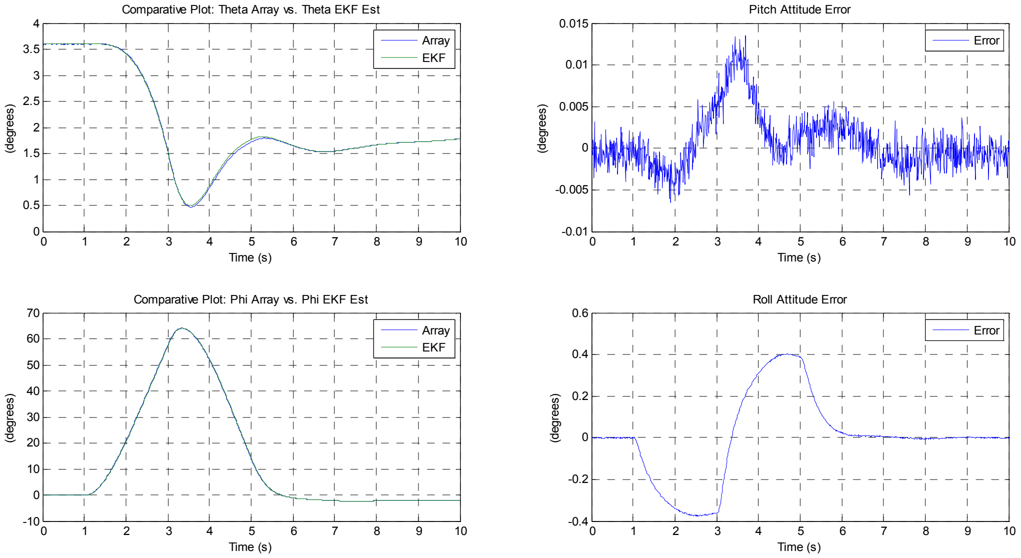

Figure F.43: Phase II Non-Turbulent Attitude Estimation Results using Sensor Noise Values: Part II - Study A

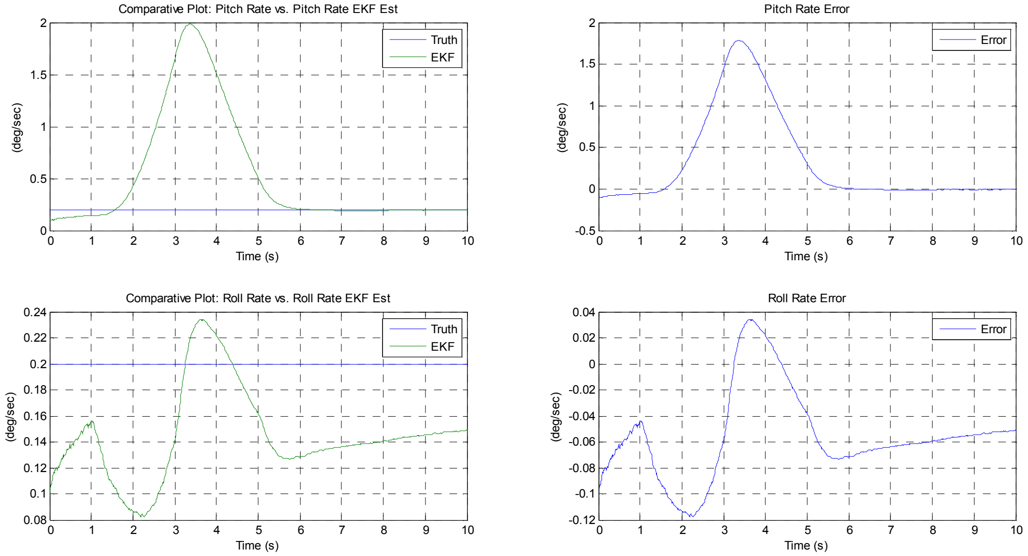

Figure F.44: Phase II Non-Turbulent Bias Estimation Results using Sensor Noise Values: Part II - Study A

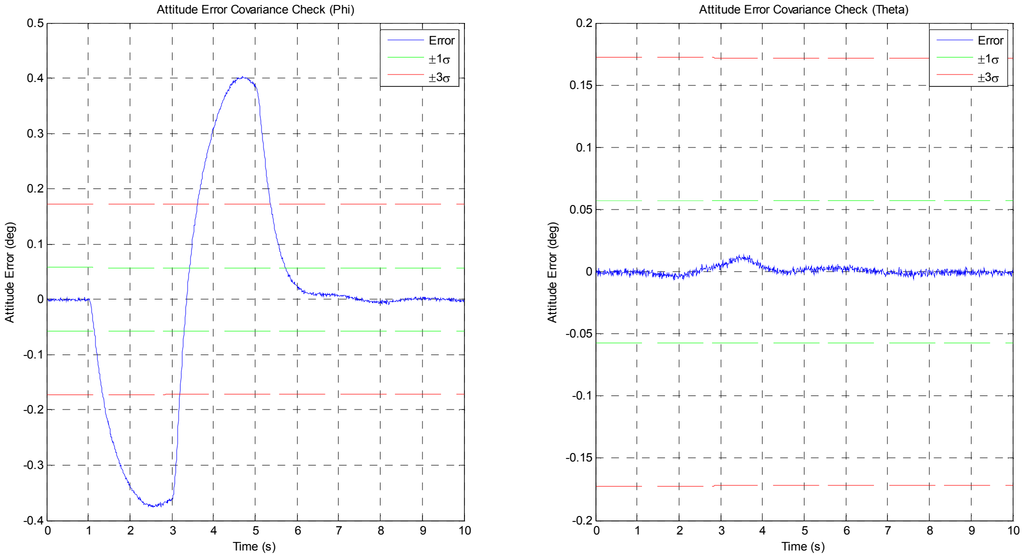

Figure F.45: Phase II Non-Turbulent Attitude Error Covariance Check using Sensor Noise Values: Part II - Study A

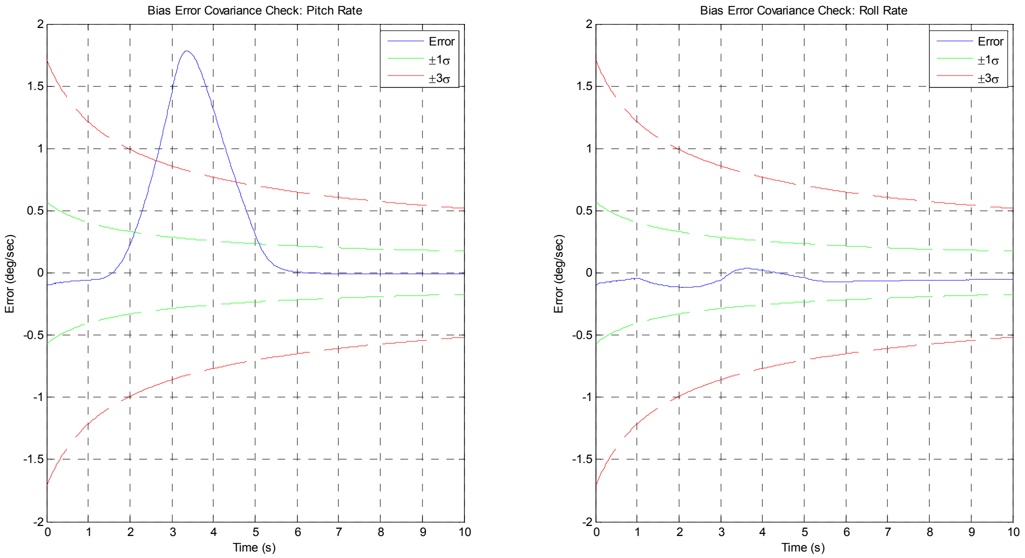

Figure F.46: Phase II Non-Turbulent Bias Error Covariance Check using Sensor Noise Values: Part II - Study A

Nonlinear Aircraft Simulation: Study B

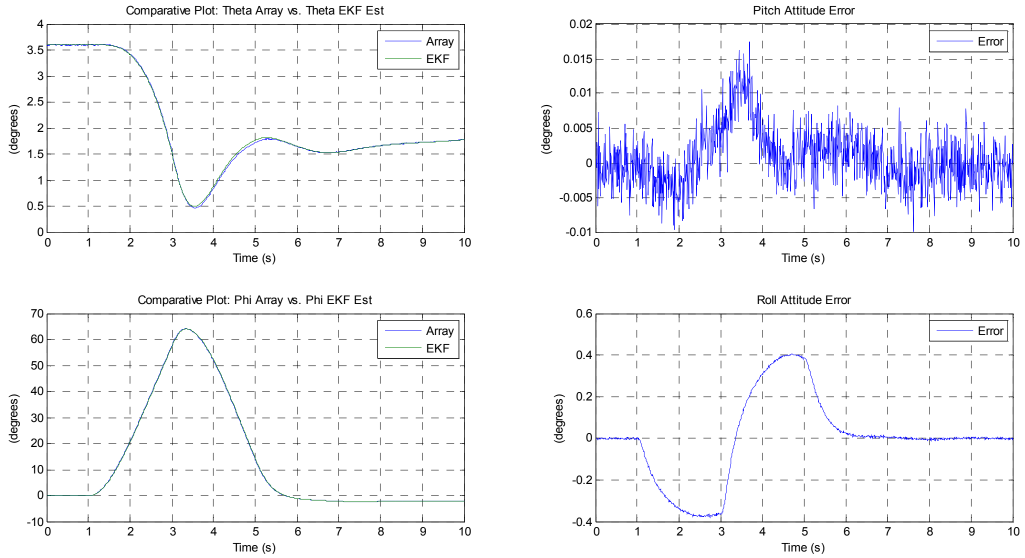

Figure F.47: Phase II Non-Turbulent Attitude Estimation Results using Sensor Noise Values: Part II - Study B

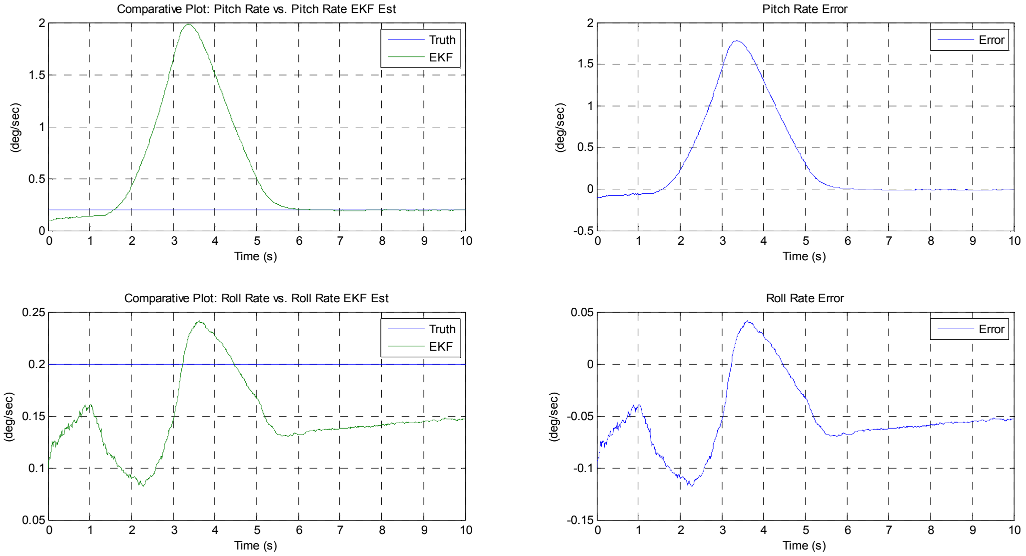

Figure F.48: Phase II Non-Turbulent Bias Estimation Results using Sensor Noise Values: Part II - Study B

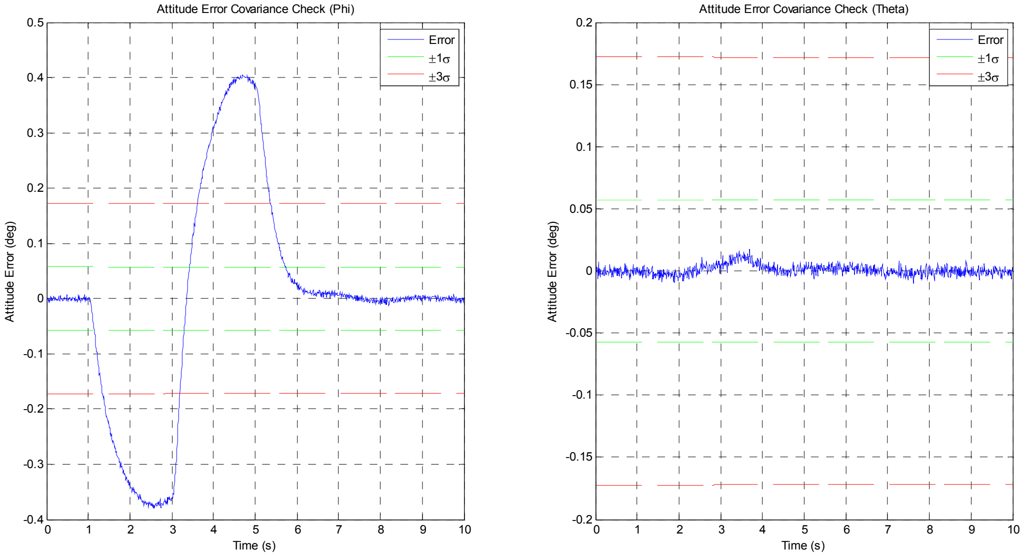

Figure F.49: Phase II Non-Turbulent Attitude Error Covariance Check using Sensor Noise Values: Part II - Study B

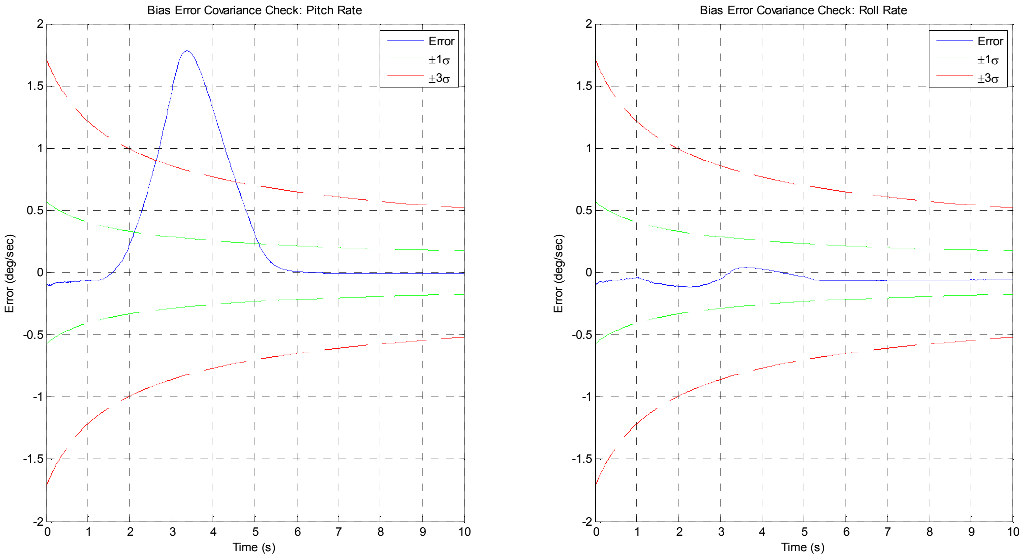

Figure F.50: Phase II Non-Turbulent Bias Error Covariance Check using Sensor Noise Values: Part II - Study B

Nonlinear Aircraft Simulation: Study C

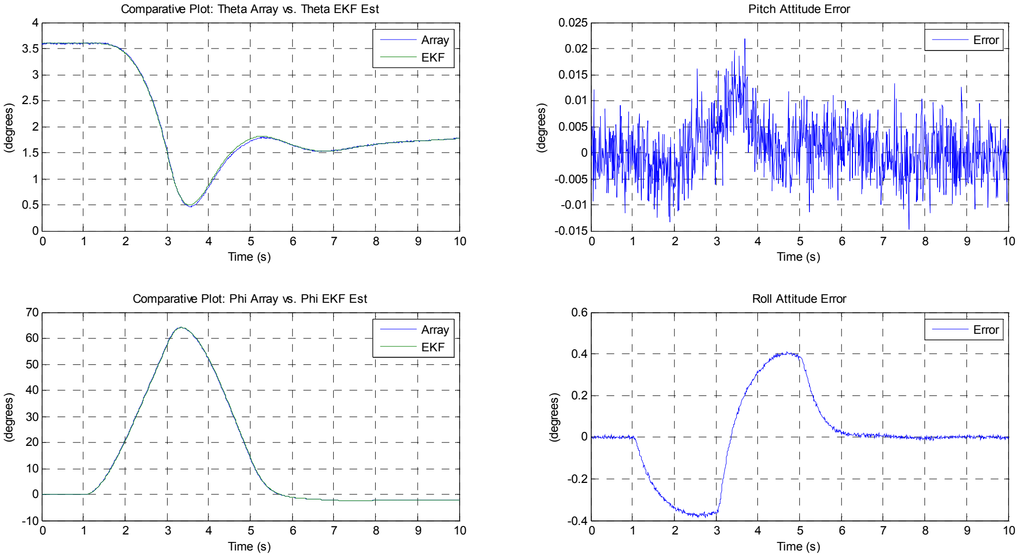

Figure F.51: Phase II Non-Turbulent Attitude Estimation Results using Sensor Noise Values: Part II - Study C

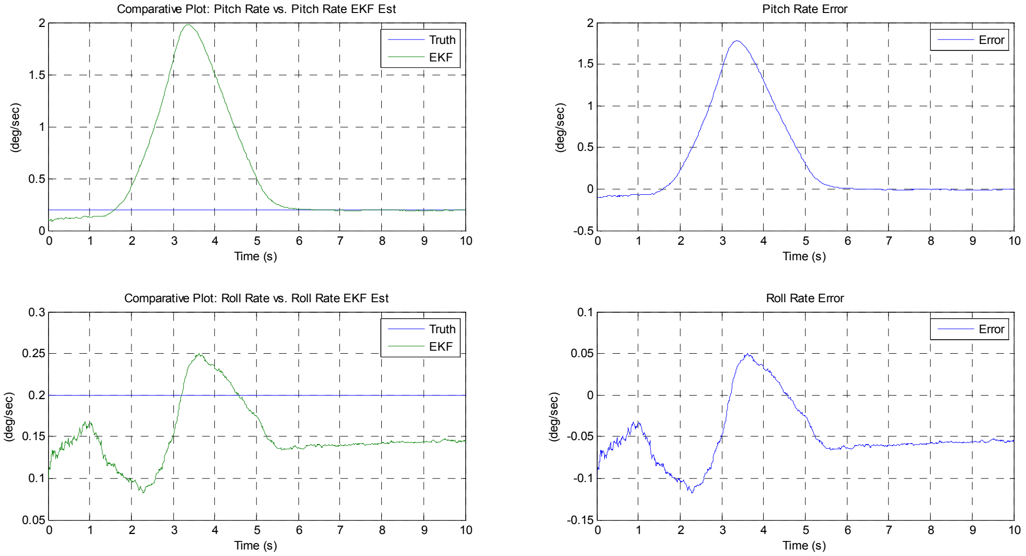

Figure F.52: Phase II Non-Turbulent Bias Estimation Results using Sensor Noise Values: Part II - Study C

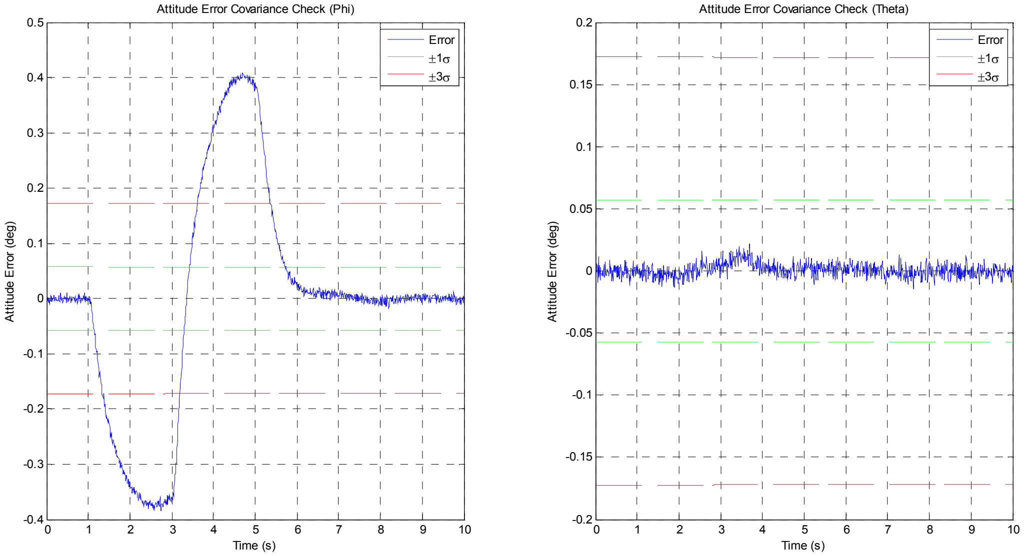

Figure F.53: Phase II Non-Turbulent Attitude Error Covariance Check using Sensor Noise Values: Part II - Study C

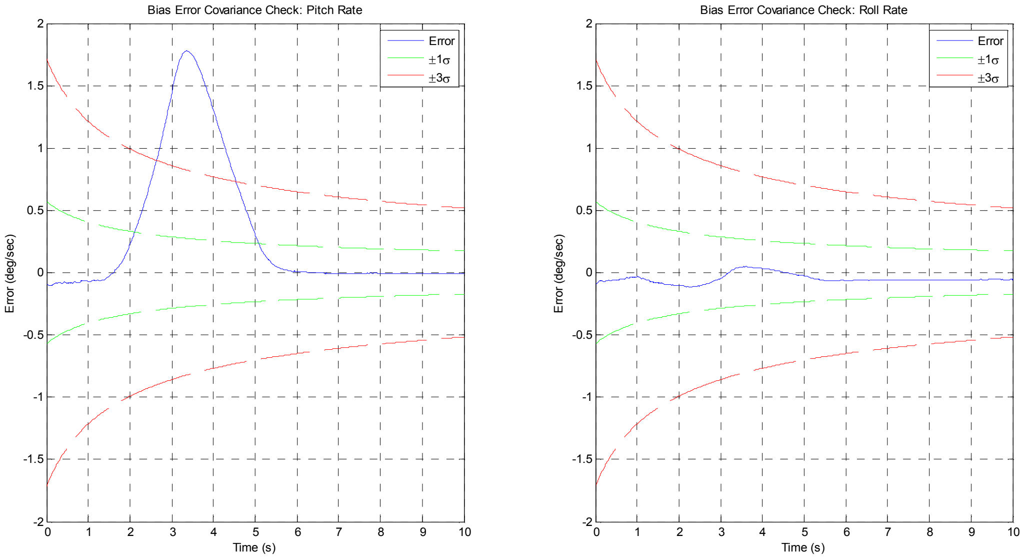

Figure F.54: Phase II Non-Turbulent Bias Error Covariance Check using Sensor Noise Values: Part II - Study C

F.2.4 Phase II: Turbulent Transverse Aircraft Simulation Maneuver – Part II

Nonlinear Aircraft Simulation: Study A

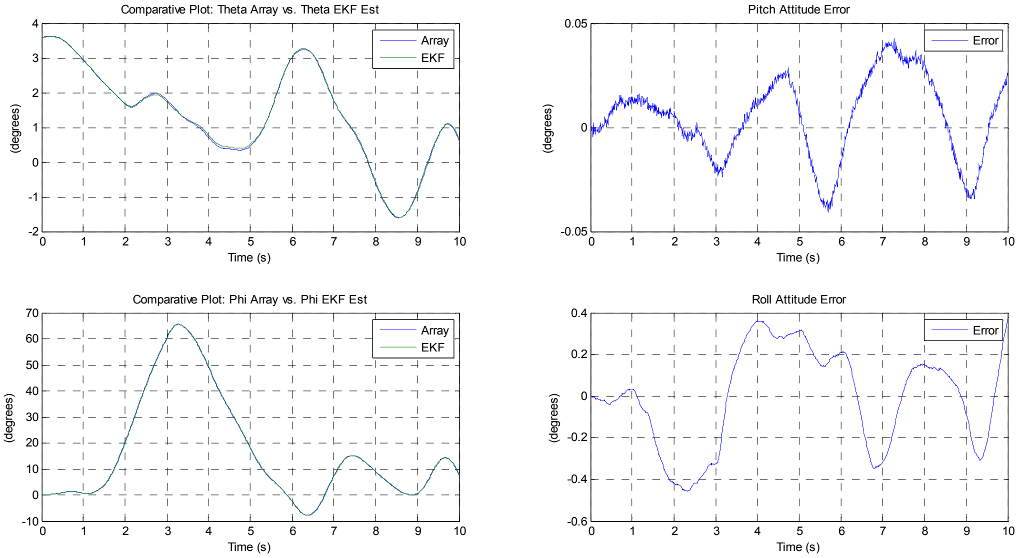

Figure F.55: Phase II Turbulent Attitude Estimation Results using Sensor Noise Values: Part II - Study A

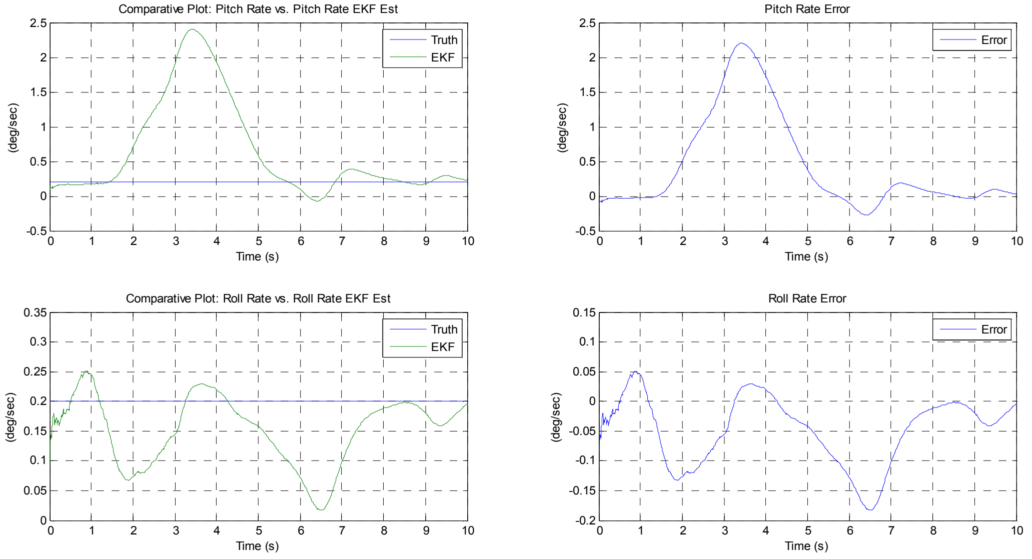

Figure F.56: Phase II Turbulent Bias Estimation Results using Sensor Noise Values: Part II - Study A

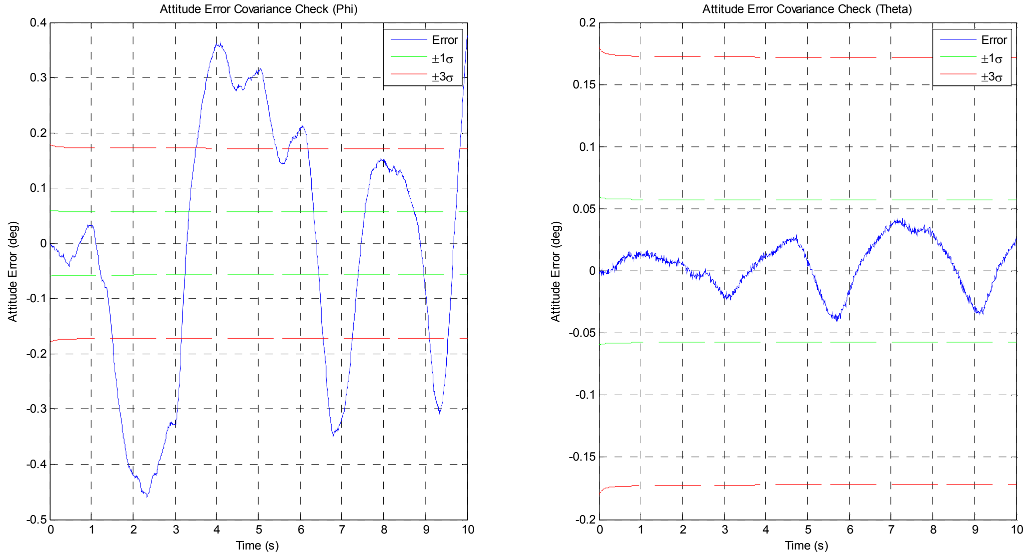

Figure F.57: Phase II Turbulent Attitude Error Covariance Check using Sensor Noise Values: Part II - Study A

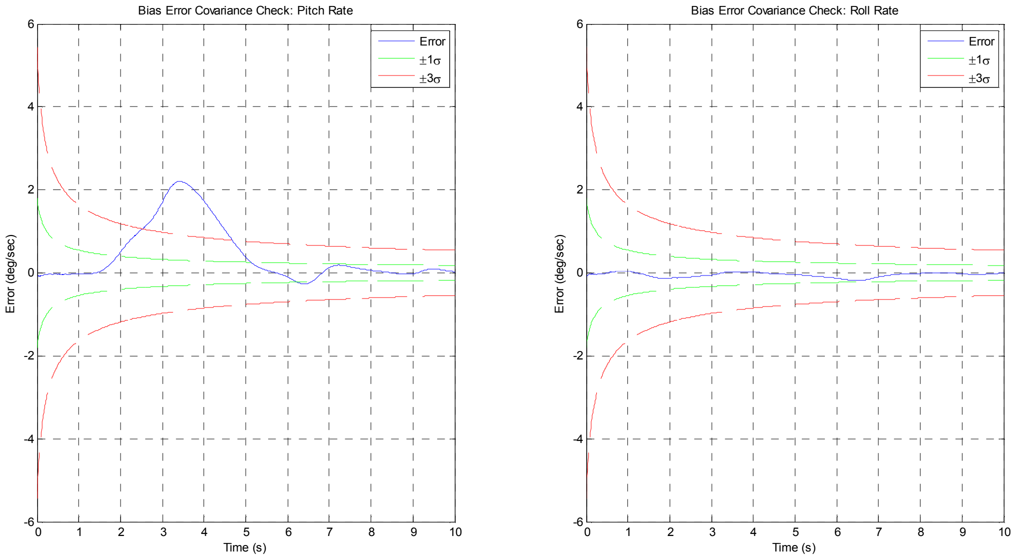

Figure F.58: Phase II Turbulent Bias Error Covariance Check using Sensor Noise Values: Part II - Study A

Nonlinear Aircraft Simulation: Study B

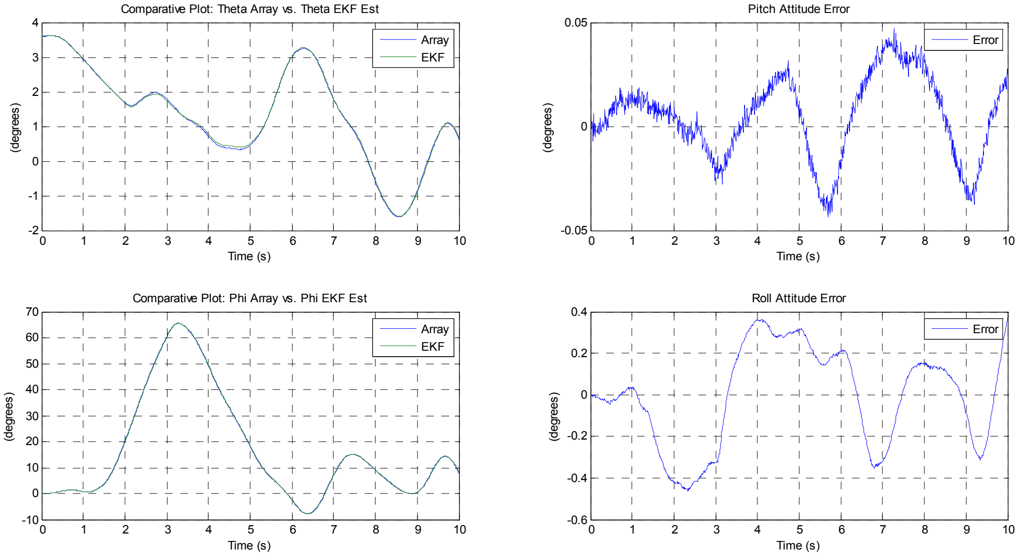

Figure F.59: Phase II Turbulent Attitude Estimation Results using Sensor Noise Values: Part II - Study B

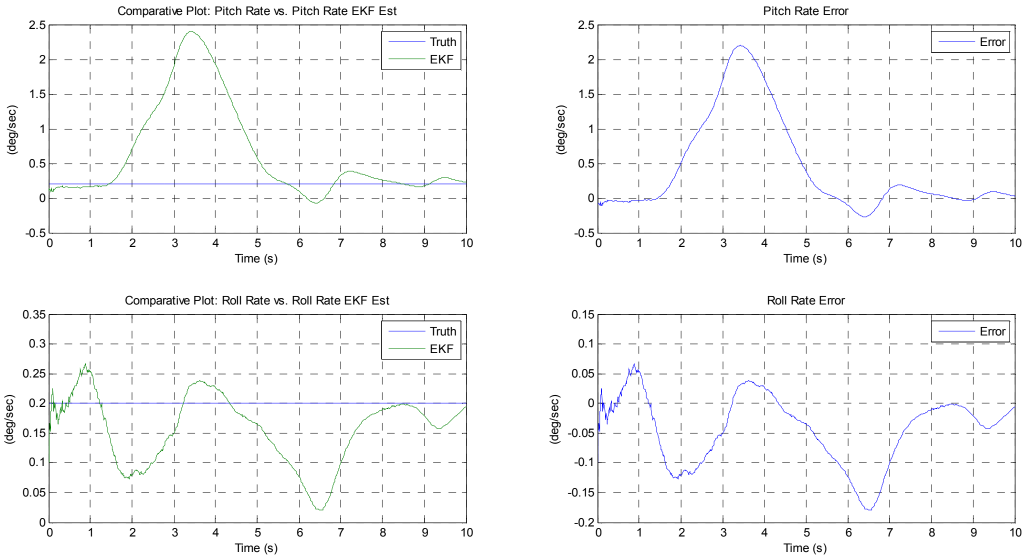

Figure F.60: Phase II Turbulent Bias Estimation Results using Sensor Noise Values: Part II - Study B

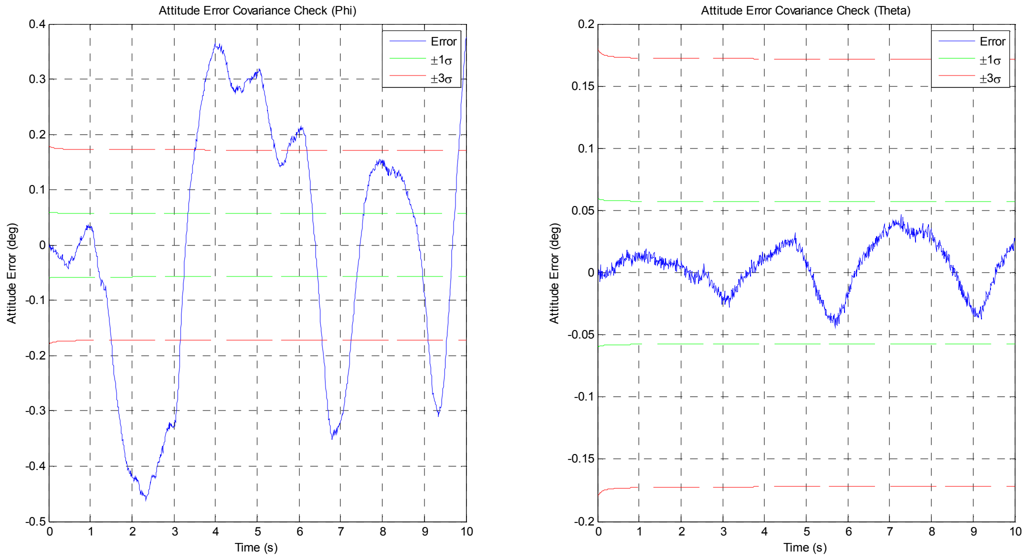

Figure F.61: Phase II Turbulent Attitude Error Covariance Check using Sensor Noise Values: Part II - Study B

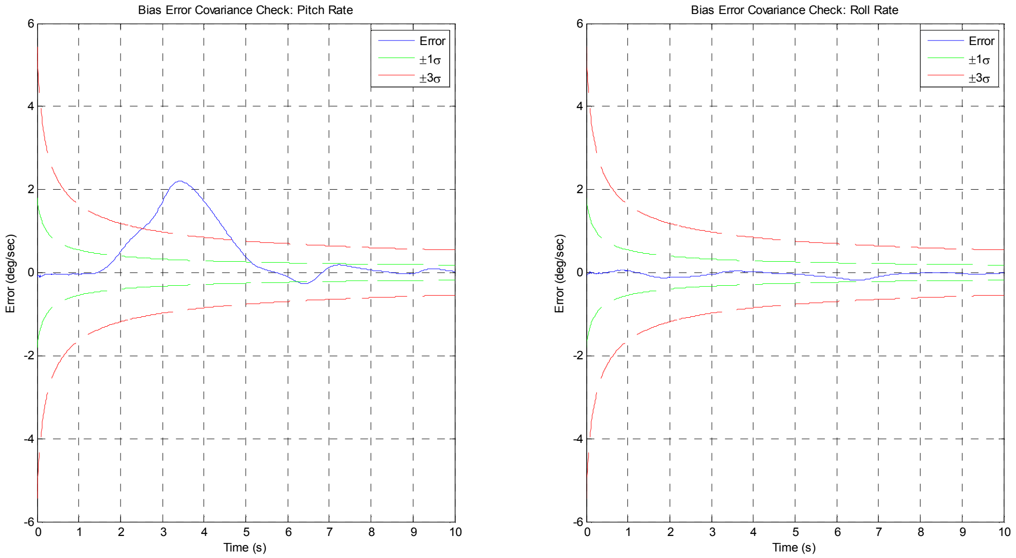

Figure F.62: Phase II Turbulent Bias Error Covariance Check using Sensor Noise Values: Part II - Study B

Nonlinear Aircraft Simulation: Study C

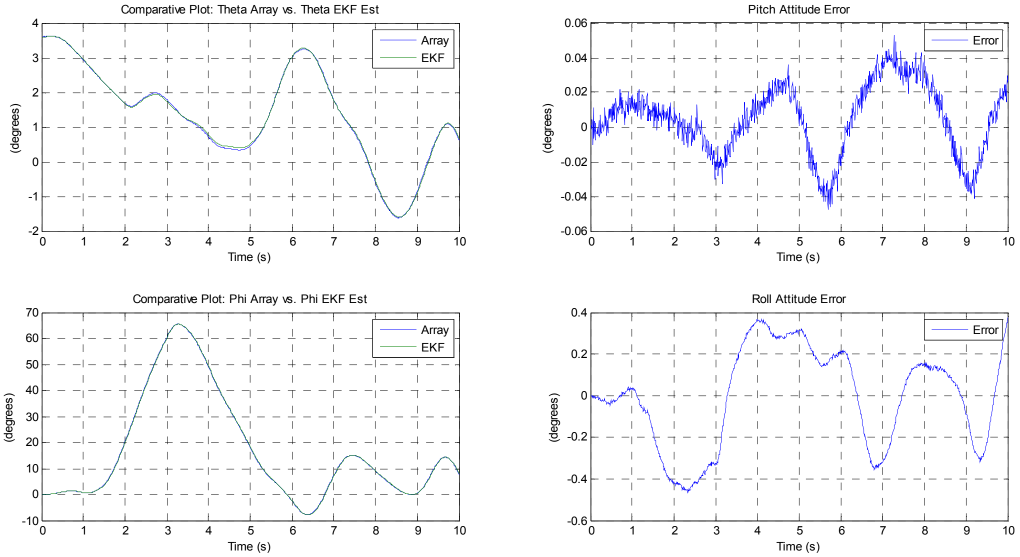

Figure F.63: Phase II Turbulent Attitude Estimation Results using Sensor Noise Values: Part II - Study C

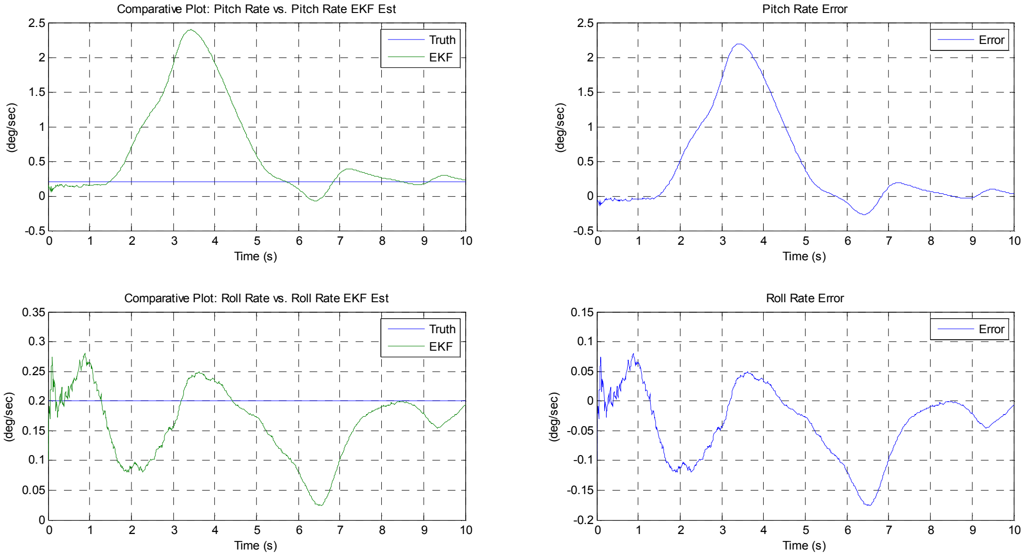

Figure F.64: Phase II Turbulent Bias Estimation Results using Sensor Noise Values: Part II - Study C

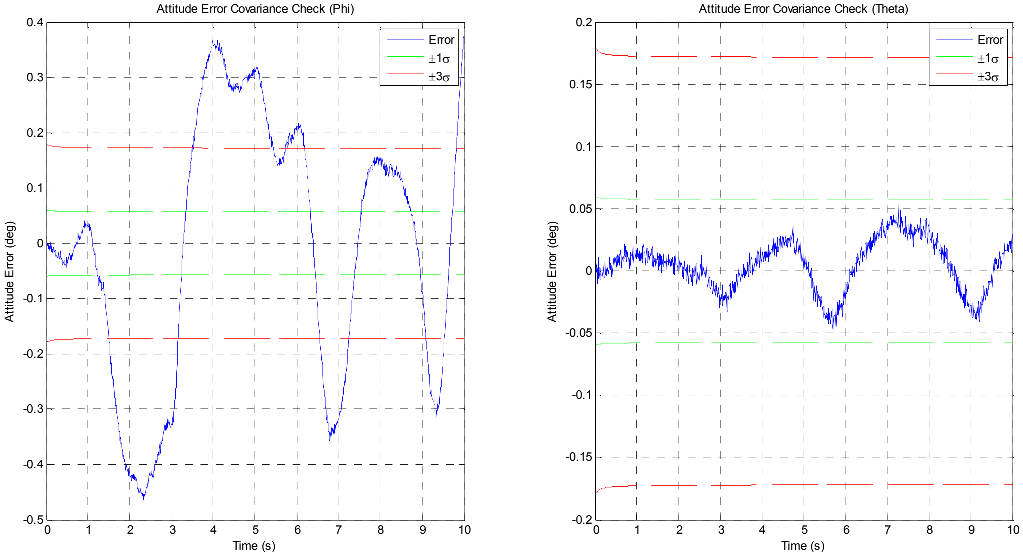

Figure F.65: Phase II Turbulent Attitude Error Covariance Check using Sensor Noise Values: Part II - Study C

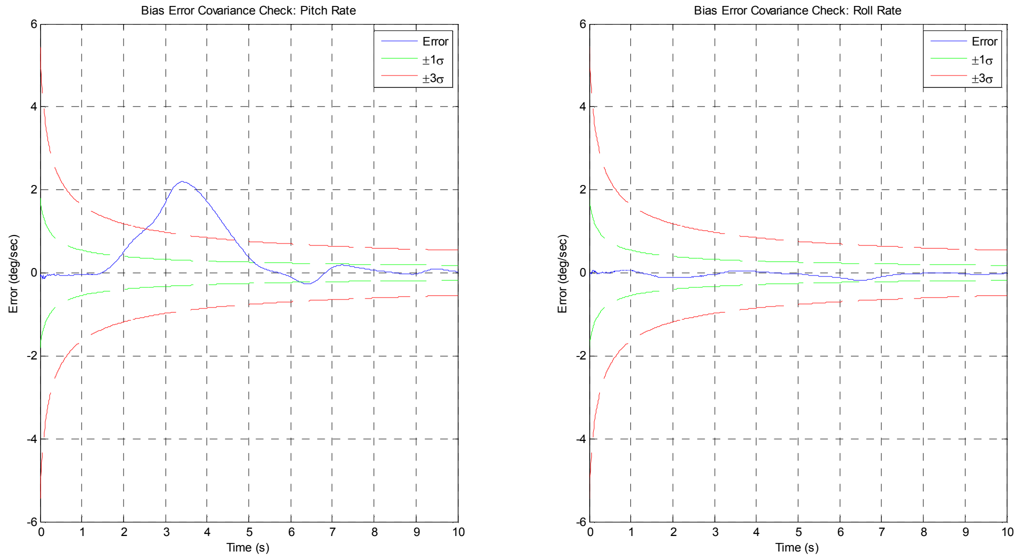

Figure F.66: Phase II Turbulent Bias Error Covariance Check using Sensor Noise Values: Part II - Study C

F.2.5 Phase III: Non-Turbulent Longitudinal/Transverse Aircraft Simulation Maneuver – Part II

Nonlinear Aircraft Simulation: Study A

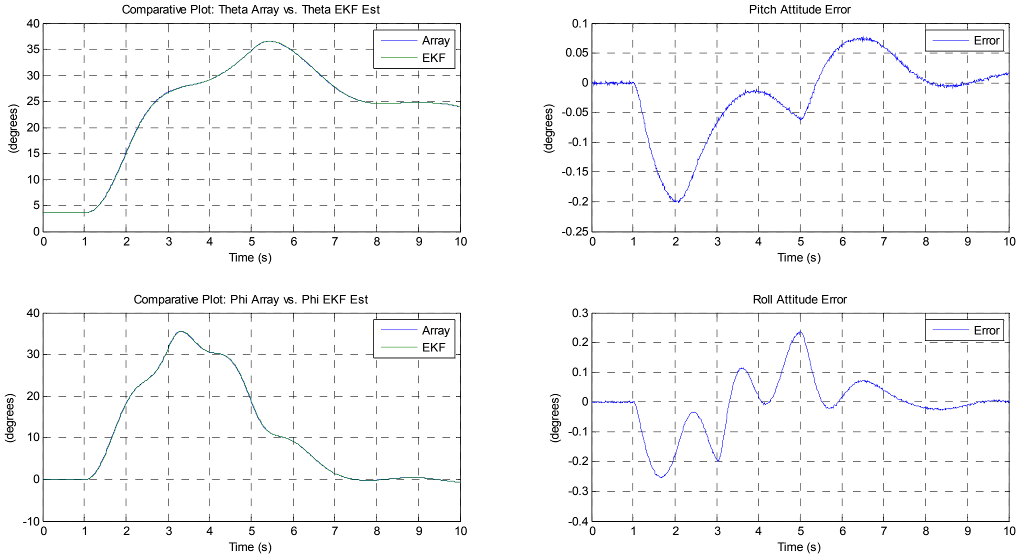

Figure F.67: Phase III Non-Turbulent Attitude Estimation Results using Sensor Noise Values: Part II - Study A

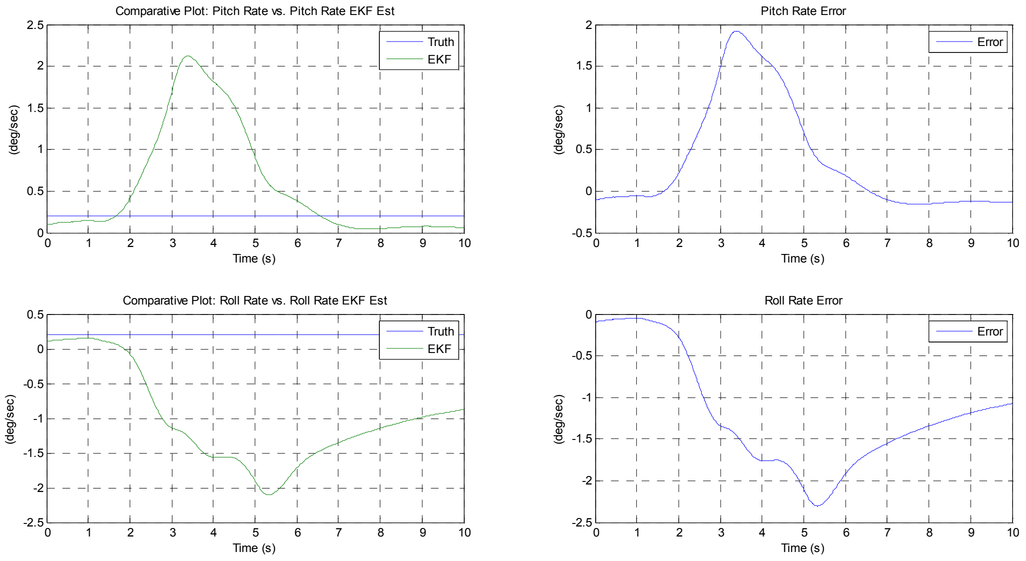

Figure F.68: Phase III Non-Turbulent Bias Estimation Results using Sensor Noise Values: Part II - Study A

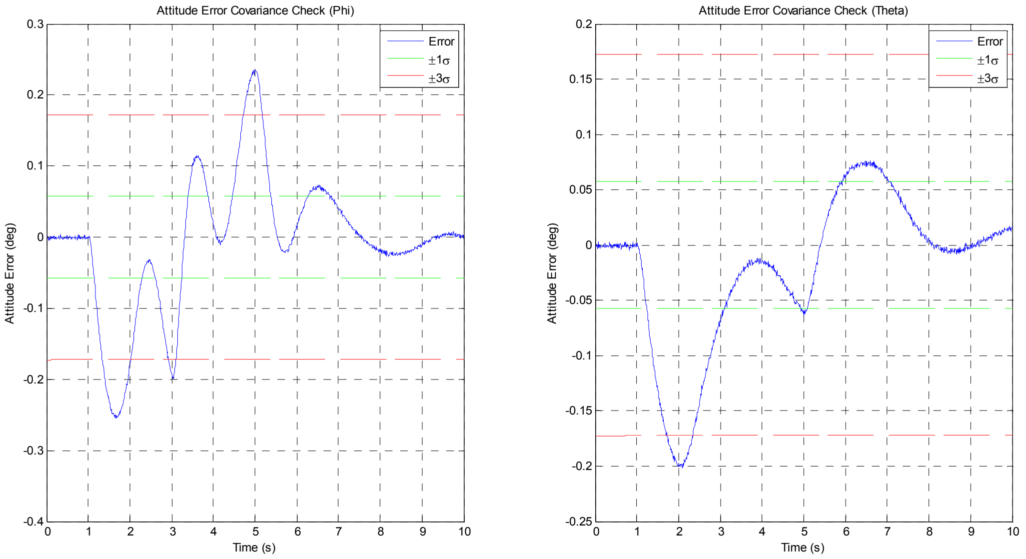

Figure F.69: Phase III Non-Turbulent Attitude Error Covariance Check using Sensor Noise Values: Part II - Study A

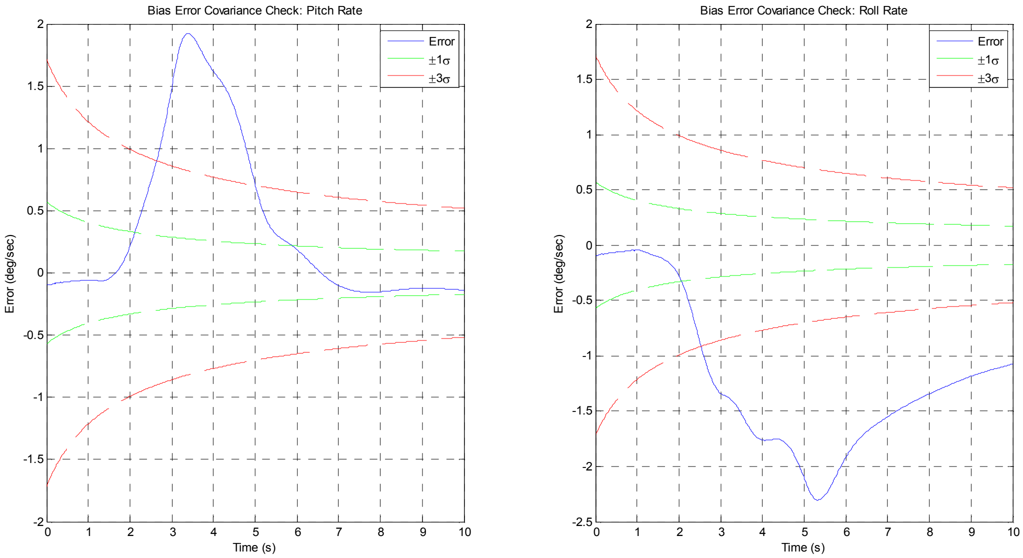

Figure F.70: Phase III Non-Turbulent Bias Error Covariance Check using Sensor Noise Values: Part II - Study A

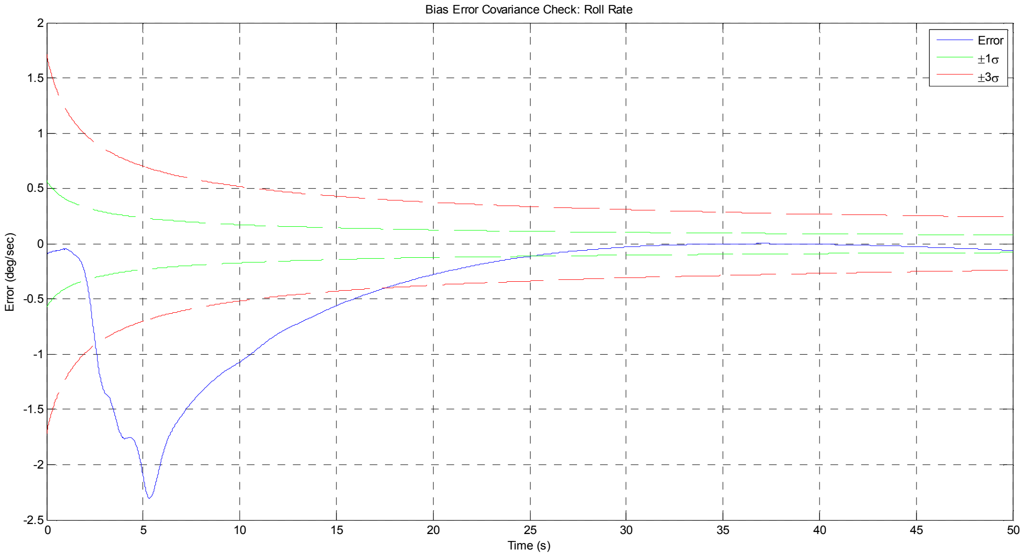

Figure F.71: Phase III Non-Turbulent Roll Rate Bias Error Covariance Check using Sensor Noise Values with Simulation Extended to 50 Seconds: Part II - Study A

Nonlinear Aircraft Simulation: Study B

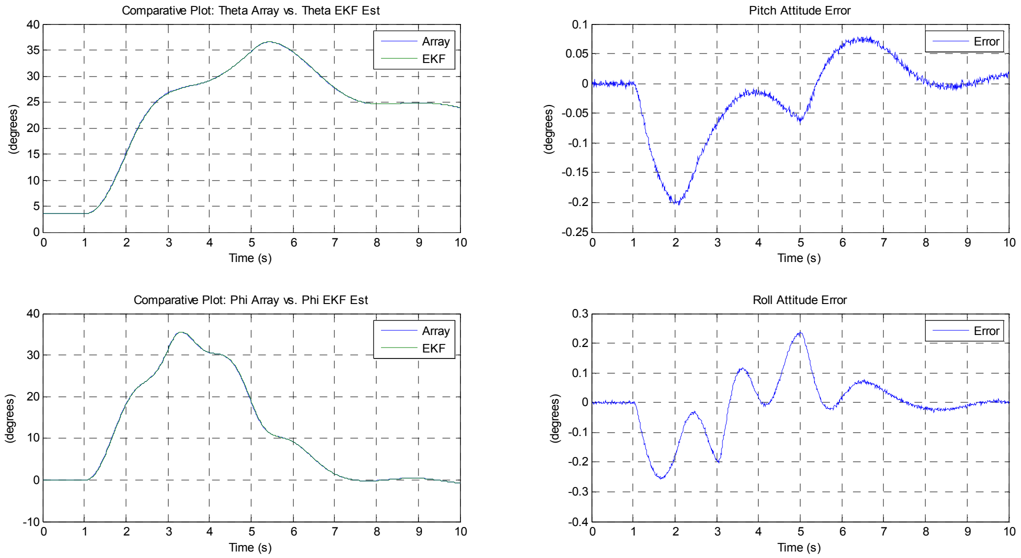

Figure F.72: Phase III Non-Turbulent Attitude Estimation Results using Sensor Noise Values: Part II - Study B

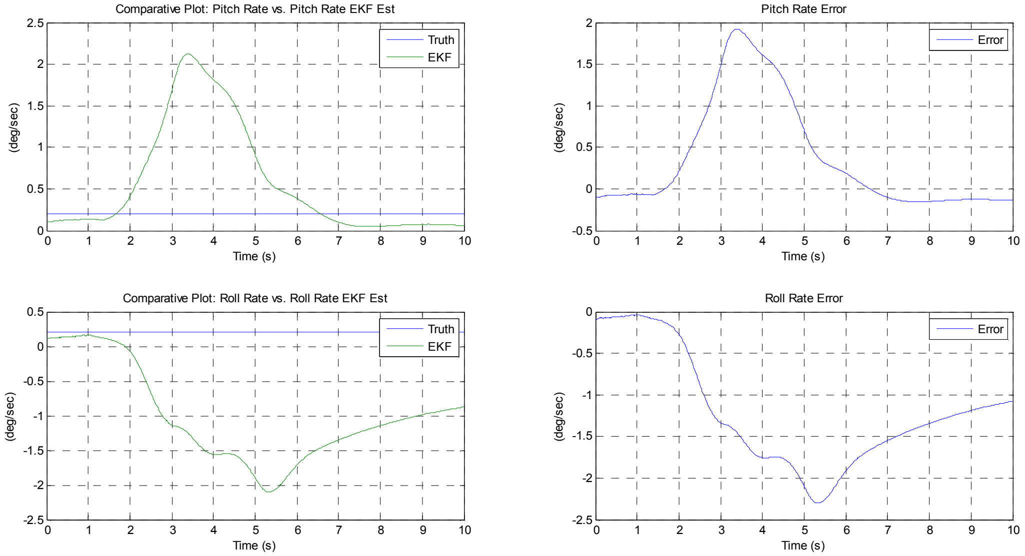

Figure F.73: Phase III Non-Turbulent Bias Estimation Results using Sensor Noise Values: Part II - Study B

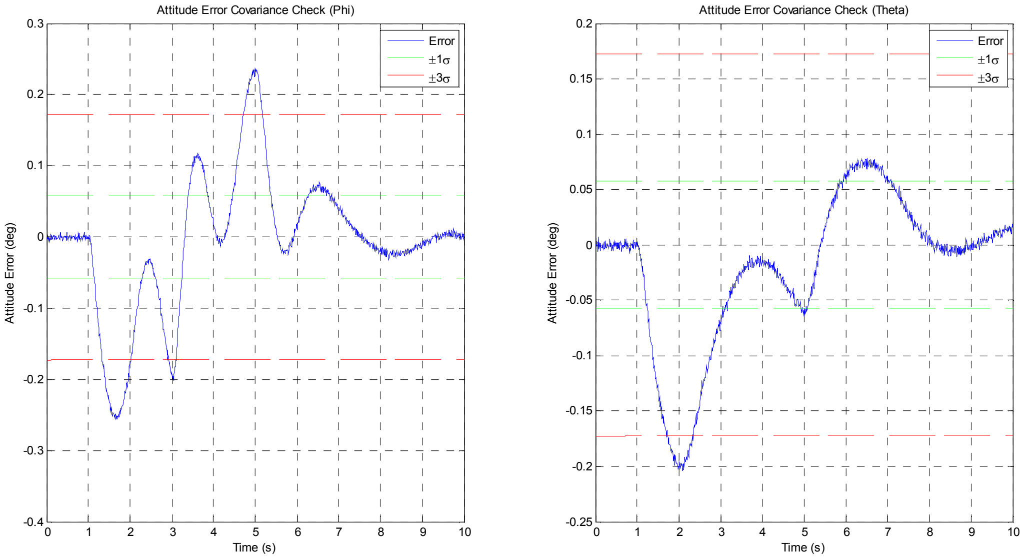

Figure F.74: Phase III Non-Turbulent Attitude Error Covariance Check using Sensor Noise Values: Part II - Study B

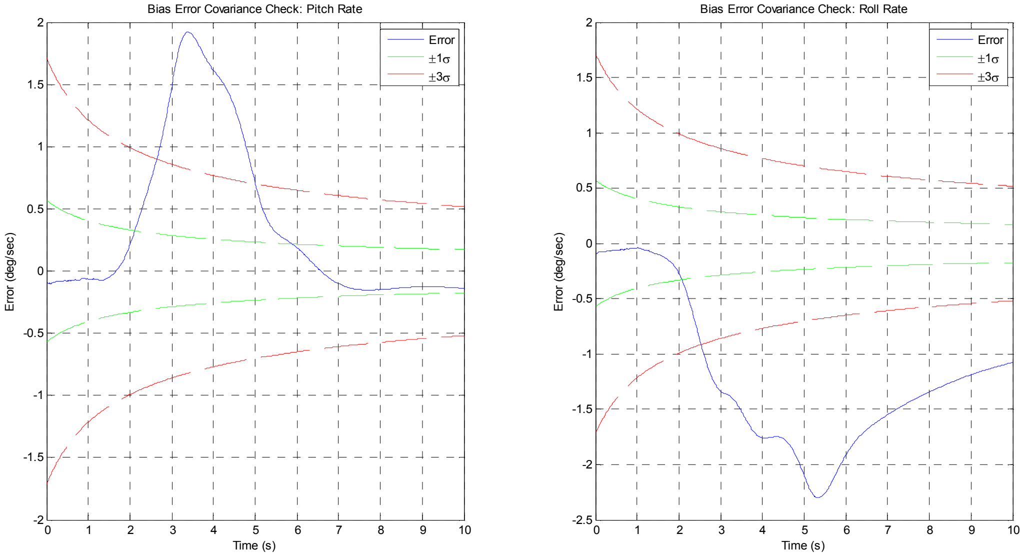

Figure F.75: Phase III Non-Turbulent Bias Error Covariance Check using Sensor Noise Values: Part II - Study B

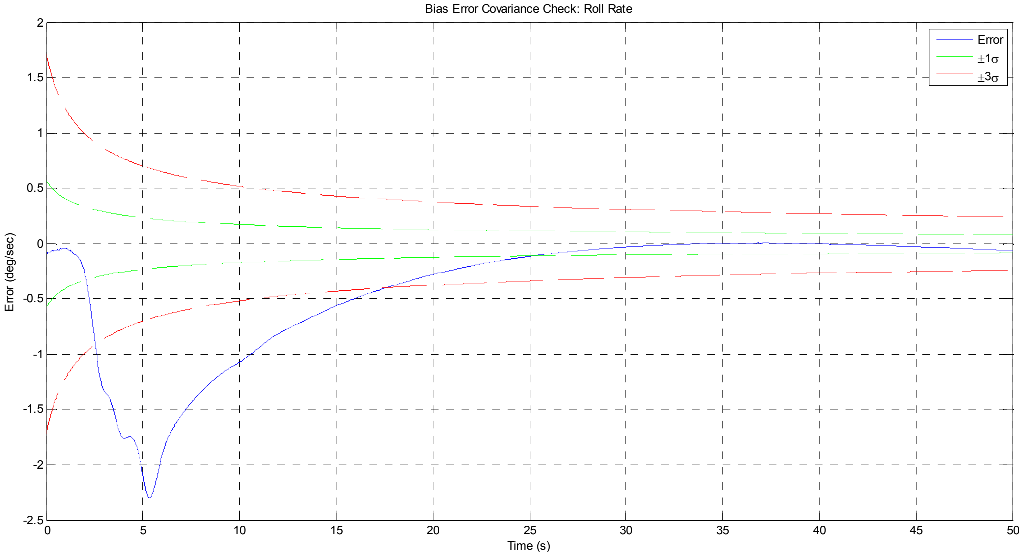

Figure F.76: Phase III Non-Turbulent Roll Rate Bias Error Covariance Check using Sensor Noise Values with Simulation Extended to 50 Seconds: Part II - Study B

Nonlinear Aircraft Simulation: Study C

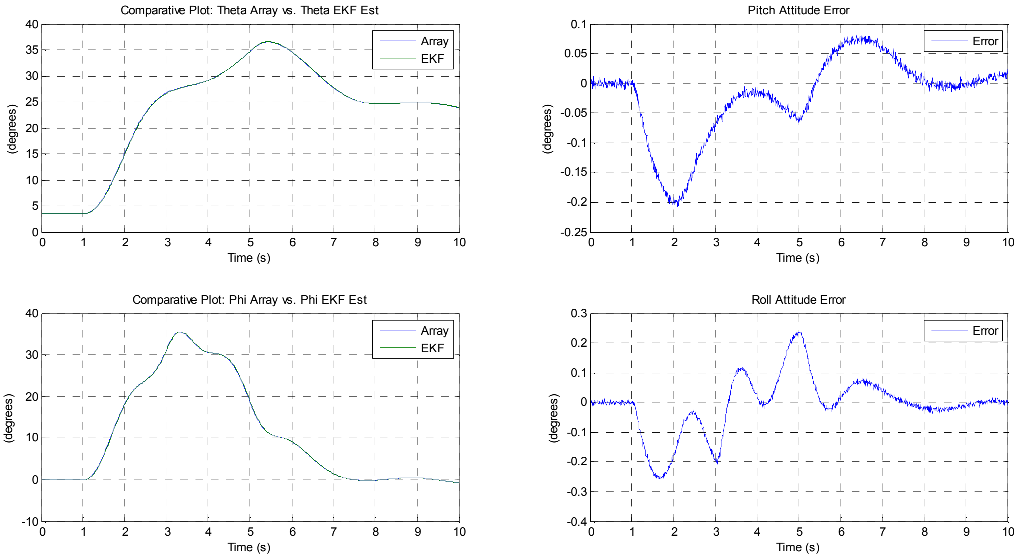

Figure F.77: Phase III Non-Turbulent Attitude Estimation Results using Sensor Noise Values: Part II - Study C

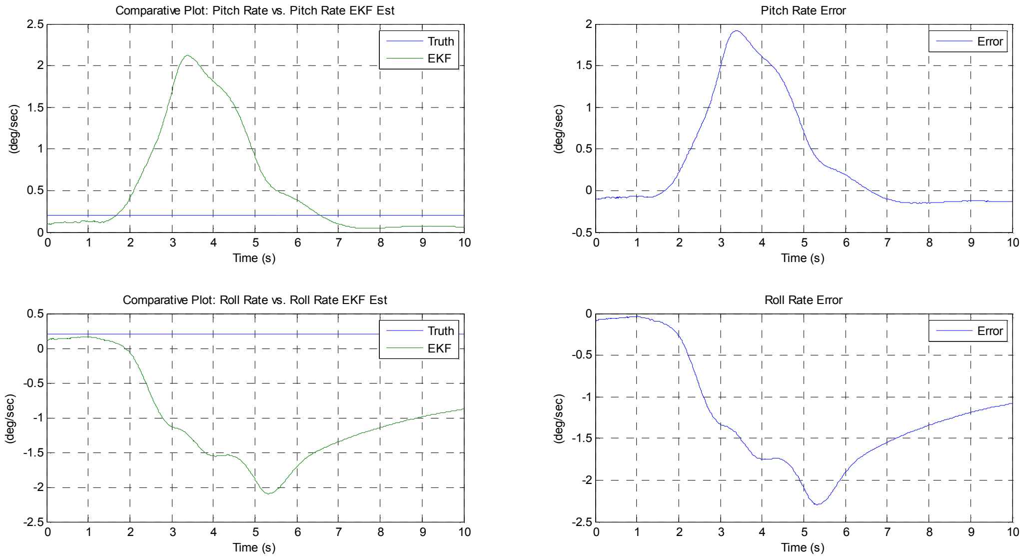

Figure F.78: Phase III Non-Turbulent Bias Estimation Results using Sensor Noise Values: Part II - Study C

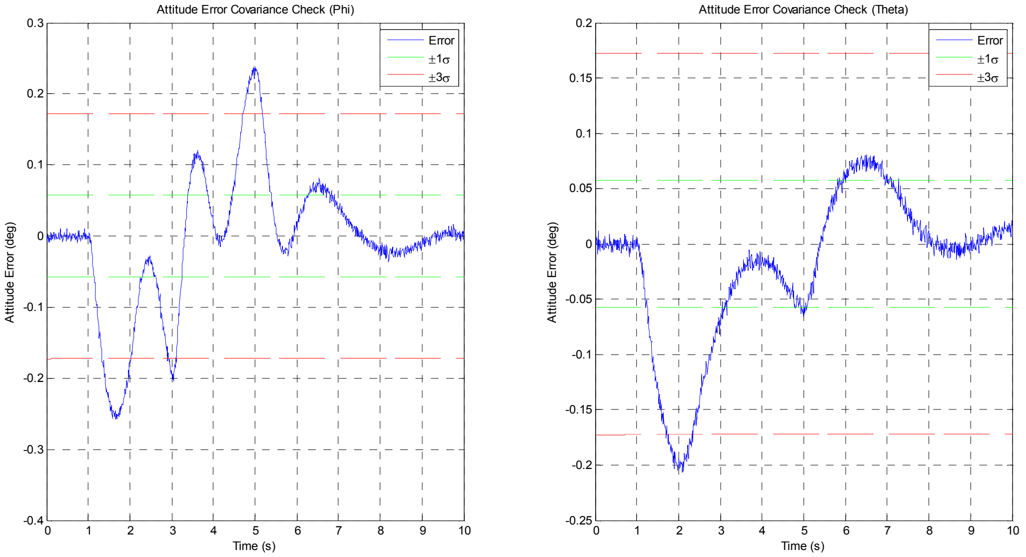

Figure F.79: Phase III Non-Turbulent Attitude Error Covariance Check using Sensor Noise Values: Part II - Study C

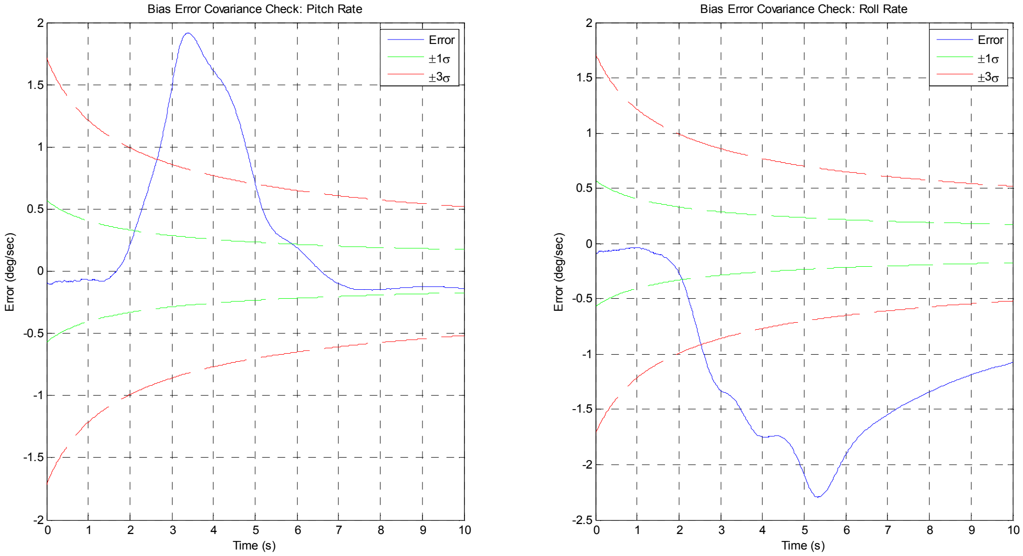

Figure F.80: Phase III Non-Turbulent Bias Error Covariance Check using Sensor Noise Values: Part II - Study C

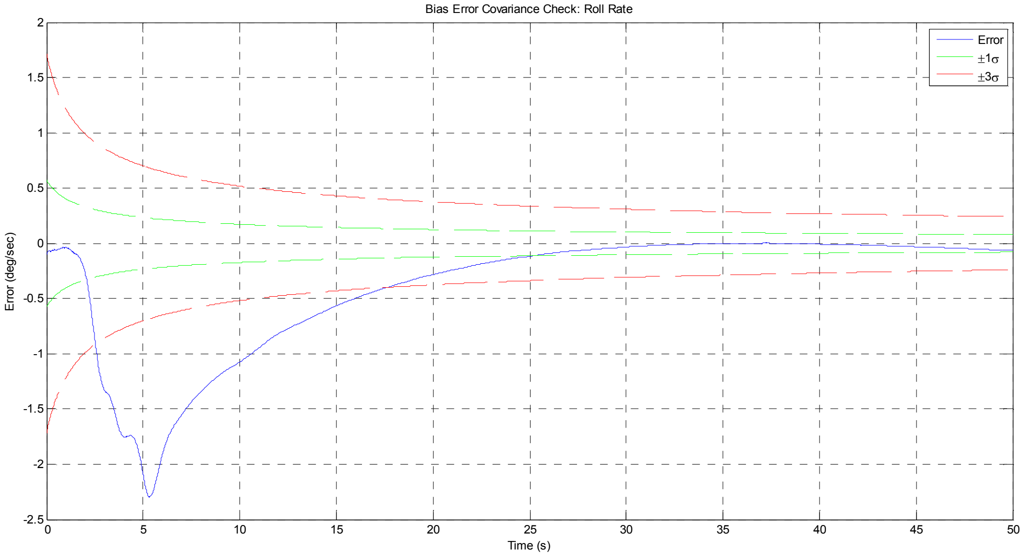

Figure F.81: Phase III Non-Turbulent Roll Rate Bias Error Covariance Check using Sensor Noise Values with Simulation Extended to 50 Seconds: Part II - Study C

F.2.6 Phase III: Turbulent Longitudinal/Transverse Aircraft Simulation Maneuver – Part II

Nonlinear Aircraft Simulation: Study A

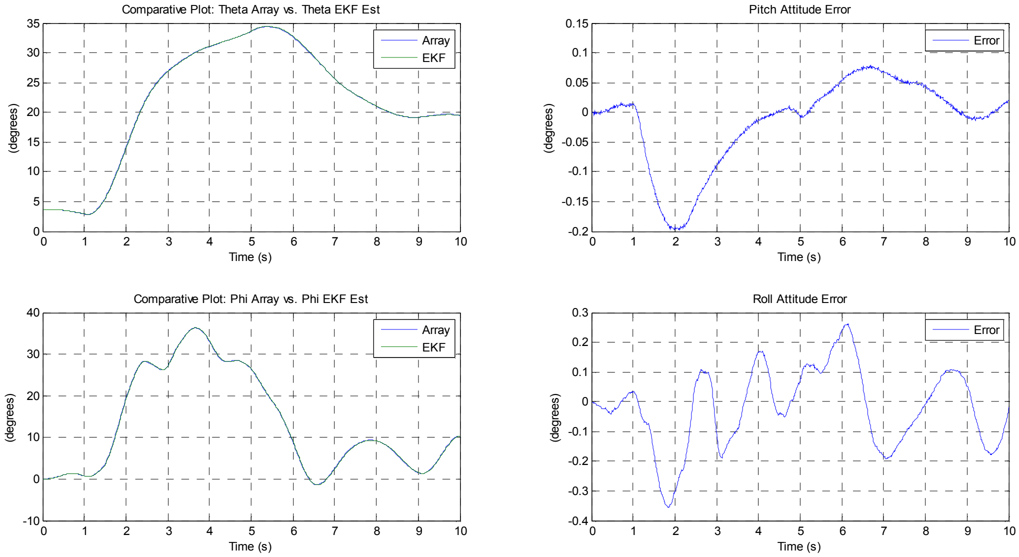

Figure F.82: Phase III Turbulent Attitude Estimation Results using Sensor Noise Values: Part II - Study A

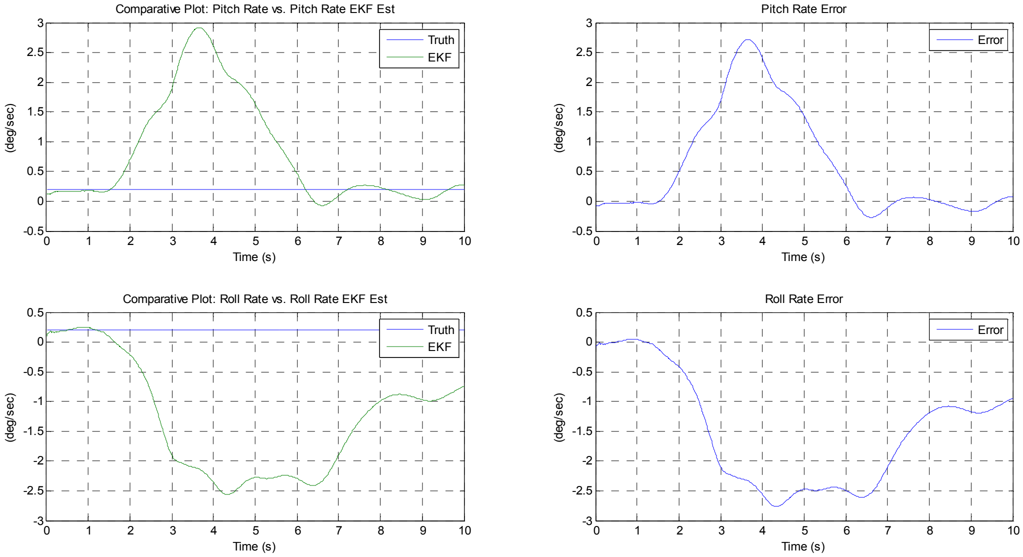

Figure F.83: Phase III Turbulent Bias Estimation Results using Sensor Noise Values: Part II - Study A

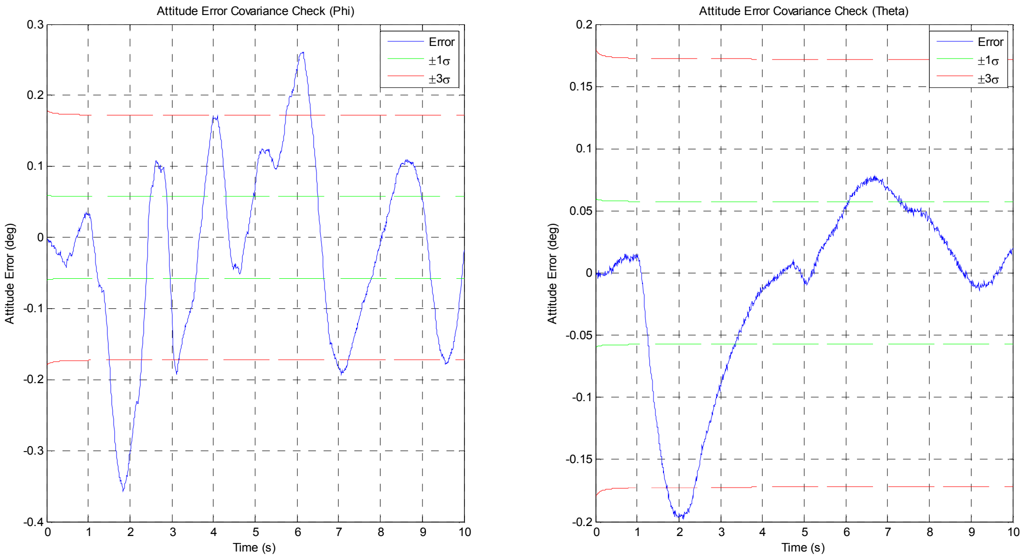

Figure F.84: Phase III Turbulent Attitude Error Covariance Check using Sensor Noise Values: Part II - Study A

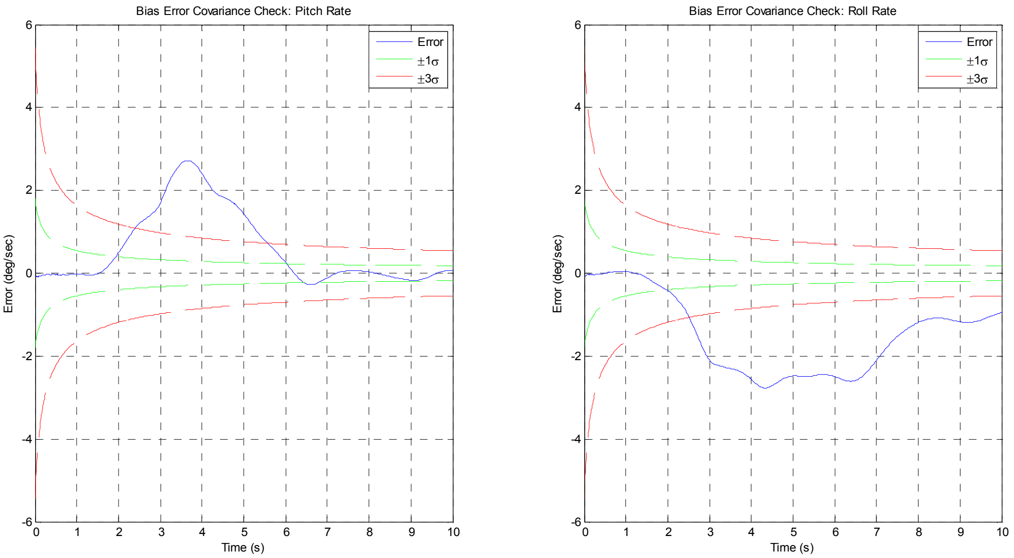

Figure F.85: Phase III Turbulent Bias Error Covariance Check using Sensor Noise Values: Part II - Study A

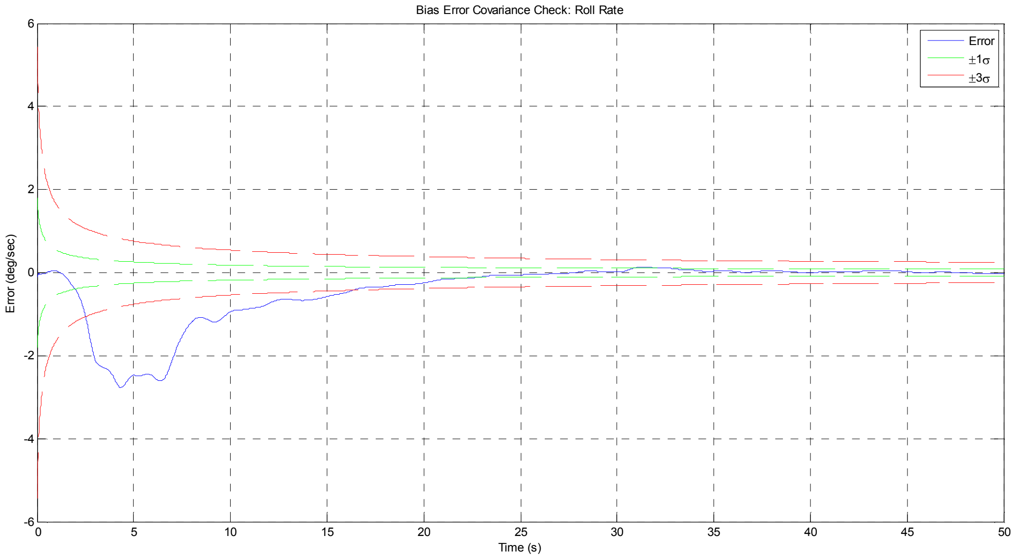

Figure F.86: Phase III Turbulent Roll Rate Bias Error Covariance Check using Sensor Noise Values with Simulation Extended to 50 Seconds: Part II - Study A

Nonlinear Aircraft Simulation: Study B

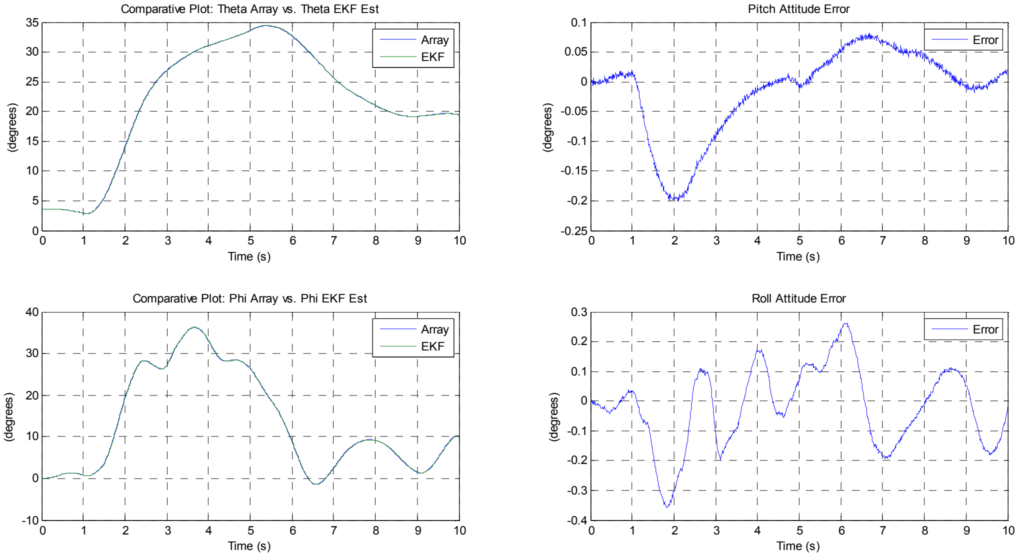

Figure F.87: Phase III Turbulent Attitude Estimation Results using Sensor Noise Values: Part II - Study B

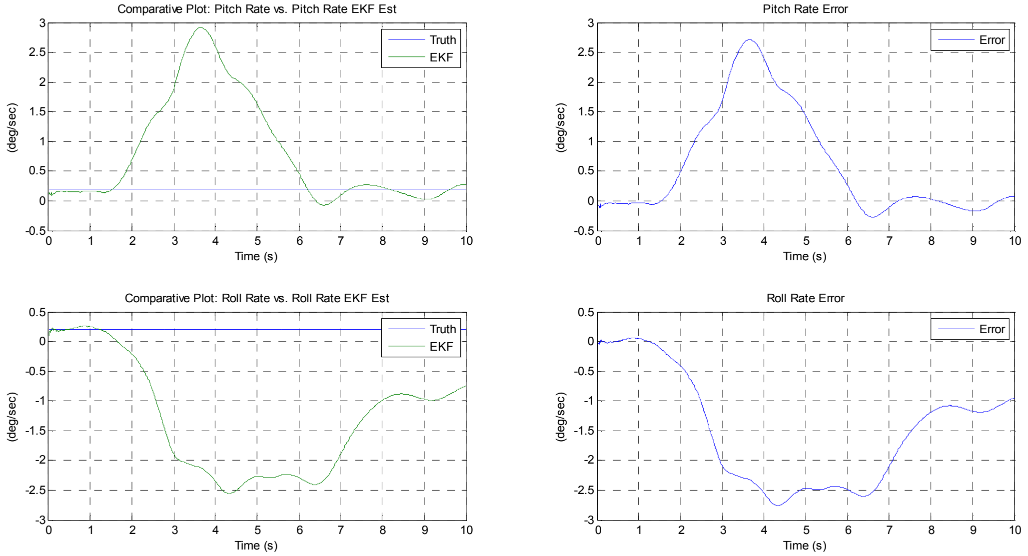

Figure F.88: Phase III Turbulent Bias Estimation Results using Sensor Noise Values: Part II - Study B

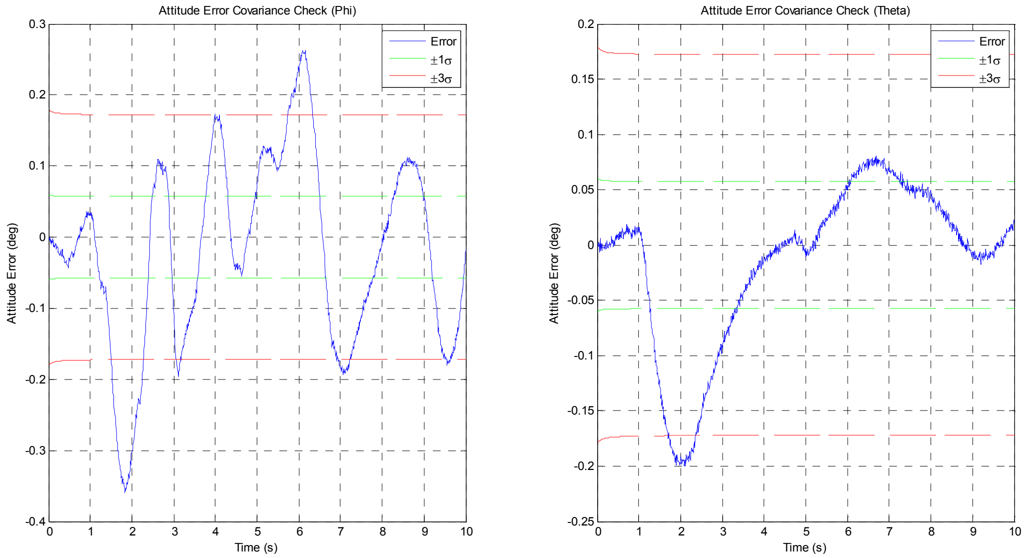

Figure F.89: Phase III Turbulent Attitude Error Covariance Check using Sensor Noise Values: Part II - Study B

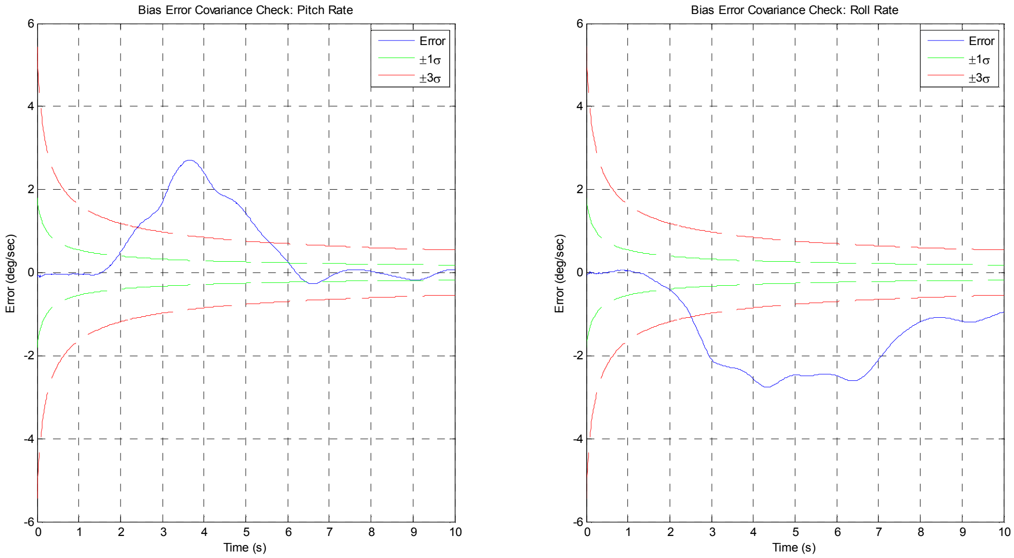

Figure F.90: Phase III Turbulent Bias Error Covariance Check using Sensor Noise Values: Part II - Study B

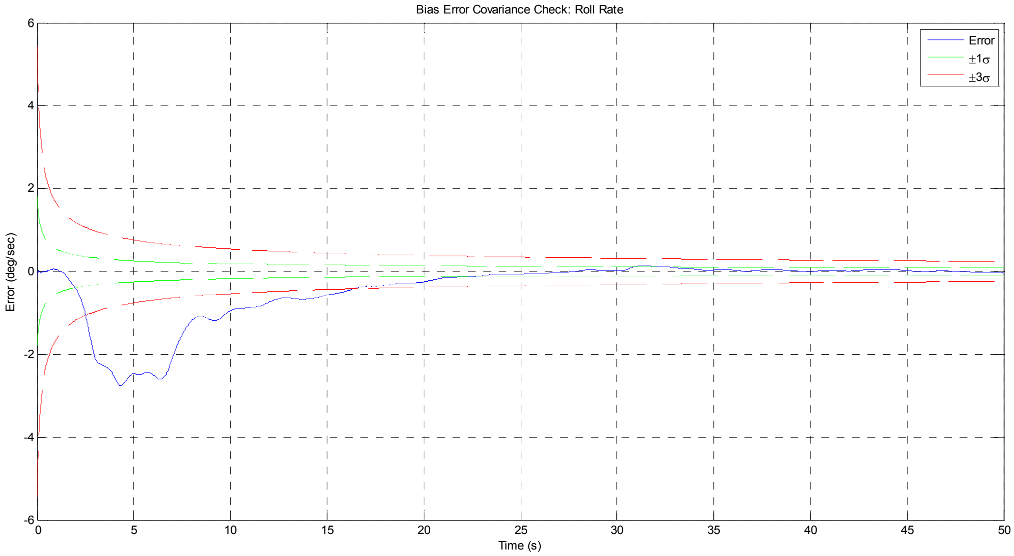

Figure F.91: Phase III Turbulent Roll Rate Bias Error Covariance Check using Sensor Noise Values with Simulation Extended to 50 Seconds: Part II - Study B

Nonlinear Aircraft Simulation: Study C

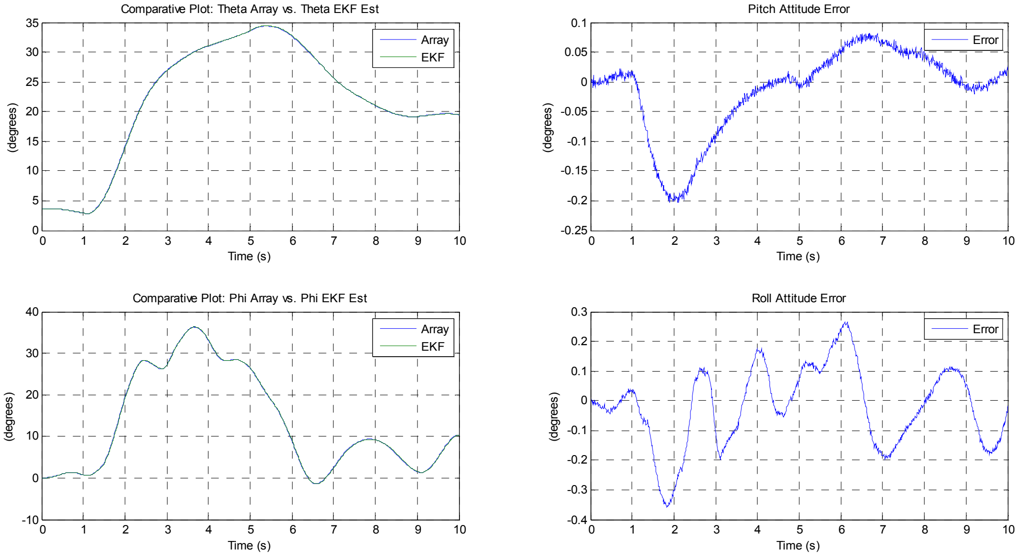

Figure F.92: Phase III Turbulent Attitude Estimation Results using Sensor Noise Values: Part II - Study C

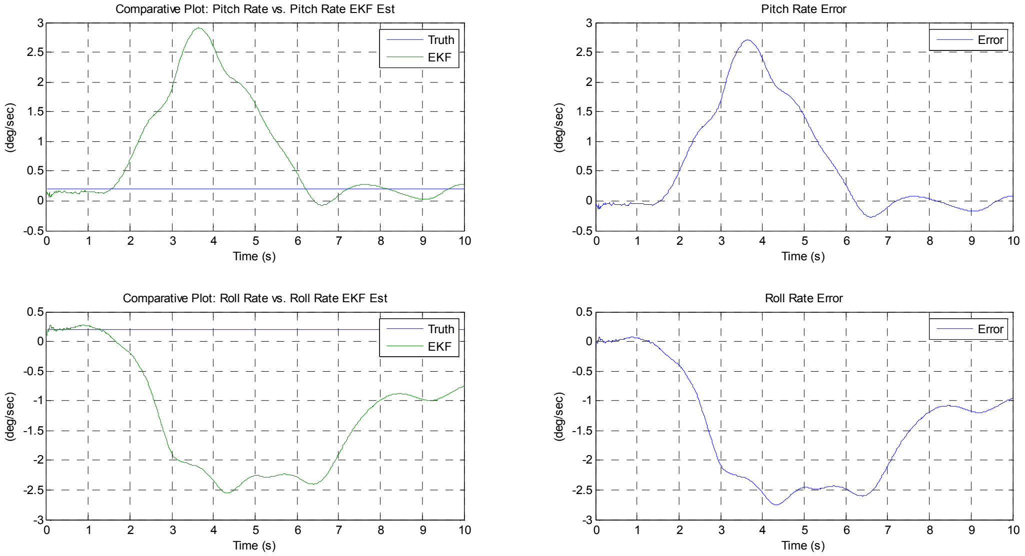

Figure F.93: Phase III Turbulent Bias Estimation Results using Sensor Noise Values: Part II - Study C

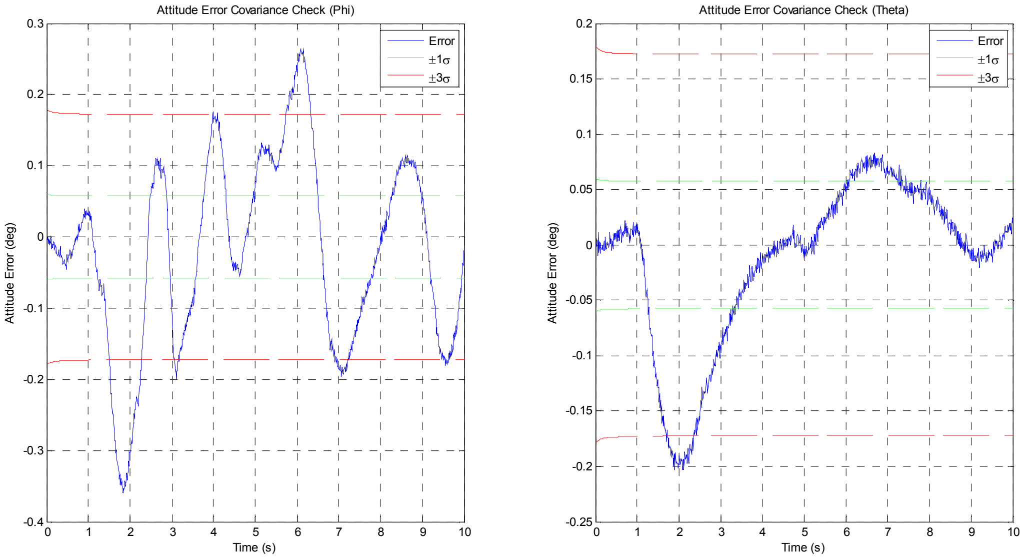

Figure F.94: Phase III Turbulent Attitude Error Covariance Check using Sensor Noise Values: Part II - Study C

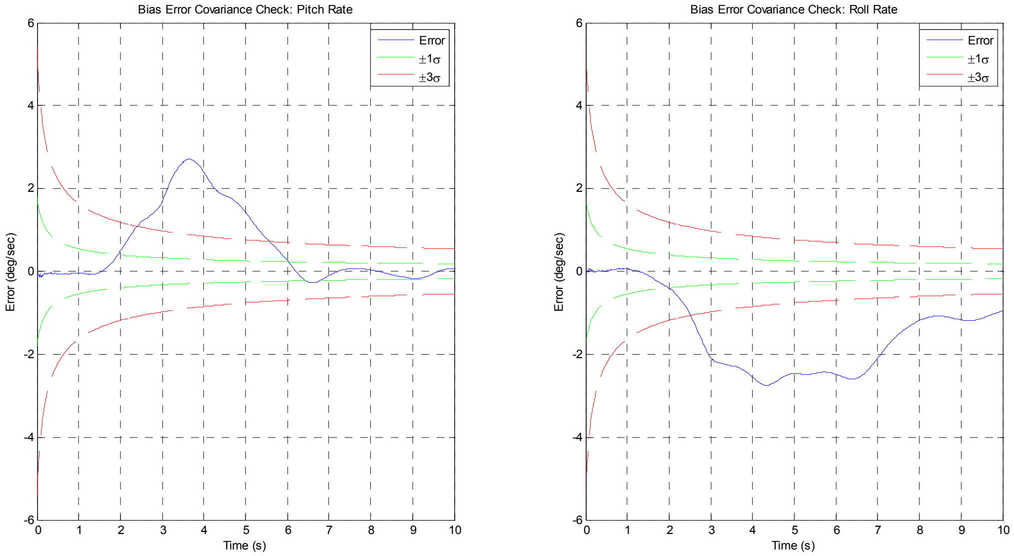

Figure F.95: Phase III Turbulent Bias Error Covariance Check using Sensor Noise Values: Part II - Study C

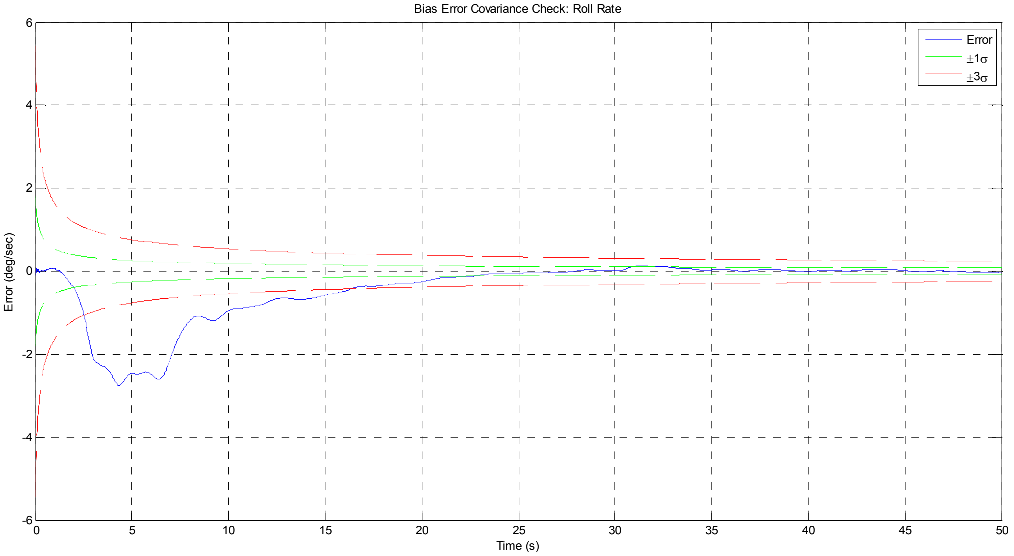

Figure F.96: Phase III Turbulent Roll Rate Bias Error Covariance Check using Sensor Noise Values with Simulation Extended to 50 Seconds: Part II - Study C